Proceedings of the

FLUID AMPLIFICATION SYMPOSIUM

May 1964

394P.

#7.00

Volume 1

HARRY DIAMOND LABORATORIES
FORMERLY: DIAMOND ORDNANCE FUZE LABORATORIES
ARMY MATERIEL COMMAND
WASHINGTON 25. D. C.

Milton S. Hochmuth
Lt. Col, Ord Corps
Commanding

B. M. Horton
Technical Director

MISSION

The mission of the Harry Diamond Laboratories is:

(1) To perform research and engineering on systems for detecting, locating, and evaluating targets; for accomplishing safing, arming, and munition control functions; and for providing initiation signals: these systems include, but are not limited to, radio and non-radio proximity fuzes, predictor-computer fuzes, electronic timers, electrically-initiated fuzes, and related items.

(2) To perform research and engineering in fluid amplification and fluid-actuated control systems.

(3) To perform research and engineering in instrumentation and measurement in support of the above.

(4) To perform research and engineering in order to achieve maximum immunity of systems to adverse influences, including countermeasures, nuclear radiation, battlefield conditions, and high-altitude and space environments.

(5) To perform research and engineering on materials, components, and subsystems in support of above.

(6) To conduct basic research in the physical sciences in support of the above.

(7) To provide consultative services to other Government agencies when requested.

(8) To carry out special projects lying within installation competence upon approval by the Director of Research and Development, Army Materiel Command.

(9) To maintain a high degree of competence in the application of the physical sciences to the solution of military problems.

Proceedings of the

FLUID AMPLIFICATION SYMPOSIUM

Volume I

CONTENTS

(continued)

CONTENTS

THE VISCOUS DISSIPATION OF ENERGY IN FREE TURBULENT FLOWS OCCURRING IN FLUID AMPLIFIER OPERATION

by

J. E. Cox

ABSTRACT

A discussion of the solutions of the equations of motion and the energy equations is presented for the cases of free turbulent flows occurring in fluid amplifier operation. The effect of turbulent viscosity on these two equations is discussed. In order to determine the effects of the viscosity on the energy equation, the mechanism of the viscous dissipation of energy must be investigated. Evaluating the dissipation function independently provides expressions for the distribution of the viscous dissipation of energy. To illustrate the evaluation techniques involved, the simple case of the jet boundary is considered in detail.

THE VISCOUS DISSIPATION OF ENERGY IN FREE TURBULENT FLOWS OCCURRING IN FLUID AMPLIFIER OPERATION

by

J. E. Cox

of

Department of Mechanical Engineering
University of Houston

INTRODUCTION

Many types of flow situations occur in fluid amplifier operation. These flows may be classified into two groups - contained flows and free flows. The free-flow situation differs from the contained-flow case in that there are no solid interfaces at the outer boundaries of the flow pattern. Primary interest to date has been directed to solutions of the equations of motion describing the physical flow phenomena in fluid amplifier elements.

In this presentation, solutions of the energy equations are also reviewed with particular emphasis on the effects of viscosity through the consideration of the viscous dissipation of energy. Free-flow phenomena are adopted as a vehicle of study.

REVIEW OF BASIC EQUATIONS

The two types of free flows frequently encountered in fluid amplifier elements are the jet boundary and the free jet as illustrated in Figure 1 and 2. These types of flow are generally grouped together since the relations describing the physical phenomena are similar in nature.

The classical relations of Schlichting[1] are employed in the presentation. The equation of motion and the continuity equation for the steady-flow, two-dimensional case may be written as

$$u \frac{\partial u}{\partial x} + v \frac{\partial u}{\partial y} = \frac{1}{\rho} \frac{\partial \tau}{\partial u} \qquad (1)$$

$$\frac{\partial u}{\partial x} + \frac{\partial v}{\partial y} = 0 \tag{2}$$

The velocity distributions are obtained by solving the equation of motion by a dimensional-analysis technique and employing the definition of the stream function from potential flow theory. The axial velocity distributions for the cases under consideration are given as

$$u(x,y) = \frac{\bar{u}}{2}\left\{ 1 + erf\left[\frac{\sigma y}{x}\right]\right\} \tag{3}$$

$$u(x,y) = \frac{3}{8\pi}\frac{K}{\mu}\frac{1}{x}\left(1 + \frac{\sigma_1^2 y^2}{4x^2}\right)^{-2} \tag{4}$$

for the jet boundary and the circular free jet, respectively. A few comments of a quantitative nature may be in order concerning the constants appearing in equations (3) and (4). The quantities σ and σ_1 are related to the rate of spread of the jet perpendicular to the direction of flow and are functions of the viscosity - laminar or turbulent - of the media. The mass momentum, K , is assumed to be a constant throughout the jet and may be evaluated by the relation

$$K = 2\pi \int_0^\infty u^2 y\, dy \tag{5}$$

Equations (3) and (4) are simplified forms for jets discharging into a fluid at rest. More general relations are available for jets discharging into fluids with relative motion. The quantitative velocity distributions are shown in Figure 1 and 2.

The general energy equation contains four individual sets of terms representing the energy stored in the element, the energy transferred by convection, the energy transferred by conduction and the viscous dissipation of energy. In steady-state, two-dimensional free flows, the energy equation has been solved for the forms

7
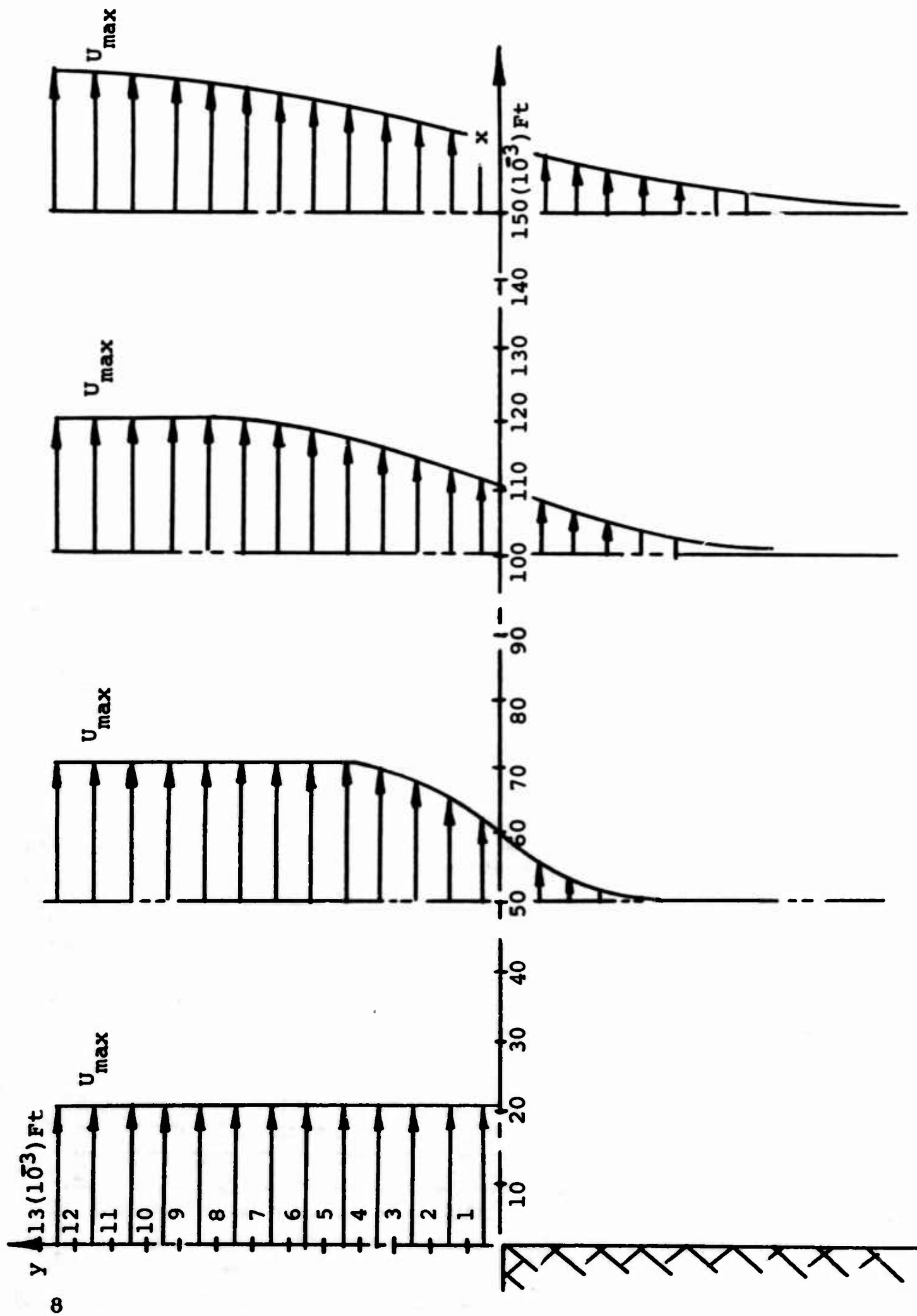
FIGURE 1 - THE VELOCITY DISTRIBUTION IN A TURBULENT JET BOUNDARY
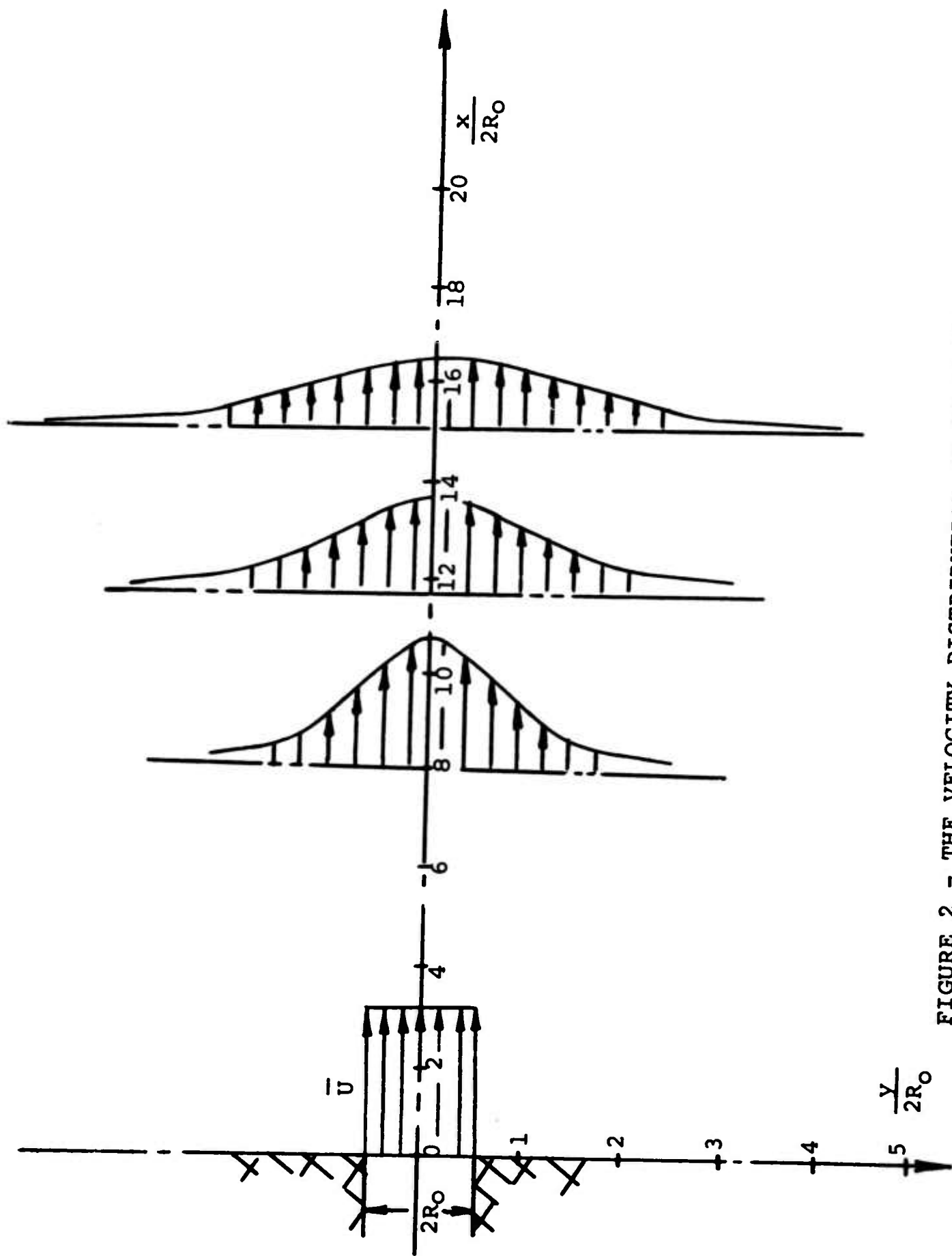
FIGURE 2 - THE VELOCITY DISTRIBUTION IN AN AXIALLY SYMMETRICAL JET

$$ u \frac{\partial T}{\partial x} + v \frac{\partial T}{\partial y} = \alpha \frac{\partial^2 T}{\partial y^2} \tag{6} $$

for the jet boundary and plane jet, and

$$ u \frac{\partial T}{\partial x} + v \frac{\partial T}{\partial y} = \frac{\alpha}{y} \frac{\partial}{\partial y} \left(y \frac{\partial T}{\partial y} \right) \tag{7} $$

for the circular jet. These equations represent only important convection and conduction terms. Since the partial differential equations of energy can be shown to be of the same form as the equations of motion, the solutions are then assumed to be similar in form. This is the technique which has been used to date for solving the energy equation.

EFFECTS OF VISCOSITY

Viscosity is a physical property of fluids which character-izes the resistance of a fluid to flow; more specifically, it is a transport property expressing the transport of momentum across a velocity gradient. The effects of viscosity are evident in simple flow situations; for the no-slip requirement at the surface together with the viscosity characteristics of the fluid determine the shape of the velocity gradient. Therefore, the effect of viscosity on the equations of motion is a predominate one. Viscosity also plays a role in the energy equation in the form of dissipated energy, which is the conversion of mechanical energy into thermal energy by the shearing action. This is a familiar term in the fields of fluid mechanics and heat transfer and is often thought of as "heat generation." This terminology is poor from two standpoints - first, it seems to indicate a viola-tion of the first law of thermodynamics; and second, it implies the transfer of energy across a boundary.

The relative importance of the viscous dissipation of energy depends upon the fluid medium and the flow patterns. Generally, its quantitative contribution is small thus accounting for its omission in equations (6) and (7). In many cases it is difficult to detect viscous dissipation in the fluid by temperature measure-ments; but, its presence can be established in some cases by determining the decrease in mechanical energy - more commonly called pressure drop. As well as increasing the internal energy of the

fluid, the viscous forces produce mechanical work (i.e., compressing or expanding the fluid element). If the viscous dissipation of energy is included in the energy equations (6) and (7), they then become

$$u\frac{\partial T}{\partial x} + v\frac{\partial T}{\partial y} = \alpha\frac{\partial^2 T}{\partial y^2} + \frac{\mu}{\rho c}\phi \tag{8}$$

and

$$u\frac{\partial T}{\partial x} + v\frac{\partial T}{\partial y} = \frac{\alpha}{y}\frac{\partial}{\partial y}\left(y\frac{\partial T}{\partial y}\right) + \frac{\mu}{\rho c}\phi \tag{9}$$

where ϕ is the dissipation function, which reduces to its simplest form as

$$\phi = \left(\frac{\partial u}{\partial y}\right)^2 \tag{10}$$

A few words are in order concerning viscosity for laminar flow and turbulent flow. In laminar flow, the viscosity is a property of the fluid and is generally treated as a constant for a particular media. Being able to treat viscosity as a constant simplifies the degree of difficulty in solving partial differential equations. When the flow is of a turbulent nature, some means must be available for taking into account the effects of turbulent mixing. A hypothetical viscosity is employed and is given the name turbulent or eddy viscosity. The eddy viscosity is generally a function of position since the turbulent mixing process is a function of position. The eddy viscosity is evaluated, in this case, by a conservation of momentum technique attributed to Prandtl.

EVALUATION OF THE VISCOUS DISSIPATION OF ENERGY

Since solutions of the partial differential equations of energy including the dissipation function is not feasible due to the complexity of the mathematics, the viscous dissipation of energy can be investigated independently; according to Lamb[2] the evaluation is accomplished by

$$\tag{11}$$

Using this analytical approach, the distribution of the dissipated energy can be expressed as functions of the coordinates x and y.

Suppose a simple situation such as the jet boundary is selected to illustrate the evaluation procedure. Substituting equation (10) into equation (11) gives

$$dq = \mu \left(\frac{\partial u}{\partial y}\right)^2 dV \tag{12}$$

and for the two-dimensional jet boundary, the element of volume is

$$dV = dx \cdot dy \tag{13}$$

The velocity gradient may be evaluated by the use of equation (3)

$$\frac{\partial u}{\partial y} = \frac{\bar{u}}{2} \frac{\partial}{\partial y}\left\{erf\left[\frac{\sigma y}{x}\right]\right\} \tag{14}$$

where "erf" indicated the error function as defined by

$$erf\, z \equiv \frac{2}{\sqrt{\pi}}\int_{0}^{z} e^{-\lambda^2} d\lambda \tag{15}$$

So that it follows

$$\frac{d}{dz}\left(erf\, z\right) = \frac{2}{\sqrt{\pi}}\frac{d}{dz}\left\{\int_{0}^{z} e^{-\lambda^2} d\lambda\right\} = \frac{2}{\sqrt{\pi}} e^{-z^2} \tag{16}$$

Applying equation (16) gives

$$\frac{\partial u}{\partial y} = \frac{\bar{u}}{\sqrt{\pi}} e^{-\left(\frac{\sigma y}{x}\right)^2} \cdot \frac{\partial}{\partial y}\left(\frac{\sigma}{x}y\right) = \frac{\bar{u}}{\sqrt{\pi}}\frac{\sigma}{x} e^{-\left(\frac{\sigma y}{x}\right)^2} \tag{17}$$

Making this substitution into equation (12) results in an expression for the dissipated energy in an element of fluid in a jet boundary

$$dq = \mu \frac{\bar{u}^2}{\pi} \frac{\sigma^2}{x^2} e^{-2\left(\frac{\sigma y}{x}\right)^2} dy\, dx \qquad (18)$$

the values of σ and μ must be established from empirical data; according to Schlichting, $\sigma = 13.5$ and $\mu/\rho = 0.00137 x\bar{u}$ for the turbulent case. These empirical constants are based on experimental data obtained for air. Equation (18) may now be written as

$$dq = 0.00137 \frac{\bar{u}^3}{\pi} \frac{\sigma^2}{x} e^{-2\left(\frac{\sigma y}{x}\right)^2} \cdot dy\, dx \qquad (19)$$

from which the evaluation of the viscous dissipation of energy for the turbulent jet boundary can be determined.

DISTRIBUTION OF DISSIPATED ENERGY

By evaluating equation (19) by a finite difference technique, the distribution shown in Figure 3 is obtained. The results are presented in a normalized manner. The dependency of the dissipation of energy upon the velocity gradient is visible in the figures; the more pronounced the velocity gradient, the greater the dissipation of energy.

The case of the axially symmetrical jet is considered in detail by the author.[3] The viscous dissipation of energy for the free circular jet using the velocity relations of Schlichting is shown in Figure 4. It should be pointed out that in this case, Schlichting's relations are valid for $x \geq 8D$; in the critical region $0 < x < 8D$, other velocity expressions must be employed.

Variation in the behavior patterns characteristic of the viscous dissipation of energy are evident upon comparison of Figures 3 and 4. In the case of the axially symmetrical jet and the jet boundary, the dissipation of energy spreads in a y direction as x increases since the velocity patterns do likewise. For the axially symmetrical jet, the amount of dissipated energy diminishes as x increases because the average velocity of the fluid in the jet decreases with increasing x. This characteristic is not evident in the case of the jet boundary since the average velocity does not change but rather remains $\bar{u}/2$.
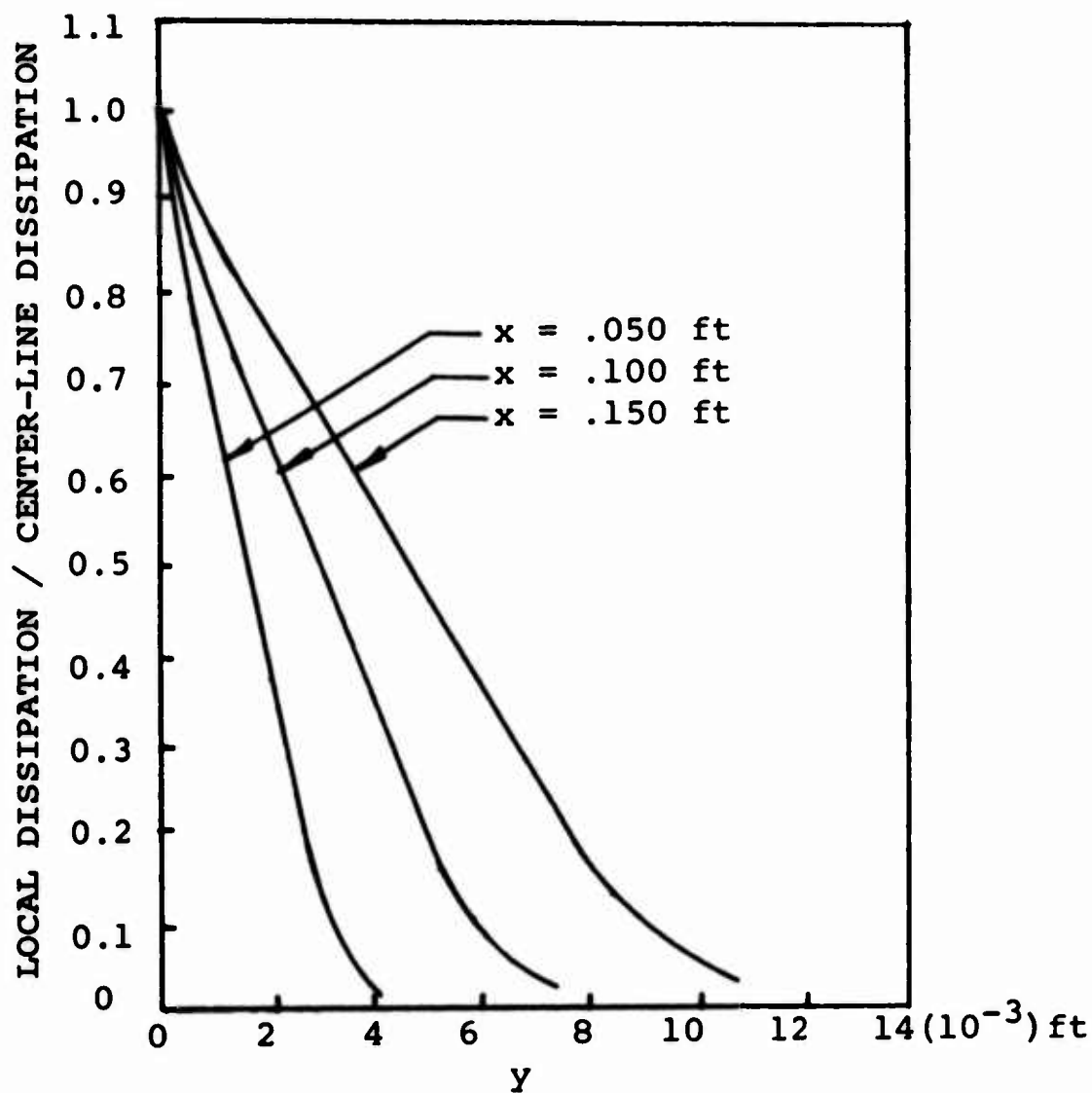
FIGURE 3 - THE DISTRIBUTION OF THE VISCOUS DISSIPATION
OF ENERGY IN A TURBULENT JET BOUNDARY

14
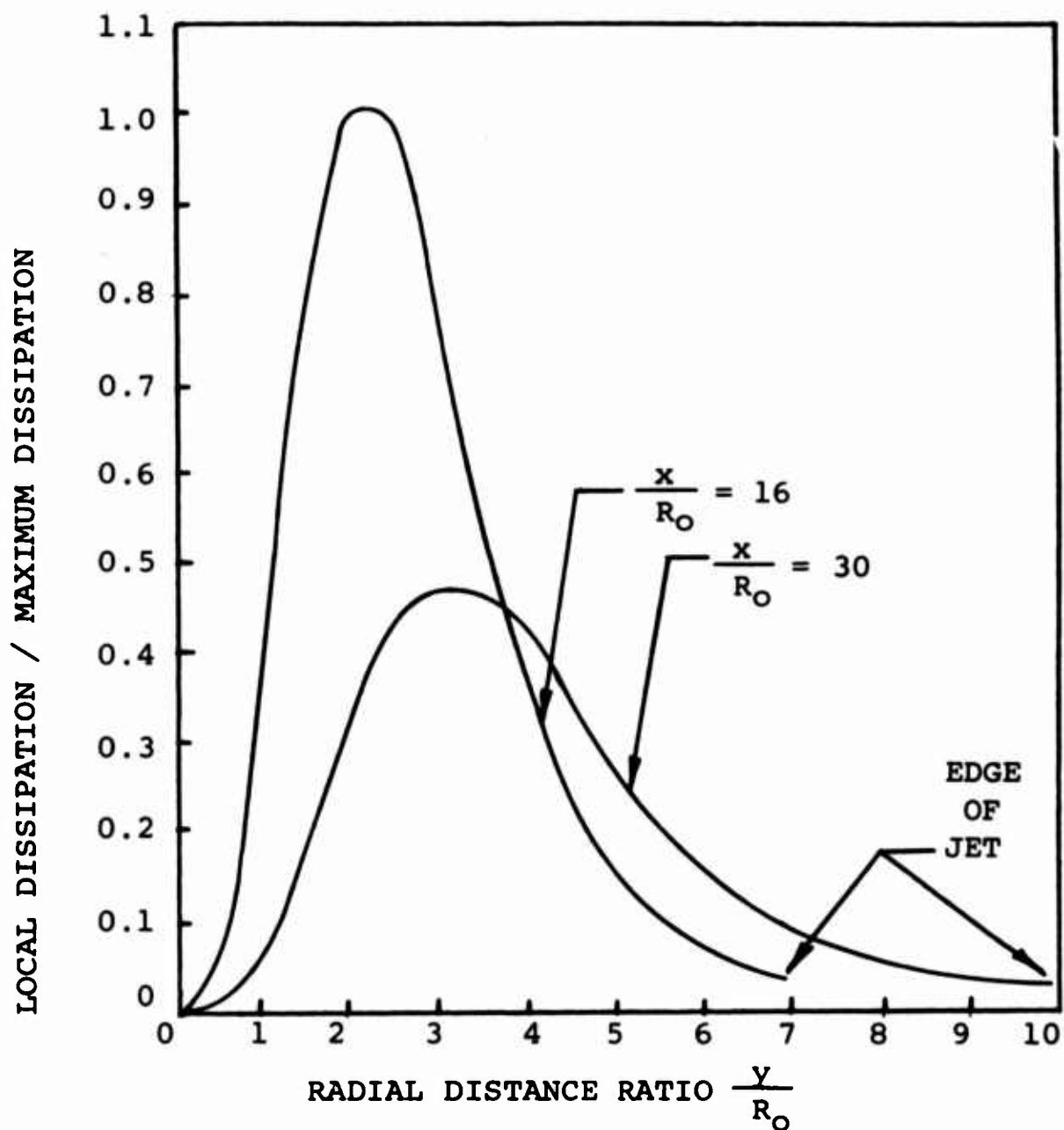
FIGURE 4 – THE DISTRIBUTION OF THE VISCOUS DISSIPATION
OF ENERGY IN A TURBULENT AXIALLY SYMMETRICAL JET

CONCLUDING REMARKS

The characteristics of the viscous dissipation of energy
have been investigated for free-flow situations. The techniques
demonstrated in free flows may also be applied to contained flows.
If flow patterns can be assigned to the various fluid-amplifier
elements, then the viscous dissipation of energy for the element
can be described remembering that care must be taken in evaluating
the eddy viscosity properly.

If fluid-amplifier systems are to be employed in continuous
operations, the thermal characteristics of the circuits must be
understood--the more critical the local temperatures become, the
greater the need to be aware of the temperature distributions
throughout the system. In order to establish the actual tempera-
ture distribution, it is necessary that the energy equation be
solved with the inclusion of the important terms in the dissipation
function. A superposition technique may give _qualitative_ results--
i.e., using the similarity principle to establish a temperature
distribution neglecting the dissipation function and then impos-
ing the equivalent temperature of the dissipated energy. The
inclusion of this effect of the conversion of mechanical energy
into internal energy may prove to be an important consideration
in a critical system.

REFERENCES

1. Schlichting, H. _Boundary Layer Theory_; McGraw-Hill, 1960.

2. Lamb, H. _Hydrodynamics_; Dover Publications, 1932.

3. Cox, J. E. "Investigation of the Viscous Dissipation of
    Energy in Turbulent Flows"; Dissertation, Oklahoma State
    University; August, 1963.

NOMENCLATURE

c	Specific heat
D	Orifice diameter
K	Mass momentum
q	Dissipated energy
R_o	Orifice radius
T	Temperature
u	Velocity component in x direction
$\bar{u}$	Upstream velocity
v	Velocity component in y direction
V	Volume
x	Axial coordinate parallel to primary flow
y	Coordinate perpendicular to axis of flow
α	Thermal diffusivity
μ	Viscosity, laminar or turbulent
ϕ	Dissipation function
$\sigma, \sigma_,$	Emperical constants
τ	Shearing stress

Some Aspects of Curved Turbulent Mixing
Important in Fluid Amplifiers and Fluid Logic Devices

by

D. P. Margolis
Assistant Professor
Mechanical Engineering

The Pennsylvania State University

ABSTRACT

In a curved turbulent mixing layer the flow is dynamically either stable or unstable depending on whether the radial gradient of angular momentum is positive or negative. In the unstable case mass entrainment is greater than for either the stable case or a straight mixing layer. The rate of dissipation of turbulent energy is an order of magnitude less in the unstable case than in the stable case. Based on present results a fairly good prediction of the mean velocity profiles is possible.

Nomenclature

r, ϕ, z	Cylindrical coordinates
V, U, W	Mean velocities in the r, ϕ, z directions
v, u, w	Turbulent velocities in the r, ϕ, z directions
D	Channel height
D_n	Primary nozzle height
M_p	Primary mass flow
M_s	Secondary mass flow
p	Fluctuating component of the static pressure
q^2	$= \overline{u^2} + \overline{v^2} + \overline{w^2}$
t	Time
U_n	Primary nozzle velocity
X_c, X_m	Curvilinear distance: In curved channel distance from the nozzle to the point measured along the mean radius; for curved plate distance measured from nozzle along surface of the plate.
y	Distance from the wall over which the jet issues
$Y_{1/2}$	Width of mixing layer
ϵ	Rate of dissipation of turbulent energy
ϵ	Eddy viscosity
ν	Kinematic viscosity

Introduction

To date most analyses of the fluid mechanics in fluid amplification devices has ignored viscosity or has taken its effect into account by corrections in an inviscid analysis. Considering the complexity of the problem such approaches have been desirable in an effort to introduce simplification. The time comes, however, when no new information can be extracted from these first order approaches so that it becomes necessary to investigate the flow mechanism in more detail. Since curved turbulent mixing flows are so common in fluid amplification devices it seems appropriate to discuss some of the features of curved mixing flows that would be of interest to designers of fluid amplification devices.

A curved turbulent mixing flow can be said to exist whenever two fluid streams having different momenta, temperature, or mass concentration mix in such a way that the mean streamlines of the resulting flow have appreciable curvature. The most common mixing flow is that between two streams with different momenta and this is the case that is found so often in fluid amplifiers.

With regard to fluid amplification devices the subjects that seem most important to discuss are mass entrainment, the rate of dissipation of turbulent energy, and methods for predicting the mean flow. The remainder of this paper will be concerned with those aspects of the curved mixing flows. **

Theoretical Considerations

If one considers the radial equilibrium of a fluid element in an inviscid curved flow one finds that the equilibrium is stable if the radial gradient of the angular momentum is positive, and that the equilibrium is unstable if the radial gradient of the angular momentum is negative. Several investigators (1, 2, 3, 4)[1] have shown that these considerations can be applied successfully to curved turbulent flows, and, furthermore, that the structure of the turbulence is markedly different between the two cases. In the curved mixing layer these differences are exaggerated because of the large momentum gradients present.

If one starts with the Navier-Stokes equations for turbulent flow in a cylindrical coordinate system an energy balance for the turbulent flow can

---

**For a more detailed discussion of the turbulence mechanism in a curved mixing layer see the author's paper, "A Curved Turbulent Mixing Layer," to be published in the Physics of Fluids.

[1]Numbers in parentheses refer to references in the bibliography.

be obtained. In this equation $\overline{q^2}$ is the mean square turbulent kinetic energy; u, v, w are the turbulent velocity components in the ϕ, n, z directions, p is the fluctuating component of the static pressure, and an overbar denotes temporal average.

$$\frac{1}{2}\frac{\partial \overline{q^2}}{\partial t} + \frac{1}{2}\left[\frac{U}{r}\frac{\partial \overline{q^2}}{\partial \phi} + V\frac{\partial \overline{q^2}}{\partial r} + W\frac{\partial \overline{q^2}}{\partial z}\right] + \frac{1}{2}\left[\frac{\partial \overline{uq^2}}{r\partial \phi} + \frac{\partial \overline{vq^2}}{\partial r} + \frac{\partial \overline{wq^2}}{\partial z} + \frac{\overline{vq^2}}{r}\right]$$

$$+ \left[\overline{u^2}\frac{\partial U}{r\partial \phi} + \overline{uv}\frac{\partial V}{r\partial \phi} + \overline{uv}\frac{\partial W}{r\partial \phi} + \overline{v^2}\frac{\partial V}{\partial r} + \overline{uv}\frac{\partial U}{\partial r} + \overline{vw}\frac{\partial W}{\partial r} + \overline{uw}\frac{\partial U}{\partial z}\right.$$

$$\left. + \overline{vw}\frac{\partial V}{\partial z} + \overline{w^2}\frac{\partial W}{\partial z} + V\frac{\overline{u^2}}{r} - U\frac{\overline{uw}}{r}\right] = -\frac{1}{\rho}\left[\frac{\partial \overline{pu}}{r\partial \phi} + \frac{\partial \overline{pv}}{\partial r} + \frac{\partial \overline{pw}}{\partial z} + \frac{\overline{pv}}{r}\right]$$

$$+ \gamma\left[\overline{u\nabla^2 u} + \overline{v\nabla^2 v} + \overline{w\nabla^2 w} - \frac{\overline{u^2}}{r^2} + \frac{\overline{v^2}}{r^2} + \frac{2}{r^2}\overline{u\frac{\partial v}{\partial \phi}} - \frac{2}{r^2}\overline{v\frac{\partial u}{\partial \phi}}\right]$$

The significance of the terms is as follows: the first term is the rate of change of the mean-square of the turbulent kinetic energy in an unsteady flow; the terms in the first bracket represent the transport of turbulent energy by the mean flow, the terms in the second bracket represent the transport of turbulent energy by the turbulent flow, the terms in the third bracket represent the production of turbulent energy, the terms in the fourth bracket represent the transport of turbulent energy by the fluctuating pressure, and the terms in the last bracket represent the viscous transport terms and the dissipation terms. If we assume that the flow is steady and two dimensional and further make an order of magnitude analysis for the case where the thickness of the mixing layer is of the same order of magnitude as the radius of curvature (4) the energy balance becomes:

$$\frac{1}{2}\left[\frac{U}{r}\frac{\partial \overline{q^2}}{\partial \phi} + V\frac{\partial \overline{q^2}}{\partial r}\right] + \frac{1}{2}\left[\frac{\partial \overline{vq^2}}{\partial r} + \frac{\overline{vq^2}}{r}\right] + \left[\overline{uv}\frac{\partial U}{\partial r} - \overline{uv}\frac{U}{r} + \overline{u^2}\frac{V}{r}\right]$$

$$= -\frac{1}{\rho}\left[\frac{\partial \overline{pu}}{r\partial \phi} + \frac{\partial \overline{pv}}{\partial r} + \frac{\overline{pv}}{r}\right] - \epsilon$$

where,

$$\epsilon = \nu\left[2\overline{\left(\frac{\partial v}{\partial r}\right)^2} + \overline{\left(\frac{\partial v}{r\partial \phi} + \frac{\partial ru}{r\partial r} - \frac{2u}{r}\right)^2} + 2\overline{\left(\frac{\partial ru}{r^2\partial \phi} + \frac{v}{r}\right)^2}\right.$$

$$\left. + \overline{\left(\frac{\partial v}{\partial z} + \frac{\partial w}{\partial r}\right)^2} + \overline{\left(\frac{\partial u}{\partial z} + \frac{1}{r}\frac{\partial w}{\partial \phi}\right)^2} + 2\overline{\left(\frac{\partial w}{\partial z}\right)^2}\right]$$

21

Since the production term represents energy extracted from the mean flow and the dissipation term is the rate at which this energy is dissipated into heat an experimental determination of the energy balance is very important.

Experimental Apparatus

Figure 1 shows a schematic of the wind tunnel used. Figure 2 shows a detail of the nozzle and movable partition.

The test sections used in the investigation were a curved channel with an inner and outer radius of 9" and 12" respectively and curved plates having radii of curvature of 3", 9", 13.5" and 18". The included angle of all test sections was 90 degrees.

When the curved channel was used the nozzle height was only a fraction of the channel height. The high velocity primary flow and the low velocity flow subsequently induced into the channel formed the mixing layer.

With the curved channel in the position shown in Figure 1 the unstable case was produced. If the curved channel was turned upward the stable case resulted.

Because of their simplicity of construction, the curved plates were used to determine the effect of changing the radius of curvature.

The measurements of the mean and turbulent velocities were made with a Hubbard Instrument Company Constant-Temperature, Linearized, Hot-Wire Anemometer. The spectral measurements were made with a Hewlitt-Packard 302-A Wave Analyzer.

Experimental Results

Figure 3 shows the mean velocity profiles for both the stable and unstable cases in the curved channel and in a straight channel at $X_c/D = 4.59$. Note that the degree of mixing (indicted by the uniformity of the velocity profile) is better in the unstable case than either the stable or straight case. Since the primary flow was the same in all three cases the area under the curves is proportional to the amount of secondary mass entrained. For the three cases shown the ratio of secondary mass flow to the primary mass flow is:

unstable	1.1
straight	0.7
stable	0.4

Thus, if entrainment is an important consideration the unstable case should be used.

Figures 4 and 5 show the energy balances for the stable and unstable cases in a curved channel. Note that in both cases the production of turbulent energy and the transport of turbulent energy by the turbulent velocities are the dominant terms.

In the stable case the production and transport terms decrease as the flow develops until finally, in the later stages, dissipation becomes important and a balance between production and dissipation exists. In the unstable case, on the other hand, the transport and production terms increase rapidly as the flow develops, and even at the last measuring station (75 degrees) the dissipation term has not yet assumed importance.

One way to show the striking difference between the energy balances in the stable and unstable cases is to plot the ratio of dissipation rate to the rate of production. Figure 6 is such a plot. For the unstable case the ratio is essentially constant; for the stable case the ratio rises rapidly. In the unstable case the rate of energy dissipation is a constant percentage of the rate of energy production. This means that a constant percentage of the turbulent energy produced can be transported to other regions of the flow. In the stable case, on the other hand, more and more of the turbulent energy produced is dissipated leaving less and less energy for transport.

Figure 7 shows the rate of dissipation of turbulent energy for the stable and unstable cases. Note that in the unstable case the rate of dissipation is an order of magnitude less than for the stable case.

Figure 8 is a correlation of the mean velocity data taken at several angular positions with a 9" and 18" radii plates. The scaling velocity is the difference between the maximum and minimum velocity of a particular profile and the scaling length is the distance from the point of maximum velocity to the point where the velocity is one-half the maximum.

Figure 9 is a correlation of the mean velocity data taken in a straight channel and in the curved channel for both the stable and unstable cases. The scaling length and velocity are the same as those for Figure 8. The slope of the curves in Figures 8 and 9 are different.

A prediction for $Y_{1/2}$ would yield a method of predicting the mean velocity profiles. Some preliminary work has been done in this vein. Figure 10 shows some measurements of $Y_{1/2}$ made with curved plates having radii of curvature of 3", 9", 13.5" and 18". A log-log plot of the data reveals that the relation

$$\frac{Y_{1/2}}{X_c} = \left(\frac{X_c}{D_n}\right)^{-3/4}$$

is a close approximation to the data for $X_c/D_n < 20$

It is interesting to note that the mean velocity distribution and ratio of secondary to primary mass flow M_s/M_p display Reynolds similarity for Reynolds' numbers, based on the primary nozzle height D_n and the nozzle velocity U_n, greater than 30,000. Figures 11 and 12 show these results.

Many times an attempt to solve problems in turbulent flows is made by introducing an "eddy viscosity" in analogy to the molecular viscosity. This approach is basically wrong because it does not predict from first principles and does not describe the mechanism of the turbulence. The popularity of this method stems from the fact that it has been able to produce simple results to hitherto insoluble problems. It would seem interesting to determine to what extent an "eddy viscosity" can be defined in a curved mixing flow. For a two-dimensional curved <u>laminar</u> flow the viscous term can be written

$$\frac{1}{r^2} \frac{\partial}{\partial r} \left(r^2 \, \tau_{r\phi} \right)$$

where,
$$\tau_{r\phi} = \nu \, r \frac{\partial}{\partial r} \left(\frac{U}{r} \right)$$

so that we would be led to write

$$\left(\tau_{r\phi} \right)_{turb} = \epsilon_0 \, r \frac{\partial}{\partial r} \left(\frac{U}{r} \right)$$

Using the experimentally determined turbulent shear stresses and mean velocity distribution the values of ϵ_0 were calculated. The results show that an "eddy viscosity" cannot be defined. This is not surprising when one considers the energy balances. The "eddy viscosity" concept is successful only for flows where the turbulence mechanism is governed by local conditions, and breaks down where the turbulent mechanism is strongly dependent on non-local conditions, for instance where there is considerable transport of turbulent energy.

Conclusions

Considerably more work is required both to determine the structure of turbulence in a curved mixing layer and to determine methods of predicting the important mean quantities.

It has been demonstrated that mass entrainment is greater in the unstable case of the curved mixing layer than in either the stable case or a straight mixing layer.

The rate of dissipation of turbulent energy is an order of magnitude less in the unstable case than in the stable case. The ratio of the rate of dissipation of turbulent energy to the rate of production of turbulent energy is constant as the flow in the unstable case develops but rises rapidly as the flow in stable case develops.

A fairly good correlation of the mean velocity data is possible if the total variation of the velocity across the flow is used as the scaling velocity and the width of the layer is used as the scaling length. For the unstable case produced by flow over curved plates the width of the mixing layer can be predicted with a fair degree of accuracy.

An "eddy viscosity" does not exist for the curved mixing layer.

BIBLIOGRAPHY

1. Eskmazi, S., and Yeh, H., "An Investigation on Fully Developed Turbulent Flows in a Curved Channel," Journal of Aero. Sci., Vol. 23, pp. 23-34, January 1956.

2. Traugott, S. C., "Influence of Solid-Body Rotation on Screen-Produced Turbulence," NACA Technical Note 4135, August 1958.

3. Rose, W. G., "A Swirling Round Turbulent Jet," ASME Paper No. 62-WA-59, 1962.

4. Margolis, D. P., "An Investigation of a Curved Mixing Layer," Ph. D. Thesis, Pennsylvania State University, June 1963.
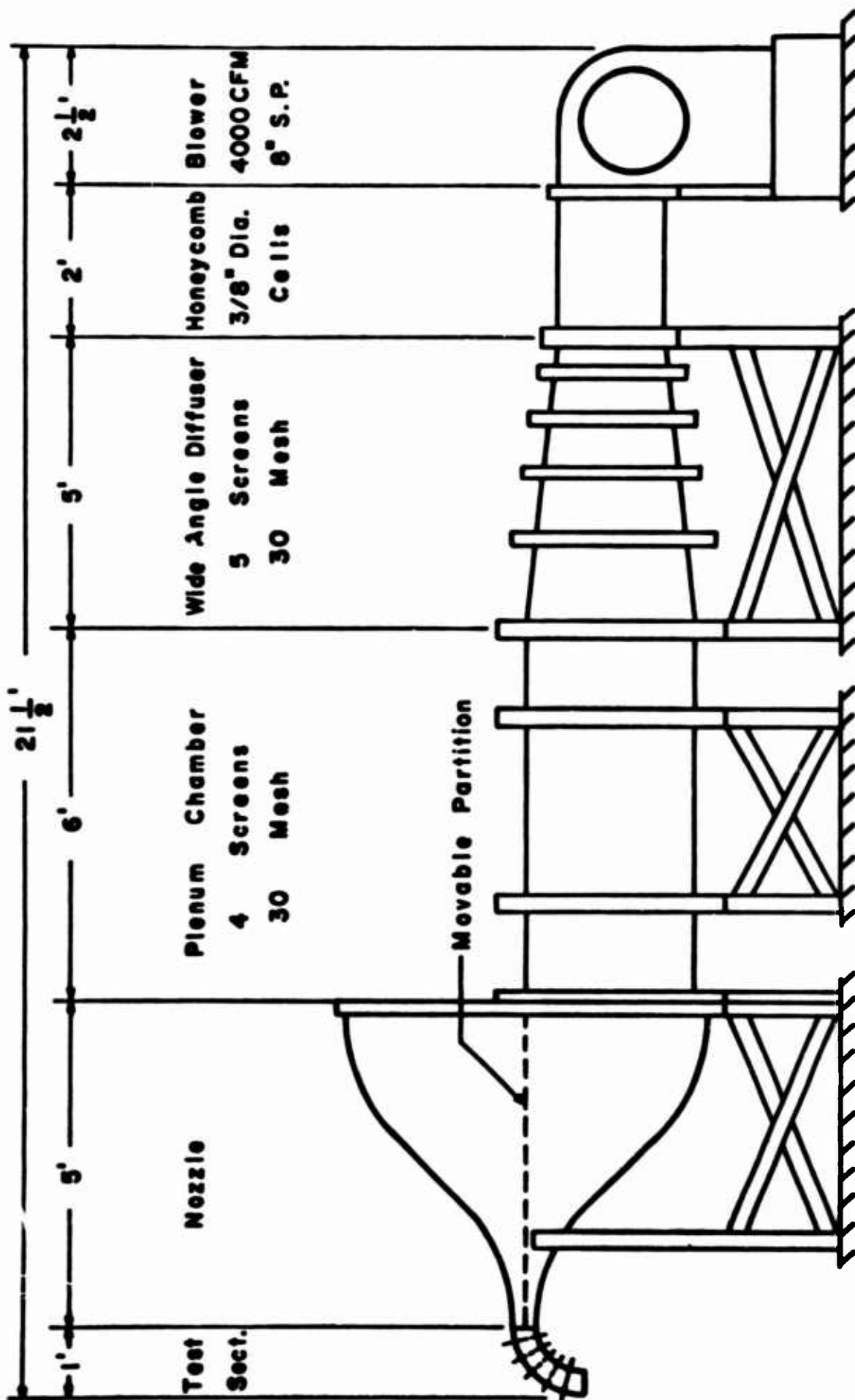
FIGURE I SCHEMATIC DRAWING OF THE WIND TUNNEL

27

SECONDARY FLOW

PRIMARY FLOW

REMOVABLE TOP
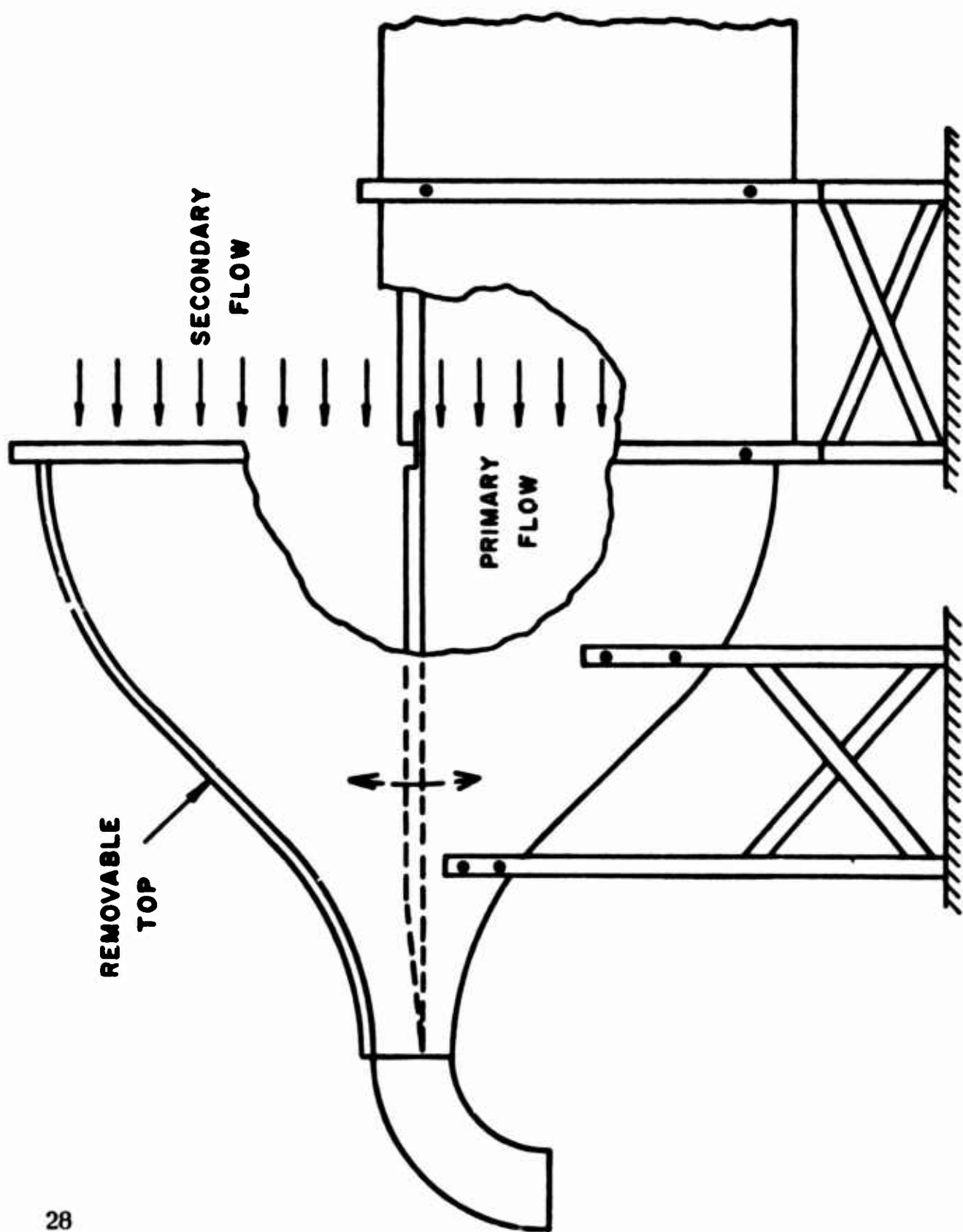
FIGURE 2 DETAIL OF NOZZLE AND MOVABLE PARTITION
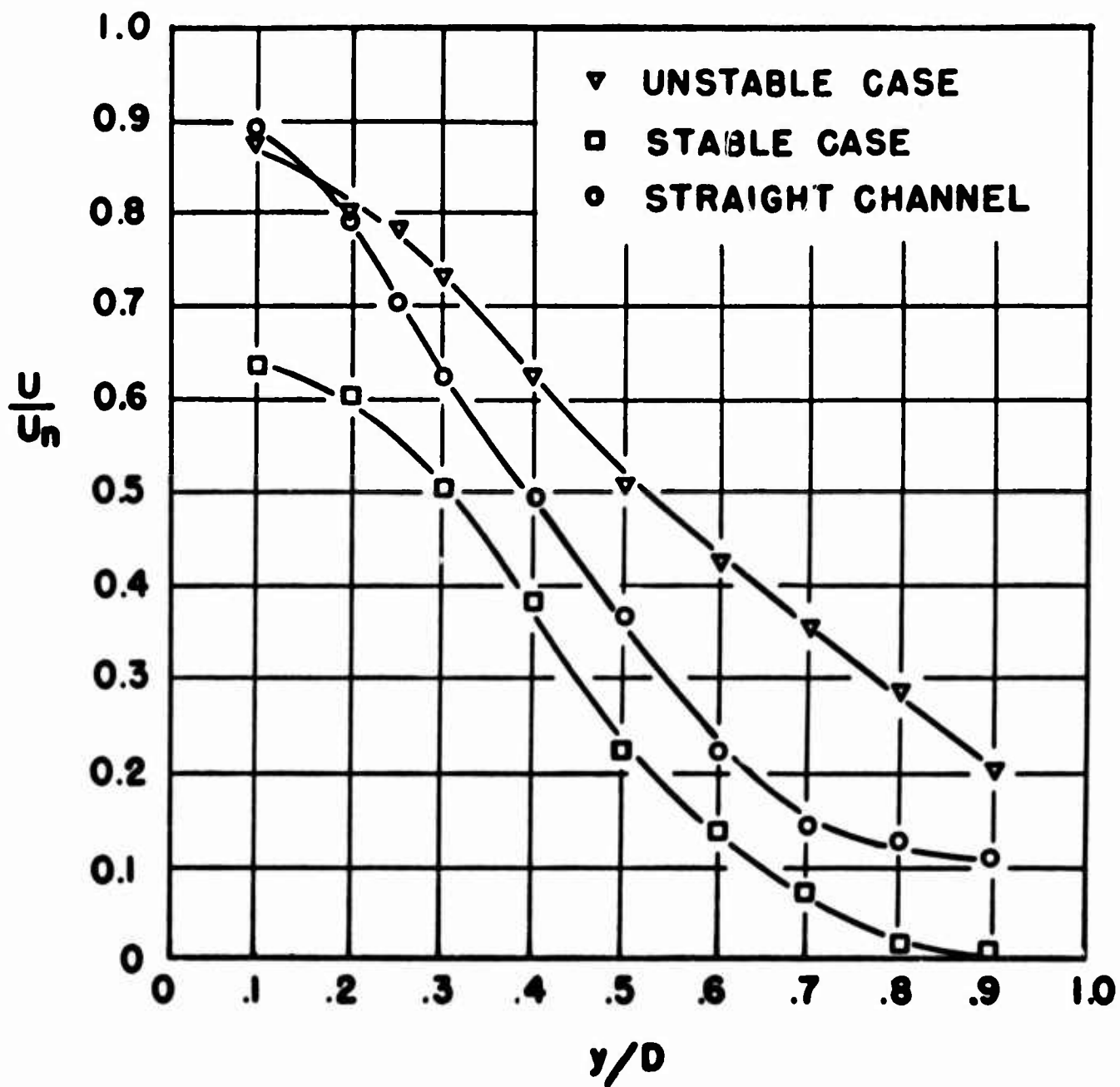
FIGURE 3. COMPARISON OF MEAN VELOCITY PROFILES AT $X_c / D = 4.59$
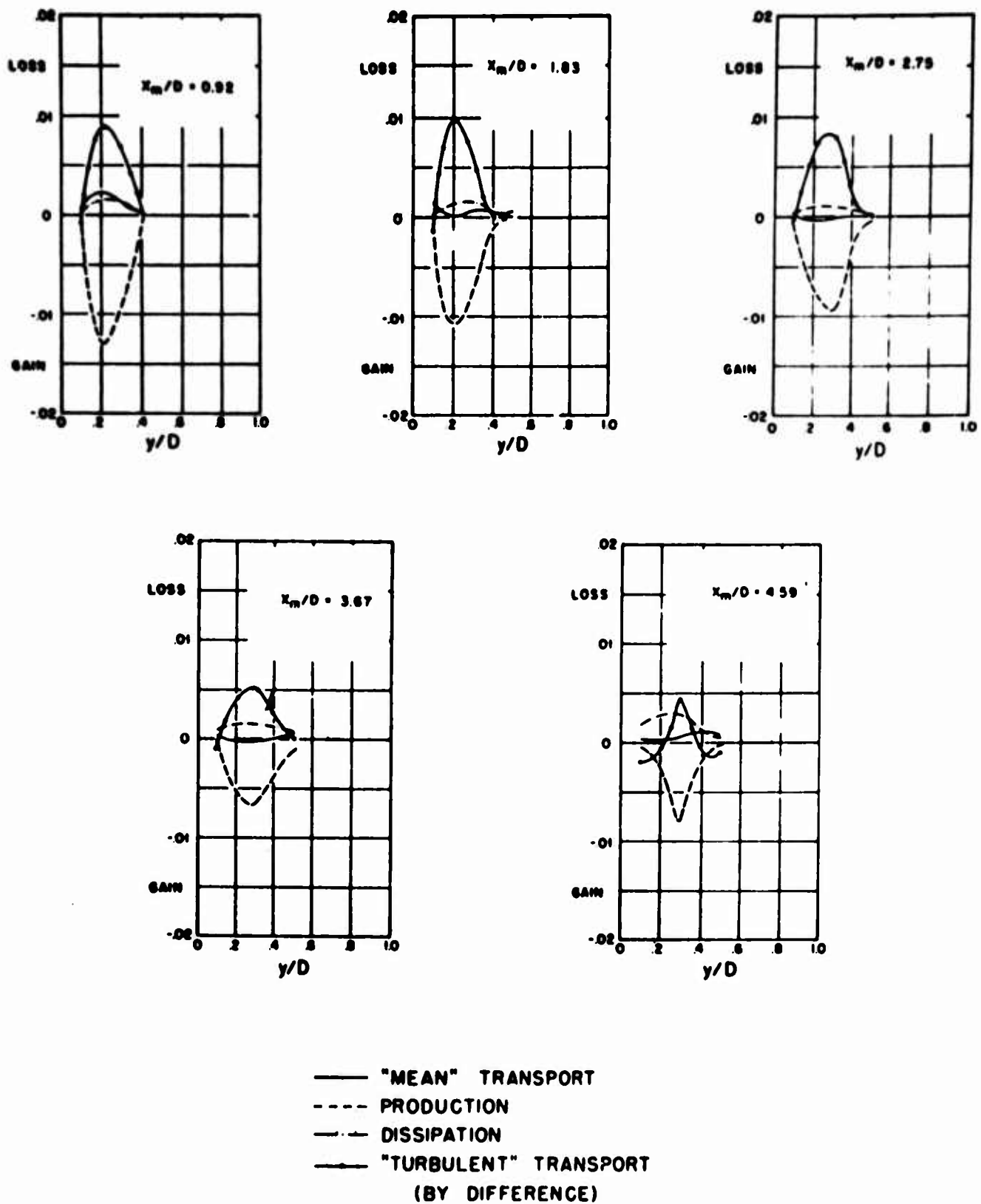
FIGURE 4   TURBULENT ENERGY BALANCES IN
CURVED CHANNEL (STABLE CASE)
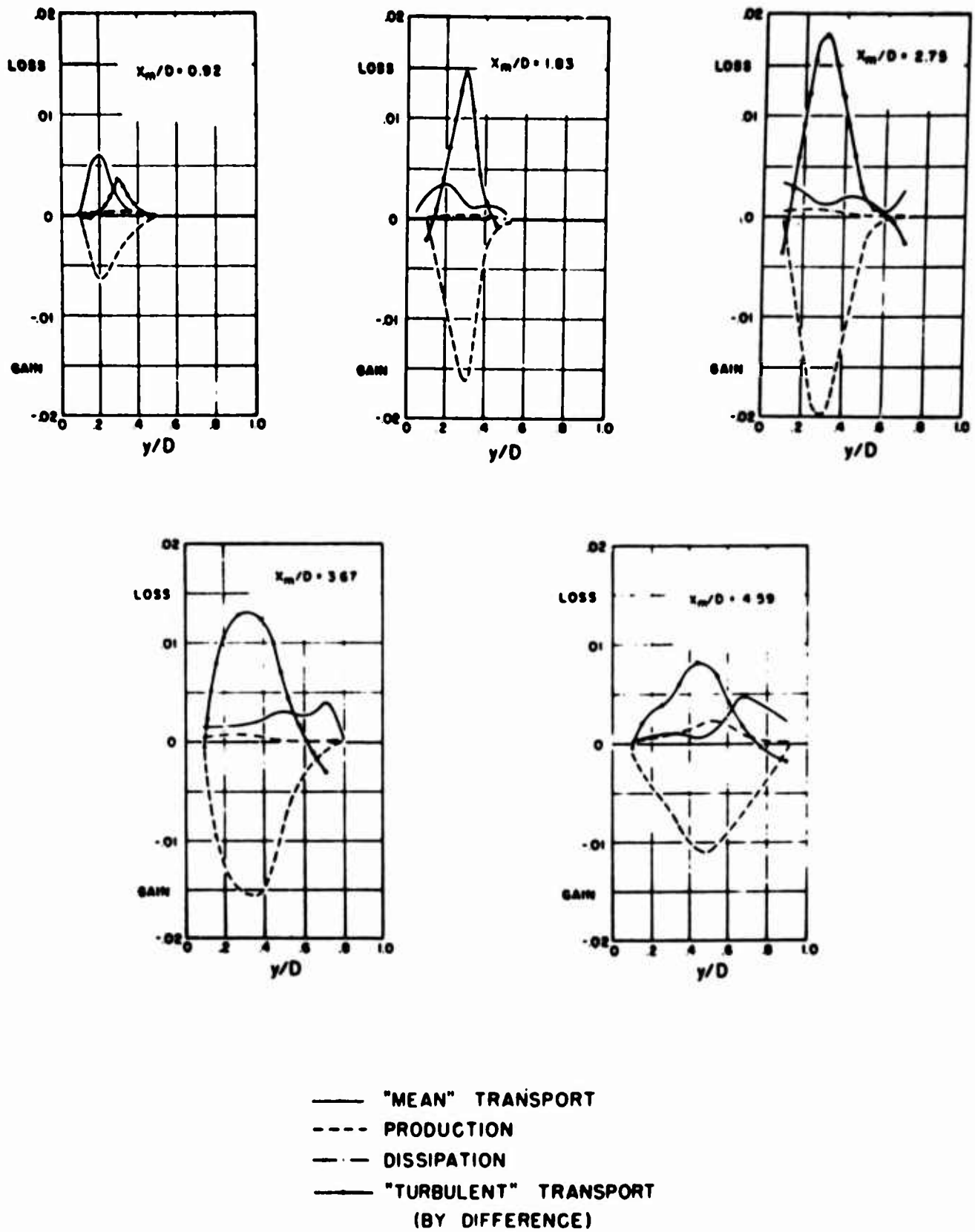
FIGURE 5 TURBULENT ENERGY BALANCES IN CURVED CHANNEL (UNSTABLE CASE)
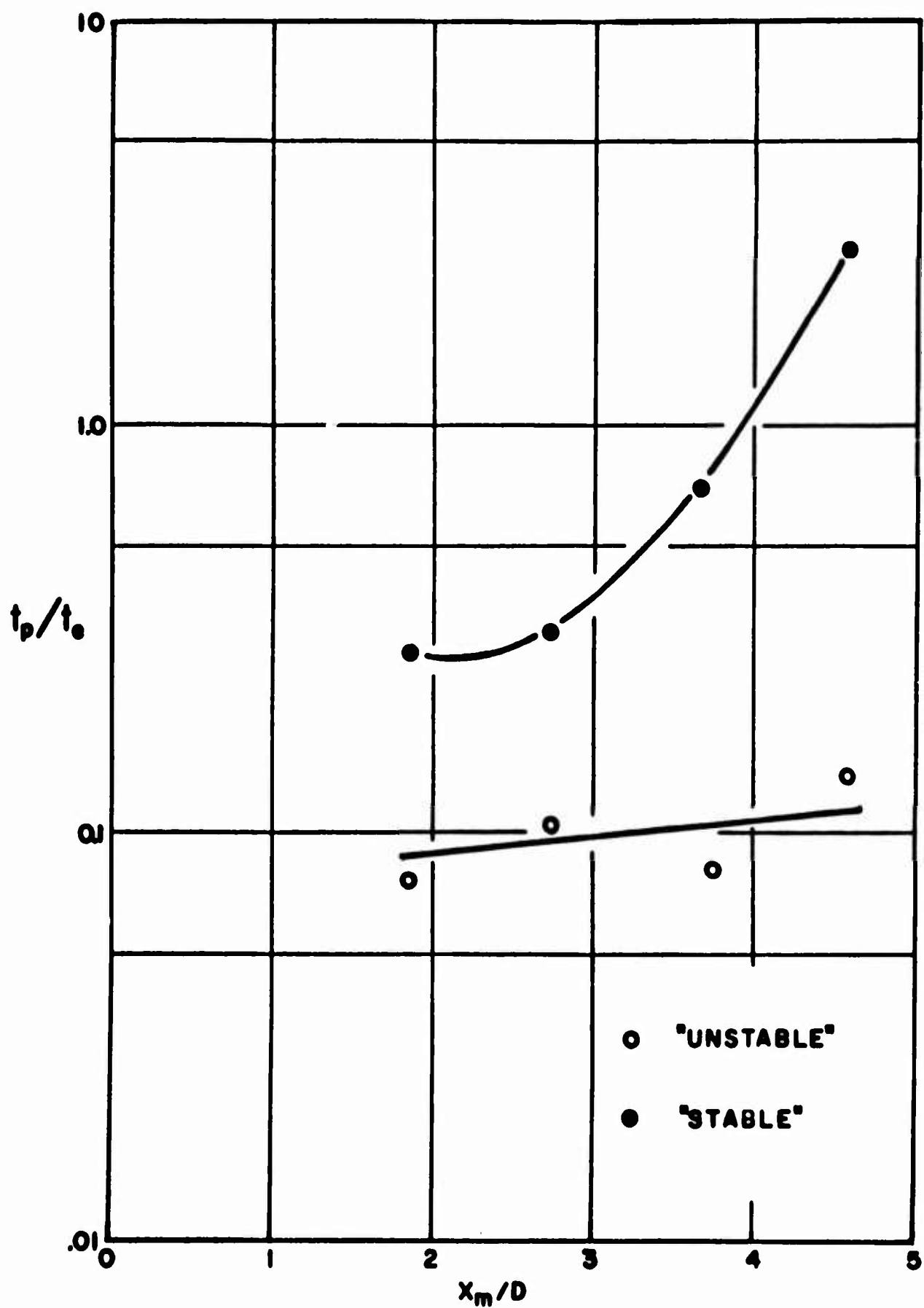
FIGURE 6. RATIO OF RATE OF DISSIPATION TO RATE OF PRODUCTION
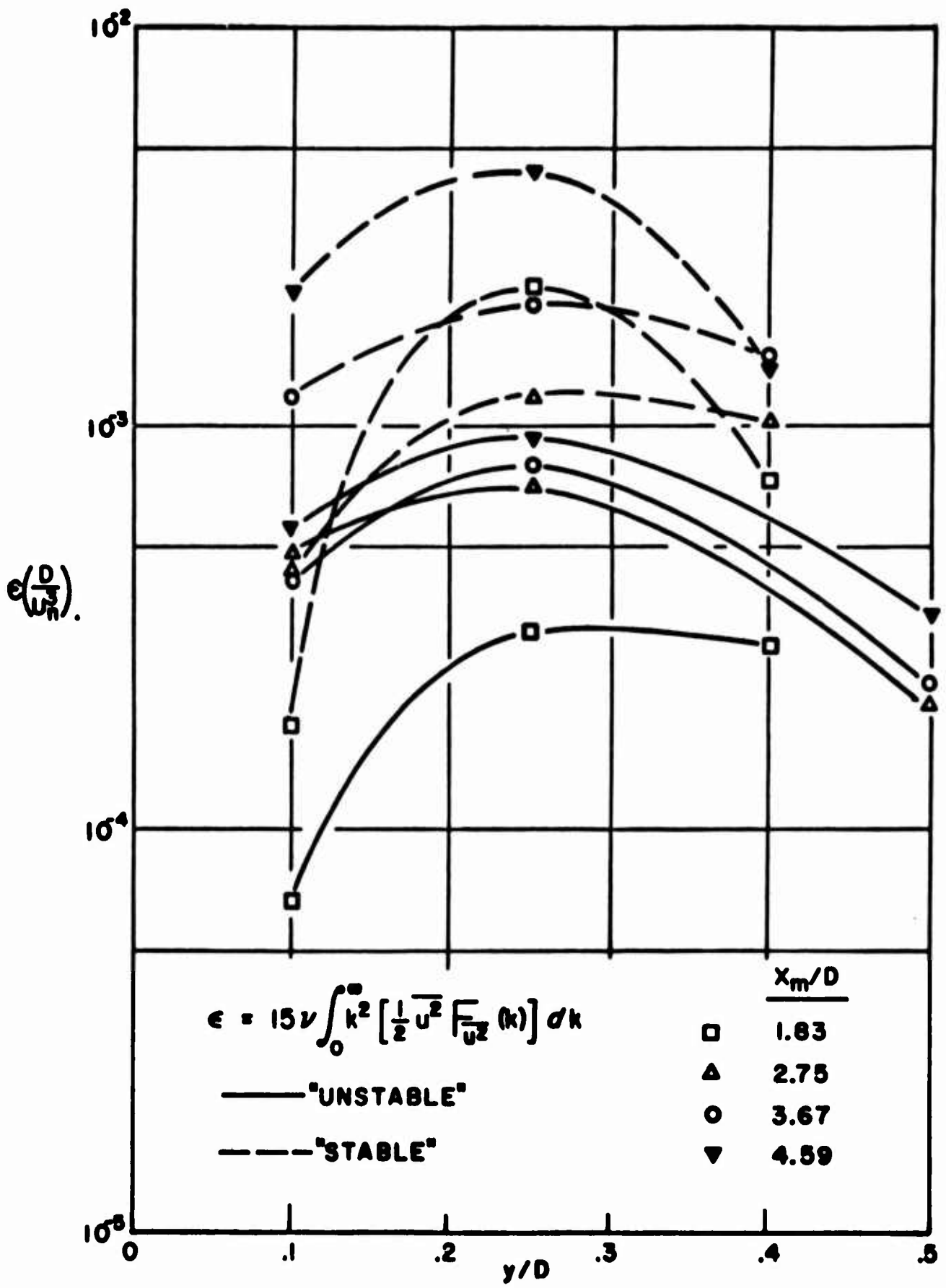
FIGURE 7. DISSIPATION RATES IN CURVED CHANNEL
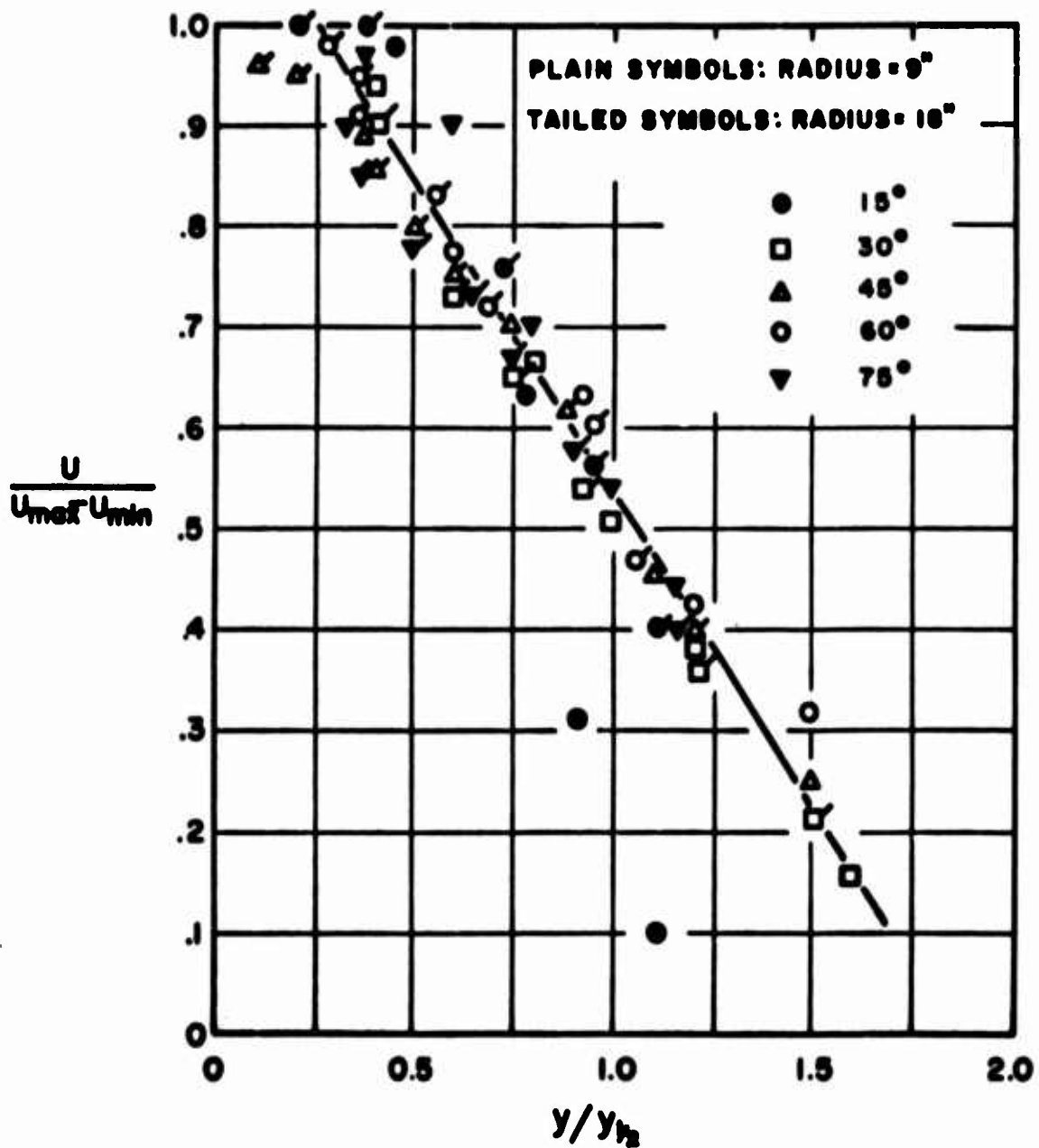
FIGURE 8. CORRELATIONS OF MEAN VELOCITY FOR 9" AND 18" CURVED PLATES
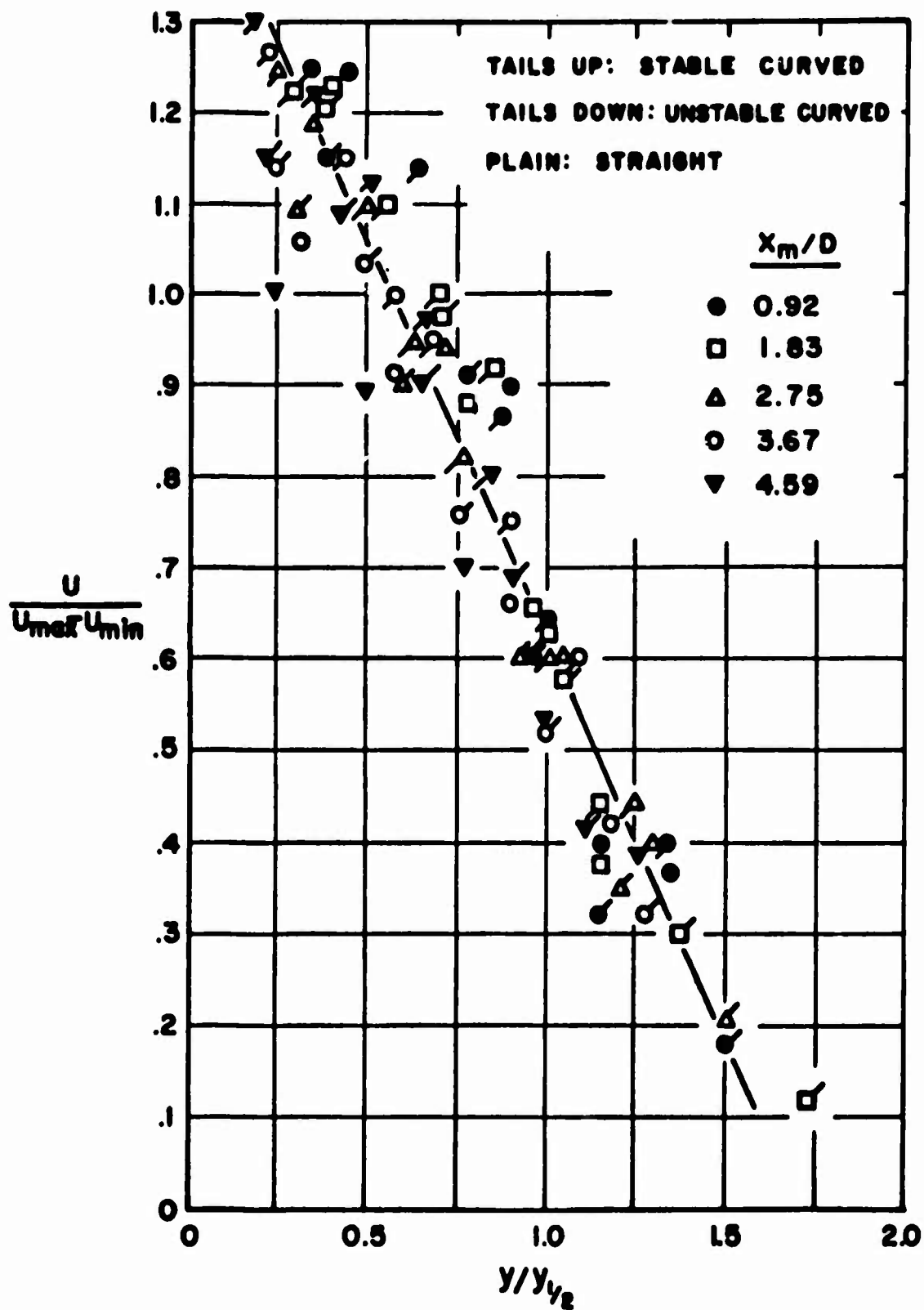
FIGURE 9. CORRELATIONS OF MEAN VELOCITY FOR CURVED CHANNEL AND STRAIGHT CHANNEL
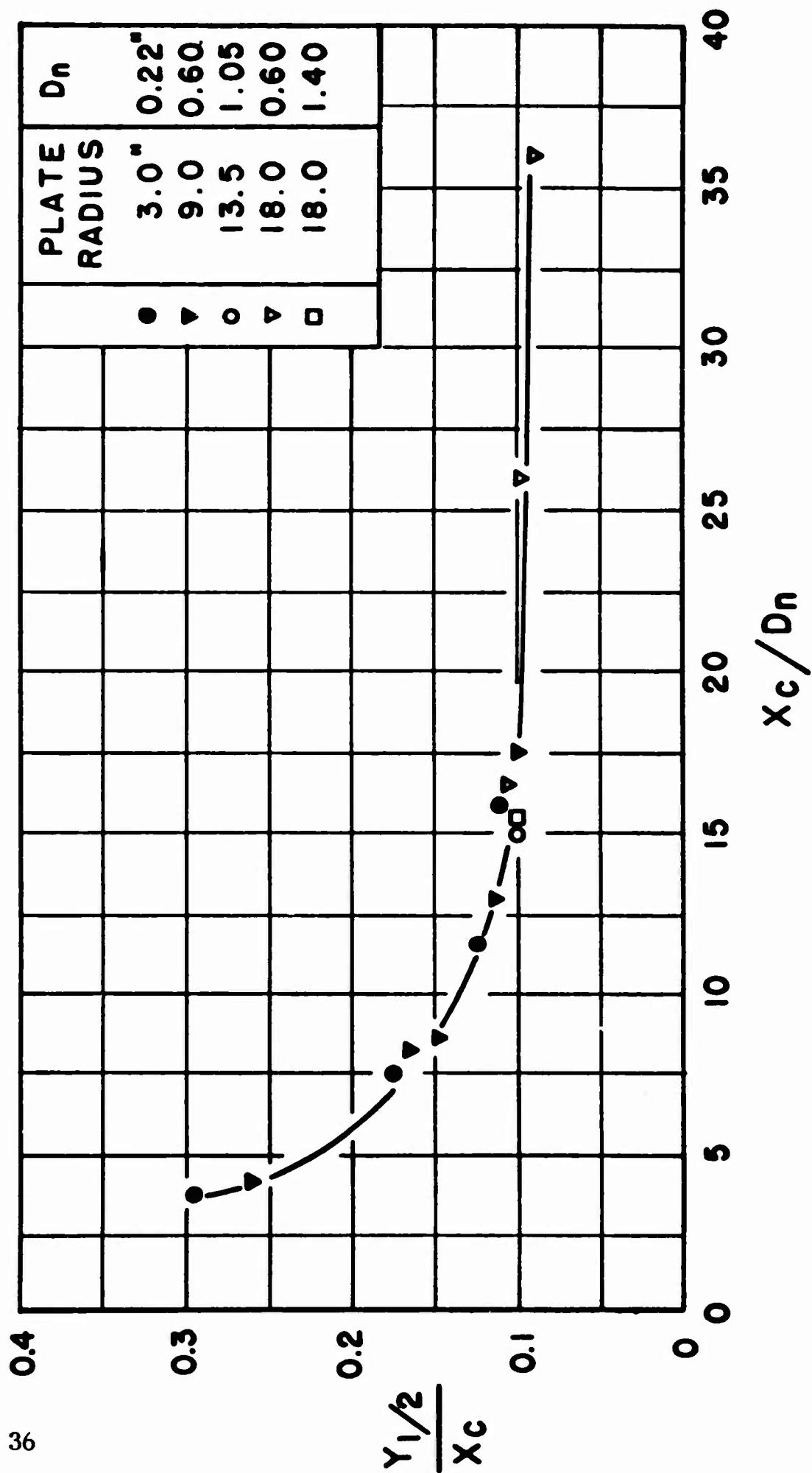
FIGURE 10. CORRELATION OF $Y_{1/2}$
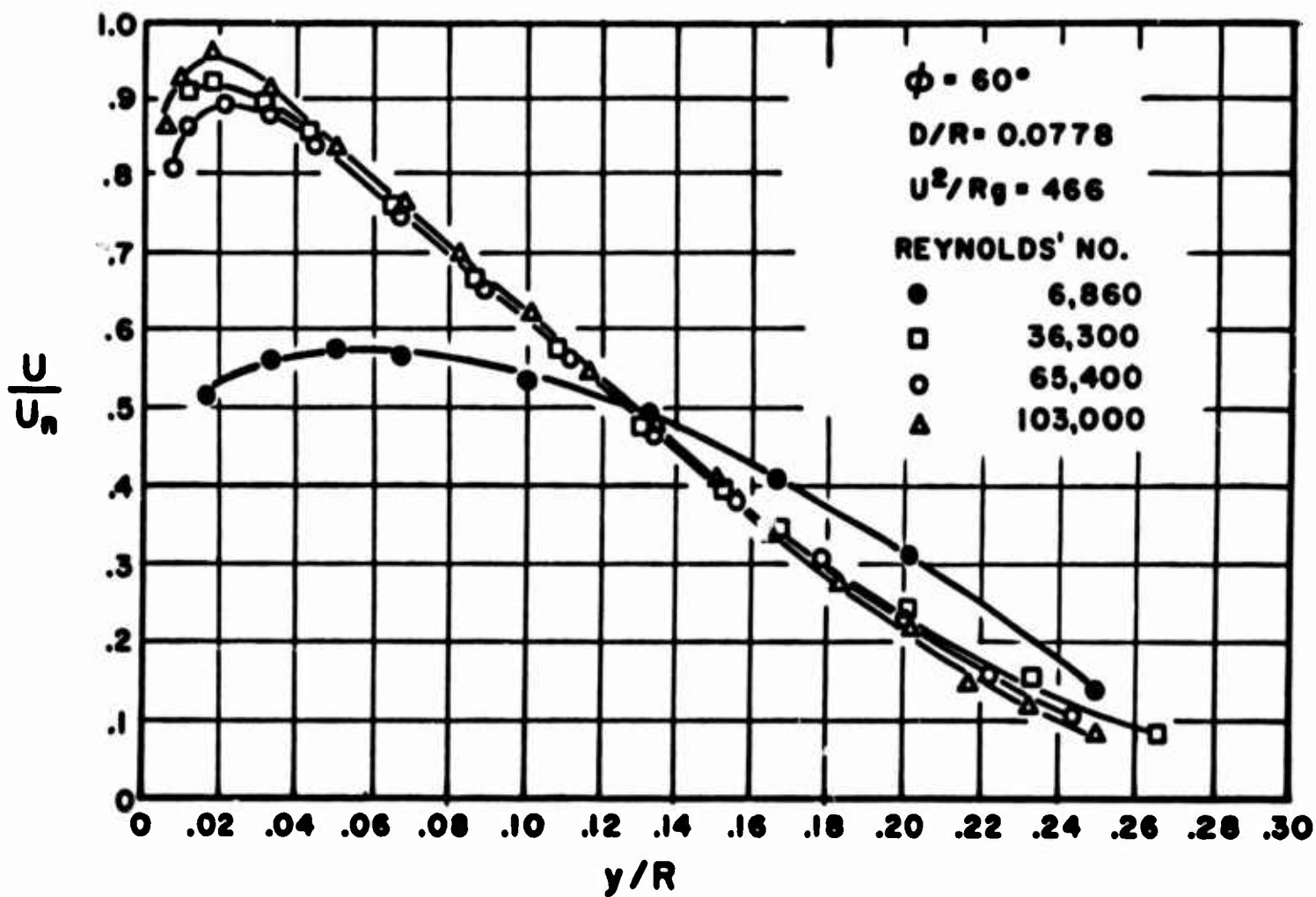
FIGURE 11. MEAN VELOCITY DISTRIBUTIONS AT SEVERAL REYNOLDS' NUMBERS

37
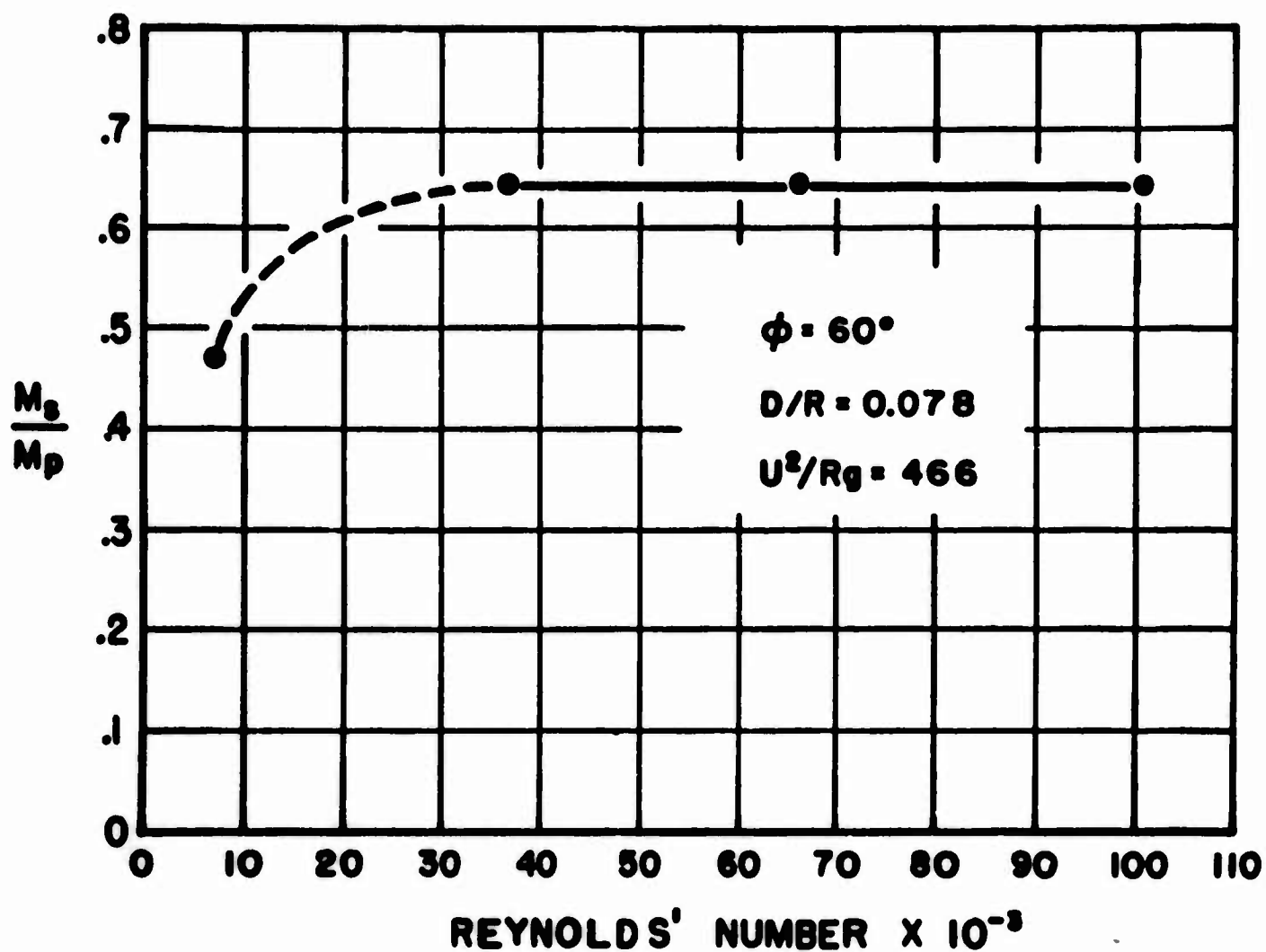
FIGURE 12. MASS FLOW RATIO AT SEVERAL
REYNOLDS' NUMBERS

INVESTIGATIONS OF INTERACTING UNDEREXPANDED JET FLOWS[*]

by

William J. Sheeran[**]
Darshan S. Dosanjh[***]

ABSTRACT

Some further experiments were performed with transversely impinging two-dimensional underexpanded jet flows as an extension of the work reported at the Diamond Ordnance Fuze Laboratories Fluid Amplification Symposium held in October 1962. The previous observations on the radical changes in shock structure and recovery stagnation pressure distribution in a highly underexpanded jet flow due to the transverse impingement of a relatively low pressure jet flow were investigated further. From pitot pressure traverses and shadowgraphs it was determined that while an earlier proposed interaction model can be used to explain the pitot pressure distributions, certain new observations suggest a possible modification which is discussed in the paper. Also, the removal of the side walls downstream of the jet exits (i.e. the use of free, rectangular exit, underexpanded jet flows) did not cause significant changes in the basic interaction phenomena that were observed with the side walls in place (i.e. with two-dimensional jet flows). Additionally, a brief investigation with a thin wire stretched through the first shock cell of the highly underexpanded power jet flow showed that while the shock structure behavior was similar to that in the impinging jet arrangement (in that the Riemann Wave in the underexpanded jet flow was eliminated), the pitot pressure distribution behavior was radically altered.

The previously proposed method of determining the approximate Mach number distribution along the flow centerline in the inner region of a single highly underexpanded jet by using the area-Mach number relation in conjunction with the assumption that the jet flow boundaries were simply an extension of the sonic nozzle was further examined. The jet spread (therefore the local flow cross-sectional area) does vary with changes in jet operating pressure ratio, thus the proposed method predicts a varying inner flow region Mach number distribution; however, the actual Mach number distribution is independent of the operating pressure ratio for a choked jet. Upon further investigation it was then established that the proposed approximate method could be used to some advantage only over a limited range of jet operating pressures.

[**] Graduate Student, L. C. Smith College of Engineering
[***] Professor of Mechanical Engineering, L. C. Smith College of Engineering

INTRODUCTION

During the past year in the Mechanical Engineering Department at Syracuse University some further experiments were conducted with transversely impinging, two-dimensional, underexpanded jet flows[1]. These investigations, among other things, may provide background for the design of supersonic momentum exchange fluid amplifiers. For two-dimensional flows it has been found that when a relatively low pressure jet (control jet) is perpendicularly impinged onto a highly underexpanded jet flow (power jet), such that the impingement point occurs between the nozzle exit and the normal shock (Riemann Wave) of the power jet, the normal shock front is replaced by an oblique shock structure[2,3]. Associated with this change in shock structure the pitot pressure distribution in the highly underexpanded jet flow is altered considerably; the maximum centerline recovery stagnation pressures at locations downstream of the previous location of the Riemann Wave being substantially increased. In Ref. 2 a mechanism for this recovery stagnation pressure behavior was proposed and in the present study this mechanism is examined further.

As there was some question as to the extent of the influence of the nozzle arrangement on the phenomena recorded in the previous studies, the side walls downstream of the jet exits were removed (i.e. free, transversely impinging, rectangular exit, underexpanded jet flows were used) and the resulting shock structure and pitot pressure distribution behavior compared to that previously observed with the side walls in place.

Since it has been established that the pitot pressure distribution change is caused by the replacement of the Riemann Wave by the oblique shock structure due to the control jet impingement[1], it may be conjectured that the same effect might be obtained by stretching a wire through the supersonic flow upstream of the normal shock. The detached bow shock structure associated with the wire would then eliminate the Riemann Wave. This use of a wire was tried and the resulting pitot pressure distribution compared to that recorded in the impinging jet case.

In Ref. 2, the authors made an additional miscellaneous observation that at the particular jet operating pressure ratio used the approximate average Mach number at axial positions upstream of the normal shock front in a highly underexpanded, two-dimensional jet flow could be calculated from the isentropic, one-dimensional area-Mach relationship by simply assuming the jet flow boundary to be an extension of the sonic nozzle. The feasibility of such an approach has been more closely examined here.

EXPERIMENTAL FACILITY AND PROCEDURE

The compressed air facility and pressure control system used in these studies are reported in detail in Ref. 3, the only change being the installation of an aftercooler between the compressor and the storage tanks. The aftercooler reduced the amount of water vapor in the air supply. Its separator also removed some of the oil which had become a problem in the recording of some earlier optical data[3].

The construction details of the two-dimensional converging jet nozzles, as well as the arrangement used in these studies are seen in Fig. 1. All of the two-dimensional nozzles were identical in construction, converging smoothly from

5" x 3/8" x 5/16" supply chambers down to the 1/32" x 3/8" (aspect ratio of 12) nozzle exits. A short 1/32" straight portion was provided just before the exit. In the $90°$ arrangement used, the two nozzle centerlines were perpendicular to each other with the relatively low pressure jet (referred to here as the control jet) nozzle centerline being located one nozzle width, w, (w is the small dimension of the rectangular exit, 1/32") downstream of the highly underexpanded jet (referred to here as the power jet) exit. The power jet nozzle centerline was in turn located two nozzle widths (1/16") from the control jet exit. Measuring x along the power jet nozzle centerline from the power jet exit and y along the control jet nozzle centerline from the control jet exit, the two nozzle centerlines intersected at $x/w = 1$, $y/w = 2$. This jet arrangement was mounted between the parallel side walls of the test section thus producing a two-dimensional jet flow, if boundary layer affects are neglected. No gap was provided between the power and control jet nozzle blocks, with the result that the "free" entrainment by the jet flows was asymmetric.

Two methods of mounting optical glass in the side walls were used to allow for shadowgraphic, schlieren and interferometric studies of the flow. The section used in the majority of the studies, and described in detail in Refs. 2 and 3, had the glass such that neither the jet exits nor the impingement point of the nozzle centerlines was exposed by the windows. When this section was constructed the jet interaction problem to be studied was such that the flow close to the nozzle exits was not of immediate interest so that this method of mounting the glass was used to avoid the problem of affecting a seal between the glass windows and the metallic nozzle blocks for the high operating pressures involved. However, in the more recent studies it was important to have the flow near the exits visible, therefore a second test section was constructed where the glass windows were located over the nozzle blocks themselves[1]. Several sealing problems have been encountered with this section and as yet the results from it have been only of a qualitative nature.

For both test sections, the power and control jet supply chamber absolute stagnation pressures, P_{OP} and P_{OC} respectively, were measured in large settling chambers which were connected to the supply chambers of the jet nozzles through short rigid fittings; the maximum loss between the settling chamber and the supply chambers was only 1/4 per cent of the settling chamber pressure.

SHOCK STRUCTURE AND RECOVERY STAGNATION PRESSURE

The recovery stagnation pressure distribution and shock structure of the impinging jet flow field was investigated using a highly underexpanded power jet (200 psig settling chamber pressure) interacting with various relatively low pressure control jet flows. The per cent control was defined as $100 \times \overline{P_{OC}}/\overline{P_{OP}}$; $\overline{P_{OP}}$ and $\overline{P_{OC}}$ being the power and control jet settling chamber gage pressures respectively.

For the power jet flow alone, i.e. zero per cent control, with a settling chamber pressure $\overline{P_{OP}} = 200$ psig (or in the usual designation: for a pressure ratio $P_N/P_a = 7.81$ jet flow, where P_N is the absolute static pressure at the power jet sonic nozzle exit and P_a is the ambient or receiver absolute pressure) the usual shock structure of a highly underexpanded jet flow was exhibited (see shadowgraph,

41

Fig. 2)[*]. The shock structure was comprised of the usual intercepting and normal (Riemann Wave) shocks. In order to match the downstream pressures the intersection of the intercepting and normal shocks gave rise to the reflected oblique shocks.

In Refs. 2 and 3 it was reported that, in the jet arrangement described in the previous section, the transverse impingement of the control jet flow gave rise to a repetitive shock structure in the downstream direction, similar to but not as well defined as the cellular shock structure of a single and somewhat lower pressure ratio jet. This is illustrated by shadowgraphs taken for 2 and 10 per cent control jet flow (Fig. 3).

The effect of the transverse impingement on the jet flow recovery stagnation pressures was recorded by pitot tube traverses. The plots of the ratio of the local absolute pitot pressure, P_{Tj}, to the power jet settling chamber absolute pressure, P_{op}, versus the y-location at $x/w = 10$ are shown in Fig. 4 for 0, 2 and 10 per cent control impingement[**]. Traverse results for 2 per cent control at $x/w = 5$ and 10 were previously reported in Ref. 3; however, these made use of an arc traverse and were repeated in the present studies using a straight traverse perpendicular to the jet flow centerline. This traversing method made the correlation between the pitot pressure distributions and the wave structure more direct[1]. The $y = 0$ location in the plot corresponds to the centerline of the power jet nozzle; negative locations are measured toward the control jet side. The direction of impingement of the control jet flow is indicated by the arrow.

The most interesting result of the impingement, at least from the point of fluid amplification, is seen at $x/w = 10$ (Fig. 4) in the change from the zero per cent control double peak distribution to the smooth, almost Gaussian distribution with the impingement of 10 per cent control. This change resulted in a tremendous increase in the jet flow centerline pitot pressure. The 2 per cent control impingement also caused a large increase in centerline pitot pressure; however, the last vistages of the separate peaks are still apparent. These pitot pressure distributions are discussed in detail in Ref. 1.

A mechanism for this behavior of the pitot pressure distributions was proposed in Ref. 2 and is illustrated in the sketches shown in Fig. 5. In this model the impingement of the control jet flow upstream of the Riemann Wave causes new velocity and static pressure boundary conditions to be imposed on the power jet flow which crosses the intercepting shock on the control jet side. In order to meet these new boundary conditions the intercepting shock moves inward towards the power jet centerline and at the same time adjusts at larger wave-angles to the power jet flow streamlines. One of the sketches of Fig. 5 shows the successive positions of the intercepting shock with increasing control jet operating pressures, as observed in shadowgraphs. For 2 per cent control this shock is moved just enough to completely

_____

[*] Unless indicated otherwise shadowgraphs discussed here were taken using the test section described in Refs. 2 and 3 (thus the jet exits are not visible in the photographs) and with the film 1.75" from the centerplane.

[**] The calculation of velocity profiles from the pitot traverse results was attempted; however, the lack of reliable static pressure or static temperature information made such attempts fruitless.

42

replace the normal and control jet side intercepting shock with a single oblique shock. The intercepting shock on the far side remains in its original zero per cent control location. With increasing per cent control (i.e. increasing control jet operating pressure) the relocated intercepting shock adjusts at greater and greater wave-angles to the flow and thus meets the far-side intercepting shock closer and closer to the power jet exit. For 2 per cent control it met the far-side shock at approximately $x/w = 9.0$, therefore just replacing the entire normal shock; however, for 10 per cent control this relocated intercepting shock intersected the far-side shock at an x/w of approximately 5.8. The power jet flow in the region enclosed by the relocated intercepting shock, the power jet exit, and the far-side intercepting shock is unaffected by the control jet impingement. It was proposed that a contact surface* is formed between the deflected control jet flow and the power jet flow which crosses the relocated intercepting shock. Across this contact surface the pressure and flow directions are the same; however, the velocity magnitudes, the temperature and the density may be different. In optical records this contact surface will appear somewhat similar to a shock due to different density on either side.

In this model for both the 2 and 10 per cent control cases the normal shock has been replaced by an oblique shock which causes smaller losses in stagnation pressure than those encountered in crossing the normal shock. Additionally, the relocated intercepting shock occurs closer to the power jet exit, at positions where the local Mach number just ahead of it is lower and the static pressure higher than those encountered at the farther downstream location just upstream of the Riemann Wave. Thus the strength of the relocated shock and the stagnation pressure losses associated with it are further reduced. Both these effects account for the increase in P_{Tj} with control jet impingement. Also, whereas the flow downstream of the normal shock was subsonic, the flow downstream of the relocated oblique shock structure is supersonic thus giving rise to the repetitive wave structure.**

In order to check the validity of this proposed model, the pitot pressure distributions were compared with the corresponding shadowgraphs. (See Ref. 1 for details.) On the basis of this detailed comparison the interaction model proposed by the authors in Ref. 2 and illustrated in Fig. 5 can be used to explain most of the experimental results. However, some more recent observations have cast doubt on certain aspects of this model. Since shock waves and contact surfaces appear similar in shadowgraphs, schlieren and also interferograms (due to the density dependence of such systems), the primary point of doubt in the proposed model was whether or not the contact surface and the relocated oblique shock had been correctly identified.

It was shown from shadowgraphs and schlieren pictures that what has been referred to as the relocated intercepting shock is actually a shock[1]. However, while the pitot pressure results have been explained on the basis of the contact surface appearing downstream of the relocated intercepting shock, they could as easily have been explained if it had been another oblique shock. One of the arguments in favor of its being a shock was found in the increasing distinctness of

---

*This interface is also often referred to as a slip surface.

**This repetitive shock structure will cause further losses at locations farther downstream than those considered here.

its shadowgraphic appearance in the downstream direction (Fig. 3). In the previously proposed model this contact surface separated the deflected control jet flow and the power jet flow which crossed the relocated intercepting shock. However, in order for the control jet flow to be deflected in the downstream direction of the power jet centerline it would first have had to interact with at least the outside portion of the power jet flow near the point of impingement. This mixed jet flow could still have had a different density and temperature than the power jet flow that crossed the relocated intercepting shock farther downstream. However, once this mixing of the two jet flows was initiated, and since the jet exit Reynolds number per foot was on the order of 10^5 or greater, it would seem that the extent of mixing would have increased in the downstream direction. This would have meant that any boundary between the mixed jet flow and the power jet flow that crossed the relocated intercepting shock would have been less distinct in the downstream direction and certainly not have shown up as a sharply defined contact surface.

Additional evidence available at present that lends credence to the shock rather than the contact surface theory was seen in schlieren pictures[1] which showed that the supposed contact surface C (see sketches) definitely crossed the portion B of the far-side intercepting shock downstream of the intersection point A with the relocated intercepting shock D.

Continuation of far-side intercepting shock

B

A

Previously proposed contact surface

C

D

Relocated intercepting shock
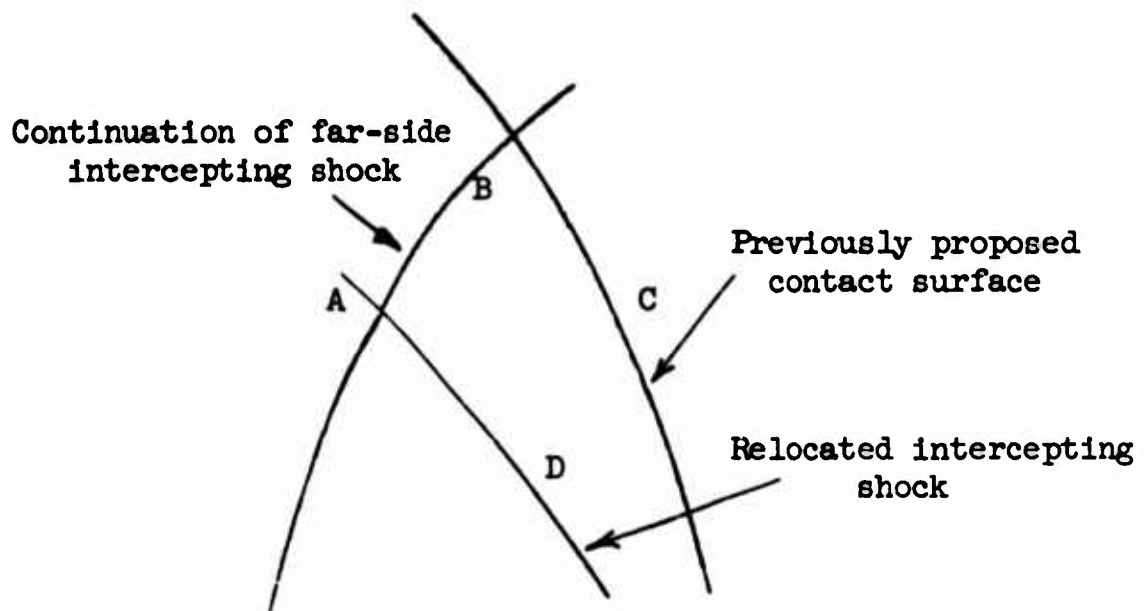
Sketch of Previously Proposed Contact Surface and Far-side
Intercepting Shock Crossing

This crossing of the shock and contact surface does not in itself rule out the contact surface model since this phenomenon has been observed in other studies. However, it does mean the contact surface separated two regions of supersonic flow. Due to the curvature in the supposed contact surface (Fig. 3) additional structure on both sides of the contact surface would have been required in order to turn these supersonic flows tangent to such a curving surface. Such structure does not show in the optical records. However, expansion and weak compression regions do not clearly show up in shadowgraphic records; thus leaving open the possibility that such structure could actually have been present to turn the supersonic flows. The foregoing discussion casts some doubt on the identification of the previously proposed contact surface in that it could have been another oblique shock. Since the velocity is tangent to a contact surface and at some

angle to a shock, by simply determining the direction of the velocity it is hoped in the near future to more positively identify this structure. If it is a shock wave, the problem is to justify its existence in the flow.

The possible appearance of the second oblique shock downstream of the relocated intercepting shock may be explained by examining the details of the shadowgraphs (Figs. 6 and 7) taken with the newer test section where the nozzle exits were visible. In Fig. 6, taken for 10 per cent control, it appears that an expansion region formed between the relocated intercepting shock and this supposed second oblique shock (for details see Ref. 1). However, the shadowgraph for 2 per cent control (Fig. 7) seems to indicate, instead, that both the intercepting and supposed second oblique shock apparently originate very close to the power jet exit, cross just above the control jet impingement point, and extend downstream to appear as separate shock structures. These contradictions from the optical records alone concerning essentially the same basic flow phenomenon have not been resolved yet. Similar phenomenon was observed in interacting jets without side walls (see subsequent discussion).

As mentioned under Experimental Facility and Procedure, the nozzle arrangement used previously[2,3] did not provide for any gaps between the power and control jet nozzles. Therefore with the jets operating there was a small cavity between the power and control jet nozzles which had no communication with the atmosphere (see following sketch).

C.J.

Low Pressure
Cavity

$\leftarrow$ W = 1/32" $\rightarrow$

P.J.
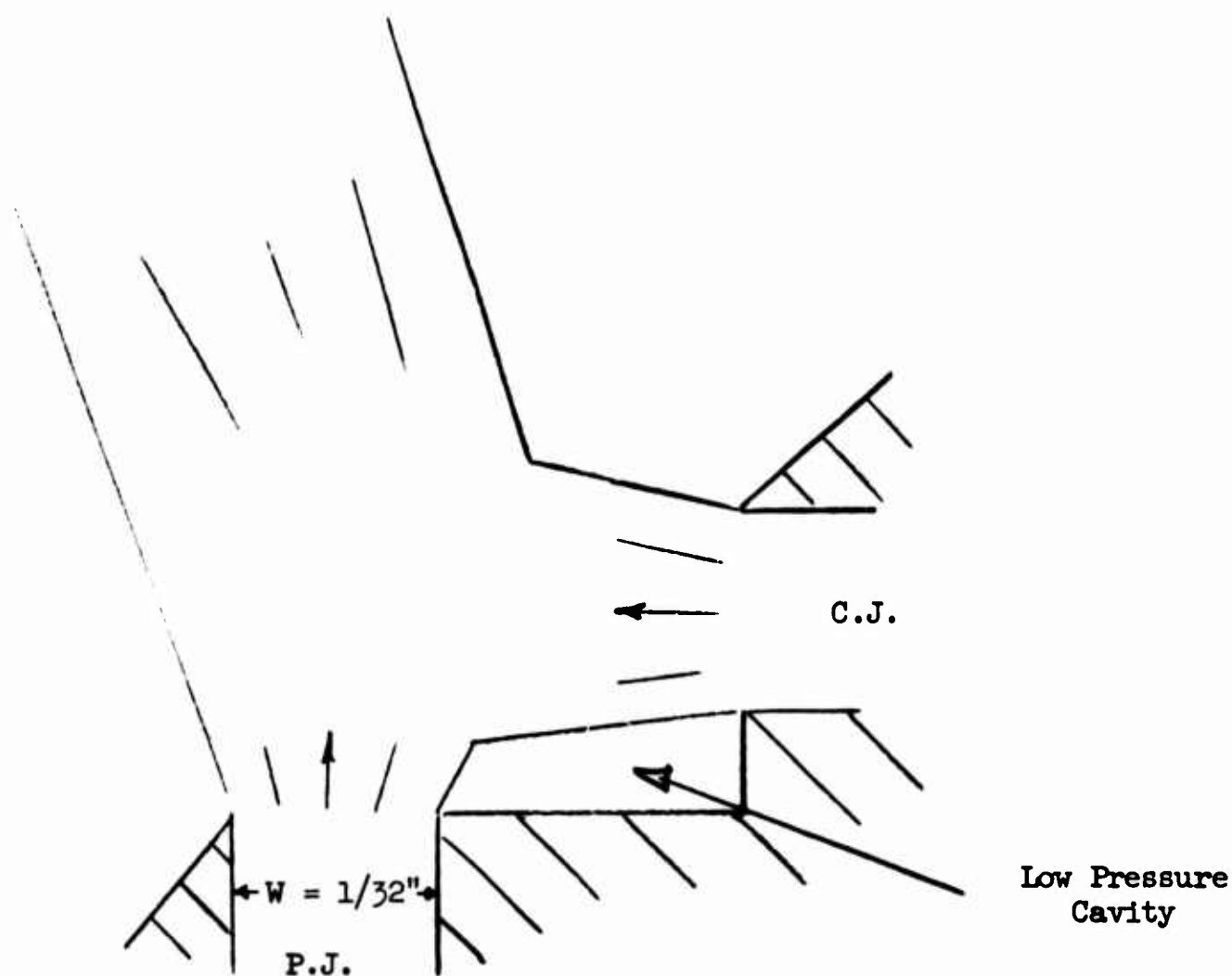
The entrainment demands of the power and control jets caused this cavity to become a region of lower than atmospheric pressure. The extent of the influence of this low pressure region and the walls on the changes in jet flow shock structure and on the corresponding changes in pitot pressure distribution when the control jet was impinged was not known. To determine such possible effects a separate setup was constructed with exactly the same nozzle arrangement and dimensions as used in the studies discussed previously; however, the side walls downstream of the nozzle exits were eliminated (i.e. free, rectangular exit, 1/32" x 3/8", jets were used). With the side walls removed the region between the jet nozzles had free communication with the atmosphere in the direction parallel to the 3/8" dimension of the exits (i.e. normal to the plane of the section shown in the previous sketch).

In this arrangement, the shock structure behavior due to 10 per cent control jet impingement is shown in Fig. 8. The power jet flow alone (P_{OP} = 214.5 psia), as seen in Fig. 8a, corresponds to the flow shown in the shadowgraph presented in Fig. 1 taken when the side walls were present. Comparison of Fig. 8b to Fig. 3b or Fig. 6 illustrates that the basic shock structure pattern in the 10 per cent control impingement case was the same whether or not the side walls were used (i.e. whether or not the cavity between the jet nozzles had free communication to the atmosphere). The apparent expansion region or shock crossing, discussed earlier, also clearly shows in Fig. 8b. However, the shock structure for this arrangement was located closer to the jet exits than was the case when the side walls were used (e.g. for the power jet alone the Riemann Wave was at x/w = 6.8 as contrasted to x/w = 8.5 with the side walls in place[1]). This was expected since with the side walls removed the jet flow could expand in directions around the entire periphery of the jet, whereas with the side walls in place the expansion was restricted to only two sides. These differences in shock location, however, did not alter the basic shock structure behavior. As would be anticipated, since the shock structure behavior was similar, the pitot traverses of the flow field resulting from a 10 per cent control jet impingement onto a P_{OP} = 214.5 psia power jet, with side walls removed, revealed the same type of pitot pressure distribution behavior as that observed with the side walls in place. From the initial observations of pitot pressure distribution and shock structure behavior with the side walls removed, it appears that the side walls and cavity between the jet nozzles do not significantly influence the basic interaction phenomena observed.

As was discussed in connection with the proposed interaction model, it is the replacement of the Riemann Wave of the power jet flow by the oblique repetitive shock structure of the resultant impingement flow that is responsible for the radical change in pitot pressure distribution at locations downstream of the original position of the Riemann Wave in the power jet flow alone. Therefore, an alternate and simpler method of eliminating the Riemann Wave was examined.

A thin wire (0.018" dia.) was mounted parallel to the 3/8" dimension of the jet exit such that it was located at an initial x/w of 3 in the power jet supersonic flow upstream of the Riemann Wave (i.e. in the first shock cell). The power jet flow, however, caused a bowing and thus a slight shift of the wire to approximately x/w = 3.18, in the center of the flow. A free, rectangular exit jet, having the same construction details as those in the impingement studies, was used since the presence of the optical glass side walls downstream of the exit ruled out the stretching of the wire across the flow. A shadowgraph, taken with the film parallel to the 1/32" dimension of the jet exit, illustrating the nature of the jet flow for P_{OP} = 214.5 psia (the same as used for the experiments discussed previously) is shown in Fig. 9a. This shadowgraph thus corresponds to the one shown in Fig. 8a.

46

Shadowgraphs of the flow field corresponding to Fig. 9a, but with the wire in place, are presented in Figs. 9b and 9c. The pitot probe shown in these shadowgraphs was located along the centerline of the flow (i.e. y = 0) at x/w = 10. The shadowgraph in Fig. 9c is of the same flow as in Fig. 9b, however, with the film parallel to the 3/8" dimension of the jet exit. The probe bow shock shown in Fig. 9c was quite plane and parallel (i.e. constant detachment distance) to the wire which illustrates the extent of the two-dimensional flow region produced by the free jet of aspect ratio 12. This view could not be shown for either of the interacting jet flow arrangements since the control jet nozzle blocked light passage in this direction.

It can be seen in Fig. 9b that, as expected, the detached bow shock wave ahead of the wire replaced the Riemann Wave of the undisturbed jet flow. This bow shock had a normal portion in the center, just ahead of the forward stagnation point of the cylindrical wire, and oblique segments to either side. This meant of course that the Riemann Wave was not entirely replaced by oblique shocks, as in the impinging jet case, but rather partially by oblique shocks, which influenced the outer portions of the flow, and partially by another normal shock. The flow which passed through the oblique segments of the bow shock remained supersonic, as evidenced by the repetitive shock structure on each side which was formed by the interaction of these oblique segments with the intercepting shocks of the first cell. The jet flow in the center which passed through the normal (or the nearly normal) portions of the bow shock became subsonic, as shown by the lack of a bow shock at the probe tip when it was located on the jet centerline downstream of the wire (Figs. 9b and 9c). The wire thus effectively split the power jet flow into two separate outer supersonic flows[*] separated by a central region of subsonic flow.

The normal portion of the detached bow shock was located closer to the power jet exit than was the Riemann Wave and thus the stagnation pressure losses across it were less than those for the Riemann Wave (in the first shock cell Mach number increases with increasing distance from the jet exit). Thus, from the point of view of the losses associated only with the shock structure, when the wire was in place, higher centerline recovery stagnation pressures could be expected at locations, such as x/w = 10, downstream of the original Riemann Wave location.

The actual pitot pressure distributions for the jet flow alone and the jet flow with the wire in place are shown in Fig. 10. The undisturbed jet flow distribution at x/w = 10 was similar in form to that of the zero per cent control case in the arrangement with side walls discussed earlier (Fig. 4). However, with the wire in place, instead of an increase in centerline recovery pressure the nature of the distribution remained the same, just being spread more, while less stagnation pressure was recovered in the central region. This decrease in centerline recovery pressure was associated with the presence of the turbulent wake behind the wire; the wake being a region of reduced stagnation pressure with a velocity minimum occurring along the centerline (instead of a velocity maximum as in the case of a free jet flow). No region with characteristics comparable to the wake occurred in the impinging jet arrangement. Thus, even though the loss in centerline stagnation pressure encountered in crossing the normal shock (center portion of the bow shock when wire was inserted, Riemann Wave for the undisturbed

---

[*] It is quite likely that the use of a thinner wire would not cause such a noticeable splitting of the flow. However, because of their lack of rigidity, any thinner wires were not used.

jet) was less when the wire was inserted, the presence of the low stagnation pressure wake flow in the central region, when the wire was in place, more than nullified any possible gain in centerline recovery pressure at locations downstream of the original position of the undisturbed jet Riemann Wave. Therefore to take advantage of the induced increase in jet centerline pitot pressure an impinging jet arrangement would be preferable to the wire insertion technique. The increased spread of the distribution was due to the splitting effect of the wire on the flow, as discussed earlier.

Impinging jet studies are continuing under an NSF grant in the Department of Mechanical Engineering at Syracuse University with new instrumentation (interferometer etc.), and larger jets being developed. In addition to a study sponsored by NSF to examine the basic flow phenomena involved, and thus to answer some of the unresolved questions mentioned in this paper, a separate study under NASA sponsorship is underway to examine the sound field of the impinging jets[1].

AREA-MACH NUMBER STUDIES

Besides the main point of Ref. 2, an additional miscellaneous observation was made that at the operating pressure ratio used the approximate average centerline Mach number distribution upstream of the normal shock front in a highly underexpanded, two-dimensional jet flow could be calculated from the isentropic, one-dimensional area-Mach number relationship by simply assuming the actual jet boundary to be an extension of the sonic nozzle. The area-Mach number relation used is:

$$\frac{A^*}{A} = M \left[\frac{\gamma + 1}{2(1 + \frac{\gamma-1}{2} M^2)} \right]^{\frac{\gamma+1}{2(\gamma-1)}} \tag{1}$$

where A^* is the sonic nozzle exit area and A is the full local cross-sectional area of the jet flow at a given inner region centerline location as determined from pitot traverses or shadowgraphs, M is the Mach number at the centerline location corresponding to A, and γ is the ratio of specific heats for air (taken as 1.4). The use of the full cross-sectional area of the jet flow (based on the locations where $P_{T1} = P_a$) in Eq. (1) required that the presence of the intercepting shocks, with their attendant anisentropy, be neglected. For the relatively low ratios of nozzle-exit to ambient pressure used in these studies this assumption may be justified for approximate results because the expanded inner region jet flow crossed the weak intercepting shocks at small wave-angles. Using the Mach numbers obtained in this manner, the expected stagnation pressure losses due to the probe bow shock and the Riemann Wave at x/w = 5 and 10 respectively were calculated in Ref. 2 for a $P_N/P_a = 7.81$ jet. These results were found to be in surprisingly close agreement with the experimental results, in spite of the crude assumptions used in this procedure.

Since the jet spread, and thus A, does vary with changes in jet pressure ratio, P_N/P_a, the method proposed in Ref. 2 predicts a varying inner flow region Mach number distribution. However, in reality the inner region Mach number distribution for the underexpanded jet is fixed and independent of P_N/P_a once the

nozzle is choked.[4] This can be easily seen upon examination of the governing equations for two-dimensional, non-viscous, irrotational flow

$$\frac{(M^2 - 1)}{(1 + \frac{\gamma-1}{2} M^2)} \frac{1}{M} \frac{\partial M}{\partial s} - \frac{\partial \theta}{\partial n} = 0 \qquad (2)$$

$$\frac{1}{(1 + \frac{\gamma-1}{2} M^2)} \frac{1}{M} \frac{\partial M}{\partial n} - \frac{\partial \theta}{\partial s} = 0 \qquad (3)$$

where s and n are the streamline co-ordinates and θ is the direction with respect to the centerplane. For M > 1 these equations are hyperbolic and the necessary initial conditions for their solution, as applied to jet flows, are generally taken along the first characteristic from the nozzle lip. For isentropic flow and a given nozzle geometry, the nozzle exit Mach number and flow direction are independent of the nozzle pressure ratio and thus the initial conditions for the jet flow solution are unchanged for varying P_N/P_a. It was confirmed experimentally[1] (using the same arrangement as used in Ref. 2) that over the range of P_N/P_a available in the laboratory the Mach number at a given centerline location in the inner region was constant as theoretically predicted (Fig. 11). At x/w = 8 for $P_N/P_a < 8.5$ no experimental data were recorded since the probe tip was downstream of the Riemann Wave, i.e. no longer in the inner flow region, due to the decreasing length of the inner flow region with decreasing P_N/P_a values.

Shown in this plot are the corresponding Mach numbers for the probe tip at x/w = 5 as calculated from the area-Mach relation[1]. At $P_N/P_a = 7.81$ the ratio of the sonic nozzle exit area, A^*, to the experimentally determined local jet flow full cross-sectional area, A, was found to be 0.128. This yielded a Mach number of 3.65 which is only 6.4 per cent lower than the constant value of 3.90. (Slight differences in the value of A^*/A and the Mach numbers from those of Ref. 2 can be attributed to experimental scatter.) Even closer agreement would have been established if somewhat higher operating P_N values had been used since the area-Mach results appear to approach the actual constant value at the slightly higher pressure ratios. Also shown in Fig. 11 are the centerplane Mach numbers determined from the characteristic solution reported in Ref. 1. In Ref. 1 it was shown that at x/w = 5, the Mach number determined from the approximate Area-Mach Number method is only about 4 per cent lower than that calculated by the characteristic method.[*]
It is thus apparent that while the procedure suggested in Ref. 2 gives close results over a certain range of P_N/P_a values, it is not too promising for use over the entire range. The validity of the main point of Ref. 2, however, is not affected by this modification in the miscellaneous statements.

---

[*] The characteristics solution described in Ref. 1 was of a crude nature (i.e. to facilitate hand calculation the characteristic net was quite coarse) and did not give very close agreement with the experimental shock locations; however, it was adequate for the determination of the centerline Mach number distribution, as comparison with existing partial characteristic solutions and the experimental results showed. Recently Eastmann[4] has formulated a detailed characteristics program which has given good agreement with the normal shock location, etc. for underexpanded axisymmetric jets. However, the authors have not as yet encountered a detailed, complete characteristic solution for a two-dimensional, sonic exit jet flow.

REFERENCES

[1] Sheeran, W. J. and Dosanjh, D. S., "Interacting Jet Flow Investigations, Part I. Further Experiments with Two-Dimensional Underexpanded, Transversely Impinging Jet Flows," Report No. ME 1058-63091, Mechanical Engineering Department, Syracuse University, Syracuse, New York 13210 (copies available from authors),(Sept. 1963).

[2] Dosanjh, D. S. and Sheeran, W. J., "Experiments with Two-Dimensional, Transversely Impinging Jets," AIAA Journal, Vol. 1, No. 2, pp. 329-333, (February 1963).

[3] Dosanjh, D. S. and Sheeran, W. J., "Interaction of Transversely Impinging Jets," Proceedings of the Fluid Amplification Symposium, October 1962, Vol. 1, Diamond Ordnance Fuze Laboratories, Washington, D. C., pp. 217-265, AD 297935 (November 15, 1962).

[4] Eastmann, D. W., "Two-Dimensional or Axially Symmetric Real Gas Flows by the Method of Characteristics, Part II: A Summary of Results from the IBM 7090 Program for Calculating the Flow Field of a Supersonic jet," Boeing Company Report D2-10599 (1962).

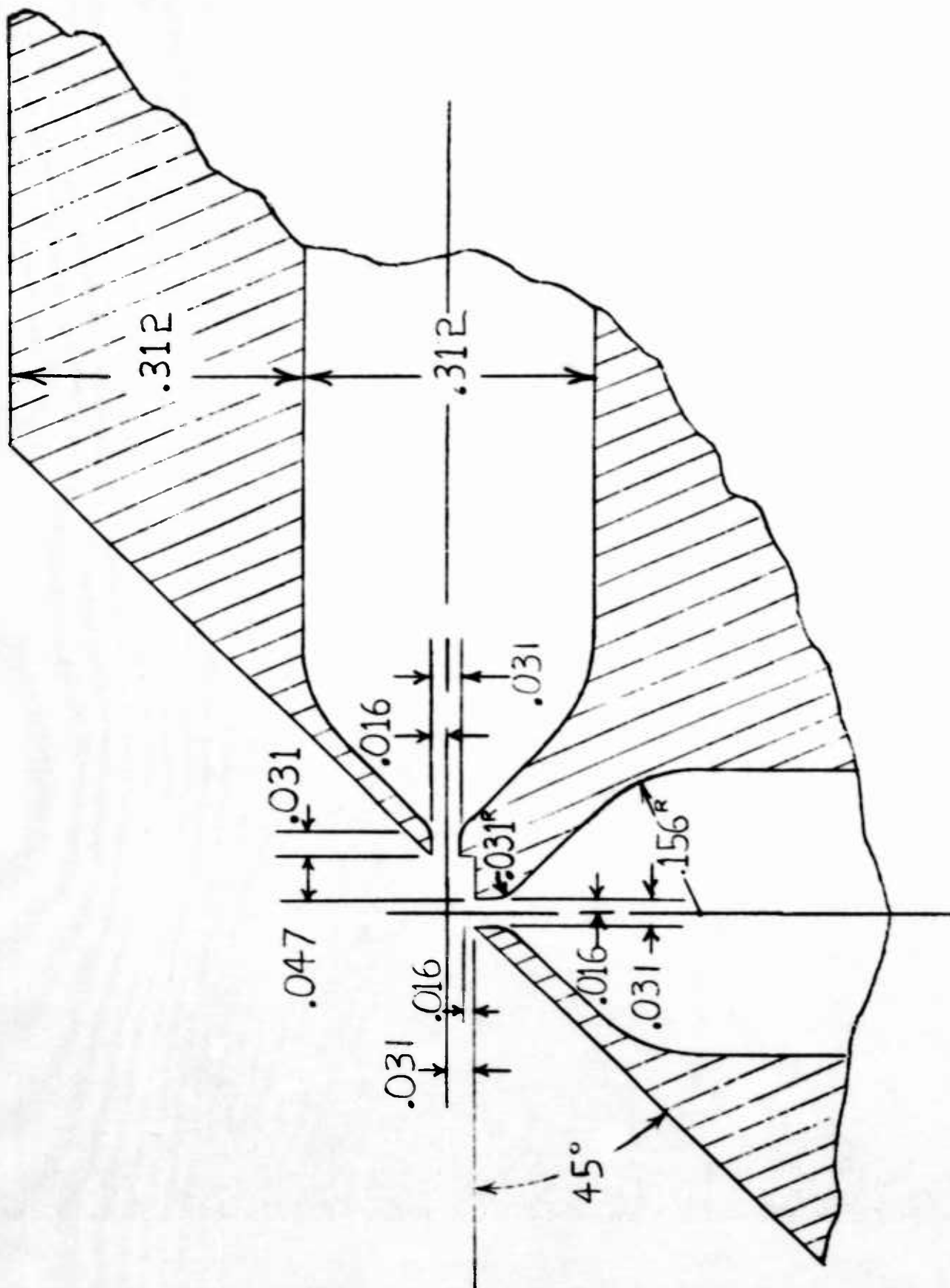FIG. 1. DETAILS OF THE CONVERGING NOZZLES AND THE JET ARRANGEMENT

51
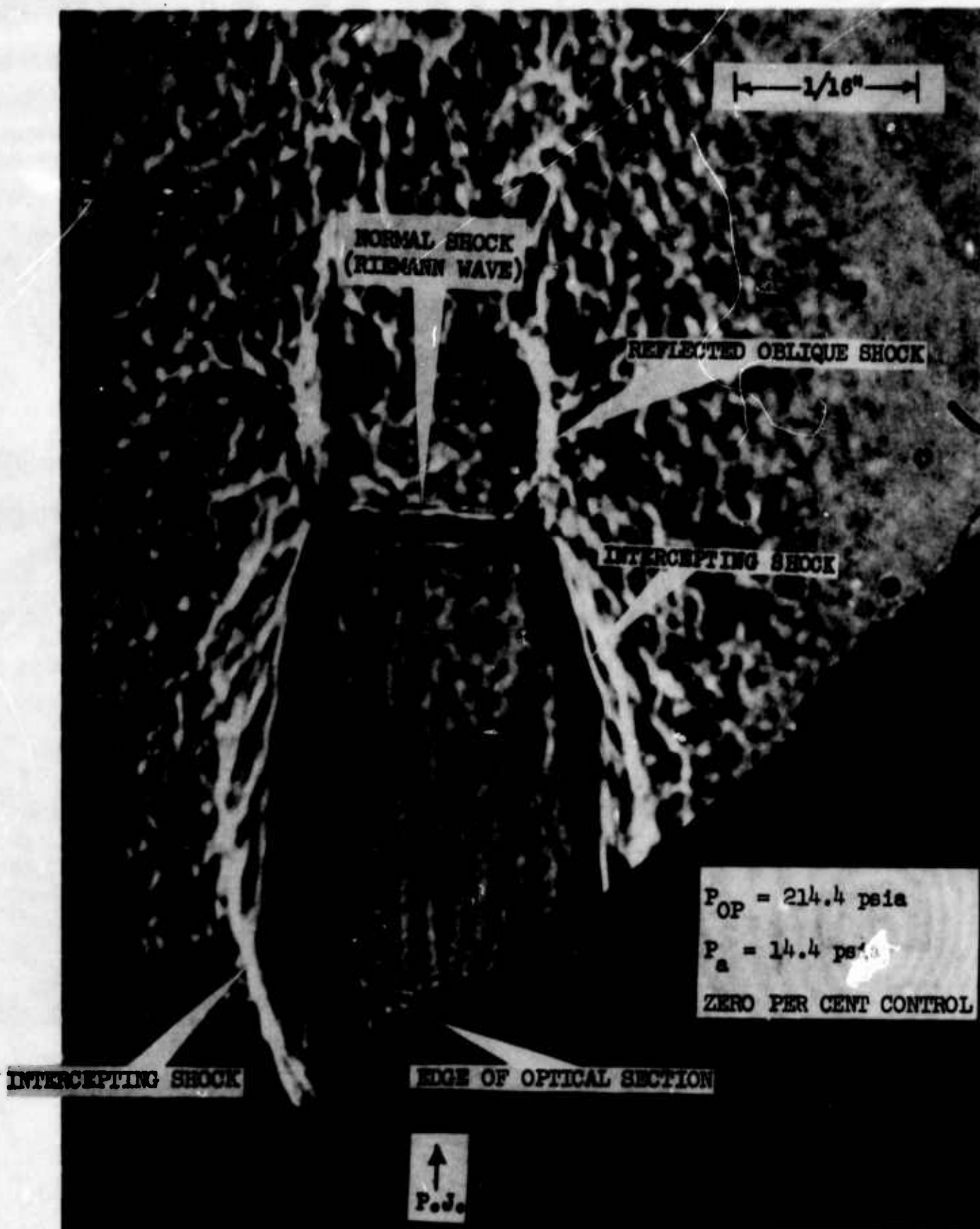
FIG. 2. SHADOWGRAPH OF HIGHLY UNDEREXPANDED TWO-DIMENSIONAL POWER JET FLOW
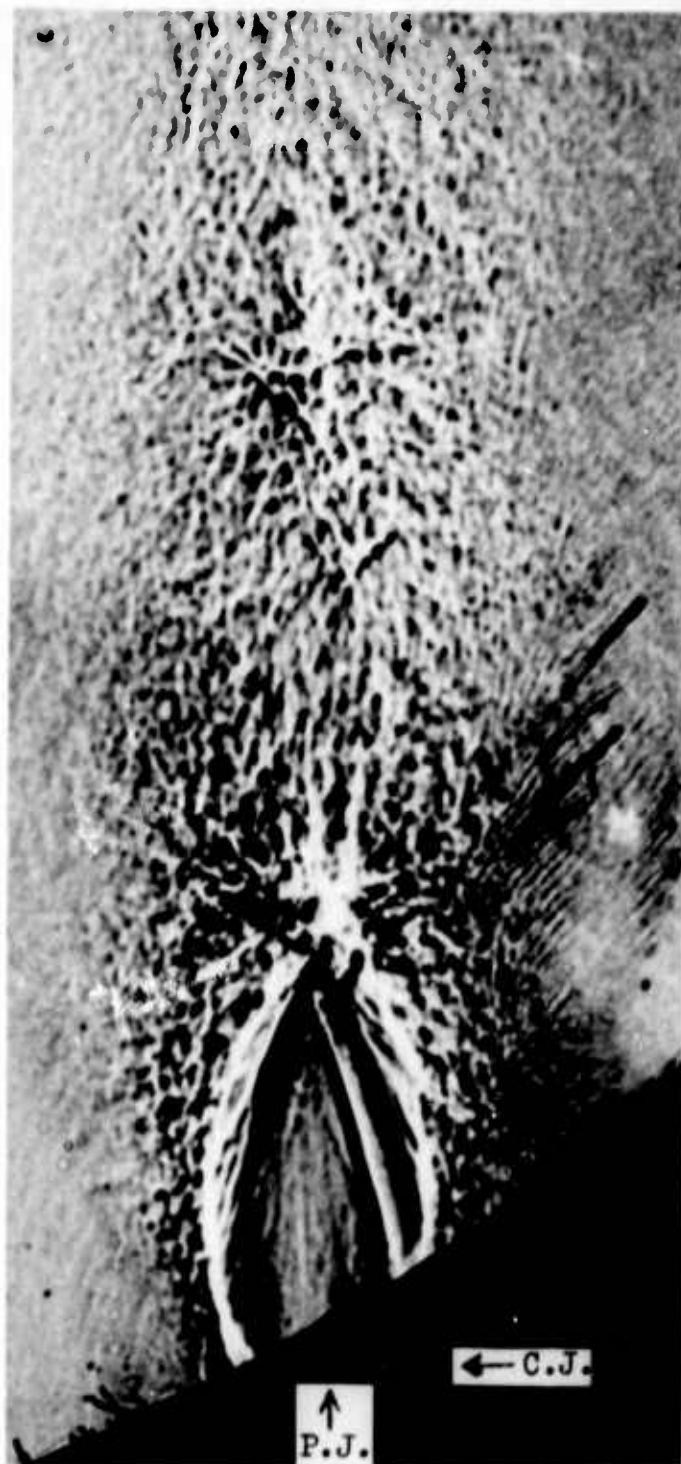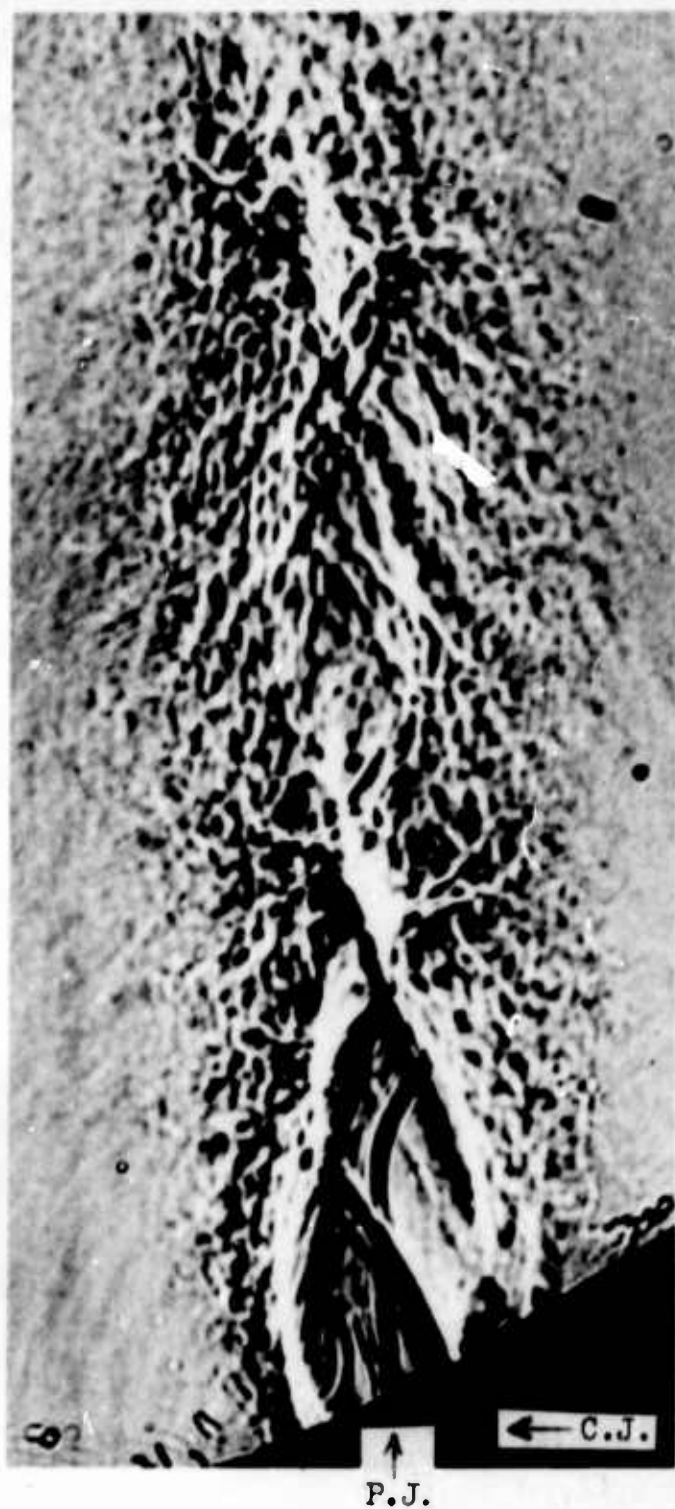
(3a)　2 PER CENT CONTROL　　　　　(3b)　10 PER CENT CONTROL

FIG. 3.　SHADOWGRAPH OF INTERACTING TWO-DIMENSIONAL JET FLOWS
$P_{OP} = 214.6$ psia　　　　　$P_a = 14.6$ psia
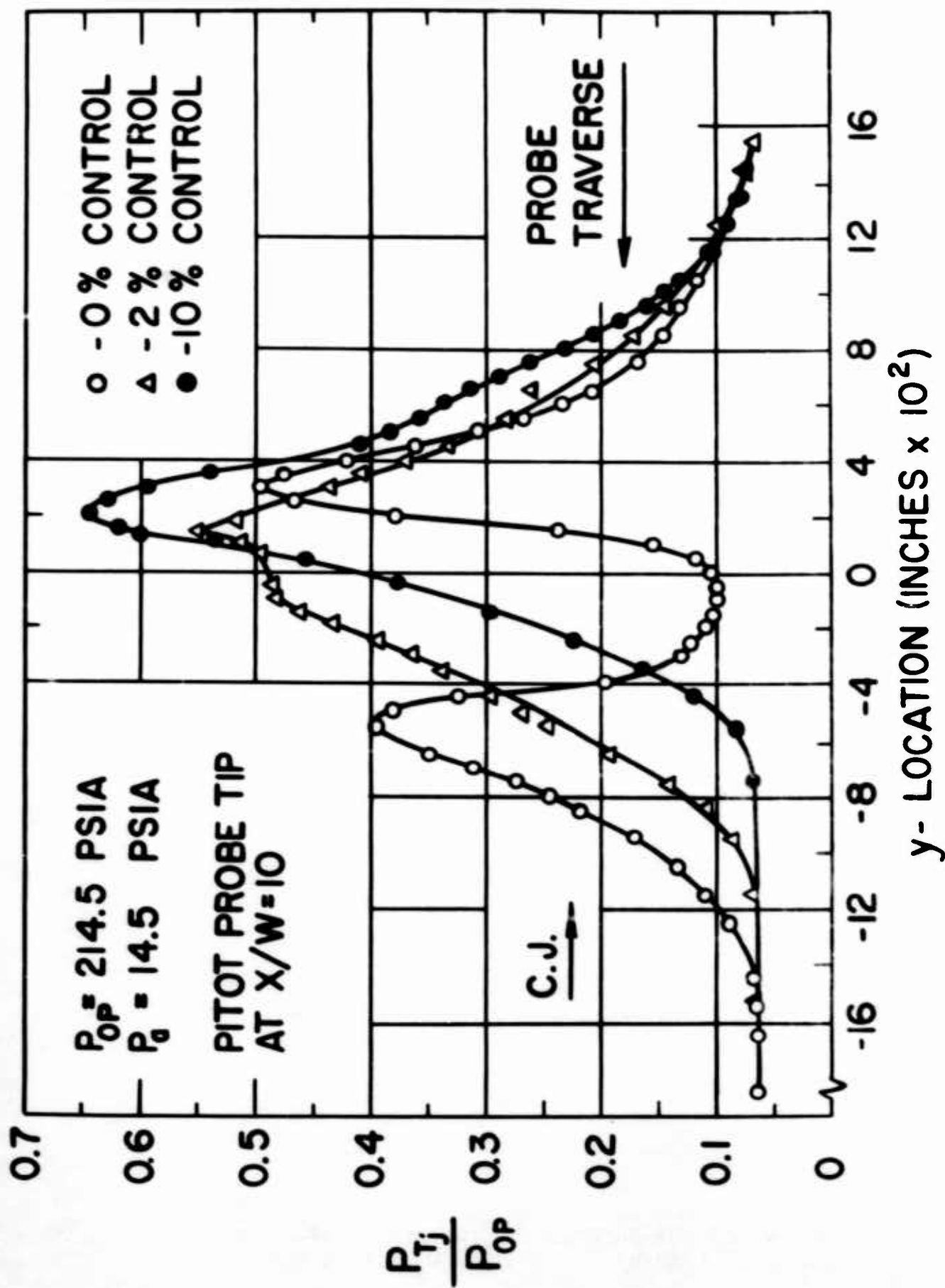
FIG. 4 PITOT PRESSURE DISTRIBUTION AT VARIOUS PERCENT CONTROL
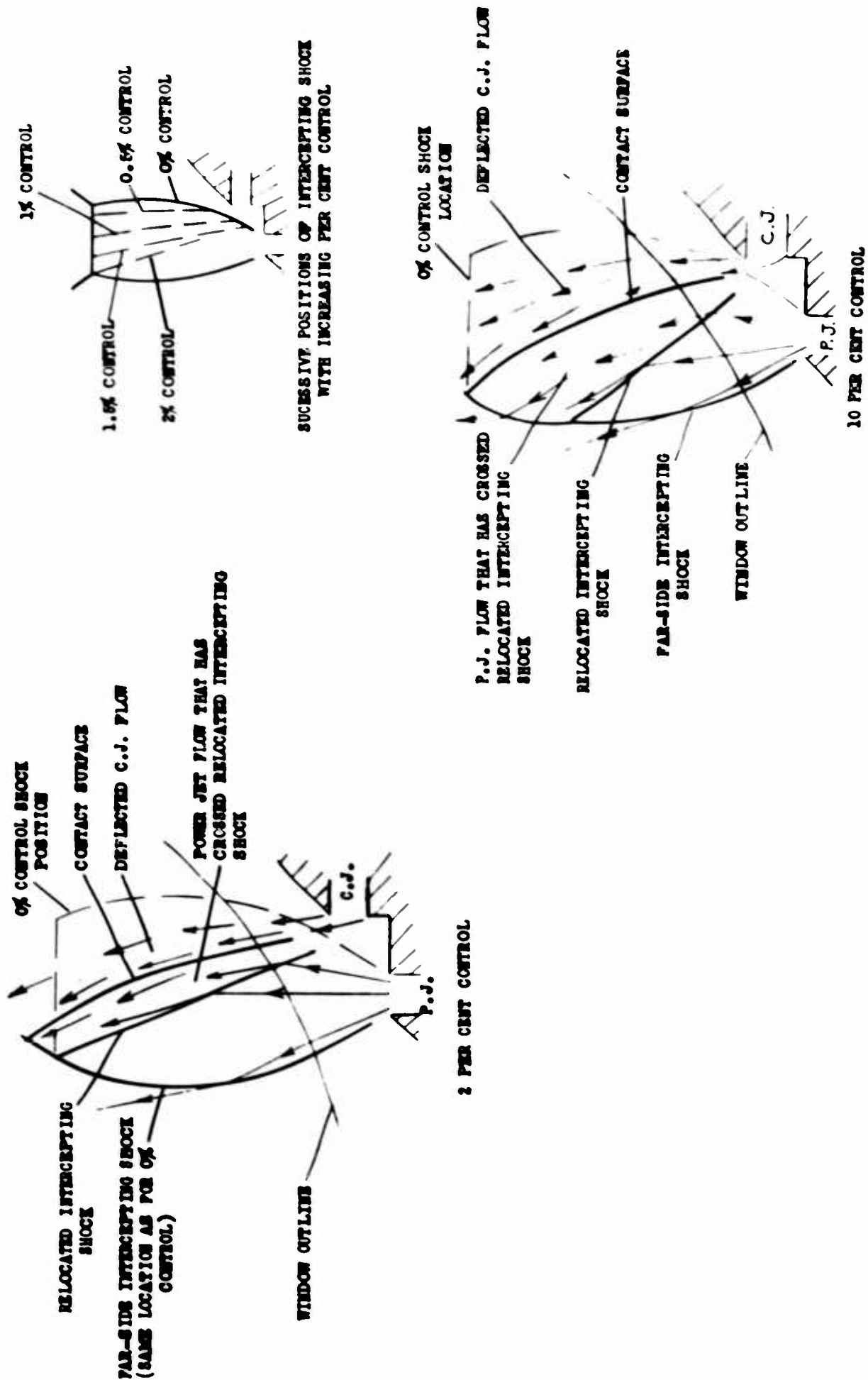
FIG. 5. PROPOSED JET INTERACTION MODEL

55

Within the figure:

$P_{OP} = 214.5$ psia

$P_a = 14.5$ psia

10 PER CENT CONTROL

CONTROL JET NOZZLE BLOCK

APPARENT EXPANSION CENTER

POWER JET EXPANSION CENTER

FIG. 6. SHADOWGRAPH OF TRANSVERSELY IMPINGING JET FLOWS

Labels visible in the figure:

P_OP = 214.5 psia
P_a = 14.5 psia
2 PER CENT CONTROL

CONTROL JET NOZZLE BLOCK

APPARENT CROSSING OF SHOCK STRUCTURE
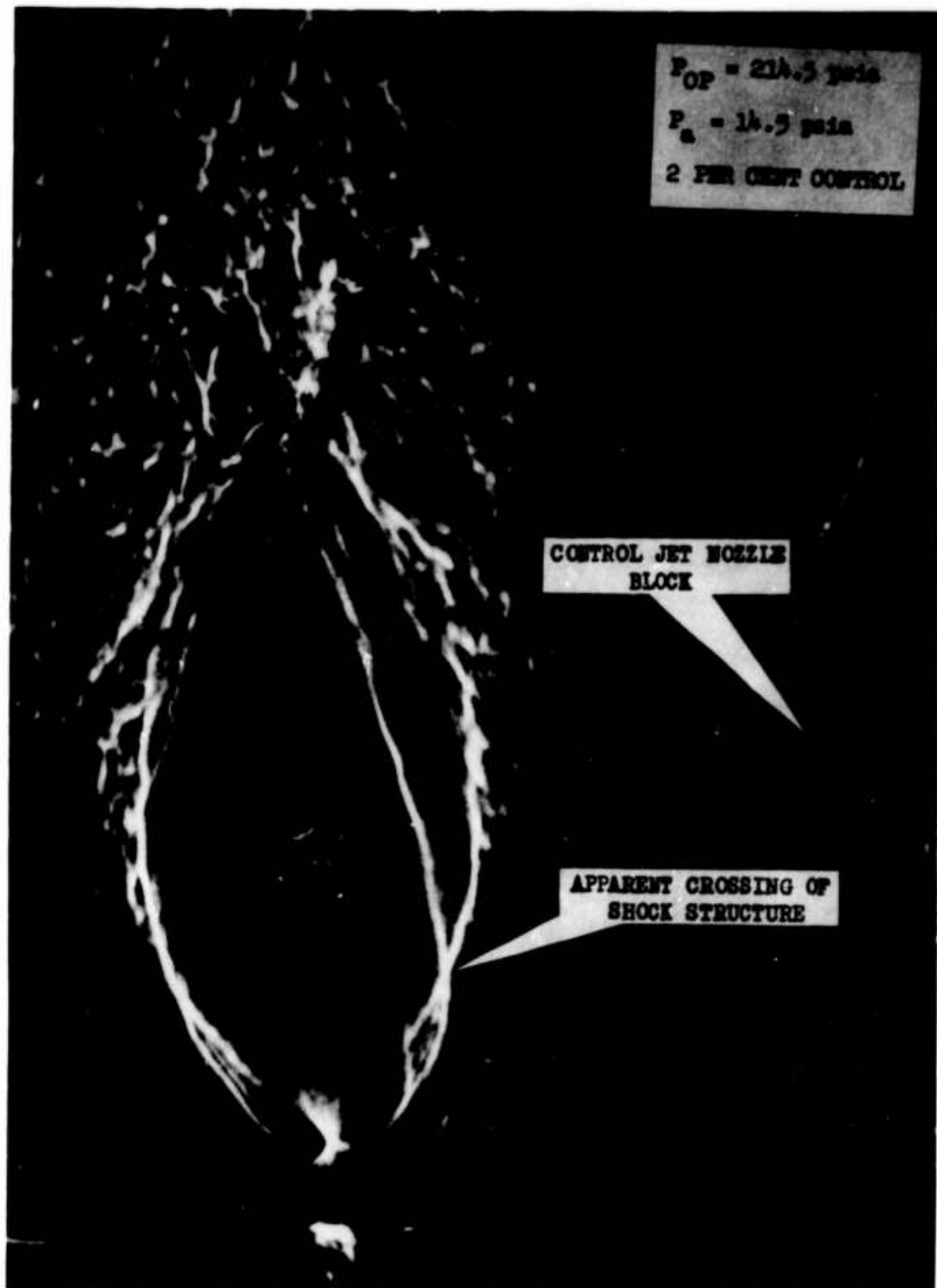
FIG. 7.   SHADOWGRAPH OF TRANSVERSELY IMPINGING JET FLOWS

57

(8b) 10 PER CENT CONTROL

$P_a = 14.5$ psia

(8a) ZERO PER CENT CONTROL

$P_{OP} = 214.5$ psia

FIG. 8. SHADOWGRAPH OF TRANSVERSELY IMPINGING JET FLOWS (SIDE WALLS REMOVED)

58
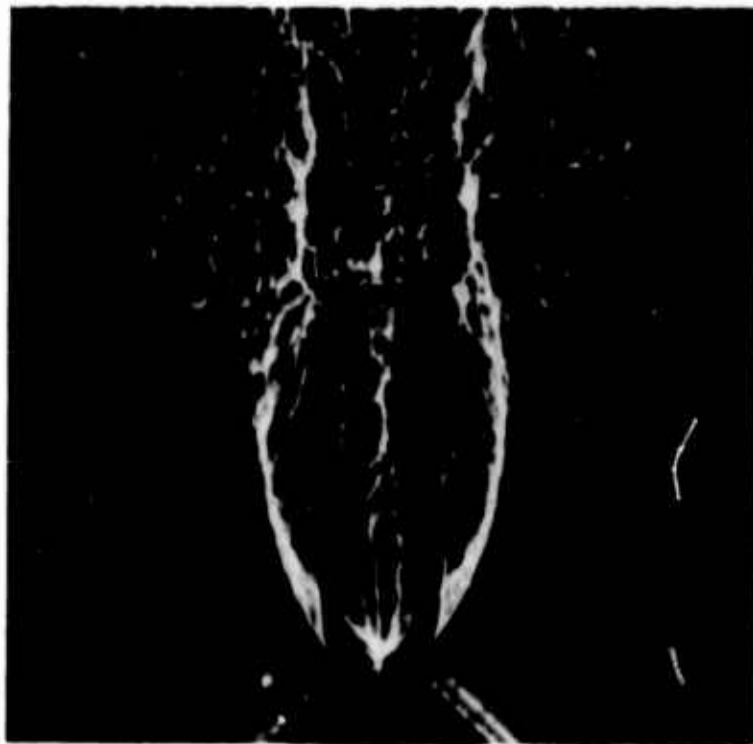
(9a) WITHOUT WIRE
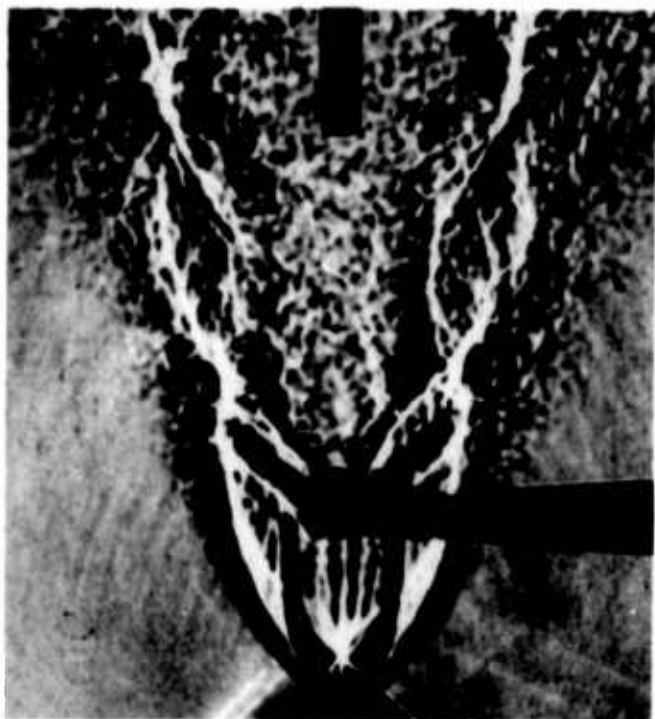
(9b) WIRE AT X/W = 3.18
FILM PARALLEL TO 1/32" DIM.

(9c) WIRE AT X/W = 3.18
FILM PARALLEL TO 3/8" DIM.

FIG. 9. SHADOWGRAPHS OF HIGHLY UNDEREXPANDED, RECTANGULAR EXIT, FREE JET FLOWS

P_{OP} = 214.5 psia P_a = 14.5 psia

59
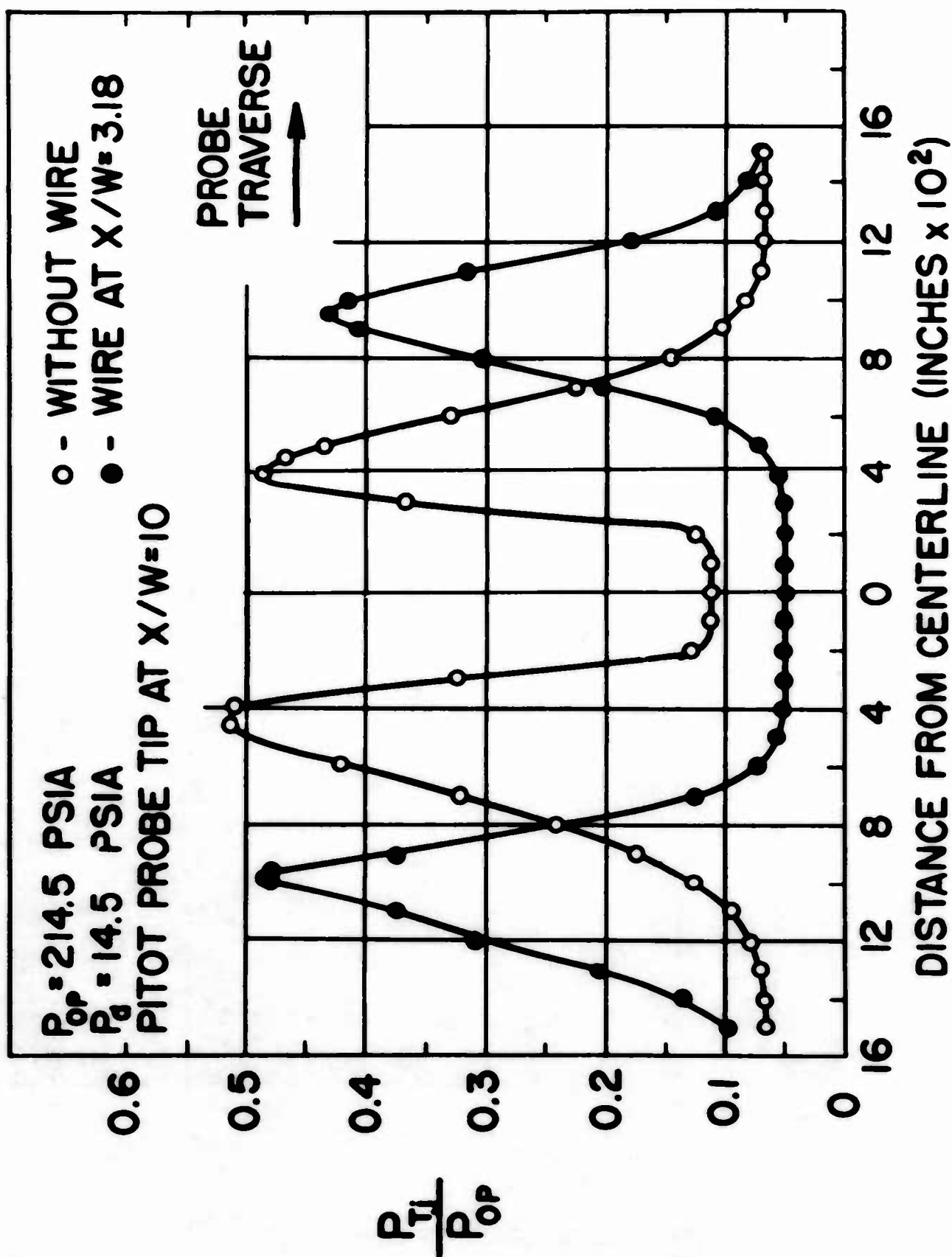
FIG. 10 PITOT PRESSURE DISTRIBUTION OF A FREE JET FLOW WITH AND WITHOUT WIRE

60
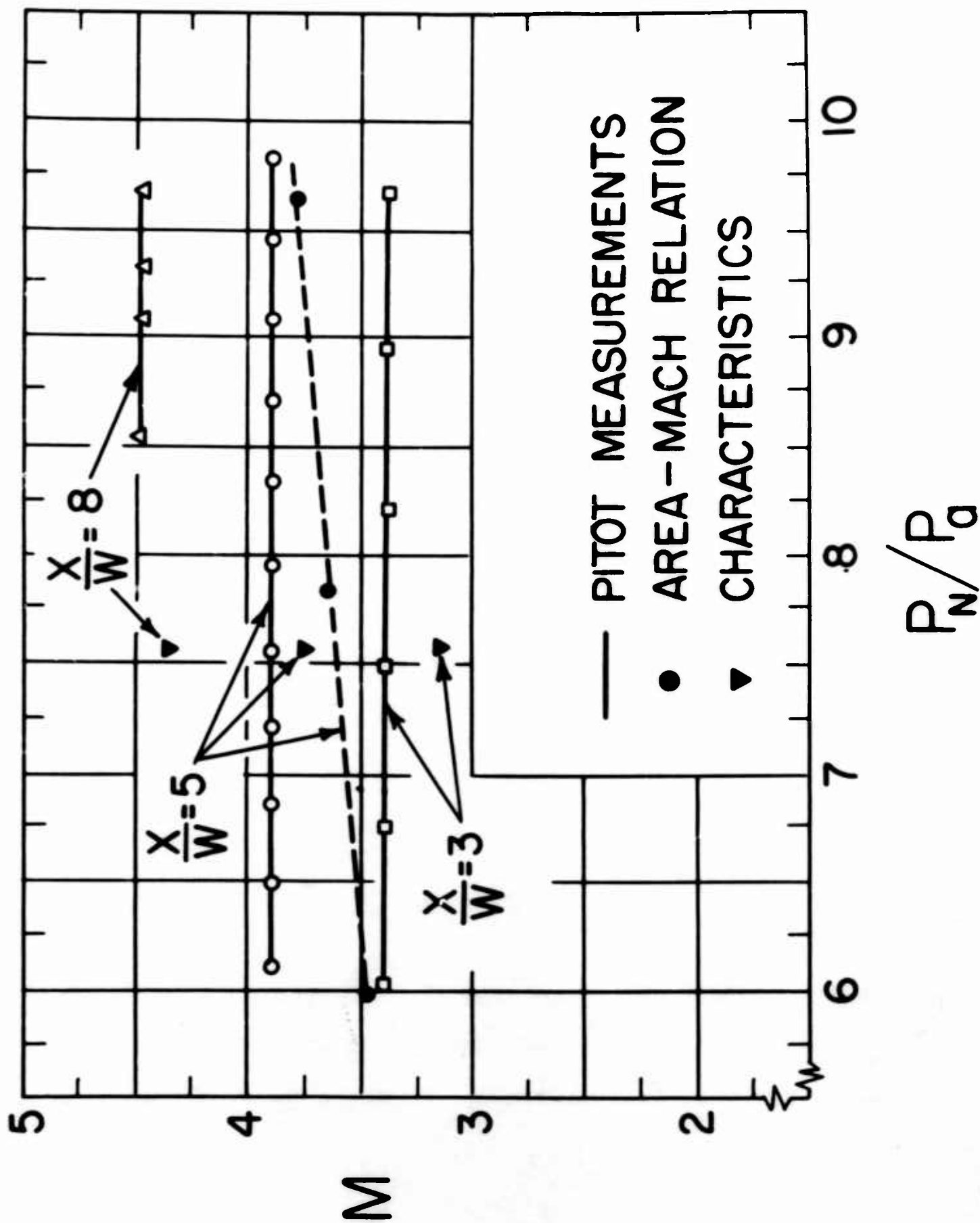
FIG. 11. INNER REGION CENTERLINE MACH NUMBER VS. OPERATING PRESSURE RATIO

61

SPREADING RATES OF COMPRESSIBLE
TWO-DIMENSIONAL REATTACHING JETS

by

Thomas J. Mueller
and
Robert E. Olson

of

United Aircraft Corporation Research Laboratories
East Hartford, Connecticut

ABSTRACT

The results of an investigation of the spreading rates of compressible two-dimensional reattaching jets and tangential wall jets are reported. For the reattaching jets four initial jet Mach numbers - two subsonic and two supersonic - were investigated for each of two setback distances and two angles of the adjacent wall. Three initial jet Mach numbers - two subsonic and one supersonic - were employed for the tangential wall jet. These data are presented along with previously reported free jet data.

Velocity profiles were obtained from a combination of pitot pressure surveys across the jet and static pressure measurements along the wall and jet-centerline by assuming a constant total temperature throughout the jet.

Values of the spread parameter were obtained for each type of jet flow by fitting the nondimensional velocity profiles to the Gaussian profile and the error function profile in the region where the velocity ratio is 0.5. Using these values of the spread parameter, a comparison was made of typical experimental nondimensional velocity profiles with the theoretical error function and Gaussian velocity profiles. The significance of this comparison and the spreading rates obtained are discussed in relation to the velocity profile development characteristics of jet flows in fluid amplifiers.

This investigation was undertaken as part of a general study of the aerodynamic characteristics of two-dimensional turbulent compressible jets being conducted for the Harry Diamond Laboratories under Contract DA-49-186-AMC-66(X).

INTRODUCTION

The spreading rates of both axisymmetric and two-dimensional com-
pressible turbulent jet flows have been the subject of continued interest
because of their frequent use in analytical models of jet mixing phenomena. The center of attention in the jet spreading phenomena has been the
empirical coefficient referred to as the jet spread parameter or similarity
parameter. This jet spread parameter is an aggregate empirical coefficient
which is introduced to describe such aspects of turbulent mixing as
velocity profiles, shear stresses and the equivalent turbulent eddy
viscosity.

Because the jet spread parameter is an aggregate empirical coefficient
its exact determination by strictly analytical means is not possible.
Recently a semi-empirical formulation of this parameter for constant
pressure mixing was presented [Ref. 1]. Although this formulation shows
reasonable agreement with available free jet data within limited ranges of
the flow variables, more experimental verification is needed. It should be
pointed out that since the assumption of constant pressure mixing is used,
this method would not be suitable for the non-constant pressure mixing
zones of reattaching jets.

Usually the jet spread parameter is determined by fitting experimental
nondimensional velocity profiles to the theoretical velocity distribution
which shows the best correlation of the data [Refs. 2 and 3]. In addition
to the tedious calculations involved, the value of the jet spread parameter
obtained is sensitive to the theoretical velocity distribution chosen
[Ref. 4]. However, since the jet spread parameter is usually identified
with the rate of change of the inflection point tangent of the velocity
profile, the numerical values of this parameter obtained using one theoreti-
cal velocity distribution may be interpreted for another theoretical
velocity distribution by matching the slopes of the two velocity distri-
butions in the region of the inflection point.

Since the underlying motive for this work is to supply empirical in-
formation necessary to improve analytical methods of predicting the aero-
dynamic characteristics of digital fluid jet control devices, the primary
concern will be jet flows within two-dimensional models. For purposes
of comparing the spreading rates of reattaching jets and tangential wall
jets to free jets, however, axisymmetric free jet data will be used because
of its availability from a single source for both subsonic and supersonic
flows.

EXPERIMENTAL APPARATUS AND PROCEDURE

The test rig (described in detail in Refs. 5 and 6) was two-dimensional and was provided with hinged sidewalls 3 inches apart. Removable nozzle blocks were utilized so that both subsonic and supersonic jet Mach numbers could be obtained. Subsonic jet Mach numbers were obtained with an ASME elliptical convergent nozzle. Convergent-divergent nozzles designed for uniform flow at the exit were employed to obtain supersonic jet Mach numbers. The exit height, w , for all nozzles was equal to 0.50 inch, thereby providing an aspect ratio equal to 6.0. The plates downstream of the nozzle blocks were adjustable to vary both setback, S , and wall angle, Θ . A separate plate was used for the tangential wall jet experiments. Airflow was supplied at an upstream total pressure of approximately 22 psia and a total temperature of 80° F and was exhausted through laboratory vacuum pumps for all tests. Reynolds numbers based on the nozzle exit width of approximately 2.5 x 10^5 (depending on jet Mach number) were obtained with these upstream conditions.

For the plates which were adjustable to vary both setback and wall angle, fifty pressure taps were provided along one of the boundary walls. These pressure taps were located along the centerline and on a line 0.75 inch from the centerline. The separate tangential wall jet plate also had fifty pressure taps located along the centerline and along a line 0.75 inch from the centerline. These pressure taps were used to measure the wall static pressure distributions.

A variable-position pitot pressure probe was employed to obtain surveys through the stream. In order to obtain static pressure measurements along the jet centerline (defined as the locus of points of maximum stream velocity) a special probe was employed. This probe consisted of a slotted hypotube which was bent to the contour of the jet centerline. A second movable hypotube with a static pressure orifice was contained within the first. The slot in the first hypotube was oriented so that the static pressure orifice faced the side plate. The hypotube extended upstream into the plenum chamber and downstream to the end of the boundary walls.

The boundary layer thickness on one side of the nozzle at the exit which forms an initial condition for the ensuing mixing process was less than 0.01 inches. This resulted in a maximum boundary layer momentum thickness of less than 0.001 inche

MIXING CHARACTERISTICS OF REATTACHING JET FLOWS

The general features of reattaching jets, tangential wall jets, and free jets are shown in Fig. 1. An examination of these three jet flows indicates that the mixing in the core regions of these flows is of the jet boundary type. This observation together with insufficient data to the contrary has prompted many investigators to assume that all of these jet boundary mixing zones spread at the same rate. Certainly at subsonic velocities there is little reason to suspect different spreading rates for the jet boundary mixing in the free jet and the tangential wall jet; that is, unless the stabilizing effect of the wall significantly affects the mixing process. For supersonic velocities where the interactions of compression and rarefaction waves are significant and somewhat different for the free jet and tangential wall jet, it can be expected that the spreading rates for these two jet flows will differ slightly.

On the contrary, there is little reason to believe, á priori, that the spreading rates for reattaching jets - either subsonic or supersonic - will be identical to those of the free jet and/or the tangential wall jet. At subsonic velocities it seems logical to expect that the spreading rates for the outer mixing zone in the core region of a reattaching jet will probably not be significantly different from those of a free jet and a tangential wall jet. For the inner mixing zone, however, a somewhat lower spreading rate would be expected due to the dampening influence of the wall. It is precisely the spreading rate of this inner mixing zone which is an important factor in analyzing the separation bubble and in determining the location of jet reattachment [Ref. 7] . For supersonic reattaching jet flows the presence of strong compression waves and rarefaction waves modifies the mixing processes in both the inner and outer mixing zones. Hithertofore, the assumption that this inner mixing zone spreads like a free jet has been used [Ref. 5] .

As for the outer mixing zone downstream of reattachment (no longer jet boundary type mixing), after some initial adjustment length downstream of reattachment the spreading rates should approach those of the tangential wall jet in the developed region. The spreading rate of this outer mixing zone is an important consideration in optimizing the location of the diffuser entrance in digital fluid jet devices.

All in all there are as many similarities as there are dissimilarities in these three types of jet flows and a comparison of their spreading rates should be helpful in pointing this out.

66

Since the jet spread parameter is sensitive to the theoretical velocity distribution chosen for the correlation it is important at the outset to support any such choice.

Figures 2 and 3 indicate the correlation of the two-dimensional tangential wall jet data with the Gaussian and frequently used error function distribution. It is clear from these figures that the Gaussian velocity distribution given as:

$$u/u_c = e^{-B_1(\xi/\xi^*)^2} \tag{1}$$

where $B_1 = 0.6931$ FOR $u/u_c = 0.5$ AT $\xi/\xi^* = 1.0$

represents the best fit of this data. It was also found that the Gaussian distribution offered the best correlation of the data taken in both the inner and outer mixing zones of the reattaching jet. Typical nondimensional velocity profiles for the inner and outer mixing zones upstream of reattachment[1] and for the outer mixing zone downstream of reattachment are shown in Figs. 4 and 5.

JET SPREAD PARAMETER

The jet spreading rate is defined as the rate of increase of the width of the mixing zone in the downstream direction. Furthermore, the jet spread parameter is inversely proportional to this spreading rate; i.e., the larger the value of σ the smaller the spreading rate.

Once a particular theoretical velocity distribution has been chosen and velocity profile similarity demonstrated, it is a relatively simple matter to compute the jet spread parameter. For the Gaussian velocity distribution given in Eq. (1), $\xi^* = x/\sigma_G$. The mixing zone width, ξ^* , can be presented in explicit form by differentiating Eq. (1) with respect to ξ as follows:

$$\frac{d(u/u_c)}{d\xi} = - \frac{2(0.6931)}{\xi^*} e^{-0.6931(\xi/\xi^*)^2} \tag{2}$$

---

[1] For reattaching jets studied the flow field can be conveniently divided by the reattachment location since the end of the core region occurs near this location.

However, $\xi = \xi^*$ at $u/u_c = 0.5$; therefore

$$\xi^* = \frac{-0.6931}{\left[\dfrac{d(u/u_c)}{d\xi}\right]_{\frac{u}{u_c} = 0.5}} \tag{3}$$

The quantity ξ^* can be determined for the Gaussian velocity profile by knowing the slope of the experimental velocity profile at the location where $u/u_c = 0.5$. While taking slopes from experimental curves was somewhat less than desirable, every precaution was exercised to insure accurate results.

Finally, σ_G is obtained by taking the inverse of the slope of the ξ^*/w versus x/w plot as shown in Fig. 6. In all the cases for which data are presented in this paper the plots of ξ^*/w versus x/w (of which Fig. 6 is a typical example) were linear.

It should be noted that the curves in Fig. 6 for the inner and outer mixing zones upstream of reattachment were drawn through the origin. Theoretically, if curves of this type are extrapolated to zero mixing region width, an approximate virtual origin of the mixing process is obtained. This virtual origin of the mixing region is a consequence of the boundary layer build-up along the nozzle wall and results in a finite mixing region width at the nozzle exit. According to the method of Ref. 9, for our maximum boundary layer momentum thickness at the nozzle exit of 0.001 inches, the virtual origin would be located approximately 0.03 inches upstream of the nozzle exit. This very small change in the origin of the mixing process from the nozzle exit was neglected in this investigation.

Values of σ_G obtained for the reattaching jets and tangential wall jets as a function of Mach number are shown in Fig. 7. For purposes of comparison, Fig. 7 also includes available axisymmetric free jet data and an incompressible two-dimensional free jet data point - in the core region - evaluated for the Gaussian velocity profile by the method suggested in Ref. 4.

In the outer mixing zone upstream of reattachment, the jet spread parameter shows good agreement with the axisymmetric free jet values at subsonic Mach numbers, see Fig. 7A. However, as the Mach number increases above one, the σ_G for the reattaching jet does not increase as rapidly as that for the axisymmetric free jet. This indicates that for supersonic flow the outer mixing region upstream of reattachment spreads faster than

68

does a free jet at the same Mach number. The difference in the free jet
and the reattaching jet spreading rates may be attributed to the differences
in the compression and rarefaction wave interactions with the mixing region
for the two jet flows. While the values of σ_G for the tangential wall jet
also shown on Fig. 7A agree with the axisymmetric free jet at subsonic Mach
numbers, at a Mach number of 2.0 the value of σ_G is somewhat lower.

For the inner mixing zone upstream of reattachment, the jet spread
parameter is larger than for the axisymmetric free jet at subsonic and
supersonic Mach numbers as indicated in Fig. 7B. These larger values point
out how the dampening influence of the wall produces lower spreading rates.
The data for the tangential wall jets are also included on Fig. 7B for
purposes of comparison.

The variation of the jet spread parameter with Mach number for the outer
mixing zone downstream of reattachment (i.e., downstream of the core region)
is shown in Fig. 7C. These values are about twice as large as those for
mixing in the core region of the axisymmetric free jet. This is contrary
to what has been found to be the case for free jets. For free jets - both
compressible [Ref. 6] and incompressible [Ref. 8] - experiments show that
the spreading rate is larger in the developed region than in the core region
(i.e., the value of σ in the developed region is smaller than that in the
core region). These lower spreading rates in reattaching jets may be
traced to the rapid decay of turbulent transport quantities across and
beyond the reattachment region [Ref. 10] .

REFERENCES

1. Channapragada, R. S.: Compressible Jet Spread Parameter for Mixing Zone Analyses. AIAA Journal, Vol. 1, 1963, pp. 2188-2189.

2. Maydew, R. C., and J. F. Reed: Turbulent Mixing of Axisymmetric Compressible Jets (in the Half-Jet Region) with Quiescent Air. Saudia Corp. Research Report SC-4764, March 1963.

3. Maydew, R. C., and J. F. Reed: Turbulent Mixing of Compressible Free Jets. AIAA Journal, Vol. 1, 1963, pp. 1443-1444.

4. Rosler, R. S.: Comment on "Turbulent Mixing of Compressible Free Jets". AIAA Journal, Vol. 1, 1963, pp. 2413-2414.

5. Olson, R. E.: Reattachment of a Two-Dimensional Compressible Jet to an Adjacent Plate. ASME Symposium on Fluid Jet Control Devices, 1962.

6. Olson, R. E., and D. P. Miller: Aerodynamic Studies of Free and Attached Jets. United Aircraft Corporation Research Laboratorie Report A-1771-24, December 1963.

7. Mueller, T. J.: An Experimental Investigation of the Reattachment of Compressible Two-Dimensional Jets. Submitted for presentation at the Symposium on Fully Separated Flow, ASME Hydraulic Conference, May 18-21, 1964, Philadelphia, Pennsylvania.

8. Schlichting, H.: Boundary Layer Theory. Fourth Edition, McGraw-Hill Book Co., 1960.

9. Kirk, F. N.: An Approximate Theory of Base Pressure in Two-Dimensional Flow at Supersonic Speeds. R.A.E. Tech. Note Aero. 2377, 1954. (Published 1959.)

10. Mueller, T. J., and J. M. Robertson: A Study of the Mean Motion and Turbulence Downstream of a Roughness Element. Published in Developments in Theoretical and Applied Mechanics, Vol. 1, Plenum Press, New York, 1963, pp. 326-340.

NOMENCLATURE

B_i Constant in Eq. (1)

L   Distance along plate measured from nozzle exit

L_R Distance between nozzle exit and reattachment point measured along plate

M_0 Initial jet Mach number

p_e Static pressure on free boundary of jet

p_0 Nozzle exit static pressure

p_{t_0} Nozzle exit total pressure

S   Distance between plate and inner contour of nozzle at nozzle exit - referred to as setback

u   Mean velocity parallel to jet centerline

u_c Mean velocity on jet centerline

u_0 Mean velocity at nozzle exit

u_{MAX} Maximum mean velocity in jet at a given streamwise station

w   Total height of nozzle at exit

x   Distance along jet centerline

x_c Distance between nozzle exit and end of core region

y   Distance perpendicular to jet centerline

y_B Distance perpendicular to boundary wall

y' Distance perpendicular to jet centerline measured from location where $u/u_c = 0.5$

Θ Angle of plate relative to nozzle centerline

η $\eta = \sigma \dfrac{y'}{x}$

ξ Distance from boundary of mixing zone perpendicular to jet centerline

ξ^* Distance from boundary of mixing zone to location where $u/u_c = 0.5$

σ Jet spread parameter

σ_G Jet spread parameter obtained from correlation with Gaussian velocity distribution

72
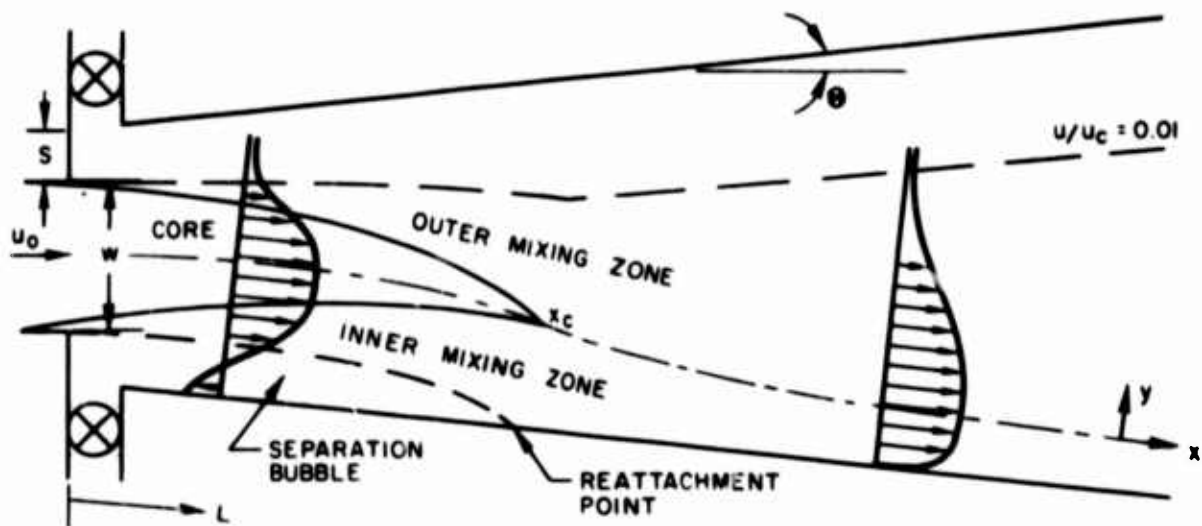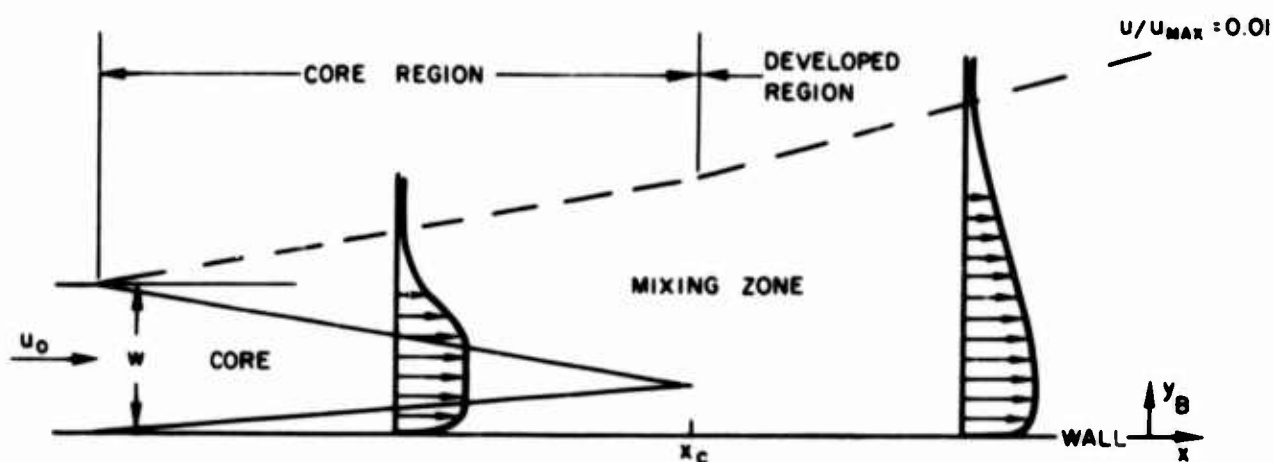
A. REATTACHING JET

B. TANGENTIAL WALL JET
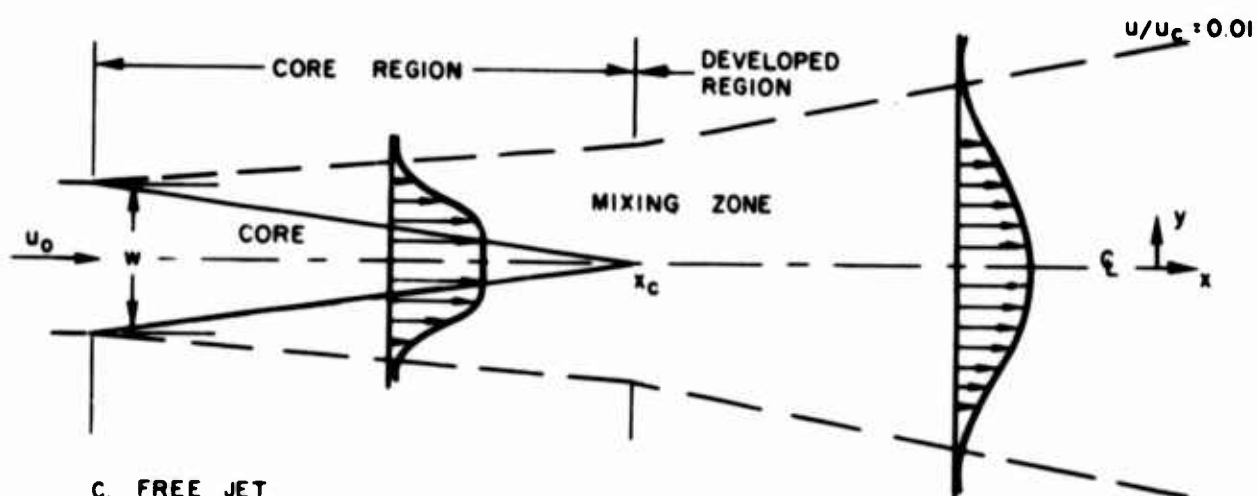
C. FREE JET

FIGURE 1 GENERAL FEATURES OF REATTACHING JET, TANGENTIAL WALL JET,
AND FREE JET FLOW MODELS

73

$M_0 = 0.895$

$p_e = p_0$

SYMBOL	O	□	◇	◖	▽	◗	△
x/w	1	2	3	4	5	6	7

$$u/u_c = e^{-0.6931(\xi/\xi^*)^2}$$
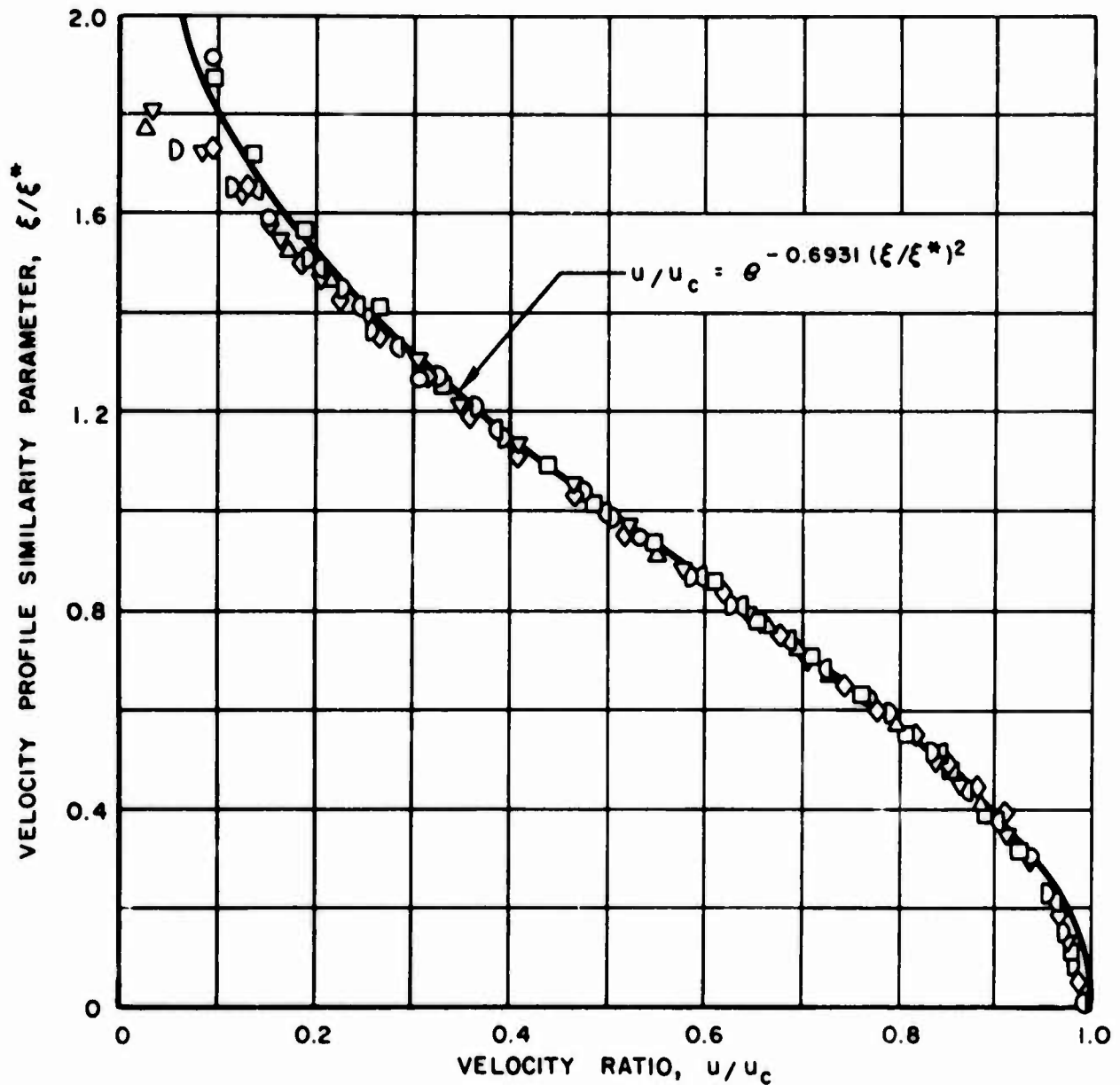
FIGURE 2 NONDIMENSIONAL VELOCITY PROFILES IN MIXING ZONE OF CORE REGION FOR TANGENTIAL WALL JET
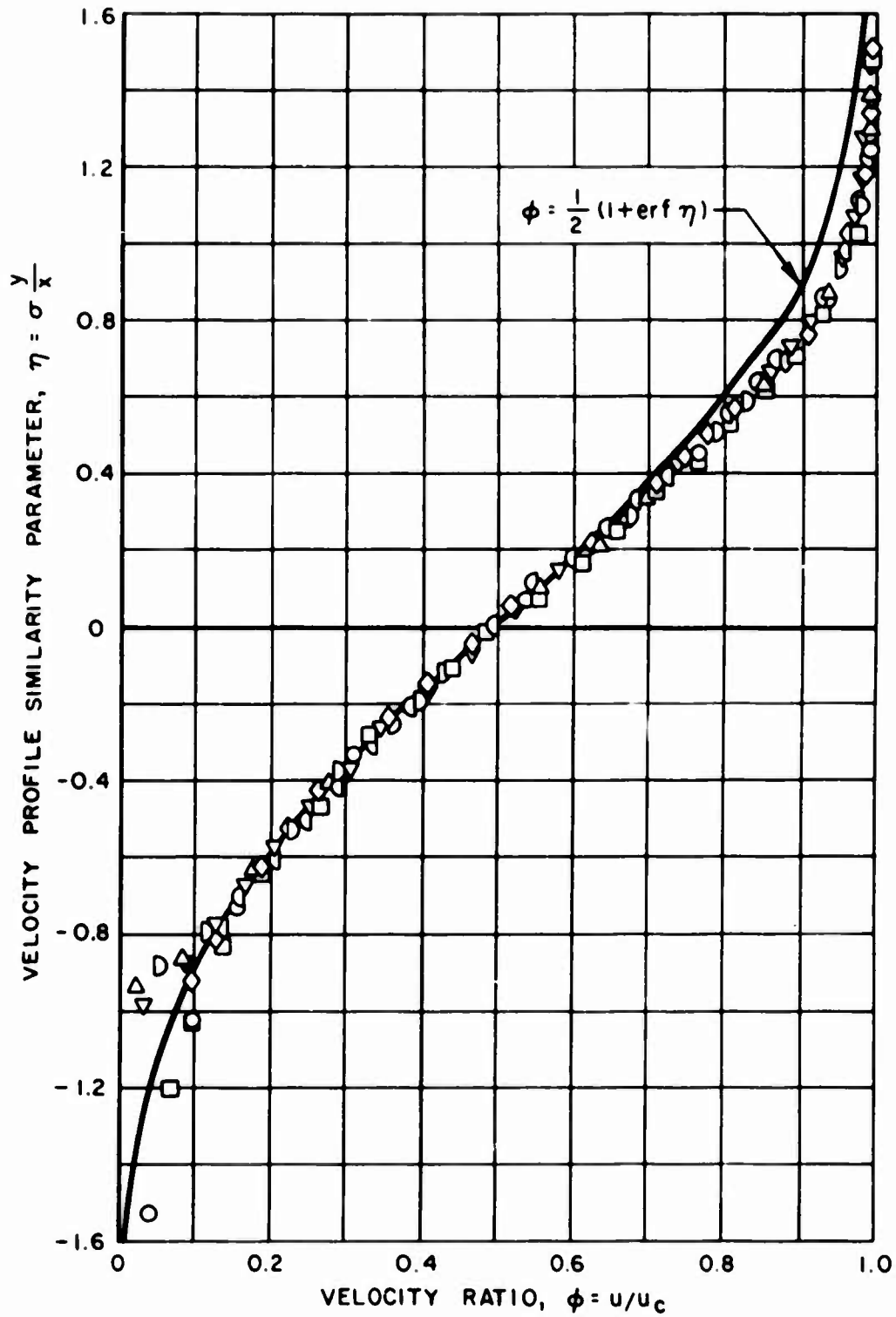
FIGURE 3 NONDIMENSIONAL VELOCITY PROFILES IN MIXING ZONE OF CORE REGION FOR TANGENTIAL WALL JET

75

$M_0 = 0.66$
$S/w = 0.5$
$\theta = 14°$
$p_e = p_0$

SYMBOL	O	□
x/w	1.3	2.3

OPEN SYMBOLS DENOTE OUTER MIXING ZONE
SOLID SYMBOLS DENOTE INNER MIXING ZONE

$$u/u_c = \theta^{-0.6931(\xi/\xi^*)^2}$$

VELOCITY PROFILE SIMILARITY PARAMETER, ξ/ξ^*

VELOCITY RATIO, u/u_c
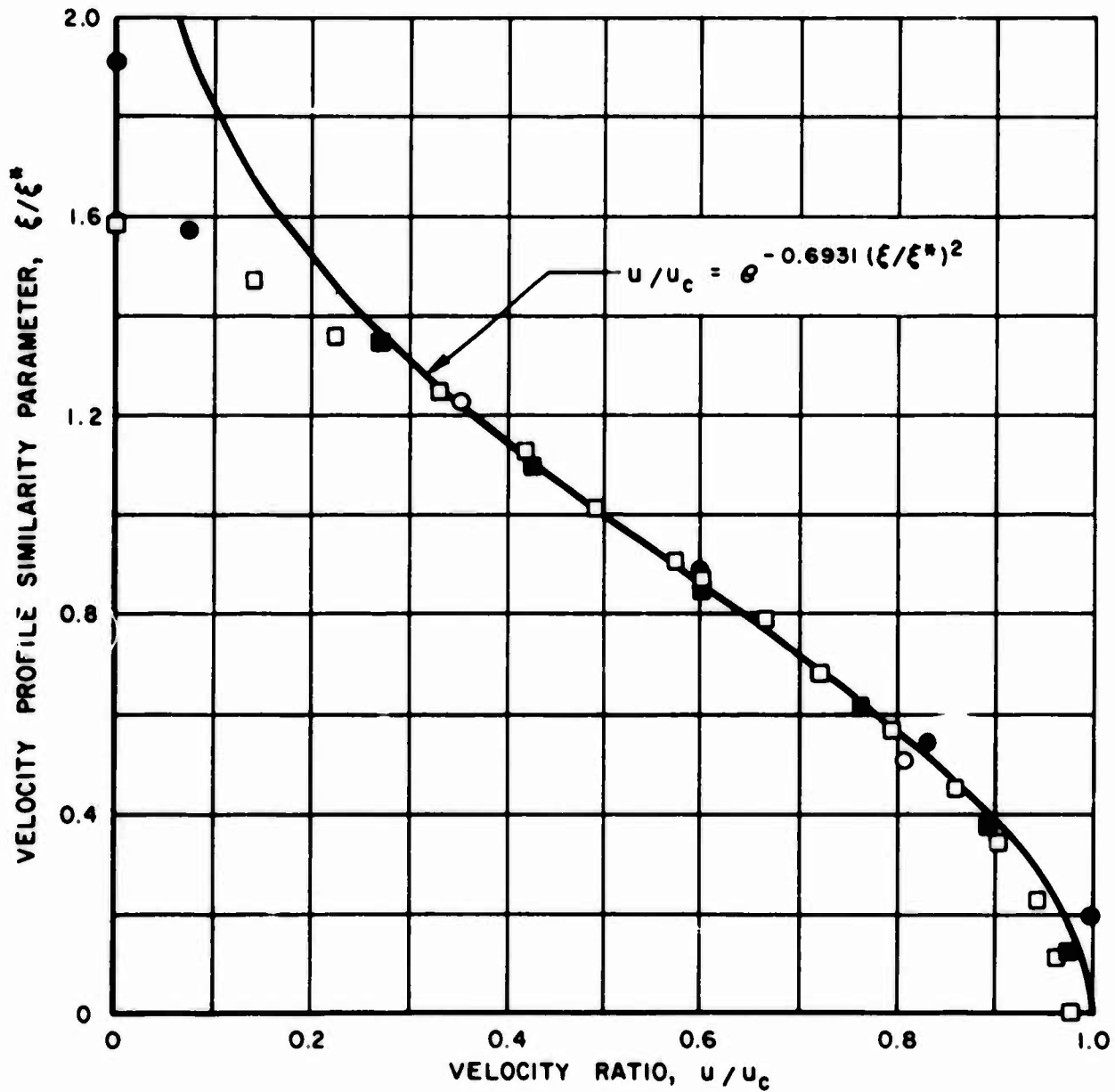
FIGURE 4 NONDIMENSIONAL VELOCITY PROFILES UPSTREAM OF REATTACHMENT
FOR INNER AND OUTER MIXING ZONES

76

SYMBOL	O	□	◇	◁	▽
x/w	4.3	6.3	8.3	10.3	12.3

FIGURE 5 NONDIMENSIONAL VELOCITY PROFILES DOWNSTREAM OF REATTACHMENT FOR OUTER MIXING ZONE

77
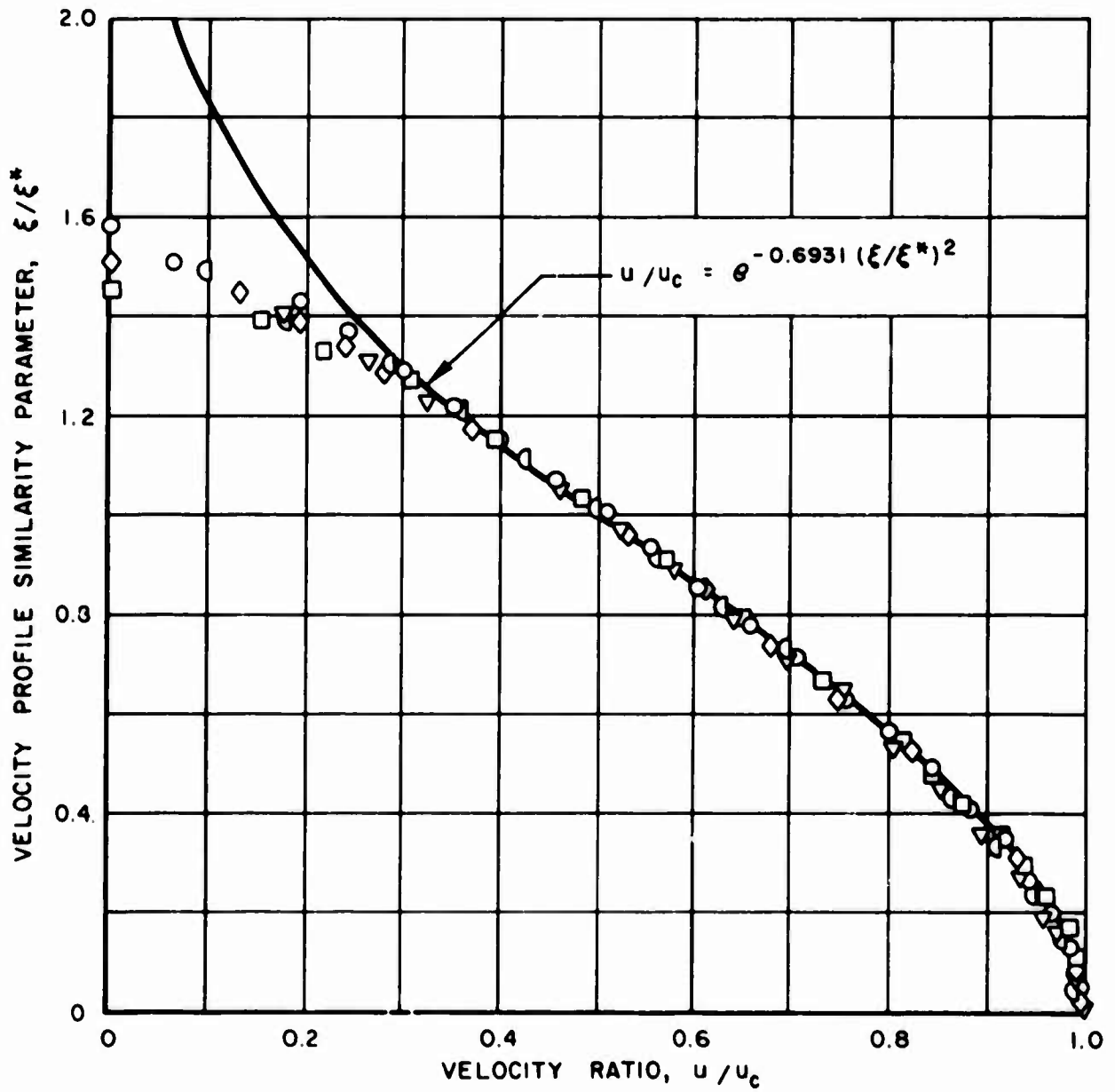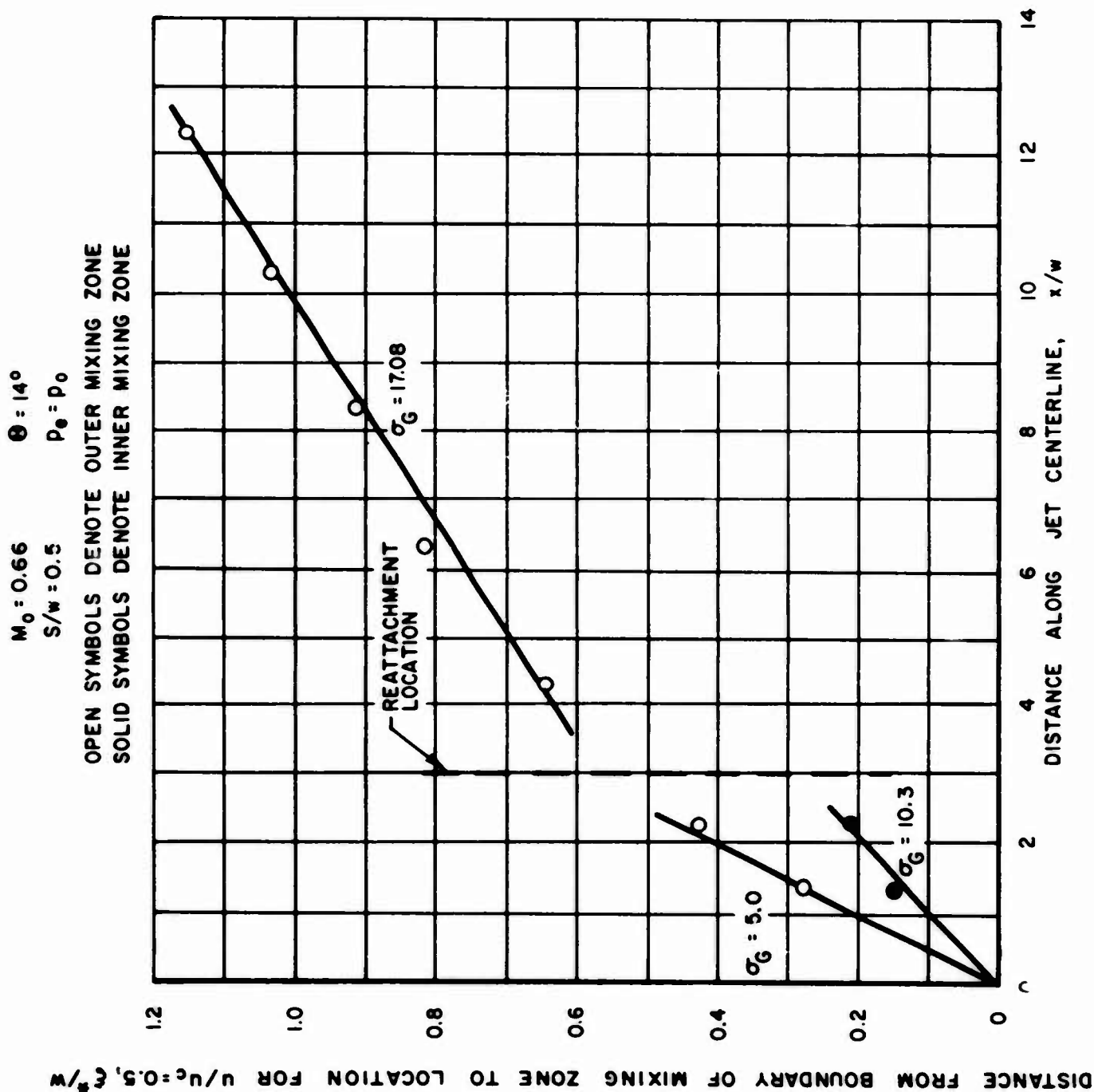
FIGURE 6 REATTACHING JET SPREADING CHARACTERISTICS FOR GAUSSIAN VELOCITY DISTRIBUTION

78
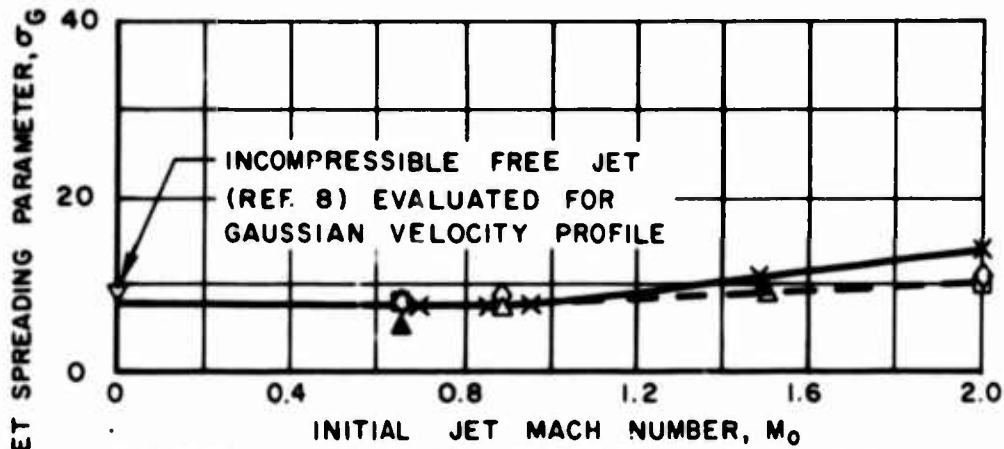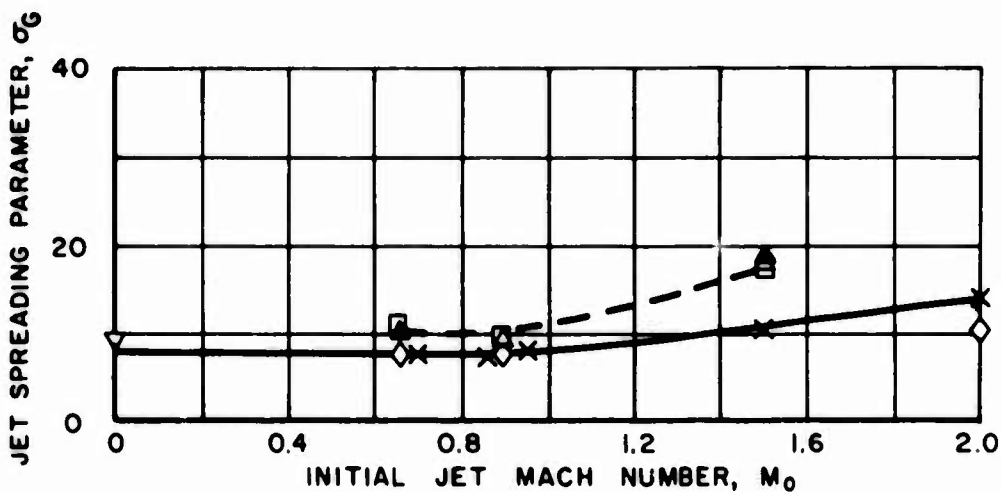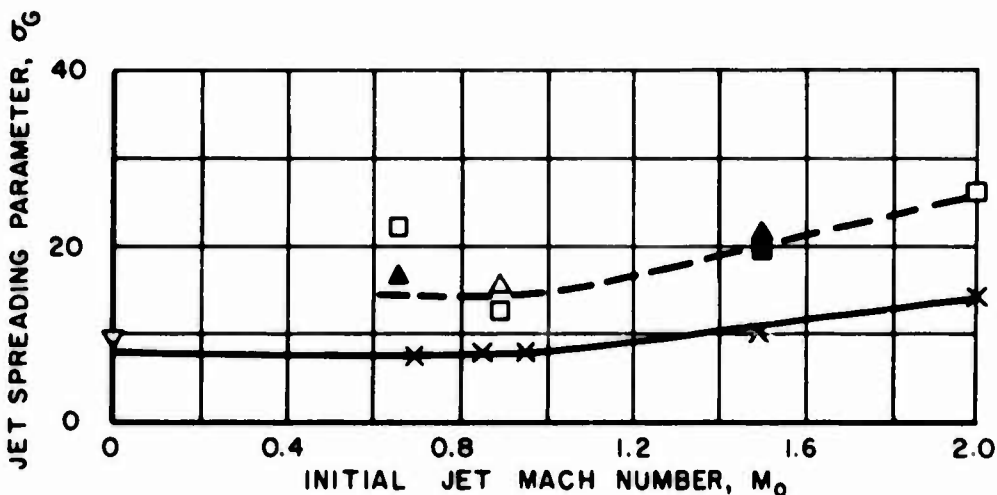
FIGURE 7   VARIATION OF JET SPREADING PARAMETER WITH INITIAL JET
MACH NUMBER FOR REATTACHING JETS

79

THE INTERACTION OF OBLIQUE SHOCKS AND EXPANSION WAVES
WITH A JET BOUNDARY MIXING ZONE

by

Robert E. Olson
and
David P. Miller

of

United Aircraft Corporation Research Laboratories
East Hartford, Connecticut

ABSTRACT

Studies of the interaction of oblique shocks and expansion waves with a jet boundary mixing zone were conducted and analytical procedures are presented for computing the location and strength of the reflected waves associated with such interactions. The procedures involve a graphical step-wise calculation with the mixing zone divided into a finite number of constant Mach number regions. Results obtained from the analytical procedures for upstream Mach numbers of 2.0 are presented and shown to be in good agreement with experimental results. Also presented is an illustration of the applicability of the analytical procedures described to the prediction of pitot pressure profiles at various stations in a representative fluid amplifier.

These studies were conducted as part of a general investigation of the aerodynamic characteristics of fluid amplifiers under Contract DA-49-186-ORD-912.

INTRODUCTION

The prediction of the flow characteristics in fluid amplifiers having supersonic power jet Mach numbers frequently requires the determination of the characteristics of the interaction of oblique shock waves and expansion waves with a jet boundary mixing zone. Although the characteristic interaction of oblique shocks and expansion waves with an idealized inviscid jet boundary can be found in most textbooks on supersonic aerodynamics, the influence of the shear layer along the jet boundary, to the authors' knowledge, has not been previously considered.

Consequently, studies were undertaken to develop procedures for predicting the characteristics of these fundamental interactions including the influence of jet boundary mixing and further to demonstrate the applicability of the procedures developed to the prediction of the flow profiles for jet flows encountered in fluid amplifiers. The information presented herein represents the significant results of these studies.

CHARACTERISTICS OF JET BOUNDARY MIXING ZONE

Before proceeding with the discussion of the interaction of oblique shocks and expansion waves with a turbulent jet boundary mixing zone, it is first necessary to discuss the flow characteristics of such a shear layer. A schematic diagram illustrating the nature of turbulent mixing along the boundary of a submerged jet exhausting into quiescent surroundings is presented in Fig. 1. As shown in Fig. 1, the mixing layer, which originates at the outer boundary of the jet because of viscous shearing with the quiescent surroundings, spreads inwardly into the core of the jet and also spreads outwardly entraining fluid from the surroundings. Within the conservation of total momentum, there is a continuous momentum exchange in the mixing process between layers of fluid moving at different velocities with the quiescent fluid from the surroundings gaining momentum at the expense of the fluid originally in the jet.

Although the mixing layer is shown to have zero thickness at the nozzle and increase linearly in width from that point, in actuality this shear layer has a finite thickness at its origin with the velocity profile being that of the initial boundary layer. Therefore, a transition region exists downstream of the nozzle in which: 1) the velocity profile adjusts to that corresponding to fully-developed mixing, and 2) the spreading rate

approaches a linear value. Kirk (Ref. 4) suggested that at some distance, x , downstream of the nozzle exit the turbulent shear layer behaves in much the same manner as an equivalent layer developing from zero thickness over a greater distance $x + x'$. By assuming that over the distance x' the equivalent mixing layer attains a momentum thickness equal to the momentum thickness, θ , of the real boundary layer and employing Görtler's first approximation that the momentum thickness of an asymptotic turbulent shear layer increases as 1/30th of the distance from the origin, Kirk reasoned that the distance to the vertical origin, x' , could be expressed as

$$x' = 30\theta \tag{1}$$

Nash (Ref. 5) concludes from a more rigorous treatment of this transition region that Kirk's approximation is valid from downstream distances greater than approximately 8 boundary layer thicknesses. For thin boundary layers relative to the nozzle exit the shift in origin of the mixing layer is not significant and can be neglected. For thick boundary layers the correction of Kirk or a similar correction should be applied.

From the discussion of jet boundary mixing in Ref. 1, the angle between the inner boundary of the mixing zone and the reference inviscid boundary (i.e., the jet boundary for no mixing between the jet and external surroundings), can be expressed as

$$\beta_i = \tan^{-1} \frac{\kappa}{\left\{ \dfrac{0.5\left[f_2(1) + f_4(1)\right] - f_1(1)}{f_3(1)f_4(1)} \right\}} \tag{2}$$

where κ is an empirical shear stress constant expressing the rate of momentum exchange in the mixing layer and $f_1(1)$, $f_2(1)$, $f_3(1)$ and $f_4(1)$ are Mach number functions given in APPENDIX III. Values of the shear stress constant, κ , obtained experimentally by various investigators for jet boundary mixing are presented in Fig. 2 for a range of jet Mach numbers. Although considerable scatter exists in the experimental results, it appears that the shear stress constant can be considered nearly a constant for Mach numbers from 0 to 1.5 with a decrease indicated for higher Mach numbers.

Also from Ref. 1 the distance from the inviscid boundary to the location in the mixing zone where the velocity is one-half of its value in the inviscid core can be expressed as

$$\xi^* = \frac{\kappa x}{\left\{ \dfrac{0.5\left[f_2(1) + f_4(1)\right] - f_1(1)}{f_3(1)} \right\}} \tag{3}$$

where x is measured parallel to the reference inviscid boundary. It can be seen from Eqs. (2) and (3) that any line having a constant value of ξ/ξ^* is at an angle to the reference inviscid boundary of

$$\beta = \tan^{-1}\left[\frac{\kappa}{2C_2} - \frac{(\xi/\xi^*)\kappa}{2f_4(1)C_2} \right] \tag{4}$$

where the angle β is positive when measured in a direction toward the inviscid core and

$$C_2 = \frac{0.5\left[f_2(1) + f_4(1)\right] - f_1(1)}{2f_3(1)\,f_4(1)} \tag{5}$$

Assuming a Gaussian velocity distribution in the mixing zone, the local velocity nondimensionalized with respect to the velocity at the inviscid boundary becomes

$$\frac{u}{u_i} = e^{-0.6931(\xi/\xi^*)^2} \tag{6}$$

Correspondingly, the Mach number distribution in the mixing zone for iso-energetic mixing can be expressed as

$$\frac{M}{M_i} = \frac{u}{u_i}\left\{ \frac{1}{1 + \dfrac{\gamma-1}{2}M_i^2\left[1 - \left(\dfrac{u}{u_i}\right)^2\right]} \right\}^{\frac{1}{2}} \tag{7}$$

Consequently, from Eqs. (4), (6) and (7), lines of constant Mach numbers (constant ξ/ξ^*) can be constructed in the mixing zone.

84

INTERACTION OF OBLIQUE SHOCKS WITH MIXING ZONE

A schematic diagram illustrating the characteristic interaction of an oblique shock with an idealized constant pressure inviscid boundary is presented in Fig. 3. In order to satisfy the condition of constant static pressure on the jet boundary the shock wave reflects from the boundary as a centered expansion fan with the total strength of the reflected waves equal to the strength of the oblique shock. For any real case, however, a shear layer exists along the jet boundary, as discussed previously, and the shock is reflected as a series of expansion waves distributed throughout this shear layer rather than from a point as indicated in Fig. 3. A rigorous analysis of the interaction requires long and tedious computation employing the method of characteristics for rotational flow. A considerably less tedious approximate method which was developed for determining the location of the reflected expansion waves is outlined and compared with experiment.

A schematic diagram of the flow model employed in the development of the approximate method is presented in Fig. 4. Noting the relationship of this interaction region shown in Fig. 4 to the inviscid core of the jet, it is observed that the strength of the reflected expansion waves is specified by the condition that the pressure in region 3 of the inviscid core must equal the pressure in region 1. In general, the techniques employed for determining the location of the reflected expansion waves involves constructing the incident shock wave through the mixing zone, specifying the segment of the wave from which the expansion waves are shed, and, finally, tracing the boundaries of the reflected expansion waves (Mach lines) through the mixing zone to the inviscid boundary. This is accomplished by first dividing the supersonic portion of the mixing zone upstream of the shock into segments of constant Mach number. Secondly, the shock wave is traced through the mixing zone by calculating for each interval the shock wave angle required to maintain the pressure ratio across the incident shock. This procedure is continued through successive intervals to the point in the mixing zone where the Mach number behind the shock wave is reduced to 1.0. For subsequent intervals to the sonic line, the shock wave angles are chosen to produce a downstream Mach number of 1.0. Finally, the mixing zone downstream of the shock is divided into intervals of constant Mach·number; and Mach lines, originating from the position in the mixing zone where the Mach number first becomes 1.0, and the sonic line are traced back through the mixing zone to the inviscid boundary. The reflected expansion waves are then located in the center of equal intervals between the intersections of these two Mach lines with the inviscid boundary. A detailed step-wise calculation procedure is presented in APPENDIX I.

A comparison between experimental pitot pressure profiles obtained in Ref. 1 for a wall jet near the impingement of an oblique shock on the jet boundary mixing zone and the pitot pressure profiles in the inviscid core obtained by employing the above procedure for locating the position of the reflected expansion waves is presented in Fig. 5. The good agreement shown between the experimental and predicted values of pitot pressure downstream of the shock substantiate the validity of the procedure for locating the position of the reflected expansion waves for the conditions of the comparison. Although similar comparisons have not been made for initial Mach numbers other than 2.0, the accuracy of the procedure over a range of Mach numbers is expected to be within acceptable limits for most practical applications of the method.

INTERACTION OF EXPANSION WAVES WITH MIXING ZONE

A schematic diagram illustrating the characteristic interaction of a family of expansion waves with an idealized constant pressure inviscid boundary is presented in Fig. 6. In order to satisfy the condition of constant static pressure on the jet boundary each expansion wave reflects as a compression wave thereby forming a family of reflected compression waves opposite in sense to the incident expansion waves. For any real case, however, as discussed previously, a shear layer exists along the jet boundary thereby altering the pattern of the reflected compression waves. An approximate method for locating the position of these reflected compression waves is outlined and compared with experiment.

A schematic diagram of the flow model employed in the development of the approximate method is presented in Fig. 7. The incident expansion waves are treated as several finite waves for convenience of calculation even though in reality the expansion process is continuous. In the actual expansion process, the initial and terminal expansion waves arrive at the inviscid boundary along Mach lines. The angles of the two Mach lines relative to the local flow directions are specified by the Mach numbers in regions 1 and 2. The strength of the reflected compression waves separating regions 2 and 3 is determined by the boundary condition that the pressure in region 3 must equal the pressure in region 1, the ambient pressure external to the jet. Therefore, since the incident and reflected waves are nearly isentropic, the Mach numbers in regions 1 and 3 will be approximately equal and the flow will be turned by the reflected compression waves through an angle equal to the amount that the flow is turned by the incident expansion waves. In general, the technique employed for determining the location of the reflected compression waves involves tracing the two incident Mach lines through the mixing zone to the sonic line and back along

Mach lines of the opposite family to the inviscid boundary and subsequently locating the reflected expansion waves between the reflected Mach lines. This is accomplished by first dividing the supersonic portion of the mixing zone into regions of constant Mach number with the sonic line being deflected through an angle, 2ω, at the intersection with the extrapolated incident expansion waves, where ω is the angle through which the flow in the inviscid core is deflected by each incident expansion wave. Secondly, the incident Mach lines are traced through the mixing zone to the sonic line and back to the inviscid boundary. Finally, the reflected compression waves are then located in the center of equal increments between the reflected Mach lines. A detailed step-wise calculation procedure is presented in APPENDIX II.

A comparison between experimental pitot profiles obtained in Ref. 1 for a wall jet near the impingement of a family of expansion waves on the jet boundary mixing zone and the pitot pressure profiles in the inviscid core obtained by employing the above procedure for locating the position of the reflected compression waves is presented in Fig. 8. The good agreement shown between the experimental and predicted values of pitot pressure downstream of the interaction substantiate the validity of the procedure for locating the position of the reflected compression waves. Although similar comparisons have not been made for initial Mach numbers other than 2.0, the accuracy of this procedure over a range of Mach numbers is again expected to be within acceptable limits for most practical applications of the method.

APPLICATION TO COMPUTING JET FLOWS IN FLUID AMPLIFIERS

Jet flows involving the interaction of expansion waves and oblique shocks with a jet boundary mixing zone are encountered in most supersonic fluid amplifiers. Two jet flows characteristic of the types encountered in supersonic wall-attachment digital amplifiers are illustrated in Fig. 9. Prediction of the flow profiles throughout the jet for both types of jet flows requires the determination of the characteristics of the interaction between expansion waves and shock waves and a jet boundary mixing zone. (For simplicity, the jet boundary mixing zone is not shown in Fig. 9).

To illustrate the applicability of the methods developed previously for determining the location of waves reflected from the jet boundary downstream of the impingement of an oblique shock or a family of expansion waves, the flow field in the inviscid core of an oblique wall jet was computed and compared with the flow profiles obtained experimentally. A diagram of the theoretical flow field for a Mach number 2.0 oblique wall jet having a wall deflection angle of 8 deg and an initial jet

boundary deflection of 5 deg is presented in Fig. 10. The flow field in the inviscid core was computed by the method of characteristics for supersonic irrotational flow with the spreading rate of the jet boundary mixing zone, and the position of the waves reflected from the mixing zone determined by the procedures presented previously. The boundary layer growth along the wall was computed by the method outlined in Ref. 1 and the waves impinging on the boundary layer were assumed to be reflected from the displacement thickness, δ^*, with no distortion.

A comparison of the calculated pitot pressure profiles in the inviscid core, corresponding to this flow model, with experimental pitot profiles is shown in Fig. 11 for stations extending downstream from the nozzle to a distance of 3 nozzle widths. Separation of the boundary layer near the impingement of the compression waves reflected from the jet boundary downstream of the impingement of the initial expansion waves precluded any valid comparison for stations further downstream than 3 nozzle widths. Good agreement is shown for the position of the shock wave emanating from the wall discontinuity, both before ($L_W/w = 0.5$) and after ($L_W/w = 1.5$) their interaction at $L_W/w = 0.8$. The good agreement between the measured and predicted values of pitot pressure at $L_W/w = 2.0$ shows that the flow model can be employed for both the reflection of a compression wave from a boundary layer and the interaction of expansion waves with the mixing zone. The usefulness of the procedure for predicting the location of the inner boundary of the mixing zone is evidenced by the good agreement at all stations. Somewhat poorer agreement is noted, however, for the prediction of the boundary layer thickness, δ . This discrepancy can be attributed to neglecting the effect of streamwise pressure gradient in the boundary layer calculations. Better agreement between the theoretical and experimental results could be obtained by taking into account the effect of the static pressure gradient along the boundary wall.

APPENDIX I

Calculation Procedure for the Interaction of an Oblique Shock

with a Jet Boundary Mixing Zone

A graphical, step-wise procedure for determining the location of the reflected expansion waves downstream of the impingement of an oblique shock on a jet boundary mixing zone is outlined below with reference to Fig. 4.

1. Construct line AE normal to the flow in region 1 (point A is the intersection of the incident shock wave and the inviscid boundary). Divide the mixing region into intervals having widths of $\xi/\xi^* = 0.1$. In order to simplify the construction of the shock wave, extend the lines of constant ξ/ξ^* parallel to the line $\xi/\xi^* = 1.0$. From Eq. (7), calculate the average Mach number in each interval.

2. Construct the continuation of the shock wave from the inviscid core into the mixing zone. This is accomplished by calculating for each interval the shock wave angle required to maintain the pressure ratio across the incident shock, p_2/p_1 , in the inviscid core. Initiate construction at point A and continue through successive intervals to point B in the mixing zone where the Mach number behind the shock wave is reduced to 1.0.

3. Construct the shock wave from point B to point C using shock wave angles in each interval that produce sonic velocity behind the shock wave rather than maintaining the pressure ratio p_2/p_1 . Since point C is located on the sonic line of the mixing zone, the shock wave will become normal to the flow at this point.

4. Construct the path of the Mach line from point B through the nonuniform Mach number field of the mixing zone in region 2 to the inviscid boundary at point F. As a first step, using the Mach number and flow direction in the inviscid section of region 2, locate the inviscid boundary AF $(\xi/\xi^* = 0)$ using Eq. (2). Secondly, extend the lines of constant ξ/ξ^* from region 1 into region 2 parallel to the inviscid boundary AF. Finally, starting at point B, construct the Mach line through each interval using the Mach number calculated behind the shock wave in step (2).

5. Construct the $\xi/\xi^* = 1.0$ line in region 3 by deflecting it at its intersection with the line CD through an angle equal to the difference in flow directions in regions 1 and 3. Line CD is perpendicular to the flow direction in region 3.

6. Construct the inviscid boundary in region 3. This line is located with respect to the $\xi/\xi^* = 1.0$ line by calculating the downstream growth of ξ^* by,

$$\xi^* = \xi^* |_{x = x_0} + \frac{d\xi^*}{dx} (x - x_0) \tag{8}$$

where the coordinates x and ξ are measured parallel and perpendicular respectively to the flow direction in region 3. The derivative $d\xi^*/dx$ is obtained from Eq. (3).

7. Construct the path of the Mach line from point C through the mixing zone in region 5 to the inviscid boundary at point G. This Mach line forms the downstream boundary of the reflected expansion waves since the last expansion wave is taken to emanate from the intersection of the shock wave and the sonic line. In a method similar to step (1), divide the mixing zone of region 5 into intervals having widths of $\xi/\xi^* = 0.1$ that are located using the $\xi/\xi^* = 1.0$ line as a reference. The average Mach number, and hence the average Mach angle, is calculated using Eq. (7). Therefore, using step-wise construction starting at point C, the intersection of the Mach line with the inviscid boundary at point G is determined.

8. Construct the location of the expansion waves between points F and G. Although the expansion process between points F and G is continuous, for calculation purposes it is convenient to consider the expansion fan to consist of several finite waves. Since the net change in flow direction from region 2 to region 3 is calculated from the pressure boundary condition ($p_3 = p_1$), the number of intervals is selected so that the flow deflection by the wave in each interval is about 2 deg. The angle of each wave and the change in the flow properties and flow direction across each wave at the boundary of the inviscid core are calculated using the Prandtl-Meyer equations for inviscid flow.

APPENDIX II

Calculation Procedure for Interaction of Expansion Waves

with a Jet Boundary Mixing Zone

A graphical, step-wise procedure for determining the location of the reflected compression waves downstream of the impingement of a family of expansion waves on a jet boundary mixing zone is outlined below with reference to Fig. 7.

1. Construct lines in the mixing zone, upstream of the incident expansion waves, corresponding to (1) the sonic line, (2) the line of $\xi/\xi^* = 1.0$ ($u/u_i = 0.5$), and (3) the inviscid boundary ($\xi/\xi^* = 0$). The angles between these lines and the reference inviscid boundary (the line coincident with the position of the outermost streamline of the jet if no mixing occurred) are obtained from Eq. (5).

2. Construct a sonic line through the interaction region by assuming that deflection occurs at the intersection with each projected incident expansion wave (points A, B, C, and D). The sonic line is deflected an amount 2ω toward the inviscid core at each reflection of an incident wave, where ω is the angle through which the flow in the inviscid core is deflected by each incident expansion wave.

3. Construct the $\xi/\xi^* = 1.0$ line through the interaction region by assuming that a deflection angle of 2ω occurs at each of the intersections with lines which pass through points A, B, C, and D normal to the average local flow direction. The angle between the $\xi/\xi^* = 1.0$ line and sonic is given by Eq. (4) employing also Eqs. (6) and (7).

4. Construct the inviscid boundary downstream of point E by calculating the value of ξ^* and subtracting this value from the $\xi/\xi^* = 1$ line of step (3). With the coordinates x and ξ measured along and perpendicular to the flow direction in each region respectively, the value of ξ^* is given by

$$\xi^* = \xi^*\Big|_{x=x_A} + \frac{d\xi^*}{dx}(x - x_A) \tag{9}$$

The derivative $d\xi^*/dx$, based on the Mach number in regions 1 and 3, is given by Eq. (3).

5. Construct the continuation of the Mach line EF that bounds region 1. To simplify construction, divide the mixing zone into intervals having widths of $\xi/\xi^* = 0.1$, obtain an angle of the Mach line for each interval based on an average Mach number calculated from Eq. (7), and then construct the Mach line through successive intervals starting at point E. In a similar manner, construct the reflected Mach line from point F to point G. The spreading characteristics of the mixing zone throughout the interaction region are assumed to be specified by the Mach number in region 1 with the downstream growth in ξ^* being given by Eq. (9).

6. Construct the continuation of Mach line HI that bounds region 2. The Mach number in the mixing zone is calculated from Eq. (7) while the flow direction and values of ξ/ξ^* are located with respect to the $\xi/\xi^* = 1.0$ line established in steps (3) and (4). Employing a similar procedure, construct the Mach line from point I to point J.

7. Construct the location of the reflected compression waves along the inviscid boundary ($\xi/\xi^* = 0$) by dividing the line GJ into equal intervals (select a number so that the flow deflection per interval is about 2 deg). Locate the initial point of each reflected compression wave in the center of an interval.

APPENDIX III

Auxiliary Mach Number Functions

$$f_1(1) = \int_0^1 \frac{\left(\frac{u}{u_0}\right)^2}{1 + \frac{\gamma-1}{2} M_0^2 \left[1 - \left(\frac{u}{u_0}\right)^2\right]} \, d\left(\frac{\xi}{\xi^*}\right)$$

$$f_2(1) = \int_0^1 \frac{\frac{u}{u_0}}{1 + \frac{\gamma-1}{2} M_0^2 \left[1 - \left(\frac{u}{u_0}\right)^2\right]} \, d\left(\frac{\xi}{\xi^*}\right)$$

$$f_3(1) = \frac{0.3465}{1 + \frac{\gamma-1}{2} M_0^2 (1 - 0.25)}$$

$$f_4(1) = \int_0^\infty \frac{\left(\frac{u}{u_0}\right)^2}{1 + \frac{\gamma-1}{2} M_0^2 \left[1 - \left(\frac{u}{u_0}\right)^2\right]} \, d\left(\frac{\xi}{\xi^*}\right)$$

LIST OF REFERENCES

1. Olson, R. E., and D. P. Miller: Aerodynamic Studies of Free and
   Attached Jets. United Aircraft Corporation Research Laboratories
   Report A-1771-24, Final Report on Contract DA-49-186-ORD-912,
   December 1963.

2. Reichardt, H.: Gesetzmässigkeiten der freien Turbulenz. VDI -
   Forschungsheft, No. 414, May 1942. (Translated as Ministry of
   Aircraft Production, R.T.P. Trans. No. 1752).

3. Maydew, R. C. and J. F. Reed: Turbulent Mixing of Axisymmetric
   Compressible Jets (in the Half-Jet Region) with Quiescent Air.
   Sandia Corporation SC-4764 (RR), March 1963.

4. Kirk, F. N.: An Approximate Theory of Base Pressure in Two-Dimensional
   Flow at Supersonic Speeds. R.A.E. Tech. Note Aero. 2377, 1954.
   (Published 1959.)

5. Nash, J. F.: The Effect of an Initial Boundary Layer on the Deve-
   lopment of a Turbulent Free Shear Layer. National Physical Labora-
   tory, Aerodynamics Division, NPL AERO REP. 1019, June 6, 1962.

C_2 Constant in Eq. (4)

L_w Distance along boundary wall

M Mach number

p Static pressure

p_e Static pressure on free boundary of jet

p_p Pitot pressure

p_t Total pressure

u Velocity parallel to reference inviscid boundary

w Total height of nozzle at exit

x Distance along jet centerline

x' Virtual origin of mixing zone

y_B Distance perpendicular to boundary wall

β Angle between lines of constant ξ/ξ^* and reference inviscid boundary (see Eq. (4))

γ Ratio of specific heats

δ Boundary layer thickness

δ^* Boundary layer displacement thickness

θ Boundary layer momentum thickness

Θ Angle of boundary wall relative to nozzle centerline

κ Shear stress constant

ξ Transformed coordinate perpendicular to jet centerline

| ω | Flow turning angle |

Subscripts

| i | Denotes conditions on inviscid boundary |
| o | Denotes conditions at nozzle exit |

Superscripts
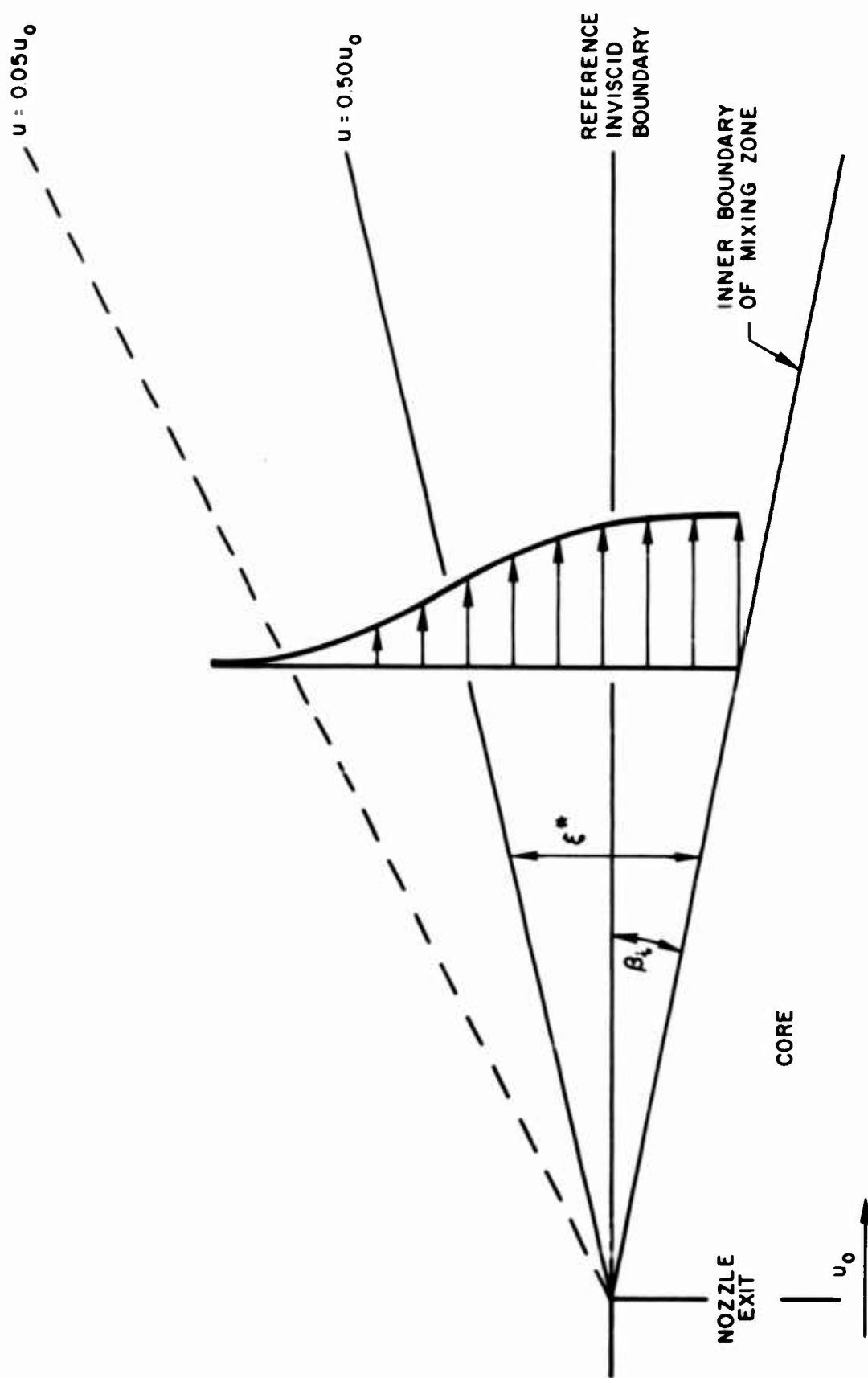
| $*$ | Denotes conditions where $u/u_i = 0.5$ |

FIGURE I FLOW MODEL FOR JET BOUNDARY MIXING ZONE

97
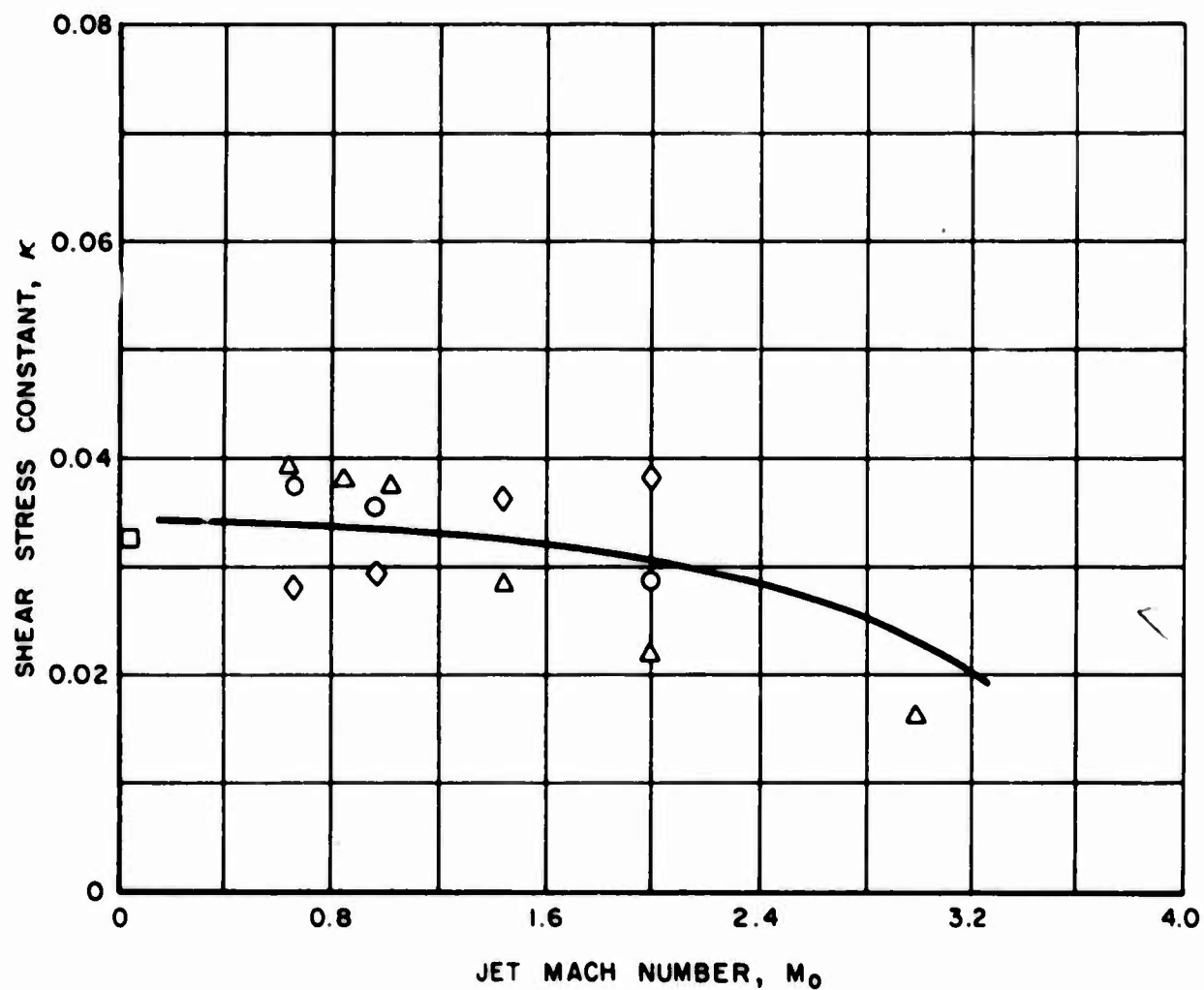
FIGURE 2 SHEAR STRESS CONSTANT FOR JET BOUNDARY MIXING ZONE
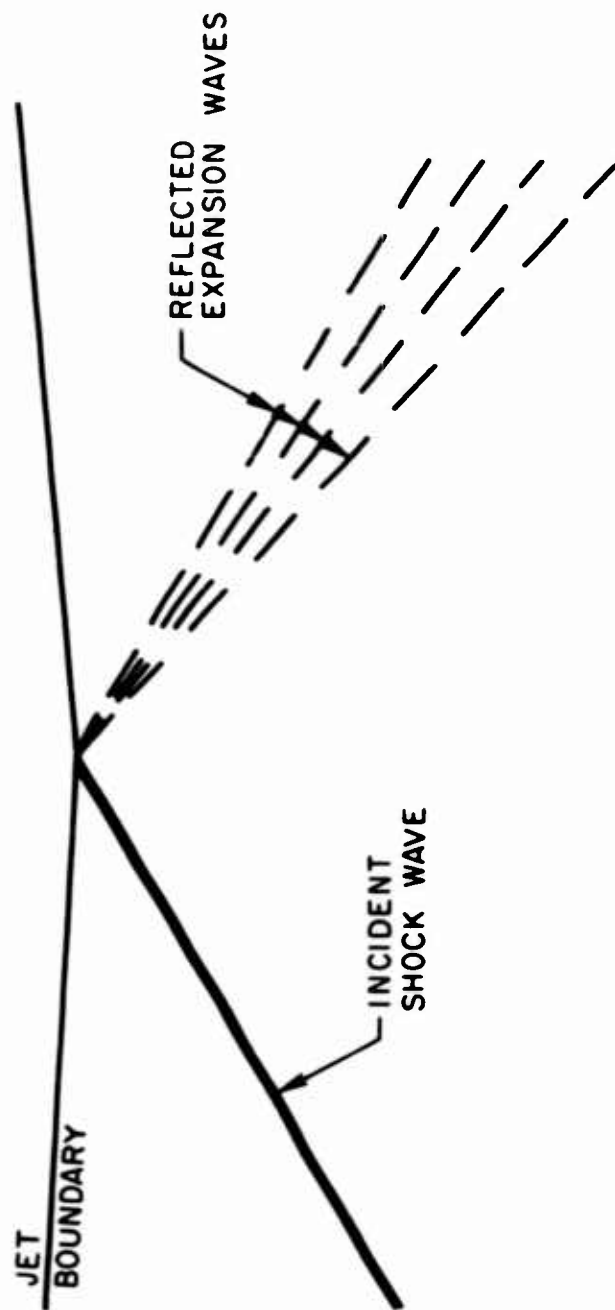
98

JET
BOUNDARY

REFLECTED
EXPANSION WAVES

INCIDENT
SHOCK WAVE

FIGURE 3   INTERACTION OF OBLIQUE SHOCK WITH INVISCID JET BOUNDARY
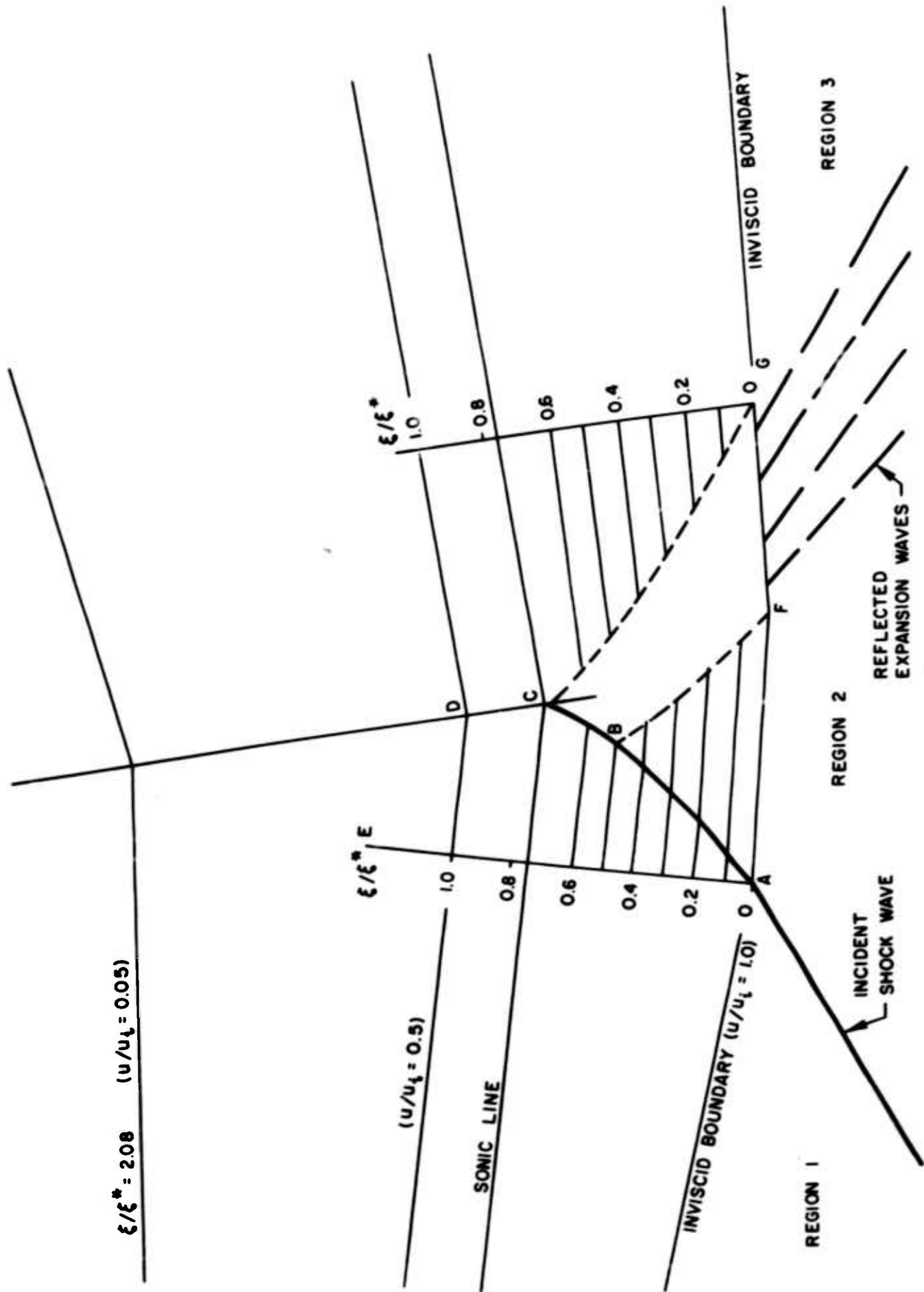
FIGURE 4 FLOW MODEL FOR INTERACTION OF OBLIQUE SHOCK WITH MIXING ZONE
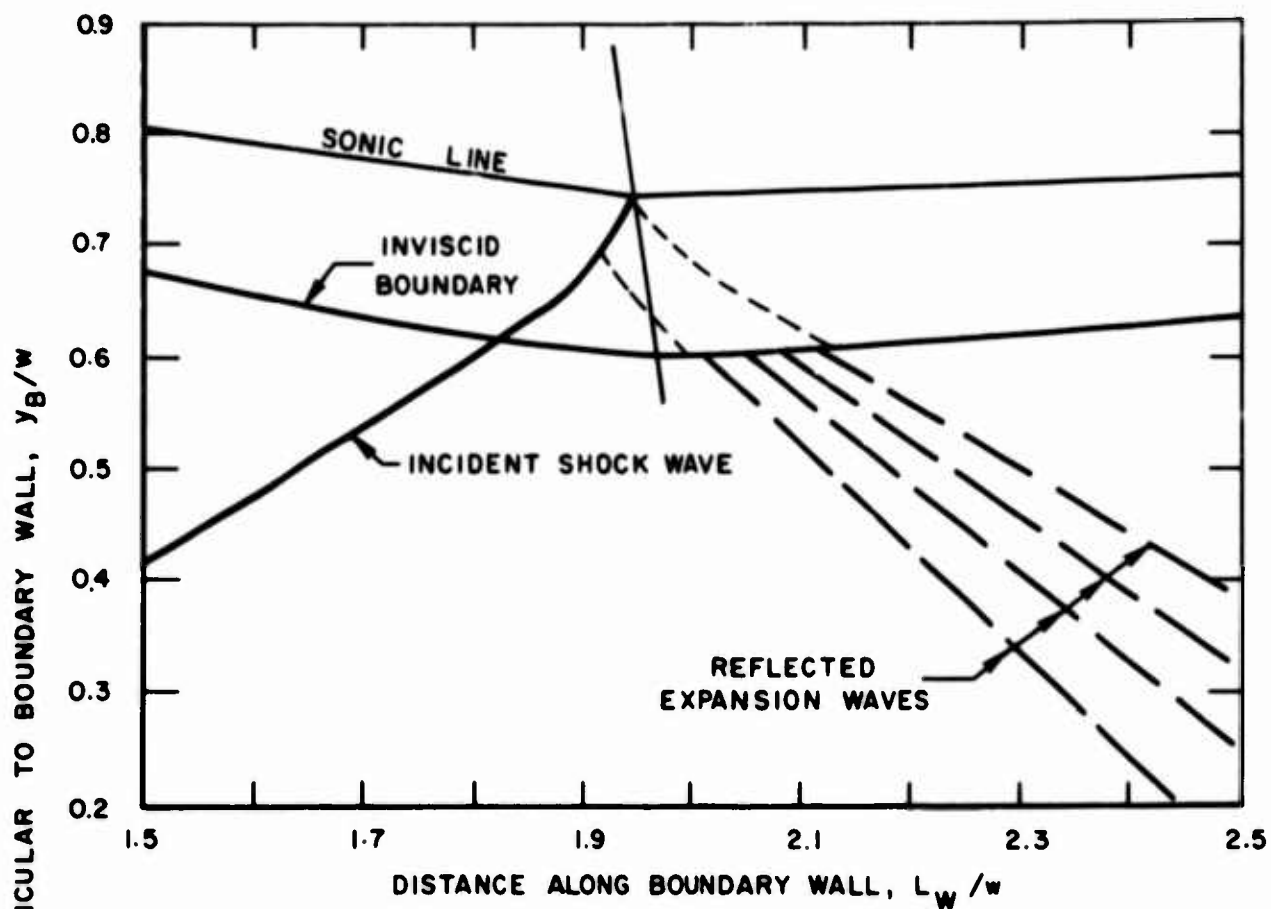
100
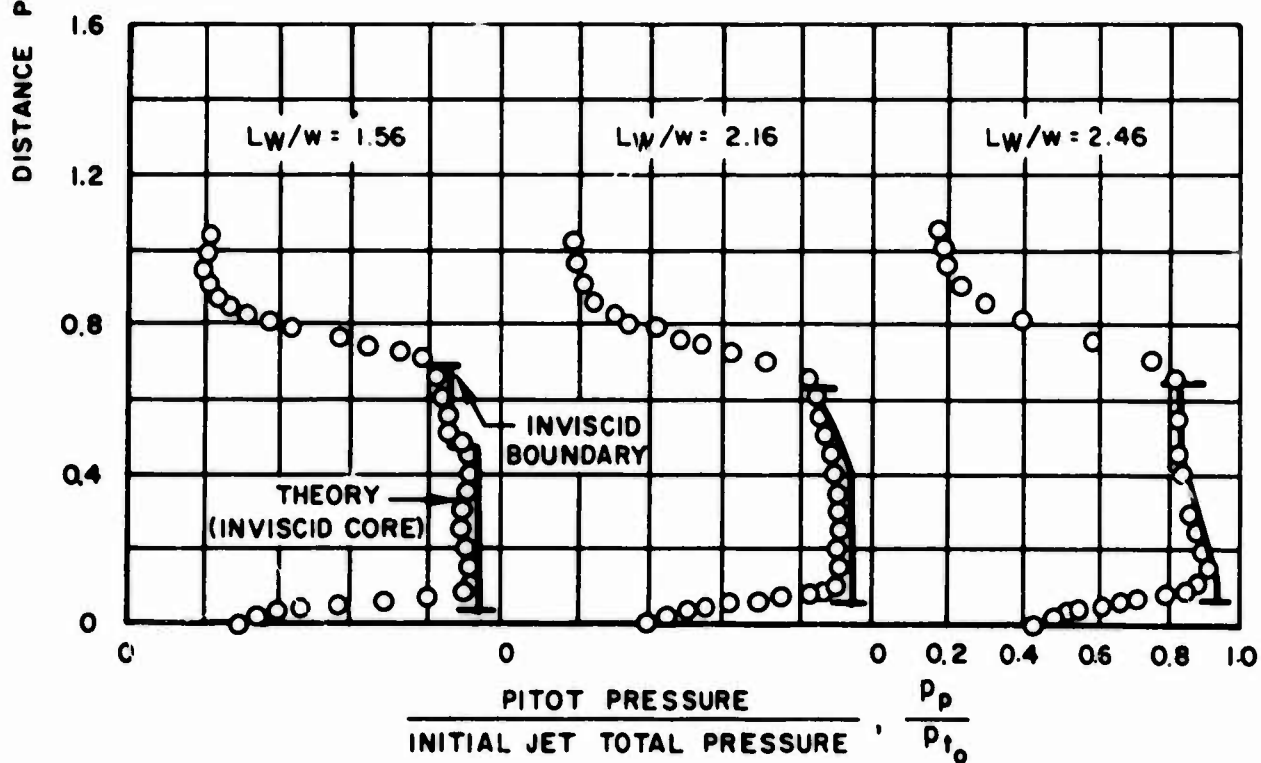
FIGURE 5 COMPARISON OF THEORY AND EXPERIMENT FOR INTERACTION OF SHOCK WAVE WITH MIXING ZONE

101
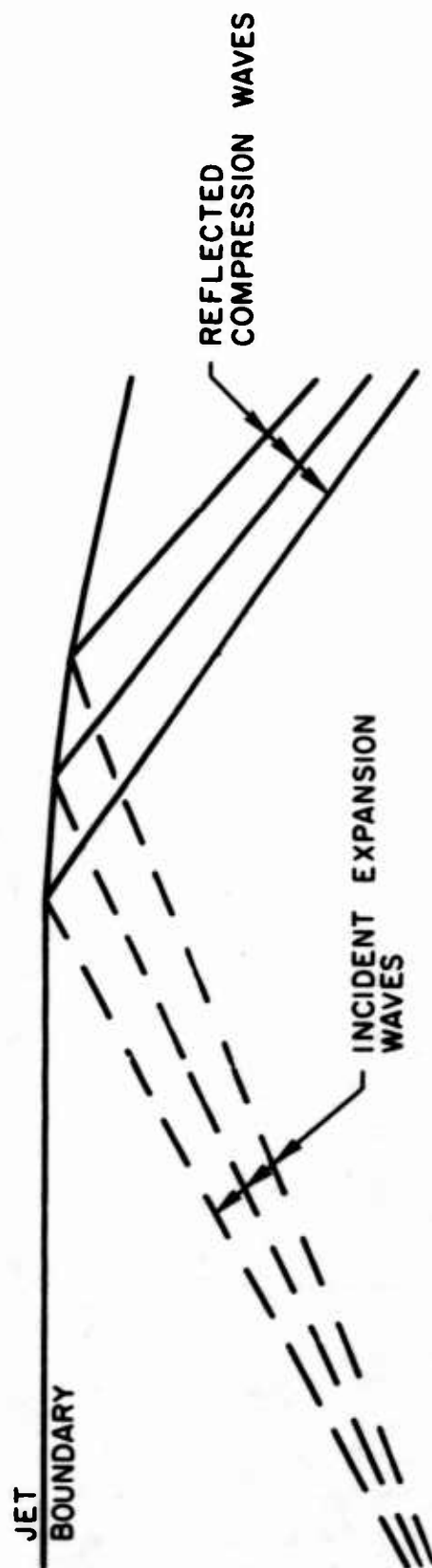
FIGURE 6 INTERACTION OF EXPANSION WAVES WITH INVISCID JET BOUNDARY

102
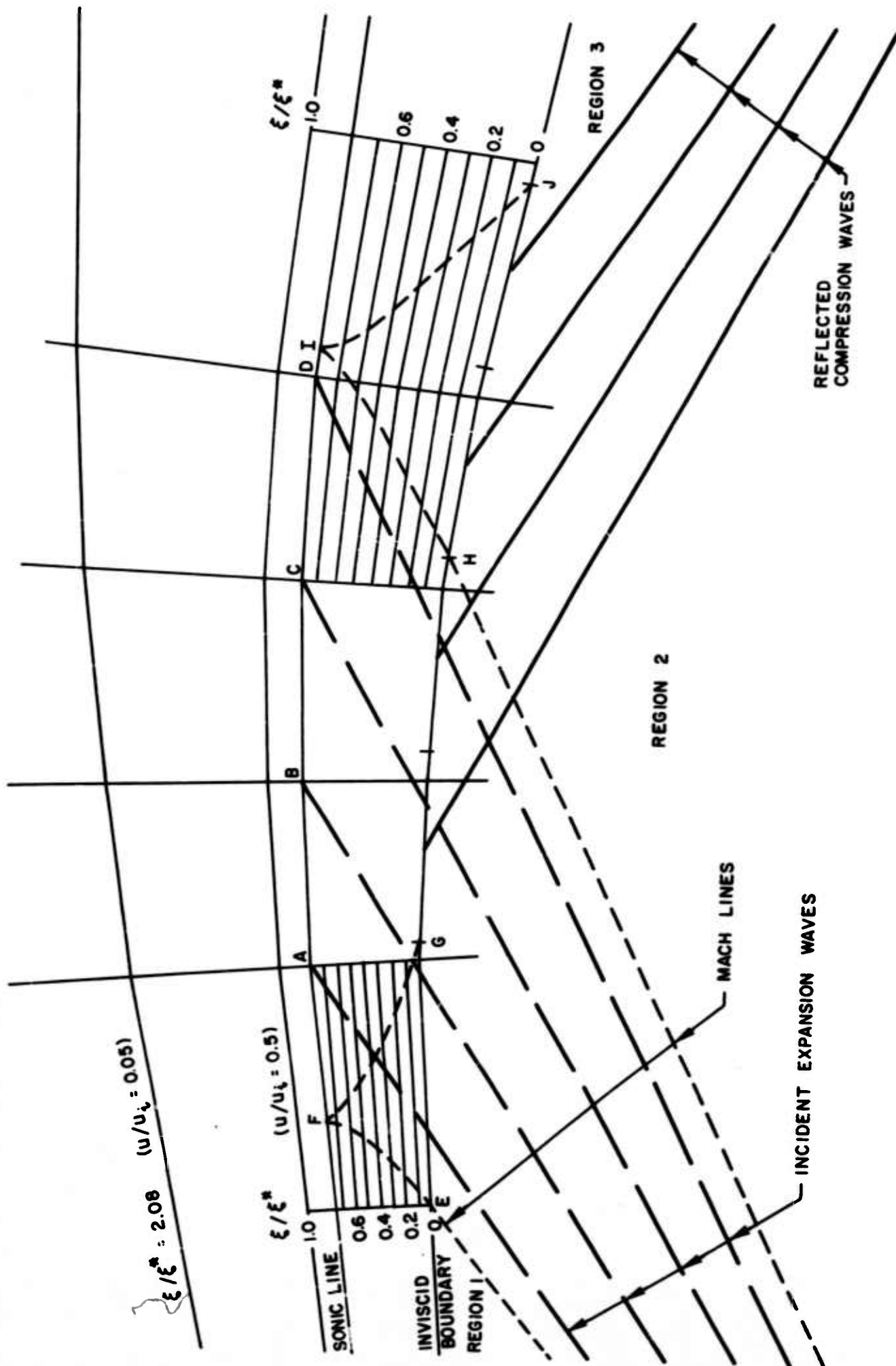
FIGURE 7 FLOW MODEL FOR INTERACTION OF EXPANSION WAVES WITH MIXING ZONE
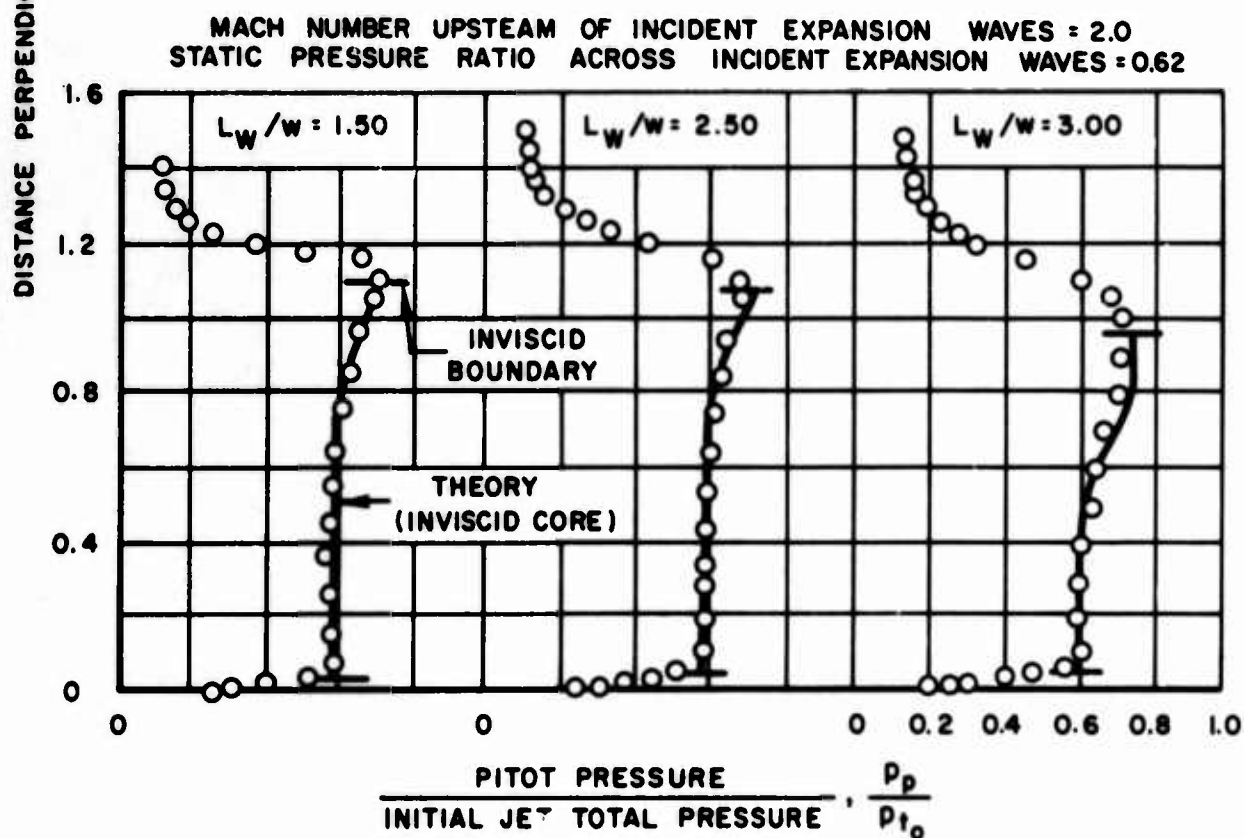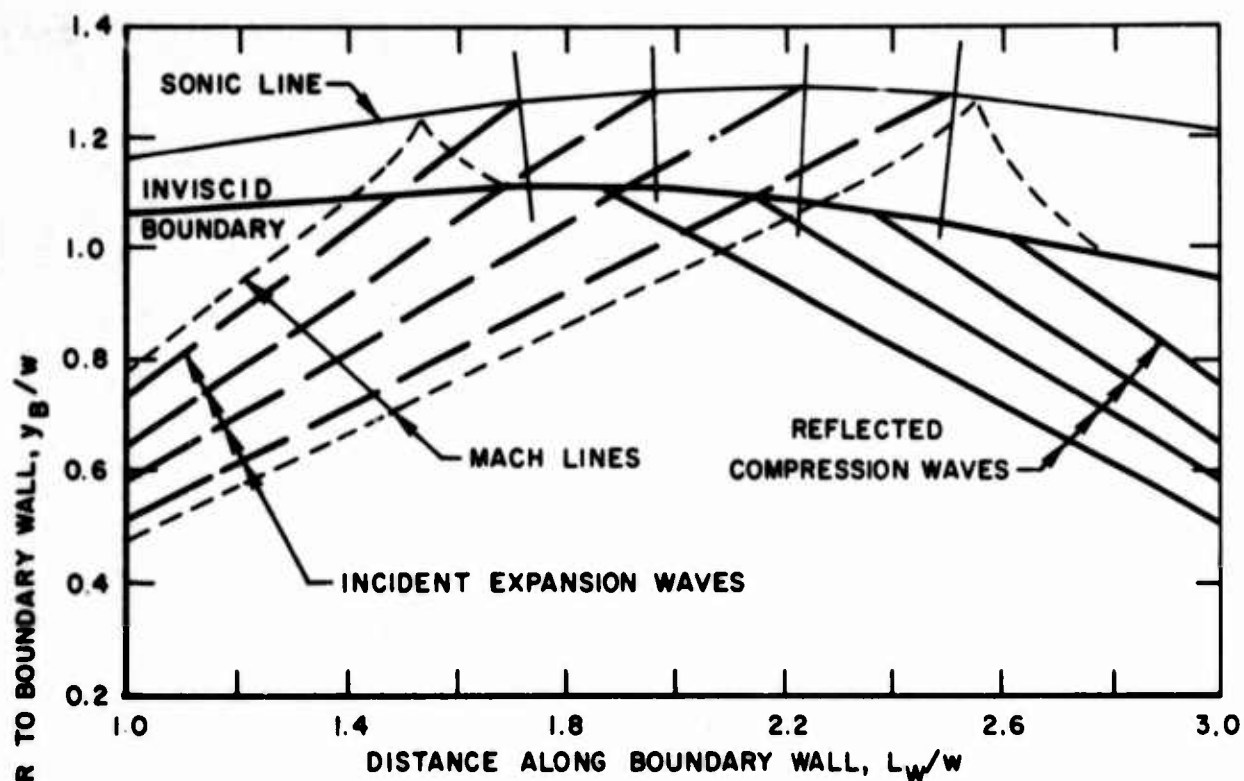
FIGURE 8 COMPARISON OF THEORY AND EXPERIMENT FOR INTERACTION OF EXPANSION WAVES WITH JET BOUNDARY

104

REATTACHED JET
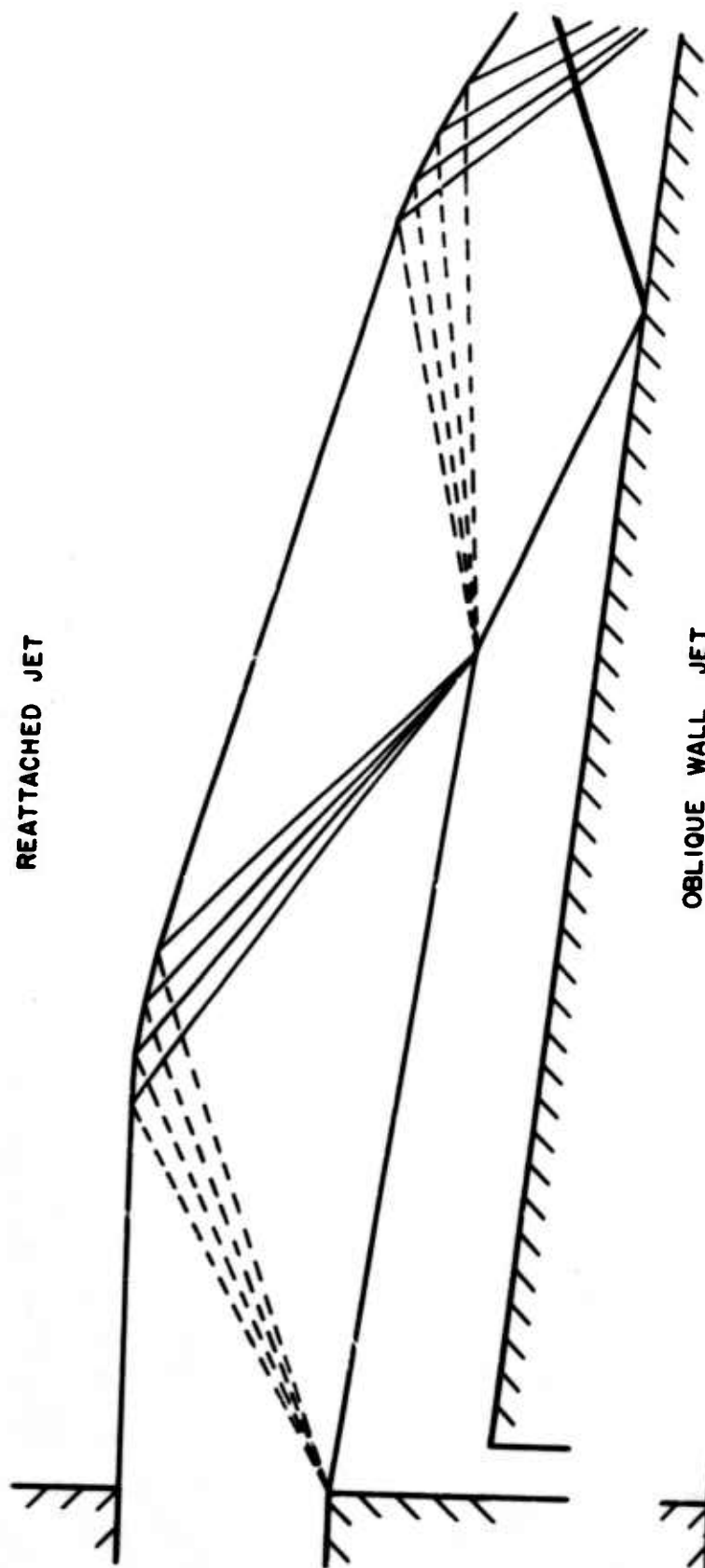
OBLIQUE WALL JET
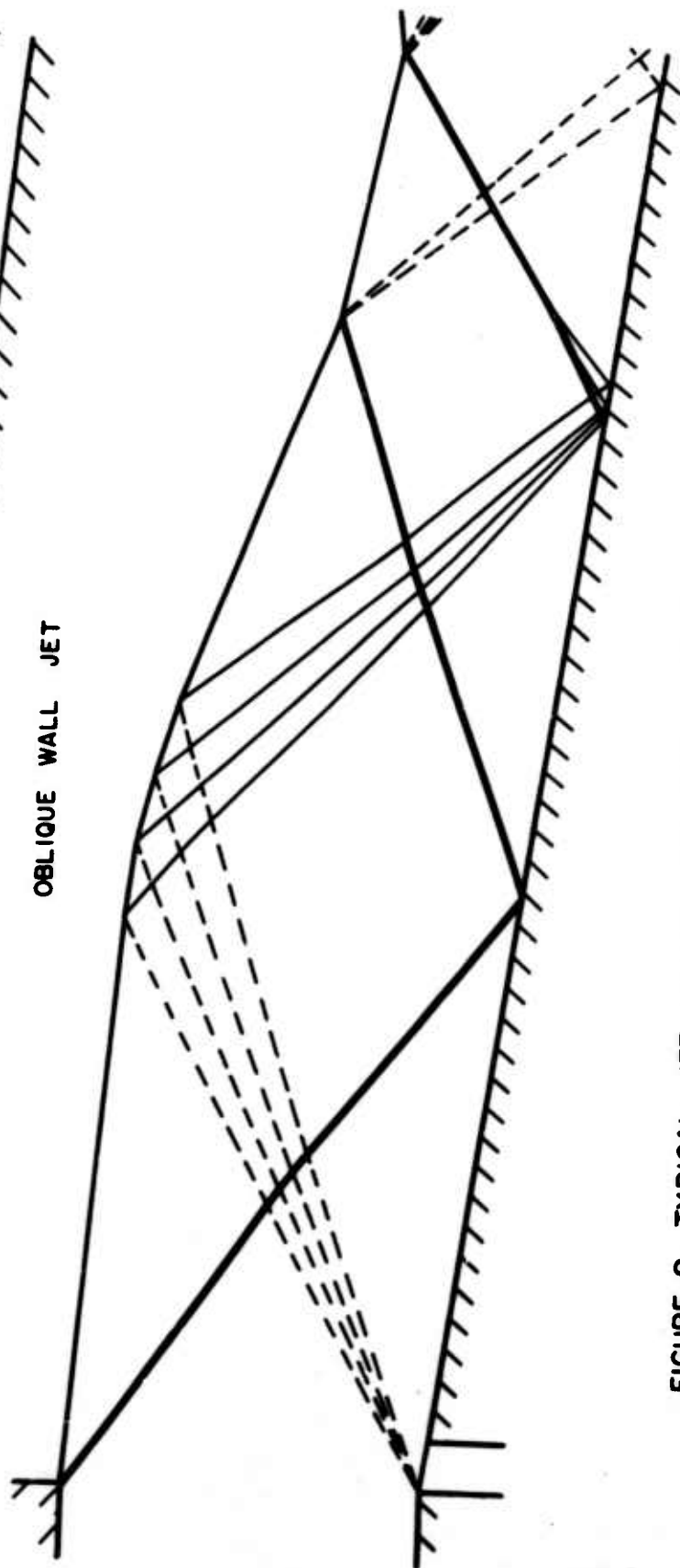
FIGURE 9 TYPICAL JET FLOWS IN WALL-ATTACHMENT DIGITAL AMPLIFIERS

$M_0 = 2.0$

$\Theta = 8°$ $P_e/P_o = 1.31$

$u/u_t = 0.05$

SONIC LINE

INVISCID BOUNDARY

MACH LINE

P_e

P_o

MACH LINE

EXPANSION WAVES

SHOCK WAVE

REFLECTED COMPRESSION WAVES

Θ

β^*

$\frac{L_W}{W} = 0$

W

0.5   1.0   1.5   2.0   2.5

FIGURE 10   DIAGRAM OF THEORETICAL FLOW FIELD FOR SUPERSONIC OBLIQUE WALL JET

$M_0 = 2.0$, $\theta = 8°$, $p_e/p_0 = 1.31$
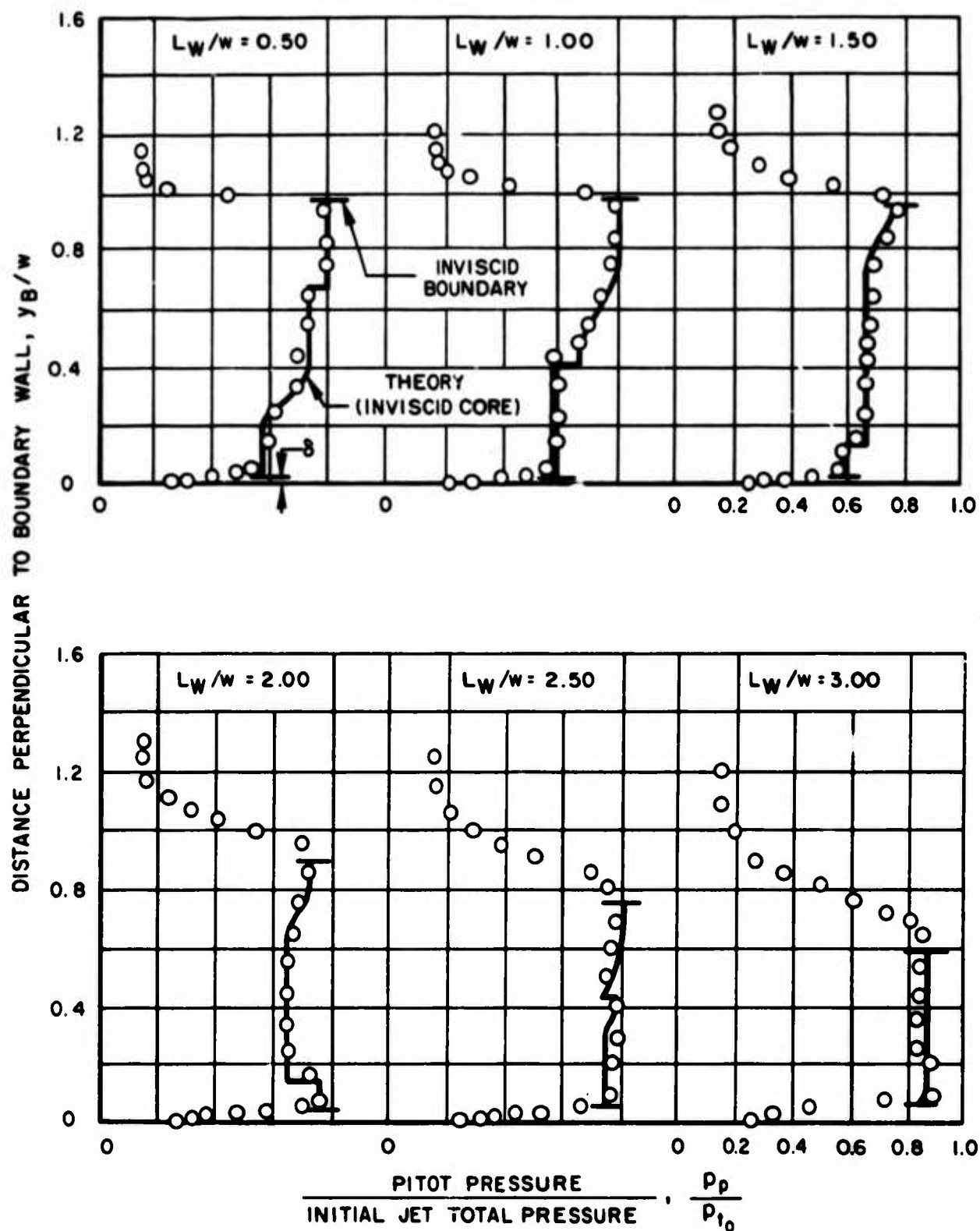
FIGURE II   COMPARISON OF EXPERIMENTAL AND THEORETICAL PITOT PRESSURE
PROFILES FOR SUPERSONIC OBLIQUE WALL JET

107

Abstract:
SEPARATED FLOW IN CURVED CHANNELS

by

H.A. Curtiss
O.G. Feil
D.J. Liquornik

Giannini Controls Corporation
Astromechanics Research Division

Fluid flow in a curved channel, or elbow, that has sufficiently small curvature to promote separation is shown to be the basis of a powerful technique for use in fluid state amplification. Modulation of this sensitive flow is accomplished by injection of a small secondary flow in the separation region to either encourage or retard flow separation. This separation point movement results in a redistribution of the main stream momentum which, with appropriate design 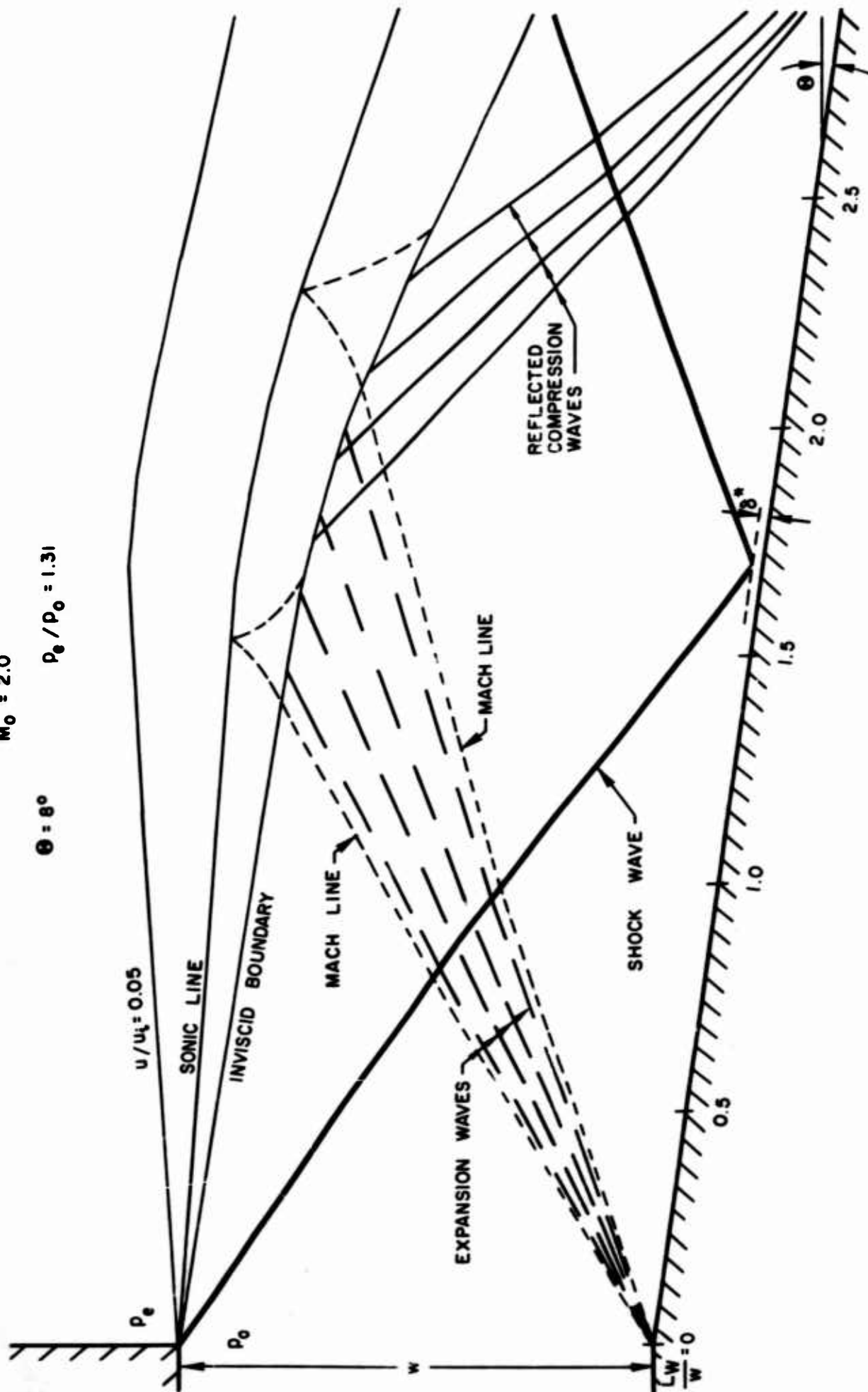of an output receiver, represents a significant flow modulation gain. When combined with two other flow phenomena; i.e., oblique flow impingement and entrained flow separation, the method provides a basis for very large proportional fluid state flow amplification.

This report presents some results of a fundamental experimental study of separating curved channel flow both with and without secondary injection. Some of these results are compared with a preliminary analytical technique based on an empirically modified classical approach. The complex nature of the flows involved precludes the early derivation of a completely general theory. A discussion of published literature applicable to separating curved flow shows that very little prior work, either theoretical or experimental, has been reported; and that, to the authors' knowledge, nothing has been reported on secondary injection into this type of flow. A method for predicting the flow redistribution resulting from secondary injection into a straight channel is presented in this report and compared with the experimental results.

The experimental studies, using air as the test medium, included tests of different aspect ratio elbows and a series of elbow curvatures ranging from a sharp edge turn to a straight channel. In addition, various secondary flow injection rates and several main stream velocities were investigated. Most of the experiments were conducted under conditions of carefully controlled low level inlet turbulence. All flows had turbulent boundary layer, but not fully developed flow, entering the curved channel. Measurements of boundary layer profiles and stream velocities from both hot wire anemometer and pitot probe techniques in addition to static pressure surveys are presented. Two-component velocity measurements, which are necessary for understanding both curvature-induced and injection-induced secondary flows, were obtained by a unique hot wire anemometer X-probe technique.

These results are correlated and where possible compared with preliminary analytical techniques. The elbow geometry and secondary injection methods providing the most efficient amplification are discussed and, finally, a general discussion of the problems and most likely approaches to the full understanding of separated flow in sharply curved channels is presented.

109

JET INTERACTION NOISE

by

F. A. Moynihan

Honeywell
Military Products Group
Research Laboratory

ABSTRACT

Experience with proportional fluid amplifiers has shown that noise in the form of pressure fluctuations is generated within the device even after minimizing and/or eliminating the obvious noise sources such as roughness, fluid impurities and flow separation conditions caused by strong positive static pressure gradients. An additional possible noise source, the jet interaction process of the power and control streams, was investigated by measurements of the velocity fluctuations in the combined jets using a hot-wire anemometer technique. Variables, for the experiments, include the geometry of the control and power streams as well as their relative pressure levels. It was found that the various shear layers, formed by the velocity discontinuities of the power and control streams, can be a significant noise source at upstream stations where a simple free jet would be relatively quiet.

INTRODUCTION

Experience with proportional fluid amplifiers has shown that noise in the form of total pressure fluctuations are generated within the amplifier even after minimizing and/or eliminating the obvious noise sources such as roughness, fluid impurities and flow separation conditions caused by strong adverse pressure gradients. The noise, measured in the output legs was largest at null and decreased as the combined power and control streams were deflected either way from null. For most cases, amplitude was also a function of relative velocity of the control and power streams in that as the total control flow was increased the noise level went down. These observations suggested that the jet interaction process itself could be a possible source of velocity fluctuations (total pressure noise) which were not damped out. To investigate this, an experiment was initiated to systematically measure the velocity fluctuations, using a hot-wire anemometer technique, in the interaction region of three impinging streams, simulating the geometry found in proportional amplifiers.

Velocity fluctuation measurements in simple two and three dimensional free jets, for example, references 1-4, when interpreted as total pressure fluctuations

show that the entrainment process in a free jet can be a significant noise source. Data reported by Sato (reference 2, Figure 10) for velocity fluctuation measurements across a two-dimensional, initially laminar free jet are replotted here in terms of total pressure noise to illustrate the shape and trends of the noise profiles. The profiles show peaks which, according to many authors, are located at the inflection point in the velocity profile and the trend of increasing magnitude in the downstream direction at least for the range of jet lengths associated with fluid amplifiers. In the case of the initially laminar jet, the amplitude of the peak noise is approximately 2.5% at $x/W_p = 6.7$ (reference 1) and for a turbulent jet the peak noise is approximately 3% at $x/W_p = 6.0$ (reference 4).

The approximate relative velocities of the control and power streams across the shear layer, $(v_c/v_p)_a$, at small x/W_p are calculated from

$$\left(\frac{v_c}{v_p} \right)_a = \frac{Q_c}{Q_p} \frac{W_p}{W_c} \sqrt{\frac{q_p{}'}{q_c{}'}}$$

This expression is derived by continuity using the geometric interpretation of q' described in reference 5. $q_p{}'$ is primarily a function of $P_c{}^o/P_p{}^o$ and decreases with it while $q_c{}'$ is essentially a function of just the offset, reference 5. Verification of this approximate calculation is shown in the upstream velocity profiles of Figures 4 and 5 by comparing the velocities across the discontinuity.

EXPERIMENT

The apparatus, Figure 2, has the three jets mounted between two parallel plastic sheets. Power jet channel was 1/2 in. wide with an aspect ratio of 6. Control port width, W_c and offset, s, see Figure 3, were geometric variables. Fluid was air at subsonic speeds (maximum velocities on the order of 60 to 70 ft/sec) and low pressure (power jet total pressures on the order of 1 to 2 in. H_2O gage). Velocity fluctuations were measured with a hot-wire anemometer (Flow Corporation Model HWB) with the wire axis oriented perpendicular to the x-y plane. Readout was by a true RMS voltmeter. Simultaneous mean velocity measurements were made with an adjacent pitot probe and static tap. The probes, mounted to the top plate, were located by sliding the plate relative to the jets in the x and y directions by means of jack screws. Nomenclature is illustrated in Figure 3.

Measured RMS velocity fluctuation normalized by the maximum velocity of the profile (at the profile centerline) is squared to give the ratio of the fluctuating dynamic pressure to the centerline dynamic pressure. This ratio can be interpreted as total pressures if the ambient static pressure, assumed constant across the profile, is used as the zero reference. Thus, $P_N{}^o/P_E{}^o$, is plotted and provides a quality measure of the noise level to be captured by receivers with a width of some y/W_p at which were located at some x/W_p station.

112

DISCUSSION

A set of data were taken where the control ports were pressurized but there was little or no control stream flow, Figure 3. It is apparent that the noise profiles are similar in both shape (quiet centercore) and trend (increasing peak amplitude in the downstream direction) with those reported for the referenced simpler free jet.

Introducing a relatively larger control stream velocity, Figure 4, (although for a different geometry) illustrates that the shear layer formed between the control and power streams as well as the outer edges of the combined jets can form a noise source. This is indicated by the four noise peaks in the profile at $x/W_p = 1.5$ in Figure 4. Location of the shear layer is indicated by the discontinuities in the velocity profile. Downstream at $x/W_p = 9.5$, the velocity discontinuities are gone and both the velocity and noise profiles are similar to that of a single free jet.

Effect of varying the relative velocity of the control and power stream on the noise profiles at an upstream location, $x/W_p = 1.5$, is shown in Figure 5 for the same W_c/W_p as Figure 4 except that the offset, s/W_c is reduced from 1.25 to .50. Data in Figure 5(b) are for approximately the same relative velocities $(v_c/v_p)_a = .61$ but of course the relative flow rate (mass ratio) is reduced. The noise profile, 5b, is similar to that of Figure 4 in that the four noise peaks at the shear layers are apparent, and have similar magnitudes but the overall width of the combined jets is reduced at the station due to the smaller offset. Reduction of the control stream velocity, Figure 5(a), increases the noise at the inner shear layers (larger velocity discontinuity) and appears to reduce the noise peaks at the outer edges. By increasing the control stream velocity to match the power stream, Figure 5(c), the inner noise peaks are eliminated but raises the noise peaks at the outer edges. These comparisons serve to illustrate that at upstream stations the noise profiles can be shaped by controlling the effective relative control and power stream velocities by either the control stream total pressure or by variation of the control port offset.

Downstream profiles, $x/W_p = 9.5$ corresponding to the configurations of Figure 5(b) and 5(c) plotted in Figure 6. While similar to each other in shape neither one has the relatively 'quiet' core shown for the larger offset configuration, Figure 4, at a similar x/W_p station. By noting that the overall jet width is the same ($y/W_p \approx 3.6$) at $x/W_p = 9.5$ for both the large and small offset means that jet spreading rate is larger for the small offset case which might be a cause for the phenomena. In any event, there are no apparent noise peaks attributable to either the shear layers observed upstream and appear to have a larger noise level over the whole jet width than those measured upstream.

As the combined jets are deflected by an unbalance of control flows, the relative velocities would change on either side of the power jet and could be expected to alter the noise profile peaks. A comparison of the noise profiles before and after deflection, Figure 7, show that the magnitude of the noise peaks are changed at both the upstream location, Figure 7(a), and the downstream location, Figure 7(b), but only by small amounts. These particular data

113

indicate that the change in overall noise level of the fluid captured by receiver ports as the jet is deflected would depend more on the amount of the 'quiet' core being captured rather than the alteration of the upstream velocity discontinuity.

SUMMARY

The experimental results show that a free jet itself is a 'noise' process which grows in the downstream direction and for jet lengths applicable to fluid amplifier, the total pressure fluctuations can be on the order of 4 to 6 percent, which is a significant noise. At the downstream stations addition of the control streams doesn't markedly alter the noise profile from that of a free jet except for small control port areas and small offsets where the 'quiet' center core was eliminated. Upstream receiver locations (short jet lengths) could be a means of reducing the noise generation. But if this is done, care should be used in minimizing the velocity discontinuity of the power and control streams to avoid excessive noise generation from this source. This can be done by increasing the mass flow ratio for a given geometry or altering the geometry by decreasing the offset.

114

REFERENCES

1. Sato, H. "The Stability of a Two Dimensional Jet," Journal of Fluid Mechanics, Vol. 7, pp. 53-80, January 1960.

2. Amramovich, G. N. "Turbulent Jets Theory," Gasudarstvennoye Izdatel' stvo Fiziko - Matematicheskoy Literatury 1960, Translation in ASTIA Document AD 283,858, August 1962.

3. Heskestad, G. "Measurements in a Two-Dimensional Turbulent Jet," AFOSR 2456, April 1962.

4. Miller, D. R. and Comings, E. W. "Static Pressure Distribution in a Free Turbulent Jet," Journal of Fluid Mechanics, $\underline{3}$, 1957-8.

5. Moynihan, F. A. and Reilly, R. J. "Deflection and Relative Flow of Three Interacting Jets," Proceedings of the Second Fluid Amplification Symposium, May 1964 at Harry Diamond Laboratories.

NOMENCLATURE

Symbols

P^o	total pressure
q	dynamic pressure
q'	relative dynamic pressure q/p^o. Measured upstream in control or power stream channel where transverse conditions are uniform
Q	volume flow rate per unit height
s	control port offset, see Figure 3
v	velocity
W	channel width
x,y	coordinates, see Figure 3

Subscripts

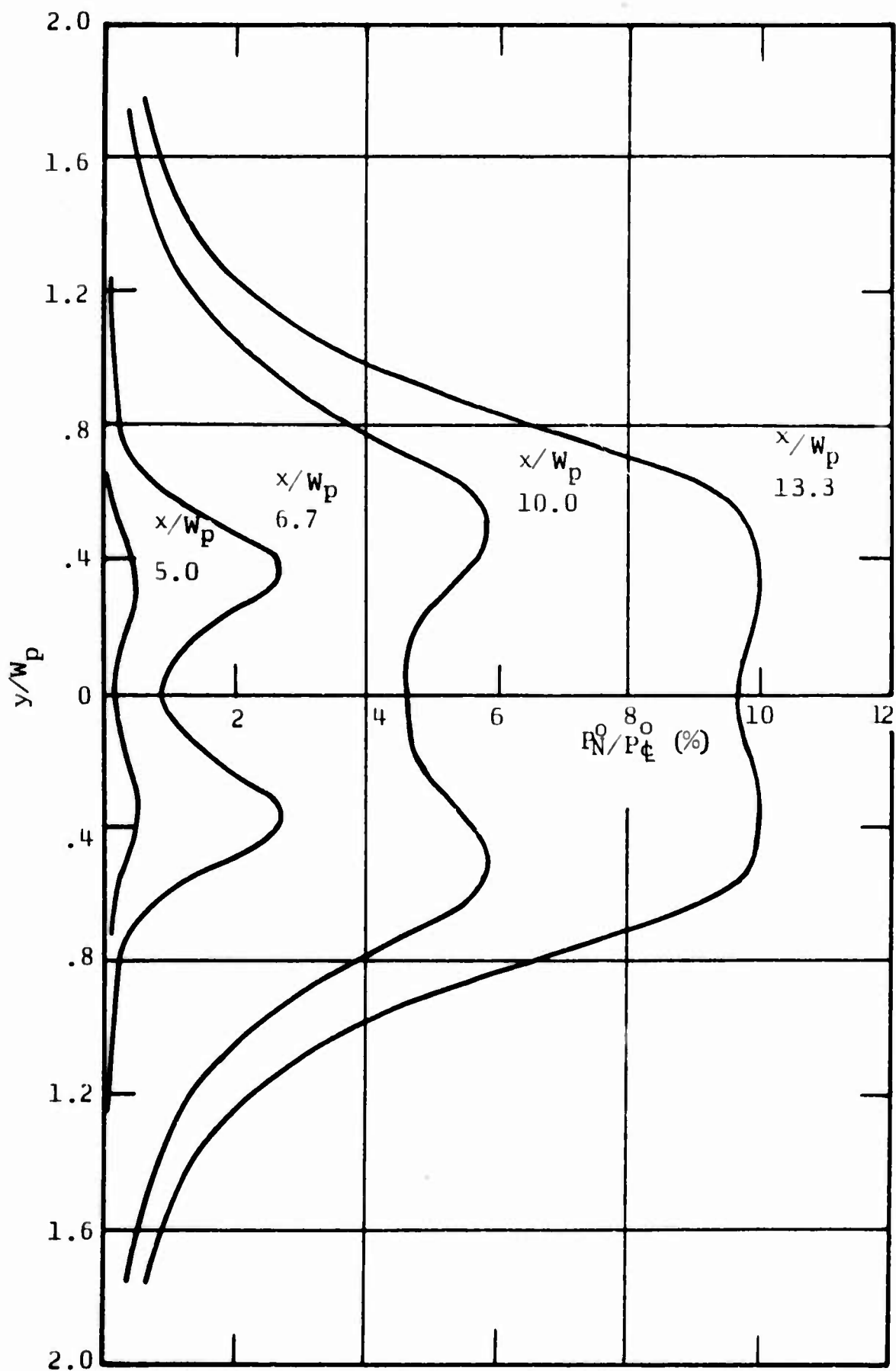|	
a	upstream station of combined jets where control and power streams are identifiable and parallel
c	control stream
$\mathfrak{L}$	velocity profile centerline
p	power stream
N	noise due to velocity fluctuations

FIGURE 1.   TOTAL PRESSURE FLUCTUATIONS IN AN INITIALLY
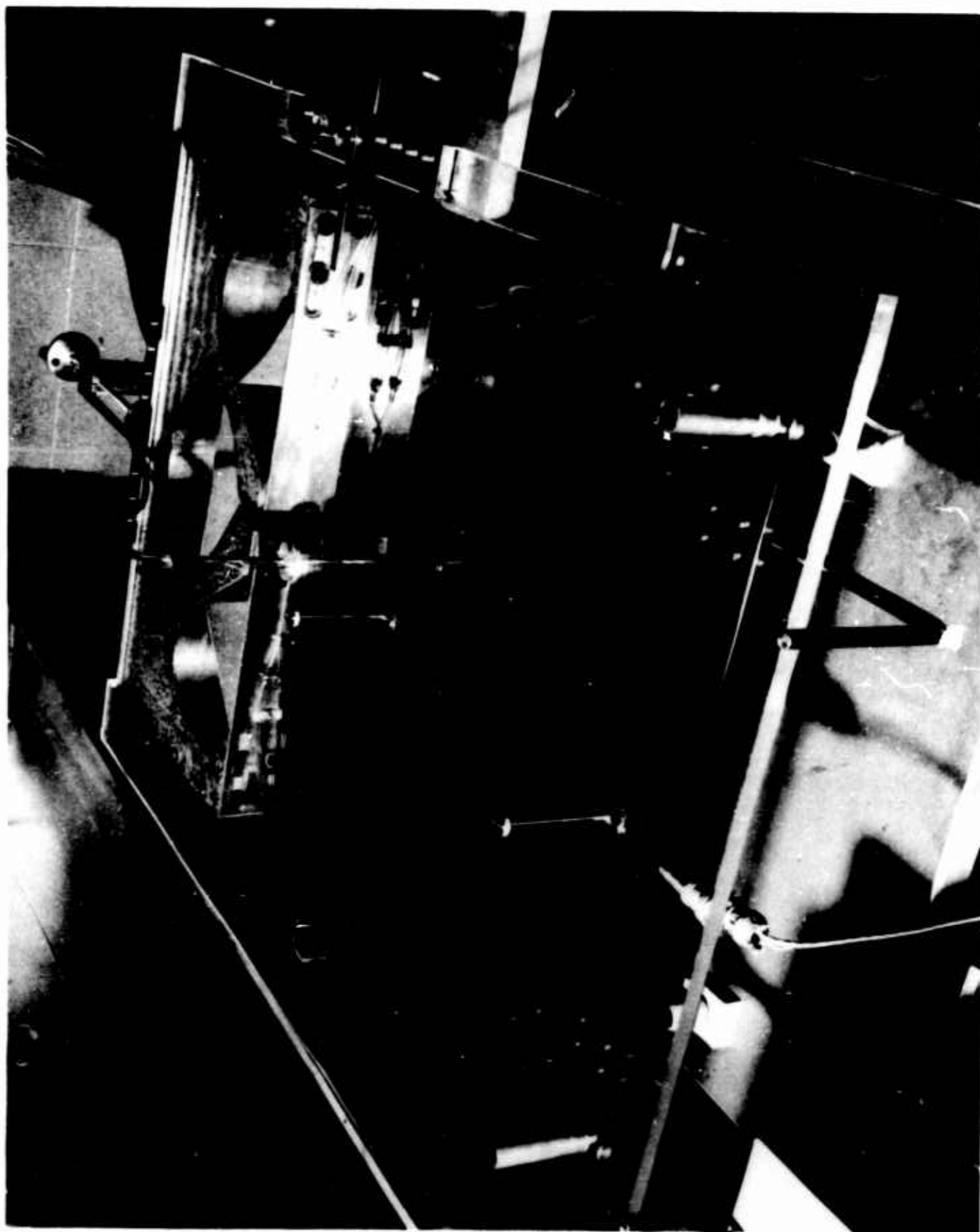   LAMINAR FREE JET (SATO, Ref. 2)

116

FIGURE 2. JET INTERACTION EXPERIMENTAL APPARATUS

117
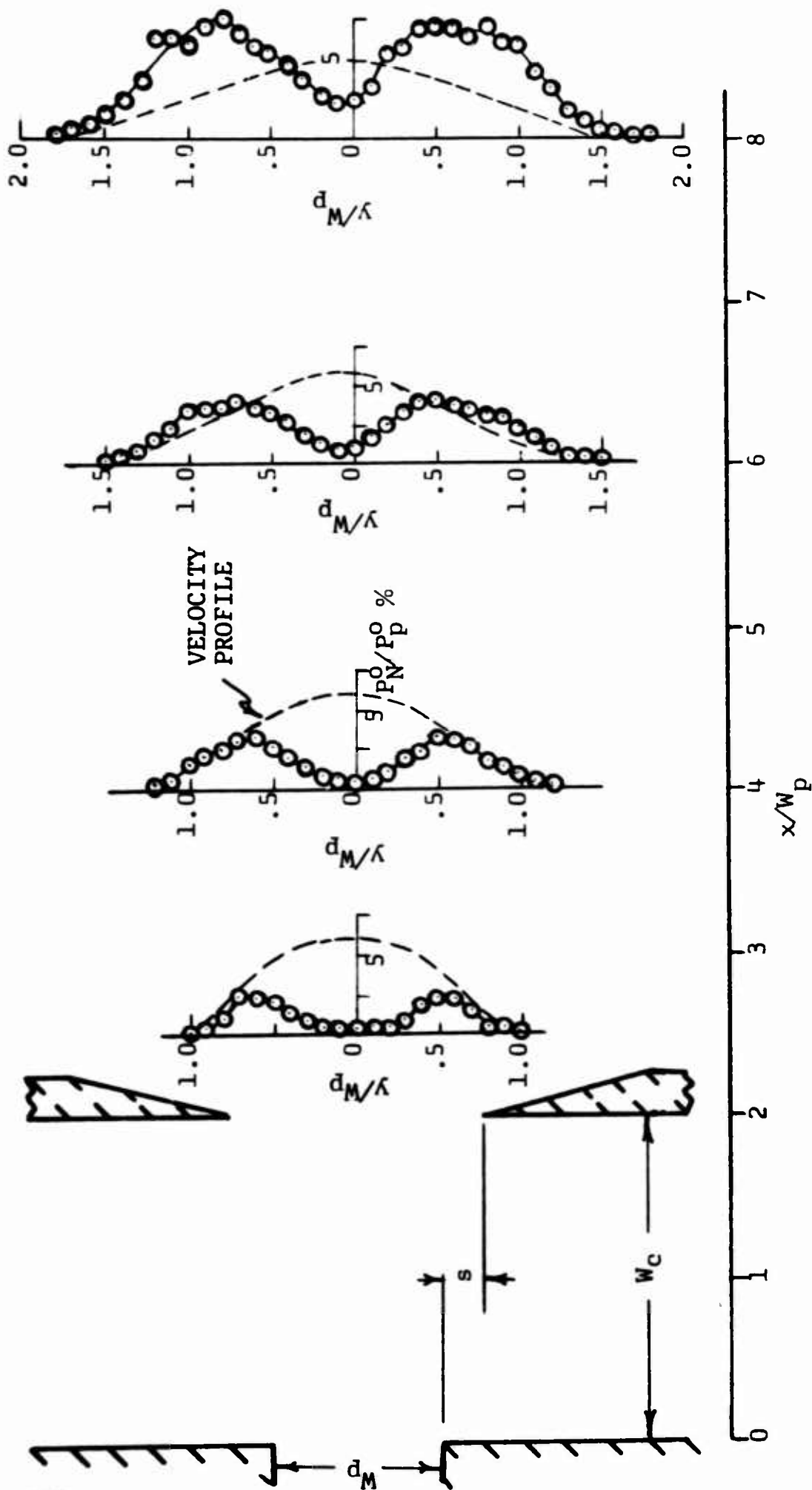
FIGURE 3. NOISE PROFILES ; $W_c/W_p = 2.0$, $s/W_p = .125$, $\Delta \bar{P}_c^o/P_p^o = 0$, $\bar{P}_c^o/P_p^o = .17$, MR≈0

118

FIGURE 4. NOISE PROFILES ; $W_C/W_p = 1.0$, $s/W_C = 1.25$, $\Delta P_C^O/P_p^O = 0$, $\bar{P}_C^O/P_p^O = .40$, $MR = .84$, $(v_C/v_p)_a = .62$

119
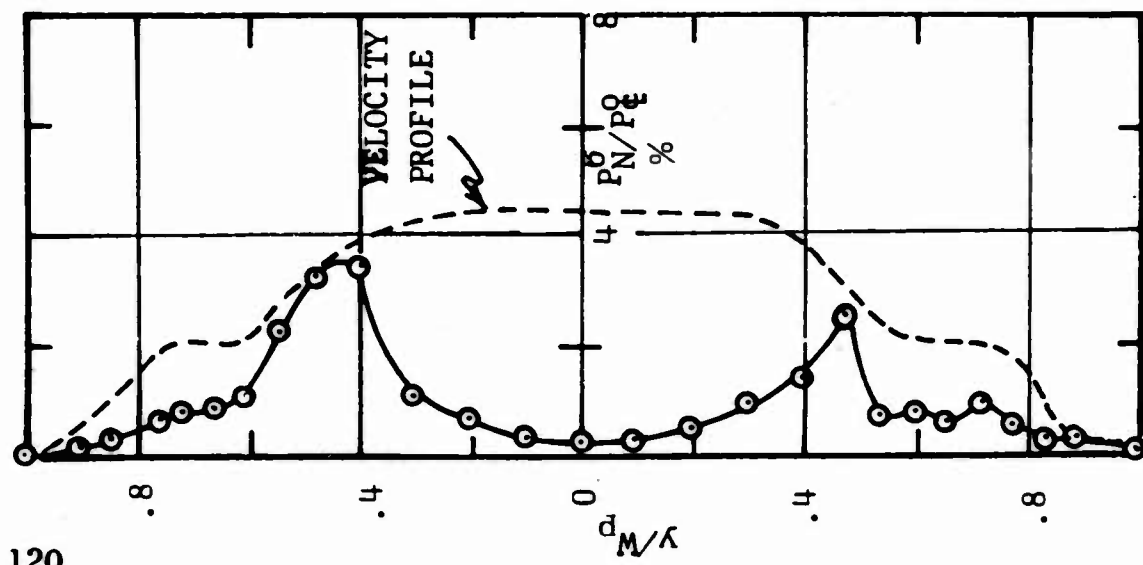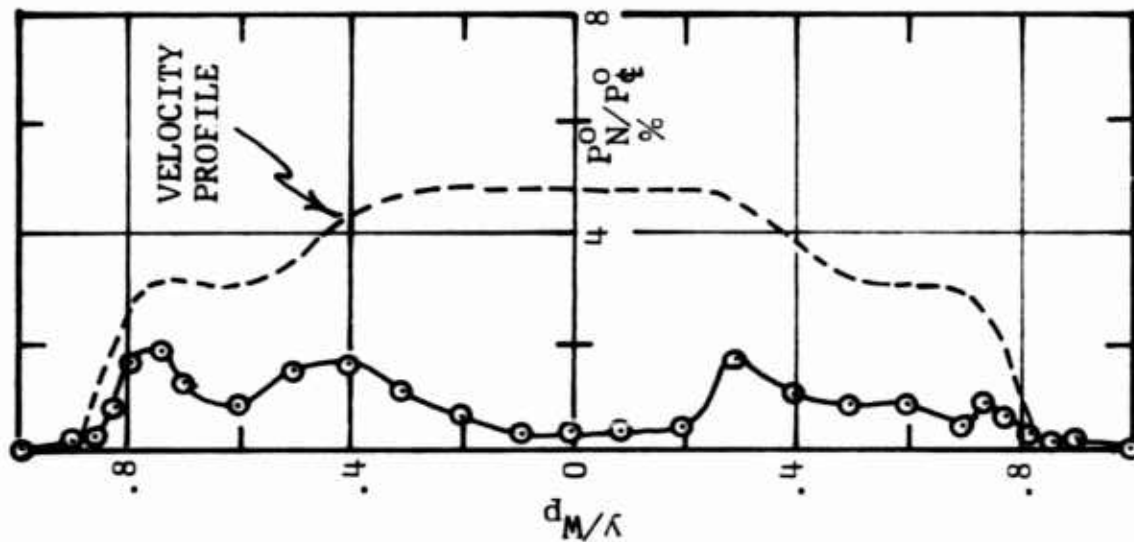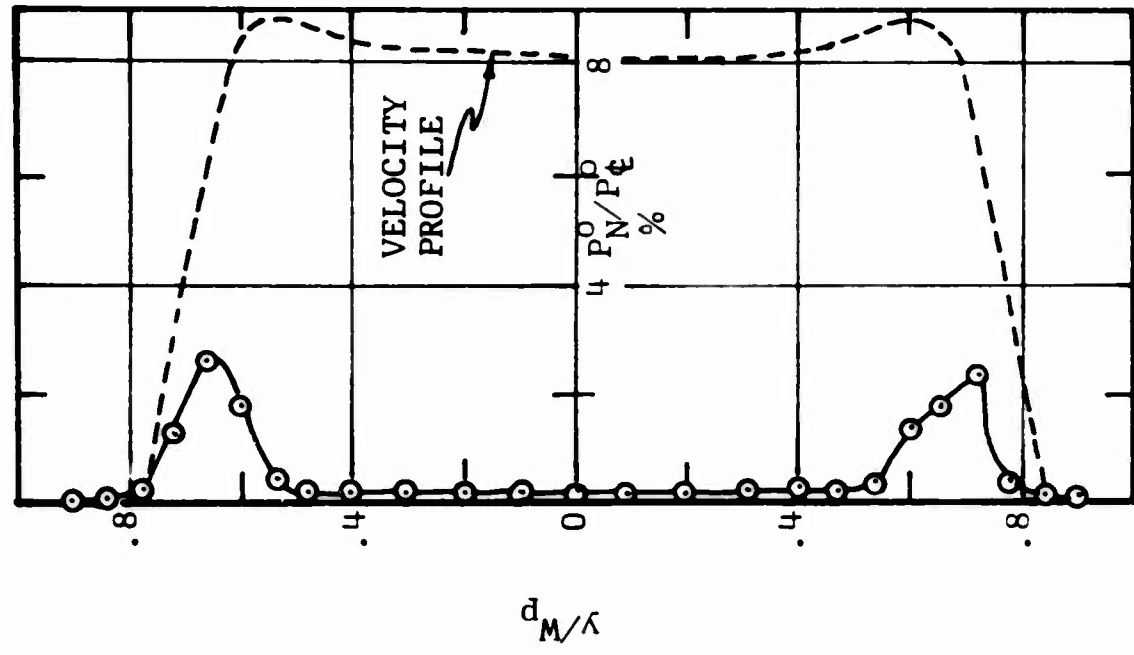
FIGURE 5. NOISE PROFILES AT $x/W_p = 1.5$, $W_c/W_p = 1.0$, $s/W_c = .50$, $\Delta P_c^o/P_p^o = 0$

a) $\bar{P}_c^o/P_p^o = .20$, MR=.36
$(v_c/v_p)_{a} = .45$

b) $\bar{P}_c^o/P_p^o = .40$, MR=.57
$(v_c/v_p)_{a} = .61$

c) $\bar{P}_c^o/P_p^o = .96$, MR=2.0,
$(v_c/v_p)_{a} = 1.0$

120

FIGURE 6. NOISE PROFILES AT $x/W_p = 9.5$; $W_c/W_p = 1.0$; $s/W_c = .50$; $\Delta P_c^\bullet/P_p^\bullet = 0$

a) $\bar{P}_c^O/P_p^O = .40$, MR=.57, $(v_c/v_p)_a = .61$

b) $\bar{P}_c^O/P_p^O = .96$, MR=2.0, $(v_c/v_p)_a = 1.0$

121

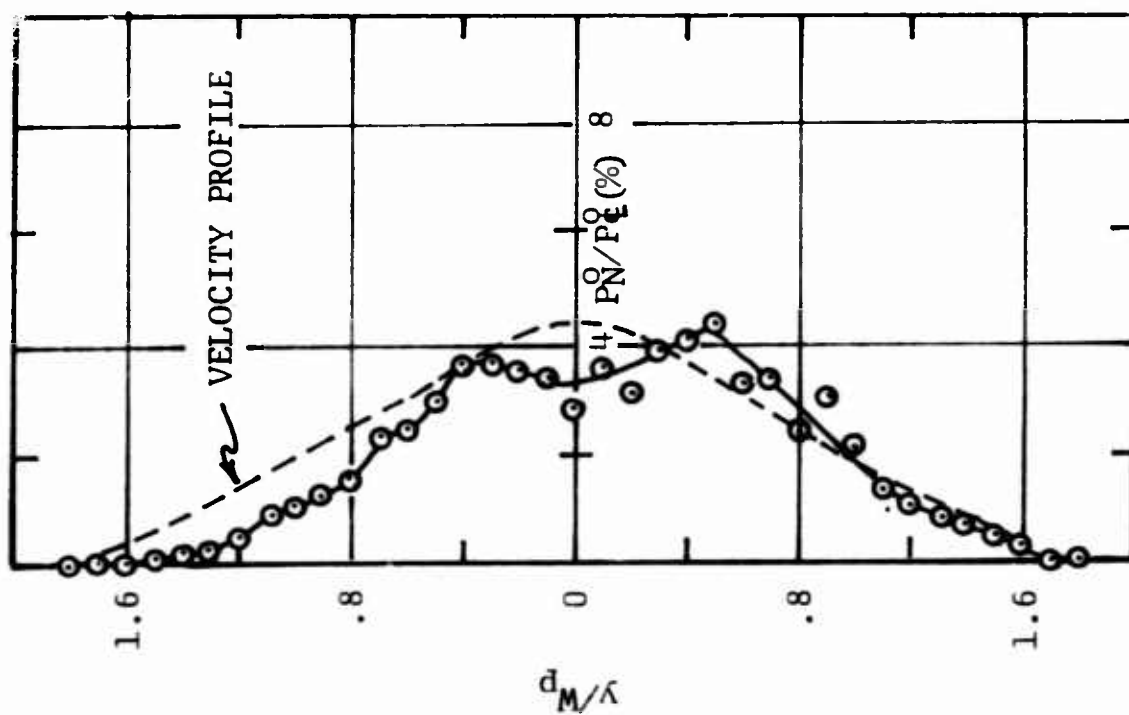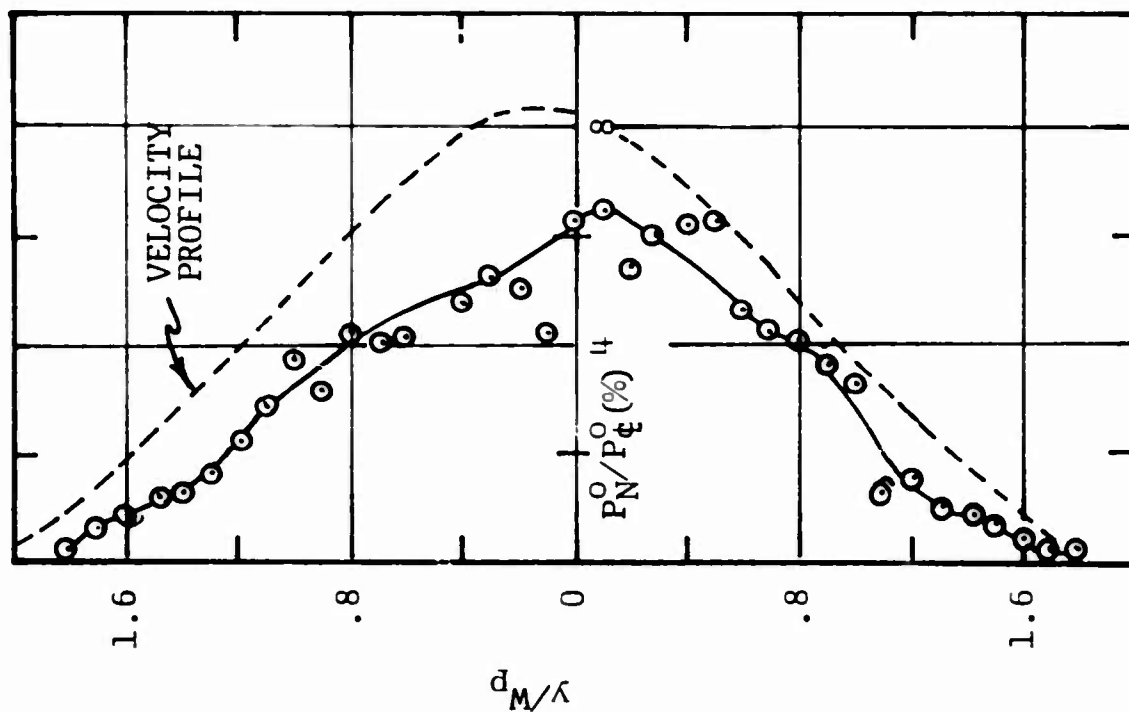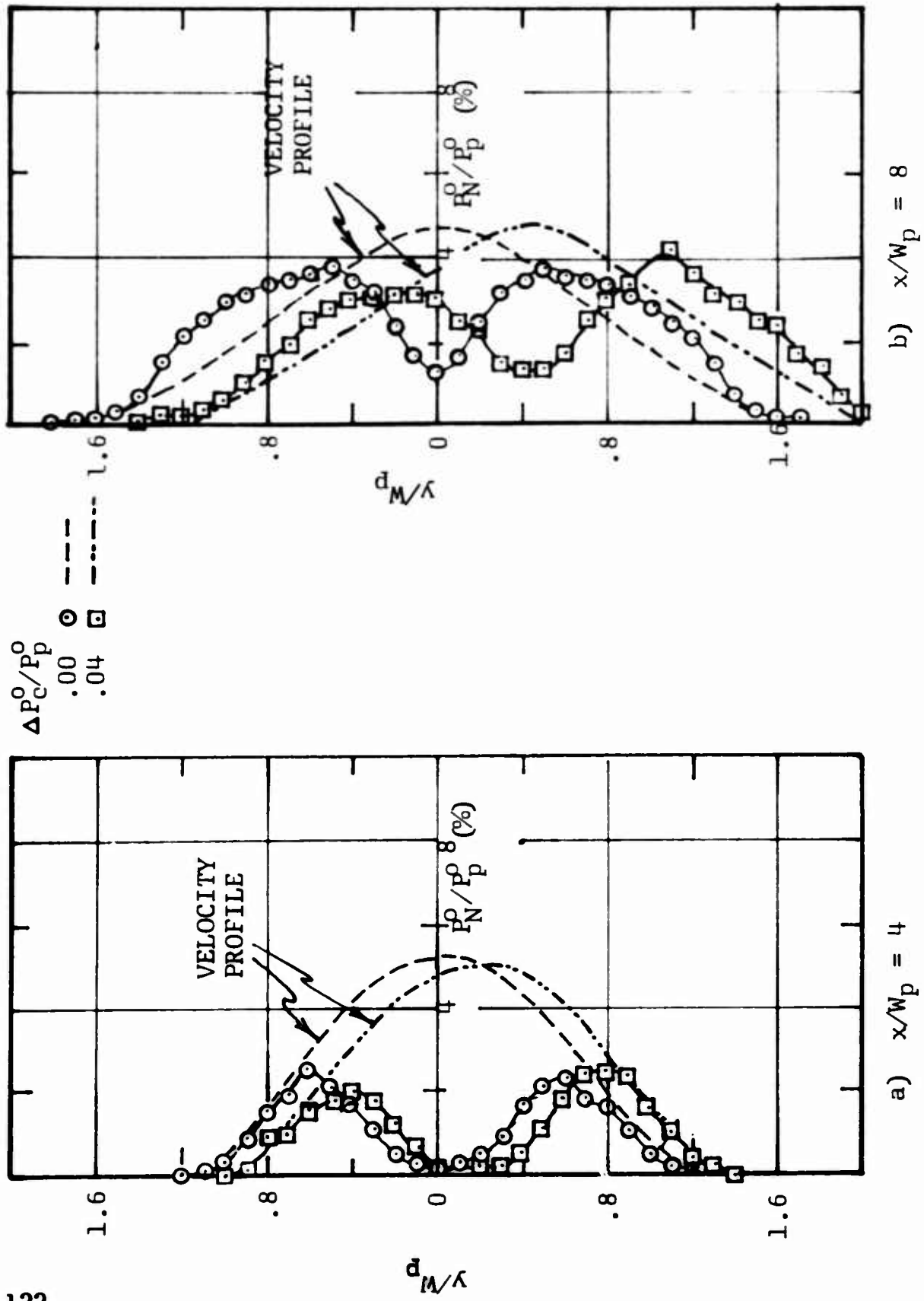FIGURE 7. NOISE PROFILES ; $W_c/W_p = 2.0$, $s/W_c = .125$, $\bar{P}_c^0/P_p^0 = .30$, MR = .20

122

DEFLECTION & RELATIVE FLOW OF THREE INTERACTING JETS

by

F. A. Moynihan and R. J. Reilly

Honeywell
Military Products Group
Research Laboratory

ABSTRACT

Deflection of a power stream by means of interaction with unbalanced control streams, a phenomena basic to fluid amplifiers, was investigated experimentally. An expression for the combined stream deflection in terms of the acting forces is derived and verified by detailed measurements for two-dimensional incompressible flow. Presence of free boundaries and viscosity make it difficult to solve the jet deflection equation explicitly in terms of amplifier design parameters so the relation of the interaction forces, as they affect the jet deflection, and the relative mass flows of the three streams were determined experimentally for a range of amplifier design variables. It is shown that all the forces (momentum, static pressure and centrifugal) are significant in determining the deflection and that their relative importance is a function of the control stream average pressure for both small and large control ports. Average control stream mass flow, relative to the power stream mass flow is essentially independent of jet deflection and is a function of the geometry and average control stream total pressure.

INTRODUCTION

A phenomena basic to many classes of fluid amplifiers is the interaction of small control streams with a power stream to deflect the combined jet. Prediction of the flow deflection and the incoming flow rates in terms of channel geometry and pressures is of interest for the design of fluid amplifiers and proportional devices in particular. Various analysis and experiments have been reported, for example, references 1, 2 and 3, to predict flow deflection, but in general they do not show clearly the effects of altering the geometry or relative pressure level of the streams; nor, as shown by the present experiments, do they always account for all of the significant forces. For example, reference 1 uses only the momenta to predict the deflection, reference 2 and 3 include both the momentum and static pressure forces, while the present results indicate that momentum, static pressure and centrifugal forces can be significant. As an aid to clarifying this, the present paper

presents typical results of detailed measurements of the interaction region
for a range of geometries and pressures and a simplified analysis is advanced
to organize the results.

It is recognized that there are many possible geometric variables for the
interaction process other than those reported here. But it is hoped that
these data can act as an aid to the understanding of what is occurring when
changes are made and as a guide in designing geometries to control the jet
deflection and relative mass flows for particular fluid device applications.

The experiments and analysis are for two-dimensional interaction of three
incompressible fluid streams whose basic geometry is as shown in Figure 1.
Geometric variables were the relative width of the control streams, W_c/W_p,
and the control stream offset, s/W_c. Fluid stream variables include the con-
trol stream's relative pressure level, P_c^o/P_p^o, as well as the unbalance of
the control stream pressures.

The apparatus, Figure 2, has the three jets mounted between two parallel
large plastic plates. A pitot probe and static pressure tap mounted in the
top plate can be located at any point in the interaction region by sliding
the top plate relative to the jets by means of fine thread jack screws in
both the x and y directions. A "cobra" probe, interchangeable with the pitot
probe, provides flow direction measurements. Flow deflections resulting from
the interaction were measured at downstream stations at from x/W_p = 4 to 6.
Reference conditions for the three streams are measured by pitot probes and
static taps located upstream in each of the three channels. Pressure read-
outs are by conventional inclined manometers.

The fluid was air at subsonic speeds (maximum velocities on the order of 60
to 70 ft/sec) and low pressures (power jet total pressures on the order of 1
to 2 inches of H_2O gage). Power jet channel was 1/2 inch with an aspect ra-
tio of 6 and the Reynolds number based on W_p was approximately 16,000.

ANALYSIS

Jet Deflection

A control volume type of analysis is applicable because the interest is in
the end result of the interaction as a function of known incoming flow condi-
tions. In order to use this method, the entering flow conditions of velocity
magnitude and direction and static pressure distributions in each channel
must be known to solve for the exit flow conditions providing the intervening
external forces acting on the fluid are known. Then, if the exit static pres-
sure is known, the resulting flow direction can be solved for if one assumes
a uniform exit velocity direction.

The first problem then is to accurately define the limits of the control
volume to satisfy the requirements of known entering flow conditions. This
is the station in each entering channel where the transverse velocity

24

distribution was uniform and parallel with the walls. Measurements across the exit of the control ports show that flow direction, velocity magnitude and the static pressure distributions are all non-uniform and not readily predictable, Figure 3. However, approximately one channel width upstream, the flow is uniform as illustrated by the uniform transverse static pressure distributions of Figure 3. Thus, the control volume must be drawn upstream in each channel and the unbalance of wall pressure forces acting on the fluid (equal and opposite to fluid forces on the wall), shown in Figure 3, must be accounted for in the force balance. Origin of the transverse pressure gradients are the internal centrifugal forces of the deflected fluid streams.

The downstream portion of the control volume is drawn so that all of the exit flow is through the face B-C, Figure 1. Referring to Figure 1, it is necessary to assume that:

(1) The flow direction through B-C is uniform.

(2) The static pressure is uniform and equal to the ambient, which is substantially correct if B-C is sufficiently far downstream, Figure 3.

(3) The flows through A-B and D-C (entrained flow) are equal in magnitude but opposite in direction.

(4) The static pressure distributions along A-B and D-C are equal.

With these assumptions, the force balance can be written in the x and y directions using the theorem that for a control volume the difference of the outgoing and incoming momenta are equal to the sum of the forces acting between them.

In the y direction

$$\dot{m}_a \, \overline{v}_a \, \sin \theta - \dot{m}_1 \, v_1 + \dot{m}_2 \, v_2 \;=\; W_c \, P_1 - W_c \, P_2 + \Sigma F_{wy} \qquad (1)$$

In the x direction

$$\dot{m}_a \, \overline{v}_a \, \cos \theta - \dot{m}_p \, v_p \;=\; W_p \, P_p - a \, P_a + \Sigma_{wx} \qquad (2)$$

Where Γ_w is the pressure force of the walls on the fluid in the respective directions.

Letting P_a be the reference pressure and equal to zero and combining equations 1 and 2

125

$$\tan \theta = \frac{\dot{m}_1 v_1 - \dot{m}_2 v_2 + W_c (P_1 - P_2) + \Sigma F_{wy}}{m_p v_p + W_p P_p + \Sigma F_{wx}} \qquad (3)$$

Putting equation 3 in terms of total pressures, P°, and dynamic pressures, q,

$$\tan \theta = \frac{W_c [(P_1^\circ + q_1) - (P_2^\circ + q_2)] + \Sigma F_{wy}}{W_p [P_p^\circ + q_p] + \Sigma F_{wy}} \qquad (4)$$

It is convenient to reference the dynamic pressure (kinetic energy) to the total pressure (total energy) to define the condition of the incoming flow. So let

$$q' \equiv q/p^\circ \qquad (5)$$

Then

$$\tan \theta = \frac{W_c [(1 + q_1') P_1^\circ - (1 + q_2') P_2^\circ] + \Sigma F_{wy}}{W_p [(1 + q_p') P_p^\circ] + \Sigma F_{wx}} \qquad (6)$$

q' can be given a geometric interpretation if one imagines that the three streams do not mix, illustrated in Fig. 1 by phantom lines for control stream 1, so that the continuity equation can be written for each stream and further if it is assumed no total pressure loss in the stream. Then it can be shown that

$$q' = \left(\frac{a}{W}\right)^2 \qquad (7)$$

where "a" is the exit area of the particular stream and W is the original channel width, illustrated in Figure 1 for number one control stream as "a_1." Thus $\sqrt{q'}$ represents an effective area ratio and further because $q \leq P^\circ$ then $q' \leq 1.0$, so $\sqrt{q'}$ represents an effective channel constriction. Experimental measurements of q' are presented and discussed later.

In order to examine the net effect of the various forces on the jet deflection in the following experimental results, one can write expressions for the deflections including only portions of the acting forces. For example, if one neglects the centrifugal forces, the net deflection due just to the entering fluid momenta and static pressure forces would be

126

$$\tan \beta = \frac{W_c}{W_p} \left[\frac{1 + q_1'}{1 + q_p'} \frac{P_1^{\,\circ}}{P_p^{\,\circ}} - \frac{1 + q_2'}{1 + q_p'} \frac{P_2^{\,\circ}}{P_p^{\,\circ}} \right] \qquad (8)$$

and further, if one considered only the entering fluid momenta

$$\tan \beta_m = \frac{W_c}{W_c} \left[\frac{q_1'\, P_1^{\,\circ} - q_2'\, P_2^{\,\circ}}{q_p'\, P_p^{\,\circ}} \right] \qquad (9)$$

Net effect of the centrifugal forces would then be the difference between θ and β.

A check on the assumptions made in the force balance is afforded by comparing the θ measured by a flow direction probe with calculated θ; where θ calculated is from equation 4 and the data from Figure 3 for the incoming total and dynamic pressures and the integrated wall pressures for ΣF_{wy} and ΣF_{wx}. Tabulation of the various forces as well as the resulting flow directions are listed in Table 1 for the three sets of data shown in Figure 3. Comparison of the measured and calculated θ's in the table show agreement for all three sets of data indicating that assumptions are reasonable. Also of interest is the relatively large size of the wall static pressure forces indicating the possible influence of the centrifugal forces on the net jet deflection. The actual net influence of the centrifugal forces can be seen by comparing θ and β. For the first configuration, $W_c/W_p = 1.0$, $s/W_c = .5$, $\beta < \theta$ indicating that the net effect of the centrifugal force is to add to the deflection, for the second configuration $\theta \approx \beta$ so the effect of the centrifugal forces is negligible while for the third configuration $\beta > \theta$ which shows that the net effect of the centrifugal forces can be to subtract from the possible jet deflection. The table also hints that, except for the third configuration, β_m is insufficient to predict the deflection. Further comparisons of θ, β and β_m as functions of geometric and pressure variables are discussed later.

Relative Flow

The incoming flow rates of the control and power streams are of interest in design of fluid amplifiers; and in particular the relative flow rates of the sum of the control streams and the power streams denoted as Mass Ratio.

By definition

$$MR = \frac{\dot{m}_1 + \dot{m}_2}{\dot{m}_p} \qquad (10)$$

127

Assuming the same incompressible fluid for control and power streams and using equation 5,

$$MR = \frac{W_c}{W_p} \left[\frac{\sqrt{q_1' \, P_1^{\,\circ}} + \sqrt{q_2' \, P_2^{\,\circ}}}{\sqrt{q_p' \, P_p^{\,\circ}}} \right] \tag{11}$$

The mass ratio is not clearly an independent parameter in the jet deflection expression as formulated in equation 6 but is a dependent variable of the interaction process in that it contains q'. Equation 11 shows that MR is a function of the area ratio W_c/W_p and the sum of the control pressures or their average. The mass ratio was determined experimentally for all configurations investigated and the results are discussed later.

EXPERIMENTAL RESULTS

Jet Deflection

As expected, equation 6 indicates that for a given geometry θ should be primarily a function of $\Delta P_c^{\,\circ}/P_p^{\,\circ}$ which can be a controlled variable for the interaction. That this is true is illustrated later in Figure 7. The q's and the centrifugal forces are functions of the interaction process and are best determined experimentally. The centrifugal forces do not enter simply into the deflection expression so it is difficult to predict what their net effect will be and indeed this is true as illustrated for the configurations in Table 1 where the net effect was both + and -. The effect of the q's on θ are more simply seen. If q_1' and q_2' are nearly the same then anything that increases q_1' should increase θ and anything decreasing q_p' would reduce θ. Let us first examine the parameters affecting the q's.

Interpreting q' as an effective channel constriction, it would follow that q_1' and q_2' be a function of θ, and the offset "s" in that these variables alter the constriction for the respective flows. The geometrical interpretation of q' also predicts that q_p' would be a function of the relative total pressure of the control and power streams, $\overline{P}_c^{\,\circ}/P_p^{\,\circ}$, in that the control streams tend to "pinch" off the power stream.

Sample data, Figure 4, illustrate how q_1' increases with θ and q_2' decreases with θ. Increase of q_1' can be interpreted as an effective enlargement of the offset for control port number 1 as the combined jets are deflected away from that port and the decrease of q_2' is a corresponding decrease in the effective discharge area for the other control stream. It is interesting to note that variation of q_1' and q_2' with θ are essentially linear, within the data accuracy, and that their average is a constant. This was true for most all configurations investigated. Using this observation, the behavior of q_c' (defined as the average of q_1' and q_2') with the other parameters was investigated. Although not shown here, the data showed that q_c' was essentially independent of the average control pressure. But as shown in Figure 5, q_c'

128

increased nearly linearly with offset, s/w_c, and is essentially independent of the control port area ratio W_c/W_p.

Although q_p' is independent of θ, Figure 4, it is primarily <u>a</u> function of the average control stream pressure and decreases linearly with P_c^o/P_p^o, for a given geometry, Figure 6. This follows from the "pinching" action of the control streams on the power stream postulated previously. q_p' is also a function of area ratio, Figure 6(a), and offset, Figure 6(b). Enlarging the control ports and/or decreasing the offset have the effect of reducing q_p' and thus possibly increasing θ according to equation 6.

The measured jet deflection, θ, was essentially a linear function of $\Delta P_c^o/P_p^o$, for all configurations, as illustrated in Figure 7 for two typical configurations. Thus the slope, called jet deflection slope, can be used to describe the jet deflection performance. Figure 7(a) illustrates a case where the $\theta > \beta$ showing that the centrifugal forces are adding to the deflection and 7(b) illustrates a case where $\theta < \beta$ and the centrifugal forces have the opposite effect. If the difference of β and β_m is attributed to just the incoming fluid static pressure forces, 7(a) shows that even though the area ratio is small, the static pressure forces are more significant than the momentum forces and in 7(b), with a larger control port area, the deflection due to the momentum forces are larger than that due to the static pressure forces. Thus, amplifiers cannot be simply classed as "Momentum" or "Pressure" according to the size of the control ports. Of more importance, Figure 7 illustrates that θ, β and at least for small deflections β_m are essentially linear with $\Delta P_c^o/P_p^o$ and that neither β nor β_m are sufficient to describe θ under a variety of conditions. This is brought out further in Figure 8 where the jet deflection slopes are shown for a larger variety of geometries and pressures.

Figure 8 indicates that for small control ports, on the order of $W_c/W_p < 1.0$, the centrifugal forces aid the deflection and for larger W_c they detract from β. The effects of average control pressure and offset on the centrifugal forces appear interrelated so it is difficult to make a general observation. However, it appears that the centrifugal forces become more significant at large offsets and low control pressures.

Figure 8 and 9 illustrate that in general large control port areas and small offsets increase the jet deflection slope. Choice of the average control pressure needed to enhance the deflection slope depends on the geometry as shown in Figure 9.

The effective pivot point of the deflected combined jets, which is of interest in designing fluid amplifiers, is approximately at the intersection of the centerlines of the power and control ports for all configurations investigated. This is illustrated in Figure 10 by the line connecting the velocity profile centerlines. During the experiments the effective pivot point was determined by geometry from the flow direction measurement at a known location (the midpoint of profile).

129

Relative Flows

The relative flow rates, mass ratio, as expressed in equation 11 are primarily functions of the area ratio and the average control pressure and depend on θ only as θ is related to $\sqrt{q_1}'$ and $\sqrt{q_2}'$ vary only slightly with θ, Figure 4, so one could expect that the mass ratio be nearly independent of θ.

This was borne out in all the experimental results for deflection angles in the range used by fluid amplifiers. This leaves q_c' and q_p' as variables for the mass ratio and, as discussed previously, they are functions of area and offset. Plots of mass ratio vs average control pressure, Figure 11, illustrate that the mass ratio will increase with $\bar{P}_c{}^o/P_p{}^o$, area ratio and offset.

REFERENCES

1. Reilly, R. and Moynihan, F. "Notes on a proportional Fluid Amplifier,"
   ASME Publication Fluid Jet Control Devices, 28 November 1962.

2. Peperone, S., Katz, S. and Goto, J. "Fluid Amplification, Gain Analysis
   of the Proportional Amplifier," TR-1073; Diamond Ordnance Fuze Labora-
   tories, 30 October 1962.

3. Brown, F. "A Combined Analytical and Experimental Approach to the Develop-
   ment of Fluid Jet Amplifiers," Paper 62-WA-154; ASME Winter Meeting, 25
   November 1962.

LIST OF SYMBOLS

a	effective channel width
$\dot{m}$	mass flow rate
P	static pressure
P^o	total pressure
$\Delta P_c^{\ o}$	$P_{c_1}^{\ o} - P_{c_2}^{\ o}$
$\overline{P}_c^{\ o}$	$\frac{1}{2}(P_{c_1}^{\ o} + P_{c_2}^{\ o})$
q	dynamic pressure
q'	relative dynamic pressure (q/P^o)
v	velocity
W	channel width
MR	mass flow ratio, see equation 10
θ	combined jet deflection angle
β	combined jet deflection angle due to entering fluid static pressure and momenta, eq. 8
β_m	combined jet deflection angle due to entering fluid momenta, eq. 9

Subscripts

a	interaction region
c	control port
p	power port or stream
1	control stream 1
2	control stream 2

TABLE I

Interaction Region Measured Forces

	Configurations		
NOTE: Pressure dimensionless by $P_p{}^o$	W_c/W_F =	1.00	1.00	2.00
Area dimensionless by W_p	s/W_c =	.50	1.00	.25
	$\Delta P_c{}^o/P_p{}^o$ =	.10	.10	.20
	$\overline{P}_c{}^o/P_p{}^o$ =	.25	.25	.50

Y Direction Forces	1.00	1.00	2.00
Control Streams net momentum	.040	.066	.280
Control Streams net static pressure	.080	.067	.260
Power Stream net wall static pressure	.039	.033	.145
ΣF_y	.159	.166	.632

X Direction Forces			
Power Stream momentum	1.544	1.612	.890
Power Stream static pressure	.228	.194	.555
Control stream net wall static pressure	.228	.446	.640
ΣF_x	2.00	2.252	2.085

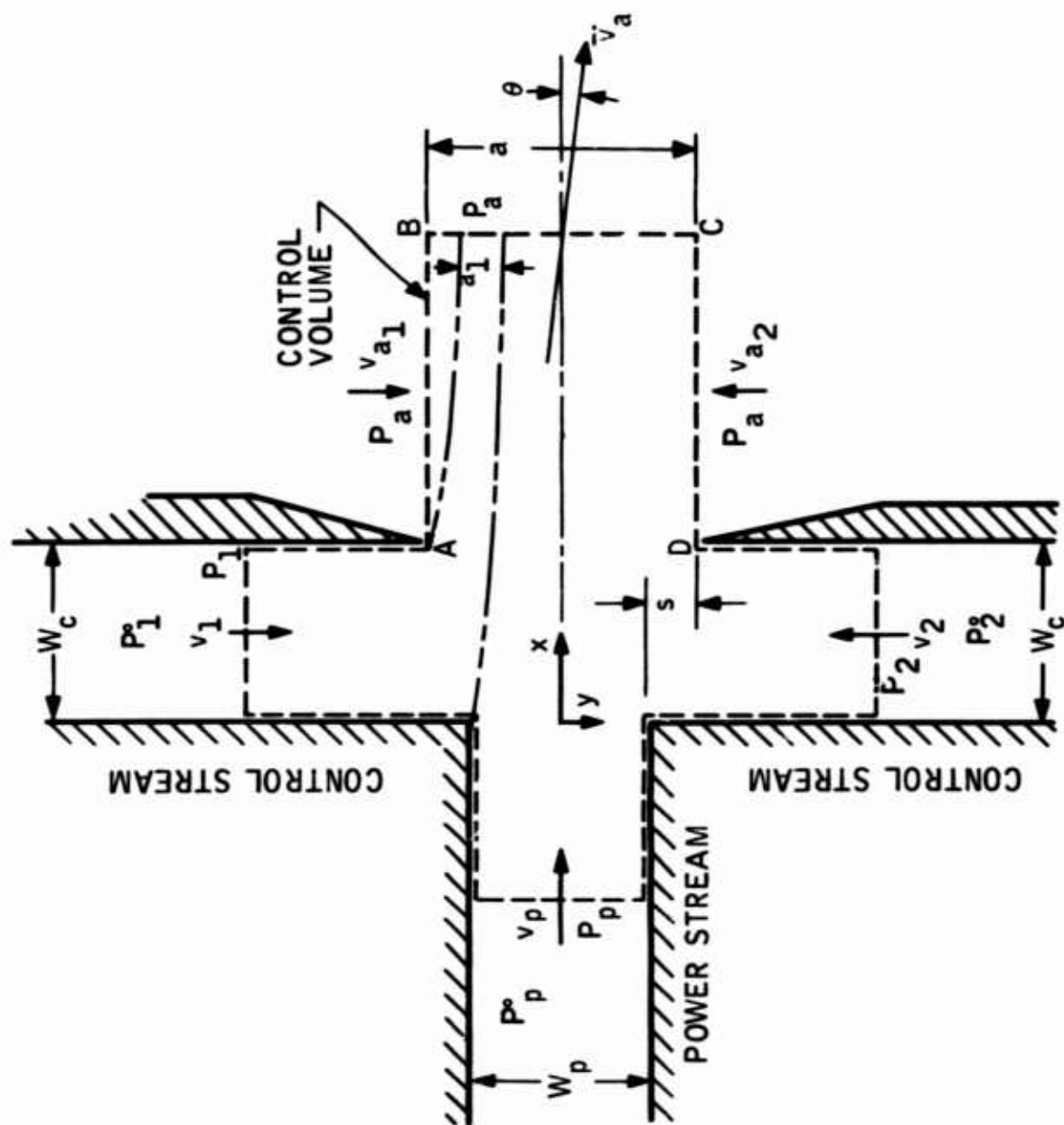| Flow Deflection			
$\theta = \tan^{-1}\dfrac{\Sigma F_y}{\Sigma F_x}$ (eq. 4)	4.6°	4.2°	16.8°
θ measured by probe	4.8°	4.3°	17.4°
β (eq. 8)	3.9°	4.2°	20.6°
β_m (eq. 9)	1.5°	2.4°	17.5°

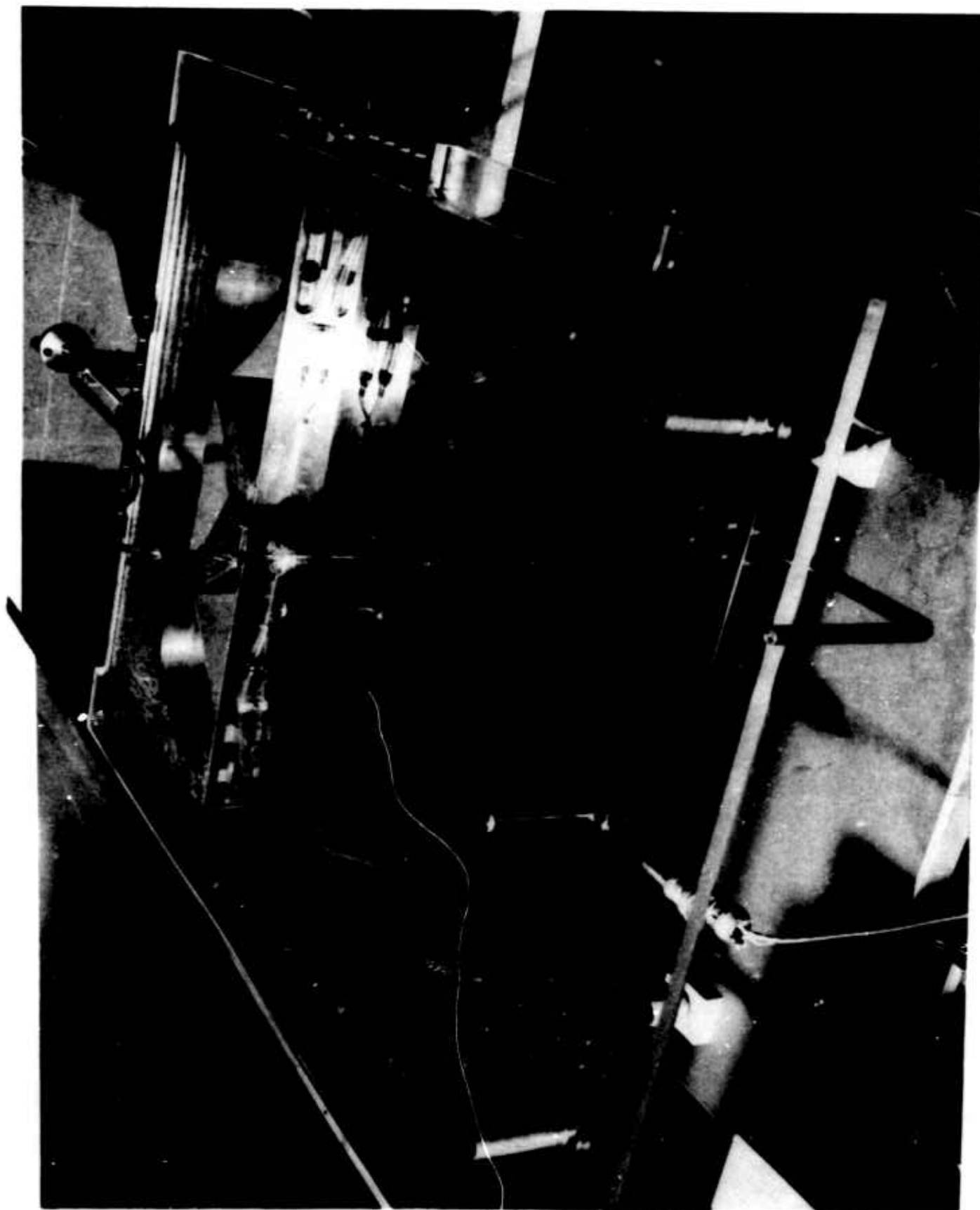FIGURE 1. CONTROL VOLUME AND NOMENCLATURE
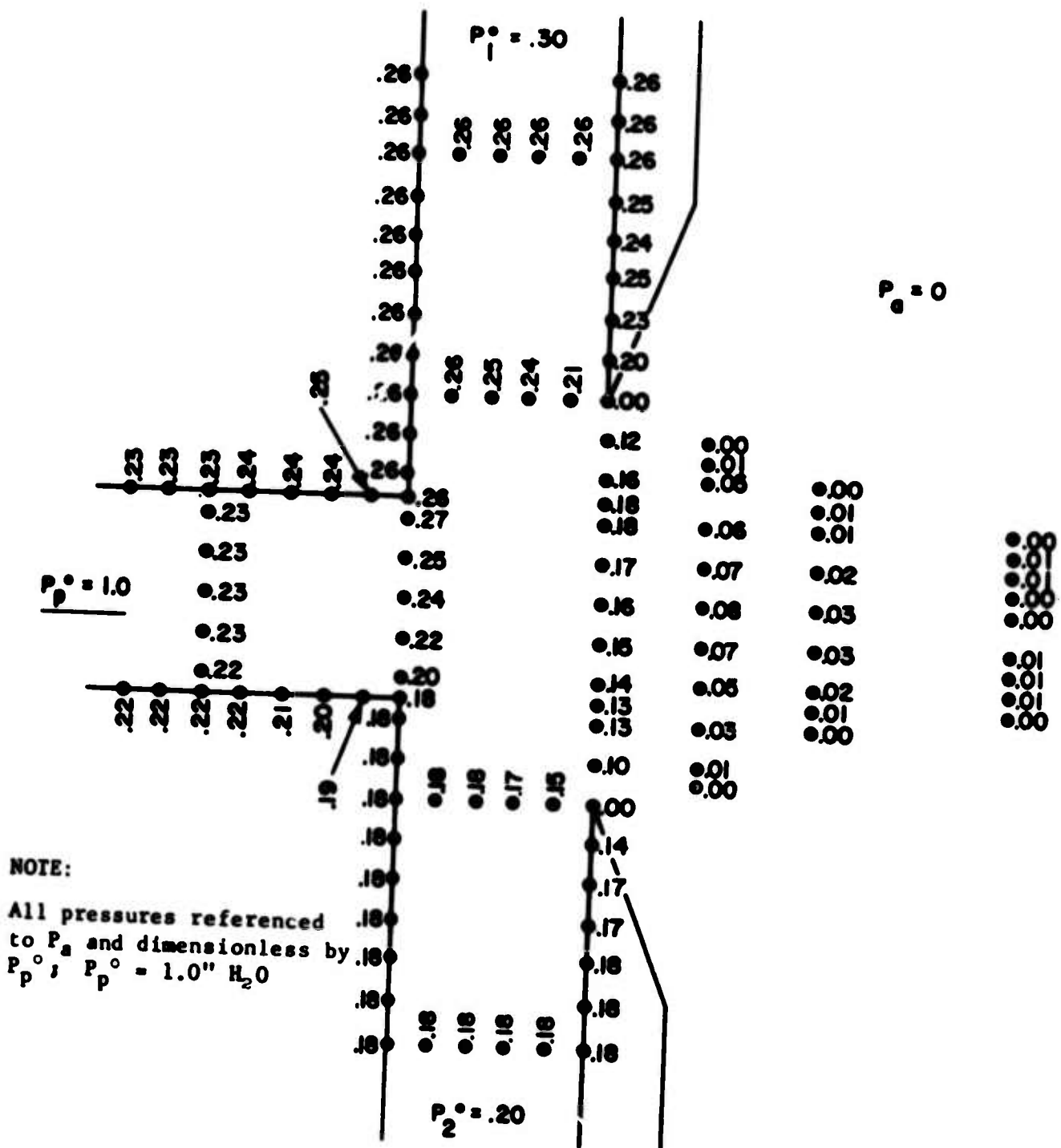
FIGURE 2. JET INTERACTION EXPERIMENTAL APPARATUS

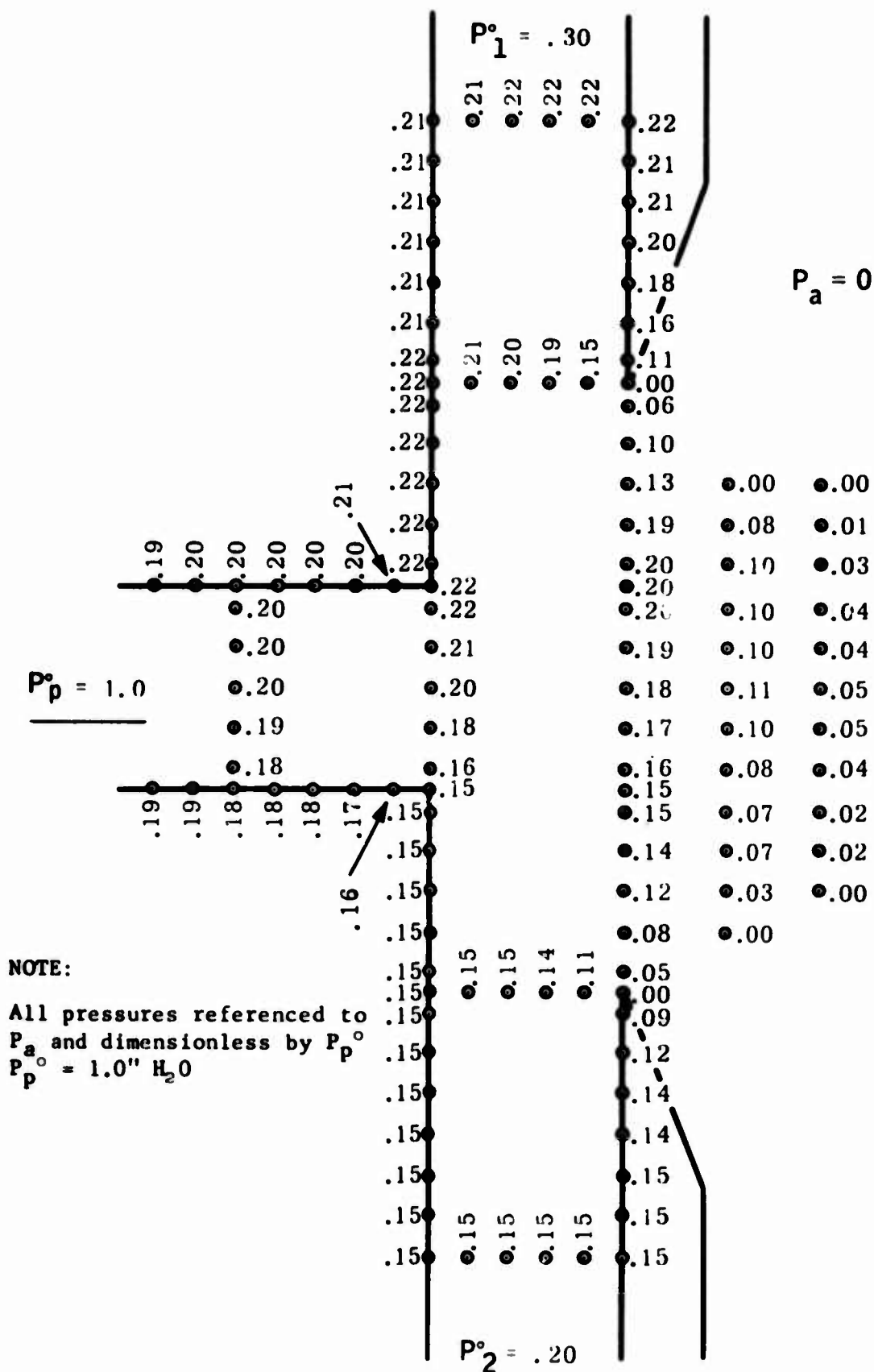FIGURE 3(a). STATIC PRESSURE DISTRIBUTION IN THE INTERACTION REGION
$W_c/W_p = 1.0$, $s/W_c = 0.5$, $P^\circ_c/P^\circ_p = 0.25$, $\Delta P^\circ_c/P^\circ_p = 0.10$

135

FIGURE 3(b). STATIC PRESSURE DISTRIBUTION IN THE INTERACTION REGION
$W_c/W_p = 1.0$, $s/W_c = 1.0$, $\bar{P}^\circ_c/P^\circ_p = 0.25$, $\Delta P^\circ_c/P^\circ_p = 0.10$
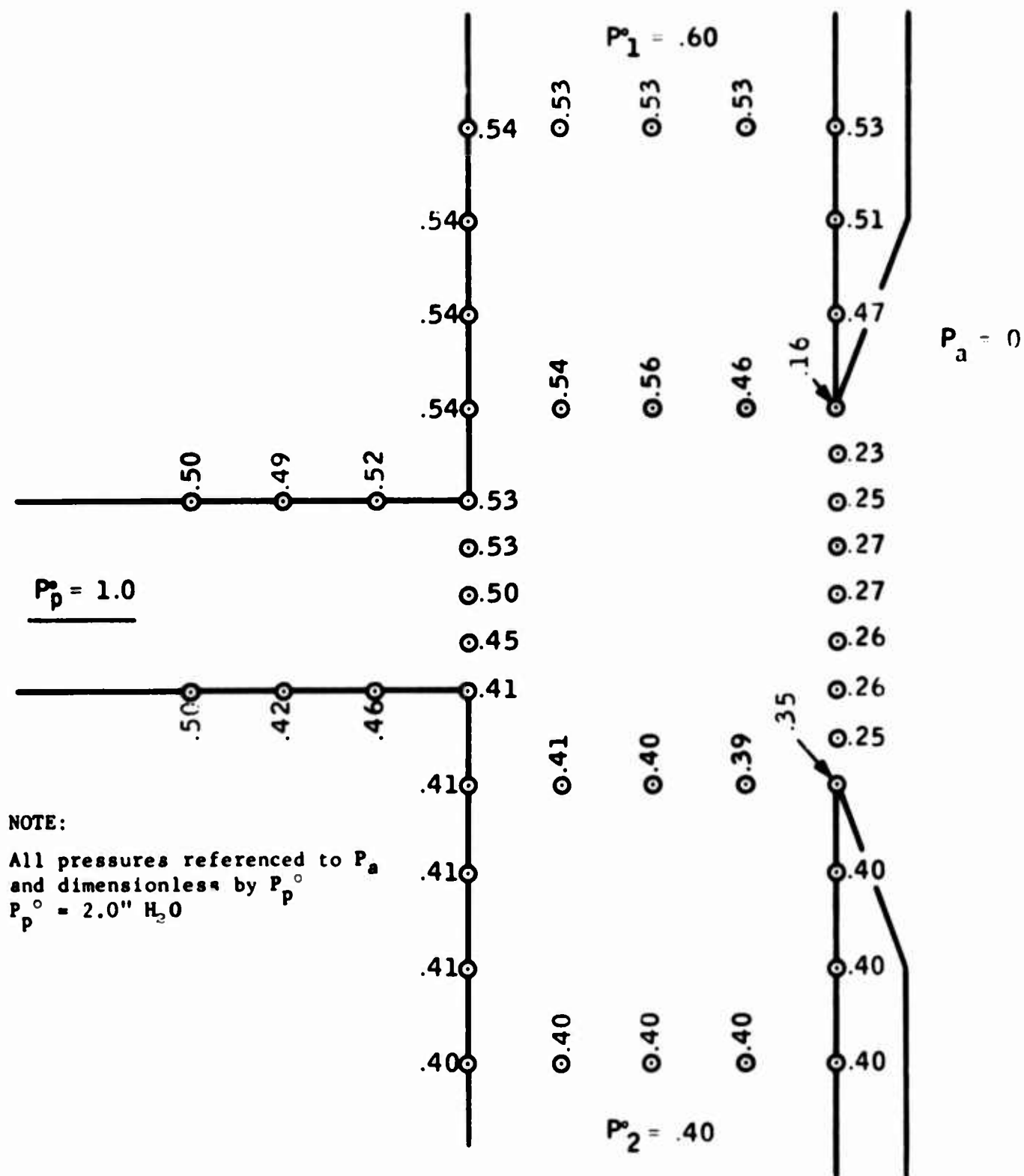
136

$P_1^\circ = .60$

$P_a = 0$

$P_p^\circ = 1.0$

$P_2^\circ = .40$

NOTE:

All pressures referenced to P_a
and dimensionless by P_p°
$P_p^\circ = 2.0'' \ H_2O$

.54   .53   .53   .53   .53

.54   .51

.54   .47

.54   .54   .56   .46   .16

.50   .49   .52   .53   .23

.53   .25

.53   .27

.50   .27

.45   .26

.50   .42   .46   .41   .26

.41   .41   .40   .39   .35   .25

.41   .40

.41   .40

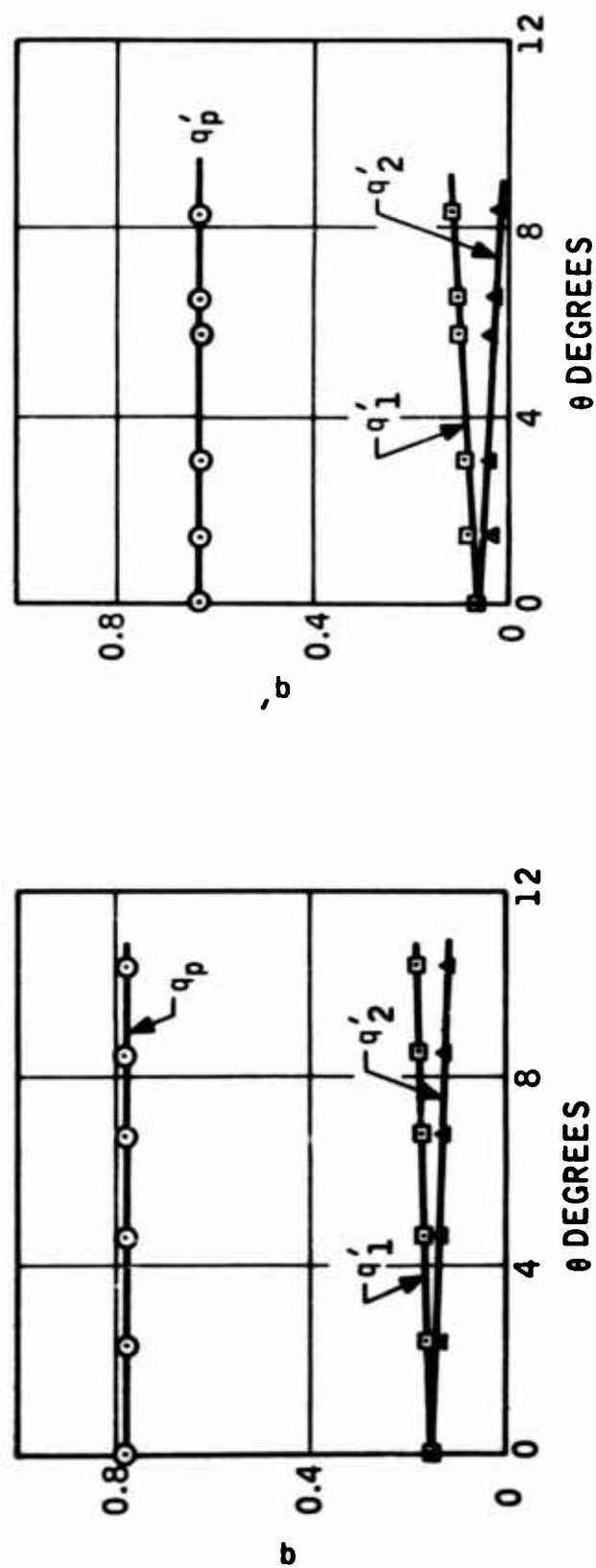.41   .41   .40   .40   .40   .40

FIGURE 3 (c). STATIC PRESSURE DISTRIBUTION IN THE INTERACTION REGION
$W_c/W_p = 2.0$, $s/W_c = 0.25$, $P_c^\circ/P_p^\circ = 0.50$, $\Delta P_c^\circ/P_p^\circ = 0.20$

137

(a) $W_c/W_p = 1.0$, $s/W_c = 0.50$, $\bar{P}_c^\circ/P_p^\circ = 0.2$

(b) $W_c/W_p = 2.0$, $s/W_c = 0.50$, $\bar{P}_c^\circ/P_p^\circ = 0.3$

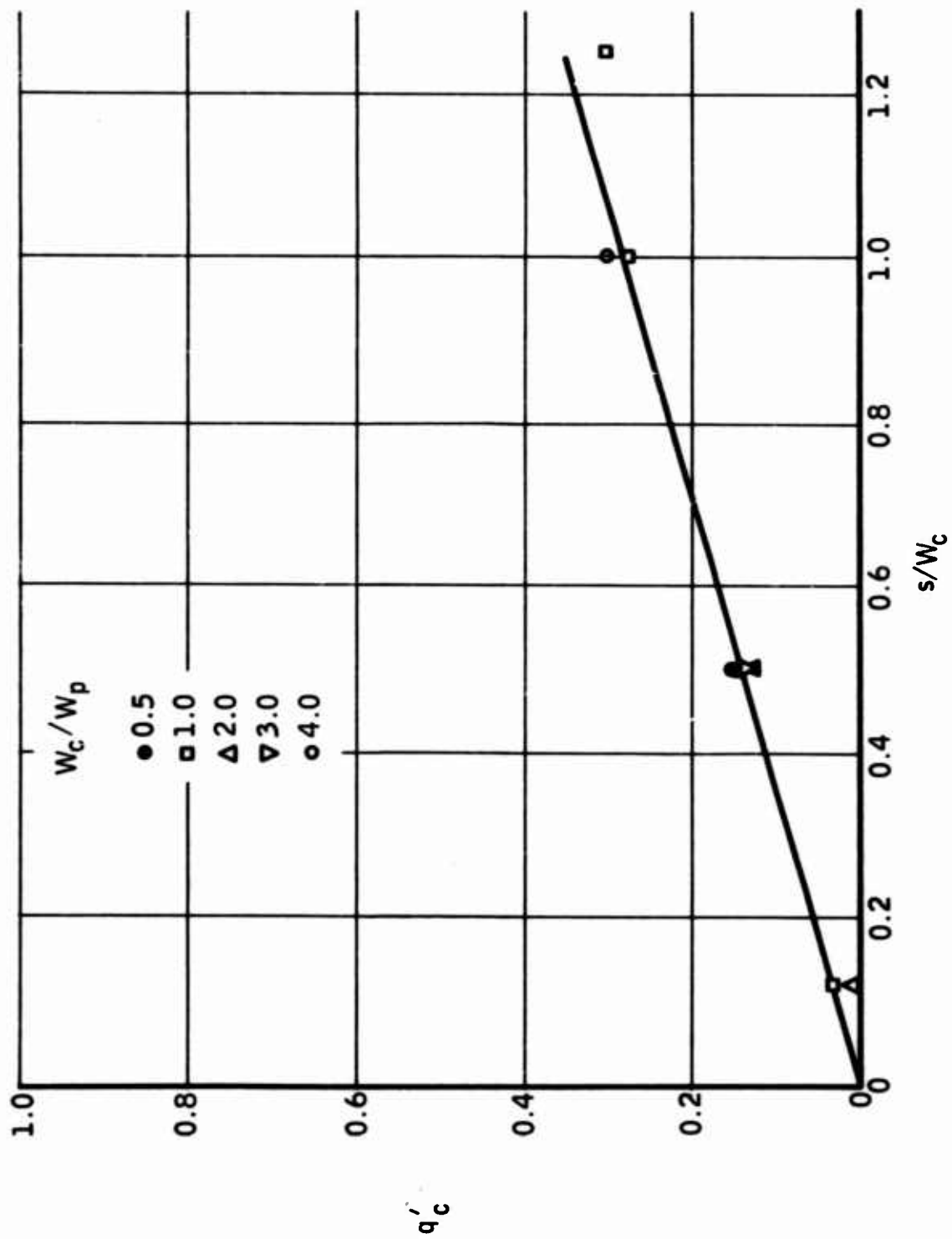FIGURE 4. TYPICAL, VARIATION OF q's WITH JET DEFLECTION

138

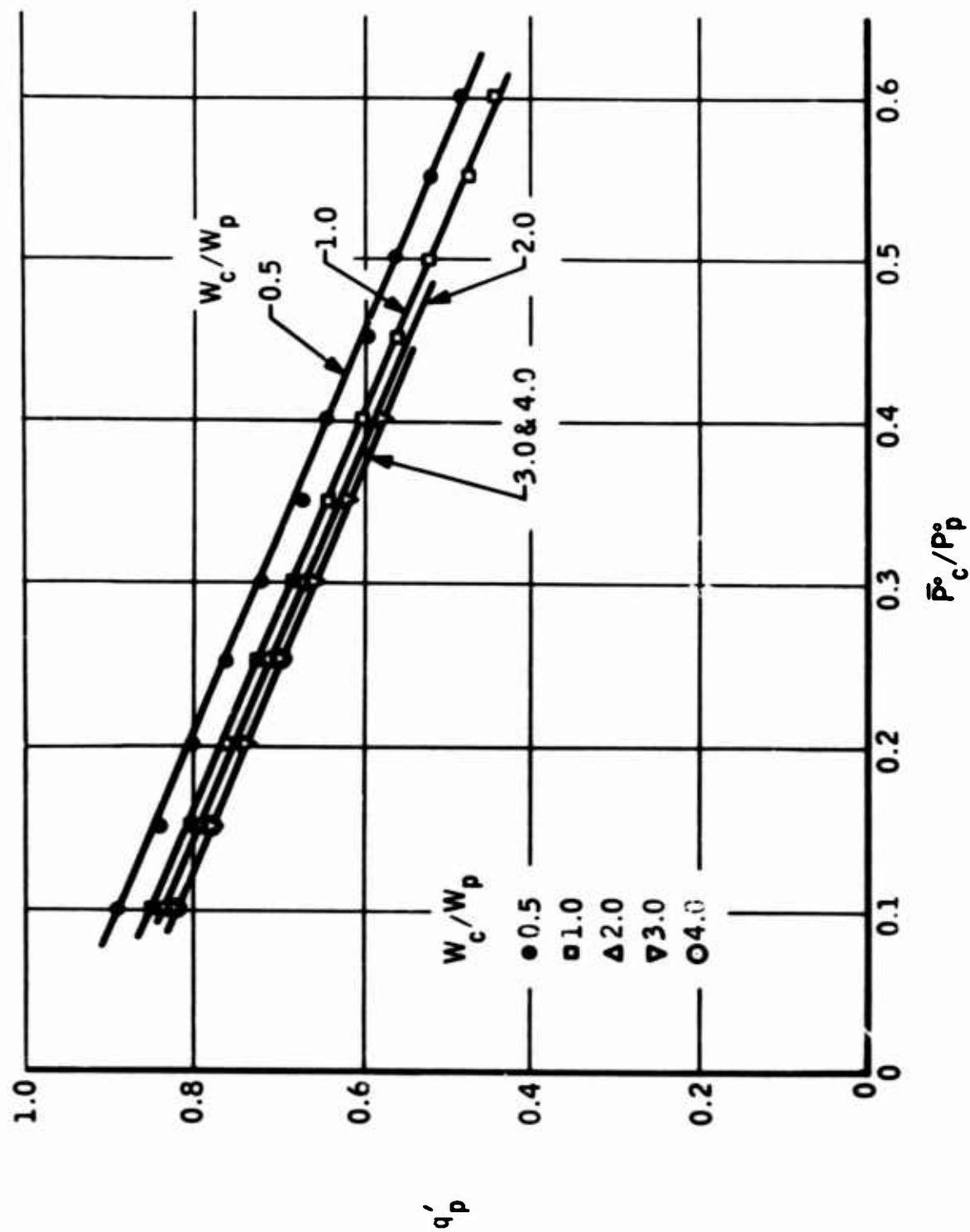FIGURE 5. q'_c VERSUS s/W_c FOR VARIOUS CONTROL PORT AREAS

FIGURE 6 (a). q'_p VERSUS $\bar{P}^*_c / P^*_p$ FOR VARIOUS CONTROL PORT AREAS, ALL WITH $s/W_c = 0.50$
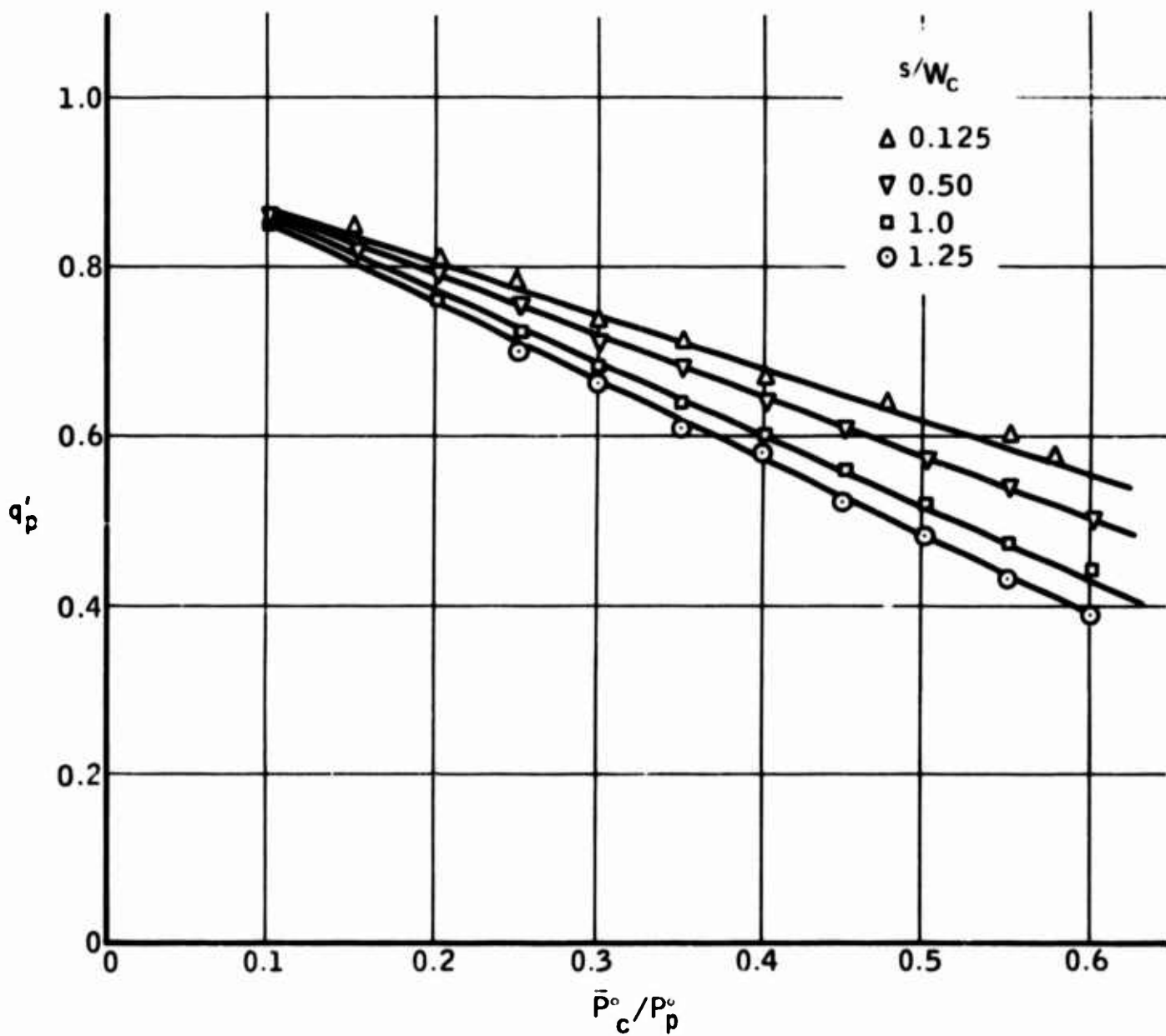
FIGURE 6 (b). q'_p VERSUS $\bar{P}^o_c/P^o_p$ FOR VARIOUS CONTROL PORT OFFSETS, ALL WITH $W_c/W_p = 1.0$

(a) $W_c/W_p = 1.0$, $s/W_c = 0.50$, $\bar{P}^o_c/P^o_p = 0.2$

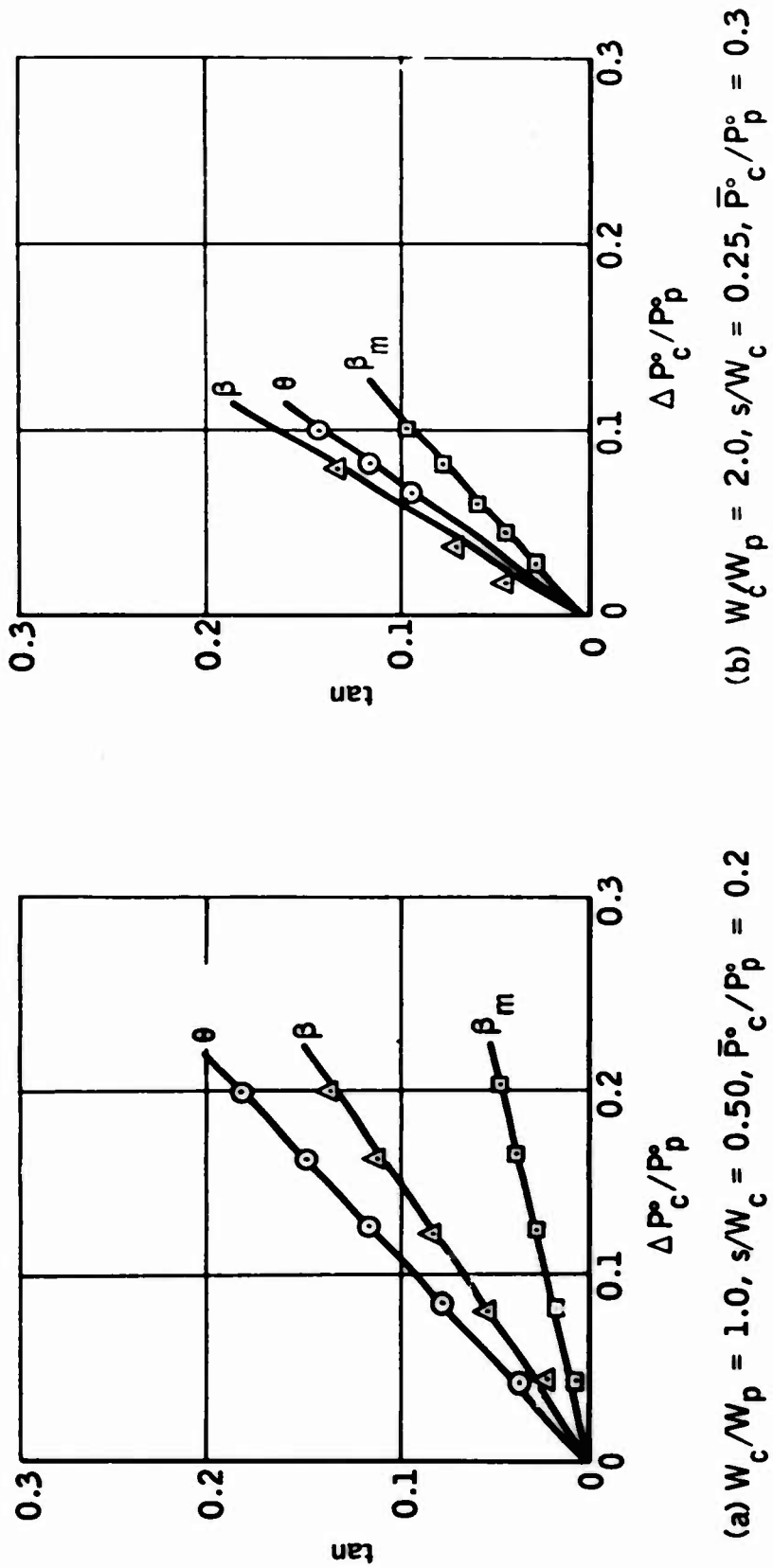(b) $W_c/W_p = 2.0$, $s/W_c = 0.25$, $\bar{P}^o_c/P^o_p = 0.3$
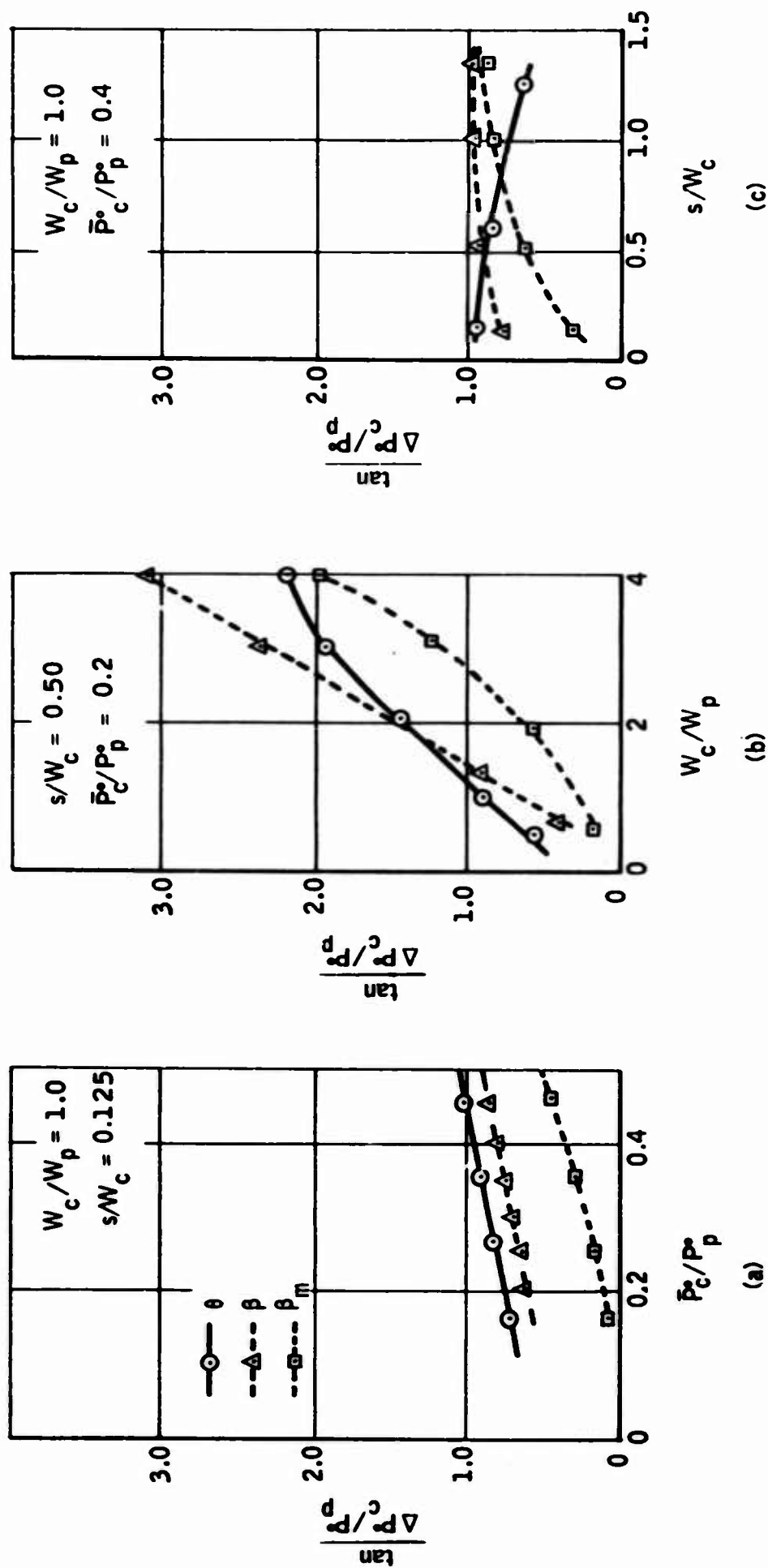
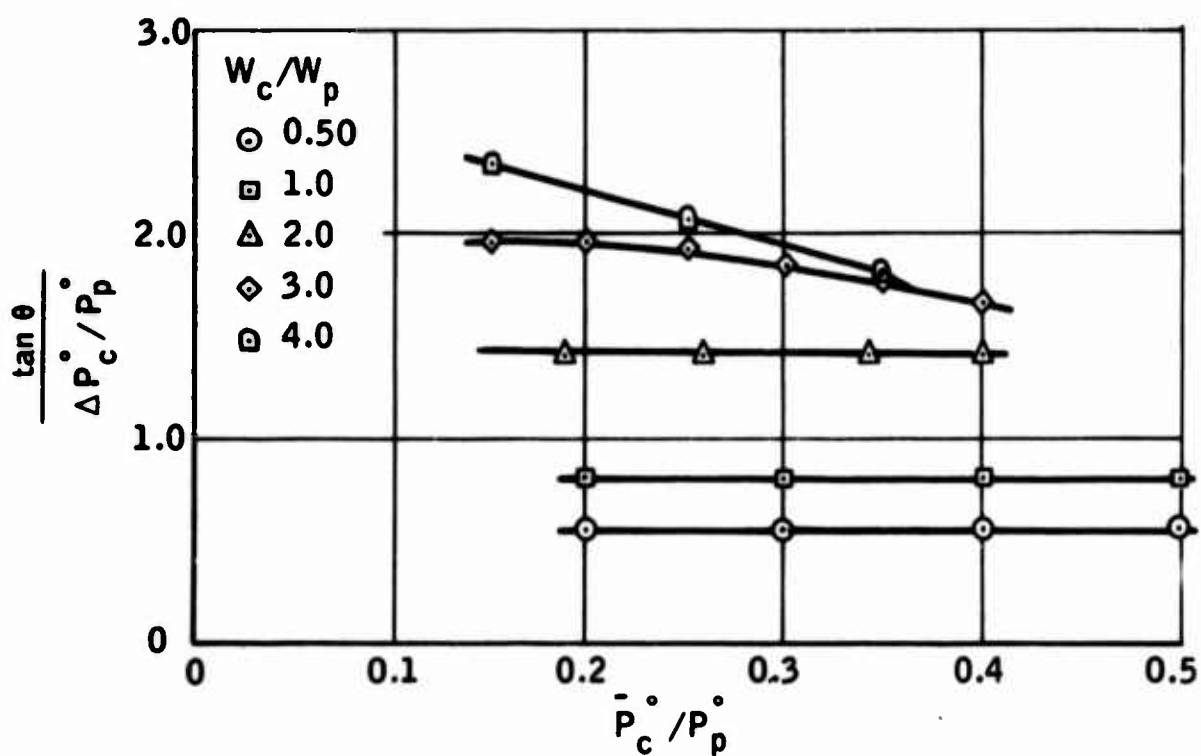FIGURE 7. TYPICAL JET DEFLECTION CURVES

FIGURE 8. TYPICAL VARIATION OF JET DEFLECTION SLOPE WITH AVERAGE CONTROL PRESSURE, CONTROL PORT AREA, AND CONTROL PORT OFFSET

143

(a) FOR VARIOUS CONTROL PORT AREAS, ALL WITH $s/W_c = 0.50$

(b) FOR VARIOUS CONTROL PORT OFFSETS, ALL WITH $W_c/W_p = 2.0$

FIGURE 9. JET DEFLECTION SLOPE VERSUS AVERAGE CONTROL PRESSURE
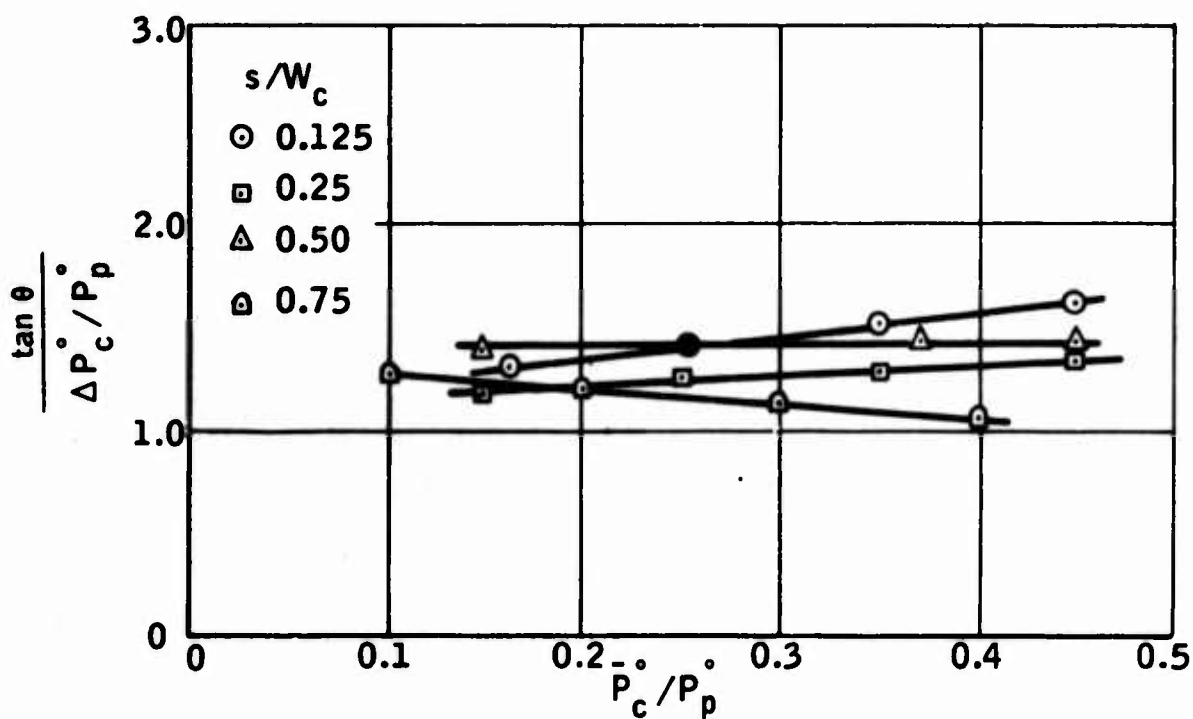
144

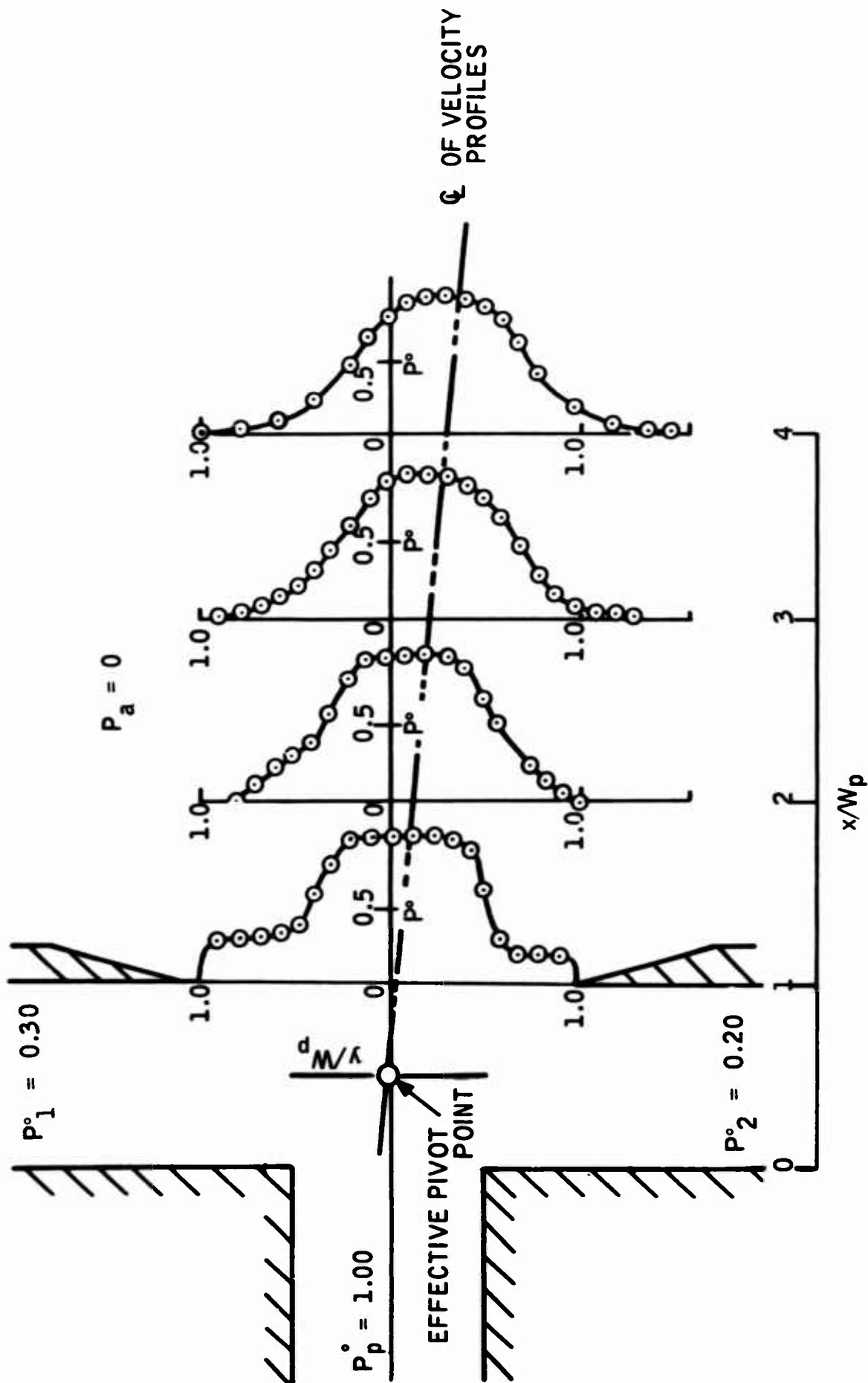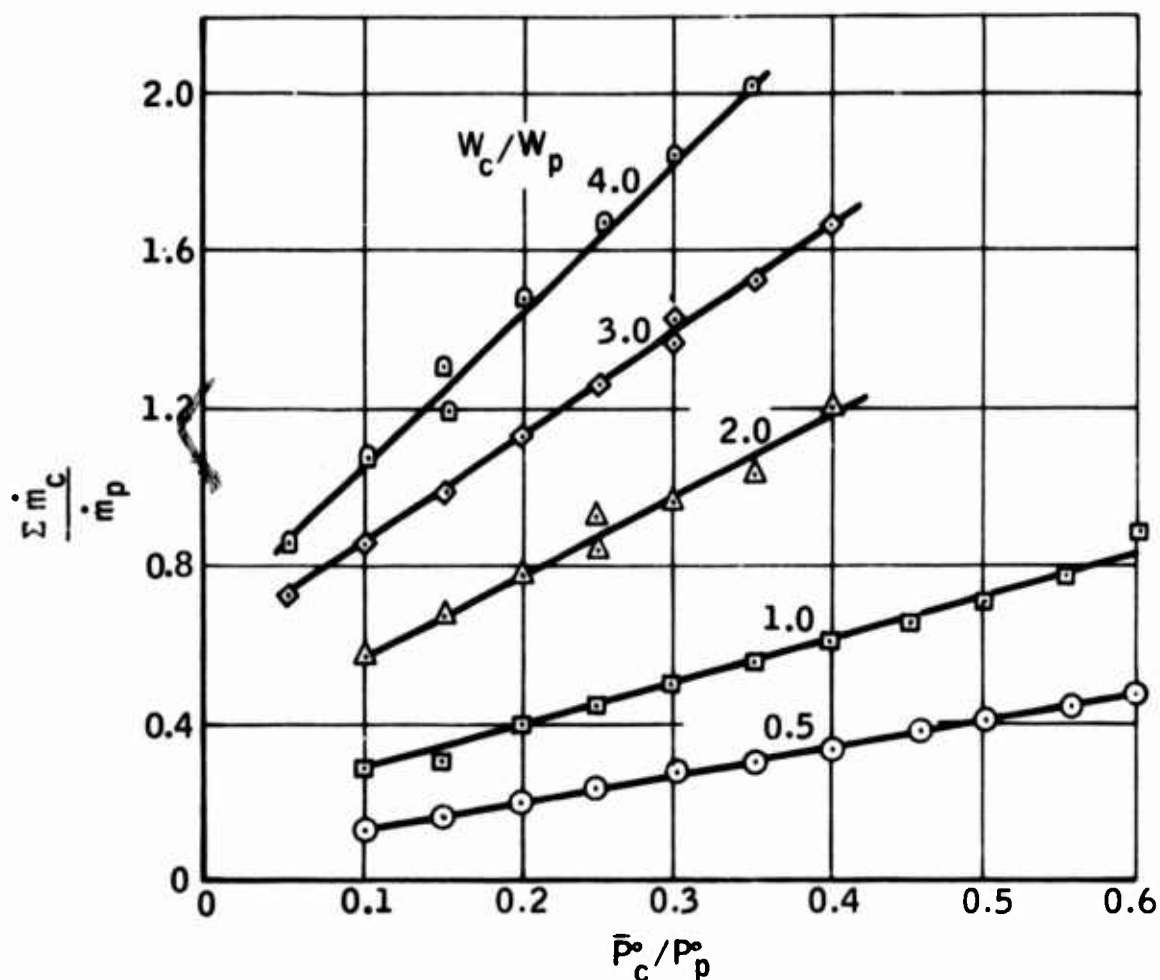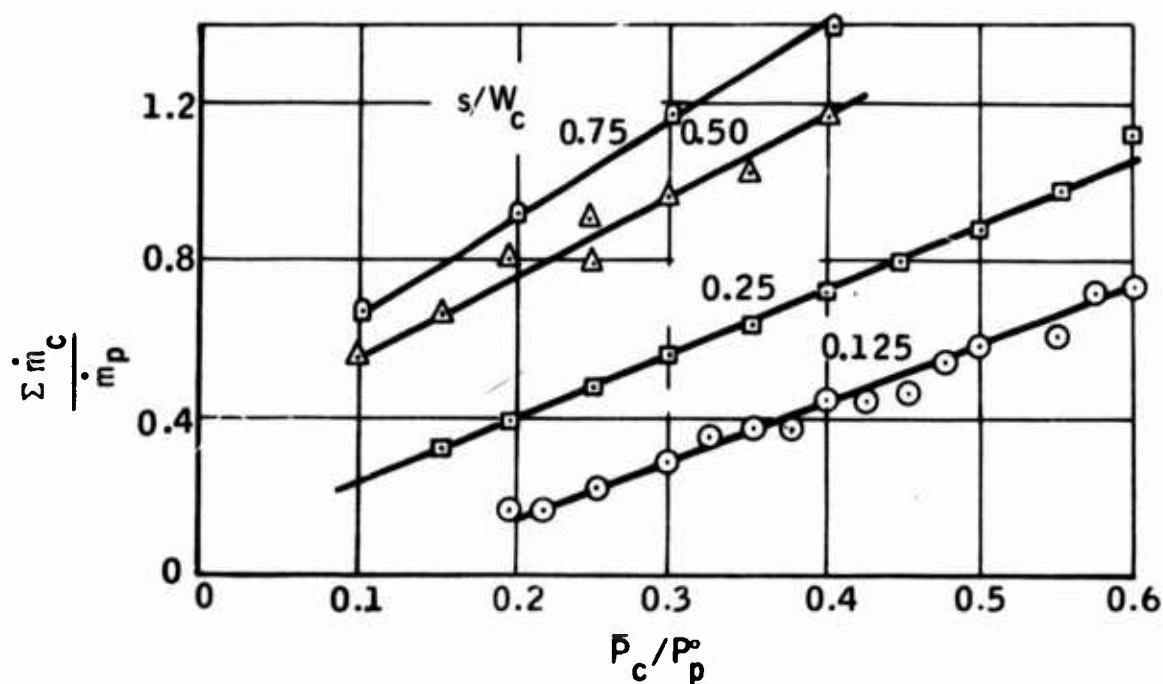FIGURE 10. TOTAL PRESSURE PROFILES, $W_c/W_p = 1.0$, $s/W_c = 0.50$, $P_c^o/P_p^o = 0.25$, $\Delta P_c^o/P_p^o = 0.10$

(a) FOR VARIOUS CONTROL PORT AREAS, ALL WITH $s/W_c = 0.50$

(b) FOR VARIOUS CONTROL PORT OFFSETS, ALL WITH $W_c/W_p = 2.0$

FIGURE 11. MASS RATIO VERSUS AVERAGE CONTROL PRESSURE

NOISE REDUCTION BY
JET-EDGE AND RESONATOR COUPLING

by

RICHARD N. GOTTRON
Captain, U. S. Army

147

ABSTRACT

It is found that noise of only relatively low amplitude is present in pneumatic amplifiers when the jet-edge frequency and the resonant-cavity frequency are approximately the same. When these two oscillations are out of tune, broadband audible noise is present. The amplitude of the noise in several successive velocity regions is shown by a series of photographs of a spectrum analyser. Proportional amplifiers can be designed to effectively reduce the noise for chosen input parameters. Experiments indicate a reduction in pressure of the noise up to 80% for certain velocity ranges. The design criteria of splitter distance and cavity length are investigated and related to the design of proportional amplifiers.

INTRODUCTION

Pneumatic proportional amplifiers exhibit large-amplitude broadband audible noise when operated in certain jet-velocity ranges. This noise is unpleasant and can reduce the efficiency of the amplifier considerably. However, the noise is largely absent in jet-velocity regions in which the system oscillates at an eigenfrequency of a lateral resonating cavity. This system oscillation consumes little system energy, and is therefore a much more desirable range in which to operate.

If broadband noise is produced in the operation of a proportional amplifier, it theoretically may be reduced by shifting the jet-edge frequency to an eigenfrequency of lateral resonating cavities or by changing the cavity dimension to make one of the eigenfrequencies approximately equal to the jet-edge frequency. The jet-edge frequency may be shifted either by changing the distance between the splitter and jet exit (which may result in a change in performance characteristics) or by changing the jet velocity (a change in operating condition). The cavity eigenfrequencies are shifted by changing the length of the cavity, which involves a change neither in performance nor operating condition. Slight changes in performance characteristics or operating conditions may be permissible in the early design stages, and it would seem advisable to consider all three means of avoiding the noise ranges in designing an amplifier for a particular application.

Since little data is available on the actual effectiveness of eliminating noise in proportional amplifiers by adjusting these parameters, an experimental study was made. A proportional amplifier in which these parameters are varied was tested, and the

148

sound produced was analyzed and recorded. These tests showed that the broadband noise can be reduced as much as 80 per cent in pressure by increasing the jet velocity, so that the jet-edge frequency increases to an eigenfrequency of the cavities. Changes in design parameters (the distance between the splitter and jet exit, and the cavity length) are also shown to reduce the noise predictably with a few exceptions.

JET-EDGE SYSTEM AND NOISE CONSIDERATIONS

A jet impinging on a wedge produces transverse oscillations in the jet. Brown (ref 1) gave an empirical formula for the frequency of these oscillations, usually called the jet-edge frequency.

$$f_e = 0.466 \ j \ (u\text{-}40) \ (\frac{1}{h} - 0.07)$$

where u is the jet exit velocity in cm/sec,. h is the distance from the jet exit to the edge in cm, and j is an experimental constant that can assume values of 1, 2.3, 3.8, or 5.4, corresponding to the "stages" of the oscillating jet. The constants 40 and 0.07 can be neglected without introducing appreciable error.

Since a lateral cavity is an inherent feature of proportional amplifiers, this simple jet-edge situation is altered. Nyborg (ref 2) found that the presence of a lateral cavity could tune the jet-edge frequency, so that the jet-edge and cavity system would oscillate approximately at the eigenfrequencies of the cavity rather than at the jet-edge frequency. The cavity eigenfrequencies f_n are given by

$$f_n = \frac{(n - \frac{1}{2})a}{2(L + e)}$$

where n = 1, 2, 3, a is the speed of sound in cm/sec, L is the cavity length, and e is a small end correction that is usually neglected. Nyborg called this type of oscillation "the jet-edge system" oscillation as opposed to the simpler "jet-edge" oscillation, and this nomenclature will be applied in this report.

Figure 1a shows the jet-edge frequency (sloping straight line) for j = 1 and the cavity eigenfrequencies (n = 1, 2, 3) plotted against the jet velocity. Only the first stage of the jet-edge

FIGURE I-A
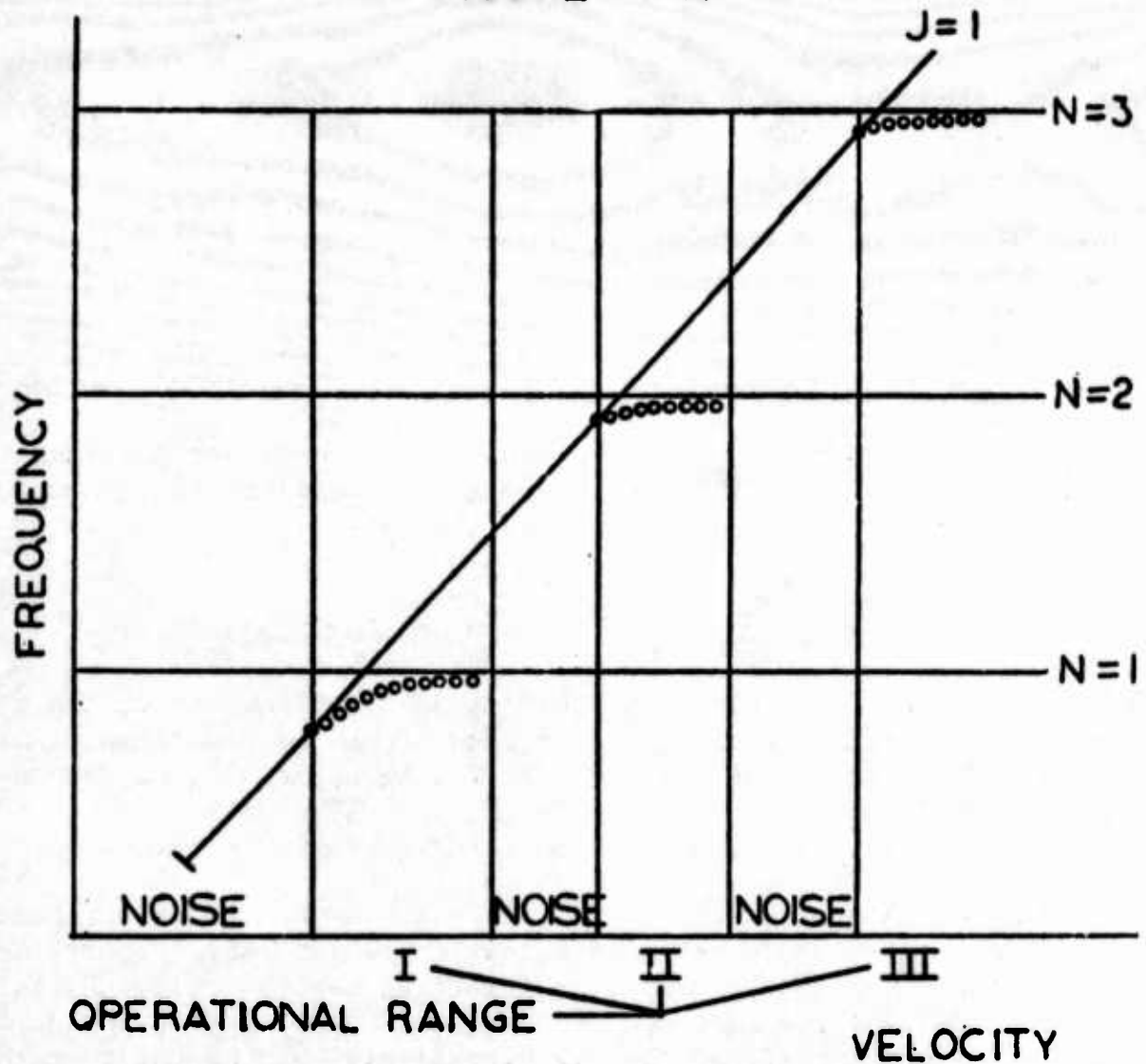
FREQUENCY VS. VELOCITY FOR THE
JET-EDGE SYSTEM
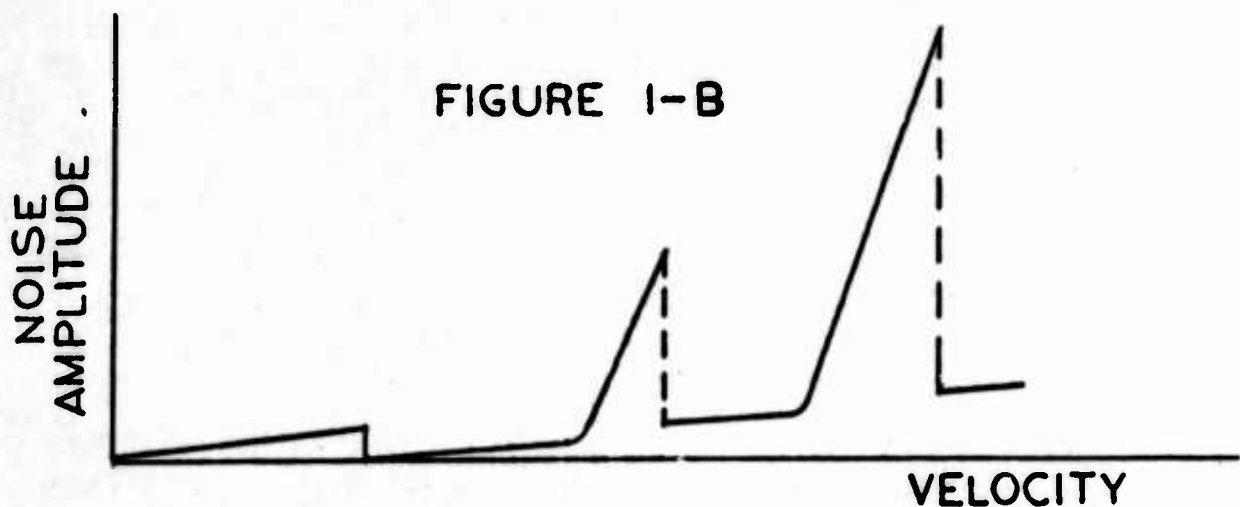
FIGURE I-B

NOISE AMPLITUDE VS. VELOCITY FOR
THE JET-EDGE SYSTEM

frequency is considered since the higher stages (j = 2.3, 3.8, etc.) are not tuned by the cavities. (This was experimentally determined during these tests.) The lines of dots in Figure 1a traverse the jet velocity ranges over which the jet-edge system is tuned (called operational range). This tuning commences near the intersection of the stage-1 jet-edge frequency and each cavity eigenfrequency. Between the velocity ranges of jet-edge system oscillation are ranges in which there is considerable noise. For convenience, the velocity ranges in which there is considerable broadband noise will be called noise ranges.

Figure 1b shows the relative amplitude of the broadband noise. The velocity scale is identical to Figure 1a. As the velocity is increased there is a slow transition from a jet-edge system oscillation to a noise range. However, there is a sudden drop in noise amplitude when the velocity is increased from a noise range to a jet-edge system oscillation.

The noise in the first noise range is of low amplitude since the jet velocity is small. The first eigenfrequency (n = 1) occurs below an input pressure of 3 psig. The second noise range exhibits broadband noise of considerable amplitude, and noise in the third range is of very high amplitude, often beyond the pain threshold. These noise ranges can be large or small, depending on the design parameters, h and L.

It is undesirable to operate units where the jet-edge frequency is tuned at the first cavity eigenfrequency (for n = 1) if L is greater than 5 mm, since the jet-edge system frequency will be audible and intense. Thus, the first operational range may also be considered an undesirable range of operation for L greater than 5 mm.

TEST SETUP AND RESULTS

The experimental setup is shown in Figure 2. The unit has a movable splitter and movable cavity walls. Thus various values of h and L can easily be obtained. The velocity of the air is determined from a flowmeter. A microphone picks up the noise generated within the unit and, after passing through an amplifier, it is monitored on a sonic analyzer. An X-Y recorder is used to obtain the frequency spectrum from a wave form analyzer. Photographs of the sonic analyzer were taken at selected settings of flow velocity.

Tests were conducted for a setting of L = 20 mm and h = 3, 5, and 7 mm. Tests were also conducted for h = 30 mm and L = 10, 20, 30, and 40 mm. In the first set of tests the stage-1 jet-edge frequencies were shifted and in the second set the eigenfrequencies were shifted. As a result, the noise ranges also were shifted. General trends can be deduced from the observed results.
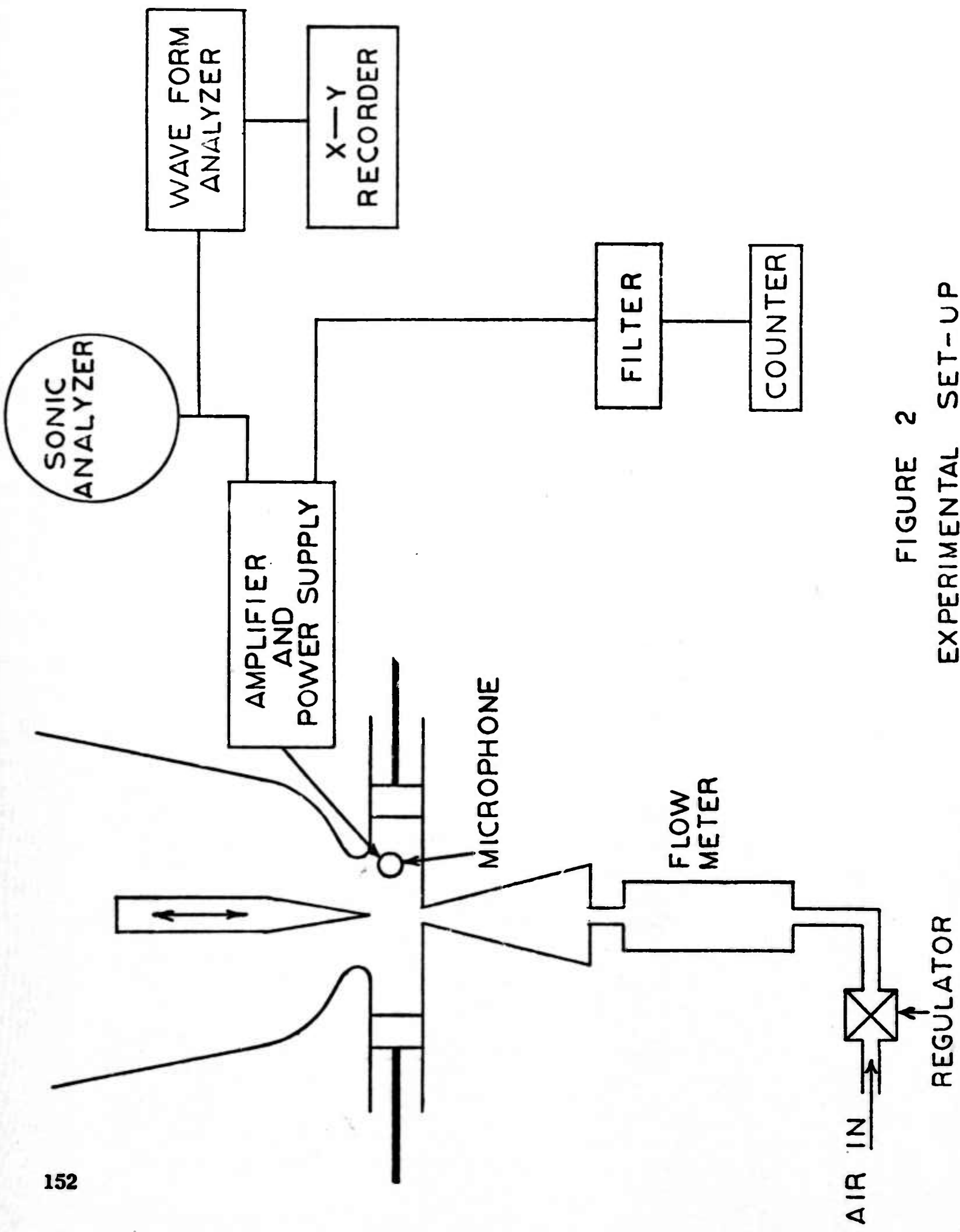
FIGURE 2
EXPERIMENTAL SET-UP

152

Figure 3 shows sonic analyzer outputs for a setting of h = 3.0 mm and L = 20 mm. Figure 3a is a photograph for a case with no input flow. The pulse shown in 3a is an extraneous signal inherent in the microphone readout system.

Figure 3b shows the frequency spectrum for a velocity of 6000 cm/sec. This is equivalent to an input pressure of approximately 2 psig. Figure 3b consists of low broadband noise with the high amplitude jet-edge system frequency at 3.9 kc. Even though the broadband noise is low, this is not considered a good operating point, since the system frequency is audible and of high amplitude.

Figure 3c shows the increase in noise at a jet velocity of 9000 cm/sec. There is no jet-edge system oscillation present, and the unit is operating in the second noise range.

Figure 3d shows the noise spectrum at an input velocity of 11,500 cm/sec. The jet-edge system frequency is at 19.1 kc. It is evident in comparing 3c to 3d that the broadband noise has been reduced about 50 per cent.

Figure 3e shows that the noise increases as the jet velocity is increased. Figure 3e was taken at a jet velocity of 18,000 cm/sec, which is at the end of the second jet-edge system range.

Figure 3f shows the noise spectrum for a jet velocity of 26,000 cm/sec. This is in the third noise range. The broadband noise is very large in amplitude.

Figure 3g depicts the noise spectrum for an input velocity of 28,000 cm/sec. The jet-edge system frequency is 29 kc, far above the audible range. Comparing figures 3f and 3g shows a decrease in the noise of approximately 80 per cent.

Figure 3h shows the noise spectrum for a velocity of 43,000 cm/sec. Comparing this with 3g shows that the broadband noise gradually increases as the jet velocity is increased, but never exceeds the amplitude of the noise in the noise ranges.

At 28,000 cm/sec, the system oscillates at 29 kc. However, as the velocity is increased, there is a jump in the cavity eigenfrequency from n = 4 to n = 5 and the frequency shifts to 38 kc. This occurs without going through a noise range as the jet velocity is increased.

When the edge or splitter is moved from 3.0 to 5.0 mm from the jet exit, the slope of the jet-edge curve is reduced and one expects that the noise ranges should occur at higher jet velocities. Like-

a
u = 0

b
u = 6000 cm/sec

c
u = 9000 cm/sec

d
u = 11,500 cm/sec

e
u = 18,000 cm/sec

f
u = 26,000 cm/sec

g
u = 28,000 cm/sec

h
u = 43,000 cm/sec

1694-63

Figure 3. Sonic analyzer photographs at designated velocities.

wise, for a setting of 7.0 mm, the noise ranges should occur at
even higher velocities. As stated previously, only three settings
of h were used. The noise bands did occur at higher velocities
when h was increased from 5.0 to 7.0 mm, however, there was no
change in the noise band when h was changed from 3.0 to 5.0 mm.

When the cavity length L is changed, the noise ranges should
also change. For decreasing L, the noise ranges should occur at
higher jet velocities, and for increasing L, the ranges should
occur at lower velocities. When L was decreased from 20 to 10 mm,
the noise range did occur at higher velocities as expected. When
L was increased from 20 to 30 mm, the range occurred at lower velo-
cities, again as expected. However, at 40 mm, the range occurred
at higher jet velocities. Since there was only one range at a set-
ting of 40 mm, the higher velocity range could have been the third
noise range instead of the second range.

CONCLUSIONS

It has been demonstrated that broadband noise (pressure) can be
reduced up to 80 per cent by operating units in a velocity range
near the intersection of the first stage of the jet-edge oscillation
and the cavity eigenfrequencies. Ranges of broad band noise occur
when the jet-edge and cavity frequencies are different. The noise
ranges can be shifted by changing either the splitter distance or the
cavity length.

Since audible sound is unpleasant and detrimental to the opera-
tion of pneumatic proportional amplifiers, jet-edge systems oscil-
lating below 15 kc can also be considered undesirable. Thus, pro-
perly designed amplifiers should have small resonant cavities and a
small splitter distance. Since the jet-edge system frequency is
independent of the exit width of the jet, the ratio of splitter dis-
tance to jet exit width can be varied. As an example, most of the
results reported in this report are for h = 3.0 mm; thus for a ra-
tio of 10 to 1, the jet width w would be 0.3 mm.

The higher frequencies would also be more rapidly attenuated,
since the absorption coefficient for acoustic compressional waves is
proportional to the frequency.

REFERENCES

1. Brown, G. Burniston, "The Vortex Motion Causing Edge Tones," Proc. Phys. Soc. (London) 49, 493 (1937).

2. Nyborg, W. L., Burkhard, M. D. and Schilling, H. R., "Acoustical Characteristics of Jet-Edge and Jet-Edge Resonator Systems," The Journal of the Acoustical Society of America, Vol. 24, No. 3, May 1952.

A HYDRODYNAMIC STUDY OF THE FREE-JET CLASS
OF FLUID-JET AMPLIFIERS*

by

RICHARD T. CRONIN

Senior Mechanics Engineer
CHRYSLER CORPORATION MISSILE DIVISION
Detroit, Michigan

ABSTRACT

A theoretical two-dimensional solution is presented for the free-jet class of fluid-jet amplifiers. As a preliminary investigation, it is assumed that both the primary and secondary streams of perfect fluid are guided by two-dimensional channels with straight and parallel walls. The deflection angle and the free streamline profile of the resulting jet are solved by using "Free Streamline Theory" of Kirchhoff.

The jet deflection angle has been related in closed form to both channel flows, both channel widths, the included angle between the channels, the jet flow and its speed. The amplifier geometrical configuration is completely specified when certain mapping equations, usually requiring numerical integration, yield the free streamline profile of the jet and the coordinates of both channel exits.

INTRODUCTION

The amplifier shown in Figure 1-a controls its free jet when a primary stream (power stream) and a secondary stream (control stream) emerge together to form a free jet. The secondary stream determines the jet deflection angle and its flow rate.

Since a theoretical investigation of this type has not been made to study this device, the postulates of this preliminary investigation are:

1. Both the primary and secondary streams are guided by two-dimensional channels with straight and parallel side walls.

2. Both guided streams flowing at a constant rate consist of a perfect working fluid.

3. The effects of gravity are neglected.

With these assumptions, the actual device is simplified to the idealized flow system in Figure 1-a. If U_1, U_2, α, h_1 and h_2 are given, the problem is to determine the angle of jet deflection β, the jet velocity U, and its width h. Additionally, this study will show how to make the primary exit-port perpendicular to its side walls.

This analytical study is based on the well-known "Free Streamline Theory" which involves a series of transformations from the physical plane (Z-Plane) to the complex potential plane (W-Plane). The resulting relation between the complex potential and physical planes furnish two equations to determine the X- and Y-coordinates of the free streamline profile. Due to the complexity of the problem, it is shown that numerical integration and some iteration may have to be performed for a complete solution.

TRANSFORMATION FROM Z-PLANE TO ζ-PLANE

The physical plane is first transformed to the log-inverse velocity plane (Q-Plane) defined by

$$Q = Ln \frac{U}{q} + i\theta \tag{1}$$

From given conditions in Figure 1-a, the velocity vectors across D_∞ D_∞', B_∞ B_∞', and I_∞' I_∞'' may be constructed as shown in Figure 2. Since E is the intersecting point of streamlines ED_∞ and EB_∞, q = 0. Hence Q is infinite. The coordinates of various points in the Q-Plane are summarized as follows:

Point	Q
D_∞' , D_∞	$Ln \dfrac{U}{U_1} + i\alpha$
E_∞ to E_∞'	$\infty + i\theta \qquad 0 \leq \theta \leq \alpha$
B_∞ , B_∞'	$Ln \dfrac{U}{U_2}$

A	0
I'_∞, I''_∞	$i\theta_c$
A'	$i\alpha$

Based on this information, the diagram in the Q-Plane is constructed as shown in Figure 3. Now the interior of the polygon is mapped on the upper half of the ζ-Plane in such a way that I'_∞ and I''_∞ go to their respective infinite positions on the real axis while E maps to $\zeta = 0$. The vertices A and A' correspond to $\zeta = a_3$ and a_4, respectively. Thus the ζ-Plane is traced out in Figure 4. By the theorem of Schwarz-Christoffel, the transformation function is given by:

$$\frac{dQ}{d\zeta} = \frac{K_1}{\zeta \sqrt{(\zeta - a_3)(\zeta - a_4)}}.$$ (2)

After integrating, we get

$$Q = \frac{K_1}{\sqrt{-a_3 a_4}} \sin^{-1} \frac{2a_3 a_4 - (a_3 + a_4)\zeta}{(a_4 - a_3)\zeta} + K_2$$ (3)

The constants K_1 and K_2 may be determined by the following conditions:

At A $Q = 0$ and $\zeta = a_3$

At A' $Q = i\alpha$ and $\zeta = a_4$

Substitution of these corresponding values in Equation (3) yields the following two equations:

$$\frac{K_1}{\sqrt{-a_3 a_4}} \frac{\pi}{2} + K_2 = 0$$ (4)

$$\frac{-K_1}{\sqrt{-a_3 a_4}} \frac{\pi}{2} + K_2 = i\alpha$$ (5)

Thus $K_2 = \frac{i\alpha}{2}$ and $\frac{K_1}{\sqrt{-a_3 a_4}} = \frac{i\alpha}{\pi}$

Equation (3) becomes

$$Q = \frac{\alpha}{\pi} \cosh^{-1} \frac{2a_3 a_4 - (a_4 + a_3)\zeta}{(a_4 - a_3)\zeta}$$ (6)

The values of a_3 and a_4 will be determined after the transformation from the W-Plane to the ζ-Plane is completed.

Advantage is taken of certain characteristics of the complex potential function, W, along the flow system periphery in Figure 1-a. First of all, W is defined as

$$W = \phi + i\psi \tag{7}$$

A polygon is constructed by selecting values of ψ and ϕ along the flow system periphery. First, the stream function, ψ, is assigned equal to the constant flow rate along the free streamlines in the Z-Plane of Figure 1-a. Secondly, the velocity potential function, ϕ, is made proportional to the physical coordinates of the uniform velocity profiles in the Z-Plane. Hence, the resulting polygon in Figure (5) is found from

$$\psi = 0 \qquad\qquad \text{on } D'_\infty \ A' \ I''_\infty$$

$$\psi = U_1 h_1 \qquad\qquad \text{on } D_\infty \ E, \ B_\infty \ E$$

$$\psi = U_1 h_1 + U_2 h_2 = Uh \qquad \text{on } B'_\infty \ A \ I'_\infty$$

$$\phi = \infty \qquad\qquad \text{on } I'_\infty \ I''_\infty$$

$$\phi = 0 \qquad\qquad \text{on } E$$

$$\phi = -\infty \qquad\qquad \text{on } B_\infty \ B'_\infty \ , \ D_\infty \ D'_\infty$$

The polygon in Figure 5 is degenerated to a simpler form in Figure 6. Three vertices are selected in the ζ-Plane to satisfy certain requirements of the problem. Since E in the W-Plane of Figure 6 and both E_∞ and E'_∞ in the Q-Plane of Figure 3 correspond to E in the Z-Plane of Figure 1-a, then E in the W-Plane must map to the same point (the origin of the ζ-Plane of Figure 4) as both E_∞, E'_∞ in the Q-Plane do. Both I'_∞ and I''_∞ in the ζ-Plane must be selected so that Equation (6) yields one and the same value for both I'_∞ and I''_∞ in the Q-Plane. Hence, the following selection of points in Figure 4 satisfies this requirement of Equation (6).

Point	ζ	Q
I'_∞	$-\infty$	$i\theta_c$
I''_∞	∞	$i\theta_c$

Upon substitution of these values, Equation (6) becomes

$$-\cos \frac{\pi}{\alpha} \ \theta_c = \frac{a_4 + a_3}{a_4 - a_3} \tag{8}$$

The transformation to map the W-Plane on the ζ-Plane is given by

$$\frac{dW}{d\zeta} = \frac{K_3 \zeta}{(\zeta - a_5)(\zeta - a_7)} \tag{9}$$

160

After integration, we get

$$W = \frac{-K_3}{a_5 - a_7} \left[-a_5 \, \text{Ln} \, (\zeta - a_5) + a_7 \, \text{Ln} \, (\zeta - a_7) \right] + K_4 \tag{10}$$

The following values of W and ζ correspond to each other:

Point	W	ζ
B'_∞	$-\infty + iUh$	a_7
E	$iU_1 h_1$	0
D'_∞	$-\infty$	a_5
I''_∞	∞	∞
I'_∞	$\infty + iUh$	$-\infty$

Substitution of these corresponding values in Equation (8) yields a series of relations between the constants with the following results:

K_4 = must be real and is set equal to zero for convenience

$$K_3 = \frac{Uh}{\pi}$$

$$a_5 = \gamma^{-\lambda} \tag{10a}$$

$$a_7 = -\gamma^{1-\lambda}$$

where $\gamma = \dfrac{U_2 h_2}{U_1 h_1}$ and $\lambda = \dfrac{U_2 h_2}{Uh}$

Therefore the substitution of the known constants into Equation (10) gives

$$W = \frac{U_1 h_1}{\pi} \, \text{Ln} \, (\zeta - a_5) + \frac{U_2 h_2}{\pi} \, \text{Ln} \, (\zeta - a_7) \tag{11}$$

Now the constants, a_3 and a_4 in Equation (6), may be expressed in terms of a_5 and a_7 by substituting the corresponding values of Q and ζ in Equation (6) for the points D_∞ and B_∞:

At $\quad D_\infty$, $D'_\infty \qquad\qquad Q = \text{Ln} \, \dfrac{U}{U_1} + i\alpha \qquad\qquad \zeta = a_5$

At $\quad B_\infty$, $B'_\infty \qquad\qquad Q = \text{Ln} \, \dfrac{U}{U_2} \qquad\qquad\qquad \zeta = a_7$

Therefore

$$\cosh\left[\frac{\pi}{\alpha}\ Ln\frac{U}{U_1}\right] = \frac{(a_3+a_4)\,a_5 - 2a_3\,a_4}{(a_4-a_3)\,a_5} \tag{12}$$

$$\cosh\left[\frac{\pi}{\alpha}\ Ln\frac{U}{U_1}\right] = \frac{-(a_3+a_4)\,a_7 - 2a_3\,a_4}{(a_4-a_3)\,a_7} \tag{13}$$

Solving Equations (12) and (13) simultaneously for a_3 and a_4, we get

$$a_3 = \frac{-(\omega_1+\omega_2)\,a_5\,a_7}{(1-\omega_2)\,a_7 - (1+\omega_1)\,a_5} \tag{14}$$

$$a_4 = \frac{(\omega_1+\omega_2)\,a_5\,a_7}{(1+\omega_2)\,a_7 - (1-\omega_1)\,a_5} \tag{15}$$

where

$$\omega_1 = \cosh\left[\frac{\pi}{\alpha}\ Ln\frac{U}{U_1}\right] = \frac{1}{2}\left[\left(\frac{U}{U_1}\right)^{\pi/\alpha} + \left(\frac{U}{U_1}\right)^{-\pi/\alpha}\right]$$

$$\omega_2 = \cosh\left[\frac{\pi}{\alpha}\ Ln\frac{U}{U_2}\right] = \frac{1}{2}\left[\left(\frac{U}{U_2}\right)^{\pi/\alpha} + \left(\frac{U}{U_2}\right)^{-\pi/\alpha}\right]$$

It is natural to expect that the locations of A and A′ in Figure 1-a affect the jet. Hence, certain restraints must be placed on a_3 and a_4. As the first restraint, a_3 and a_4 must be defined to fall within the limits of the cosine function in Equation (8). As the second restraint, a_3 and a_4 must be consistent with the continuity of flow.

$$Uh = U_1 h_1 + U_2 h_2 \tag{16}$$

Substitution of the known a_3 and a_4 functions from Equations (14) and (15) into Equation (8) yields

$$\cosh\frac{\pi}{\alpha}\,\theta_C = -\left[\omega_1\frac{U_1 h_1}{Uh} - \omega_2\frac{U_2 h_2}{Uh}\right] \tag{17}$$

where $\omega_1 = \frac{1}{2}\left[\left(\frac{U}{U_1}\right)^{\pi/\alpha} + \left(\frac{U}{U_1}\right)^{-\pi/\alpha}\right]$

$$\omega_2 = \frac{1}{2}\left[\left(\frac{U}{U_2}\right)^{\pi/\alpha} + \left(\frac{U}{U_2}\right)^{-\pi/\alpha}\right]$$

Equation (17) is related to the physical deflection angle, $\beta_c = \alpha - \theta_c$, from Figure 2.

$$\cos \frac{\pi}{\alpha} \beta_c = \omega_1 \frac{U_1 h_1}{Uh} - \omega_2 \frac{U_2 h_2}{Uh} \tag{18}$$

By the nature of the amplifier, $U_2 h_2$ is made smaller than $U_1 h_1$. If the limit of $U_2 h_2 \rightarrow U_1 h_1$ and $U_2 h_2 \rightarrow 0$ are studied for various velocity conditions, the jet deflection angle β_c in Equation (18) is bounded and made single-valued.

Velocity Condition	Limits on Right Hand Side of Equation (18)	Limits on β_c	
$U_1 = U_2 \quad (\omega_1 = \omega_2)$	$0 < \omega_1 \dfrac{U_1 h_1}{Uh} - \omega_2 \dfrac{U_2 h_2}{Uh} < 1$	$0 < \beta_c < \alpha/2$	
$U_2 > U_1 \quad (\omega_1 > \omega_2)$	$0 < \omega_1 \dfrac{U_1 h_1}{Uh} - \omega_2 \dfrac{U_2 h_2}{Uh} < 1$	$0 < \beta_c < \alpha/2$	
$U_1 > U_2 \quad (\omega_2 > \omega_1)$	$-1 < \omega_1 \dfrac{U_1 h_1}{Uh} - \omega_2 \dfrac{U_2 h_2}{Uh} < 1$	$0 < \beta_c < \alpha$	(19)

Now, the mapping to the known values of a_3, a_4, a_5 and a_7 in Equations (6) and (11) is verified in Appendix A.

DIFFERENTIAL EQUATIONS FOR FREE STREAMLINE PROFILE

Along a free streamline, ψ is constant so that

$$dW = d\phi = \frac{d\phi}{ds} \, ds = Uds \tag{20}$$

Since $dX = dS \cos \theta$ and $dY = dS \sin \theta$, Equation (20) becomes

$$\frac{dX}{h} = \frac{\cos \theta \, dW}{Uh} \tag{21}$$

$$\frac{dY}{h} = \frac{\sin \theta \, dW}{Uh} \tag{22}$$

To express W in terms of θ, advantage is taken of the fact that $Q = i\theta$ along the free streamlines. After using Equations (14) and (15), substitution of this value in Equation (6) results

$$\cos \frac{\pi}{\alpha} \theta = \frac{- (\omega_1 + \omega_2) \, a_5 a_7 + (\omega_1 a_5 + \omega_2 a_7) \, \zeta}{(a_7 - a_5) \, \zeta} \tag{23}$$

As ζ approaches the limits of $+ \infty$ and $- \infty$ in Figure 6, Equation 23 reduces to

$$\cos \frac{\pi}{\alpha} \theta_C = \frac{\omega_1 a_5 + \omega_2 a_7}{a_7 - a_5} \tag{24}$$

After elimination of ζ between Equations (11) and (23), substitution of Equation (24) into the resulting equation yields

$$W = \frac{U_1 h_1}{\pi} \, \text{Ln} \left[\frac{\omega_3}{\cos \frac{\pi}{\alpha} \theta_C - \cos \frac{\pi}{\alpha} \theta} - a_5 \right]$$

$$+ \frac{U_2 h_2}{\pi} \, \text{Ln} \left[\frac{\omega_3}{\cos \frac{\pi}{\alpha} \theta_C - \cos \frac{\pi}{\alpha} \theta} - a_7 \right] \tag{25}$$

where $\omega_3 = \frac{(\omega_1 + \omega_2) \, a_5 a_7}{a_7 - a_5}$

164

Differentiating Equation (24) and substituting Equations (21) and (22) into the result produces

$$\frac{dX}{h} = - \left[\frac{U_1 h_1}{Uh} \frac{a_7}{\cos \frac{\pi}{\alpha} \theta + \omega_1} + \frac{U_2 h_2}{Uh} \frac{a_5}{\cos \frac{\pi}{\alpha} \theta - \omega_2} \right]$$

$$\times \left[\frac{(\omega_1 + \omega_2) \sin \frac{\pi}{\alpha} \theta \cos \theta \, d\theta}{\alpha (a_5 - a_7) \left(\cos \frac{\pi}{\alpha} \theta - \cos \frac{\pi}{\alpha} \theta_c \right)} \right] \tag{26}$$

$$\frac{dY}{h} = - \left[\frac{U_1 h_1}{Uh} \frac{a_7}{\cos \frac{\pi}{\alpha} \theta + \omega_1} + \frac{U_2 h_2}{Uh} \frac{a_5}{\cos \frac{\pi}{\alpha} \theta - \omega_2} \right]$$

$$\times \left[\frac{(\omega_1 + \omega_2) \sin \frac{\pi}{\alpha} \theta \sin \theta \, d\theta}{\alpha (a_5 - a_7) \left(\cos \frac{\pi}{\alpha} \theta - \cos \frac{\pi}{\alpha} \theta_c \right)} \right] \tag{27}$$

INTEGRAL EQUATIONS FOR FREE STREAMLINE PROFILE

Before Equations (26) and (27) are integrated, several computations are required to input the appropriate constants into the integral equations. The following series of steps are used to fulfill this end:

1. Assume U, U_1, U_2, h_1, h_2 and α

2. Compute h, a_7, a_5, $\cos \frac{\pi}{\alpha} \beta_c$ and θ_c from

$$h = \frac{U_1 h_1 + U_2 h_2}{U} \tag{16}$$

$$a_7 = - \gamma^{1-\lambda} \text{ and } a_5 = \gamma^{-\lambda}$$

$$\text{where } \gamma = \frac{U_2 h_2}{U_1 h_1} \text{ and } \gamma = \frac{U_2 h_2}{Uh}$$

constants summarized in Equation (10a).

$$\omega_1 = \frac{1}{2} \left[\left(\frac{U}{U_1}\right)^{\pi/\alpha} + \left(\frac{U}{U_1}\right)^{-\pi/\alpha} \right] \qquad (17)$$

$$\omega_2 = \frac{1}{2} \left[\left(\frac{U}{U_2}\right)^{\pi/\alpha} + \left(\frac{U}{U_2}\right)^{-\pi/\alpha} \right] \qquad (17)$$

$$\cos \frac{\pi}{\alpha} \beta_c = \omega_1 \frac{U_1 h_1}{Uh} - \omega_2 \frac{U_2 h_2}{Uh} \qquad (18)$$

$$0 < \beta_c < \alpha/2 \quad \text{when } U_1 \le U_2 \qquad (19)$$

$$0 < \beta_c < \alpha \quad \text{when } U_1 > U_2 \qquad (19)$$

3. Compute θ_c as defined in Figure 2

$$\theta_c = \alpha - \beta_c$$

4. Integrate and plot the free streamline profile from A to I_∞' with the X- and Y-coordinates

$$\frac{X}{h} = - \int_0^{\theta_c} \left[\frac{U_1 h_1}{Uh} \frac{a_7}{\cos \frac{\pi}{\alpha} \theta + \omega_1} + \frac{U_2 h_2}{Uh} \frac{a_5}{\cos \frac{\pi}{\alpha} \theta - \omega_2} \right]$$

$$\times \frac{(\omega_1 + \omega_2) \sin \frac{\pi}{\alpha} \theta \cos \theta \, d\theta}{\alpha (a_5 - a_7)(\cos \frac{\pi}{\alpha} \theta - \cos \frac{\pi}{\alpha} \theta_c)} \qquad (28)$$

$$\frac{Y}{h} = - \int_0^{\theta_c} \left[\frac{U_1 h_1}{Uh} \frac{a_7}{\cos \frac{\pi}{\alpha} \theta + \omega_1} + \frac{U_2 h_2}{Uh} \frac{a_5}{\cos \frac{\pi}{\alpha} \theta - \omega_2} \right]$$

$$\times \frac{(\omega_1 + \omega_2) \sin \frac{\pi}{\alpha} \theta \sin \theta \, d\theta}{\alpha (a_5 - a_7)(\cos \frac{\pi}{\alpha} \theta - \cos \frac{\pi}{\alpha} \theta_c)} \qquad (29)$$

166

5. Displace I''_∞ from I'_∞ by h consistent with continuity Equation (16) and shown in Figure 1-b. Integrate and plot the free streamline profile from I''_∞ to A' with the X- and Y-coordinates

$$\frac{X}{h} = - \int_{\theta_C}^{\alpha} \left[\frac{U_1 h_1}{Uh} \frac{a_7}{\cos\frac{\pi}{\alpha}\theta + \omega_1} + \frac{U_2 h_2}{Uh} \frac{a_5}{\cos\frac{\pi}{\alpha}\theta - \omega_2} \right]$$

$$\times \frac{(\omega_1 + \omega_2)\sin\frac{\pi}{\alpha}\theta \cos\theta \, d\theta}{\alpha(a_5 - a_7)(\cos\frac{\pi}{\alpha}\theta - \cos\frac{\pi}{\alpha}\theta_C)} + \sin\theta_C \qquad (30)$$

$$\frac{Y}{h} = - \int_{\theta_C}^{\alpha} \left[\frac{U_1 h_1}{Uh} \frac{a_7}{\cos\frac{\pi}{\alpha}\theta + \omega_1} + \frac{U_2 h_2}{Uh} \frac{a_5}{\cos\frac{\pi}{\alpha}\theta - \omega_2} \right]$$

$$\times \frac{(\omega_1 + \omega_2)\sin\frac{\pi}{\alpha}\theta \sin\theta \, d\theta}{\alpha(a_5 - a_7)(\cos\frac{\pi}{\alpha}\theta - \cos\frac{\pi}{\alpha}\theta_C)} - \cos\theta_C \qquad (31)$$

6. Arbitrarily select A and then locate A'.

7. Determine E since the channel widths h_1 and h_2 are known.

In most instances, it is not possible to find an analytical solution in closed form for the integrals in steps 4 and 5. However, numerical integration allows free streamlines AI'_∞ and A' I''_∞ to be plotted in the Z-Plane. Errors in these stream-line profiles are not only caused by numerical integration processes but also by certain approximations made on the integral limits in Equations (28), (29), (30) and (31). The limit, θ_C, must be relaxed on all four integrals because these stream-lines can never be plotted to the asymptotic jet at infinity in Figure 1-c. If these streamlines are merely made to approach the asymptotic jet, slight changes in the integral limits permit an approximate solution of the free jet profile.

From Figure 1-c, an approximate solution is obtained as

1. The upper limit on Equations (28) and (29) is changed from θ_C to

$$\theta = \lim_{\epsilon \to 0} (\theta_C - \epsilon)$$

2. The lower limit on Equations (30) and (31) is changed from θ_c to

$$\theta = \lim_{\epsilon \to 0} (\theta_c + \epsilon)$$

As ϵ becomes minute in Figure 1-c, the jet defined at the stations $\theta + \epsilon$ and $\theta - \epsilon$ is nearly identical to the asymptotic jet. Hence, the integration constants in Equations (30) and (31) represent good approximations.

Now, the problem of evaluating the integrals in Equations (28), (29), (30) and (31) is considered between the lower limit of $\theta_c - \epsilon$ to the upper limit of $\theta_c + \epsilon$. For convenience sake, let the form representing these integrals be denoted by[1]

$$\int_{\theta_c-\epsilon}^{\theta_c+\epsilon} \frac{f(\theta)\, d\theta}{\cos \frac{\pi}{\alpha} \theta - \cos \frac{\pi}{\alpha} \theta_c} = \int_{\theta_c-\epsilon}^{\theta_c+\epsilon} \left[\frac{f(\theta)}{\cos \frac{\pi}{\alpha} \theta - \cos \frac{\pi}{\alpha} \theta_c} - \frac{\alpha f(\theta_c)}{\pi(\theta - \theta_c)} \right]$$

$$\times\, d\theta \quad - \quad \frac{\alpha f(\theta_c)}{\pi} \int_{\theta_c-\epsilon}^{\theta_c+\epsilon} \frac{d\theta}{\theta - \theta_c}$$

The last term on the right side of the prior integral is zero due to symmetry. Additionally, the second to the last term removes the indeterminacy at asymptote θ_c to simplify integration processes.

---

[1] This integral evaluation was made by B. M. Watson, Senior Reentry Dynamics Engineer, Missile Division, Chrysler Corporation.

A stable and free two-dimensional jet has been defined from the theory presented in the previous section. The jet shape, its location and both exit-ports of the two-dimensional amplifier can be determined after selection of certain physical parameters are made. These parameters are the jet surface speed, the included angle between the amplifier channels, both channel widths and the fluid entrance speed to each channel.

The theory contained in this study is used to define the jet profile for the symmetrical amplifier in Figure 7. By way of definition, the desired symmetry is achieved as

- The primary channel exit-port is made perpendicular to its side walls.

- The outer wall overhang (if any) of the secondary channels does not interfere with the free jet.

Now, iteration processes are used to find the desired symmetry. With the selection of $h_1 = 1.000$, $h_2 = 0.539$, $\alpha = 18°$ and $U_1 = U_2 = 1.000$, variations of U and h consistent with continuity are studied until the desired symmetry is satisfied. The following table not only summaries the parametric values used in the first and last trials of iteration but also keys these trials to the appropriate figures depicting the jet profile and amplifier configuration.

AMPLIFIER PARAMETERS

Figure No.	Velocities				Channel Widths		Included Angle	Free Jet		
	Velocity Condition	U	U_1	U_2	h_1	h_2	α	Uh	h	β_c
8	$U_1 = U_2$	1.174	1.000	1.000	1.000	0.539	18°	1.539	1.310	3.89°
9	$U_1 = U_2$	1.116	1.000	1.000	1.000	0.539	18°	1.539	1.380	6.01°
10	$U_1 = U_2$	1.174	1.000	1.000	1.000	0.819	18°	1.819	1.548	7.50°
11	$U_1 = U_2$	1.116	1.000	1.000	1.000	0.819	18°	1.819	1.630	8.04°
12	$U_1 < U_2$	1.174	1.000	1.116	1.000	0.819	18°	1.912	1.630	3.55°
13	$U_1 < U_2$	1.174	1.116	1.000	1.000	0.189	18°	1.935	1.648	6.38°

The first trial begins by assuming U = 1.174 and computing h = 1.310 from continuity. Equations (28), (29), (30) and (31) are numerically integrated to show the asymmetrical amplifier configuration in Figure 8. The undesirable projection of rigid wall

A´ D´ beyond DE should be removed. A final trial taken for U = 1.116 and h = 1.380 attains amplifier symmetry in Figure 9.

At this point, a "one by one" variation is made on some physical parameters to evaluate the jet profile and the attending amplifier configuration. Again, the prior table keys each variation to the appropriate figure illustrating the amplifier.

- Changes in h_2 are made for high and low U and for $U_1 = U_2$. For the high speed case of U = 1.174, altering h_2 from 0.539 in Figure 8 to 0.819 in Figure 10 causes an increase of the jet deflection angle from 3.89° to 7.50°. For the low speed case of U = 1.116, altering h_2 from 0.539 in Figure 9 to 0.819 in Figure 11 causes an increase of the jet deflection angle from 6.01° to 8.04°.

- The inequality comparisons for $U_1 < U_2$ and $U_1 > U_2$ are made. Comparing the choice of $U_1 = 1.000$ and $U_2 = 1.116$ in Figure 12 to the choice of $U_1 = 1.116$ and $U_2 = 1.000$ in Figure 13 increases the jet deflection angle from 3.55° to 6.38°,

From a comparison of the resulting amplifier configurations in Figures 9 to 13, it is observed that the jet is more effectively deflected when

- The stagnation point E moves closer to the channel exits.

- The rigid wall B´ A at the channel exits projects beyond the rigid wall D´ A´.

For the velocity condition of $U_1 = U_2$, a meaningful plot is devised to measure the deflection angle from equation (17). If $(U/U_1)^{\pi/\alpha}$ is plotted against $(h_1 - h_2)/(h_1 + h_2)$ in Figure 14, the deflection angle increases when U/U_1, α, h_2 become larger or else h_1 vanishes.

LIST OF REFERENCES

1   G. Birkhoff and E. H. Zarantonello: Jets, Wakes and Cavities. New York: Academic Press Inc, 1957.

2. L. M. Milne – Thomson: Theoretical Hydrodynamics. New York: MacMillan Company, 1960. Fourth edition.

3. V. L. Streeter: Fluid Dynamics. New York: McGraw-Hill Book Company, 1948. First edition.

4. H. R. Vallentine: Applied Hydrodynamics. London: Butterworths, 1959, Second impression, 1961.

5. E. T. Copson: An Introduction to Theory of Functions of a Complex Variable. London: Oxford University Press, 1935. First edition, 1960 Reprint.

6. R. V. Churchill: Introduction to Complex Variables and Applications. New York: McGraw-Hill Book Company, 1948.

NOMENCLATURE

Symbol	Definition
U	free jet surface speed
U_1	entrance speed to primary channel
U_2	entrance speed to secondary channel
h	width of asymptotic jet at infinity
h_1	primary channel width
h_2	secondary channel width
α	included angle between channels
θ	free jet deflection angle measured with respect to secondary channel
θ_c	deflection angle of the asymptotic jet at infinity
β_c	physical deflection angle measured with respect to primary channel $\beta_c = \alpha - \theta_c$
$\omega_1,\ \omega_2,\ \omega_3$	dimensionless constants defined in Equations (15) and (25), respectively
$a_1,\ ---,\ a_9$	points on the real axis of the ζ-Plane
i	imaginary unit
Z	complex position in the physical plane $Z = X + iY$
$X,\ Y$	Cartesian coordinates of Z-Plane shown in Figures 8 to 13.
S	arc length of free streamline
ζ	position along real axis in the Schwarz-Christoffel plane
W	complex potential function $W = \phi + i\psi$
ϕ	equipotential function

172

Symbol	Definition
ψ	stream function
$\dfrac{-dW}{dZ}$	complex velocity; $-dW/dZ = u - iv$ in cartesian components and $-dW/dZ = qe^{-i\theta}$ in polar components
q	magnitude of $-dW/dZ$
θ	direction of velocity
Q	$Q = \text{Ln}\dfrac{U}{q} + i\theta$
K_1, K_3	Schwarz-Christoffel constants
K_2, K_4	constants of integration
γ, λ	dimensionless constants defined in Equation (10a)
ϵ	arbitrary constant
A, A´, B, B´, D, D´, E, E´, I´, I´´	corresponding points between Z-, Q-, ζ-, and W-Planes

SPECIAL NOTATIONS

$\rightarrow$	means "approaches"
$<$	as an example, <2 means "less than 2"
$>$	as an example, >2 means "greater than 2"
$\| \|$	operation taking absolute value
Ln	natural logarithm
lim	limit
$\neq$	a sign denoting inequality
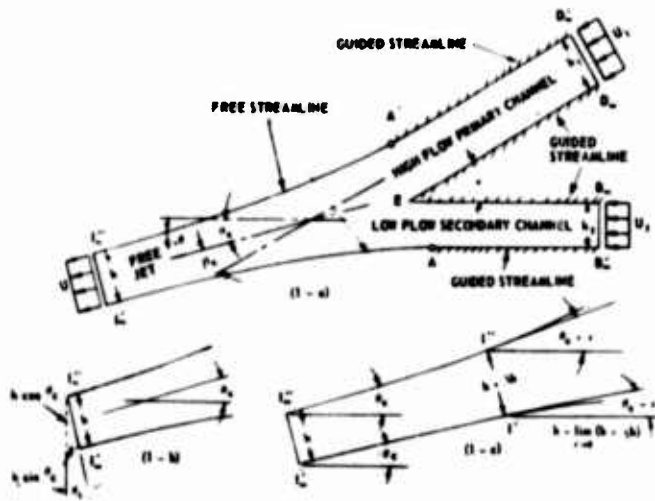
FIGURE 1 – Physical (Z) Plane
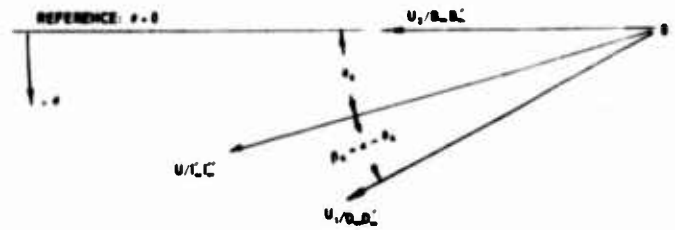
FIGURE 2 – Reference Frame for Inverse
Negative Conjugate Velocity
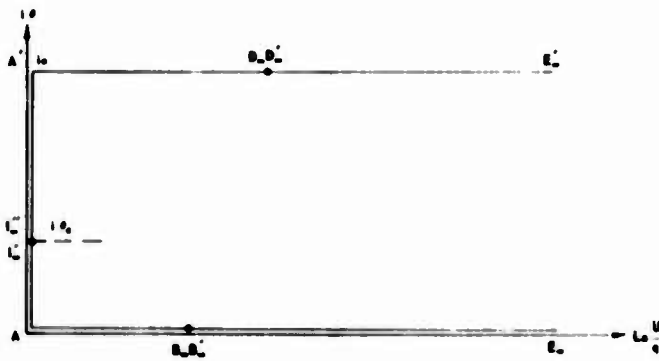
FIGURE 3 – Velocity (Q) Plane

FIGURE 4 – Schwarz-Christoffel (ζ) Plane
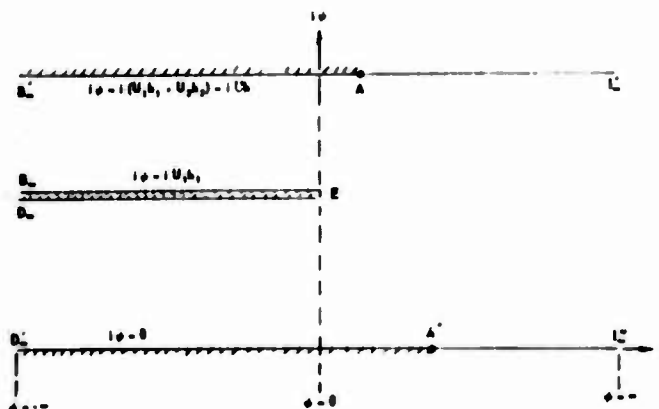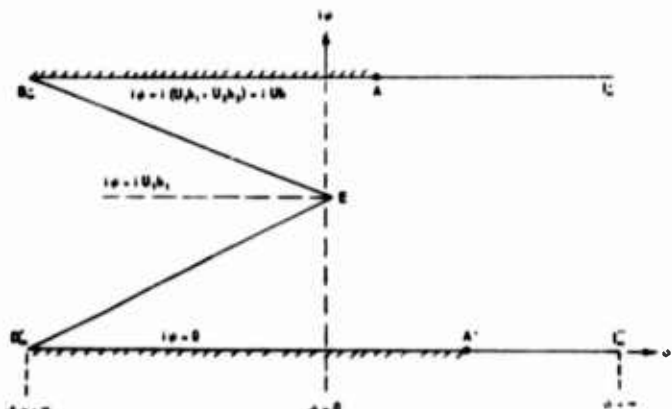
FIGURE 5 – Complex Potential (W) Plane

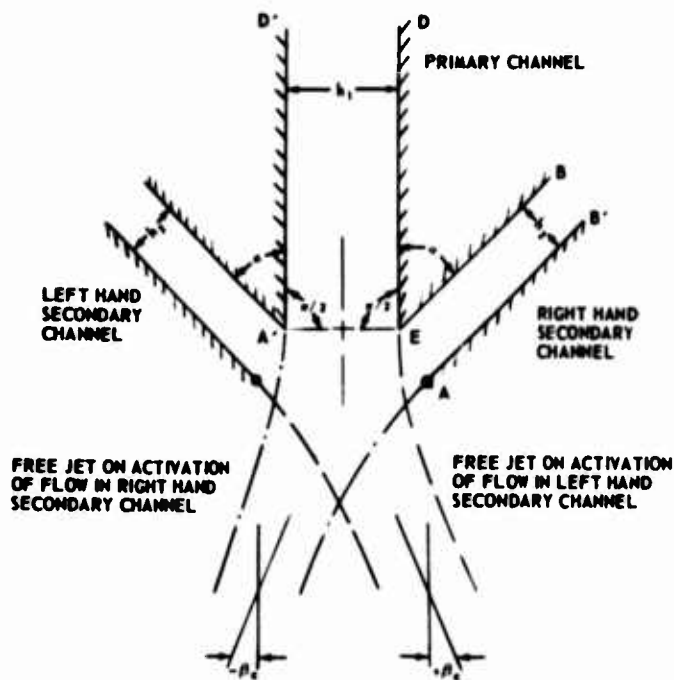FIGURE 6 – Degenerate Complex Potential
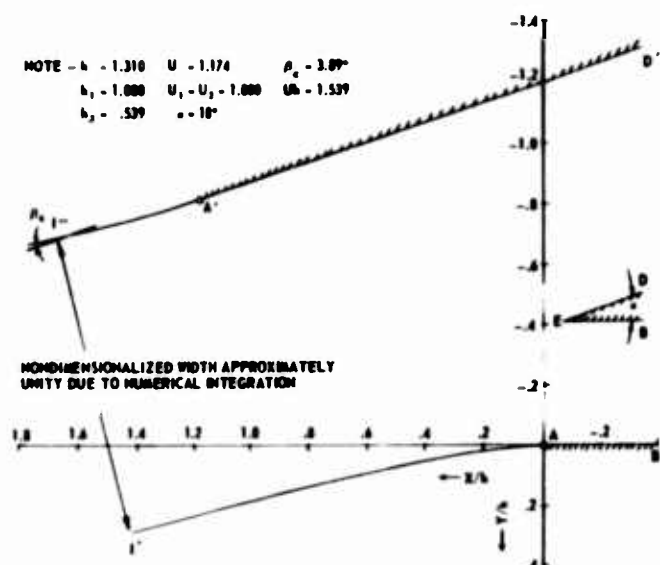(W) Plane

FIGURE 7 – Amplifier With Symmetrical Layout

FIGURE 8 – Free Streamline Profiles for High Free Jet Speed (U) and Small Secondary Channel Width (h_2) as $U_1 = U_2$
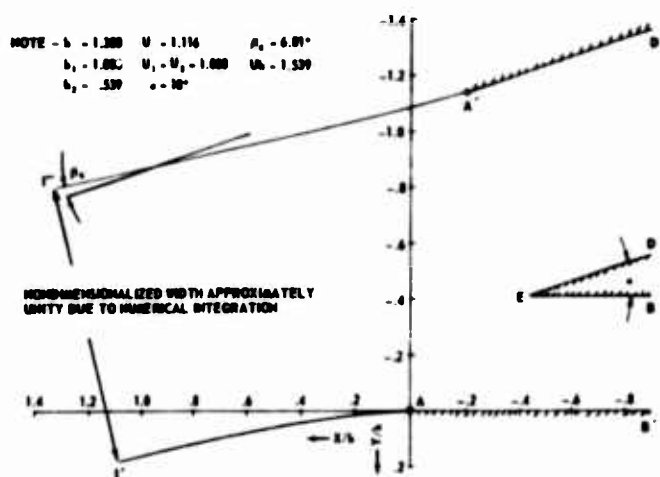

FIGURE 9 – Free Streamline Profiles for Low Free Jet Speed (U) and Small Secondary Channel Width (h_2) as $U_1 = U_2$
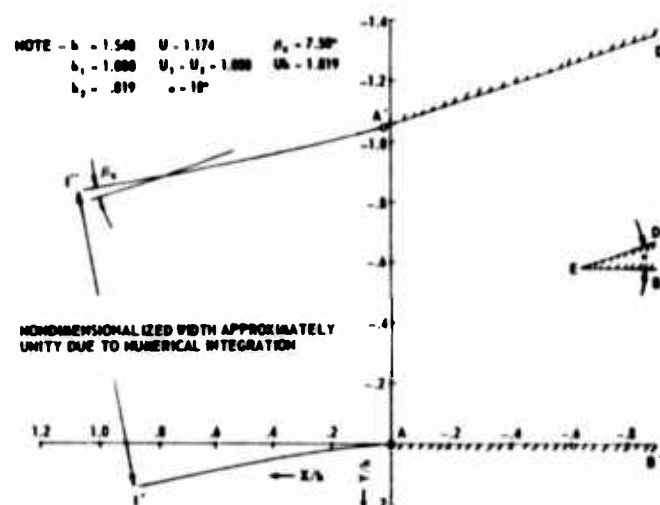

FIGURE 10 – Free Streamline Profiles for High Free Jet Speed (U) and Large Secondary Channel Width (h_2) as $U_1 = U_2$
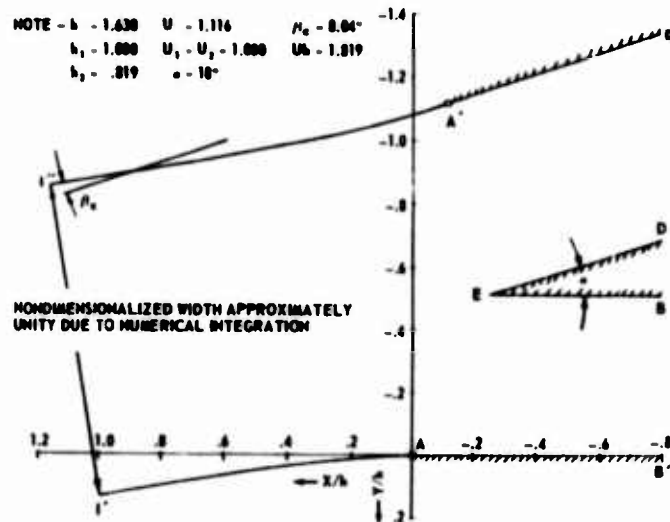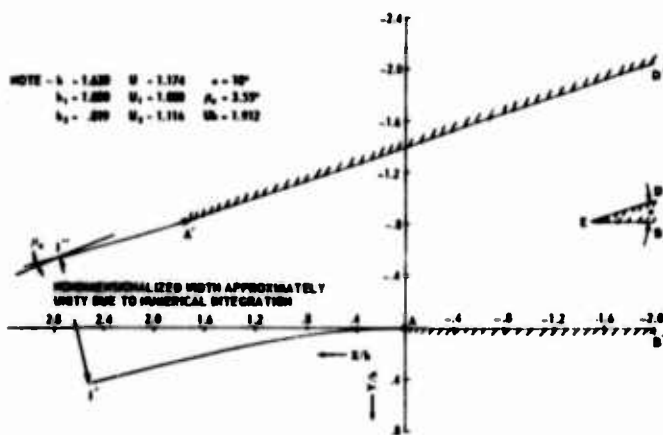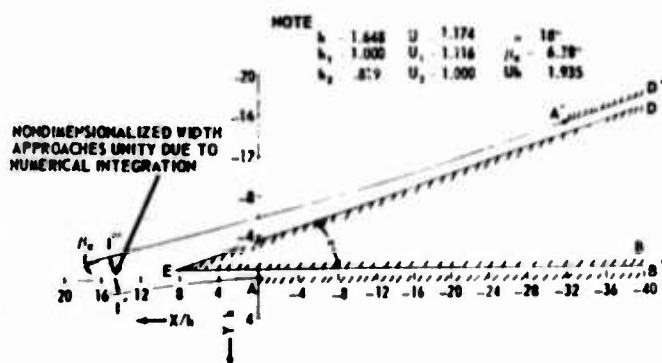
NOTE - h - 1.630   U - 1.116   β_c - 0.04°
       h_1 - 1.000   U_1 - U_2 - 1.000   Ub - 1.919
       h_2 - .819   α - 10°

NONDIMENSIONALIZED WIDTH APPROXIMATELY
UNITY DUE TO NUMERICAL INTEGRATION

FIGURE 11 – Free Streamline Profiles for Low
Free Jet Speed (U) and Large Secondary Channel
Width (h_2) as $U_1 = U_2$

NOTE - h - 1.630   U - 1.174   α - 10°
       h_1 - 1.000   U_1 - 1.000   β_c - 3.55°
       h_2 - .899   U_2 - 1.116   Ub - 1.912

NONDIMENSIONALIZED WIDTH APPROXIMATELY
UNITY DUE TO NUMERICAL INTEGRATION

FIGURE 12 – Free Streamline Profiles for High
Free Jet Speed (U) and Large Secondary Channel
Width (h_2) as $U_1 < U_2$

NOTE   h - 1.648   U - 1.174   - 10°
       h_1 - 1.000   U_1 - 1.116   β_c - 6.78°
       h_2 - .819   U_2 - 1.000   Ub - 1.935

NONDIMENSIONALIZED WIDTH
APPROACHES UNITY DUE TO
NUMERICAL INTEGRATION

FIGURE 13 – Free Streamline Profiles for High
Free Jet Speed (U) and Large Secondary Channel
Width (h_2) as $U_1 > U_2$

NOTE – SHADED BOUNDARIES
DUE TO ASSUMPTIONS
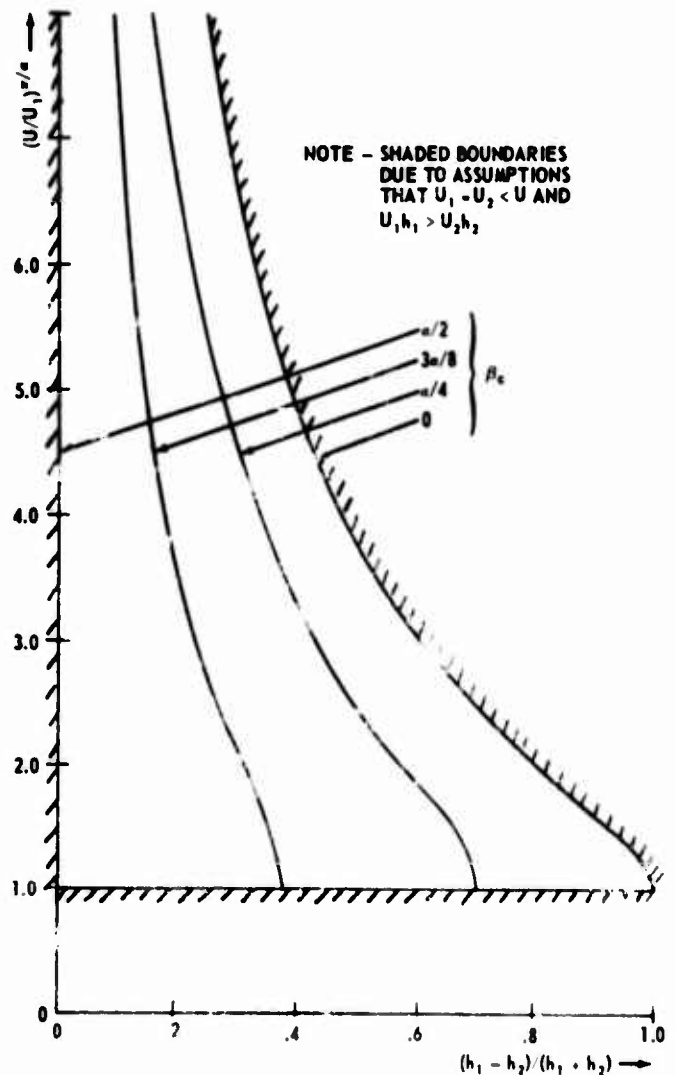THAT $U_1 - U_2 < U$ AND
$U_1 h_1 > U_2 h_2$

FIGURE 14 – Velocity Ratio $(U/U_1)^{\pi/a}$
Versus Channel Width Ratio $(h_1 - h_2)/(h_1 + h_2)$
as $U_1 = U_2$ for $\beta_C = a/2$, $\beta_C = 3a/8$, $\beta_C = a/4$
and $\beta_C = 0$

APPENDIX A

To verify the transformations in Equations (6) and (11), the inequalities, $a_3 - a_7 < 0$ $a_4 - a_5 > 0$, must be shown. Proof of these inequalities are found first by observing that $a_5 > 0$ and $a_7 < 0$ and $a_5 + a_7 > 0$ from relations appearing prior to Equation (11), and secondly substituting Equations (14) and (15) into Equation (8) to give

$$\frac{\omega_1 a_5 + \omega_2 a_7}{a_5 - a_7} = \cos \frac{\pi}{\alpha} \beta_c$$

The inequality $a_3 - a_7 < 0$ is proved by identification of its respective positive and negative terms. Details of the proof are best seen by

1. Substitution of Equation (14) into this inequality simplifies to

$$- \frac{(\omega_2 - 1)\, (a_7^2 - a_5 a_7)}{(\omega_2 - 1)\, a_7 + (\omega_1 + 1)\, a_5} < 0$$

Since $\omega_2 - 1 > 0$ and $a_7^2 - a_5 a_7 > 0$, then $(\omega_2 - 1)\, a_7 + (\omega_1 + 1)\, a_5 > 0$ must be justified.

2. Substitution of Equation (19) into $(\omega_2 - 1)\, a_7 + (\omega_1 + 1)\, a_5 > 0$ yields

$$(1 + \cos \frac{\pi}{\alpha} \beta_c)\, (a_5 + a_7) > 0$$

Since $a_5 + a_7 > 0$ and $1 + \cos \frac{\pi}{\alpha} \beta_c > 0$, the inequality is always true.

The inequality $a_4 - a_5 > 0$ is proved in a similar manner to the previous inequality. Details of this proof are best seen by considering

1. Substitution of Equation (15) into the inequality simplifies to

$$- \frac{(\omega_1 - 1)\, (a_5^2 - a_5 a_7)}{(\omega_2 + 1)\, a_7 + (\omega_1 - 1)\, a_7} > 0$$

Since $\omega_1 - 1 > 0$ and $a_5^2 - a_5 a_7 > 0$, then $(\omega_2 + 1)\, a_7 + (\omega_1 - 1)\, a_5 < 0$ must be justified.

2. Substitution of Equation (19) into $(\omega_2 + 1) a_7 + (\omega_1 - 1) a_5 > 0$ yields

$$- \left(1 - \cos \frac{\pi}{\alpha} \beta_c\right) (a_5 - a_7) < 0$$

Since $a_5 - a_7 > 0$ and $1 - \cos \frac{\pi}{\alpha} \beta_c > 0$, then the inequality $a_4 - a_5 > 0$ is always true.

WALL REATTACHMENT DEVICE WITH PULSED CONTROL FLOW

by

H. R. Müller

IBM Zurich Research Laboratory
Rüschlikon, Zurich, Switzerland

ABSTRACT: The flow gain characteristics of a monostable wall re-
attachment fluid amplifier show clearly that for high flow gain, a
double-sided element is superior to a single-sided one. The effective
angle θ^* (angle between the deflected jet and the adjacent wall, shortly
before switching) has been determined for different aspect ratios and
wall lengths, and is compared with the results of Bourque and Newman.
It can be seen that at large wall lengths, the author's curve approaches
the curve of Bourque et al, though their results have been obtained
with an element where the angle θ^* was varied by changing the wall
angle θ; whereas in the author's experiment, the angle θ was in-
creased by the injection of control flow.
The optimization of a bistable wall reattachment amplifier with re-
spect to flow and pressure gain is reported. The parameters found to
be most important are the wall offset and the control channel resist-
ance R_c.
The switching mechanism has been observed by flow visualisation and
an attempt is made to describe the switching mechanism by a simple
analytical model. A comparison with measured response times is
given. Response time measurements have also been carried out with
pulsed control flow. The results suggest that control flow has to be
injected until the separation bubble has been filled up to such an ex-
tent that the switching process becomes self-sustaining. With a con-
trol pulse duration time of 40 times the transport time τ_T, and a
control supply pressure of 0.7 times the supply pressure, the jet
could still be switched over. The control pulse duration time was 30%
of the response time measured under normal conditions.

I. INTRODUCTION

In the past few years, numerous articles have appeared which describe some of the characteristics of fluid logic devices. A large part of the articles is devoted to the study of the characteristics of proportional momentum amplifiers, single and double-sided turbulent reattachment amplifiers. The greater part of these articles describes the static characteristics of these devices and, so far, only little has been reported on the dynamic features. A number of investigations describe the so-called "Coanda effect" [1,2], namely, the reattachment of a turbulent jet to an adjacent wall. Most of these studies are limited to the case of two-dimensional flow, whereas the more interesting case is the three-dimensional one with small aspect ratios around 1. The computation of the reattachment point for large Reynolds numbers, constant bubble pressure, and long wall length for zero control flow is not very satisfactory, in so far as this is an impractical case for any application. Power considerations make it desirable to operate an element at relatively low Reynolds numbers and aspect ratios. In this range, the results will be considerably different from those achieved at high Reynolds numbers where flow gain will become relatively small, because of increased turbulence and, consequently, stabler reattachment.

It is the aim of this paper to elucidate some of the above-mentioned aspects. A comparison is made with Bourque and Newman's [3] results for a single-sided element.

The flow gain in a double-sided element was investigated in order to discover the optimum geometry. It was found that the offset and the control channel resistances were the most important parameters. Flow visualisation was used in order to study the dynamic switching in such a wall reattachment amplifier. A simple analytical model was used for the calculation of the response time. The optimization study made it possible to determine the best operation conditions of such an element and what switching speeds can be expected.

The investigation of the switching behavior for various control pulse lengths showed that switching can still take place as long as the control flow injection is sufficient to fill up the bubble to such an extent that release from the wall is possible. The use of water for experiments on switching offered the advantage of reduced switching speed and, hence, simpler experimental facilities.

II. DESCRIPTION OF THE EXPERIMENTS

Figure 4 shows the basic model chosen for this investigation. The nozzle contraction ratio was 5, the nozzle width d_N as well as the control channel width were 5 mm. The experiments with the single-sided element were carried out by removing the opposite wall and the receiver arrangement.

In order to avoid any asymmetries in the inlet velocity profile, a pipe, 35 times the length of the diameter, was incorporated into the supply line. Additionally, a bundle of small pipes was installed for straightening the flow. All experiments were carried out in the incompressible range, mainly with water.

The supply flow was kept constant for all experiments, whereas the supply pressure varied according to the amount of control flow. Though the use of a pressure source corresponds more closely to a practical application, this kind of operation would have failed in the dynamic case, where adjustment becomes impossible. At a control flow ratio of 0.1 times the supply flow, the supply pressure rose about 15% in the double-sided element. All pressures were non-dimensionalized with respect to $(\varrho/2) v_N^2$, where v_N is the nozzle mean velocity.

The source of the large scattering of the results for response time measurements, lies in the nature of the switching process (turbulence). The control supply pressure and the supply flow were kept constant within 2%.

III. THE CHARACTERISTICS OF THE WALL REATTACHMENT DEVICE

A large number of parameters influences the performance of a wall reattachment fluid amplifier, namely, aspect ratio, wall length L, divergence angle θ, offset, control channel width and receiver configuration. For relatively long elements, $L/d_N > 10$, the influence of the receiver on the stability of the reattachment is negligible as long as the Reynolds number

$$Re = \frac{v_N \cdot d_N \varrho}{\eta}$$

is not near a critical value below which the jet will no longer reattach to a wall.

One of the basic parameters is the ratio of model depth to nozzle width t/d_N (aspect ratio). Practical applications, sandwich technique and chemical processes make it desirable to keep the aspect ratio relatively small, whereas a more two-dimensional model (large aspect ratios) is needed for an analytical investigation. A description of the various manufacturing processes is given in reference 4. The

author's experiments (see companion paper, ref. 5) on the influence of the aspect ratio on the minimum Reynolds number of a symmetrical bistable element (minimum Reynolds number is defined by the ratio below which attachment to either wall no longer occurs) show clearly that below an aspect ratio of 1.5, the minimum Reynolds number increases rapidly. The asymptotic value for large aspect ratios was found to lie around 200; above an aspect ratio of 2 even laminar attachment became possible. At an aspect ratio of 1 the minimum Reynolds number already lies around 1500. This general behavior will be the same for elements with different geometries. For a single-sided element, the corresponding values will, of course, lie lower, because the asymmetry will favor a deflection. Considering the power consumption

$$N = (\frac{Q}{2}) v_N^3 \cdot t \, d_N$$

it becomes obvious that the reduction of the minimum Reynolds number allows a considerable reduction of the power consumption for a given fluid, as N is proportional to the third power of the velocity v_N.

The fact that the minimum Reynolds number can no longer be reduced above an aspect ratio of about 2, indicates that an optimum value for the aspect ratio t/d_N exists, where the power consumption is minimum. This minimum lies around $t/d_N = 3$. Gain considerations as well as fabrication techniques make it advisable to work at an aspect ratio around 1.

The nearer the Reynolds number at which an element is operated approaches the minimum below which attachment becomes impossible, the higher the flow gain will become. Experiments on pressure recovery have indicated that below a Reynolds number of 1000 and an aspect ratio of 1, the jet starts to spread rapidly after leaving the nozzle, and pressure recovery becomes, therefore, quite low. This fact also sets an upper limit to the aspect ratio, because at a given Reynolds number, the turbulence and hence the entrainment, starts to become more pronounced for increasing aspect ratio, and thus the reattachment becomes more stable. Experiments on flow gain in a single-sided element, see Fig. 1, show this behavior quite clearly.

In order to demonstrate the advantage of a double-sided over a single-sided element, the flow gain results for a single-sided element are reported in section III. 1), and then compared with those obtained for a double-sided element. Some of the special effects and limitations of fluid jet amplifiers are given in references 6 and 7.

III. 1) Monostable Single-Sided Element

The reattachment of a turbulent jet to an adjacent flat plate
has been investigated in great detail by Bourque and Newman[3],
Sawyer[8], and Levin and Manion[9], however, their results are limited
to high Reynolds numbers and large aspect ratios. No theoretical
model has so far allowed determination of the maximum divergence
angle θ at which reattachment becomes impossible for short ele-
ments. Experiments show clearly, however, that the angle θ at
which separation occurs becomes considerably lower for wall lengths
L/d_N below 15, see Fig. 1. The curve for maximum wall angle at
which separation starts has been found experimentally by Bourque
and Newman.

In an element with fixed wall angle θ the separation of the jet
from the wall is achieved by the injection of control flow. This reduces
the return flow, and, as a result, the effective angle θ^*, (θ^* is ex-
plained in Fig. 1), becomes smaller than the corresponding value
given by Bourque and Newman for zero control flow. It is obvious that
the flow gain becomes higher for elements with high initial divergence
angle θ, because less control flow has to be injected in order to
reach θ^*. The divergence angle θ was 15° in all experiments. The
author's results, given in Fig. 1, demonstrate quite clearly the in-
fluence of the aspect ratio on θ^* or flow gain v_q (see Fig. 2), re-
spectively. For an aspect ratio of 1, a wall length $L/d_N = 8$, the
effective angle θ^* is 24°, or $\Delta\theta = 9^\circ$. The corresponding ratio of
control momentum to supply momentum is 0.16 and $q_c/q_s = \sqrt{0.16} = 0.4$.
The experimental value q_c/q_s was found to be 0.2 only, the reason be-
ing that part of the control momentum is obtained by the static control
pressure built up at the control port when control flow is injected. A
flow gain of only 5 is rather low for such a short element. For a wall
length L/d_N of 15 the flow gain already decreases to 2.8 at a Reynolds
number of 5000. At an aspect ratio of 0.6 (see Fig. 2) the correspond-
ing values for flow gain are already remarkably higher due to the re-
duced turbulence (influence of bottom and top plates). The influence
of the Reynolds number becomes more pronounced at these small as-
pect ratios. The influence of receiver load on stability will already
become significant at a Reynolds number smaller than 5000 and a
wall length of $L/d_N < 8$. Figure 3 shows the flow patterns in a single-
sided element for aspect ratios of 0.6 and 1 and for two different wall
lengths. The photographs at the bottom of Fig. 3 ($L/d_N = 26$) illustrate
once again how stable reattachment becomes by means of the Coanda
effect.

Once the jet has been released from the adjacent wall, the jet deflection is determined by the control momentum. For digital operation, the jet position must be kept independent of control flow, once the jet has been switched. This feature is best achieved by introducing a second wall. A small asymmetry in the control line resistances and offsets makes it possible for the jet to switch back when the control flow q_c is reduced.

III. 2) Double-Sided Element

The introduction of a second wall (see Fig. 4) also allows increased flow gain, as the pressure drop along the second wall due to the entrainment helps to reduce the control flow necessary for switching the jet over to this second wall. The pressure reduction along the second wall helps to increase the pressure difference across the jet, so that for control flow ratios of less than 0.1, the control momentum already becomes significant; large enough to bend the jet over to the other wall. This pressure reduction on the opposite side is effective over a relatively wide region, and becomes quite effective for small divergence angles θ and small offsets, which help to reduce the control flow entrained in the bubble. Additionally, the entrained flow can be reduced by applying a larger control line resistance. The demand for a small divergence angle θ is different from that for large divergence angle θ in the single-sided one. In the double-sided element the second wall dominates by far the influence of the divergence angle θ of the wall to which the jet is attached. Furthermore, it is known that the minimum Reynolds number below which reattachment of the jet to either wall is no longer possible, increases with increasing wall angle, hence too large wall angles should be avoided. Earlier experiments on flow gain showed that the optimum divergence angle θ lies around 15°.

The experiments on a double-sided monostable element with offsets a_{c1} = 0.08 d_N, a_{c2} = 0.16 d_N, a divergence angle θ of 15°, a wall length L/d_N of 8, gave a flow gain of 13 (v_q = ratio of supply flow to critical control flow at which switching starts) at a Reynolds number of 10,000 and v_q = 20 for Re = 4000. These values lie considerably higher than the corresponding ones for the single-sided element with L/d_N = 8, at an aspect ratio of 1. For a Reynolds number of 4000, the double-sided element allows a flow gain four times higher than the corresponding single-sided one. The influence of the wall length L/d_N on flow gain was found to be relatively small for the double-sided element at a Reynolds number above 6000. Below this value the increase in flow gain with decreasing Reynolds number is higher for the shorter element. At these low Reynolds numbers the core length is already of the same length as the element itself. The influence of the receiver load also increases with decreasing wall length.

The pressure recovery was investigated for different wall lengths L/d_N. The experiments on a free turbulent jet have shown that, at an aspect ratio of 1, the results for the center plane pressure recovery still agree quite well with those reported by Albertson for large aspect ratios. At distances nine times the nozzle width downstream, the pressure recovery decays rapidly and is only 0.35 times $(\varrho/2)\, V_N^2$ at $L/d_N = 20$. For a receiver width of 2 ‡ 4 times nozzle width, the mean value is even lower than the maximum (center plane pressure recovery), and lies around 0.2· $(\varrho/2)\, V_N^2$ for $L/d_N = 20$. The pressure decay along a bounded wall jet is smaller than the corresponding one for the free jet. The pressure decay can be reduced by reducing the Reynolds number below 5000, so that the wall length no longer becomes so critical. This fact is especially important when series coupling of several elements is considered.

Figure 5 shows the output characteristics for different wall lengths L/d_N, and offsets. In Fig. 4 it can be seen that a bleed line is introduced on each side of the element. This bleed line has the task of making the supply flow independent of the receiver load, so that even with closed receivers, the main flow stays practically unchanged. The fact that the flow has to be turned over when the receiver is closed, results in an increased pressure recovery of about 30%, compared to the initial recovery.

a) Optimization

The control-input characteristic (see Fig. 6) was investigated for different control line resistances R_{c2} (see Fig. 7). Experiments were carried out for an offset of $a_{c1} = a_{c2} = 0.15 \cdot d_N$ and $a_c = 0.26\, d_N$. Though the experiments with smaller offset gave 30 - 40% more flow gain, the final experiments were made with offset $a_c = 0.26\, d_N$. It is felt that an offset of $a_c = 0.15\, d_N$ is so small that a relatively small change gives rise to relatively large deviations in the characteristics. Manufacturing tolerances become very important in miniaturized elements. The input characteristics consist of two branches A and B. The characteristics were plotted in a nondimensionalized form; the Reynolds number being 10,000. The control characteristics were measured statically, which means that the control flow was increased in small stages. Similar curves have been reported by Norwood[10]. He reported the results for an element in which quadratic resistances (orifices) were incorporated.

When the cross point Q_∞ between the resistance line R_{c1} and the characteristic A lies above the point Q_{CRIT}, switching occurs. Q_{CRIT} is the critical nondimensionalized control flow ratio above which switching can take place. The new equilibrium point will, thereafter, lie on branch B.

At low control line resistance R_{c2} (resistance in the opposite control line), the flow gain $v_q = q_s/q_{CRIT}$ becomes lowest (see Fig. 6, curve x). It becomes highest at high values of R_{c2}. However, above a certain value of R_{c2}, the flow gain becomes independent of R_{c2}. It is, therefore, not advisable to use too high resistances; R_{c1} has to be kept about equal to R_{c2}. Figure 8 shows the variation of flow gain v_q with R_{c2}; at the bottom of the figure, the minimum control supply pressure is given as a function of R_{c1} (R_{c1} is assumed equal to R_{c2}). The minimum control supply pressure must be lower than a certain value, given by the output characteristic of the "driving element". A maximum pressure of 0.4 was assumed. R_{c1} must not, therefore, exceed a value of 7. The resistances R_{c2} given in Fig. 7 were assumed linear for the flow gain curve in Fig. 8. The values for R_{c2} were taken from Fig. 7 for $q_c/q_s = 0.05$. A resistance value of $R_c = 4$ seems to be optimal; after this point, the flow gain is still maximum and $P_{cs\ min}$ is very low, namely 0.07.

Figure 6 shows quite clearly that for low values of R_{c2} the assumption of $R_{c1} = R_{c2}$ is no longer justified, because already at zero control supply pressure, the resistance line R_{c1} and the characteristic A could intersect near the switch point. Furthermore, small asymmetries introduced by the fabrication technique would make the element monostable. The end points of characteristic B for negative control flows mark the "switch back". As soon as the resistance line R_{c1} falls below this point, the jet switches back from the opposite wall. This condition is, of course, only fulfilled when suction is applied. Under normal circumstances, the control supply pressure P_{cs} is either zero or higher. A necessary condition for bistability is that the "switch back" point exist only in the left hand side. Furthermore, the "switch back" point must lie below the resistance line when passing the origin. The fact that for some resistances R_{c1}, the above-mentioned condition is not satisfied, shows that even this large scale model had a small asymmetry.

The resistances are all nondimensionalized in the form:

$$p/P_s = f(q_c/q_s) \qquad \text{(see Fig. 7)}$$

where Δp is the pressure drop across a resistance at a control flow q_c. In the case of laminar flow

$$p/p_s = f(q_c/q_s) = R \cdot q_c/q_s$$

where R is the nondimensionalized resistance coefficient

$$R = \frac{\Delta p}{q_c} \cdot \frac{q_s}{p_s}$$

When an element is operated at low Reynolds numbers, say less than 5000, the corresponding control line Reynolds number is 10 - 20 times lower for $q_c = q_{CRIT}$, due to the high flow gain. At Reynolds numbers less than 500, the flow will certainly be laminar, at least at the very beginning, because the highest Reynolds number is reached only when switching starts, when $q_c > q_{CRIT}$. When the cross section of the control line is chosen to be considerably higher than the nozzle width, the control line Reynolds number decreases even more. For laminar flow R becomes:

$$R = K \cdot \frac{l}{d_N} \; \frac{1}{Re_N\left(\frac{d_H}{d_N}\right)} \cdot \left(\frac{A_N}{A_c}\right)$$

where K is determined by the shape of the control line.

$K = 56.6$ for quadratic shape

$K = 67$ for circular shape   (see ref. 11)

Re_N is the Reynolds number defined in the usual way (with respect to the main flow)

d_H is the hydraulic diameter of the control line

$\dfrac{A_N}{A_c}$ is the ratio of nozzle area to control line area

is the control line length.

For fully turbulent flow the following relationship holds:

$$\frac{\Delta p}{p_s} = C_2^* \, (q_c/q_s)^2$$

$$C_2^* = \psi \cdot \left(\frac{l}{d_H}\right)\left(\frac{A_N}{A_c}\right)^2 \, , \qquad \psi = \frac{3.3 \cdot Re_H^{-1/4}}{10^3} \qquad \text{see ref. 11}$$

for quadratic shape.

It is especially interesting to note that in the case of laminar flow, the nondimensionalized resistance term is inversely proportional to the Reynolds number. The fact that the control input characteristic is practically independent of the Reynolds number over a large region,

shows that the ratio of pressure drop along a resistance R_c to a given output pressure must, therefore, increase with decreasing Reynolds number. The physical reason behind this interesting fact is that: Any pressure level in the element (input or output) itself is proportional to the square of the nozzle velocity v_N times a constant k, whereas the pressure drop across a resistance for laminar flow is only proportional to the corresponding velocity; for small values of v_N the ratio of $k \cdot (\rho/2) v_N^2$ over pressure drop in the resistance becomes proportional to the velocity, and decreases, therefore, with decreasing velocity.

IV. SWITCHING MECHANISM   (Double-sided element)

In this section, the dynamic switching when control flow is suddenly applied will be discussed. Careful observation of the switching action in a bistable element (see Fig. 9) allowed the construction of a simplified analytical model for the switching.

The following assumptions are made:

1) The separation bubble has to reach a critical volume V_{switch} before it is released from the wall. This critical value was determined experimentally by studying the flow patterns and by the analysis of the control flow oscillograms.

$$V_{switch} = \gamma d_N^2 \cdot t \ . \qquad \gamma \text{ was found to be } \sim 13.$$

2) The difference between the flow entrained in the jet Q_{ENT} and the return flow Q_{RET} has the form:

$$f(Y) = Q_{ENT} - Q_{RET} = K_1 Y - K_2 Y^2$$

where Y is the nondimensionalized bubble volume $Y = (V - V_o) / (V_{switch} - V_o)$, V_o is the bubble volume for zero control flow. The sketch below illustrates the shape of the curve $f(Y)$:

----- INITIAL CURVE FOR $\tau = 0$

——— ASYMPTOTIC CURVE FOR $\tau \gg$

188
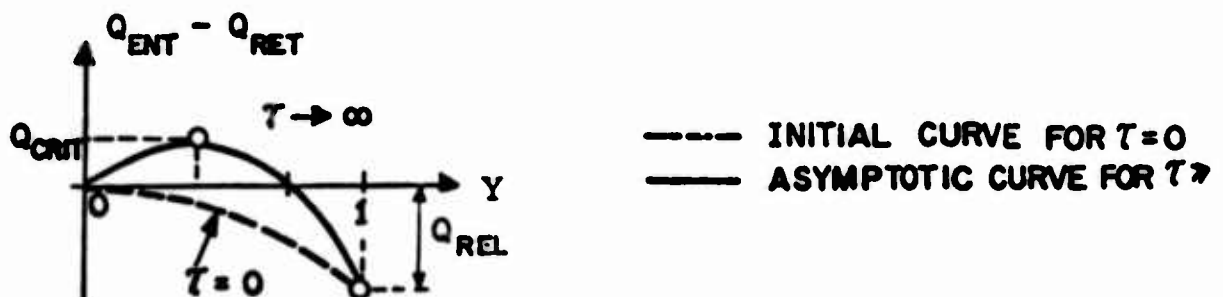
At zero control flow the entrained flow Q_{ENT} must be in balance with the return flow Q_{RET}, therefore $f(Y)$ goes through the origin. Furthermore, we know that for control flow Q_c less than Q_{CRIT} switching cannot take place; the bubble reaches a certain value Y_{CRIT} and decays again when control flow is stopped.

The bubble growth is given by the equation:

$$\frac{dY}{dS} = \frac{1}{\gamma} \; [Q_c - f(Y)]$$

$[Q_c - f(Y)]$ is the net flow filling the bubble. S is the nondimension-alized response time (τ_{REL} / τ_T) where τ_T is the transport time. The equation shows clearly that a further bubble growth $Y > Y_{CRIT}$ occurs only when Q_c becomes larger than Q_{CRIT}. As soon as the bubble has reached the critical value Y_{CRIT}, $f(Y)$ becomes smaller and changes sign. The flow patterns on switching show very clearly (see Fig. 9) how the return flow increases rapidly as soon as the bubble has reached a certain size. The value Q_{CRIT} has to be found by experiment. The value $Q_{REL} = f(Y = 1)$ must be matched so that the response time measurements fit together with the analytical curve. Q_{REL} can be seen to lie around 0.2.

The parameters K_1 and K_2 are determined by Q_{CRIT} and Q_{REL}:

$$K_1 = 2 \; [Q_{CRIT} + \sqrt{Q_{CRIT} (Q_{CRIT} + Q_{REL})}] \cdot \phi(S)$$

with $\phi(S) = 1 - \exp(-\Omega S)$

$$K_2 = K_1 + Q_{REL} \cdot$$

For $Q_{CRIT} = 0.045$ and $Q_{REL} = 0.2$, Y_{CRIT} becomes 0.3 which fits quite well with experiments.

The function $\phi(S)$ allows us to adjust the function $f(Y)$ so that the influence of the dynamic switching (initial bubble growth relatively fast) can be included in the model. When fast switching occurs, the bubble deformation is different, because then the injected control flow is not transported downstream fast enough, and the return flow is, in this case, higher. A rough estimate of the response time for the release of the jet from the wall, once more confirms that $f(Y)$ must become negative at a certain Y.

Assuming that $Q_c = 0.06$ and $f(Y) = 0$, $\gamma = 15$, S becomes at least 240, whereas $f(Y)$ is at least larger than zero for $Y < Y_{CRIT}$; and Q_c reaches its final value after $\Delta S \approx 20$. The experimental value for S, however, lies around $S = 100$.

It is interesting to note that the time dependence of the control impedance can be analyzed from the static characteristic. This fact is far from being trivial as the transient flow patterns occurring during the switching process are basically different from the stationary patterns, when the characteristic is measured statically. In order to solve this question a control flow measuring device[12] was incorporated into the control line. The device uses the electric field set up by the ions moving in a magnetic field (see Fig. 11). The differential equation for the control flow Q_c is :

$$P_{cs} - \begin{pmatrix} R_c \cdot Q_c & \text{laminar flow} \\ C_2^* \cdot Q_c^2 & \text{turbulent flow} \end{pmatrix} - A = C_1 \frac{dQ_c}{dS}$$

The equation for the characteristic A has the form :

CURVE $A = -P_{co} + R_o \cdot Q_c + C_2 Q_c^2$
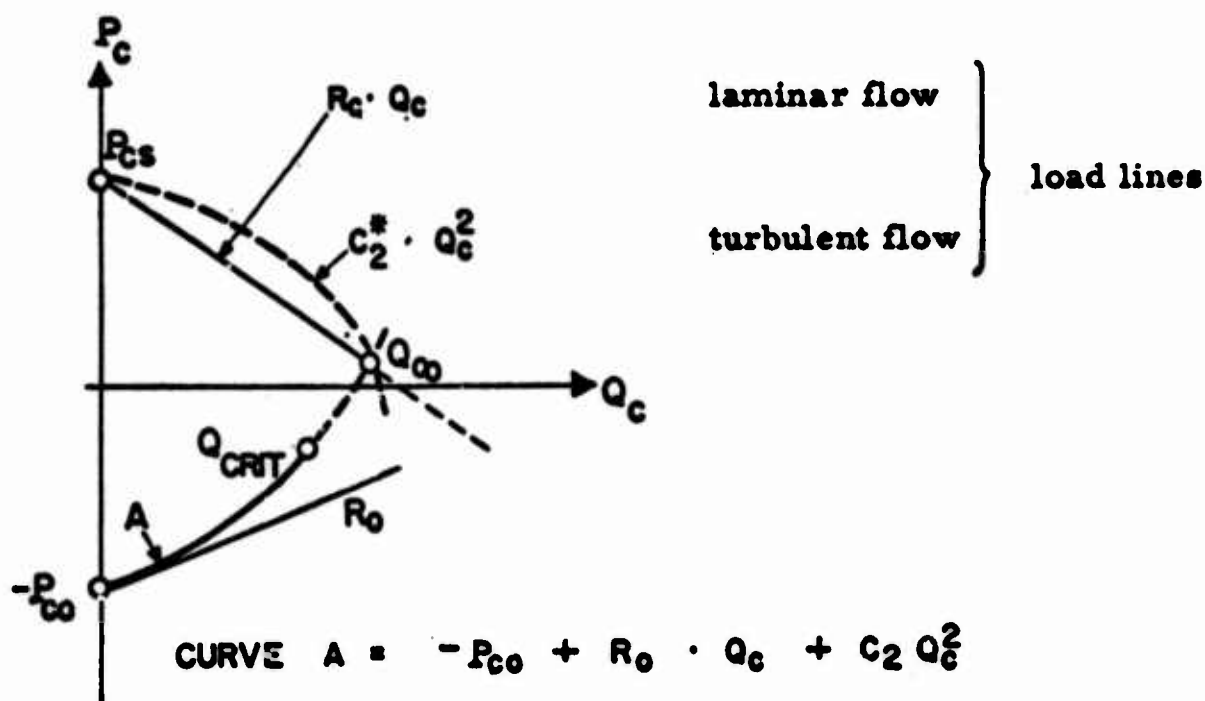
$$(P_{cs} + P_{co}) - (R + R_o) \cdot Q_c - (C_2 + C_2^*) Q_c^2 = P_{TOT} - R_{TOT} Q_c - C_{2\ TOT} Q_c^2$$

either/or

The solution of the above equation for the control flow Q_c gives:

$$Q_c (S) = \frac{Q_2 (1 - e^{-\alpha s})}{\dfrac{Q_2}{Q_\infty} + e^{-\alpha s}}$$

where

$$Q_\infty = -\frac{R_{TOT}}{2 C_2} + \sqrt{\frac{R_{TOT}^2}{4 C_{2\ TOT}^2} + \frac{P_{TOT}}{C_{2\ TOT}}}$$

$$Q_2 = \frac{R_{TOT}}{2 C_2} + \sqrt{}$$

$$\alpha = \frac{2 C_2}{C_1} \cdot \sqrt{}$$

The comparison of the results obtained from the analytical model with the experiments is given in Fig. 10. At low control supply pressure P_{cs}, where Q_∞ approaches Q_{CRIT}, the response time goes asymptotically to infinity. The argument Ω of the time function $\phi(S) = 1 - \exp(-\Omega S)$ was found to lie around 0.015. For lower control supply pressures P_{cs}, it is hard to judge how good the agreement with the experiments is, because the experimental results show large scattering in this region. The critical control flow ratio Q_{CRIT} on which the calculations were based is, in itself, not really a well-defined constant, it varies up to 10%.

The total response time (time which elapses from the moment when control flow is applied till the static pressure signal is picked up at the receiver x) can be split up into the time τ_1 which elapses until the bubble is released, and the time τ_2 which is needed to accelerate the jet downstream into the receiver. The first term is more or less independent of the wall length L, whereas the second term is proportional to (L - k), k being 7 ÷ 10 times the nozzle width. The response time will, therefore, not necessarily be doubled when the wall length is doubled.

191

The experimental set-up used for the investigation of the switching mechanism, when the control flow is pulsed, is outlined in Fig. 12. The time for the total opening of the slot in the control channel was less than 8 milliseconds, and is, therefore, negligible compared to the switching time. The results for this kind of operation are given in Fig. 13. The shorter the control pulse became, the higher the minimum control supply pressure below which switching is no longer guaranteed, rose. The results indicate that the control supply pressure has to be so high, that during the opening time, the bubble reaches the volume where it continues to grow when the control flow is stopped; this is the case when the function $f(Y) = Q_{ENT} - Q_{RET}$ becomes negative, or in other words, the switching mechanism is self-sustaining. Figure 14 shows the control flow and receiver pressure oscillograms for some typical cases. The oscillograms illustrate clearly, that at the moment when the control flow stopped, the bubble volume was already near the one where the jet became released from the wall. The point of release is marked by the sudden rise of the pressure signal.

Figure 15 shows the limiting curve below which switching is no longer 100% guaranteed. P_c^* is the control supply pressure below which switching is no longer possible for $\tau_c / \tau_T \to \infty$. Below the curve, switching becomes less and less probable.

Approximating the curve for the nondimensionalized response time by

$$S = \tau / \tau_T = \frac{C}{P_{cs} - P_{cs\,min}} + S_o \quad , \quad \text{(see Fig. 16)}$$

the response time can be given as a function of pressure gain. Pressure gain v_p is defined by P_{REC}/P_{cs}. The receiver output pressure was assumed to be 0.4. The maximum pressure gain is achieved when the control supply pressure is made minimum; at this point S approaches infinity. $1/S$ corresponds to a frequency.

V. CONCLUSION

The investigation of the flow gain characteristics in single and double-sided elements shows clearly the superiority of the double-sided element; additionally, the position of the main jet is defined by the opposite wall, whereas in the single-sided element, the position is a function of the control momentum as soon as the jet is released from the wall to which it was attached. The single-sided

element must be operated either at very low aspect ratios, very short wall length, or at a large wall angle θ. For too high wall angles, the minimum Reynolds number below which reattachment becomes impossible, increases considerably. The optimum aspect ratio for a fluid amplifier lies between 0.8 and 2.

The control line resistance is an integral part of any element and must be incorporated in any investigation. The operation of the element at a Reynolds number below 5000 favors control line resistances with laminar flow when flow gain is above 10. Assuming that the inherent characteristics of an element do not change when the Reynolds number is reduced, say from 10,000 to 5,000, (this fact has been experimentally verified), the performance of the element changes nevertheless, as the ratio of pressure drop across the resistance over the receiver output pressure, for example, becomes unfavorable at low Reynolds numbers.

The measurements of the response time of a bistable element for various control pulse lengths show that the response time is not significantly increased, when the control pulse is shortened, but a definite pressure limit exists, below which switching is no longer 100% guaranteed. This limit is a function of the control line resistance and the control line inertia. The flow visualisation study has revealed that as soon as the separation bubble has reached a certain size, the jet return flow becomes higher than the flow entrained in the jet, so that even at zero control flow, the bubble growth continues, that means, the switching process becomes self-sustaining.

The total response time of an element is given by the time τ_1 necessary to get the jet released from the wall, and the time τ_2 which elapses until the jet is accelerated downstream into the receiver. τ_1 is practically independent of the wall length for $8 < L/d_N < 17$. The analytical model formulated to calculate the response time for the bubble release, looks promising. It contains all the important features of the switching process. The measurement of the control flow allowed us to find out whether the control input characteristic is the same in the dynamic and static cases, where in the latter, control flow is increased in small stages. No significant difference has so far been found. The fact that the dynamic switching characteristic is the same for the dynamic and static cases is not trivial, because the flow pattern for the dynamic case is quite different from that of the static case.

ACKNOWLEDGEMENT

194

LIST OF SYMBOLS

A_N	Nozzle area.
A_c	Control channel area.
a	Offset (see Fig. 4).
C_1	Acceleration term, $C_1 = \dfrac{2A_N}{A_c} \cdot \dfrac{\ell}{d_N}$.
C_2	Coefficient of quadratic term used to approximate the control input characteristic A (see Fig. 6).
C_2^*	Coefficient of quadratic term used to approximate control resistance for turbulent flow.
d_N	Nozzle diameter.
K	Shape factor for control resistance with laminar flow.
ℓ	Control line length.
L	Wall length of element.
p, P	Pressure, nondimensionalized pressure, respectively.
P_s	Supply pressure $(\rho/2) V_N^2$.
P_c	Static pressure at control port.
P_{REC}	Static pressure at receiver x or $\bar{x}$.
Δp	Pressure drop along control line for flow q_c.
$P_c, P_{REC}, \dfrac{P_c}{P_s}$, or $\dfrac{P_{REC}}{P_s}$, respectively.	
P_{cs}	Nondimensionalized control supply pressure (for switching).
P_{co}	Nondimensionalized control port pressure for $q_c=0$.
q	Flow.
q_s, q_c	Supply flow, control flow, respectively.
q_{REC}	Receiver flow.

Q Nondimensionalized flow ratio.

Q_{CRIT} Nondimensionalized critical control flow necessary for switching (see Fig. 6).

$Q_{\bullet}$ Nondimensionalized limiting control flow crosspoint between curve A (see Fig. 6) and resistance R_{cl} (see Fig. 1).

$R, \; C_2^*$ Nondimensionalized control line resistance

$$P = R \cdot Q_c = \left(\frac{\Delta p}{q_c} \; \frac{q_s}{p_s} \right) Q_c \qquad \text{(laminar flow)}$$

$$P = C_2^* \, Q_c^2 = \psi \, \frac{l}{d_N} \left(\frac{A_N}{A_c} \right)^2 \cdot Q_c^2 \quad \text{(turbulent flow)}.$$

$R_{Cl}, \; R_{C2}$ Resistance in control line C_1. Resistance in control line C_2, respectively.

Re Reynolds number, $\displaystyle Re = \frac{v_N \cdot d_N \cdot \rho}{\eta}$.

S Strouhalnumber $= \tau / \tau_T$ (nondimensionalized response time).

τ Time.

τ_T Transport time $\left(\tau_T = \dfrac{d_N}{v_N} \right)$ is the time which elapses for a particle travelling the nozzle distance d_N at jet velocity v_N.

t Model depth.

t/d_N Aspect ratio (for two-dimensional flow $t/d_N = \infty$).

v_N Mean jet velocity at nozzle exit.

V Separation bubble volume.

V_0 Bubble volume for $q_c = 0$.

V_{SWITCH} Bubble volume when bubble is released (dynamic case).

Y Nondimensionalized bubble volume $Y = (V-V_0)/V_{SWITCH}-V_0)$.

v_q Flow gain, ratio of q_s over critical control flow q_{CRIT}.

v_P Pressure gain, ratio of receiver output pressure P_{REC} over control supply pressure P_{cs}.

196

γ Bubble size (for $Y = 1$), $V_{SWITCH} = \gamma \cdot t \cdot d_N^2$.

ϕ Time function, takes into account the dynamic switching process $\phi = (1 - e^{-\Omega s})$.

Ω Argument for the function $\phi(s) = 1 - e^{-\Omega s}$.

ψ Shape factor for resistance with turbulent flow.

REFERENCES

1. Métral, M.: "L'éffet Coanda", Proceedings of the Fifth International Congress on Applied Mechanics, 1938.

2. Coanda, H.: U.S.A. Patent 2052869.

3. Bourque, C. and B.G. Newman: "Reattachment of a two-dimensional incompressible jet to an adjacent flat plate", Aeronautical Quarterly, Vol. XI, Great Britain, 1959, p. 201.

4. Mitchell A.E., Müller, H.R. and R.H.W. Zingg: "Some Recent Developments in the Design of Fluid switching Devices and Circuits", Proceedings of the Fluid Power International Conference, London, April 1964.

5. Glättli H.H., Müller, H.R. and R.H.W. Zingg: "Remarks on the Limitations of Pure Fluid Elements", to be presented at the same meeting, May 1964.

6. Comparin R.A., Glättli H.H., Mitchell, A.E. and H.R. Müller: "On the Limitations and Special Effects in Fluid Jet Amplifiers", ASME Symposium on Fluid Jet Control Devices, Winter Annual Meeting, New York, Nov. 28, 1962.

7. Comparin R.A., Mitchell, A.E. and H.R. Müller: "Qualitative and Quantitative Aspects of the Wall Reattachment Amplifier", Zeitschrift für angewandte Mathematik und Physik (ZAMP), Vol. XIII, Fasc. 5, 1962.

8. Sawyer, W.A.: "Two-dimensional Turbulent Jets with Adjacent Boundaries", Dissertation: Cambridge University, October 1962.

9. Levin, S.G. and F.M. Manion: "Jet attachment distance as a function of adjacent wall offset and angle", TR 1087, 1962, Harry Diamond Laboratories Washington.

10. Norwood, R.E.: "A Performance Criterion for Fluid Jet Amplifiers", ASME Symposium Nov. 1962, see ref. 6.

11. Landolt Börnstein: "Zahlenwerte und Funktionen", 6. Auflage, VI. Band, Technik 1. Teil, page 669.

12. Thürleman, B.: "Methode zur elektrischen Geschwindigkeitsmessung in Flüssigkeiten", Helvetica Physica Acta, 14. 1941.

13. Warren, R. W. :"Some parameters affecting the design of bistable fluid amplifiers", ASME Symposium on Fluid Jet Control Devices, 1962.

14. Lachmann, G. V. :"Boundary Layer and Flow Control", Volume 1, Pergamon Press, 1961.

FIGURE CAPTIONS

Fig. 1   Variation of effective separation angle θ^* with wall length.

Fig. 2   Variation of flow gain ν_q in a single sided element with Reynolds number.

Fig. 3   Flow patterns in a single sided element shortly before switching.

Fig. 4   Wall reattachment device.

Fig. 5   Output characteristics for wall reattachment device.

Fig. 6   Control-input characteristics for various control line resistances R_{C2}.

Fig. 7   Characteristics of resistances R_{C2} used for wall reattachment amplifier.

Fig. 8   Variation of flow gain ν_q with control line resistance R_{C2}.

Fig. 9   Switching action in a wall reattachment device.

Fig. 10   Calculated and experimentally determined response time $\mathcal{T}$.

Fig. 11   Sketch of flowmeter probe.

Fig. 12   Experimental set-up for pulsed control flow measurements.

Fig. 13   Nondimensionalized response time versus control supply pressure.

Fig. 14   Pressure and flow oscillograms for different control pulse lengths.

Fig. 15   Limiting curve below which switching is no longer 100% guaranteed.

Fig. 16   Pressure gain versus inverse nondimensionalized response time S.

200

VARIATION OF EFFECTIVE SEPARATION ANGLE θ^* WITH WALL LENGTH.

OFFSET $a_{c1} = 0.2 \times d_N$
WALL ANGLE $\theta = 15°$
CONTROL CHANNEL WIDTH $= d_N$
FLUID : WATER

● BOURQUE AND NEWMAN
  MAXIMUM WALL ANGLE FOR REATTACHED FLOW
  REYNOLDS NUMBER > 10 000
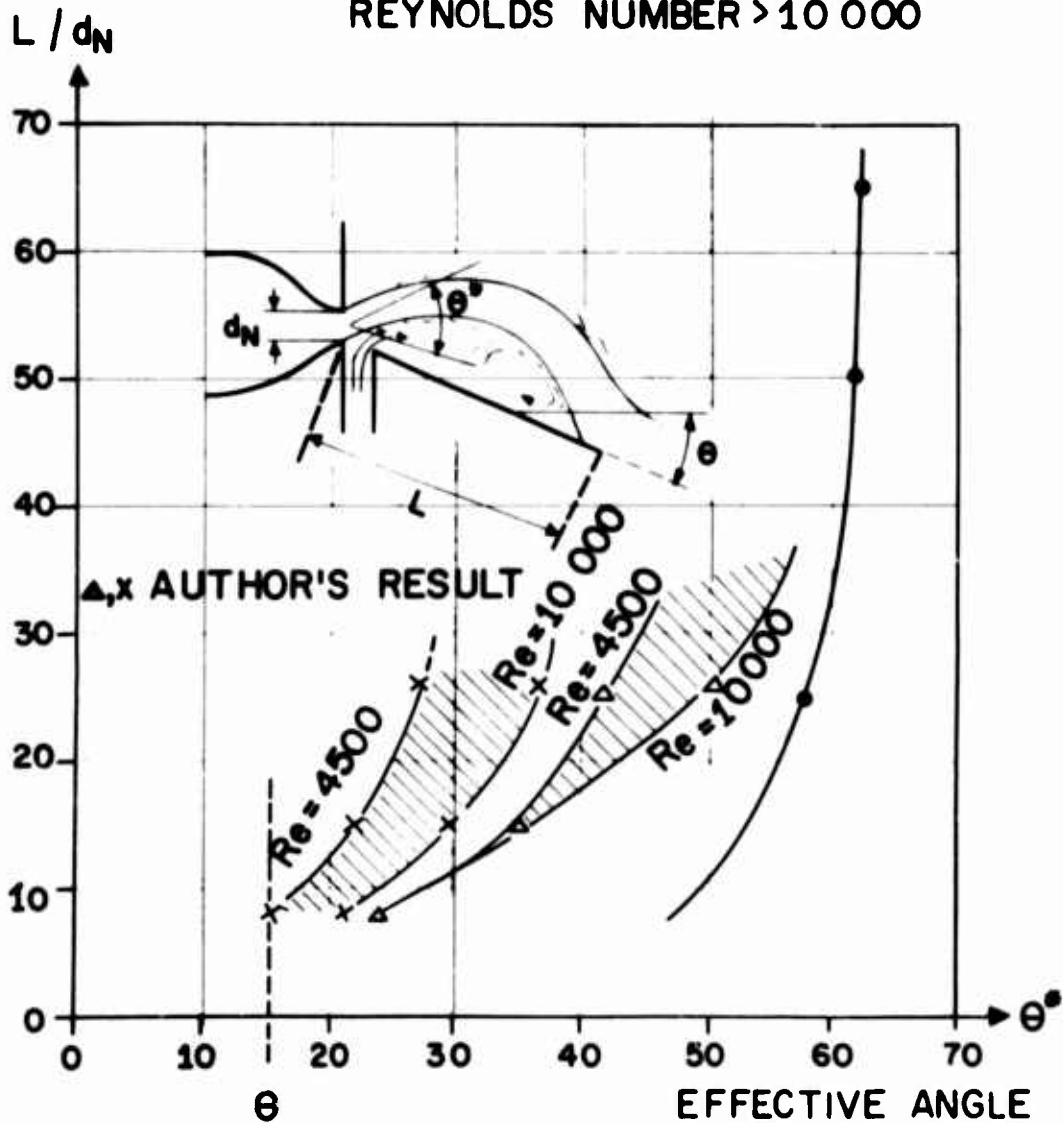
FIG. 1

● ASPECT RATIO > 1, NO CONTROL FLOW
△ ASPECT RATIO = 1, WITH CONTROL FLOW
✗ ASPECT RATIO = 0.6, WITH CONTROL FLOW

201

VARIATION OF FLOW GAIN V_q IN A SINGLE SIDED ELEMENT WITH REYNOLDS NUMBER

OFFSET $a_{c1} = 0.2 \times d_N$

CONTROL CHANNEL WIDTH = d_N

REYNOLDS NUMBER $Re = \dfrac{v_N \cdot d_N}{\eta} \cdot \rho$

ASPECT RATIO $t/d_N = 0.6$

$V_q = q_s / q_{CRIT}$

ASPECT RATIO $t/d_N = 1.0$

$V_q = q_s / q_{CRIT}$
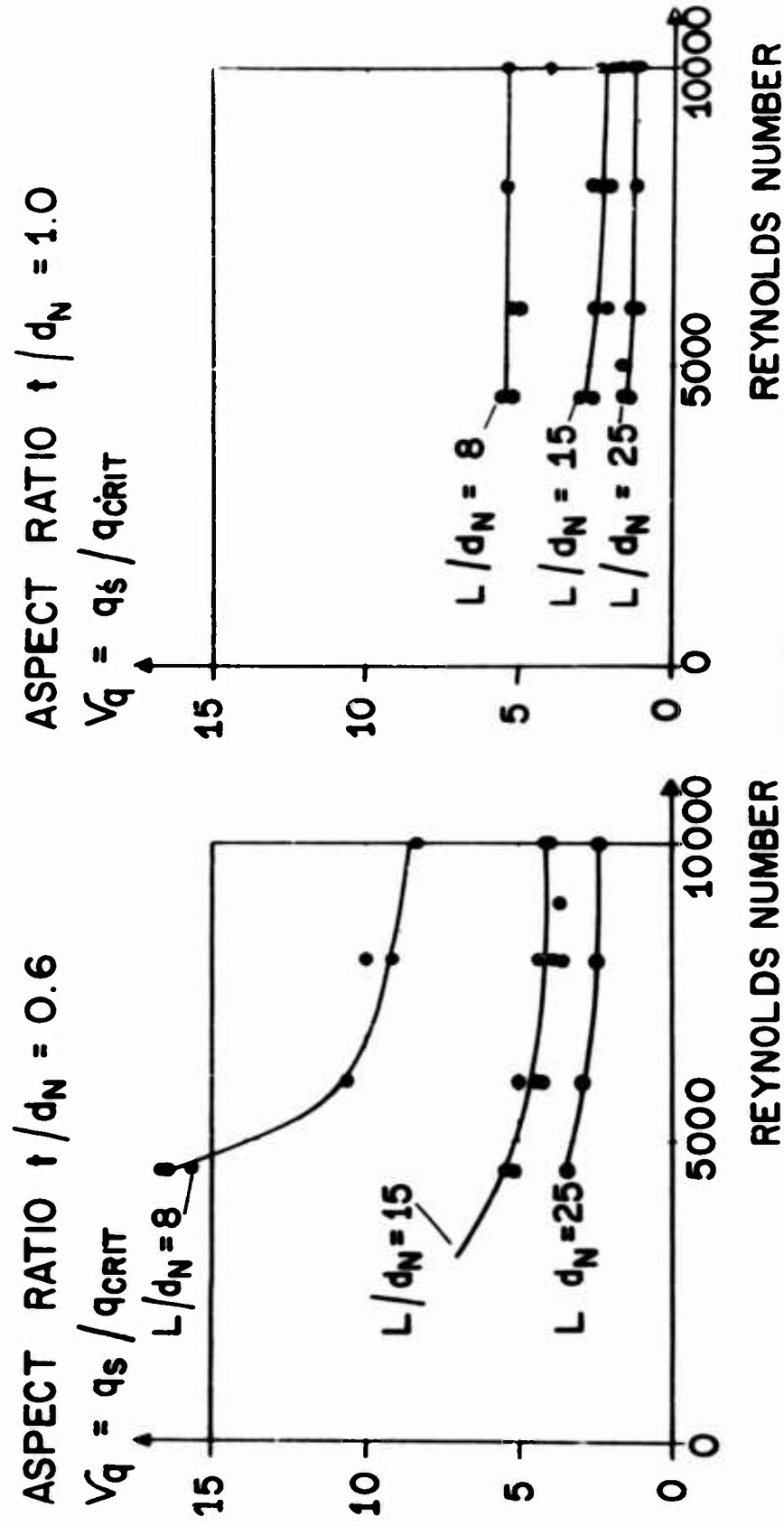
FIG. 2

FLOW PATTERNS IN A SINGLE SIDED ELEMENT SHORTLY BEFORE SWITCHING.

OFFSET a_{C1} = 0.2 x d_N

ASPECT RATIO t/d_N = 0.6

L/d_N = 16

Re = 4500
Q_{CRIT} = 0.175

Re = 10 000
Q_{CRIT} = 0.266

ASPECT RATIO t/d_N = 1

L/d_N = 16

Re = 4500
Q_{CRIT} = 0.363

Re = 10 000
Q_{CRIT} = 0.460

ASPECT RATIO t/d_N = 1

L/d_N = 26

Re = 4500
Q_{CRIT} = 0.644

Re = 10 000
Q_{CRIT} = 0.850

203
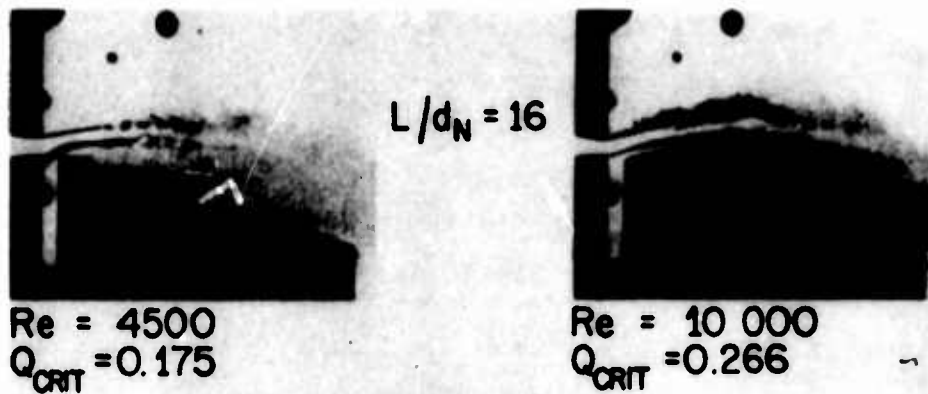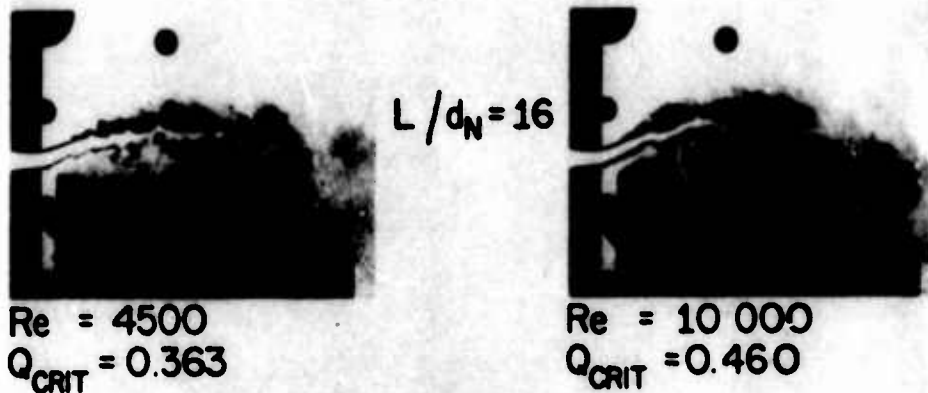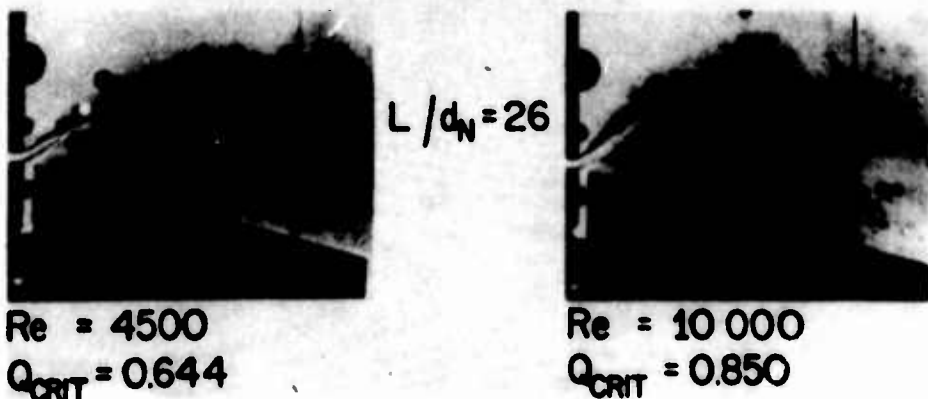
FIG. 3

WALL REATTACHMENT DEVICE
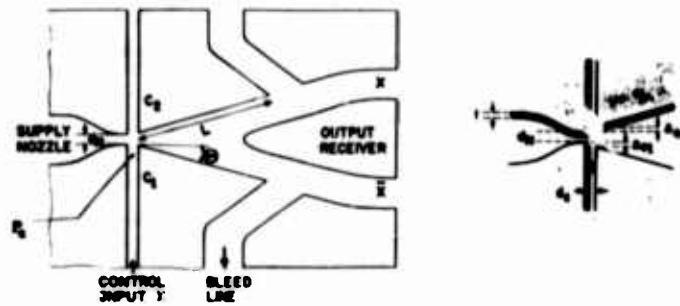
NOZZLE WIDTH d_N = 5mm

ASPECT RATIO DEPTH/WIDTH = $1/d_N$ = 1

WALL LENGTH = L

DIVERGENCE ANGLE ϑ = 15°

CONTROL CHANNEL WIDTH d_c = d_N

OFFSETS a_{c1}, a_{c2}

FIG. 4

OUTPUT CHARACTERISTICS FOR WALL REATTACHMENT DEVICE.

a) VARIATION OF OUTPUT CHARACTERISTICS WITH WALL LENGTH
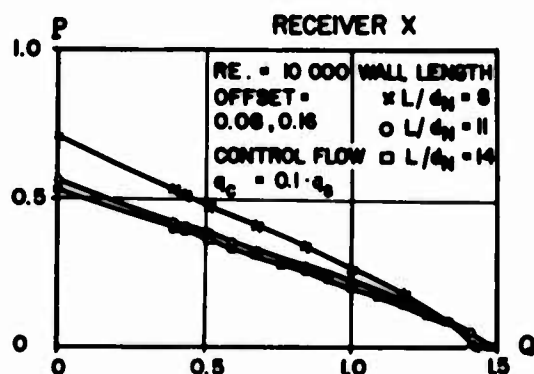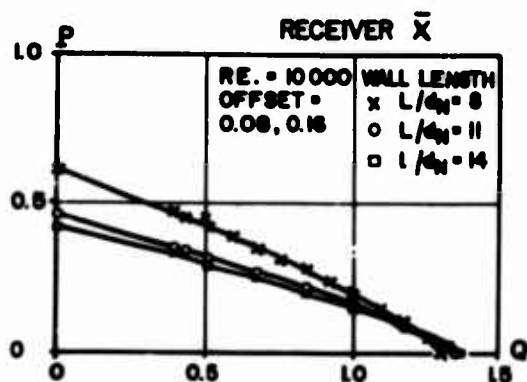
b) VARIATION OF OUTPUT CHARACTERISTICS WITH REYNOLDS NUMBER
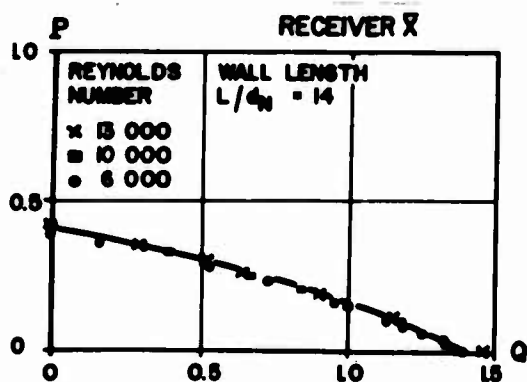
c) VARIATION OF OUTPUT CHARACTERISTICS WITH OFFSET
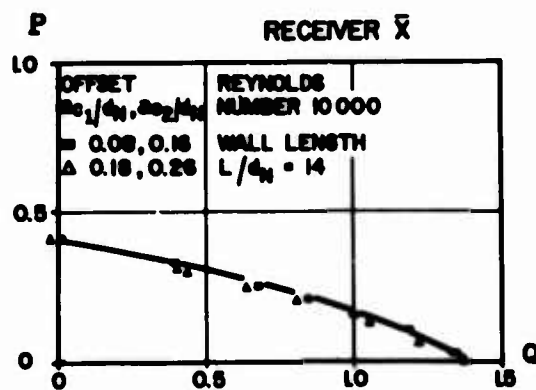
P NONDIMENSIONALIZED PRESSURE $\dfrac{P_{REC}}{P_{SUP.}}$

Q NONDIMENSIONALIZED FLOW $\dfrac{Q_{REC}}{Q_{SUP.}}$

FIG. 5

CONTROL – INPUT CHARACTERISTIC FOR VARIOUS CONTROL LINE RESISTANCES R_{C2}

ASPECT RATIO $t/d_N = 1$
DIVERGENCE ANGLE $15°$
OFFSET $(a_{c1} = a_{c2} = 0.26 \times d_N)$
WALL LENGTH $L = 14 \, d_N$
CONTROL CHANNEL WIDTH EQUAL NOZZLE WIDTH
REYNOLDS NUMBER 10 000
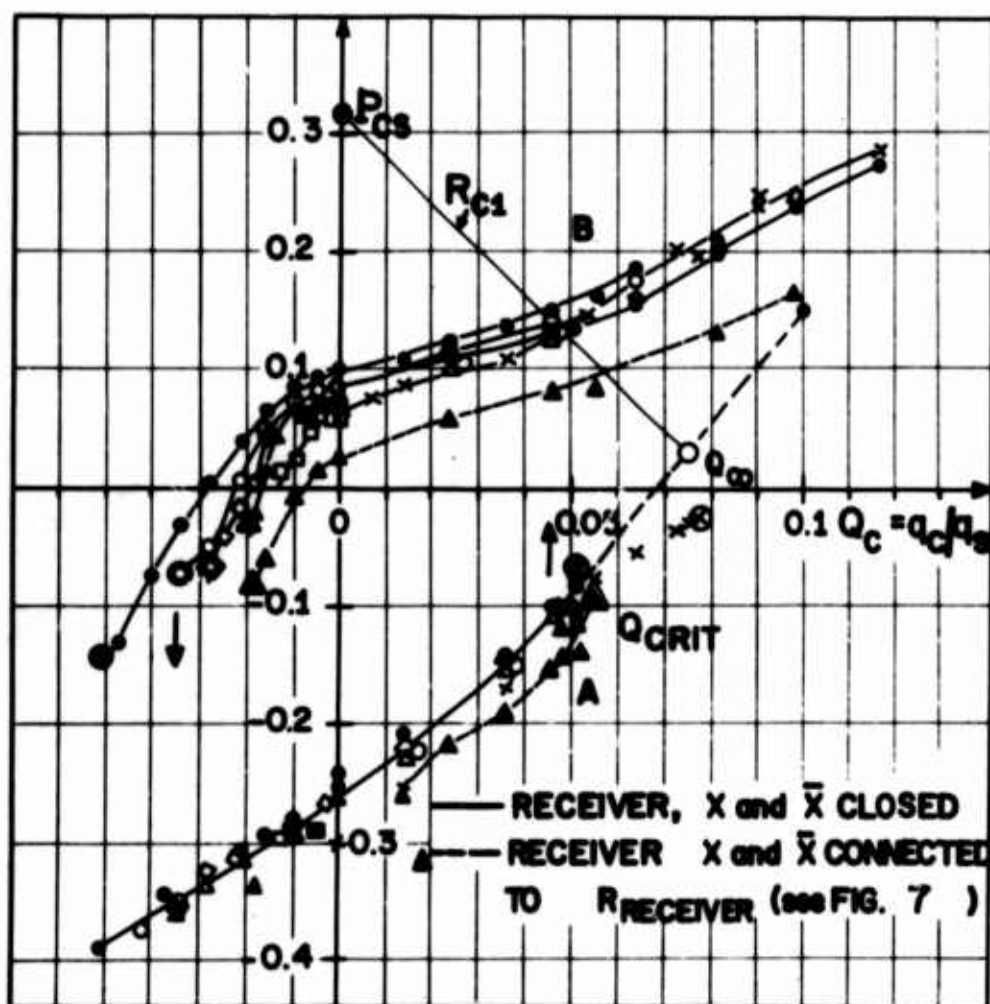
PARAMETER: RESISTANCE R_{C2}

FIG. 6

CHARACTERISTICS OF RESISTANCES R_{C2} USED FOR WALL REATTACHMENT AMPLIFIER
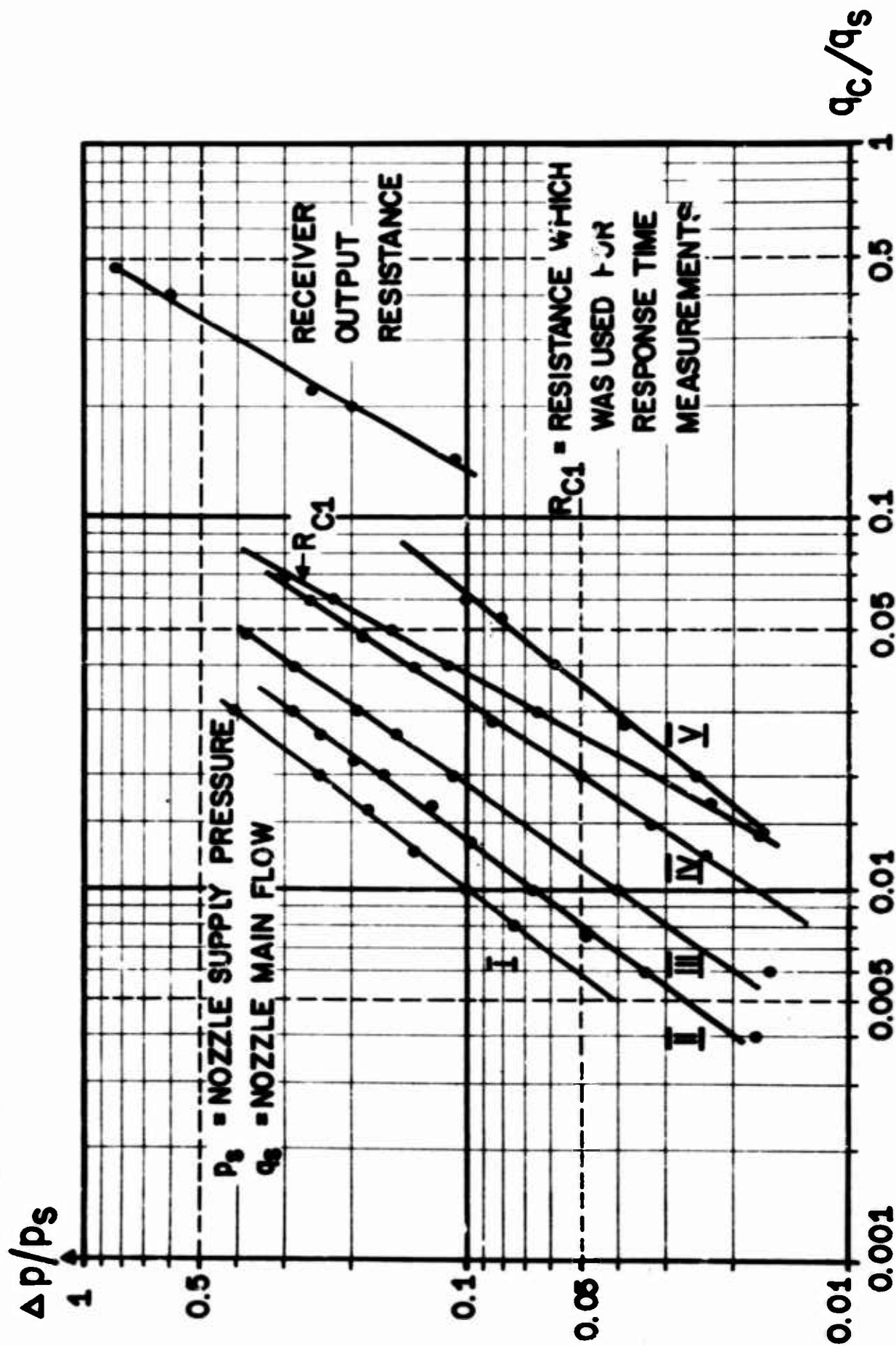
FIG. 7

207

VARIATION OF FLOW GAIN V_q WITH CONTROL LINE RESISTANCE R_{C2}

$V_q = q_s/q_{CRIT}$ OFFSET $a_{c1} = a_{c2} = 0.26 \times d_N$

$R_{C1} \to \infty$

REYNOLDS NUMBER 10 000
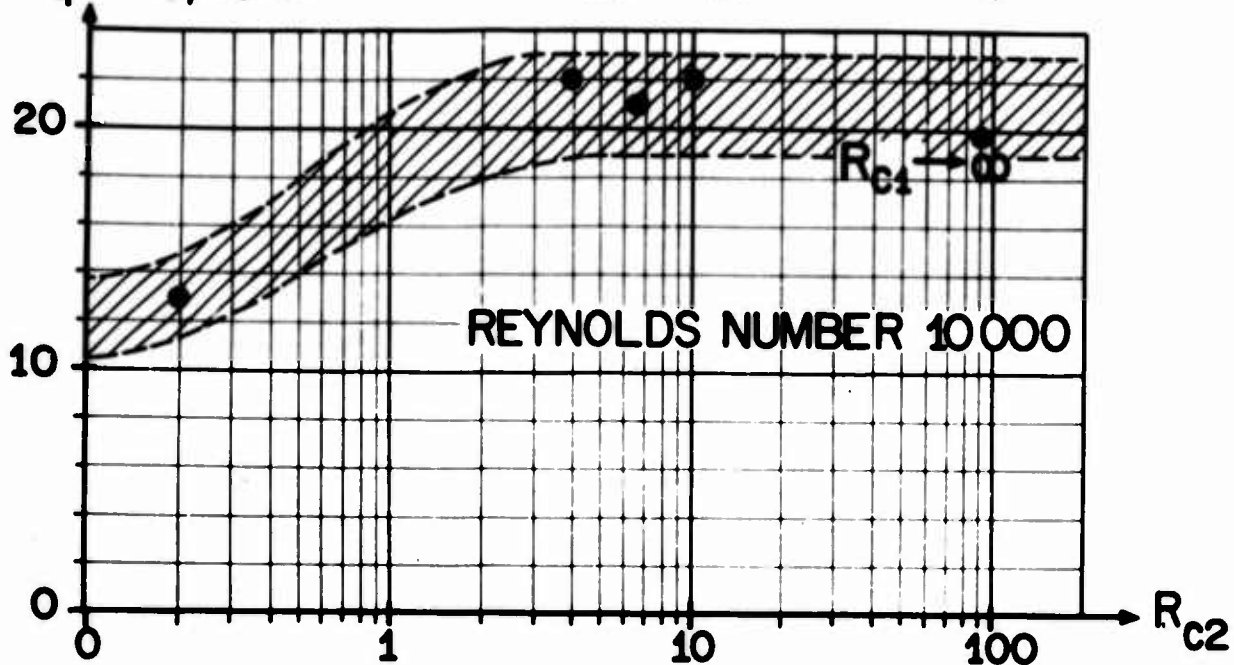
VARIATION OF MINIMUM CONTROL SUPPLY PRESSURE WITH CONTROL LINE RESISTANCE R_{C2}

$\left(P_{CS\ MIN}/P_S\right)$ OFFSET $a_{c1} = a_{c2} = 0.26 \times d_N$

$P_{CS\ MIN} = -P_{CO} + R_{C1} \cdot (q_{CRIT}/q_s)$

$= -P_{CO} + R_{C1}/V_q$

R_{C1} IS ASSUMED EQUAL R_{C2}

208

FIG. 8
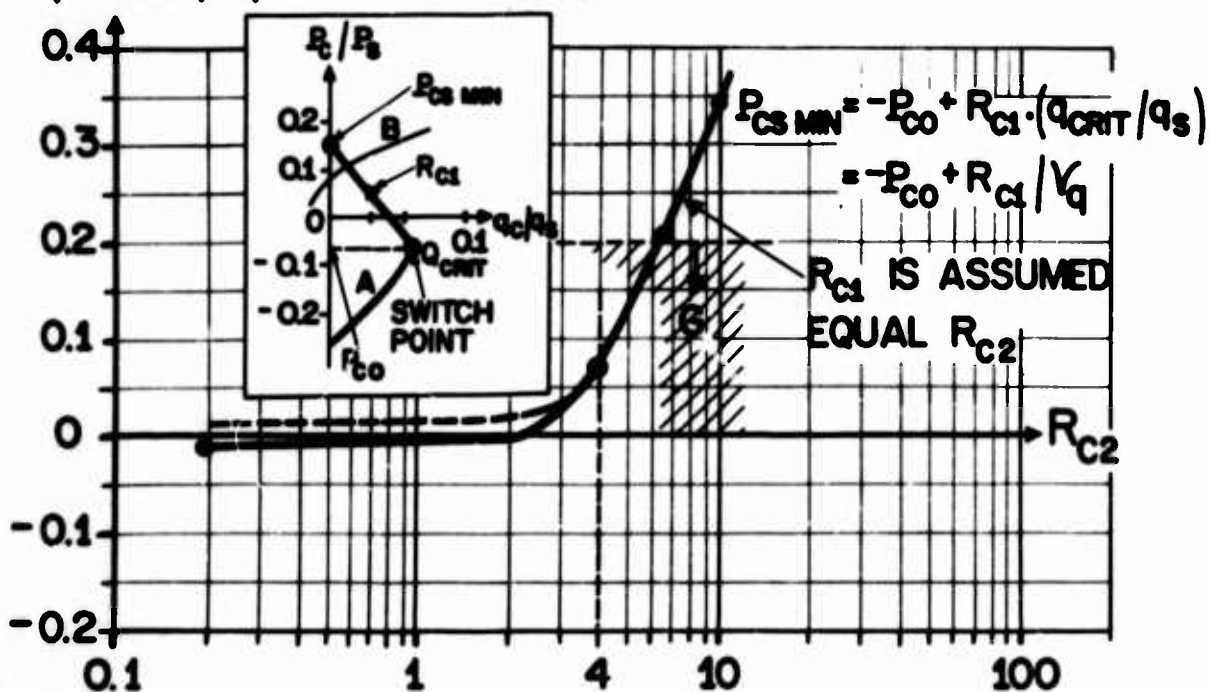
SWITCHING ACTION IN A WALL REATTACHMENT DEVICE

REYNOLDS NUMBER 10 000

OFFSET $a_{c1} = a_{c2} = 0.26 \times d_N$

DIVERGENCE ANGLE $\theta = 15°$

WALL LENGTH $L = 14 \, d_N$

CONTROL LINE LENGTH $\ell = 60 \times d_N$

CONTROL SUPPLY PRESSURE $P_{cs} = p_{cs}/p_s = 0.35$

CONTROL LINE RESISTANCE $R_{c1} = R_{c2} = 3.8$ FOR $q_c = 0.05 q_s$
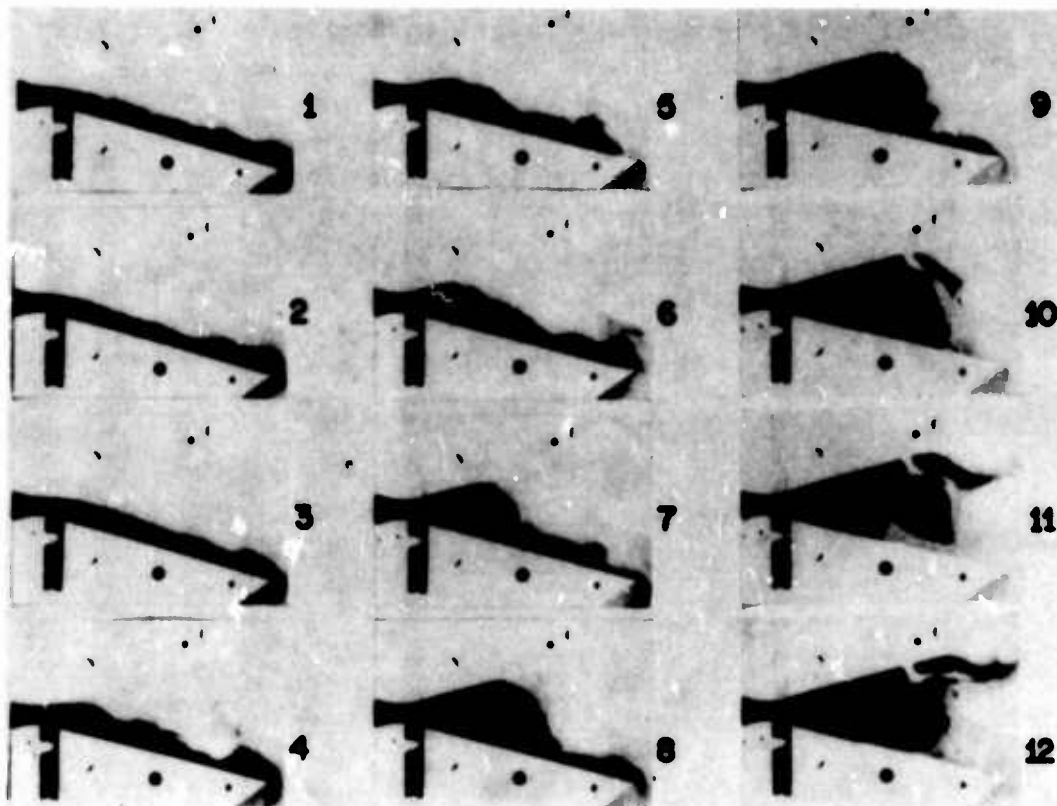
TIME INTERVAL BETWEEN TWO PHOTOGRAPHS IS 31.3 msec.

CONTROL FLOW

STATIC PRESSURE SIGNAL AT RECEIVER X

$\longrightarrow T$

$\longmapsto$ 100 msec.
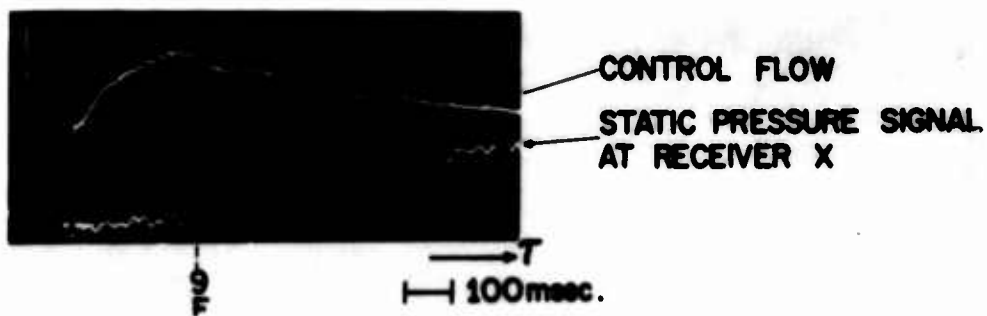
FIG. 9

209

CALCULATED AND EXPERIMENTALLY DETERMINED RESPONSE TIME τ

x CALCULATED VALUES FOR BUBBLE RELEASE

□ EXPERIMENTALLY DETERMINED VALUES FOR BUBBLE RELEASE

■ EXPERIMENTALLY DETERMINED VALUES FOR TOTAL RESPONSE TIME

S STROUHAL NUMBER $S = T/T_T$

T_T = TRANSPORT TIME $\frac{d_N}{v_N}$

REYNOLDS NUMBER Re = 10000

INERTIA $C_1 = 120$

LOAD LINE $P_{C1} = C_2^* \times Q_C^2$

$C_2^* = 68$ (see R_{C1} in Fig. 7)
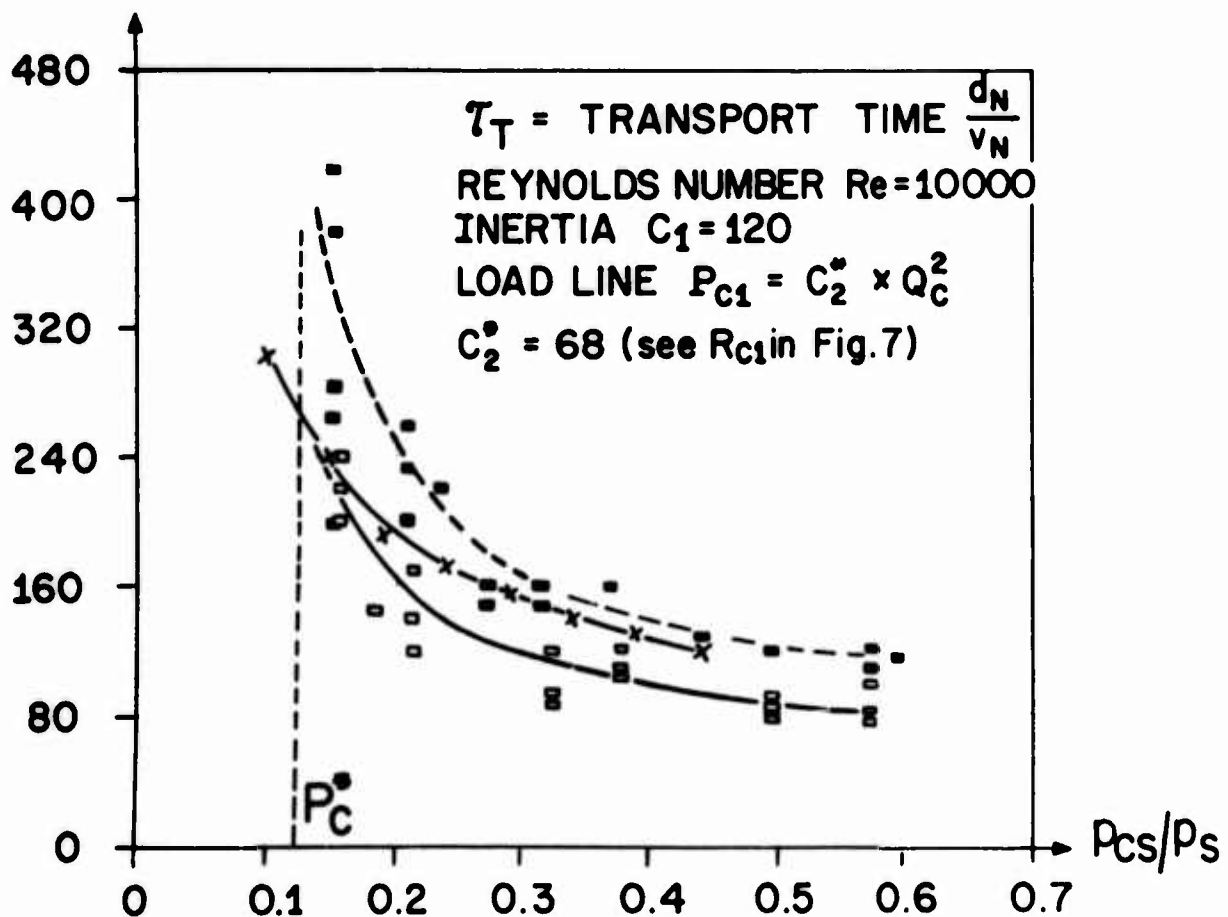
x : $Q_{REL} = 0.4$, $C_1 = 120$, $\Omega = 0.015$

$Q_{CRIT} = 0.045$

FIG. 10

SKETCH OF FLOWMETER PROBE
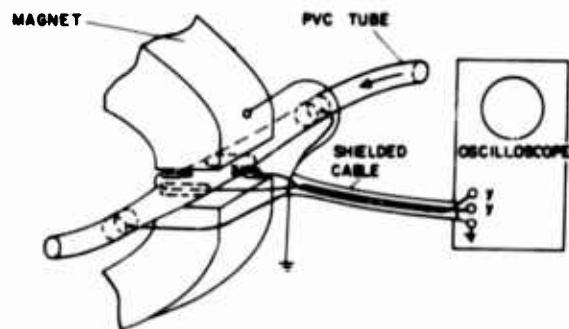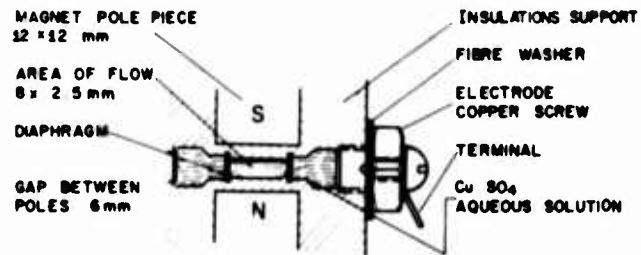
FIG. 11

EXPERIMENTAL SET-UP FOR PULSED CONTROL FLOW MEASUREMENTS

FIG. 12

NONDIMENSIONALIZED RESPONSE TIME VERSUS CONTROL SUPPLY PRESSURE

FIG. 13

PRESSURE AND FLOW OSCILLOGRAMS FOR DIFFERENT CONTROL PULSE LENGTHS.

1

$\tau_c = \infty$

$\bullet \quad \tau_c/\tau_T = \infty$

$p_c/p_s = 0.32$

4
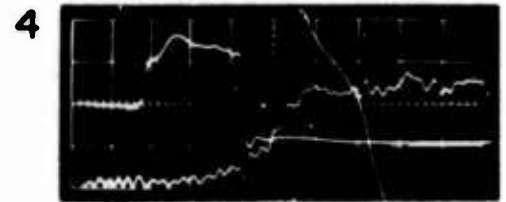
$\tau_c = 250\,\text{msec.}$

$\times \quad \tau_c/\tau_T = 100$

$p_c/p_s = 0.4$

2
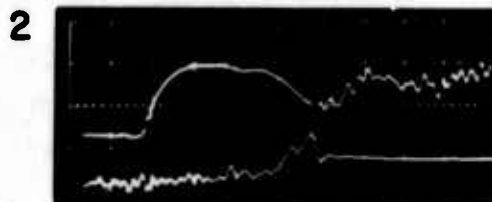
$\tau_c = 400\,\text{msec.}$

$\square \quad \tau_c/\tau_T = 160$

$p_c/p_s = 0.28$

5
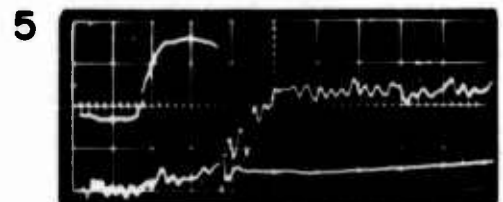
$\tau_c = 200\,\text{msec}$

$\circ \quad \tau_c/\tau_T = 80$

$p_c/p_s = 0.59$
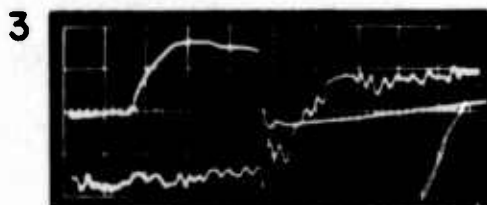
3

$\tau_c = 300\,\text{msec.}$

$\blacksquare \quad \tau_c/\tau_T = 120$

$p_c/p_s = 0.29$

6

$\tau_c = 150\,\text{mseo.}$

$\triangle \quad \tau_c/\tau_T = 60$

$p_c/p_s = 0.65$

CONTROL FLOW

PRESSURE
AT RECEIVER X
(RECEIVER CLOSED)

CORRESPONDS TO 100 msec. $\tau_c/\tau_T = 40$

214

FIG. 14
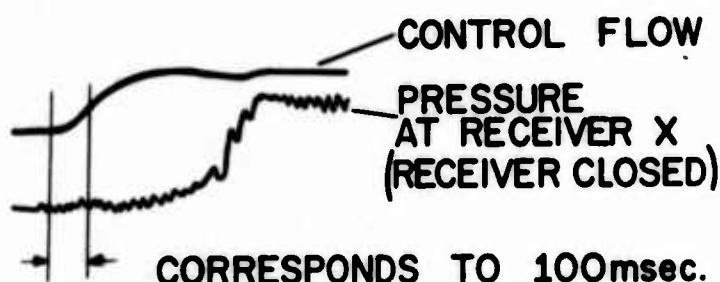
LIMITING CURVE BELOW WHICH SWITCH-ING IS NO LONGER 100% GUARANTEED

$\left(P_{C\ MIN} - P_C^*\right)/P_S$

τ_C = CONTROL PULSE LENGTH
τ_T = TRANSPORT TIME d_N/v_N

τ_C/τ_T

FIG. 15

PRESSURE GAIN VERSUS INVERSE NONDIMENSIONALIZED RESPONSE TIME S

$\gamma_p = P_{REC}/P_{CS}$

$$S = \frac{C}{\left(P_{CS} - P_{CS\ MIN}\right)} + S_0$$

P_{SUT} = 0.4
$P_{CS\ MIN}$ = 0.07
S_0 = 120
C = 8
$\mu_{p\ MAX}$ = $P_{REC}/P_{CS\ MIN}$

$\gamma_{p\ MAX}$

1/S
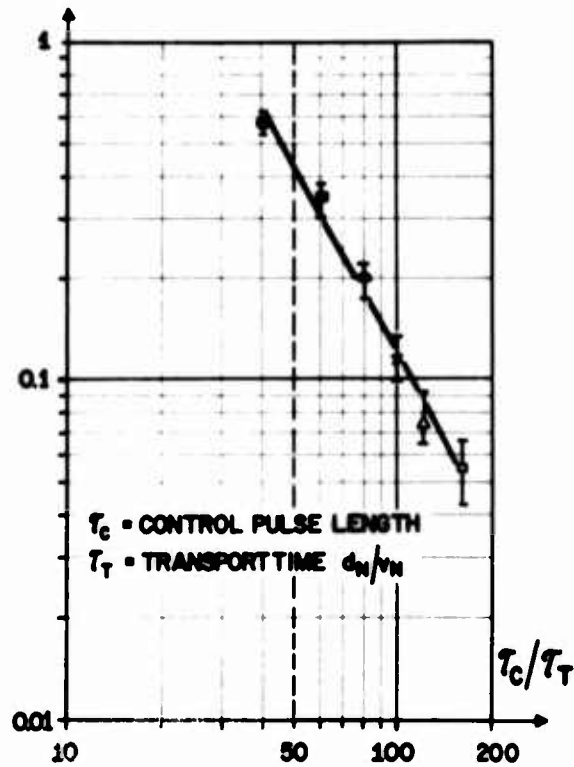
S
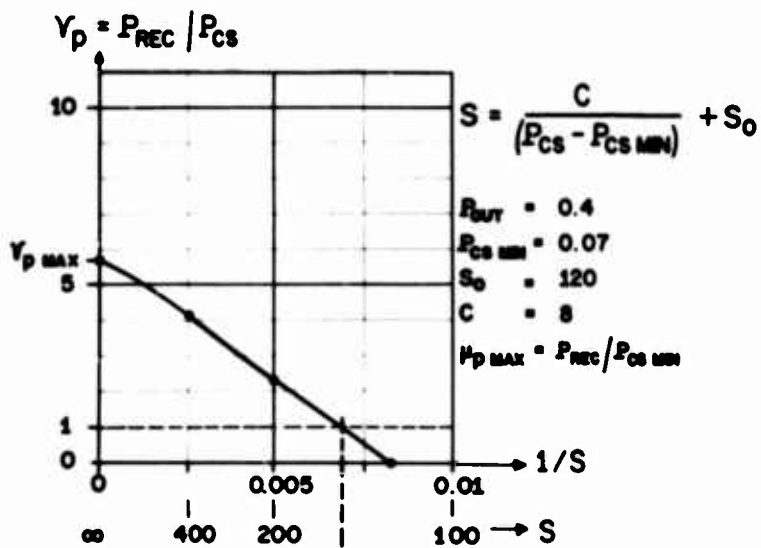
FIG. 16

REMARKS ON THE LIMITATIONS OF PURE FLUID ELEMENTS

by

H. H. Glaettli, H. R. Müller, R. H. Zingg

IBM Zurich Research Laboratory
Rüschlikon-Zurich, Switzerland

ABSTRACT: The first part is concerned with refinements of the limitation of pure fluid elements. On the one hand, basic effects in connection with the aspect ratio (turbulent reattachment, laminar attachment) are discussed; on the other hand, the influence of deviations from ideal geometries·is demonstrated. These deviations comprise oblique walls and surface roughness factors that can no longer be neglected.

The second part comprises additions to graphs and formulas published earlier. They show in a quantitative way the width of the gap to be overcome by improved or new manufacturing techniques. Consequences of requirements such as given output pressure or given response time are demonstrated. Last but not least, a new figure of merit in connection with bandwidth considerations is proposed. This figure of merit is expected to be always smaller than one. It can be applied to elements with or without intrinsic positive or negative feedback. The effect of feedback, implicitly present in various pure fluid elements, on the response time when switching in different direction occurs, is finally demonstrated by a film.

Tentative limits for the operation of pure fluid elements
were deduced in an earlier paper (ref. 1). The minimum values
for response time, size and power consumption proposed there
are based preferably on ideal geometry and on estimates as far
as a few coefficients are concerned. It is the purpose of the
first part of this paper to justify these assumptions by dealing
with further experimental evidence. The second part is concerned,
on the one hand, with some further interpretations, especially
in connection with manufacturing difficulties, on the other hand
an expression for the Strouhal number in terms of pressure
and flow rate gain, derived from a consideration of the idealized
free jet amplifier is proposed as a lower bound for fluid mechan-
ic amplifiers. Experiments show no contradictory evidence in
spite of negative or positive feedback (inherently present even
in some basic arrangements).

1.1. Effects of the aspect ratio.

The influence of bottom
and cover plates increases at small aspect ratios k_2. The mean
flow rate, therefore, has to be increased to maintain a certain
quotient of kinetic forces to viscous forces. This leads to higher
critical Reynolds numbers R_{crit} than in the really two-dimen-
sional case. - The effect of the monotonous dependence $R_{crit} = f(k_2)$
on the expression (1) for the operating power P of pure fluid
elements, namely

$$P = k_1 \cdot k_2 \cdot \frac{R^3 \cdot \eta^3}{2 \, \varrho^2 \, \ell} \qquad (1)$$

(where η = viscosity, ϱ = density of the fluid ; ℓ = nozzle width
and k_1 = ratio of operating pressure to stagnation pressure) is,
however, compensated by the multiplication with k_2 at least for
higher values of k_2 . The qualitative dependence $P = f(k_2)$, as
well as the k_2-value leading to a minimum can be derived on the
base of the hydraulic radius. The effective Reynolds number R_{corr}
corrected for the aspect ratio k_2 compared with $R(k_2 = 1)$ is
given by

$$R_{corr} = x \cdot R_{conv} = \frac{2 \, k_2}{1 + k_2} \cdot \frac{\varrho \cdot v \cdot \ell}{\eta} \qquad (2)$$

218

The dependence of the inverse of the correction factor χ on k_2 (representing the apparent dependence of measured critical Reynolds numbers on k_2) is illustrated by the broken curve in Fig. 1 .
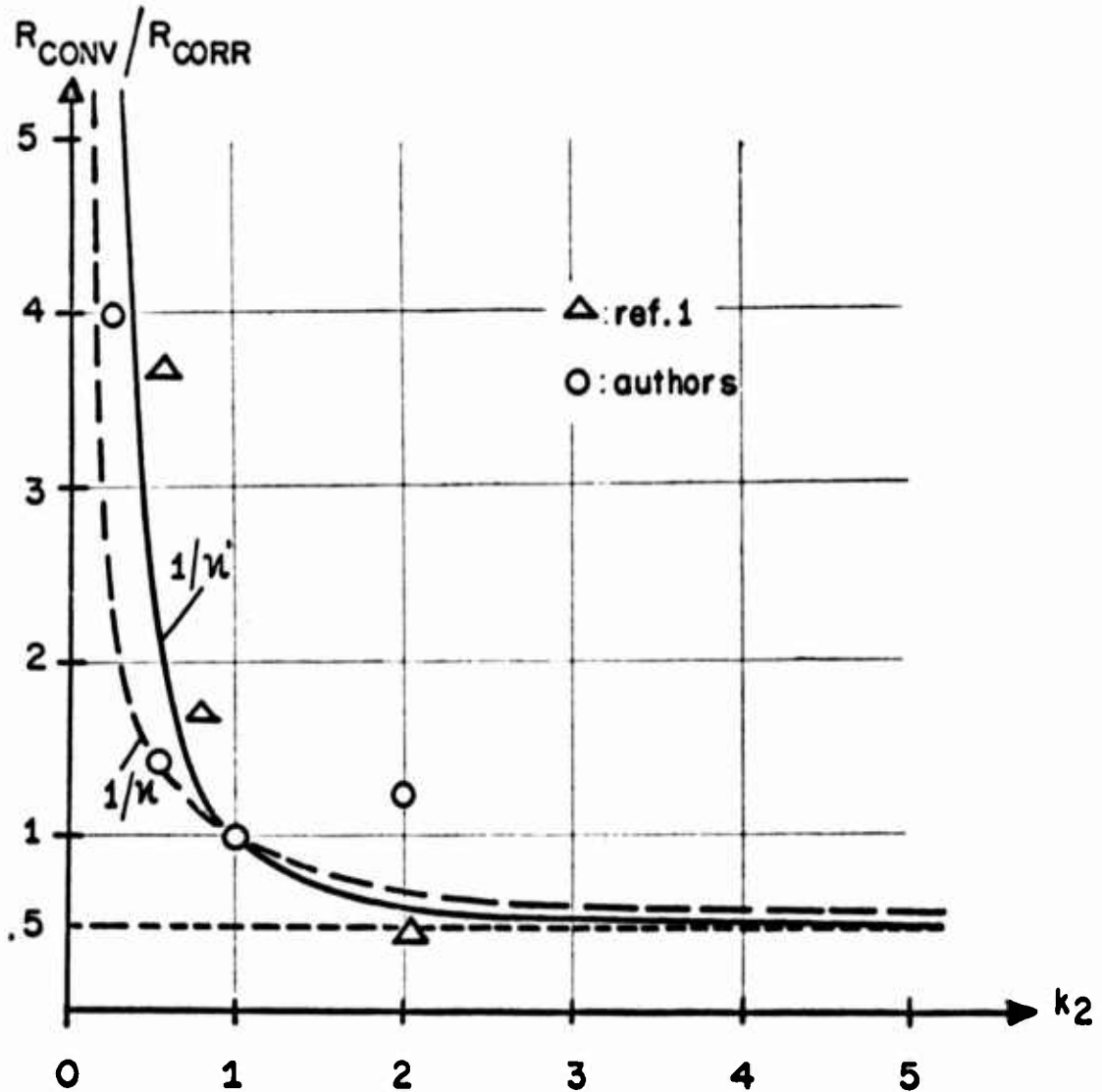

Fig. 1

Critical Reynolds number as a function of the aspect ratio.

The solid curve is based on an estimate of kinetic to viscous forces in a flow profile described by $v = f(y) \cdot f(z)$. The corresponding correction factor χ' is given by the somewhat different expression

$$\chi' = \cdot \frac{2 \cdot k_2^2}{1 + k_2^2} \tag{3}$$

Both assumptions leading to the two expressions (2) and (3) are not in full agreement with the conditions found in practical arrangements, mainly because of the flow profiles to be encountered. The resulting expressions, however, may be considered to represent useful approximations. Recent careful observations led to the results shown in Fig. 2 :
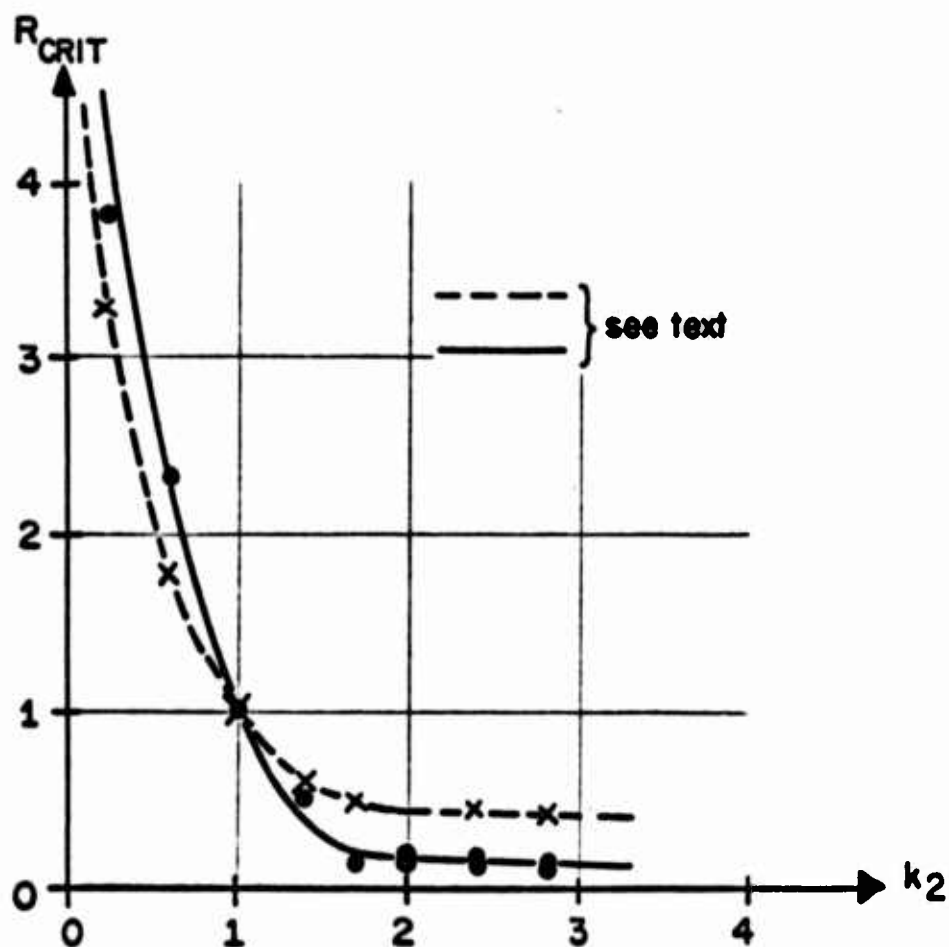
Fig. 2

Critical Reynolds number as a function of the aspect ratio.

The broken curve represents the relative critical Reynolds number for spontaneous reattachment in a bistable element (the absolute value for $k_2 = 1$ is 2770). The solid curve shows the relative minimum Reynolds number required to keep the jet in one of the attached positions (the absolute value for $k_2 = 1$ in this case is 1440).

220

One interesting observation that occurred when these measurements were being made is not shown in Fig. 2: Spontaneous laminar attachment takes place slowly at aspect ratios $k_2 > 2$ and at Reynolds numbers insignificantly higher $(R_{abs} \approx 200)$ than required to maintain attachment. Fully turbulent attachment occurs in the same k_2-range at higher Reynolds numbers $(R_{abs} \approx 1200)$ if the flow rate is increased relatively fast. This phenomenon is the object of further investigations.

The slight quantitative disagreement between Fig. 1 and Fig. 2 has no appreciable effect on the optimum k_2 leading to the minimum operating power. Figure 3 shows the qualitative dependence of P on k_2 for the two curves of Fig. 1.
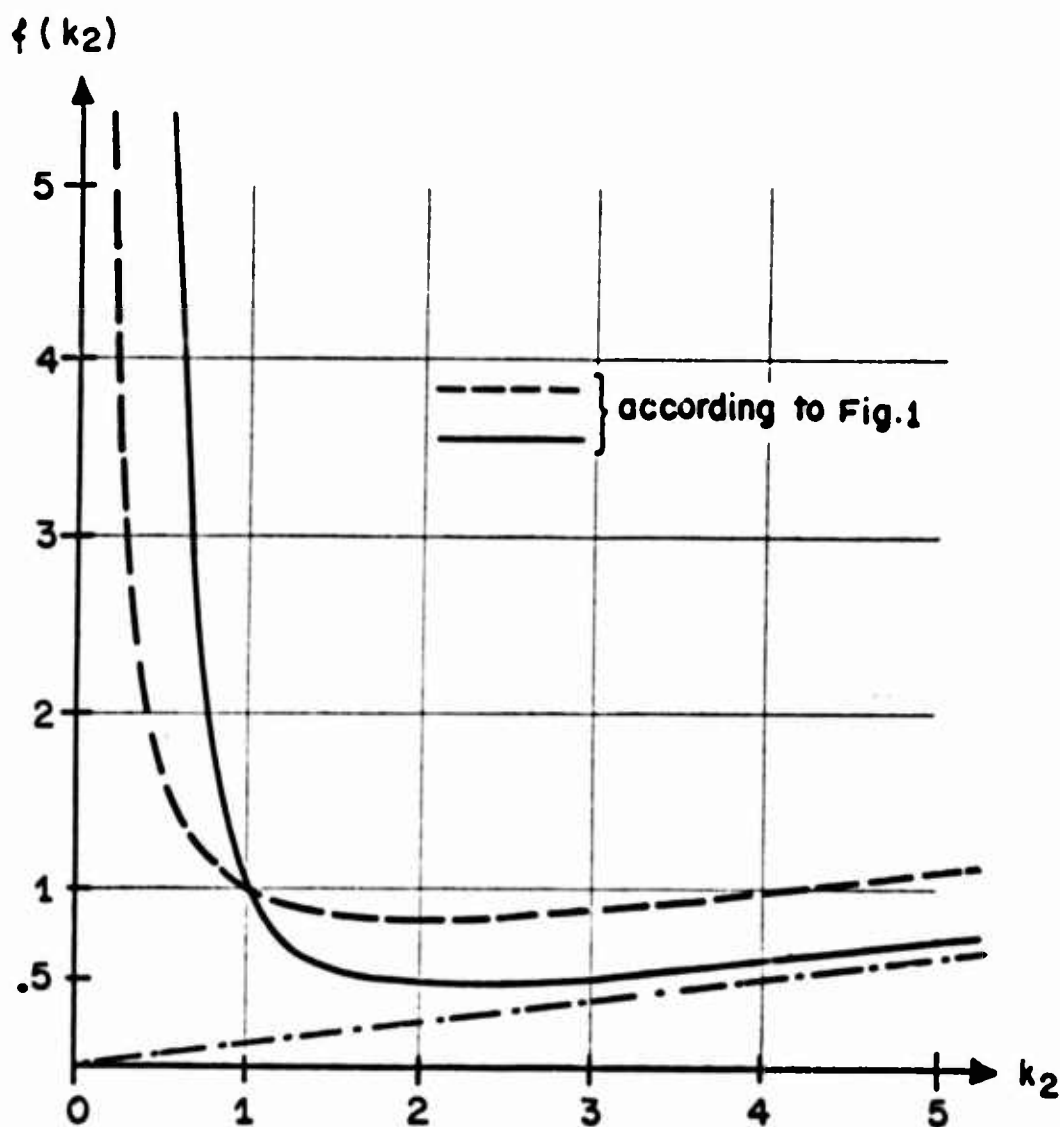
Fig. 3

Relative power consumption as a function of the aspect ratio k_2.

The dotted curve shows a minimum for $k_2 = 2$, the other for $k_2 = \sqrt{5}$. The curves of Fig. 2 suggest a minimum operating power for even slightly lower values of k_2. The important point, however, is that aspect ratios larger than 1 have no appreciable effect on the minimum power requirement.

    1.2.   Oblique walls. Several manufacturing processes are likely to result in oblique walls. Characteristic examples have been published in ref. 2. A pure fluid amplifier having oblique walls may be assumed to consist of several layers, each representing an amplifier with a slightly different geometry (different nozzle width). This causes secondary flow, the influence of which cannot easily be predicted quantitatively. Therefore, a series of experiments was set up in the following manner: Two pairs of models were built, one with an aspect ratio $k_2 = .6$, the other with $k_2 = 1.4$. One model of each pair has vertical walls, whereas the walls of the other model deviate by 16.5° from the vertical. The cross-sectional area of the nozzle of the two models of one pair is the same. The critical Reynolds numbers required to maintain attachment or resulting in spontaneous attachment in a bistable element, as well as the dependence of the flow rate gain μ_Q on the Reynolds number were observed. No significant change of critical Reynolds numbers, neither at $k_2 = .6$ nor at $k_2 = 1.4$ was detected. Typical graphs illustrating the minor influence of the wall angle on the flow rate gain are shown in Fig. 4 and Fig. 5.

Both these graphs show the same tendency as indicated by the measurements of the critical Reynolds numbers : Oblique walls result in slightly lower minimum values. The flow rate gain is decreased by oblique walls ; this means greater stability for the bistable elements in question. Higher k_2 values reinforce these effects, as can easily be expected. The proximity to the minimum Reynolds number is indicated by the sharp rise of the curves at the left. All measurements were made on elements with a full divergence angle $2\theta = 30^\circ$.
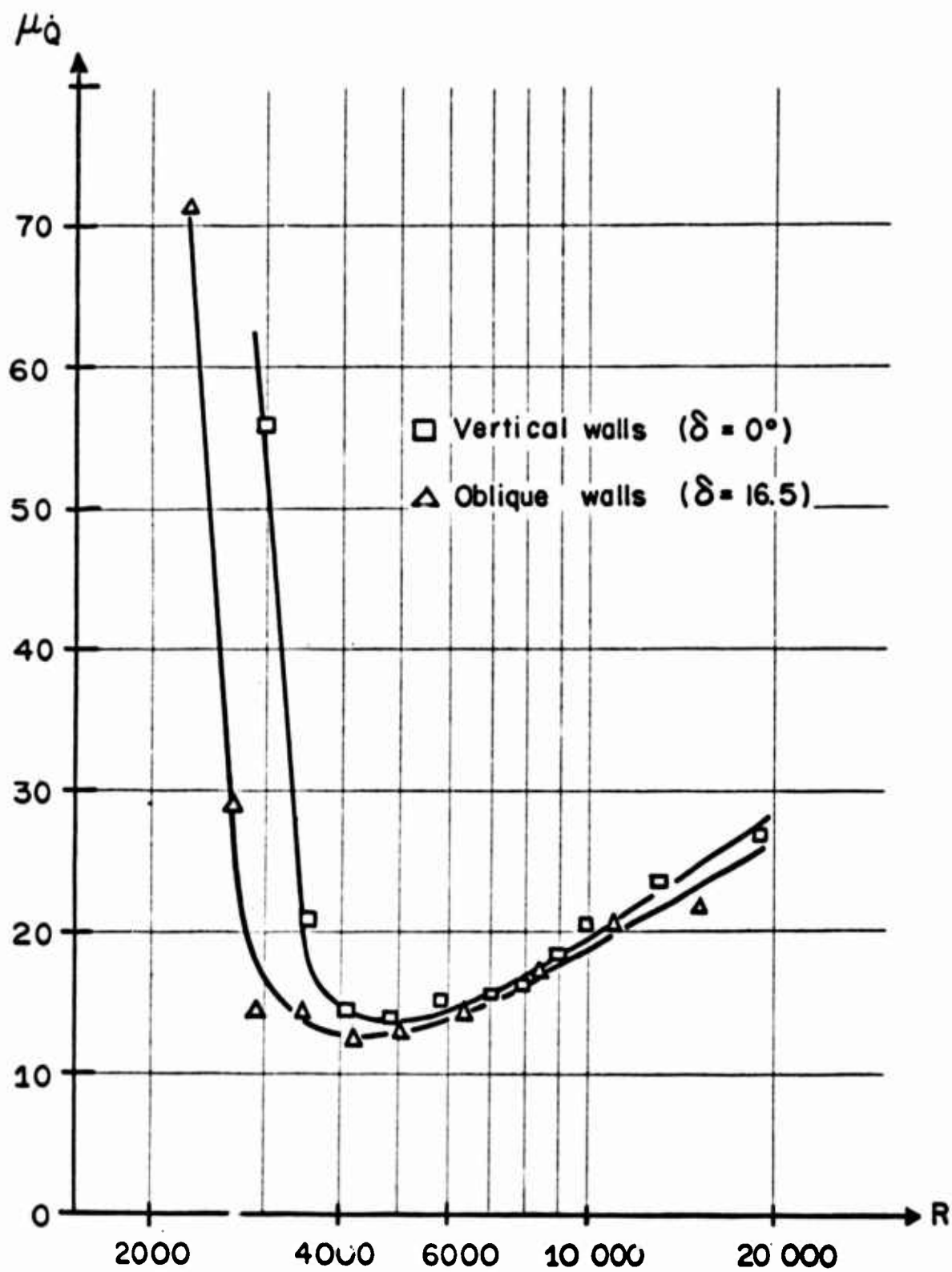
Fig. 4

Dependence of flow rate gain on Reynolds number for
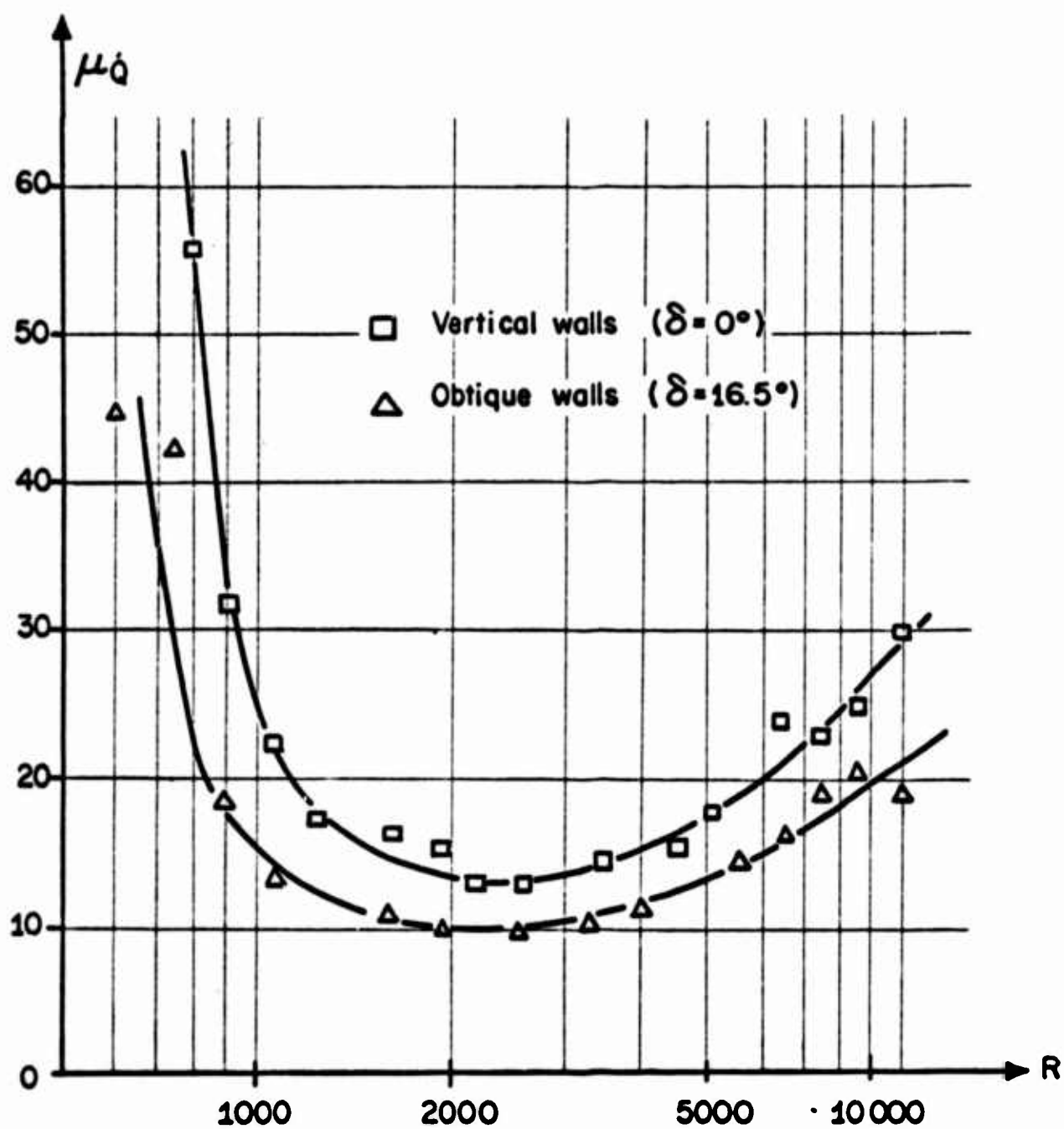two different wall angles and aspect ratio $k_2 = .6$.

Fig. 5

Dependence of flow rate gain on Reynolds number for two different wall angles and aspect ratio k_2 = 1.4.

1.3. Surface roughness effects. Most manufacturing processes result in a relatively good surface roughness. Depending on the criteria applied, the surface roughness may, however, become an important factor when miniaturized elements are considered, especially in cases where the absolute roughness increases with decreasing size. - Simple experiments were set up in order to get preliminary information: The side walls (but not bottom and cover plate) of bistable elements without control channels were covered with sandpaper of various grain size. The minimum Reynolds number for bistability and spontaneous attachment were measured. Figure 6 shows the results for aspect ratio $k_2 = 1.84$:

Fig. 6
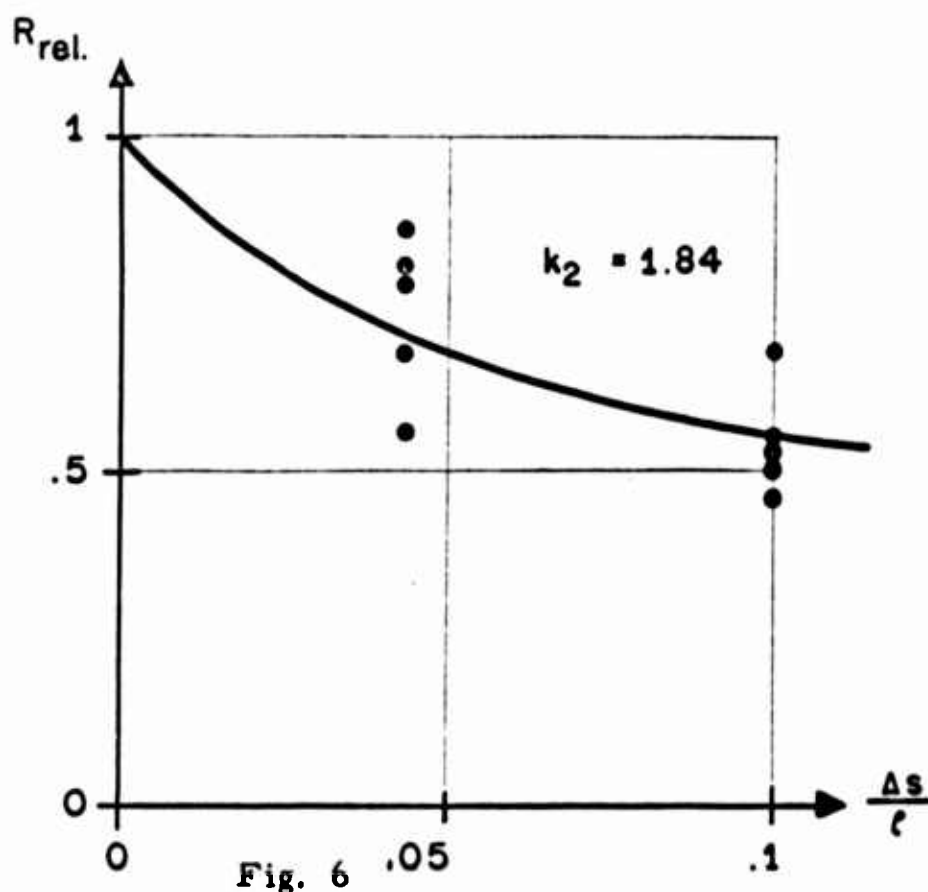
Dependence of critical Reynolds number on surface roughness.

The surface roughness was determined by microscopic inspection of thin sections of embedded sandpaper obtained by grinding. ΔS is the average difference in altitude of mountains and valleys. The results presented in Fig. 6 were obtained by observing the bistability in the laminar range. The critical Reynolds number for the model with vanishing surface roughness averages around 175.

Figure 7 shows the results for aspect ratio $k_2 = 0.79$:
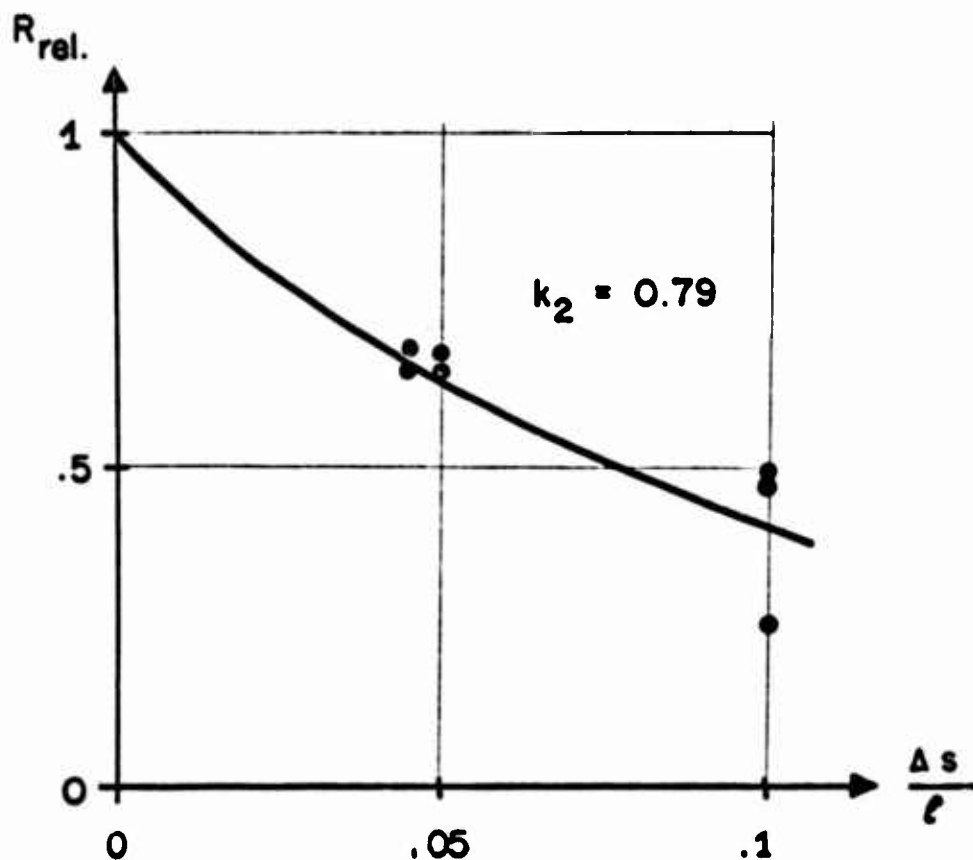

Fig. 7

Dependence of critical Reynolds number on surface roughness.

In this case, the turbulent reattachment was observed
(in agreement with observations made on models with fine sur-
faces, the laminar instability mentioned in section 1.1. could not
be observed at this aspect ratio). The absolute value for the criti-
cal Reynolds number for vanishing surface roughness was 2050.

Figure 6 and Fig. 7 demonstrate clearly that increasing
surface roughness lowers the critical Reynolds number at least in
the range covered by these experiments. Due to the fact that .1
represents a remarkable surface roughness, it may be expected
that surface roughness effects are not likely to affect the perform-
ance of pure fluid elements as far as the possibilities of present
manufacturing techniques are concerned. There is even some
optimism remaining for an approach to nozzle widths in the order
of magnitude of .01 to .05 mm.

<u>2.1. Importance of small size.</u>   An elementary way of obtaining a qualitative and quantitative synopsis of the possibilities offered by pure fluid elements has been published in ref. 3. It is certainly true that the numerical values have to be taken mainly in their order of magnitude, and it is possible in many cases to find operating conditions enabling some difficulties to be overcome at the expense of increased power consumption, for instance. Two such examples are given in the following; both point out how important or urgent a solution of the problem of producing miniaturized pure fluid elements may become under circumstances that are easily encountered.

<u>2.1.1.</u>   The first example concerns a system of pure fluid elements out of which a certain output pressure level is required. In such a case, the operating power P is given by expression (4):

$$P = \frac{k_2 \cdot \sqrt{2}}{k_1} \cdot \frac{\ell^2 \cdot p^{3/2}}{\sqrt{\rho}} . \qquad (4)$$

p is the operating pressure necessary to produce the required output pressure. As far as the well-known limits are not exceeded (minimum Reynolds number, maximum Mach number, etc.) the square law dependence of P on ℓ is noticeable. A certain correction with the aid of a suitably chosen k_2 is possible, but only to a minor extent. Matching may become difficult in cases where, even at the proper (too small) size, a relatively low efficiency would provide enough output power.

<u>2.1.2.</u>   The second example is based on the requirement of a certain response time. Again, this requirement must lie within reasonable limits, and some freedom in respect of a change of Reynolds number, Mach number, etc. must exist. In such a case the operating power is given by expression (5):

$$P = \frac{k_1 \cdot k_2 \cdot (k_3 \cdot k_4)^3}{2} \cdot \frac{\rho \ell^5}{\tau^3} . \qquad (5)$$

k_3 is the ratio of element length to nozzle width; k_4 is the ratio of mean velocity to transport velocity. The product $k_3 \cdot k_4$ represents the Strouhal number (ratio of response time τ to transport time at mean flow velocity over nozzle width ℓ).

<u>2.2. Figure of merit and bandwidth.</u>   Although the
Reynolds number is strictly bound to geometrically similar arrange-
ments, it may be used to a certain extent as a characteristic num-
ber to describe (partly) a fluid element, or it may even serve as a
figure of merit. On the one hand, it provides a good measure for
the power consumption to be expected, on the other hand, however,
it has a great disadvantage in so far as it does not include typical
amplifier data such as flow rate and pressure gain. - As to the be-
havior of most pure fluid elements, it is unfortunately true that
there is (at least presently) no way of providing an analytical re-
presentation allowing elimination of the geometry by substituting
the above-mentioned amplifier data. There is one interesting ex-
ception: the free jet amplifier (see ref. 3 and ref. 4). Assuming a
free jet of a liquid surrounded by another liquid or gas of consider-
ably lower viscosity and density, approximate formulas for the
pressure and flow rate gain, based on momentum control, can
easily be given. The most interesting expression obtained is the
one for the Strouhal number S :

$$S = \mu_{\dot{Q}} \cdot \sqrt{\mu_p} \qquad (6)$$

$\mu_{\dot{Q}}$ is the flow rate gain, μ_p is the pressure gain. The response
time τ of the idealized amplifier (a rectangular velocity profile
has also been assumed) in question then becomes

$$\tau = \mu_{\dot{Q}} \cdot \sqrt{\mu_p} \cdot \frac{\mathcal{P} \cdot \ell^2}{R \cdot \eta} \cdot \qquad (7)$$

This formula sets a lower limit for the response time which is
given by characteristic amplifier data and some magnitudes re-
lated to the physical description of the amplifier and its operation.

        The first result from (6) or (7) is a proposal concerning
a figure of merit γ

$$\gamma = \frac{\mu_{\dot{Q}} \cdot \sqrt{\mu_p}}{S_{exp}} \qquad (8)$$

where $\mu_{\dot{Q}}$, μ_p and S_{exp} are experimental data. Due to the
idealized assumptions it must be expected that γ is always smaller
than one, at least in the case of an amplifier based on momentum
control.

        One step further is suggested by the available experience
with boundary layer control: Relatively large inertias and low inter-
action forces (compared with those encountered in the free jet ampli-
fier based on momentum control) are involved in the transitions of

228

flow patterns required to effect amplification. The greatly reduced transport velocity in the boundary layer is another aspect pointing in the same direction. - The fact that momentum produced by boundary layer effects is the final agent in boundary layer control amplifiers suggests that

$$Y = \frac{\mu_{\dot{Q}} \cdot \sqrt{\mu_p}}{S_{exp}} = 1 \qquad (9)$$

may be considered to be an upper bound for all pure fluid amplifiers, independent of geometry and independent of the effects involved in providing amplification. In terms of the graph of Fig. 8 this means:
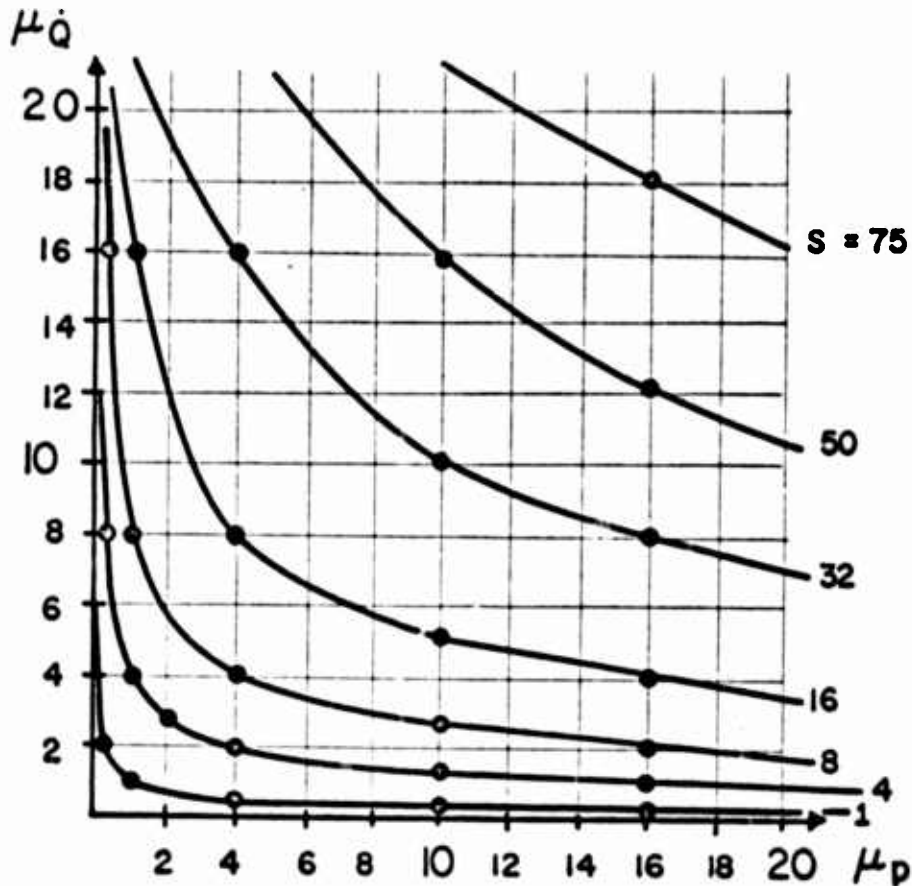
Fig. 8

Minimum Strouhal number as a function of flow rate and pressure gain.

Any Strouhal number measured in a pure fluid amplifier in connection with the corresponding values $\mu_{\dot{Q}}$ and μ_p is expected to be higher than the one represented by the curve going through $(\mu_{\dot{Q}}, \mu_p)$.

Recent investigations have shown that several amplifier types are restricted to certain regions in Fig. 8: The submerged jet amplifier for instance is no longer useful at high Strouhal numbers because of the decay of the initial velocity profile. The wall interaction type amplifier seems to be limited mainly by the difficulties in getting high pressure amplification. - The γ values determined so far, range mostly from .1 to .3. Further investigations are in progress.

In cases where negative or positive feedback is intrinsically present in a pure fluid amplifier, the average response time for the transition from state 1 into state 2, and state 2 into state 1, respectively, are to be taken to evaluate the Strouhal number. Typical examples of arrangements with intrinsic feedback are for instance, the turbulence amplifier (negative) and the vortex chamber amplifier (positive). Beyond the direct observation of positive or negative feedback, it is possible to observe these effects dynamically by slowly varying the control flow or the Reynolds number of the main flow. The reason is that due to the dependence of the feedback power on the (possibly transient) state of the amplifier and inertia effects, a significant time delay exits until feedback becomes effective.

REFERENCES

1. Comparin, R. A., Glaettli H. H., Mitchell, A. E. and H. R. Mueller: "On the Limitations and Special Effects in Fluid Jet Amplifiers", Proceedings of the ASME Symposium on Fluid Jet Control Devices, Winter Annual Meeting of the ASME, New York, 1962.

2. Mitchell, A. E., Mueller, H. R. and R. H. W. Zingg: "Some Recent Developments in the Design of Fluid Switching Devices and Circuits", Proceedings of the Fluid Power International Conference, London, April 1964.

3. Glaettli, H. H.: "Digital Fluid Logic Elements", Advances in Computers, Vol. IV, (Academic Press, New York, 1963).

4. Dexter, E. M.: "An Analog Pure Fluid Amplifier ", Proceedings of the ASME Symposium on Fluid Jet Control Devices, Winter Annual Meeting of the ASME, New York, 1962.

5. Mueller, H. R. and A. E. Mitchell: "Comparison of a Momentum with a Wall Reattachment Fluid Amplifier", Paper submitted to the organizing committee of the ASME Hydraulics Division Conference "Symposium on Fully Separated Flow", May 18-21, 1964, Philadelphia (Pennsylvania).

FIGURE CAPTIONS.

Fig. 1   Critical Reynolds number as a function of the aspect ratio.

Fig. 2   Critical Reynolds number as a function of the aspect ratio.

Fig. 3   Relative power consumption as a function of the aspect ratio k_2.

Fig. 4   Dependence of flow rate gain on Reynolds number for two different wall angles and aspect ratio $k_2 = .6$.

Fig. 5   Dependence of flow rate gain on Reynolds number for two different wall angles and aspect ratio $k_2 = 1.4$.

Fig. 6   Dependence of critical Reynolds number on surface roughness.

Fig. 7   Dependence of critical Reynolds number on surface roughness.

Fig. 8   Minimum Strouhal number as a function of flow rate and pressure gain.

232

ON THE STABILITY OF FLUID SYSTEMS

F. T. Brown, Assistant Professor of Mechanical Engineering
Massachusetts Institute of Technology, Cambridge 39, Mass.

ABSTRACT

Fluid systems, especially those containing proportional
fluid amplifiers with no moving parts, often display
little-understood bistable or cyclic instabilities.
Two general criteria for small-disturbance stability
are presented, with simple illustrations involving
amplifiers, lines, and volumes. Application of the
criteria to real systems is based on separate measure-
ments of certain static and dynamic properties of
the more complicated elements, and analysis of the
separate properties of the other elements.

Introduction

Fluid systems with no moving mechanical parts often exhibit violent bistable and oscillatory instabilities, and other staging phenomena, which do not appear during conventional testing of the separate elements. Some milder instabilities have been identified as "noise." The goal of this paper is to show how proper testing or analysis of the individual elements can indeed properly predict stability of a system.

The basis of the analysis herein is given in another paper of the author's, "On the Stability and Response of Fluid Multiport Systems," which should be available in preprint form at the time of the HDL Symposium, 26 - 28 May, 1964. The basic concept, shown in Fig. 1, is of two coupled multiport elements. For example, one element might be an amplifier, with two control ports and two output ports. Supply and exhaust ports can be neglected, since no active signal is sent through them. The second element is the environment, which consists of two control lines and two load lines. The ports on the first element are numbered 1, 2, 3, 4; and the matching ports on the second, $1'$, $2'$, $3'$, $4'$. A second example is two load lines. The four ends of the lines are the four ports of the first element, and the ports of the environment are the ports of the second element. In general, cross-coupling can exist between all the ports of any given element.

Stability Criteria

Two approaches toward predicting stability are given. The first is based on the <u>admittance</u> matrices of the elements:

234

$$\mathbf{w} = -(\mathbf{Y}_p + \mathbf{w}_o) \tag{1}*$$

$$\mathbf{w}' = \mathbf{Y}'p' + \mathbf{w}'_o \tag{2}$$

Here $\mathbf{w}, \mathbf{w}_o, \mathbf{w}'$ and $\mathbf{w}'_o$ are column matrices representing the flows out of the unprimed element and into the primed element (which in general are equal), $\mathbf{p}$ is a column matrix representing the pressures at the ports, and $\mathbf{Y}$ and $\mathbf{Y}'$ are square matrices in which the diagonal terms Y_{ii} are <u>self-admittances</u> and the other terms Y_{ij} are <u>transfer admittances</u>. If each term of $\mathbf{Y}$ and $\mathbf{Y}'$ represents a stable phenomenon, a criterion of stability is simply that the determinant $\left| \mathbf{Y}(s) + \mathbf{Y}'(s) \right|$, where s is complex frequency, have no zeroes in the right-half side of the complex s-plane. This condition can be determined by plotting the function $\left| \mathbf{Y}(j\omega) + \mathbf{Y}'(j\omega) \right|$ in the complex plane, where ω is the real frequency and j is the unit imaginary number. The absence of zeroes in the right-half side of the s-plane is indicated by a zero or negative number of net clockwise encirclements of the origin of the determinant plane, as ω goes from minus infinity to plus infinity. For special cases in which the determinant does not converge to zero or a finite number as $\omega \rightarrow \infty$, it is necessary to complete the map by having s rotate around the right-half plane from $+j\omega$ to $-j\omega$ at an infinite distance from the origin.

---

*Matrix algebra is described in numerous texts; a simple, adequate introduction is given in Ref. (1).

Equation (1) is simply a shorthand for the following set of equations:

$$w_1 = -(Y_{11}P_1 + Y_{12}P_2 + Y_{13}P_3 + \cdots + w_{01})$$

$$w_2 = -(Y_{21}P_1 + Y_{22}P_2 + Y_{23}P_3 + \cdots + w_{02})$$

The second approach toward predicting stability, which is especially useful when fluid lines produce significant delays, is based on <u>scattering variables</u>.[2] The definition

$$A = \begin{bmatrix} \sqrt{A_1} & 0 & 0 & \cdot \\ 0 & \sqrt{A_2} & 0 & \cdot \\ 0 & 0 & \sqrt{A_3} & \cdot \\ & \cdot & \cdot & \cdot & \end{bmatrix} \tag{3}$$

in which the A_1, A_2, ... are arbitrary values of flow admittance, is most useful. In practice these A's are selected as the <u>surge admittances</u> * of the respective fluid lines, where applicable. The definitions

$$\phi = A p \tag{4}$$

$$\sigma = A^{-1} w \tag{5}$$

now have identical units. The scattering variables are defined as

$$\begin{Bmatrix} u \\ v \end{Bmatrix} = \frac{1}{\sqrt{2}} \begin{bmatrix} 1 & 1 \\ 1 & -1 \end{bmatrix} \begin{Bmatrix} \phi \\ \sigma \end{Bmatrix} \tag{6}$$

with the identical reverse relation

$$\begin{Bmatrix} \phi \\ \sigma \end{Bmatrix} = \frac{1}{\sqrt{2}} \begin{vmatrix} 1 & 1 \\ 1 & -1 \end{vmatrix} \begin{Bmatrix} u \\ v \end{Bmatrix} \tag{7}$$

Note that the power transmitted through a port is

$$\text{Power} = pw = \phi \sigma = \frac{u^2}{2} - \frac{v^2}{2} \tag{8}$$

which shows that u and v are the <u>amplitudes</u> of waves travelling in the positive and negative directions, respectively.

---

*Considering mass flow (rather than volume flow), the surge admittance of a line equals the area of the line divided by the speed of sound of the fluid in the line.

At a set of ports in one element the incident waves u are reflected by the waves v. The relation between u and v is known as the scattering matrix :

$$v = Su \; ; \; v' = S' u' \tag{9}$$

The diagonal terms of the square matrix S are reflection operators or functions, or in special cases reflection coefficients, and the non-diagonal or cross-coupling terms might be described as refraction operators or functions (or coefficients).

The second criterion of stability, also derived in the before-mentioned paper by the author and again assuming that the individual terms in S and S' represent stable phenomena, is that the determinant $|I - S'S|$ have no zeroes in the right-half plane.[*] I is the unit diagonal matrix. The same sort of complex plane plot and criterion regarding encirclements of the origin applies as before.

The remainder of this paper considers special simple cases of particular relevancy to fluid systems without moving mechanical parts.

Single Volume

For a large class of problems of interest the dynamic effects can be assumed to result exclusively from fluid lines with pure delays and fluid volumes with pure compliance.

The simplest substantial problem is that of a single volume with two inlets, as shown in Fig. 2. If the "port" is selected half-way

---

[*]If a signal-flow graph of the waves u and v is drawn, adapting the approach of Mason, an equivalent criterion of stability is that the "graph determinant $\Delta(s)$" have no zeroes in the right-half plane.

through the volume,

$$Y = Y_1 = \frac{Cs}{2} + y_1 \qquad (10)$$

$$Y = Y_2 = \frac{Cs}{2} + y_2 \qquad (11)$$

where y_1 and y_2 are the non-dynamic admittances of the inlets, and C
is the compliance of the volume. The critical determinant is simply

$$|Y + Y'| = y_1 + y_2 + Cs \qquad (12)$$

The appropriate mapping, shown also in Fig. 2, shows the following nec-
essary and sufficient condition for stability:

$$y_1 + y_2 \geq 0 \qquad (13)$$

A negative y_1 or y_2 is an _active_ (power-supplying) admittance. Completely
passive systems are always stable.

Single Line

For a single line it is again possible to choose a single port mid-
way between the ends, but two ports, one at each end, are selected here.
For the environment,

$$Y' = \begin{bmatrix} y_1 & 0 \\ 0 & y_2 \end{bmatrix} \qquad (14)$$

and for the line, which is assumed to be lossless with delay time T_2 and
surge admittance A,

$$S = \begin{bmatrix} 0 & e^{-Ts} \\ e^{-Ts} & 0 \end{bmatrix} \qquad (15)$$

238

The stability criteria require expressions in terms of only the admittance or scattering matrices, but not both. The general conversion formulas are as follows:

$$S = \left(A - A^{-1}Y\right)\left(A + A^{-1}Y\right)^{-1} \tag{16}$$

$$Y = \left[(S+I)A^{-1}\right]^{-1}\left[A(I-S)\right] \tag{17}$$

Using Eq. (16) on Eq. (14), where A is a diagonal matrix of two equal elements equal to the characteristic admittance of the line, A,

$$S' = \begin{bmatrix} \dfrac{A - y_1}{A + y_1} & 0 \\ 0 & \dfrac{A - y_2}{A + y_2} \end{bmatrix} \tag{18}$$

The diagonal terms in S' are the well-known reflection coefficients for waves at the termination of a line. The determinant which the stability criterion refers to becomes

$$|I - S'S| = 1 - \left(\frac{A-y_1}{A+y_1}\right)\left(\frac{A-y_2}{A+y_2}\right)e^{-2Ts} \tag{19}$$

For $s = j\omega$ this represents a circle in the complex plane; for no encirclements of the origin,

$$\left|\left(\frac{A - y_1}{A + y_1}\right)\left(\frac{A - y_2}{A + y_2}\right)\right| < 1 \tag{20}$$

(where the vertical lines here mean magnitude of, rather than determinant of). Thus for stability the product of the two reflection coefficients must have a magnitude less than unity. Otherwise "organ-pipe" oscilla-

239

tions grow until a limit cycle is reached.

The growth of oscillations into a limit cycle is illustrated in Fig. 3[*], using the method of characteristics.[5] This problem involved a line blocked at one end with a specially contrived jet incident on the other. The dynamic prediction based on static measurements compares well with the actual observed dynamic measurements. In this particular case the damping in the line had to be taken into account, since it was nearly sufficient to prevent oscillations altogether. The slope of the surge lines was modified for this purpose.

The author has presented the attentuation and phase velocity of small-amplitude sinusoidal waves in laminar flow in liquid and gas-filled lines.[6] These results can be used to find the attentuation of a sine-wave, per round-trip cycle, at the natural and harmonic frequencies of the line. The results, shown in Fig. 4, can be introduced into the left-side of Eq. (20) as a multiplicative damping factor which in effect extends the range of stability. For other than a sine-wave the damping is always greater: hence the prediction of stability is always conservative.

Surge Instability

Consider a jet, with the active characteristics just discussed, incident on a long line. In addition, consider that a tiny compliance sep-

---

[*]The work presented in Fig. 3 was performed by Mr. K. N. Reid as part of his forthcoming doctoral thesis on the interaction of a jet and receiver port. Other graphical constructions relevant to the present discussion have been given by the author.[4]

arates the line from the jet. For high frequencies the line has simply
the characteristic admittance A; reflections from the other end affect
only the lower, organ-pipe frequencies. Equations (10) - (13) now apply,
the last of which shows the system is unstable.

The frequency of the oscillations of this <u>surge instability</u> go to
infinity as the compliance goes to zero. The author has clearly observed
such instabilities, however; they can appear as an exceedingly shrill
pitch, and quite possibly are often ultrasonic. The explanation of a
small compliance is actually not quite correct, or at least complete.
Another significant factor must be the frequency limitation of the nega-
tive jet admittance.

The amplitude of these oscillations, which may be easily confused
with "noise," should be approximately equal to the amplitude of the
nose in the S-shaped pressure-flow or admittance characteristic (see Fig.
3). They are quickly attenuated as they travel downstream.

Two Lines

The double-line problem, Fig. 1(c), has application to control
lines and load lines of fluid jet amplifiers. Note that strong coupling
usually exists between two control ports, and a weaker but often criti-
cal coupling exists between two output ports. If the problem is spec-
ialized to two identical lines with symmetric cross-coupling and reflec-
tion coefficients at either end, although the two ends are different,
the scattering matri. of the environment is

$$S' = \begin{bmatrix} s_{11}' & s_{12}' & 0 & 0 \\ s_{12}' & s_{11}' & 0 & 0 \\ 0 & 0 & s_{33}' & s_{34}' \\ 0 & 0 & s_{34}' & s_{33}' \end{bmatrix} \tag{21}$$

and of the lines is

$$S = \begin{bmatrix} 0 & 0 & e^{-Ts} & 0 \\ 0 & 0 & 0 & e^{-Ts} \\ e^{-Ts} & 0 & 0 & 0 \\ 0 & e^{-Ts} & 0 & 0 \end{bmatrix} \tag{22}$$

from which[*]

$$|\mathbf{I} - \mathbf{S'S}| = 1 + \left[(s_{11}' s_{33}' + s_{12}' s_{34}')^2 - (s_{11}' s_{34}' + s_{12}' s_{33}')^2 \right] e^{-4Ts} \tag{23}$$

When plotted in the complex plane for $s = j\omega$ this gives a circle. Stability requires no encirclement of the origin, or

$$\left| (s_{11}' s_{33}' + s_{12}' s_{34}')^2 - (s_{11}' s_{34}' + s_{12}' s_{33}')^2 \right| < 1 \tag{24}$$

This condition easily can be violated, and a wave or organ-pipe instability results.

---

[*]This result also can be found, perhaps more easily, by considering a two-port system with the ports half-way between the two ends of the line.

242

Cascaded Passive Elements

Frequently one wishes to analyze a system containing a chain of lines, volumes, and other elements. Identifying each connection as a port, in the manner of the previous examples, is entirely possible, though usually results in an over-complicated solution procedure. Usually a markedly easier approach is first to solve for the over-all properties of the chain, and then place only one port at each end.

The example of two lines connected by a volume, as shown in Fig. 5, serves as an illustration. For the volume alone,

$$
\left\{ \begin{array}{c} P_2 \\ W_2 \end{array} \right\} = \left[\begin{array}{cc} 1 & 0 \\ Cs & 1 \end{array} \right] \left\{ \begin{array}{c} P_3 \\ W_3 \end{array} \right\} \tag{25}
$$

and for the complete chain

$$
\left\{ \begin{array}{c} u_1 \\ v_1 \end{array} \right\} = \left[\begin{array}{cc} e^{T_1 s} & 0 \\ 0 & e^{-T_1 s} \end{array} \right] \frac{1}{\sqrt{2}} \left[\begin{array}{cc} 1 & 1 \\ 1 & -1 \end{array} \right] \left[\begin{array}{cc} \sqrt{A_1} & 0 \\ 0 & \frac{1}{\sqrt{A_1}} \end{array} \right] \left[\begin{array}{cc} 1 & 0 \\ Cs & 1 \end{array} \right] \left[\begin{array}{cc} \frac{1}{\sqrt{A_2}} & 0 \\ 0 & \sqrt{A_2} \end{array} \right] \frac{1}{\sqrt{2}} \left[\begin{array}{cc} 1 & 1 \\ 1 & -1 \end{array} \right] \left[\begin{array}{cc} e^{T_2 s} & 0 \\ 0 & e^{-T_2 s} \end{array} \right] \left\{ \begin{array}{c} u_4 \\ v_4 \end{array} \right\}
$$

Upon multiplication of this chain of square matrices,

$$
\left\{ \begin{array}{c} u_1 \\ v_1 \end{array} \right\} = \left[\begin{array}{cc} \left(\sqrt{\frac{A_1}{A_2}} + \sqrt{\frac{A_2}{A_1}} + \frac{Cs}{\sqrt{A_1 A_2}} \right) e^{(T_1+T_2)s} & \left(\sqrt{\frac{A_1}{A_2}} - \sqrt{\frac{A_2}{A_1}} + \frac{Cs}{\sqrt{A_1 A_2}} \right) e^{(T_1-T_2)s} \\ \left(\sqrt{\frac{A_1}{A_2}} - \sqrt{\frac{A_2}{A_1}} - \frac{Cs}{\sqrt{A_1 A_2}} \right) e^{(T_2-T_1)s} & \left(\sqrt{\frac{A_1}{A_2}} + \sqrt{\frac{A_2}{A_1}} - \frac{Cs}{\sqrt{A_1 A_2}} \right) e^{-(T_1+T_2)s} \end{array} \right] \left\{ \begin{array}{c} u_4 \\ v_4 \end{array} \right\}
$$

$$\tag{27}$$

243

Rearranging to give the outputs on the left,

$$
\left\{ \begin{array}{c} v_1 \\ u_4 \end{array} \right\} = \left[\begin{array}{c|c} \dfrac{A_1 - A_2 - Cs}{A_1 + A_2 + Cs}\, e^{-2T_1 s} & \dfrac{2\sqrt{A_1 A_2}}{A_1 + A_2 + Cs}\, e^{-(T_1 + T_2) s} \\[2mm] \hline \dfrac{2\sqrt{A_1 A_2}}{A_1 + A_2 + Cs}\, e^{-(T_1 + T_2) s} & \dfrac{A_2 - A_1 - Cs}{A_2 + A_1 + Cs}\, e^{-2T_2 s} \end{array} \right] \left\{ \begin{array}{c} u_1 \\ v_4 \end{array} \right\}
$$

(28)

This square matrix is the scattering matrix, S, of the element which contains the line, with ports at both ends of the line.

As an application of this result consider an amplifier which drives two output lines that are connected together by a volume, as also shown in Fig. 5. The accompanying signal flow graph is a useful device, either as a mnemonic or as the basis of an alternative topological approach.[*]

The properties of the amplifier will be assumed to be independent of frequency. Furthermore, symmetry of the system will be assumed. With the definitions

$$
\tau \stackrel{\leq}{=} \frac{C}{A_1 + A_2} = \frac{C}{2A} \tag{29}
$$

$$
T \stackrel{\leq}{=} T_1 = T_2 \tag{30}
$$

The scattering matrices become

---

[*]See footnote, p. 5

$$S = \begin{bmatrix} a & b \\ b & a \end{bmatrix} \tag{31}$$

in which

$$a = \frac{-2\tau s}{\tau s + 1} \; e^{-Ts} \tag{32}$$

$$b = \frac{1}{\tau s + 1} \; e^{-2Ts} \tag{33}$$

and

$$S' = \begin{bmatrix} r & c \\ c & r \end{bmatrix} \tag{34}$$

in which r is a reflection coefficient and c a cross-coupling coefficient. The matrix of interest and its determinant are, respectively,

$$I - S'S = \begin{bmatrix} 1 - (ra + cb) & -(rb + ca) \\ -(rb + ca) & 1 - (ra + cb) \end{bmatrix} \tag{35}$$

$$|I - S'S| = 1 - 2(ra + cb) + (r^2 - c^2)(a^2 - b^2) \tag{36}$$

When plotted in the complex plane for $s = j\omega$ this determinant gives a quite complicated path, dependent on the values of τ/T, r, and c. The simplest case is when $\tau = 0$ (no volume at all), for which

$$|I - S'S| = 1 - 2ce^{-2Ts} - (r^2 - c^2) \; e^{-4Ts}$$

$$= \left[1 + (r - c) \; e^{-2Ts} \right]\left[1 - (r + c) \; e^{-2Ts} \right] \tag{37}$$

245

and the condition of no clockwise encirclements of the origin gives two conditions:

$$r + c < 1$$
$$r - c < 1 \tag{38}$$

Experimental Techniques

Static values of the admittances of a fluid element are easily found experimentally, so long as the element can be stabilized long enough to make the measurements. From Eq. (1) it is seen that

$$Y_{i,j} = \frac{\partial w_i}{\partial p_j} \tag{39}$$

A minimum of two data points is required to approximate such a derivative, of course. The biggest problem experimentally is holding the pressures constant at ports other than the jth port, when these pressures are not atmospheric. A useful last resort is to attach a tee-section to the port, and to force a large quantity of flow through the leg of the tee, which is not attached to element, adjusting large valves at either end of this leg.

Static values of the scattering matrix terms are easily found from the admittances, by using Eq. (16).

For many systems the static values of the admittances or scattering coefficients of the active elements (jet amplifiers, etc.) apply up to frequencies higher than the possible instabilities of interest, which are

246

associated with the calculable dynamic properties of the attached passive elements (lines, volumes, etc.). In any case an instability predicted using these static values almost inevitably will actually exist, whether or not the values are valid at the actual frequency of the instability. The dynamics of the active elements usually increase the liklihood of instability, by adding phase lags, resonances, etc. For example, this is the only factor which can make a higher harmonic frequency of a line dominate over the fundamental, as often occurs.

Measurement of dynamic values of the admittances or scattering operators is considerably more difficult, unfortunately. The best technique known to the author at present, adapted from well-established methods used on electrical transmission lines, is shown in Fig. 6. Standing waves of small amplitude (for linearity to apply) are set up in one line, using perhaps an audio driver, or in some cases of spontaneous instabilities, a damper value. The envelope or AC magnitude of the static pressure is then measured, from which the reflection and refraction coefficients can be determined, as shown. Both magnitudes are phase are associated with these frequency-dependent coefficients. The principal problem is the measurement of the pressure peaks. One possible idea is the use of a row of simple fluid diodes (e.g. very slightly leaky check values) connected to manometer tubes. Then, only determination of the phase of the refraction coefficient requires expensive dynamic pressure transducers, and these can be located at rather arbitrary positions.

By attaching the transmission lines successively to all pairs of ports of a given element, holding the pressures constant at the other ports, the entire scattering matrix can be measured as a function of fre-

quency.

Impulse and step responses (especially the latter) can give useful but lower quality dynamic data, and are somewhat easier to obtain. Their principal use probably would be to determine the frequency above which the static characteristics are no longer valid.

Conclusions

Relationships which allow the prediction of the stability of a complicated fluid system, based on measurements of the characteristics of the individual elements, have been given. Most of the techniques actually apply to many electrical and mechanical systems as well.

The static characteristics of the active elements are relatively easily measured, and suffice for most systems, especially when long lines and large volumes are involved. The dynamic characteristics of these elements are considerably more difficult to determine.

It is proposed, therefore, that such static data accompany marketed "pure-fluid-system" elements, and that ways be sought to easily determine, if only roughly, the dynamic characteristics.

Some active elements will have a dominant ringing frequency; the natural frequency of the lines and other elements to which they are attached should be far removed. This is necessary, and almost sufficient, for a static-property analysis to be useful.

Much experimentation with commonly used elements, such as the interaction of a jet with coupled receiver ports, is clearly desired.

From the results of this paper to relations for the dynamic response is but a short step.

248

Acknowledgement

References

1. L. A. Pipes, *Applied Mathematics for Engineers and Physicists*, McGraw-Hill, New York, 1958, Chapter 4.

2. H. J. Carlin, "The Scattering Matrix in Network Theory, *IRE Transactions on Circuit Theory*, V. CT-3, n 2, June 1956, pp. 88-97.

3. S. J. Mason and J. J. Zimmerman, *Electronic Circuits, Signals, and Systems*, Wiley, New York, 1960, Chapter 1 and pp. 592-594.

4. F. T. Brown, "Fluid Jet Modulators and Systems," Chap. 16 of M.I.T. Summer Course notes, *Instrumentation for Measurement and Control*, 1963.

5. Louis Bergeron, *Water Hammer in Hydraulics and Wave Surges in Electricity*, Wiley, New York, 1961.

6. F. T. Brown, "The Transient Response of Fluid Lines," *ASME Transactions*, Series D, *Journal of Basic Engineering*, Dec. 1962.

(a) Coupled multiport elements

(b) Fluid amplifier with multiport model

(c) Fluid lines with multiport model
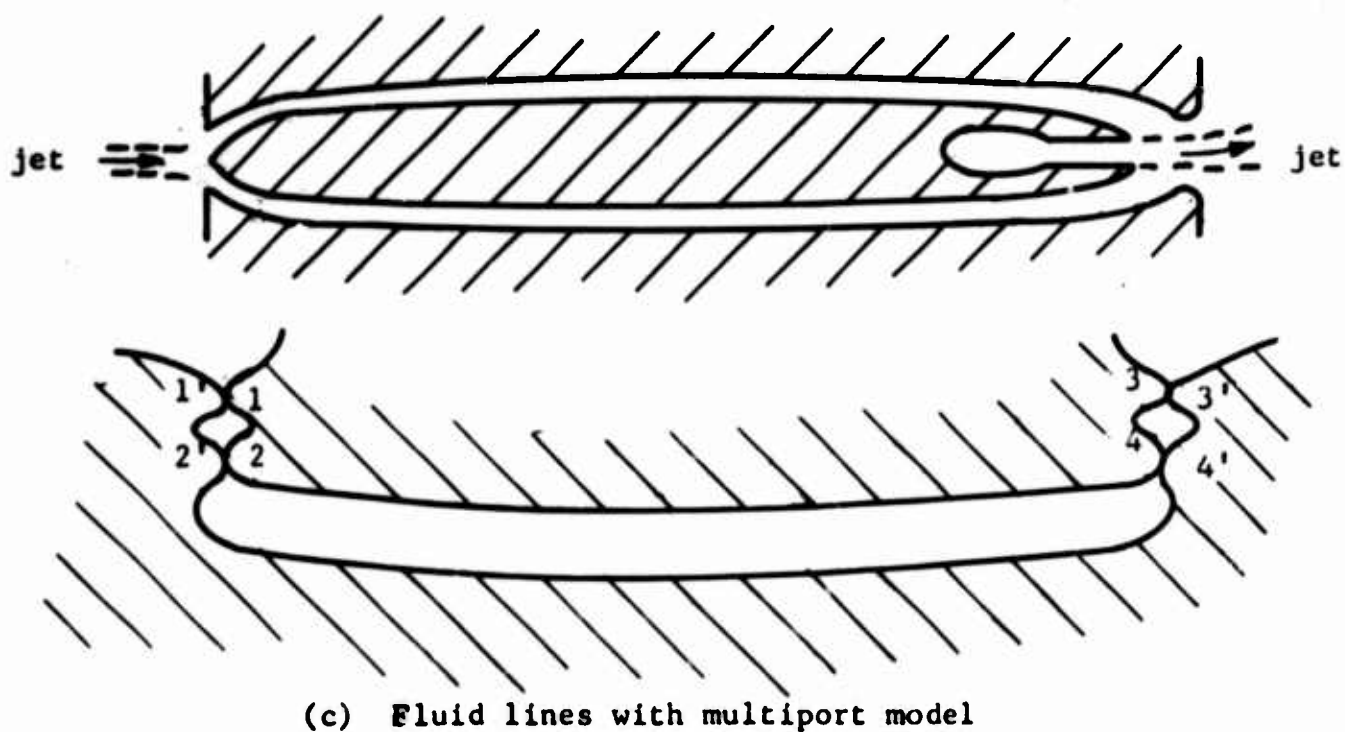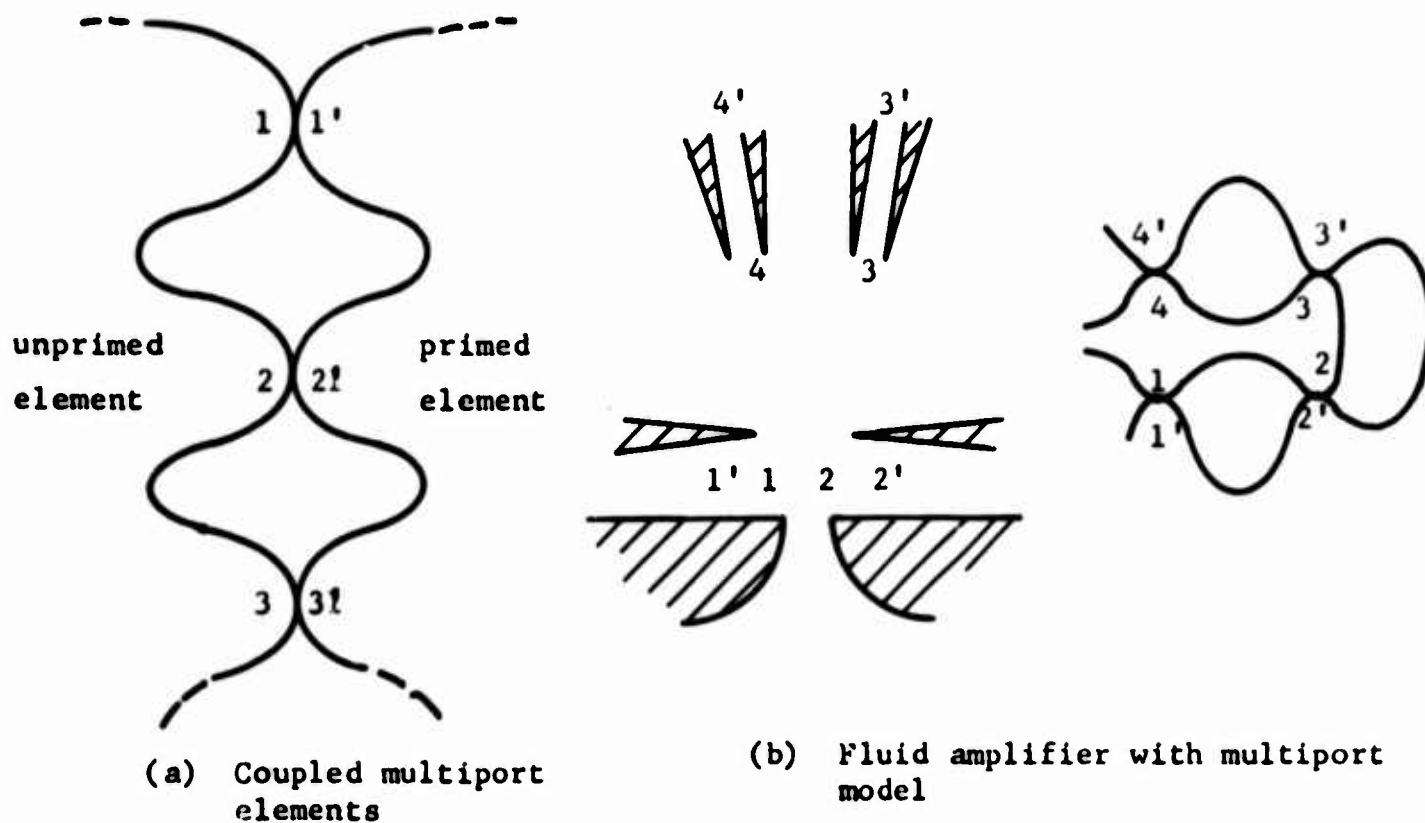
Fig. 1.   The Concept of the Multiport Model
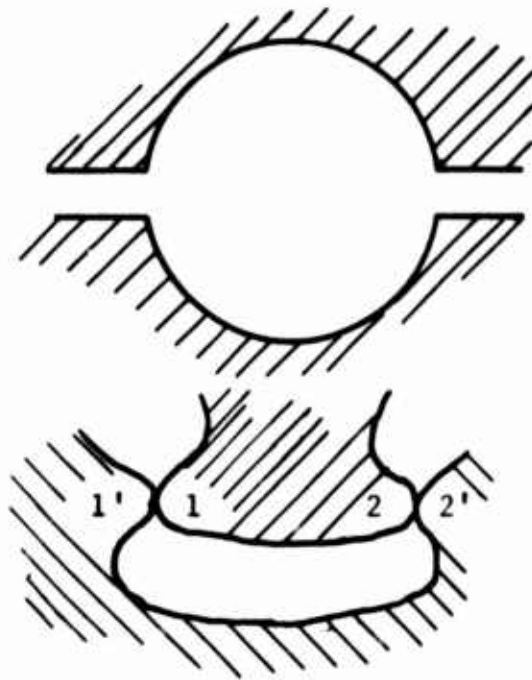
(a) Fluid volume and multiport model

(b) s-plane

(c) plane
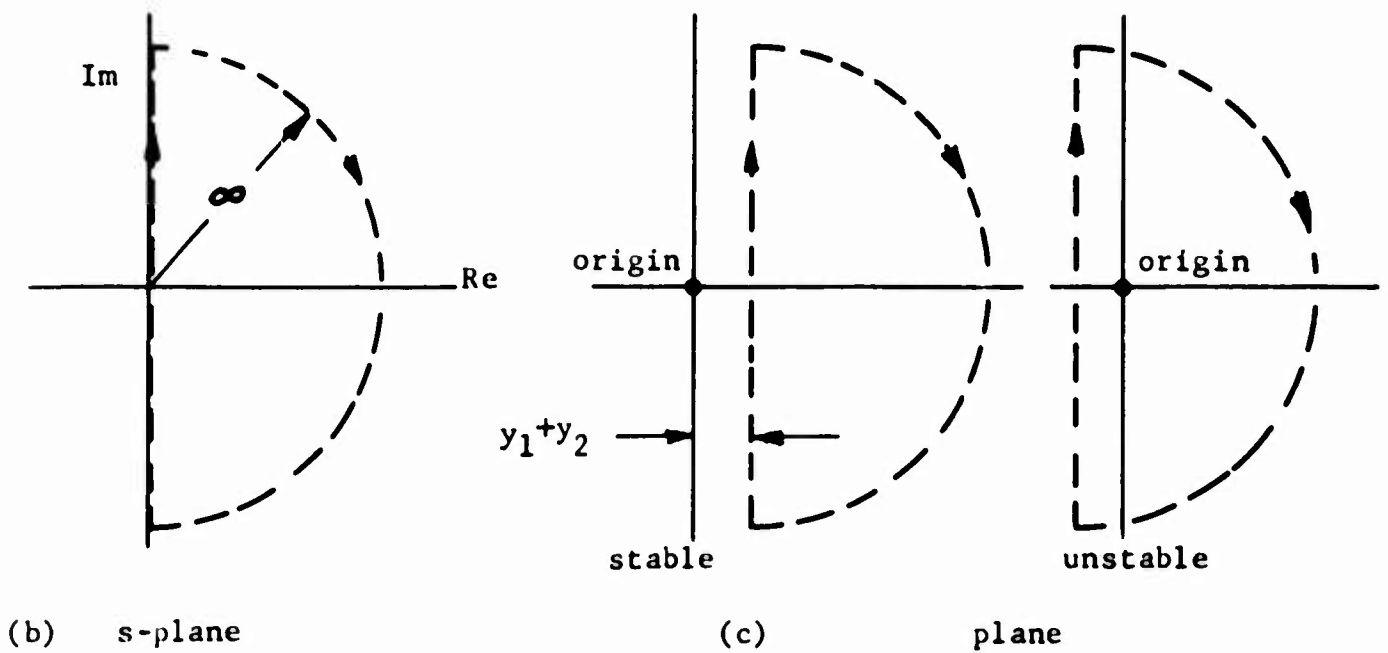
Fig. 2. Stability of Fluid Volume
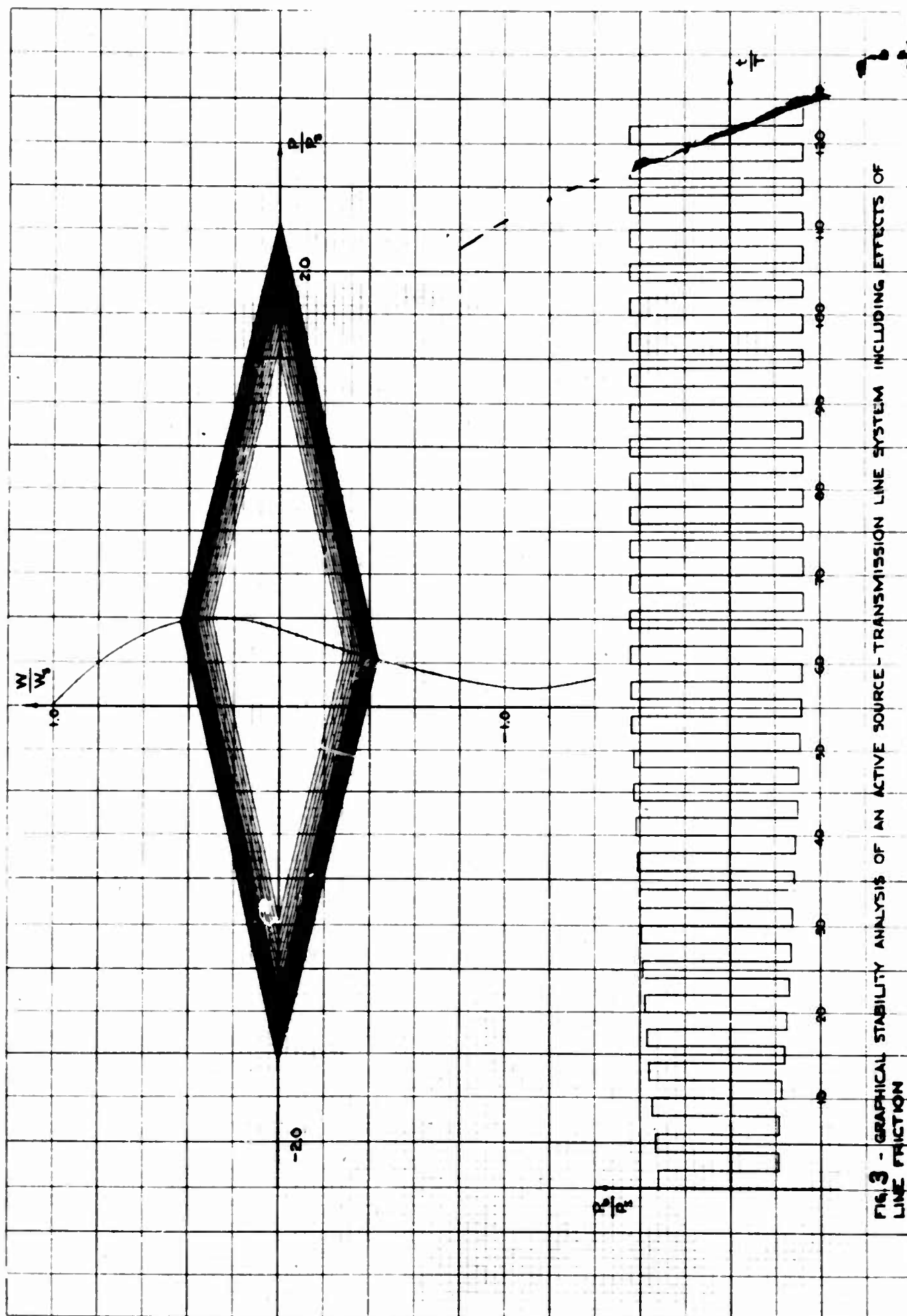
FIG. 3 - GRAPHICAL STABILITY ANALYSIS OF AN ACTIVE SOURCE-TRANSMISSION LINE SYSTEM INCLUDING EFFECTS OF LINE FRICTION
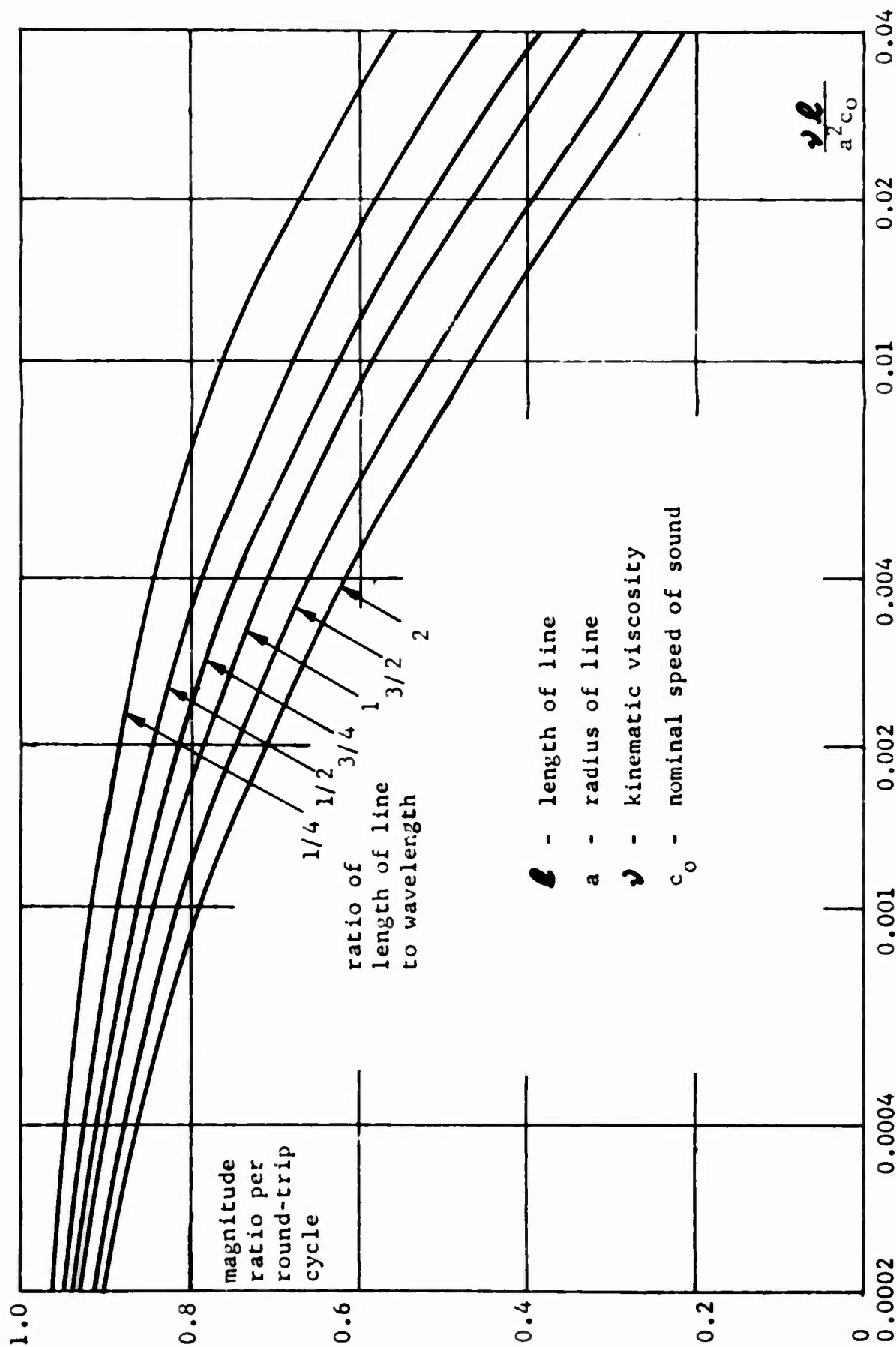
Fig. 4 Attenuation Per Cycle of Small Amplitude Sine Waves in Rigid, Isothermal-Wall, Laminar-Flow, Circular Air Line

253
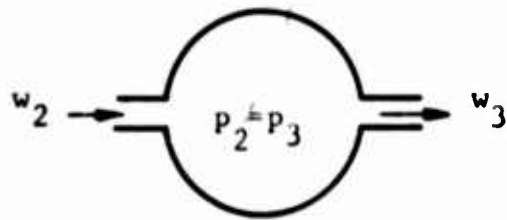
(a)   Volume showing direction of flow definitions
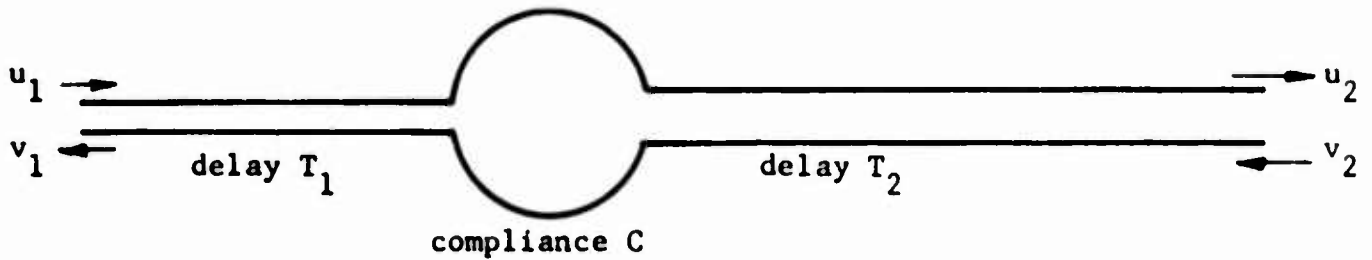
(b)   Volume between two lines showing
        consistent wave-direction definitions
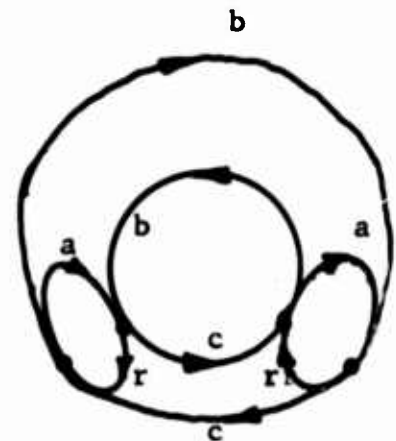
(c)   Application as fluid amplifier load, with
        multiport model and signal-flow graph

Fig. 5   Example of Cascaded Passive Elements

(a) Experimental set-up

(b) Line with standing waves

(c) Line with traveling waves
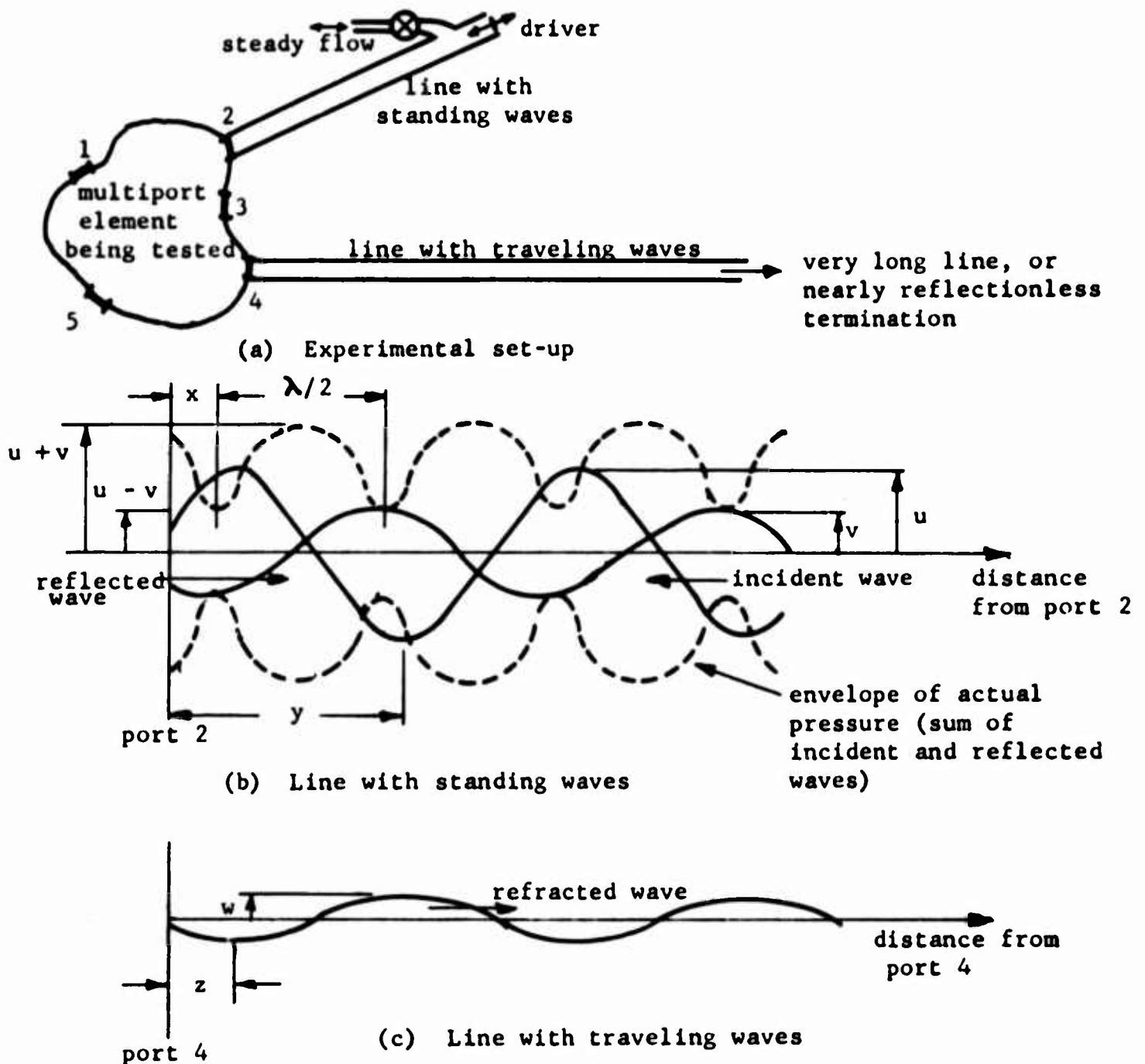
$$|s_{22}| = \frac{v}{u} = \frac{(u + v) - (u - v)}{(u + v) + (u - v)}$$

phase angle of s_{22} = $\left(\frac{x - \lambda/4}{\lambda/2}\right) \pi$ radians

$$|s_{42}| = \frac{w}{u} = \frac{2w}{(u + v) + (u - v)}$$

phase angle of s_{42} = $\left(\frac{y + z - \lambda}{\lambda}\right) 2\pi$ radians

Fig. 6 Experimental Procedure for Directly Measuring
Reflection and Refraction Functions

255

Low-Pass Filters For Pneumatic Amplifiers

by

Ronald L. Humphrey
Francis M. Manion

This paper presents some experimental results of tests performed on preliminary low-pass filter designs for pneumatic systems. The results indicate which of several methods of filtering seem most promising for application to pure fluid elements. Fluid systems, as their counterparts in electronics, are subject to noise problems. High gain pressure amplifiers have acoustic noise problems by virtue of their design. To overcome these noise problems it would be most desirable to eliminate the noise source but in these elements the source of the noise is the geometrical configuration which gives high linear gain. Therefore, any effort to reduce noise would affect a desirable gain characteristic. It appears expedient to design filters to eliminate most of the undesirable noise while passing the amplifier signal. This is possible because a great deal of the objectionable noise occurs at a frequency far greater than the useful range of the amplifier. This paper deals with the experimentation of some low-pass filter designs.

One of the cardinal rules in design of the low-pass filter is not to attenuate the amplifier signal. Therefore, a great effort was made in these tests to assure that the filter did not attenuate the DC level. The filters tested were either from theoretical adaptations of classical designs, or were merely based on experience. The theoretical adaptations were from the simplest form of acoustical-electrical

analogs and delay-line, low-pass filters. A test method was developed at Bowles Engineering to permit ready analysis of the filters effect on the noise frequency spectrum. This test arrangement is given in Figure 1, and utilizes hot-wire anemometers in conjunction with a sonic panoramic analyzer which displayed the noise frequency spectrum. The results of these tests showed that there are several useful filters by which the percent of noise generated in the analog amplifiers may be greatly reduced. The best of these are the pneumatic analogy of the electrical LC low-pass filter and the sonic delay-line filter when applied to a two-dimensional form.

This paper contains the theory and experimental results of tests performed on several pneumatic low-pass filter designs. The filters tested were as follows:

I. Filters Developed From Theory
   (1) Acoustic Theory
   (2) Adaptation of Electrical Analog Theory
   (3) Delay-line Theory

II. Filters Developed Empirically
   (1) Filtering Characteristics of a Commercially Available Device
   (2) Optiform Model of Commercial Device
   (3) Filtering Characteristics of Long Lines
   (4) Filtering Characteristics of Absorbing Walls

These filters were investigated as part of an effort to reduce the output noise of pure fluid analog amplifiers. From the various types of pneumatic filters tested the pneumatic analogy of the electrical LC low-pass filter, and the sonic delay-line filters showed the best performances. In addition, there is good correlation between test and theory.

258

The performance of a filter should be measured by how well it attenuates noise, relative to steady-state attenuation. Obviously, a small enough orifice would, by means of steady-state attenuation, reduce the noise to zero, but also the flow. However, for these tests the output flow of the analog amplifier, which provides the filter input, was never reduced more than 12% for any filter tested.

A description of how each filter was tested is shown by the instrument diagram in Figure 1.

The test method was developed at Bowles Engineering to permit analysis of the noise spectrum. The hot-wire anemometer was used to measure the complete noise spectrum both before and after the filter. The wire output was then displayed by a panoramic sonic analyzer. To obtain a permanent record the XY recorder was matched to the spectrum analyzer so that the spectrum traces would be made by the XY recorder. Special paper was then designed and fitted to the recorder so that the trace was readily available for analysis. This approach gave three definite advantages. First, the trace was greatly enlarged. Secondly, the trace could be repeated several times so that ambient perturbations could be distinguished from the steady-stage noise in the system. And finally, the trace taken before the filter could be recorded in red ink, while the trace taken after the filter was recorded in green ink giving a ready indication of the filter's effectiveness. These advantages permitted a rather exact analysis of each filter. The figures which are included in this paper are pictorial tracings of the general characteristics of the actual traces so that the effect of the filter is clear.

I. Filters Developed From Theory

(1) Acoustical Theory

Acoustical filter design was tried first since existing design data was available from <u>Fundamentals of Acoustics</u> by Kinsler and Frey.

The figure below shows the filter configuration and the basic equations used for a low-pass filter with a cut-off frequency of 1000 cps.
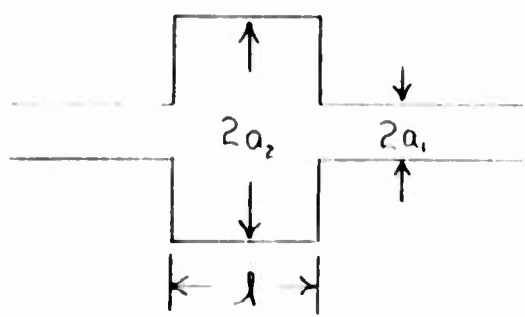
$$\text{where } l = \frac{\lambda}{4} \quad \text{where } kl \leq \frac{\pi}{2}$$

$$\therefore l = 3.36 \text{ inches at } f_c = 1000 \text{ cps}$$

The exact filter configuration and test results are shown in Figure 2.

From the test results in Figure 2, we see that the filter acted like a middle pass band filter and attenuated the low-frequency noise rather than passing it. It was decided that the filter did not work for two reasons:

(1) Eddies forming at the output of the filter due to its shape.

(2) Impedance of the filter was not matched to the line resistance and, therefore, produced many reflections.

Work on this filter was discontinued due to the test results and since with increasing frequency the acoustical filter power transmission ratio begins to increase for frequencies where $kl > \frac{\pi}{2}$. Therefore, for frequencies higher than f_c the noise would remain and continue to cause problems.

260

(2) Adaptation of Electrical Analog Theory

From the previous tests it was decided that as with electrical low-pass filters the design parameter to be considered would be the matching of the source (R_S) and load (R_1) resistance to the characteristic filter impedance (Z_C). For the design of these filters the basic electrical equations were used and made equivalent in pneumatic terms.

The equations used were as follows:

$$f_c = \frac{1}{2\pi\sqrt{LC}} \tag{1}$$

$$Z_c = \sqrt{\frac{L}{C}} \tag{2}$$

from $\quad L = \frac{f\ell}{cw} \quad$ And $\quad C = \frac{c\pi r^2}{\rho c^2} \quad$ we find that

$$LC = \frac{\ell}{w}\frac{\pi r^2}{c^2} = \text{constant}$$

$$\frac{L}{C} = \frac{\ell}{w}\frac{1}{r^2}\frac{\rho^2 c^2}{\pi^2 c^2} = \text{constant}$$

therefore, we can solve for the two variables $\dfrac{\ell}{w}$ and r

$$\frac{\ell}{w} = \frac{dR}{2\pi\rho f_c}$$

$$r = \frac{c}{\pi}\sqrt{\frac{\rho}{2f_c R d}}$$

261

Sample Calculations:

$$R_s = R_L = \frac{\frac{1}{2}\rho V}{A} = \frac{.5 \times 1.38 \times 10^{-6} \cdot 2292}{8 \times 10^{-4}} = 2.0$$

Now for $f_c = 300$ cps and $d = 0.040$ inches

$$\frac{l}{w} = \frac{d R}{2\pi \rho f_c} = \frac{.04 \cdot 2}{2 \cdot 3.142 \cdot 1.38 \times 10^{-6} \cdot .3 \times 10^{3}} = 30$$

$$\therefore r = \frac{c}{\pi}\sqrt{\frac{\rho}{2 f_c R d}} = \frac{13.44 \times 10^{3}}{3.142}\sqrt{\frac{1.38 \times 10^{-6}}{2 \cdot .3 \times 10^{3} \cdot 2 \cdot .04}} = .73$$

Now we can calculate L and C directly

$$L = \frac{\rho l}{dw} + C = \frac{1.38 \times 10^{-6}}{.04} \cdot 30 + C = 1.0 \times 10^{-3} + C$$

where C depends upon the diameter

$$C = \frac{d \pi r^2}{\rho c^2} = \frac{.04 \cdot 3.142 \cdot (.73)^2}{1.38 \times 10^{-6}(13.44 \times 10^{3})^2} = .26 \times 10^{-3}$$

We now have values for L and C in terms of $\frac{\ell}{w}$ and r, therefore, we can construct these filters in two different ways:

(1) Lumped Parameters

The low-pass filter was constructed as a π filter, where narrow lines are the L's and volumes are used as C's.

(2) Distributed Parameters

In the second case the πr^2 area of the C was converted to an $\ell \cdot w$ area and the total area was used as an LC filter.

The filter configuration and test results for the lumped parameters filter are shown in Figure 3.

Figure 4 shows the filter configuration and test results for the distributed parameter filter.

From the test results we see that the distributed parameters filter did attenuate the higher frequencies; however, the lumped parameters filter attenuated the lower frequency noise as well as the higher frequencies noise and had a 20 db/decade attenuation for frequencies above f_c.

(3) Delay Line Theory

A sonic delay-line filter was the next design tried. The figure below shows the filter configuration and the basic equations used for a low-pass filter with a cut-off frequency of 200 cps.
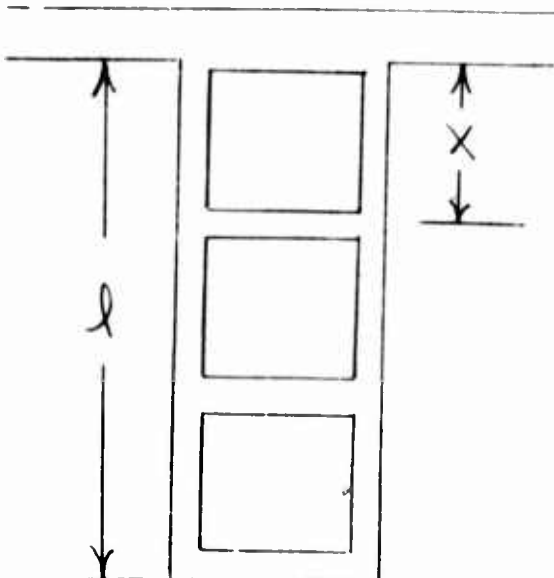
$$f_c = \frac{V_{sonic}}{4\pi\ell}$$

$$\therefore \ell = \frac{13.44 \times 10^3}{4 \cdot 3.142 \cdot 2\times 10^2} = 5.38 \text{ inches}$$

$$\text{at } f_c = 200 \text{ cps}$$

263

Since it was very toublesome to calculate the proper value for X, the λ was divided into a convenient equal number of sections.

The exact filter configuration and test results are shown in Figure 5.

From the test results in Figure 5, we see that the configuration acted as a low-pass filter for several values of P+ and had a 20 db/decade attenuation for frequencies above f_c.

II. Filters Developed Empirically

(1) Filtering Characteristics of a Commercially Available Device

It was decided to test the filtering characteristics of a commercial capillary flow meter, which are large volumes filled with a honeycomb structure as shown in Figure 6. Two flow meters were tested:

(1) National Instrument Laboratory
Vol-O-Flow Model 10-10-5
Range 0.3 scfm

(2) National Instrument Laboratory
Vol-O-Flow Model 10-10-5
Range 2.0 scfm

Figure 7 shows the test results of the two flow meters used as filters.

From the test results we see that the large range flow meter has the best filtering characteristics.

264

(2) Optiform* Model of Commercial Device

Due to the test results shown in Figure 7, it was decided to make a two-dimensional copy of the commercial flow meter in Optiform.

Figure 8 shows the Optiform model configuration used and the test results.

From the test results of Figure 8 we see that the noise was only attenuated slightly. This was due to the fact that the two-dimensional Optiform model had less surface area than the three-dimensional capillary flow meter.

(3) Filtering Characteristics of Long Lines

It was decided to study the filtering characteristics of several sections of tubing with various I.D.'s.

The table below shows a tabulation** of the test results:

	Length	I.D.	% Wide Band Noise (20 cps - 20,000 cps)
(1)	L = 0"		22.7
(2)	L = 40"	1/4"	7.9
(3)	L = 2" (1/4) -12" (3/8) -40" (1/4)		1.5
(4)	L = 2" (1/4) -12" (3/8) -2" (1/4)		5.9
(5)	L = 2" (1/4) -6" (3/8) -40" (1/4) -6" (3/8) -2" (1/4)		1.4

The effect of long line filtering is clearly seen. This type of filtering is similar to the LC filtering studied earlier, only in this case the various sized I.D. tubes simulate the L's and C's.

Figure 9 shows the filtering effect of the 40" (1/4) length of tubing.

---

*BEC Trademark
**Reference BEC TM-22

265

(4) Filtering Characteristics of Absorbing Walls

Figure 10 shows two configurations that were used to study the effect of trying to absorb the high energy noise and thus reduce the total wide band noise.

The test results are shown in Figure 11.

From the test results of Figure 11 we see that the high energy noise was absorbed, but the designs tested also generated lower frequency noise, and thus did not reduce the over-all % noise to a sufficient level.

Results - Discussion

The results of these tests indicate that the problem of proper matching from filter outputs to the exit condition is essential if the filter is to be at all effective. Second, the simple adaptation of the filter designs being tried were actually being placed in very complex RLC networks and, therefore, the results obtained were not entirely unexpected. The data indicates that the filter changes the noise-frequency spectrum that enters the filter, and not just the spectrum that leaves the filter. This is evident because the same amplifier with the same operating pressure gives different noise-frequency spectrums before different filters. This phenomenon must be due to acoustical reflections and impedance mismatches. The effect of impedance mismatch is evident from the apparent effectiveness of each filter at two different operating pressures and, therefore, different impedances. To perform a complete analysis of the filters output and all of the network elements would require an excessive amount of analytical work and then testing that would most likely prove the analysis somewhat lacking. It is far better to use some

266

preliminary experiments and then use the theoretical analysis to make the most promising designs adequate for the particular application. From the preliminary tests that have been conducted it is apparent that:

(1) The acoustical filter of Figure 2 suffers from reflections and matching problems to such an extent that it probably should not be pursued in its present form.

(2) The lumped LC filter appears promising but may need better matching to fit into the desired system.

(3) The distributed LC filter is less promising; that is, has more problems than the lumped LC filter and, therefore, probably should not be pursued.

(4) The delay-line filter appears very effective; however, it must be matched to the pressure level. The effect of higher frequencies (shorter wave lengths) on a fixed delay-line configuration is apparent in Figure 5.

(5) The commercial filter (flow meter) data of Figure 6 indicates the effect of proper matching of the impedance. The 2.0 SCFM device appears fine, but the 0.3 SCFM model which has higher resistance and less capacitance has little effect.

(6) The Optiform filter configuration essentially substantiates the data of the high-resistance lower capacitor commercial filter element.

(7) The effect of the 40" line on the noise-frequency spectrum is shown in Figure 9; however, this type of filtering always results in a reduction of the DC level (in other words, an attenuation of the signal) and for this reason is not desirable.

(8) The filter configurations of Figure 10 were attempts to see the effect of an absorbing wall on the noise spectrum. The data for these is given in Figure 11. It is apparent that these filters are completely unsatisfactory in that they appear to generate noise at some frequencies and attenuate noise at other frequencies.

In conclusion it is apparent from the filter experiments conducted that some of them are quite promising and should be properly matched into the fluid system where they are needed. The ones that are most promising appear to be the lumped LC filter and the sonic delay-line types.

Appendix

Definitions:

P – pressure (lb/in^2)

Q – volume flow (in^3/sec)

V – velocity (in/sec)

A – area (in^2)

C – velocity of sound (in/sec)

V – volume

X – wave length

Z_c – filter characteristic impedance

R_s – source resistance

R_l – load resistance

f_c – filter cut-off frequency

ℓ – length

W – width (in)

D – depth (in)

r – radius (in)

Resistance (R) $R = \dfrac{\partial P}{\partial Q}$ $\therefore R = \dfrac{\frac{1}{2}\rho V'}{A}$

Inductance (I) $P = \dfrac{dQ}{dt}$ $\therefore L = \dfrac{\rho \ell}{A}$

Capacitance (C) $V = \dfrac{1}{\ } \displaystyle\int_0^{\ } Q\,dt$ $\therefore C = \dfrac{V}{\rho C^2}$
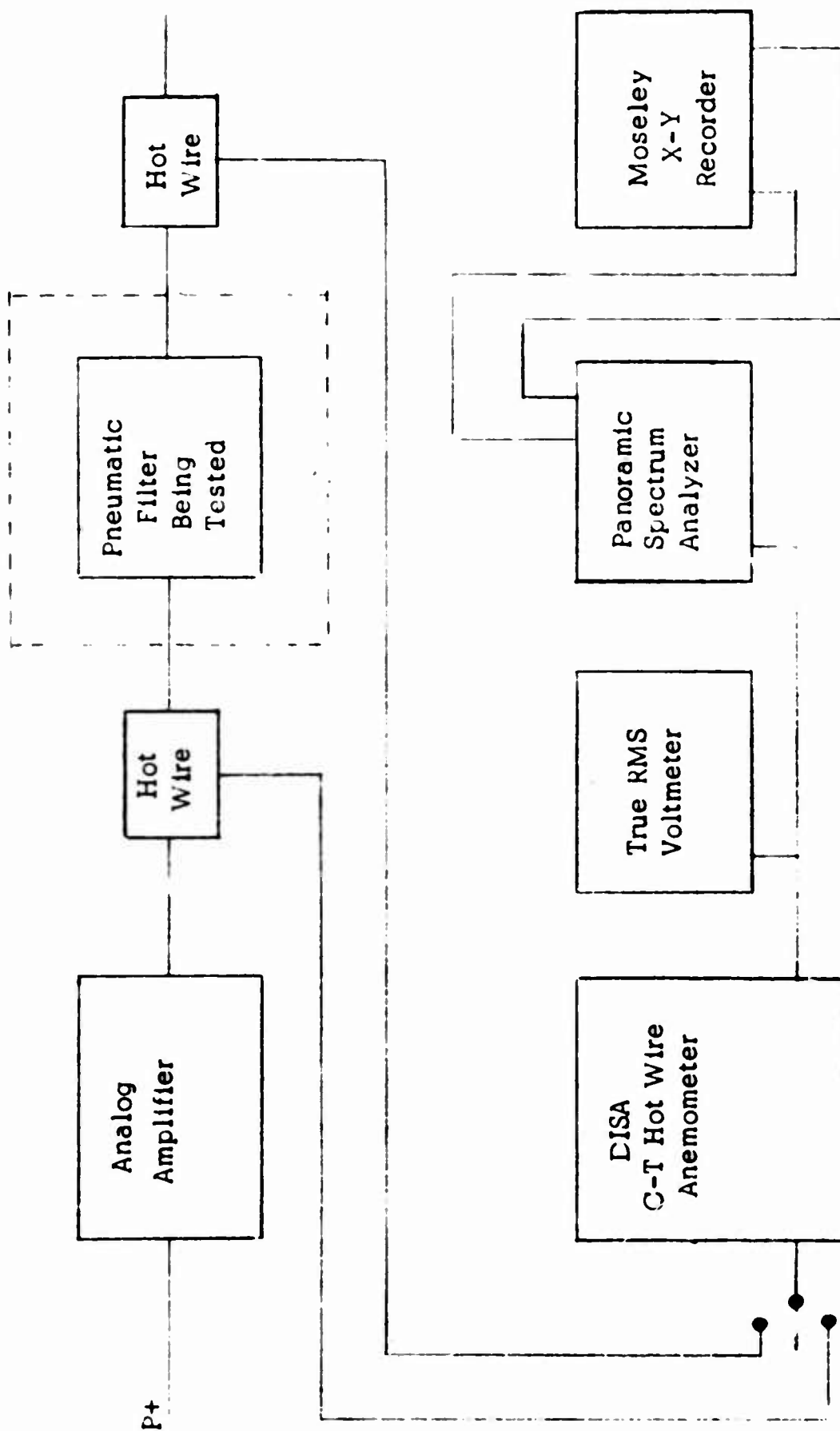
FIGURE 1

Instrumentation Diagram

FIGURE 2
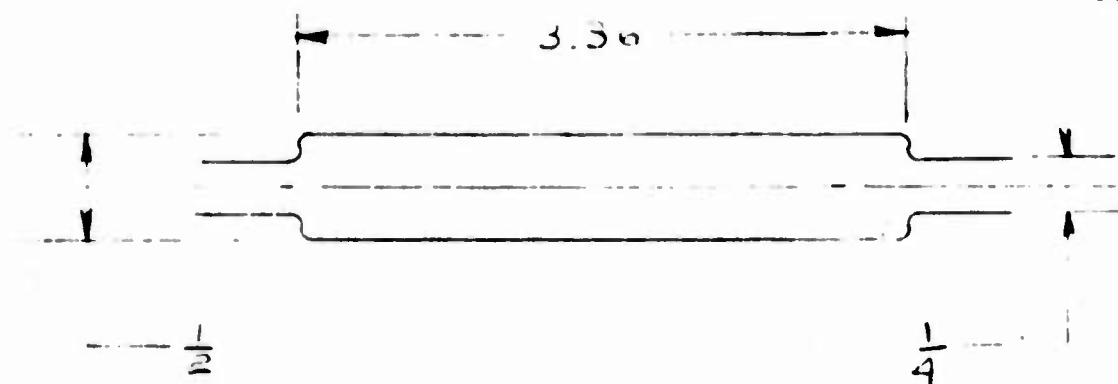
Acoustical
Filter Configuration

Filter Input _____
Filter Output -----

$Pt = 1.5 psi$

$Pt = 5.0 psi$

Frequency, cps

Frequency, cps

Filter Configuration and Frequency Spectrum Diagrams

271
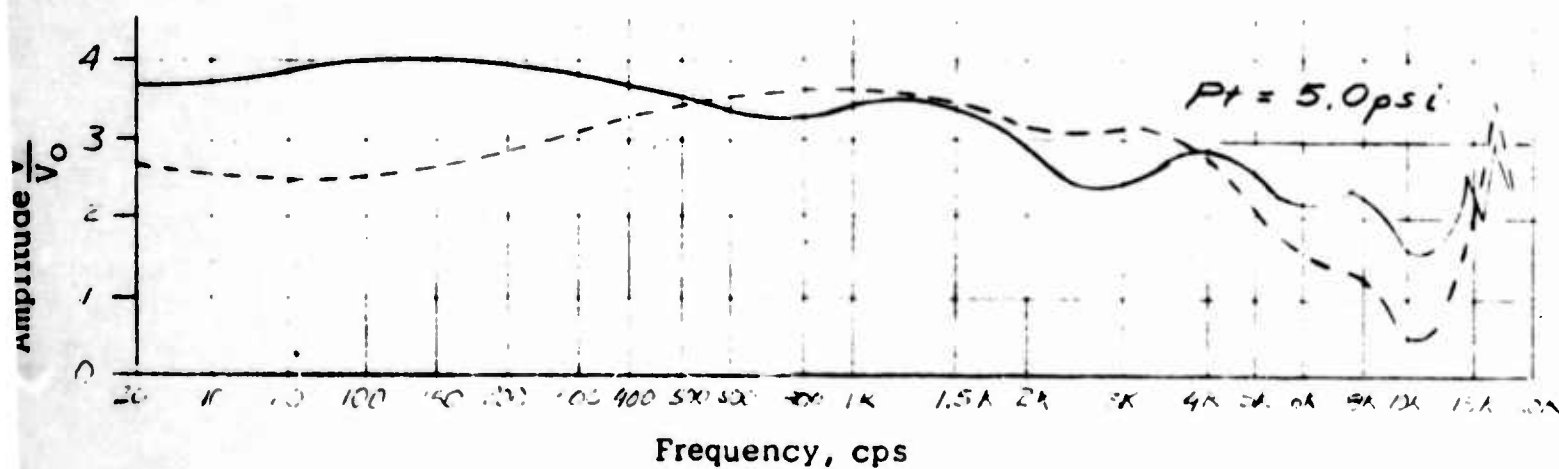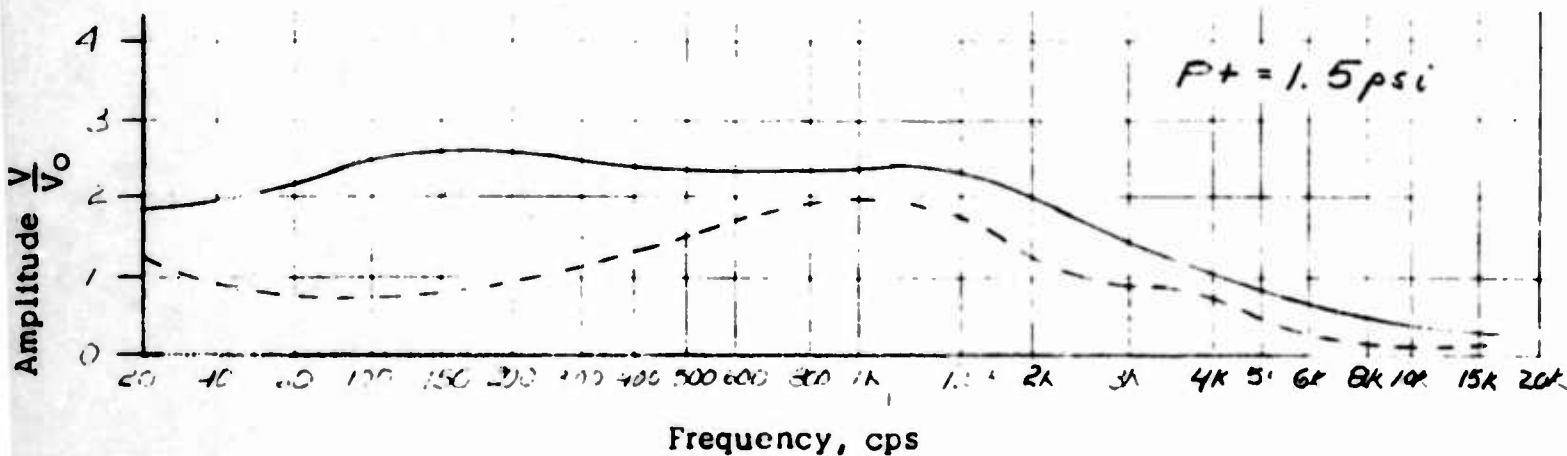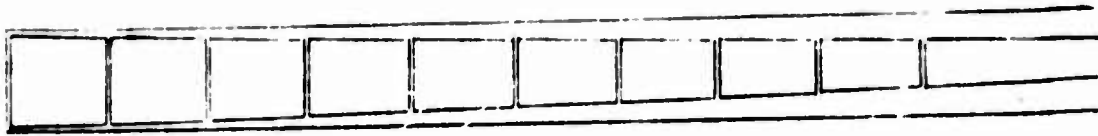
FIGURE 5

Delay Line Filter Configuration

Filter Configurations and Frequency Spectrum Diagrams

273
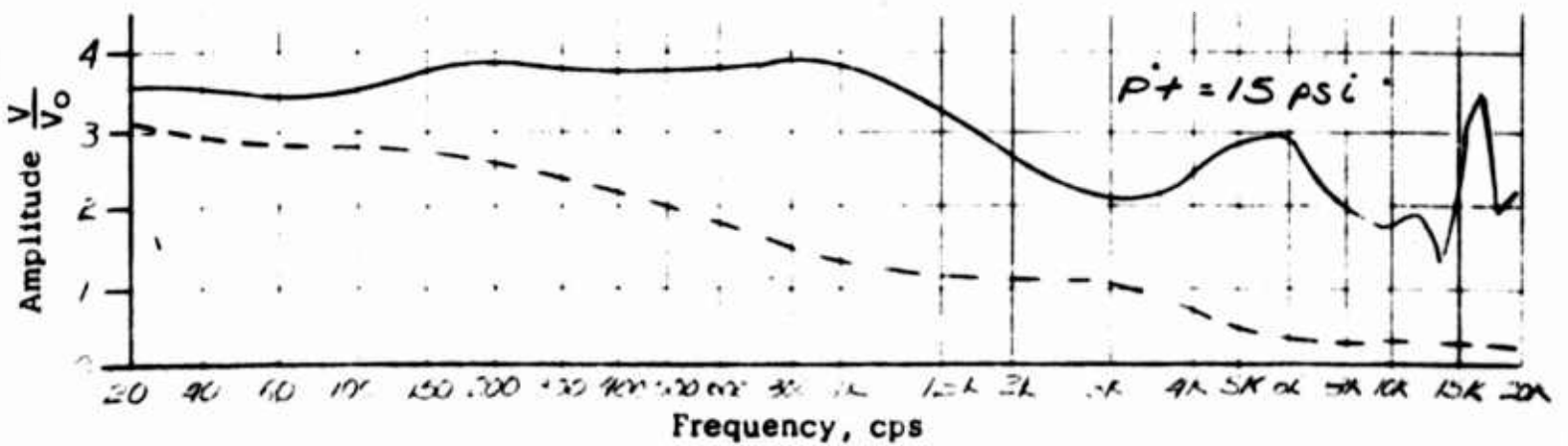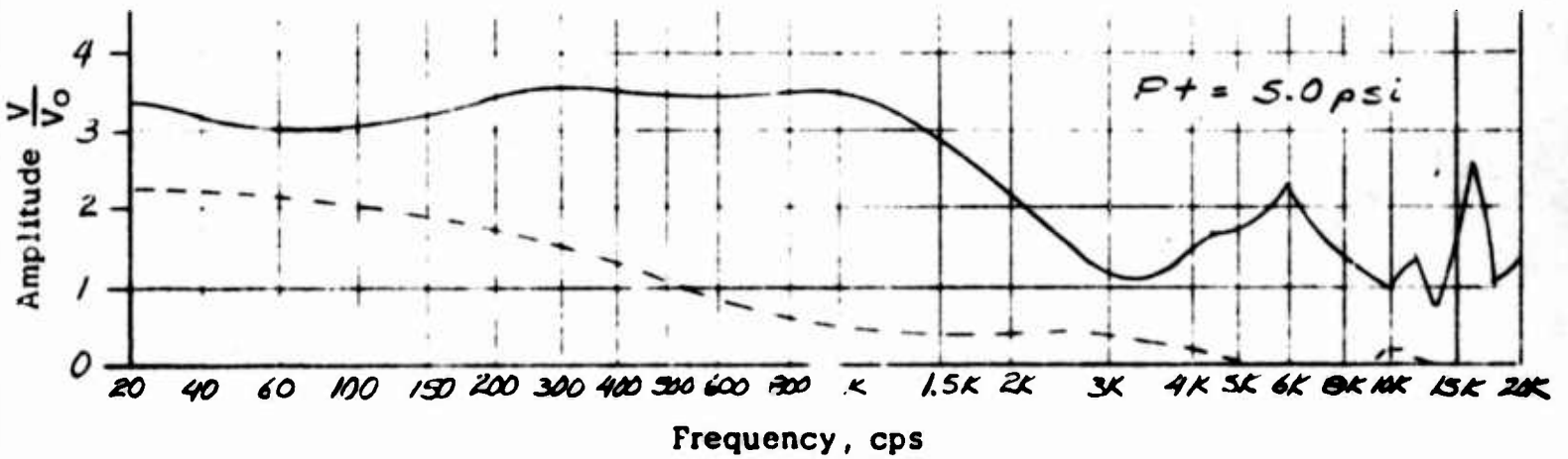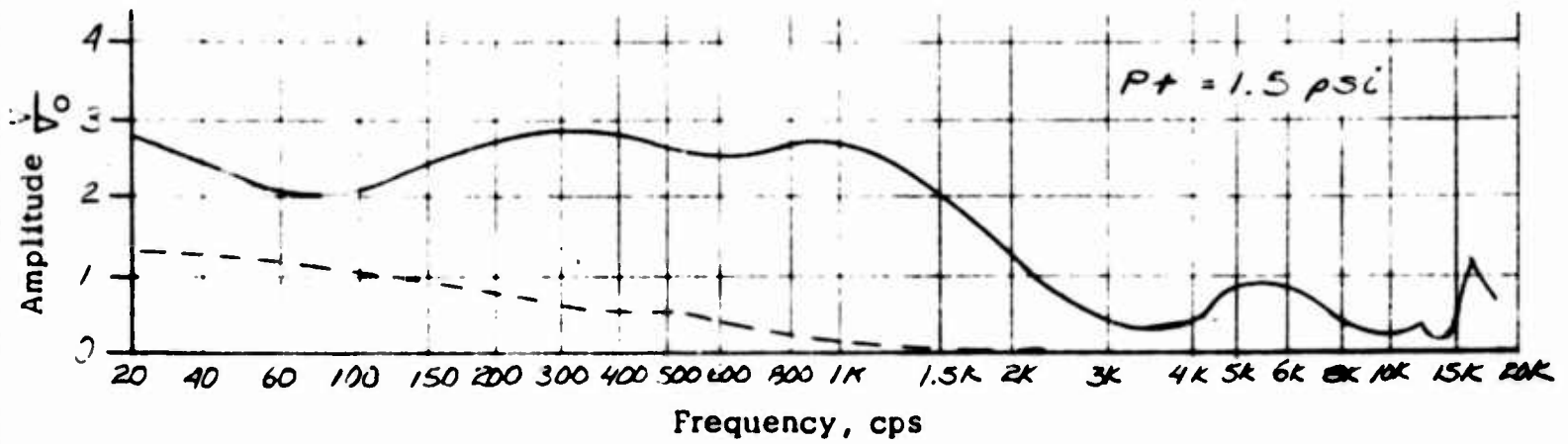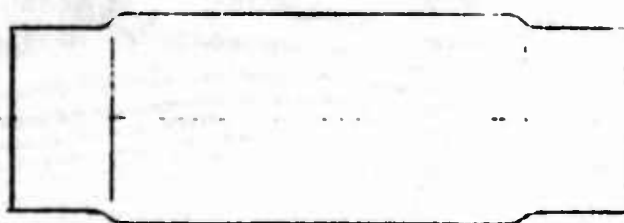
FIGURE 6

Commercial
Filter Configuration

FIGURE 7

2.0 SCFM MODEL

Frequency, cps

0.3 SCFM MODEL

Frequency, cps

Filter Configuration and Frequency Spectrum Diagrams
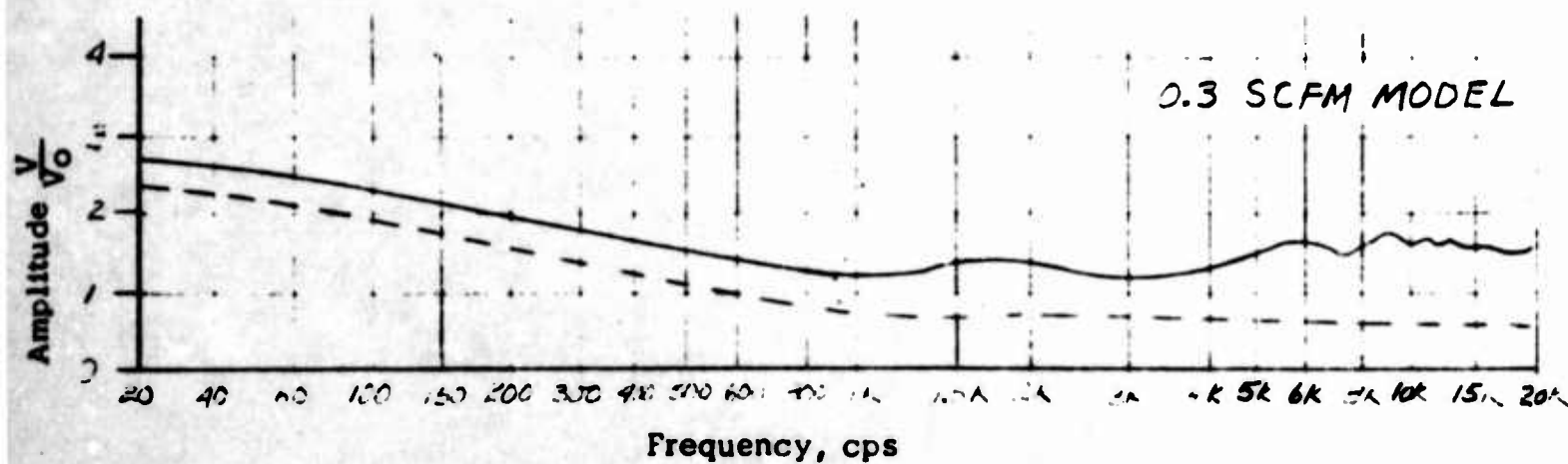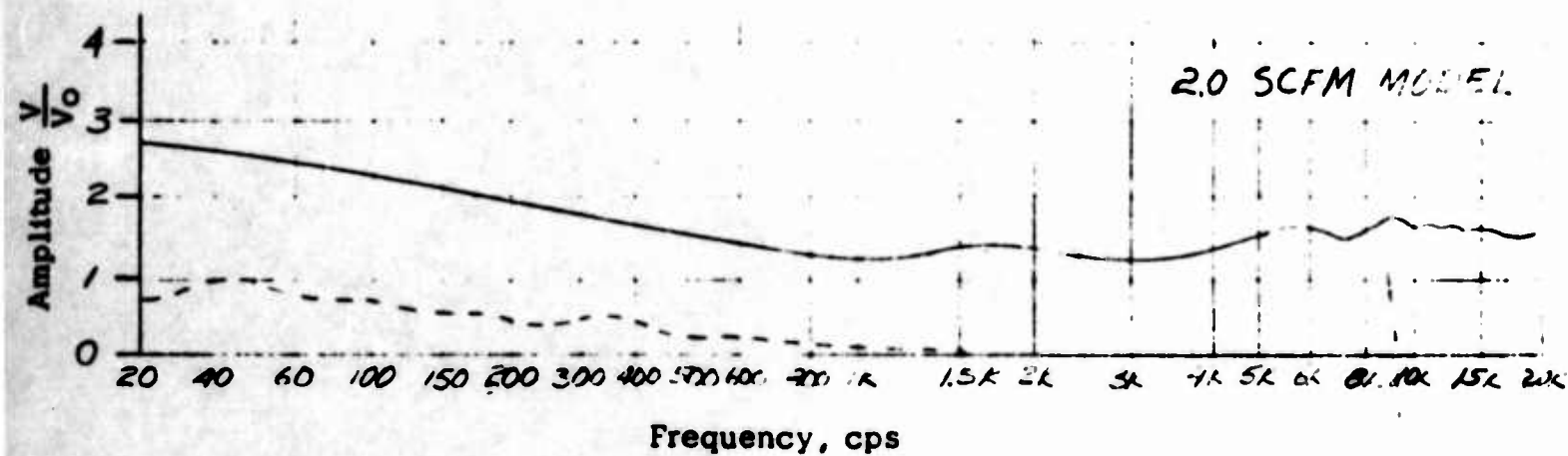
FIGURE 8

OPTIFORM Filter Configuration
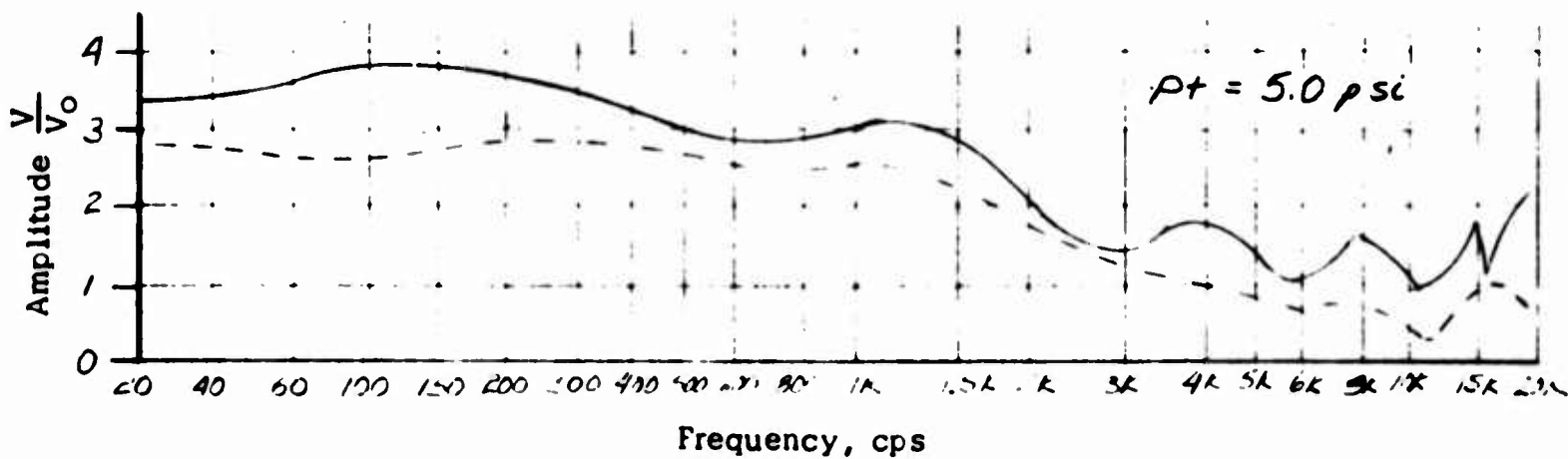
Filter Configuration and Frequency Spectrum Diagrams

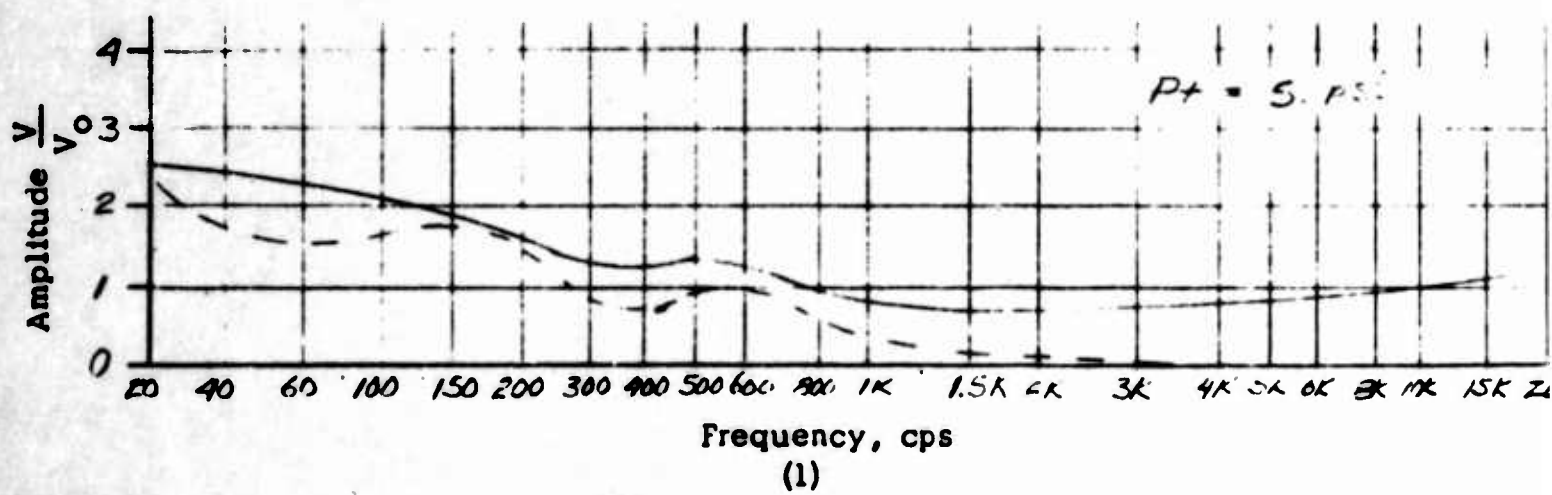**FIGURE 9**
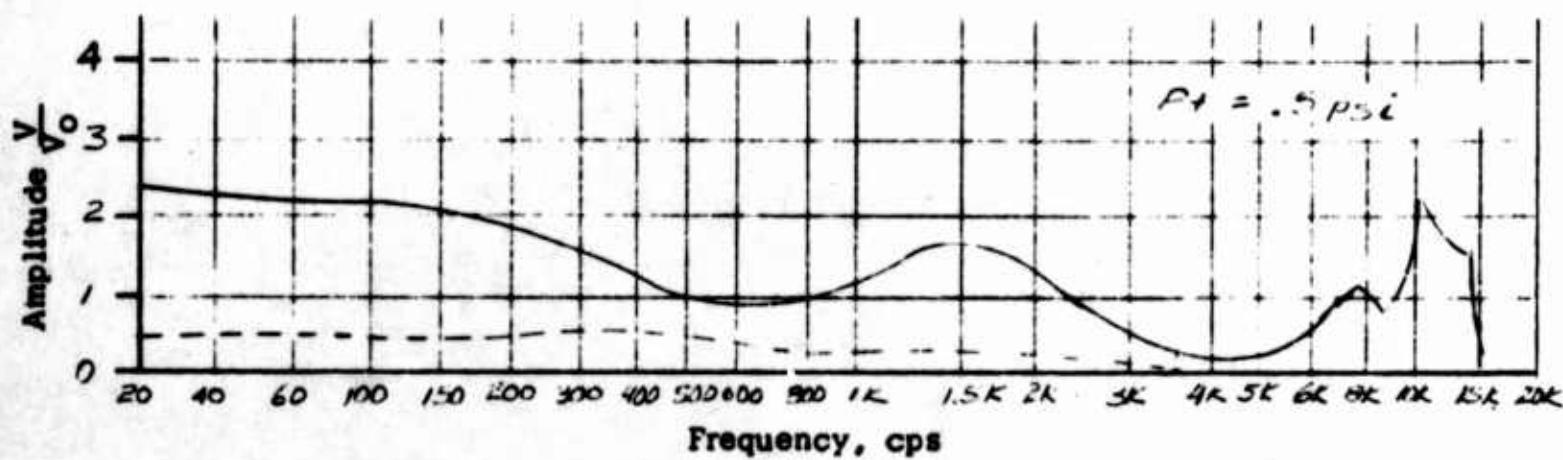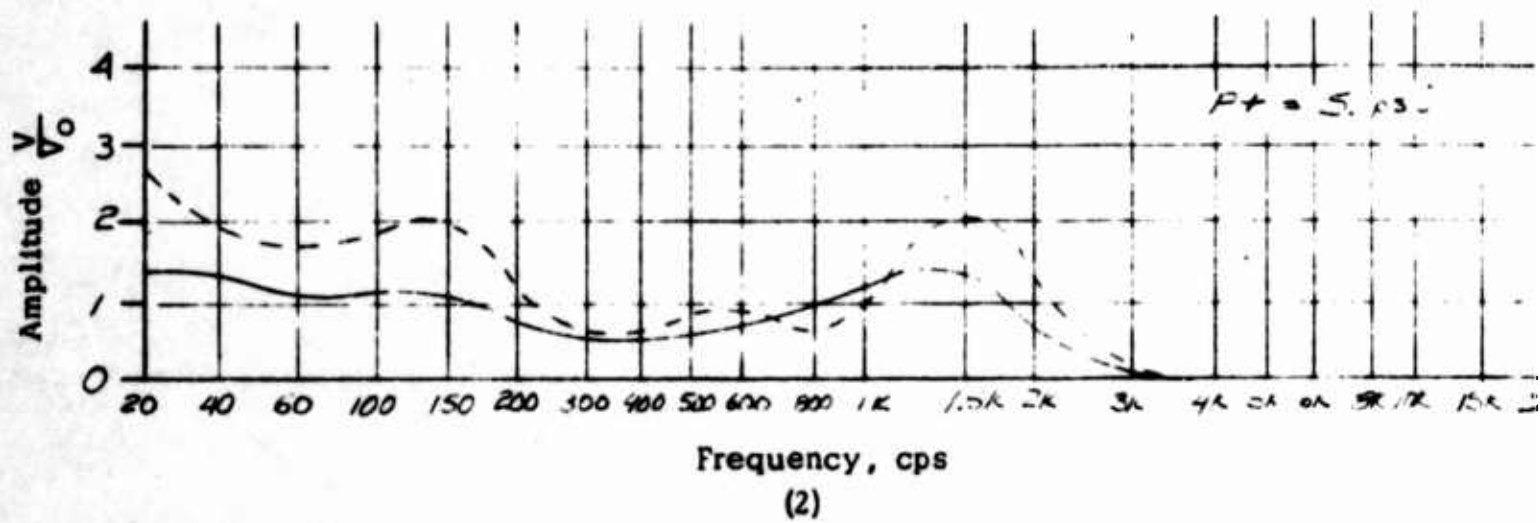

40" Line Length Frequency Spectrum Diagram

276

FIGURE 10

(1)
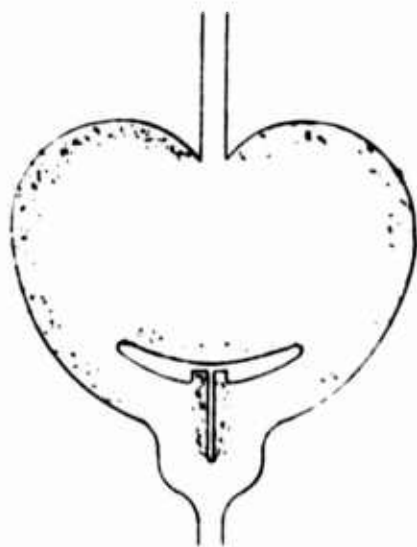
(2)

Filter Configurations with Absorbing Walls

FIGURE 11

Frequency, cps

(2)

Frequency, cps

(1)

278   Frequency Spectrum Diagrams

Harry Diamond Laboratories

Washington 25, D. C.

Acoustic Control of Pneumatic

Digital Amplifiers

by

Richard N. Gottron

Captain, U S Army

ABSTRACT

   The effect of audio-frequency acoustic waves on a pneu-
matic digital unit is considered. Experimental evidence is
presented to show that digital units can be switched with less
acoustic power than pneumatic power. The use of mixing to
reduce high frequency information to a usable range is dis-
cussed and experimental evidence is presented.

INTRODUCTION

   The effect of sound on a free jet has been investigated
extensively, but little work has been done on a confined jet.
There is reason to suspect that sound energy can be used to
control jets. This report discusses some experiments which
show that acoustic energy can be used to control power jets
in pneumatic units such as digital amplifiers and logic
elements.

   Specifically, this report is concerned with the effect
of sound on a jet with an offset wall (fig. 1). This is
closely related to work recently done by Professor Brown of
Notre Dame University, as yet unpublished. Brown discovered
that the separation point on a sphere in a flow field moved
when sound was introduced upstream of the sphere. For this
reason, we concluded that it should be possible to move the
point of reattachment of a jet in a bistable unit.

   Sound impinging on a jet produces periodically a series
of vortices at the exit of the jet, the period being equal to
that of the sound. If the jet is sensitive, Rayleigh states,
"The smallest departure from the ideal... tends spontaneously
to increase, and usually with great rapidity." (Ref. 1) Since
the jets in digital-type pneumatic amplifiers operate in this
range of sensitiveness, it is reasonable to conclude that sound
has considerable effect on digital amplifiers.

   The effect of the acoustic power on the jet is due to
several factors. Sound increases the turbulence of the jet,
causing its flow parameters to change. This change, coupled
with the second-order effects of acoustic streaming and radia-
tion pressure, causes the jet of a digital amplifier to switch
to the opposite output if the sound is injected into the separa-
tion bubble of the unit. Qualitative analysis and experimental
evidence are given for the effect of sound on digital pneumatic
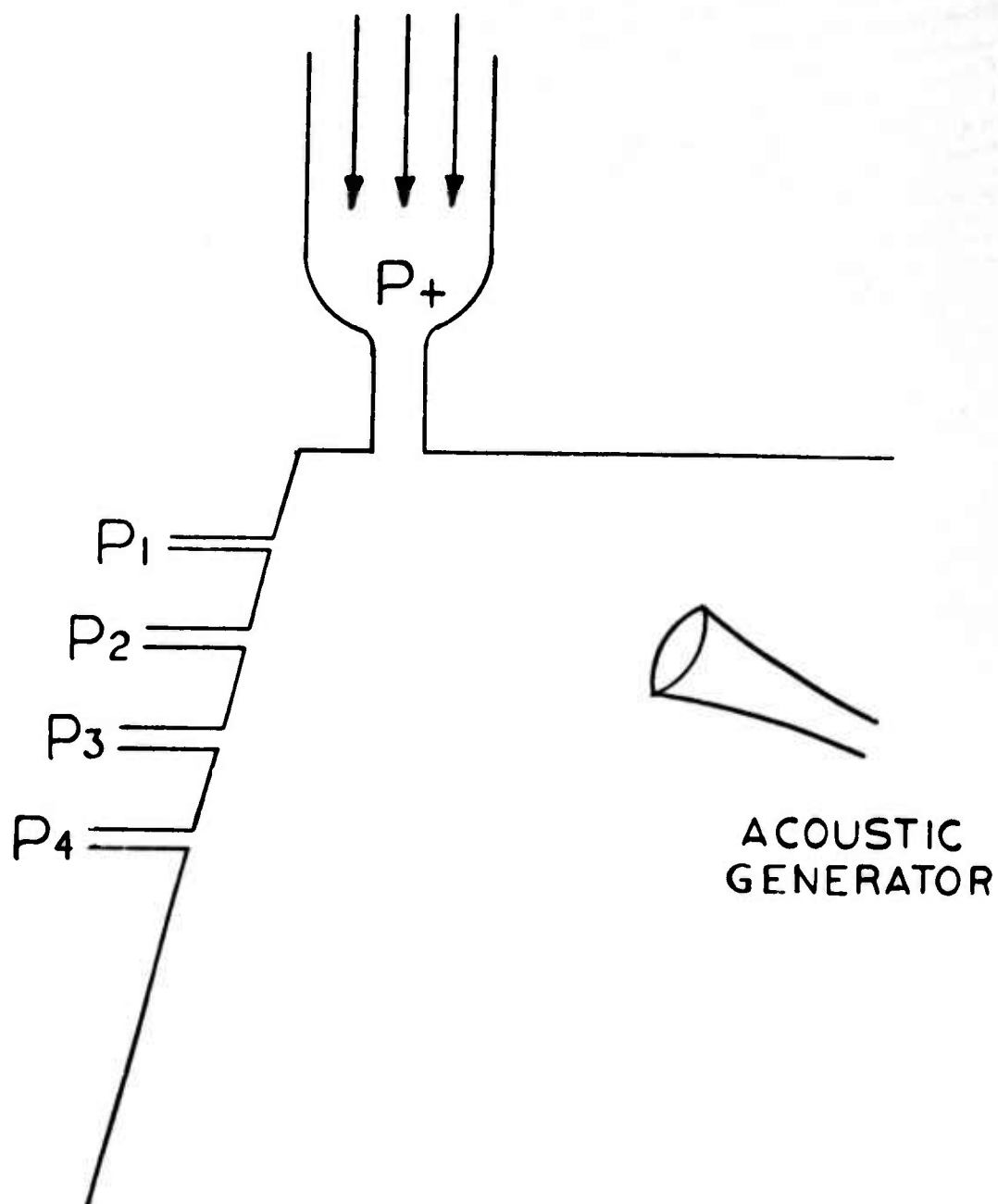amplifiers. The use of acoustic power to flip bistable units

FIGURE 1

is considered in detail, along with the effect of the beat phenomenon obtained when two audio frequency waves mix.

Figure 1 shows an experimental setup. P_t is the jet total pressure. P_1, P_2, P_3, and P_4 are static pressure taps along the offset wall. Thus the point of reattachment of the jet in tests, and any movement of this point are observable. When sound is introduced by use of an acoustic generator, the point of reattachment moves downstream. The distance the reattachment point moves depends on the amplitude and frequency of the sound.

Figure 2 shows the setup for the other experiments described in this section. It consisted of a digital pneumatic amplifier, with an acoustic generator positioned so that sound could be introduced into either the right control or the main input jet of the unit. The control input static pressure, P_s was observed during the test.

With an input pressure P_t from zero to 2.25 psig and with the jet attached to the right output offset wall, Ps indicated a pressure slightly below atmospheric. Whe sound was introduced into the right control, Ps decreased; ΔP, also decreased, indicating some flow from the left output. Ps and ΔP continued to decrease with increasing amplitude of sound until the jet switched to the left output offset wall.

When the flow switched totally to the left output, Ps rose above atmospheric. On further increasing the amplitude of the acoustic signal, Ps again decreased. As Ps decreased, ΔP decreased indicating flow from the right output even though the jet remained attached to the offset wall of the left output.

Sound was also introduced into the flow upstream of the jet. It was observed that increasing the amplitude of the sound decrease ΔP, no matter which wall the jet was locked onto. However, the jet could not be switched by introducing sound in this manner.

Another interesting phenomenon occurred in the bistable unit of figure 2 if the jet is attached to the left output wall. It has been stated previously that sound forces part of the air to be discharged from the right output. Now if the left output is loaded, the jet switches to the right wall as the sound is removed.

EXPERIMENTAL DATA

A bistable unit was setup, as shown in figure 2. The frequency was controlled by an audio oscillator. The acoustic
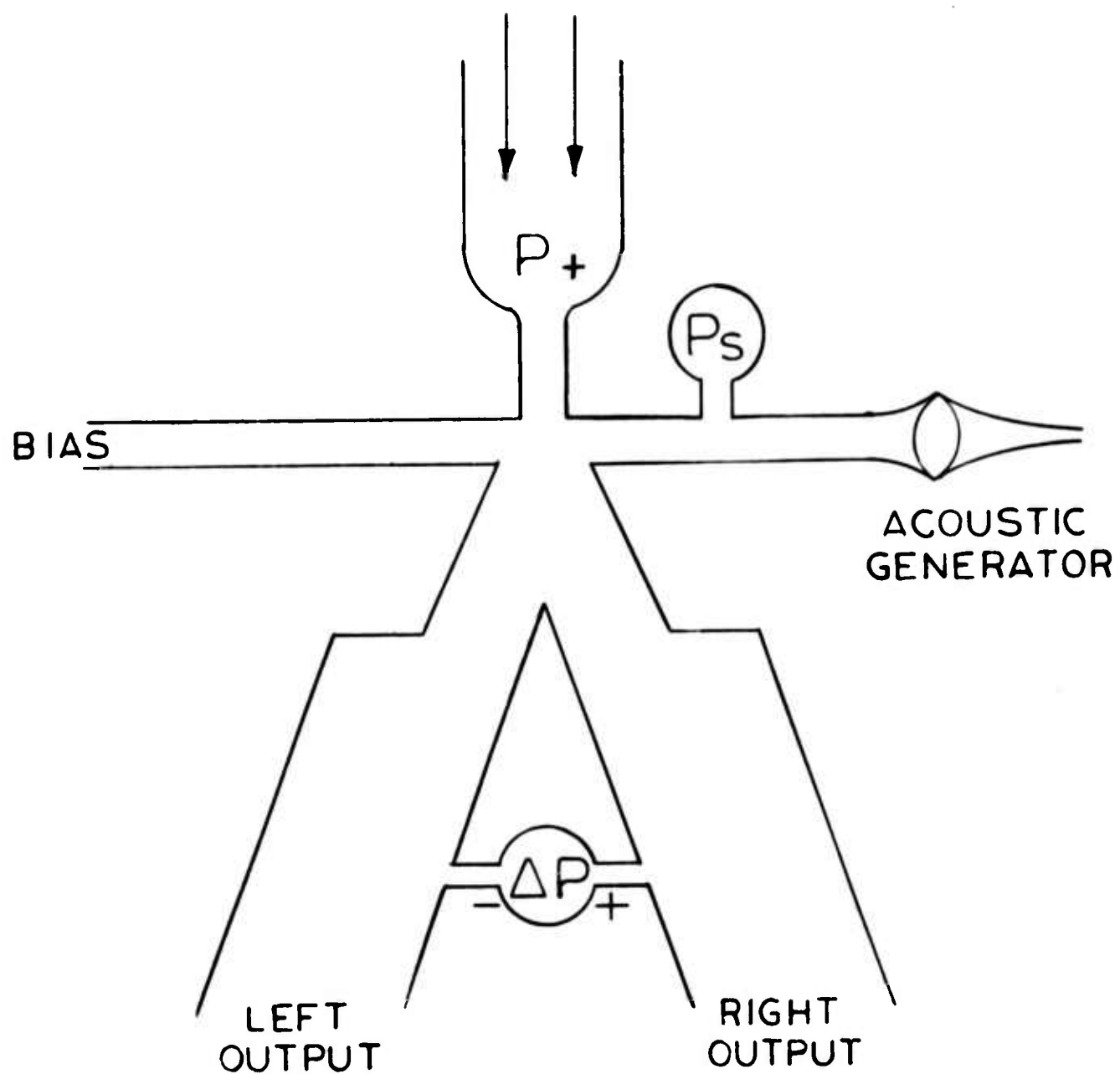
FIGURE 2

generator consisted of an acoustic driver unit. The sound was monitored and measured by placing a microphone in the right control arm in about the same location as Ps. The acoustic generator could be replaced with a flow regulator. A rotometer was placed between the regulator and Ps; thus, the pneumatic power required to switch the digital unit could be measured. This steady state, or "d-c" power was compared with the acoustic power required to switch the unit.

Figure 3 shows the required acoustic (a-c) and pneumatic (d-c) power required to switch the bistable unit under test. The unit has a main nozzle width of 0.936 inches, a splitter distance of 0.711 inches, and an aspect ratio of 15. The power curves (figure 3) are plotted against the main jet pressure and power. The sound frequency was 1818 cps.

There was no bias applied to the left control input. It is interesting to observe the different slopes of these curves. It appears that it would require much less acoustic power than pneumatic power to switch jets of increasing pressure. The set up in figure 2 could switch jets up to 2.25 psig. The limit was imposed due to the limitations of acoustic power available.
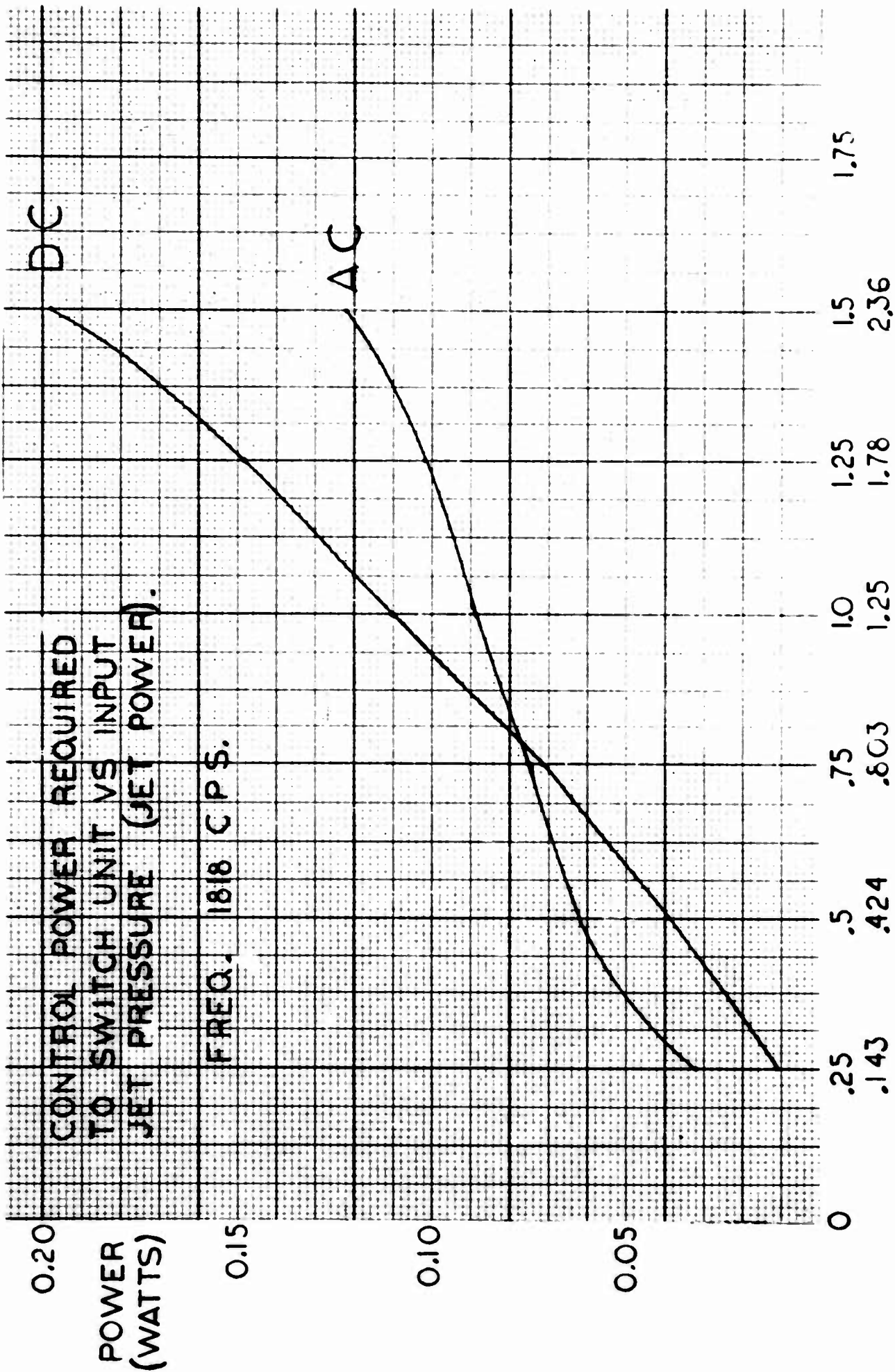
Figure 4 shows the amount of power required to switch a unit at different frequencies, from 500 to 6500 cps. It can easily be seen that, in general, the higher the frequency the less power required.

The loading effects on these units are of utmost importance. If sound cannot cause switching when the output impedance reaches a certain level, then the effect is of limited application. The memory unit of figure 2 was loaded by proportional and digital units. The unit switched when loaded, but it requires an increase of approximately 25% additional power.

APPLICATIONS

Since sound has the effect of moving the reattachment point downstream, it would appear feasible to use this effect to control a logic element (fig. 5). Pneumatic power at pressure P_r was introduced into the main jet of the logic element. After the jet reattached to the right wall sound was introduced into the second input. With both acoustic and pneumatic power applied, the flow was forced out the left output.

If the acoustic driver is replaced with some other sound producing mechanism, the unit in figure 5 could be utilized as an electro-pneumatic transducer; i.e. suppose the driver is replaced with a barium titanate crystal, then energizing the

CONTROL POWER REQUIRED
TO SWITCH UNIT VS INPUT
JET PRESSURE (JET POWER).

FREQ. 1818 C.P.S.

DC

AC

FIGURE 3

P+ PSIG
JET POWER
(WATTS)

POWER
(WATTS)

285

FIG. 4, ACOUSTIC POWER REQUIRED TO SWITCH 0.5 PSIG JET VERSUS FREQUENCY OF INPUT SOUND
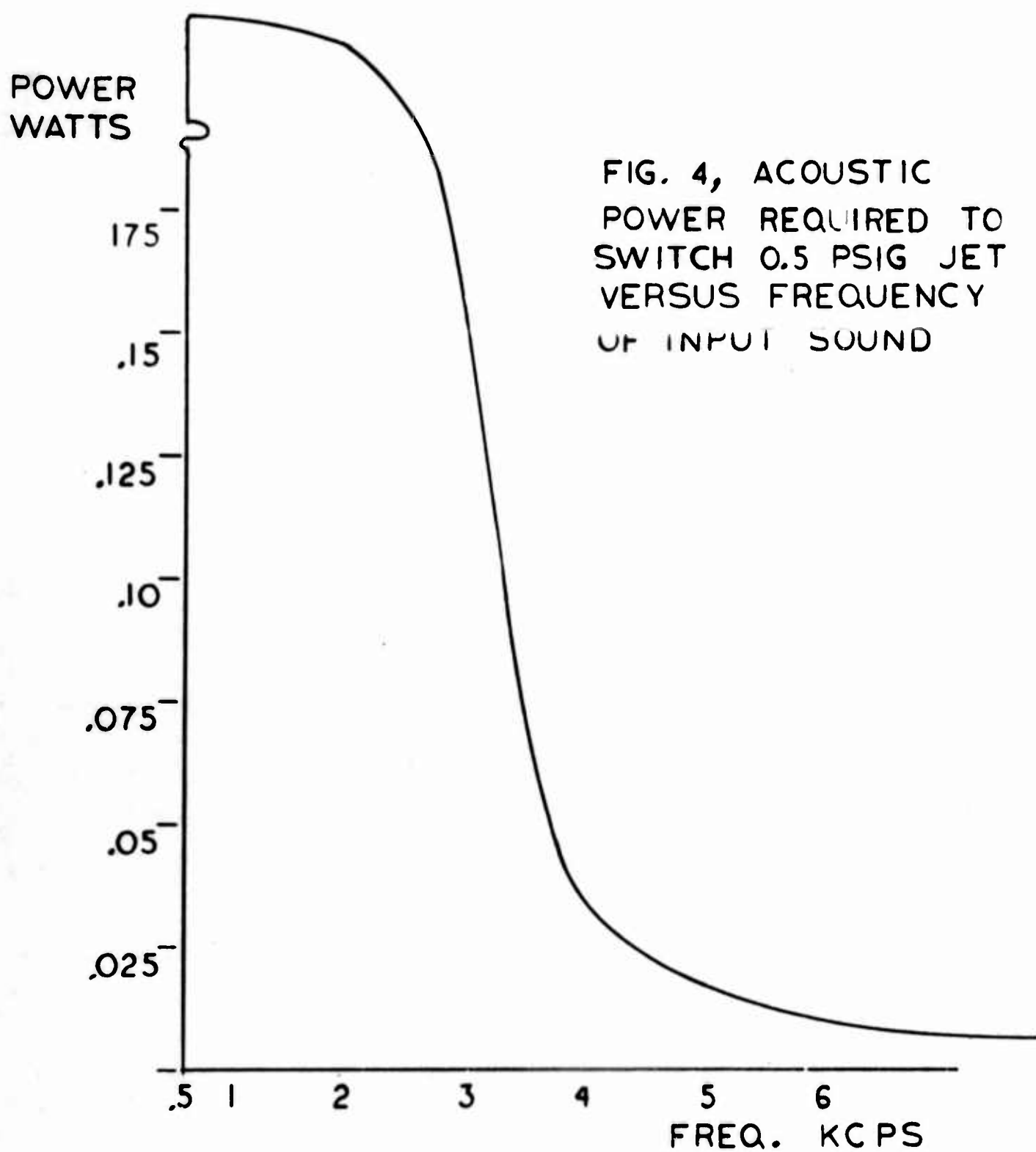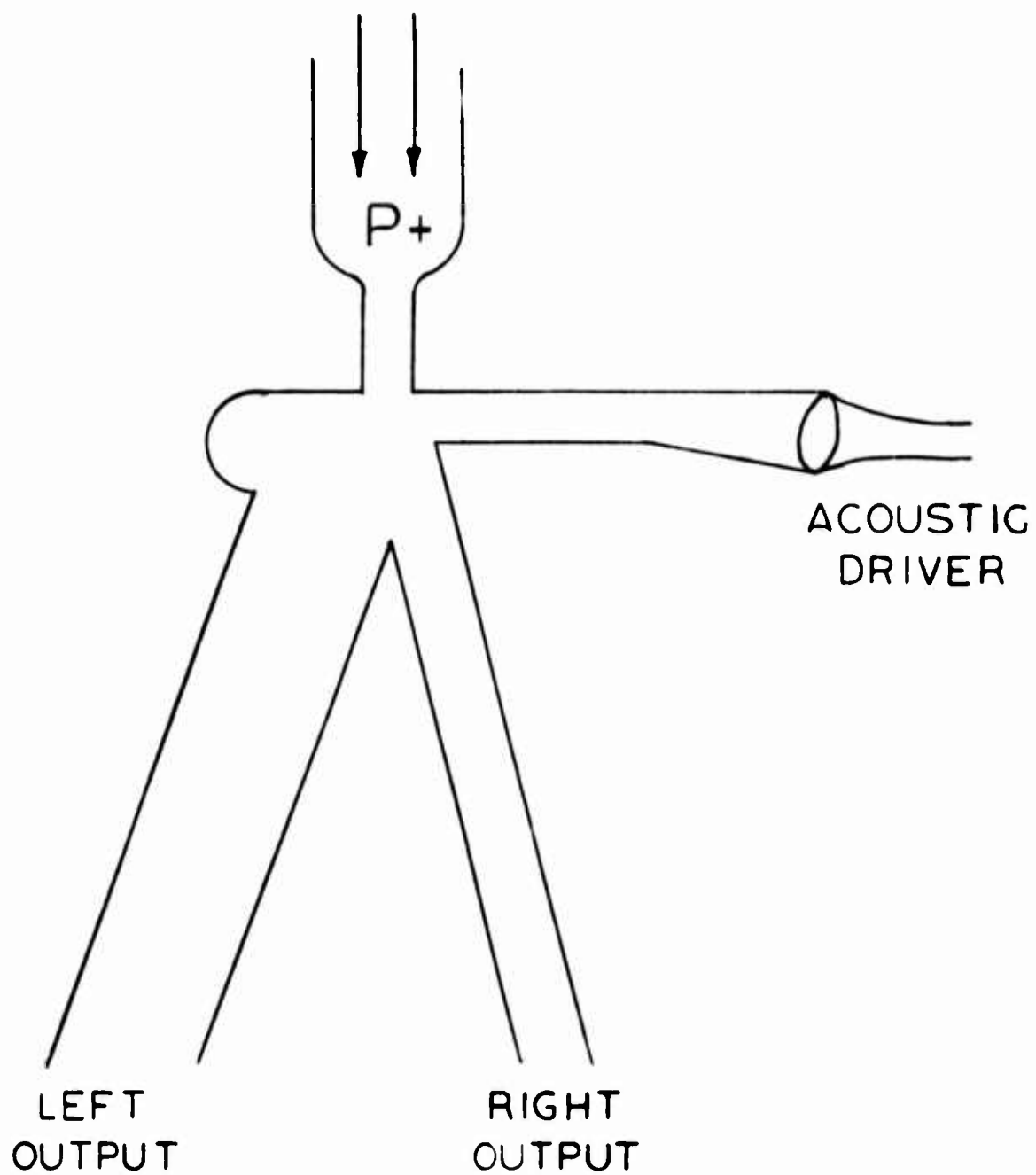
FIGURE 4

ACOUSTIC
DRIVER

LEFT

LOGIC AND UNIT

FIGURE 5

crystal at its resonant frequency will cause the crystal to resonate at this frequency resulting in acoustic waves which in turn will switch the jet.

BEAT PHENOMENON

Pneumatic signal information can presently be generated well into the ultrasonic range. For some pure fluid systems where the signal information is contained in the frequency itself, it is necessary to measure the signal frequency by pneumatic means. However, present day pneumatic counters are limited to about 250 pulses per second. By utilizing the beat phenomenon, a high frequency signal can be converted to pulsations at a lower frequency capable of being counted by present day pneumatic counters.

The beat phenomenon occurs when two sinusoidal pressure wave trains with a near equal amplitude but of slightly different frequency travel in the same direction through the same region. The beats are the maximum amplitude values of the total wave produced by the addition of the two wave train frequencies.

An experiment was designed to determine the range of operation of beat phenomenon, and by utilizing the effects of this sound in a digital unit, to convert the beats to a pulsating frequency signal. This was accomplished by the non-linearities of the digital unit, and the filtering action of the digital unit due to its limited frequency response.

Two acoustic drivers were set up as shown in figure 6. They were driven by oscillators and audio amplifiers. The counters monitored the frequency. The acoustic signals were transmitted down horns to the mixing area, then to the interaction area. The other control input had a slight bias applied to prevent switching to the left output. The output of the system was sensed by a differential pressure transducer and read out on an oscilloscope. The beat frequency was also read out on the oscillograph and oscilloscope. Thus the response of the system to the beats could be observed. Figure 7 shows a typical oscillograph plot.

With the experimental setup shown in figure 6, information was obtained on the range of operation of the system using the beat phenomenon. The number of beats per second possible is dependent on the frequencies f_1 and f_2. Letting f_1 be called reference frequency, f_2 the variable frequency, and α the difference frequency, $\alpha \leqslant 200$ for $f_1 = 500$ cps; i.e., f_2 can vary from 300 cps to 700 cps. At $f_1 = 2000$ cps and $f_2 > f_1$, α can be as large as 700 cps. However, in the total system with the digital unit, the pressure transducer will respond only up to a difference
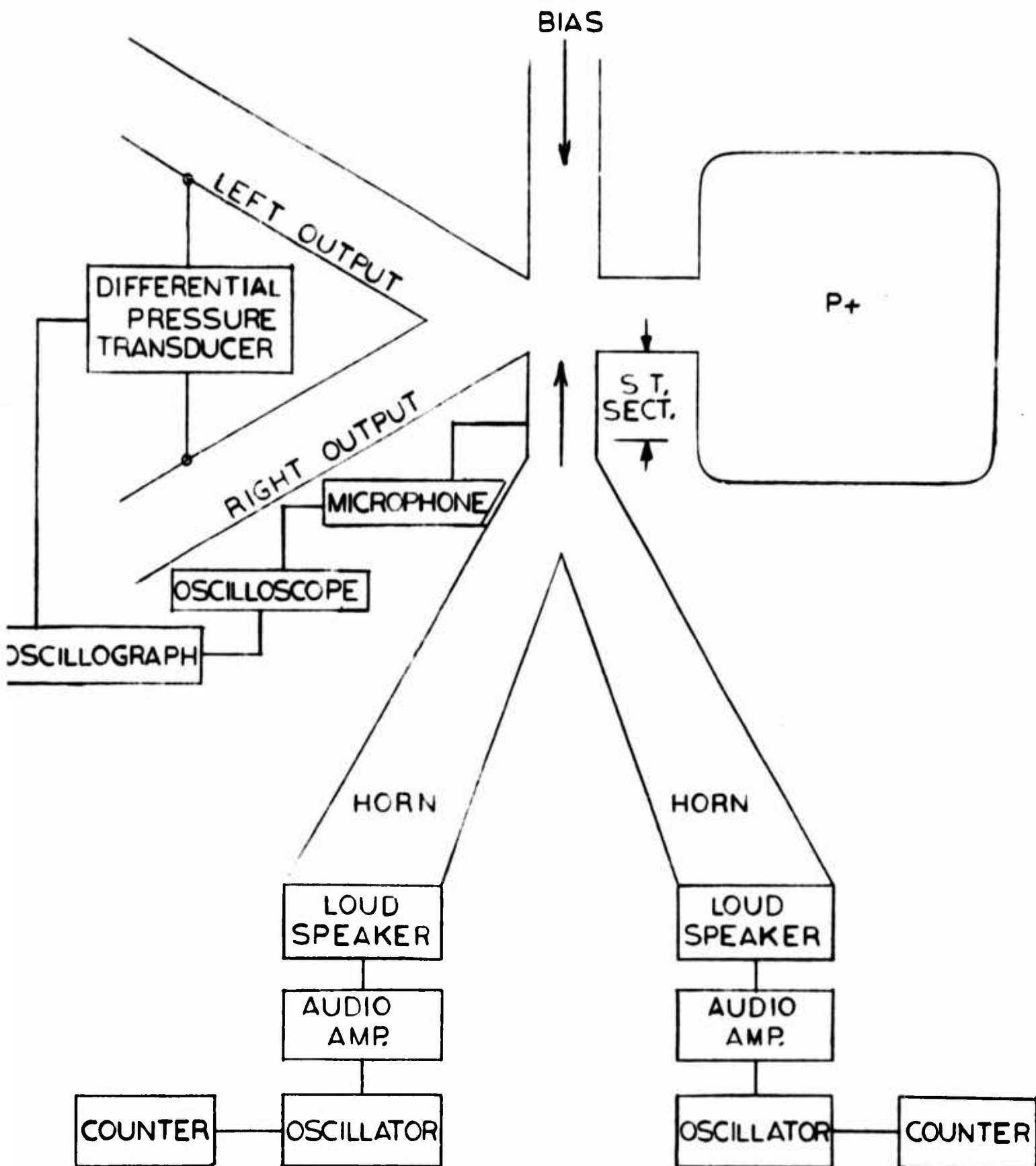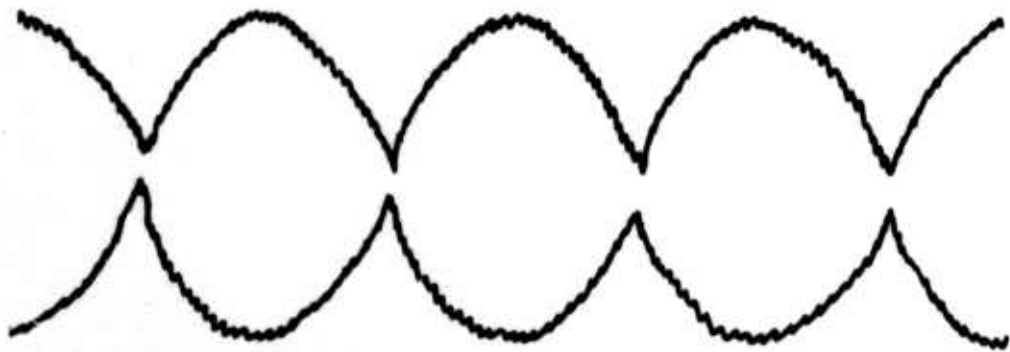
Fig. 6

Time →

FIGURE 7

frequency of 425 cps. This limitation is attributed to the digital element.

It should be emphasized that the output of the digital unit is a pulsating pressure above a reference. It is analogous to pulsating uni-directional current.

CONCLUSIONS

Experimental data were obtained that showed that it required less acoustic energy than pneumatic energy to switch a bistable device. It was also shown that the amount of acoustic power required to switch a bistable unit is frequency dependent.

Several possible applications were considered, such as an electro-pneumatic transducer. Utilization of beats to convert high frequency signal information to a usable range was shown to be feasible.

REFERENCES

1. Rayleigh, J. W. S., "The Theory of Sound," Vol. II, Dover Publications, 1945.

2. Campagnuolo, C., "Experimental Analysis of Self-Maintained Oscillations of a Jet System with a Resonating Cavity," Master Thesis submitted to Georgetown University, Washington, D. C., Sept. 1962.

3. Lindsay, Robert B., "Mechanical Radiation", McGraw-Hill Company, 1960.

4. Gray, Dwight E., "American Institute of Physics Handbook", McGraw-Hill Book Company, Inc., 1957.

5. Brown, G. Burniston, "The Vortex Motion Causing Edge Tones", Proc. Phys. Soc. London, 49, 493, 1937.

6. Nyborg, W. L.; Burkhard, M. D.; and Schilling, H. R.; "Acoustical Characteristics of Jet-Edge and Jet-Edge Resonator Systems," The Journal of the Acoustical Society of America, Vol. 24, No. 3, May 1952.

BASIC REQUIREMENTS FOR AN ANALYTICAL APPROACH
TO PURE FLUID CONTROL SYSTEMS

by

H. L. Fox
F. R. Goldschmied

of

Sperry Utah Company

A B S T R A C T

The first type of pure fluid amplifier is classified as a planar device and some of the associated analytical and experimental problems are discussed. Another type of planar device based on the edge tone phenomena is described and its operation related to the same analytical and experimental problems.

A new approach to pure fluid device design using axisymmetric geometry is discussed. The same set of problems are then related to the axisymmetric class of fluid devices. In particular, it is shown how the focussed jet axisymmetric fluid device greatly simplifies analytical work.

The work of Fromm and Harlow is displayed as a means of solving the Navier-Stokes equations for the time dependent two-dimensional viscous case. The impact of this new approach in device design and analytical techniques is discussed.

TABLE OF CONTENTS

1. Background

The public announcement in 1960 concerning the development of pure fluid amplifiers by scientists of the Diamond Ordnance Fuze Laboratories (now the Harry Diamond Laboratories) heralded a new technology and marked a major breakthrough in the science of control systems. This new technology does not replace the high speed electronic devices technology but pure fluid control systems will replace many current electro-mechanical control systems particularly for applications under severe environmental uses. The fact that a hundred and more scientific groups from industry, government, and universities have staked claims in this new field testifies to the belief in the control system application.

Bounded as the analytical treatment of this new technology is with a challenging set of non-linear partial differential equations, strict mathematical analysis of newly discovered modes of fluid flow is difficult. Thus it is that the pure fluid amplifier design has been largely an empirical approach. The empirical approach has been taken not so much by choice but by the barriers to analysis imposed by the difficulty of solving the Navier-Stokes equations, and by the fact that said equations do not completely describe the turbulent flow field. It is the purpose of this paper to explore one pathway around the impossible barriers of a complete three-dimensional time-dependent analytical treatment.

2. Problems in Current Devices

We begin with a look at the planar pure fluid bistable amplifier and the problems imposed.

Speed. The planar pure fluid flip-flop utilizes a naturally sustained and self-generated transverse pressure gradient across a flat jet of fluid to provide stable curvature of the jet and a type of "wall attachment". Empirical evidence demonstrates that the speed of switching of the "attached jet" is not as fast as the physics of the flow would suggest. For example, a fluid flip-flop with a

295

0.030 inch jet width and an aspect ratio of six, switches (in the ordinary case) in about one millisecond. The same jet flowing against a wedge in the naturally "switching" edge tone effect produces an equivalent "switching" in less than one tenth of this time period. A high-speed movie study of smoke flow-visualization shows that the switching phenomena takes place in three phases:

a. The first phase is the detachment of the jet from the wall and it can be described by quasi-steady state entrainment theory because it is comparatively slow.

b. The second phase comprises the path of the jet away from either wall and in the vicinity of the divider; here transient non-linear and acoustical effects govern the jet behavior. The jet has been observed to oscillate about the center and also to return to the starting side.

c. The third phase is the reattachment to the other wall; similarly to the first phase, it is comparatively slow.

Gain: The gain of the planar pure fluid bistable device is not as high as one would desire. This statement is true irrespective of the definition of gain. In the practical sense, "useful gain" can be defined as the number of identically sized flip-flops which can be driven or switched by a single flip-flop when all elements are operated in the same fashion. Under these restrictions, it is difficult to drive three devices with one device and very difficult to obtain consistent results with a "fan-out" of four.

Interconnections: The "useful gain" as defined is limited by the interconnection problems. Most pure fluid devices (with the notable exception of Auger's "turbulence amplifier" Reference 1) are difficult to interconnect. Nature seems almost perverse in that the combination of the fluid pressure head and velocity head are usually present in the wrong ratios. Thus, while fabricating a single device may be accomplished with a kitchen knife and a bar of soap, interconnecting even the most carefully fabricated devices is a challenging problem.

Part of the interconnection problem is related to providing the proper amount of flow, and part of the problem is acoustic in nature. Admittedly some workers, while wearing ear plugs in the laboratory, will suggest that there is no particular acoustic problem.

3. Some Problems Alleviated

Other problems exist, which will be mentioned below. For the moment, consider a planar device which resolves the problems of speed, gain, and interconnections. Starting with a basic premise that the speed of switching would perhaps be limited by the equivalent switching speed of the natural oscillation of the edge tone effect, the authors investigated the edge tone effect. The edge tone effect is illustrated in Figure 1. Here a thin jet of fluid is directed against the lip of a wedge. The naturally present acoustic feedback mechanism provides the energy necessary for a sustained oscillation. The effect is most notably used in organ pipes. (For further edge tone information see Powell, Reference 2). It was discovered that the edge tone effect could lead to a planar bistable device as illustrated in Figure 2. Here the jet is dynamically stable between the wall of the wedge (or divider) and the adjacent cusp. The "interaction region" in this device looks much like the interaction region of a proportional amplifier. The function of this rounded region is to accomodate the shedding of a vortex when the jet is switched. Let us consider this device in terms of the three problems listed above.

Speed. If it is acceptable to relate the upper switching speed of a pure fluid device to the equivalent speed of switching of an edge tone oscillation, then this device switches in less than two cycles of the thus defined upper speed limit. This speed of switching is more than ten times the speed of a comparable wall-attachment bistable fluid amplifier.

Gain. The gain of this high-speed fluid device in terms of the ratio of power jet flow to control jet flow is two to three times better than the wall-attachment

device. In other words, devices with flow gains of ten to thirty are relatively easy to obtain.

<u>Interconnections:</u> The relatively large interaction region of the high-speed fluid amplifier allows for the "OR"ing and "AND"ing of inputs almost anywhere along the periphery of the interaction region. As a matter of fact, the inputs can be introduced perpendicular to the plane of the device into the interaction region. While this fan-in capability of the high-speed device is superior to the wall attachment amplifier, the fan-out capability holds no immediate superiority. In other words, any asymmetric loading introduced into the downstream legs of the amplifier changes its basic characteristics in a similar fashion to the wall attachment device.

However, it was determined that if the higher velocity flow near the wedge was not disturbed unduly, that fluid flow could be taken from the side of the duct downstream from the cusp in the manner depicted in Figure 3. This led to a reasonably satisfying fan-out scheme and the ability to interconnect these devices by the simple expedient of "piping" outputs to inputs.

4. Planar Device Common Problems

As enticing as the above planar device may appear to the reader who has had experience with only one type of pure fluid amplifier, it pays to look a little deeper. Therefore, let us return to a discussion of problems which the planar wall attachment device shares with the high-speed device.

Other problems with planar fluid amplifiers:

<u>Analysis:</u> While the planar name of the class of devices suggests a two dimensional flow, such is not the case. Historically in fluid dynamics, the reduction to practice of two-dimensional flow has been difficult to achieve. In some interesting cases, the aspect ratio of the two dimensional jets have been of the order of 30 or more, Reference 2. Let us therefore recognize that the flow in

298

a planar device is NOT two dimensional but is characterized by complex three dimensional flow. Figure 4, adapted from reference 3, illustrates better than words the complex three dimension flow patterns in even a simple rectangular elbow. Where the flow is not two-dimensional, the solution of the Navier-Stokes equations becomes overwhelmingly difficult (at least in the near future) for any but the steady-state or quasi-steady state cases.

Heretofore, the bulk of the fluid dynamics analysis has been concerned with the steady state or quasi-steady state cases. However, the demands of the technology of the design and development of pure fluid amplifiers and pure fluid control systems require an earnest interest in the transient phenomena of fluid motion. Regrettably, the planar devices do not readily lend themselves to transient flow analysis.

Scaling Problems. Dear to the heart of the fluid-dynamicist are those non-dimensional numbers so little appreciated by many of the engineering community. These dimensionless numbers relate various parameters in such a way that scaling of a particular flow mode or flow condition can usually be assured if the ratio of the flow parameters remains unchanged. For example, the Reynolds number (Re) is the ratio of flow velocity times a linear dimension to the kinematic viscosity of the fluid used. To maintain the same flow pattern when changing to another fluid having a différent kinematic viscosity it is necessary to change the fluid velocity or the geometry of the device (or both) to maintain the same Reynolds number. Other "numbers" which are important to the fluid system designer are the Mach number (M), the Prandtl number (Pr), and the Strouhal number (St).

Sealing. The planar pure fluid devices are sensitive to any fluid flow along the top or bottom plates which may result from improper sealing. The device characteristics can be markedly changed if "leakage" occurs between portions of the power jet and the control jet. Characteristics of the devices are further changed if any

sealant oozes into critical portions of the element, particularly into the interaction region.

In general it is necessary to maintain the same Re and M numbers in order to achieve a constant St number and therefore insure linear time-scaling of fluid phenomena. (The Reynolds number is the ratio of flow velocity times a linear dimension to the kinematic viscosity. The Mach number is the ratio of flow velocity to the velocity of sound in the fluid. The Strouhal number is the ratio of frequency times a linear dimension to the flow velocity or alternatively, the ratio of flow velocity times the period of an event to a linear dimension. All of these numbers are dimensionless.) This can be accomplished and scaling is no great problem provided that the fluid devices are not so complex that they lie outside the two-dimensional fluid-dynamics assumptions which determine the model from which the scaling parameters (those nice dimensionless numbers) are derived.

There is some evidence that the planar pure fluid bistable devices are not a member of the class of devices for which the simple scaling laws can be fully met.

Fabrication. Planar devices are not easy to fabricate in small size. True, there have been elaborate graphs and charts extolling the low power consumption of planar devices with very small jet widths. But existing fabrication techniques are not adequate to reduce to practice these nice sounding extrapolations. For example, the Corning Glass "photoceram" fabrication techniques utilize a "standard" jet width of 0.015 inches for the power input jet. (The authors agree that this technique of fabrication is the best yet developed for uses up to 500°C). At this size fairly good yields (in terms of predictable device characteristics) can be maintained. Some etching techniques have produced workable devices with jet widths of 0.005 inches but not with high yields in terms of desired device characteristics.

It should be pointed out that the planar type devices are very sensitive to changes of geometry of particular portions of the interaction region. This fact

300

accounts for the difficulty of obtaining consistent device characteristics in small size elements.

In addition, it is recognized that the power consumption of a device to be used in logical circuit arrays should be low. This low power consumption can be achieved by the use of smaller jet widths, and therefore, the fabrication of small devices is highly desirable. It is to be recognized however, that the smaller devices will operate in a different flow regime because of the decrease of Re and corresponding change of St. Thus miniaturization cannot be undertaken purely from the mechanical fabrication viewpoint.

5. The Challenge

In the paragraphs above, we have presented seven major problems facing the designer of planar fluid amplifiers. In addition, we have demonstrated how to overcome about half of these problems. Investigators who have followed our path will at this point have been confronted with a choice of alternatives. The alternatives are: Do we continue with further expensive research on devices which are less than satisfacory from the fluid-dynamics point of view, or do we look for a new device approach?

We chose the latter course.

6. The axisymmetric approach.

An experienced fluid-dynamicist knows that if he desires to achieve two-dimensional flow (or at least flow which can be handled with two rather than three parameters), that the solution may be found in an axisymmetric approach to the problem. For example, the space between a cylinder nested in a pipe might provide the two dimensional equivalent of flow between two extensive flat plates. Similarly, the axisymmetric equivalent of a thin narrow jet would be an annular jet. For example, the jet made by pumping fluid through a pipe whose end is restricted with a right circular cylinder, would be an annular jet. Due to the circular nature of

the jet there are not boundaries affecting the flow which are equivalent to the top
and bottom plates in the planar type of fluid devices. The aspect ratio of such a
jet would be essentially infinite, as far as creating secondary-flow vortices and
other undesirable perturbations such as boundary-layer pressure leakage. However,
the aspect ratio of such an annular jet, defined as the circumference divided by
the width of the annulus, is important for classification of the flow response to
either the two-parameter cylindrical or cartesian Navier-Stokes equations. A high
aspect-ratio flow (> 200) will respond very closely to the cartesian analysis,
while a low aspect ratio flow (< 100) will require the cylindrical analysis.

Another immediately obvious advantage of an axisymmetric approach to a pure
fluid device would be the ease of fabrication. In other words, fabricating an
annular jet reduces to boring and turning operations. And, obviously, boring and
turning operations can be accomplished with an order of magnitude improvement in
accuracy over standard milling, routing, or filing techniques.

One of the authors, F. R. Goldschmied, was successful in inventing a pure fluid
amplifier which appears promising in meeting the requirements for a suitable "end-
run" around the problems of existing planar type devices. This device (focussed
jet NOR gate) is depicted in Figure 5 and has both a proportional and a digital
embodiment; it belongs to a new class of components which we choose to call the class
of axisymmetric fluid amplifiers.

7. <u>Fluid Amplifier Problems in the Focussed Jet Device</u>

Axisymmetric devices in general and the focussed jet device (see Fig. 5) in
particular demonstrate some advantages in resolving the problems of the planar class
of pure fluid devices. Before discussing the point, however, the authors would like
to make it quite clear that they have a belief in the usefulness of a variety of
devices. This device will provide advantages in some applications and the planar
devices may prove more advantageous in other applications. We are not claiming a

302

panacea for fluid amplifier problems. However, we do claim an approach to device design which can be handled analytically with today's techniques and today's computers.

Speed. At the time of writing of this paper, the speed of the device had not as yet been fully determined. However, the very thin jets of fluid appear to offer considerable improvements in switching time as compared with the planar type devices.

Gain. Again, the thin jets available with the axisymmetric devices provide for potential high gain performance. The early exploratory work performed with devices having jet widths of 0.003 inches to 0.010 inches indicate that interconnections having fan-in. and fan-out of four is easy to achieve.

Interconnections. In the digital focussed jet device (basically a 4 input NOR element as depicted in Figure 5) the outputs and the inputs can be readily "piped" together to provide any desired logical combination. In addition, the focussed jet device provides a natural acoustic by-pass at the output "collector" and the device can be made with sufficient gain so that an acoustic by-pass can be utilized on the control input. This capability of interconnection places this device in the same category as Auger's Turbulence Amplifier (Reference 1) insofar as interconnecting reliability is concerned.

In the above three "problem areas" the focussed jet device has not too much to offer as an improvement to the "high-speed" device. It is in the following four problem areas, however, that the focussed jet device appears capable of providing an excellent end-run around serious problems:

Scaling. For proper time-dependent scaling according to simple parameters such as Re and St, it is required that both the model and the prototype display essentially a two-parameter flow-field. If the flow is a complex three-dimensional one, then scaling will require an impractically large number of parameters; in other words it will not respond to single values of Re and St. The difference in complexities of

the planar devices and the focussed jet device are made readily apparent in Figure

The planar device requires six ratios y/t, d/t, w/t, s/t, L/t and Re, to define its

operation over a range of parametric changes. The focussed jet devices requires but

three ratios d/t, w/t, Re, for a similar parametric study (assuming in both cases

θ to be constant). As seen from Figure 8, we are dealing only with the basic flow

configuration for a NOT amplifier. If for instance a parametric study of switching

times is to be undertaken for a given input signal, then the Strouhal Number

$(St = \frac{UT}{t})$ may be plotted against the Reynolds Number $(Re = \frac{Ut}{\nu})$ for the corresponding

range of geometric ratios. For the axisymmetric device, the results may be plotted

on four sheets of paper; for a corresponding test program on the planar device, 250

sheets would be required because of the three additional geometric ratios.

Fabrication. Figure 6 illustrates the basic pieces that are necessary in making

an array of axisymmetric logic elements. The arrows illustrate the points which

have critical dimensions. Note that all critical dimensions can be fabricated with

either turning or boring operations (or by grinding of materials difficult to bore

or turn.) Tape controlled jig borers are capable of maintaining tolerances of 0.00

inches in hole location in "x" and "y" and the same tolerances in drilling or boring

operations. Thus a 0.002 inch wide jet can be fabricated with as much ease as can

a planar device with a 0.020 inch jet.

Sealing. The focussed jet device is not sensitive to "leakage". There is no

sealing problem of plates over a routed, etched, or molded element. If there is

some leakage around the shoulder of the device where the body is supported by the

supporting plate, the result is a little loss of fluid. This statement is generally

true for other types of axisymmetric elements.

Analysis. By far the most important attribute of the axisymmetric device is

that it is amenable to two-dimensional (or two-parameter) analytical investigation

using the Navier-Stokes equations. As a result, the design of the fluid device can

be performed by analytical means rather than by the slow, laborious, and costly cut-and-try methods of the empirical approach.

In early days of electronics, steady state solutions to circuit problems came first. These were followed by transient solutions to circuit analysis. This same pattern of events should be expected in the developing technology of pure fluid amplifiers. However, the authors will point out techniques by which the transient nature of the flow in axisymmetric devices can be determined analytically as a part of an iterative technique which will also converge on the steady-state solution.

8.   The Navier-Stokes Equations.

The Navier-Stokes equations of fluid motion date from approximately 1827 and are non-linear partial differential equations. The non-linear terms provide the analytical explanation to the seemingly irrational flow modes which may be observed in many   practical fluid dynamic cases.

Furthermore the equations are valid up to some critical Reynolds Number, beyond which the flow becomes turbulent. For turbulent flow, there are the Reynolds equations which yield no mathematical solution because turbulence introduces more variables than there are equations. Traditionally, simplifying assumptions are made, in order to reduce the turbulent variables.

The analysis of time-dependent viscous-flow (laminar) corresponds mathematically to the problem of solving numerically a fourth-order partial differential equation, in three independent variables, containing non-linear terms.   The most extensive attempt to solve numerically a problem of time-dependent two-dimensional incompressible viscous flow is probably that reported in 1963 by Fromm and Harlow at the Los Alamos Scientific Laboratory (Refs. 4 and 5).

It is the techniques of Fromm and Harlow upon which we can build a case for the solution of the transient behavior of the pure fluid focussed jet device. First, our axisymmetric device qualifies as being amenable to the two-dimensional analysis

305

due to the essentially infinite aspect-ratio of the annular jet. Second, for the development of an optimum low power element, we are definitely interested in the lower Mach number regime and the lower Reynolds number regime where the flow can be treated as essentially incompressible, but is very definitely viscous flow. And finally, we are interested in the transient behavior of the jet as it switches. Or, in the case of the analog element, we are interested in the signal output phase shift as a function of the frequency of the control flow signal (essentially a Bode plot).

Figure 7 illustrates the work of Fromm and Harlow as applied to the development of the von Karman vortex street on the downstream side of an obstacle. The views shown here are taken from photographs of the display of an automatic plotter as it plotted the data from an electronic computer solution of the Navier-Stokes equations.

Work being performed at the Sperry Rand Research Center and at the Sperry Utah Company has resulted in significant applications of the time-dependent solutions of the Navier-Stokes equations to selected fluid flow problems. At Sperry Utah Company we have been concerned with the transient behavior of the axisymmetric focussed jet device, while at the Sperry Rand Research Center, Dr. Robin Esch and his group have not restricted themselves to this particular device. In both cases (particularly with Dr. Esch's group) notable contributions have been and are being made to these relatively new analytical techniques.

Before one launches vigorously into the numerical analytical attack on the Navier-Stokes equations, some of the difficulties should be noted. First, it is necessary to have available a relatively large electronic computer. For example, the sequence of pictures shown in Figure 7 are selected from a run which produced 1,000 pictures in developing the fully established flow. This represents about two hours on a Univac 1107 or an IBM 7090.

It should also be mentioned that the boundary conditions which must be established to obtain a solution, present challenging problems and have not (at the time of writing) been completely solved. The solution of some of the problems requires considerable skill on the part of both mathematician and fluid-dynamicist.

The iterative process which leads to a convergence of a solution over a large number of grid points for each small interval in time provides a tremendous output of data. It is suggested that an automatic plotter be used to reduce the data to pictorial or graphical form. It is further suggested that this plotter be operated in real time in keeping with the computer output so that if the program "blows up", the computer can be stopped with the consequent saving in computer time.

And, of course, the investigator must have means for checking the computed results in the laboratory to insure adequacy of the analytical work.

9. **Expected Results from Analytical Work.**

Certain beneficial results are to be expected from a proper analytical approach to device design. The Fromm and Harlow work demonstrated that not only could the Navier-Stokes equations be solved for a complex transient flow condition but that the display of the solutions gave a better insight into the formation and shedding of vortices than had been obtained with years of experimental work.

It is expected that the current analytical program will lead to a better understanding of the switching phenomena in pure fluid devices and therefore to a better understanding of interconnection problems.

Once a suitable program for demonstrating the transient nature of the flow for a given device configuration has been proven, it then becomes easy to vary parameters in the computer and observe the results. In this fashion, a short run on the computer will replace weeks of device fabrication and test in the laboratory. This procedure will allow for the complete investigation of the changes in device parameters and the resulting device characteristics. Optimum device design for selected functions

307

is an expected result. Device design then becomes a rapid operation on the computer and plotter with the resultant savings of many dollars in laboratory work.

Certainly, this analytical approach to pure fluid device design is a much more satisfying approach (to the scientist) than is the empirical study of device characteristics.

Successfully overcoming the problems inherent in making time-dependent solution of the Navier-Stokes equations will yield useful design results for both the transient and the steady state conditions. The time dependent solutions will provide information on the transient flow behavior and the resulting convergence to a complete solution will provide the steady state flow behavior. Therefore, it is possible in this new technology to provide (at least for selected types of devices) information on both transient and steady state flow behavior early in the development stages.

Of prime importance is the reduction in the time necessary to exploit a new technology and provide for the rapid design of selected control systems to meet military and commercial requirements.

Let not the reader feel that the design approach discussed herein will replace the empirical work in fluid dynamics. Far from it. But the reduction of some portions of the design problem to analysis will enable the few well trained fluid researchers to concentrate on the thousand and one other facets of this new technology which need development.

10. The Future.

We who are working in the new technology are best equipped to extrapolate our present technical achievements into the future. Wrong as our forecast may become due to the impact of some new invention, it is of value to help the reader gain a view of the future applications of pure fluid devices.

The future holds new highs in reliable performance of low and medium speed fluid control systems. Many current electro-mechanical tasks will be accomplished in the coming months and years by pure fluid or near pure fluid systems. Some of the more demanding tasks under extreme environmental conditions will be accomplished reliably by pure fluid systems. Nuclear reactor control systems, cryogenic control systems, and control systems for industrial processes where temperature extremes or corrosive materials make control systems short-lived, will be going "fluid".

There have been many among us who have predicted very low costs for fluid control systems; who have predicted pennies or less per component; and who have hailed fluid systems as the great benefactor to the cost-effectiveness programs of several agencies. Such forecasts have not included an overly conservative prediction of how the developmental cost of pure fluid technology is to be included in the price of delivered hardware. It is the judgement of the writers that the research and development costs of pure fluid systems will be more than is required for the equivalent developmental costs of a similar electro-mechanical system. Why? Because, pure fluid systems represent a new and sophisticated technology. Logically these developmental costs can be borne only by systems which cannot be properly controlled by any but pure fluid systems, because of environmental conditions.

Another factor which will slow the advent of the highly economical system is the lack of trained engineers and technicians to do the developmental work. The commercial market for pure fluid devices is exciting, but it is the author's opinion that the military and space requirements for special purpose systems will require all and more of the current few skilled investigators in pure fluid devices.

Nevertheless, there is a future for the low cost system, or better, there is a low cost system for the future. These low costs will be seen first in high volume simple control systems, later in simple air operated digital computers and eventually

in a host of high volume "man-in-the-loop" control systems on aircraft, automobiles boats, household appliances, machine tools, and toys.

But for this year and next, don't become too excited about one. mil jets, penny gates, and 100,000 cycle oscillators. But do become excited about those difficult to mechanize control systems which you require to function reliably under adverse environmental conditions. Fluid systems are for you -- today.

LIST OF REFERENCES

1. R. N. Auger, "Turbulence Amplifier Design and Application", page 357. Proceedings of the Fluid Amplification Symposium, Vol. 1, October 1962. Diamond Ordnance Fuze Laboratories, Washington, D. C.

2. Alan Powell, "On the Edgetone", The Journal of the Acoustical Society of America, Vol. 33, No. 4, April 1961, page 395.

3. Stanitz, Osborn, and Mizisin, "An Experimental Investigation of Secondary Flow in an Accelerating, Rectangular Elbow with 90° of Turning", NACA TN 3015, October 1953.

4. J. E. Fromm and F. H. Harlow, "Numerical Solution of the Problem of Vortex Street Development", Physics of Fluids, Vol. 6, 1963, page 975.

5. J.E. Fromm, "A Method for Computing Nonsteady, Incompressible, Viscous Fluid Flows", Los Alamos Scientific Laboratory, Report LA-2910, May 1963.

6. C. E. Pearson, "A Computational Method for 2-Dimensional Time-Dependent Viscous Flow Problems", Sperry Rand Research Center Report SRRC-RR-64-8, 1964.

310

FIG. I   THE EDGETONE EFFECT
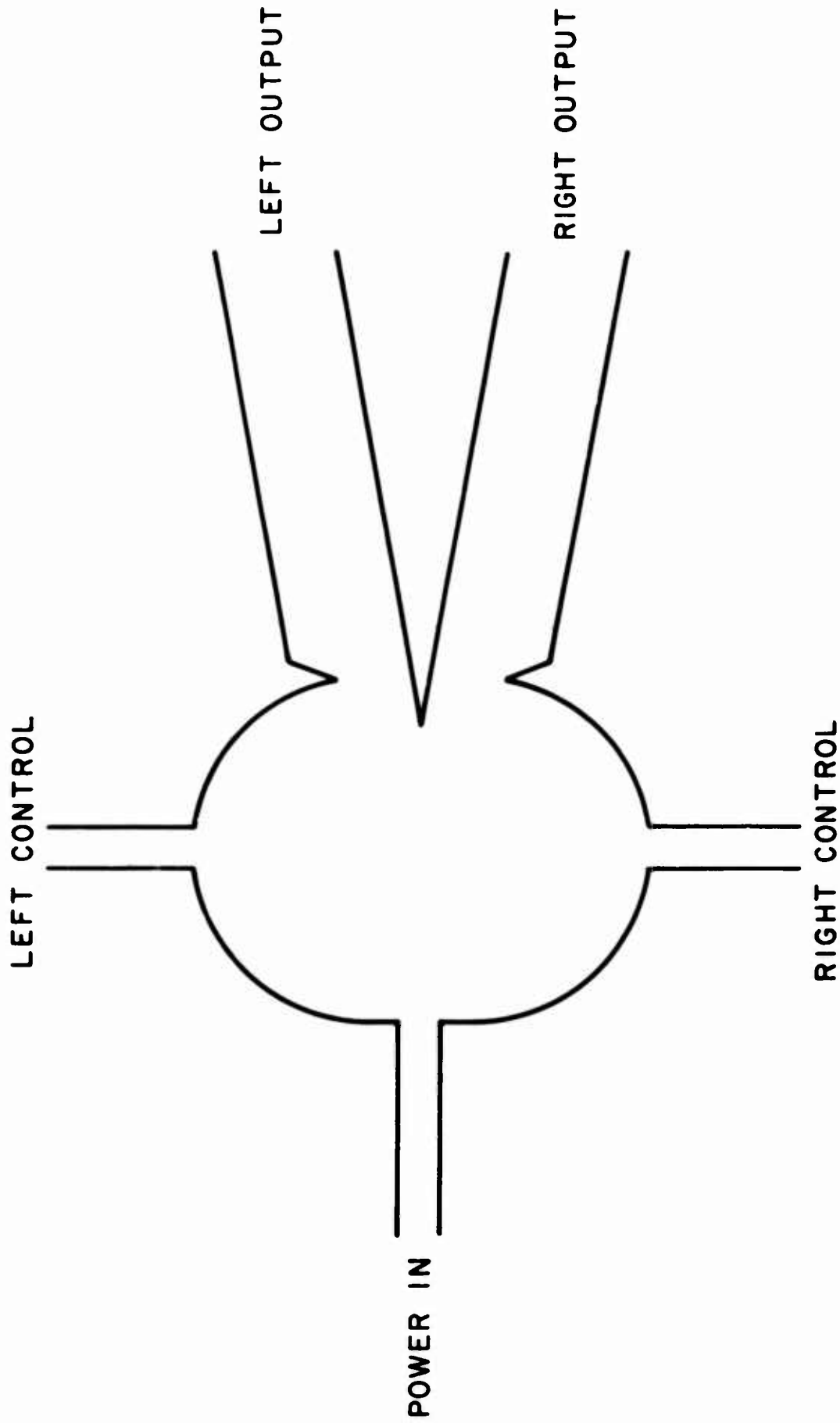
Fig. 2 HIGH SPEED FLUID FLIP FLOP

MAX. FLOW VELOCITY

DETAIL A ENLARGED
SHOWING VELOCITY PROFILE
OF FLOW

DETAIL A
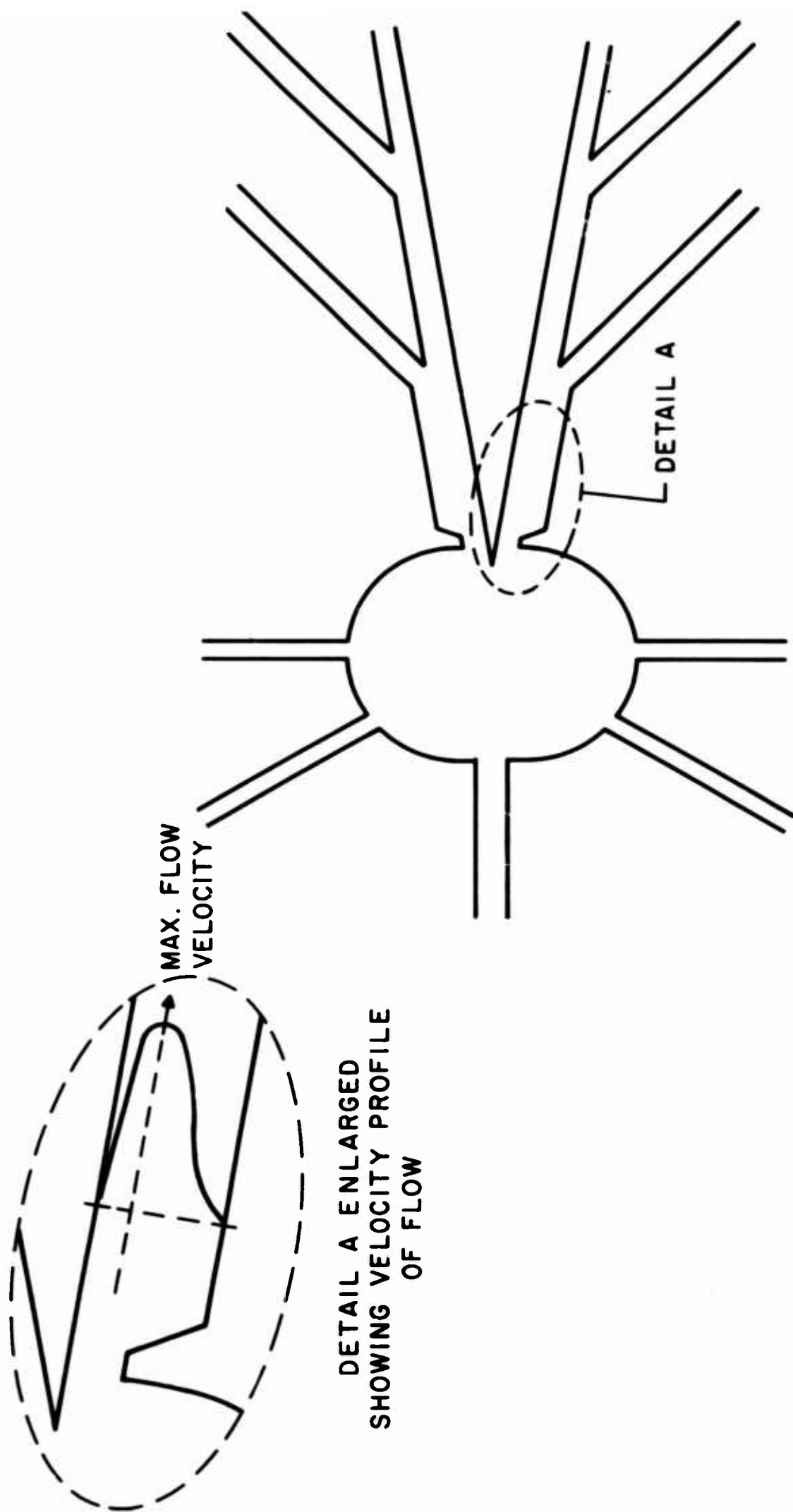
Fig. 3   MULTIPLE INPUT-OUTPUT DUCTS

313

BOUNDARY-LAYER
FLOW AT WALL

IDEAL FLOW IN TWO-
DIMENSIONAL ELBOW

U
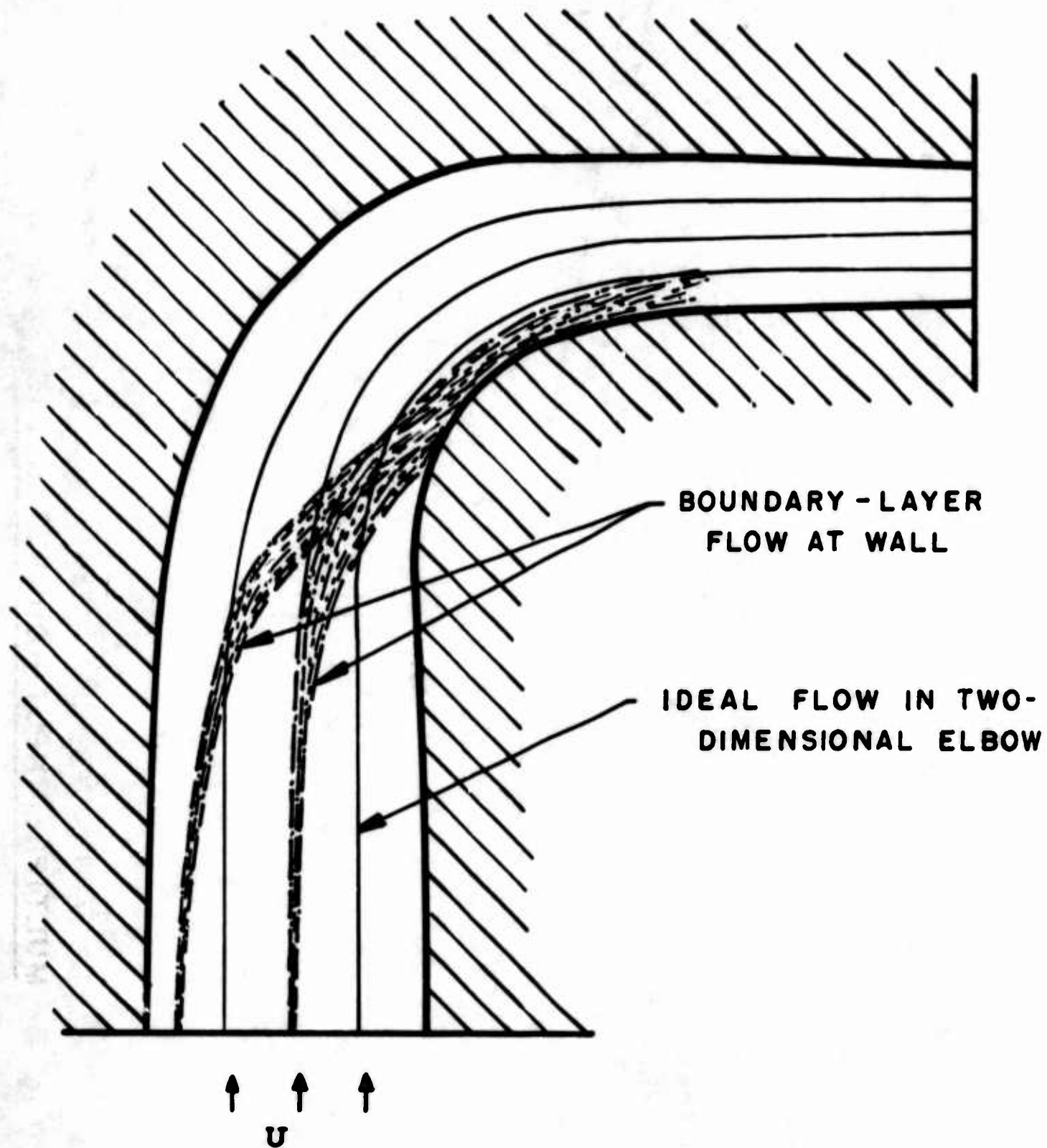
Fig. 4

RECTANGULAR ELBOW-WALL BOUNDARY-LAYER DRIFT

OUTPUT
(FANOUT OF 4)

SUPPORTING
PLATE

60° POWER
ANNULAR JET

FLUID
SUPPLY
CHAMBER

CONTROL ANNULAR JET

SUPPORTING
PLATE

FOUR "OR" INPUTS
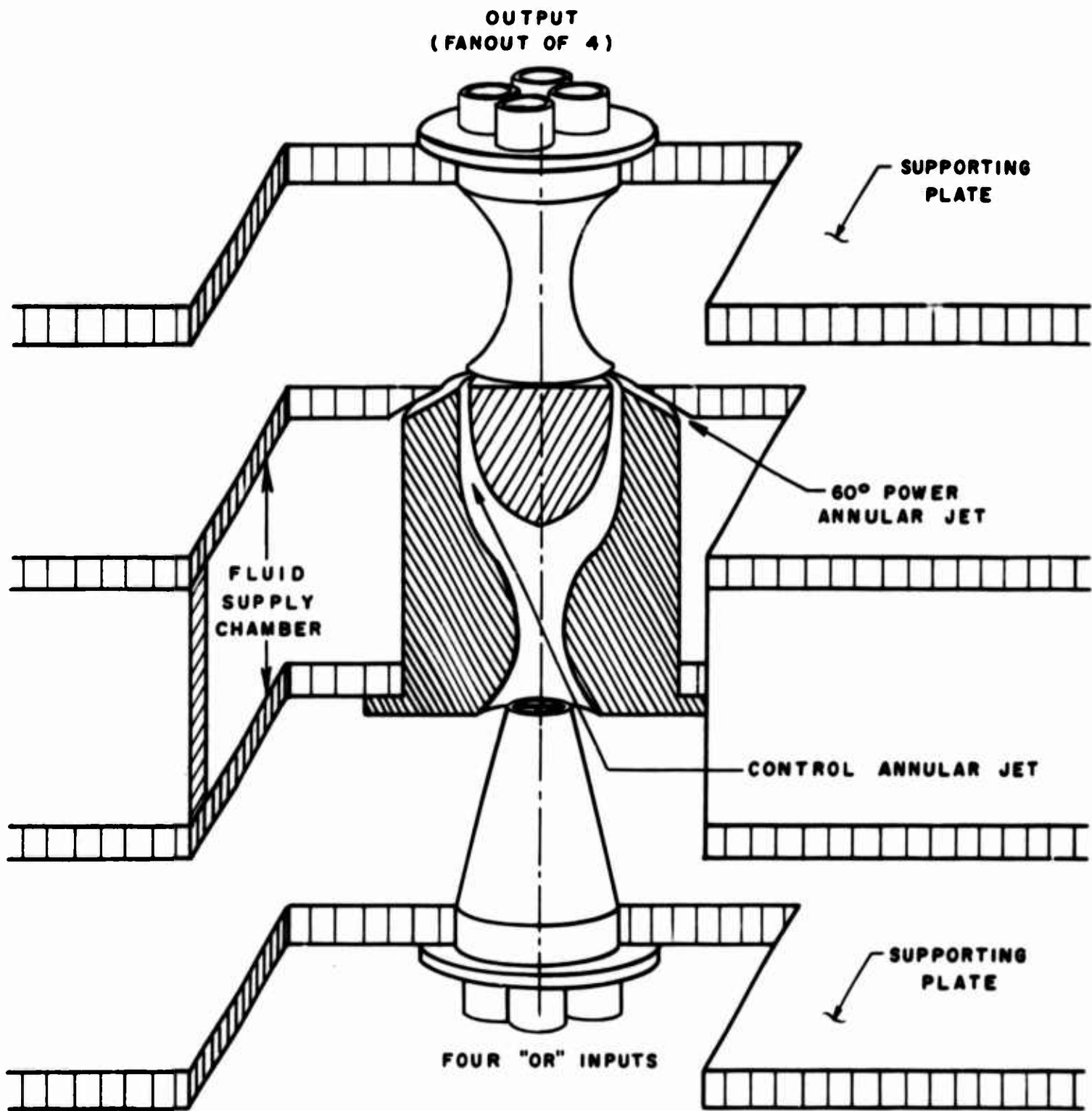
Fig. 5   FOCUSSED-JET LOGIC DEVICE
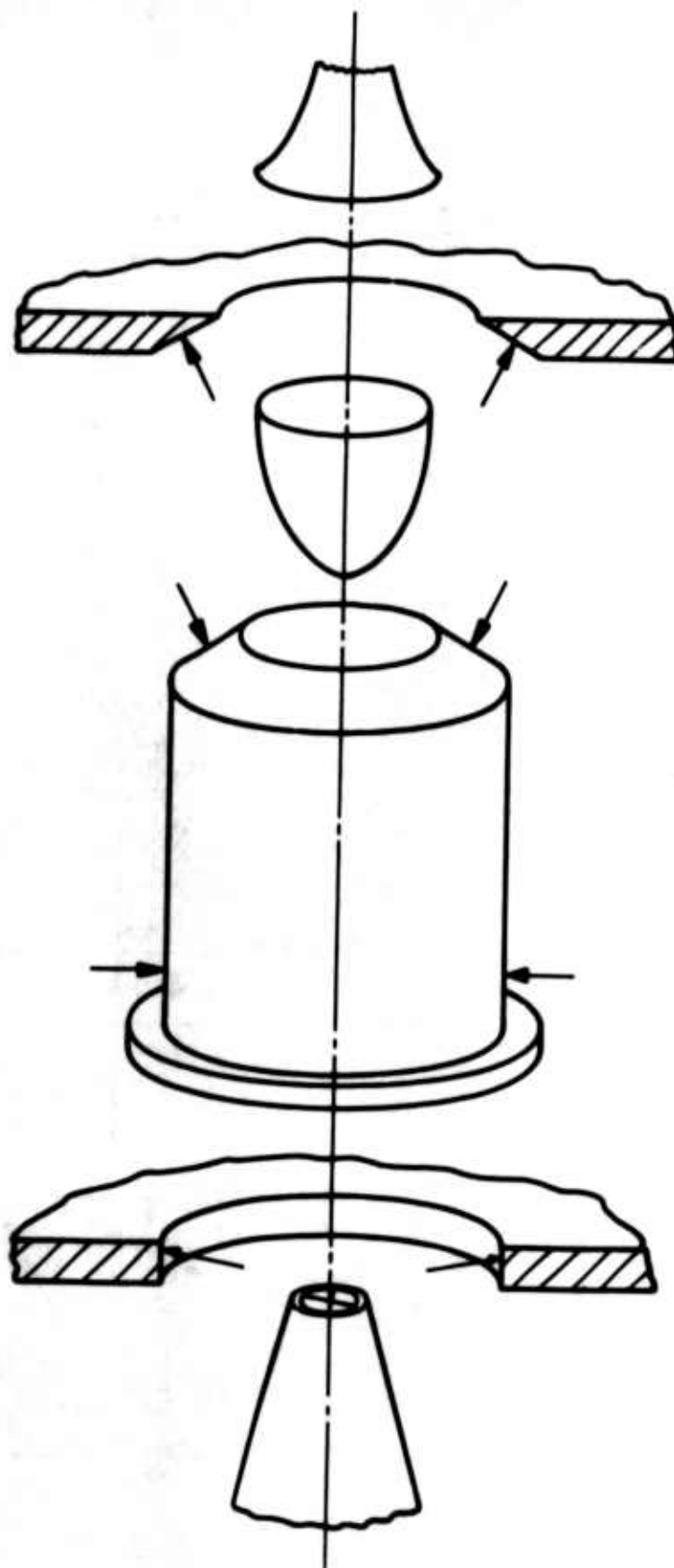
FIG. 6   Exploded view of focussed-jet device

Fig. 7A

Fig. 7B

318
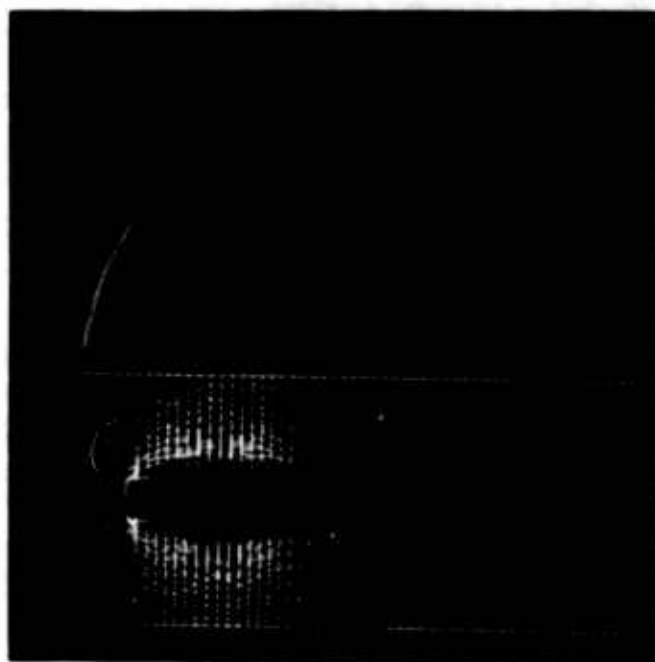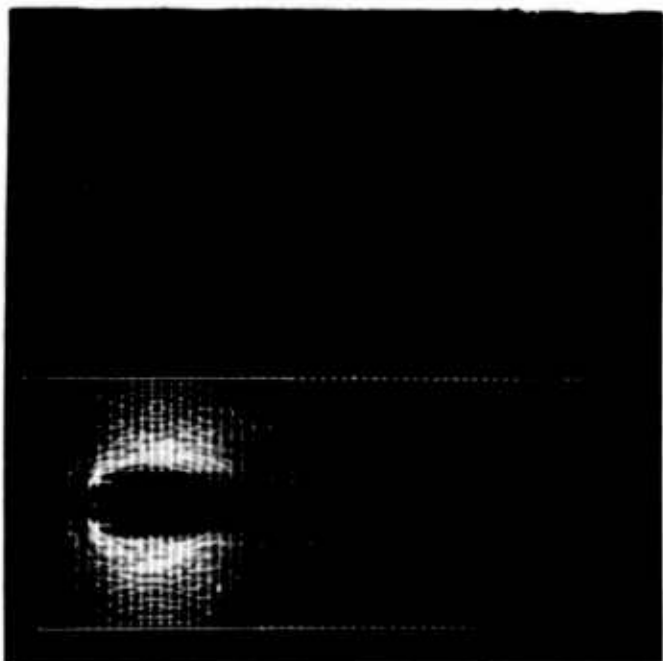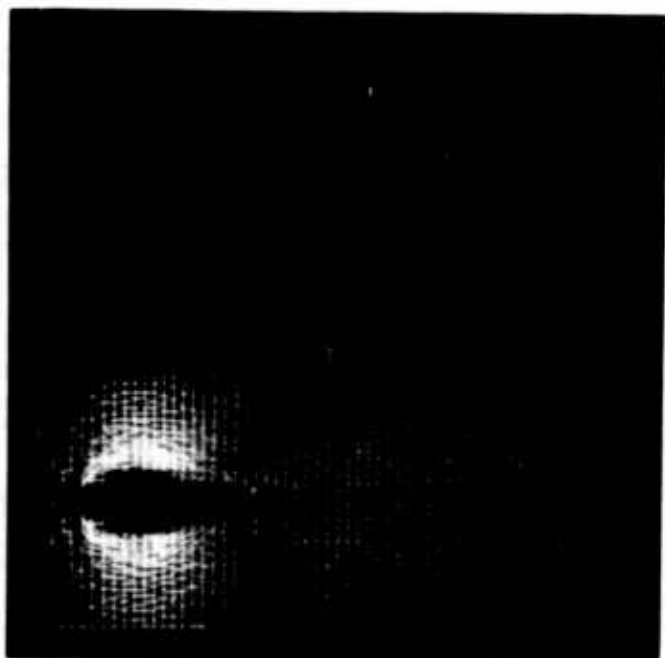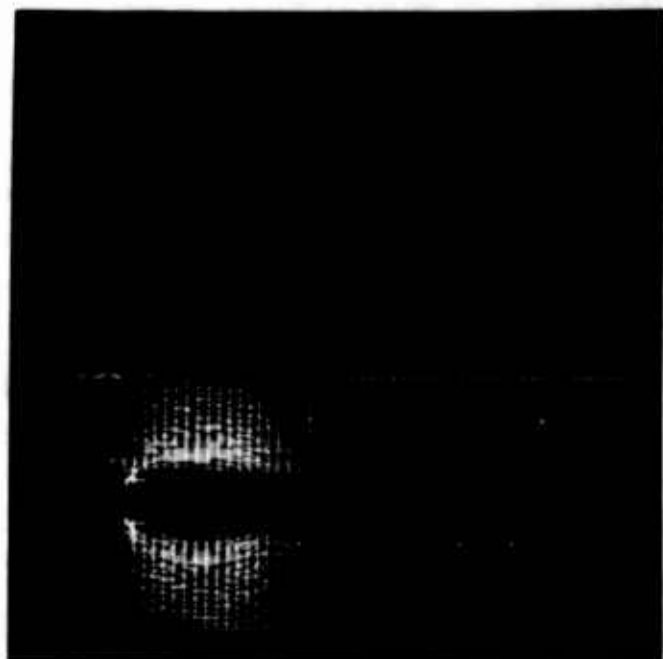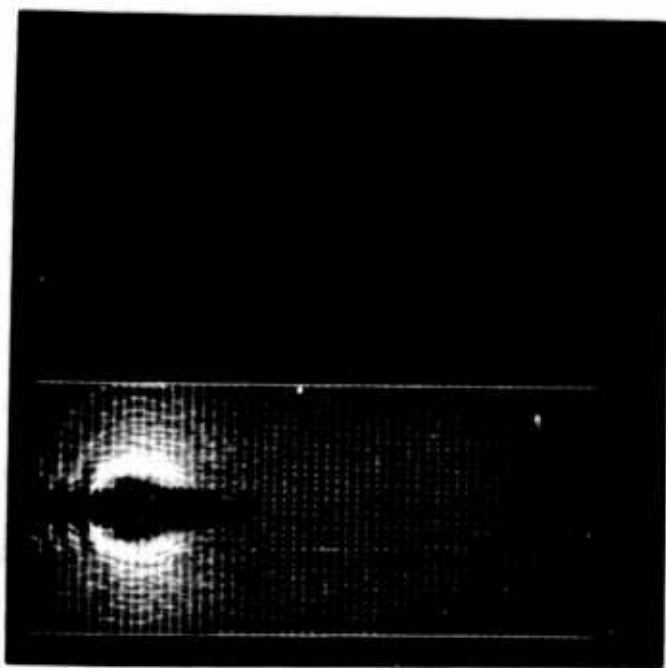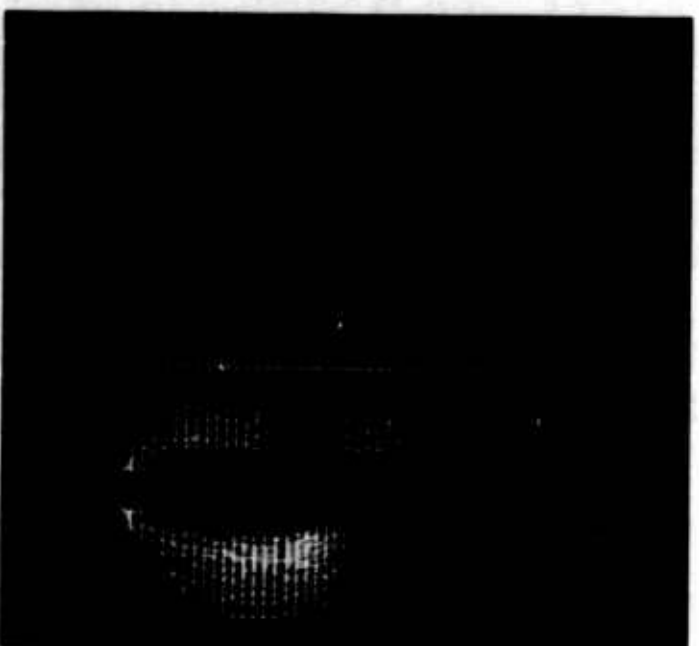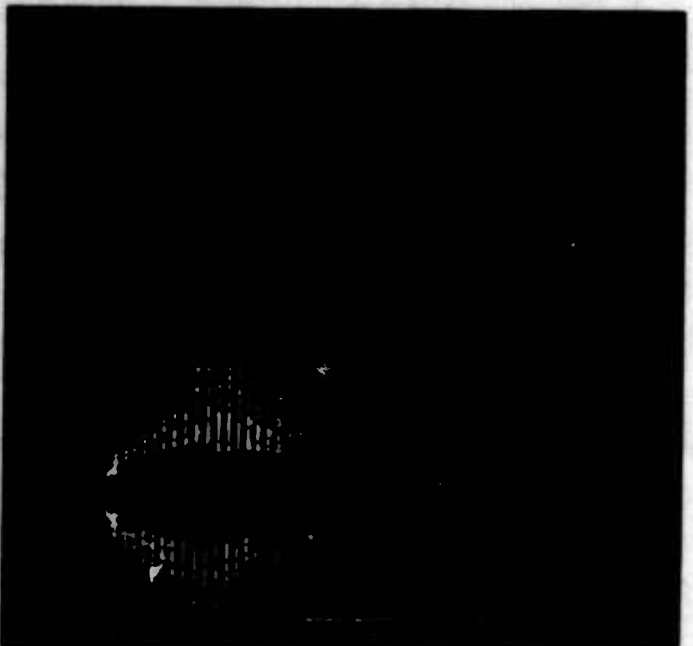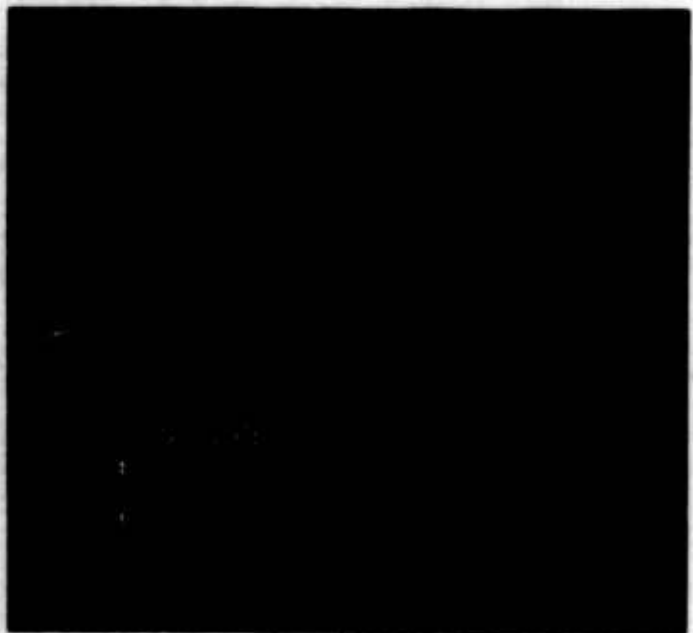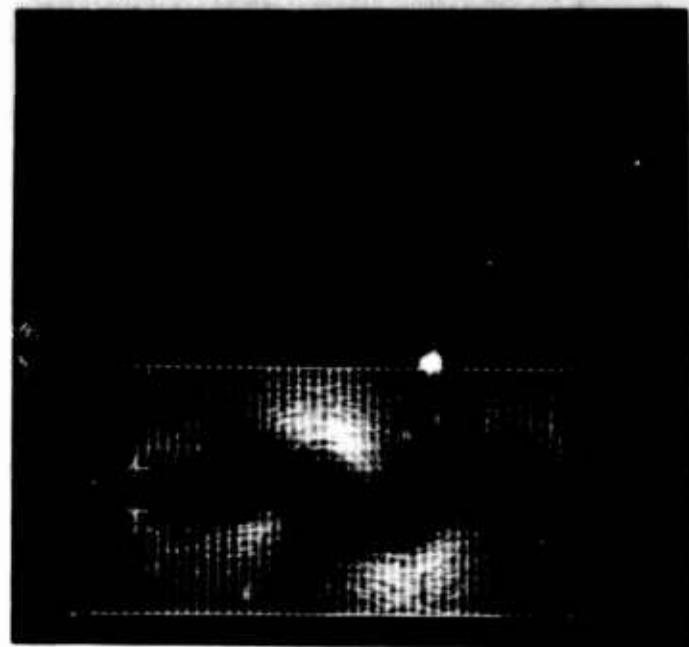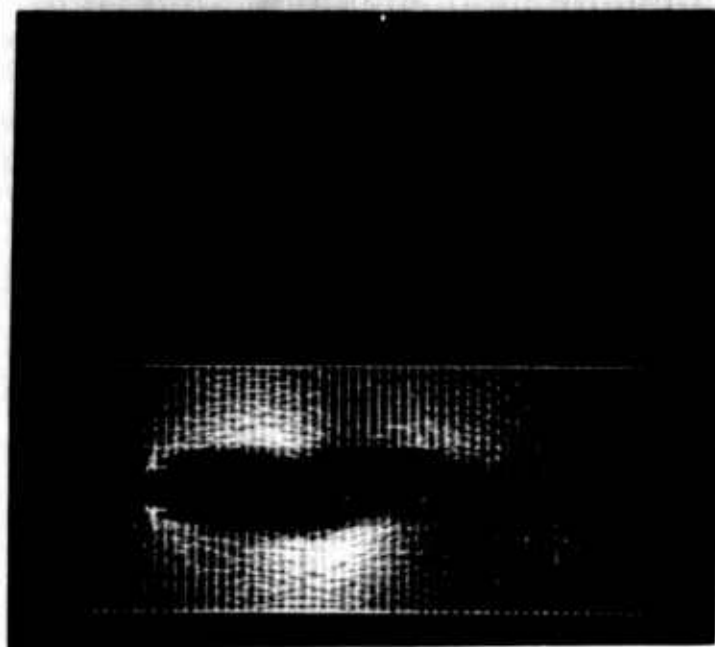
Fig. 7C
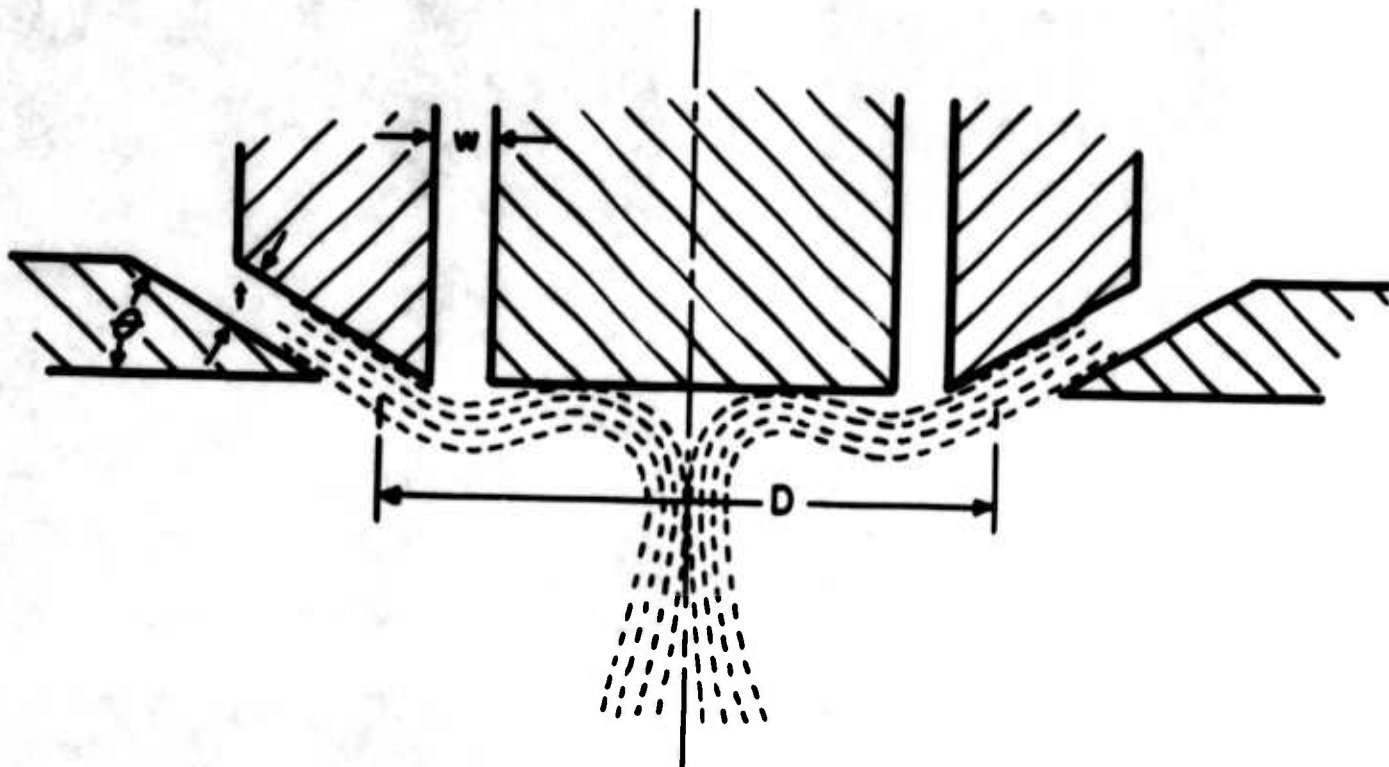
ANNULAR - JET NOT AMPLIFIER
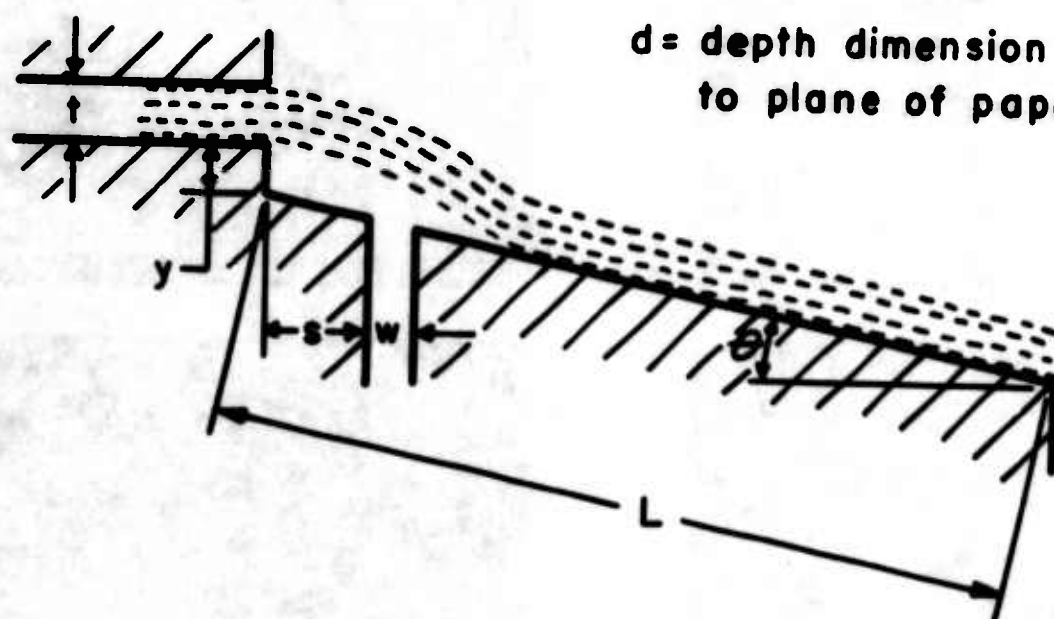
d = depth dimension perpendicular to plane of paper

PLANAR NOT AMPLIFIER

Fig. 8   BASIC FLOW CONFIGURATIONS

320

HARRY DIAMOND LABORATORIES

WASHINGTON 25, D. C.

THE RESPONSE OF A BISTABLE FLUID

AMPLIFIER TO A STEP INPUT

by

SILAS KATZ
E. T. WINSTON
P. HAWES

ABSTRACT

Switching times of two configurations of bistable fluid elements were measured at various power and control jet pressures. The units differed mainly in the ratio of control nozzle width, for element 1 this was 1.0 and for element 2 it was 0.67. The measured switching times ranged for element 1 from 13 to 44 μS and for element 2 from 100 to 150 μS. The longer switching times for element 2 are believed to be due to the relatively smaller control orifice.

The observed switching appears to be due to momentum forces. When these are not predominant, the switching times are expected to be appreciably longer.

1. INTRODUCTION

Bistable fluid amplifiers without mechanical moving parts offer interesting possibilities in the field of digital computation with fluids. However, before these bistable elements can fulfill their promise, more knowledge about their dynamic characteristics is needed. The dynamic characteristics refer to the dynamic control signal necessary for reliable activation and the time required for this signal to effect a change in state. The latter is one of the most important considerations in the design of bistable elements for digital applications. [For example, the widespread use of the electronic flip-flop for storing a single bit of information can be traced to its ability to change states in as little as a few millimicroseconds.]

At the present time there is a scarcity of data on the time constants associated with the bistable fluid amplifier. The purpose of this paper is to provide some additional quantitative data to the designer of digital fluid circuits.

2. DEFINITION OF TIME CHARACTERISTICS

The schematic of a bistable fluid amplifier is shown in figure 1. In operation, a jet of fluid is discharged from the power jet nozzle and attaches to the left or right wall. Thus the jet has a stable left-side flow position and a stable right-side flow position. Once flow is established in either position, it will remain in that position until a command signal of proper amplitude and duration is delivered to the appropriate control nozzle. Upon receipt of the signal, the flow switches from one stable position to the other. The flow then remains in this switched position after the signal is removed until another suitable command signal is introduced into the alternate control chamber. The bistable amplifier is more fully described in references 1 and 2.

The time intervals of interest in the bistable fluid amplifier are the response time, the switching time and the transport time. These are shown schematically in figure 2. The response time is defined as the time interval between the appearance of the command signal at the control nozzle and the settlement of the flow in the switched position as observed at the output. Settlement occurs when all the flow is transferred. The switching time is the time required to move the stream from one wall to the other as observed from the same distance downstream on both walls. The transport time is the interval between the issuance of a particle

of fluid from the power jet nozzle and the arrival of the same particle outside the element. It is approximately equal to the length L divided by the mean velocity of the fluid. Thus the response time is equal to the sum of the transport time and the switching time. These definitions are essentially the same as those used in reference 3.

3. TEST SETUP AND PROCEDURE

The test setup shown in figure 3 consists of a bistable fluid amplifier, a shock tube to generate the command signal, and transducers to monitor the flow in the amplifier during switching.

3.1 Generation of Command Signal

In this test arrangement the command signal is a sharp pressure step, generated in a small shock tube. The high-pressure side of the tube is separated from the low-pressure side by a cellophane diaphragm. The pressure is adjustable up to 80 psig on the high side and fixed at atmospheric on the low side. With the high-pressure side set at a desired level, the diaphragm is punctured by a sharp pointed plunger. When the diaphragm ruptures a shock front starts down the low-pressure side and then passes into the right control jet chamber. Simultaneously a conductive line, painted on the diaphragm, breaks, opening an electric circuit to establish a time reference.

3.2 Instrumentation

To make accurate and reliable dynamic measurements the instruments used should have a response faster by an order of magnitude than the function they are to measure. Although the response time and switching time of bistable pneumatic elements were unknown they were expected to be short, and instrumentation with a fast response was deemed necessary. Therefore piezoelectric pressure transducers, having rise times of about $3\mu s$, were used to sense the position of the stream.

The response time and switching time measurements are obtained from the output signals of three transducers, one at each outlet flow position of the element and the third in the right control chamber (fig. 4).

The output of the transducers is amplified and fed into an oscilloscope with provisions for a delayed sweep. Rupturing the diaphragm triggers the scope; the sweep is delayed until the shock front reaches the control jet chamber. The traces are then photographed with an oscilloscope camera. Since the time measurements are made directly from these photographs, the sweep spread of the oscilloscope was carefully checked and found to be accurate within 2 percent.

324

3.3 Test Procedure

For each test run, the static pressure of the power jet chamber is set at any desired level from 10 to 60 psig. The flow position of the power stream is determined. In this test setup the stream had to be in the right-hand position before switching. The high-pressure chamber of the shock tube is pressurized to 20, 25 or 40 psig. At these pressures the resulting pressure steps at the control jet orifice are about 8.0, 9.2 and 12.9 psig respectively. When the pressure in the high-pressure chamber has been selected, the proper delay may be set on the oscilloscope. Higher pressures require less delay time due to higher shock wave speed. Before rupturing the diaphragm, the shutter of the camera is opened. The diaphragm is ruptured by manual operation of the plunger, triggering the scope and sending the shock front down the low-pressure side of the tube. During these tests the shock pressure never failed to switch the stream.

Response and switching time measurements were made on two typical bistable elements shown in figures 5 and 6. Element 1 differs from element 2 in position of splitter--7 versus 12 power nozzle widths downstream, and in ratio of control nozzle width to power nozzle width--1.0 versus 0.67.

4. TEST RESULTS

Typical test data are shown in figures 7, 8, and 9. Figure 7 shows the signal from the control transducer in time relation to the signal from one of the output transducers. The response time can be measured as indicated on this figure. The rise time of the command signal is 20 μs. This is consistent with the shock front speed and the diameter of the transducer.

The response time can also be calculated by adding the transport time to the measurements of switching time. In these tests the transport time is approximately constant for a given test element. Typical switching time data are shown in figures 8 and 9. Initially the stream is in the right-hand position. During switching, the flow leaves this position thereby decreasing the pressure on the right-hand transducer. As the flow arrives in its new position, the pressure on the left-hand transducer increases. Examination of the signal from the right-hand transducer shows a pressure rise preceding the change to a lower level. This increase in pressure may be attributed to the control fluid superimposing a disturbance on the power nozzle flow.

Switching times are measured directly from figures 8 and 9. The transducer signals for element 1, as shown in figure 8, become

325

unsteady at the onset of switching. The dominant frequency of the oscillation is 100,000 cps. This is the natural frequency of the piezoelectric pressure transducer used. The oscillation of the transducer output signals has lower amplitude in element 2 (fig. 9) because of the slower switching time for this element.

The test results are shown in table I. Switching times are measured from the photographs. Response time is computed by adding a calculated transport time to the measured switching time.

Switching times are plotted against the ratio of power jet pressure to control jet pressure in figure 10 for test element 1.

5. DISCUSSION

Mass Flow Switching - A bistable fluid amplifier switches for various reasons. As control flow is added, the power stream attachment point is moved downstream. Whether or not attachment is maintained at a given downstream distance depends upon the geometry of the amplifier. For example, if the attachment point is driven off the end of the attached side wall, the amplifier switches to the other side. Another possibility is that before the stream reaches the end of its attached wall, the splitter diverts enough flow out of the opposite output to limit the normal entrainment to that side and a switching results. In any of these ways, switching is delayed by the time required for entrainment to lower pressures.

Momentum Switching - It is believed that for the configuration of elements used in these tests and the way the tests were performed, momentum forces determine the switching time. The momentum due to the control flow drives the power stream into the opposite wall. Once over there the stream, which is held on by entrainment-induced forces, proceeds down the wall to its equilibrium position. Switching in this manner should be faster than in situations where momentum forces are negligible. The important parameters for momentum-type switching are the setback and the ratio of control nozzle width to power nozzle width.

The switching times for test element 1 varied from 13 to 44 μS depending on power jet pressure and control jet pressure. As the power jet increased, the times showed a tendency to increase. At a given power jet pressure the time of switching depends upon the control pressure exerted. Higher control pressure tends to shorten the switching time (fig. 10).

The switching times for test element 2 varied from 110 to 150 μS. Here again increasing the power jet tends to increase the time. The

326

longer switching time in element 2 may be attributed to the lower ratio of control nozzle width to power nozzle width (0.67 versus 1.00).

The results given here show a large spread. Identical tests sometimes produce results that differ by a factor of two. This occurs partially because of the difficulty in reading the transducer output. However, it is by no means certain that the actual switching time of tests run under the same conditions are the same. While no great accuracy can be claimed for these results, they should provide order-of-magnitude information about switching times.

REFERENCES

1. Warren, R. W. and Peperone, S. J., "Fluid Amplification 1. Basic Principles", DOFL TR-1039, August 1962

2. Warren, R. W., "Some Parameters Affecting the Design of Bistable Fluid Amplifiers," Fluid Jet Control Devices - An ASME Publication, November 1962

3. Comparin, R. A., Mitchell, A. E., Mueller, H. R. and Glaettli, H. M., "On the Limitations and Special Effects in Fluid Jet Amplifiers," Fluid Jet Control Devices - An ASME Publication, November 1962

TABLE I: TEST DATA

<u>Jet Pressure (psig)</u>   <u>Time (μS)</u>

TEST ELEMENT NO. 1

Power	Control	Switching	Transport	Response
10	8.0	28	140	168
50	8.0	38	130	168
50	8.0	40	130	170
10	9.2	16	140	156
20	9.2	33	130	163
20	9.2	18	130	148
20	9.2	16	130	146
20	9.2	24	130	154
30	9.2	14	130	144
40	9.2	40	130	170
40	9.2	39	130	169
40	9.2	31	130	161
40	9.2	40	130	170
50	9.2	35	130	165
50	9.2	44	130	174
50	9.2	36	130	166
60	9.2	35	130	165
10	12.9	13	140	153
20	12.9	22	130	152
50	12.9	29	130	159

TEST ELEMENT NO. 2

Power	Control	Switching	Transport	Response
20	9.2	110	225	335
20	9.2	120	225	345
40	9.2	130	225	355
40	9.2	115	225	340
60	9.2	150	225	375
60	9.2	120	225	345

329
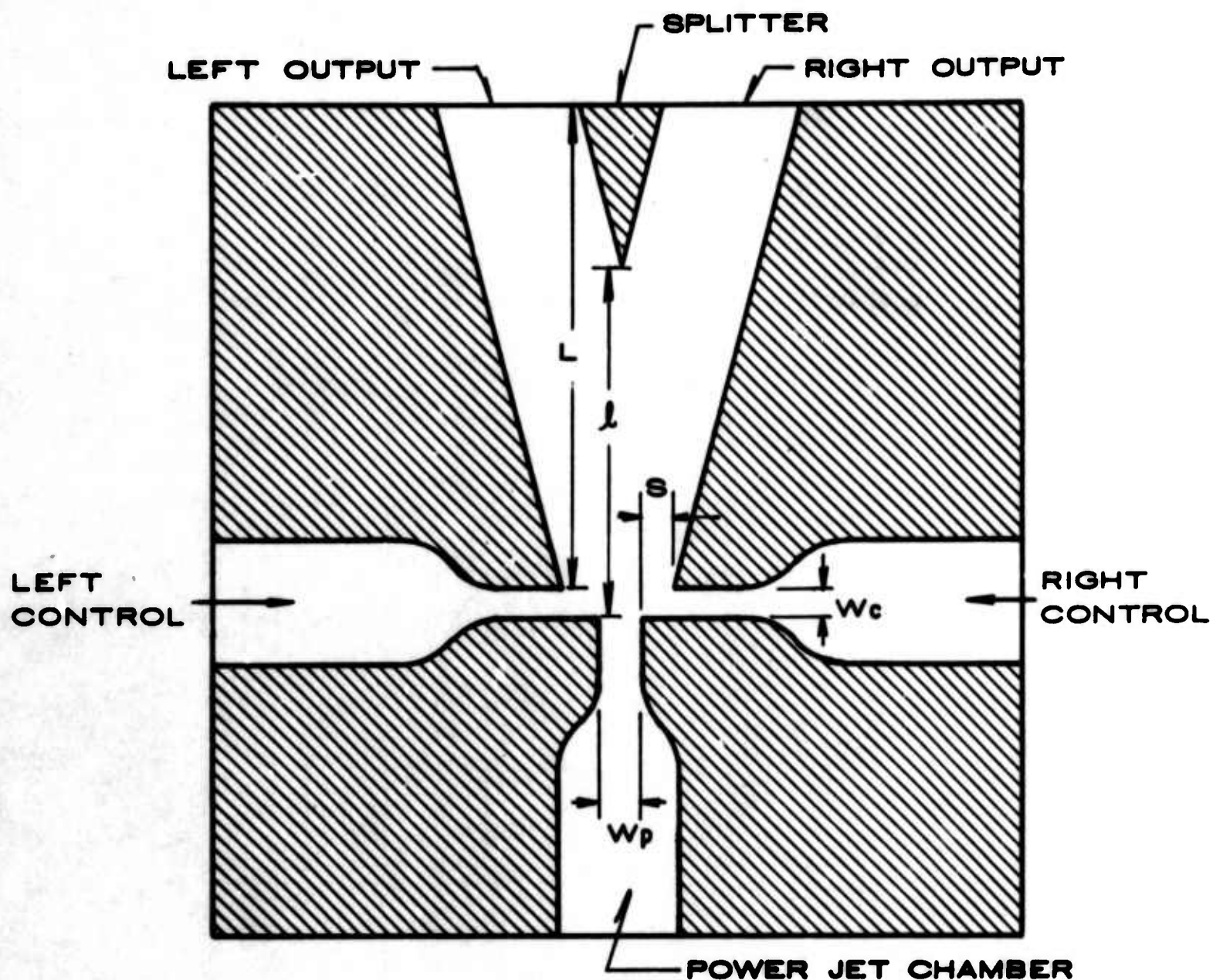
DIMENSION	MAGNITUDE IN	
	ELEMENT 1	ELEMENT 2
POWER JET WIDTH, W_p	.03	.09
CONTROL JET WIDTH, W_c	.03	.06
SPLITTER DISTANCE, l	.21	1.06
ELEMENT LENGTH, L	1.70	3.00
SETBACK, S	.02	.04
ASPECT RATIO	6	6

FIGURE 1. SCHEMATIC OF BISTABLE FLUID AMPLIFIER
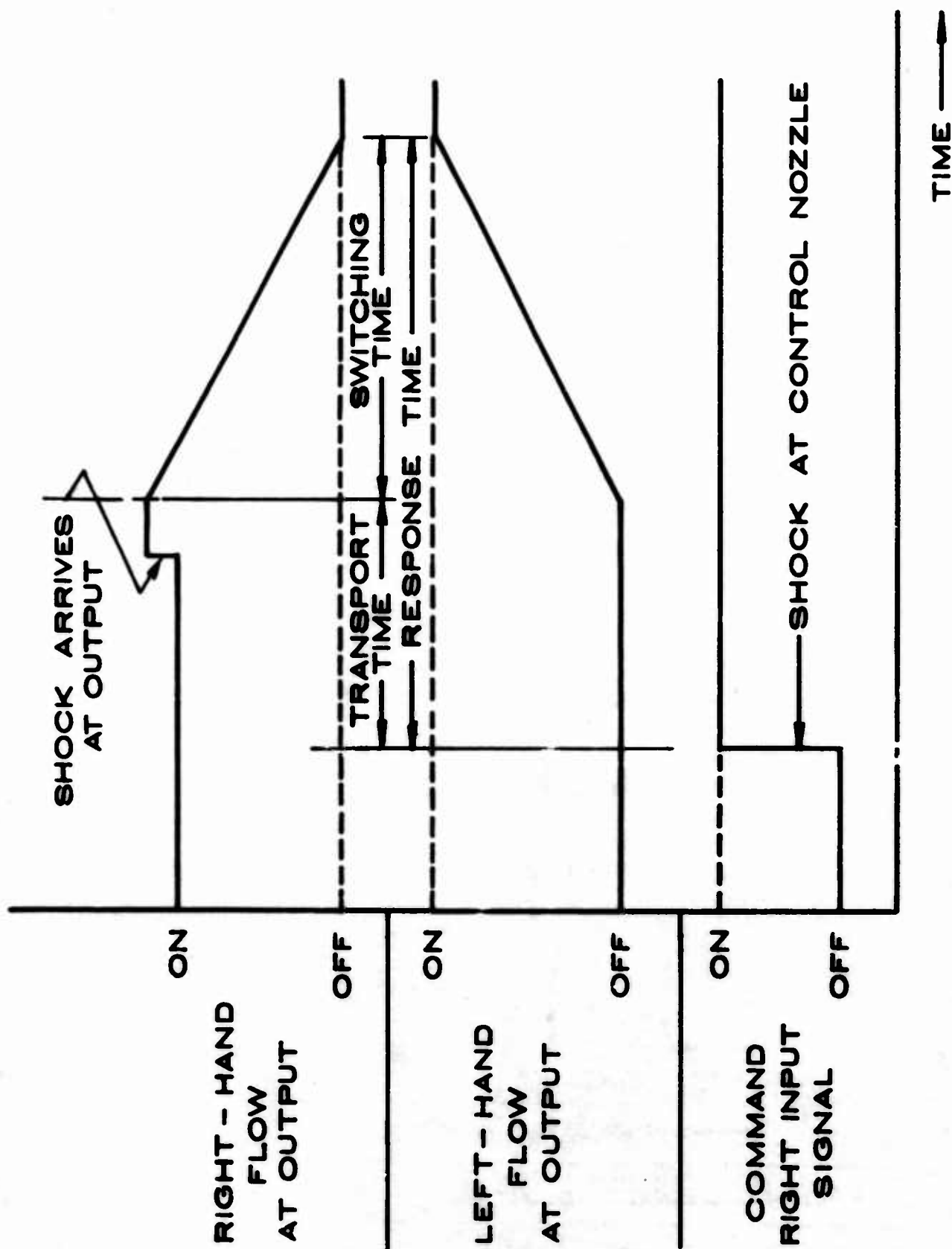
FIGURE 2. SCHEMATIC OF TIME CHARACTERISTICS

High pressure chamber
of shock tube

Low pressure chamber
of shock tube

Bistable pneumatic
element

Transducer in control
chamber

Figure 3. Experimental setup.

663-61

332
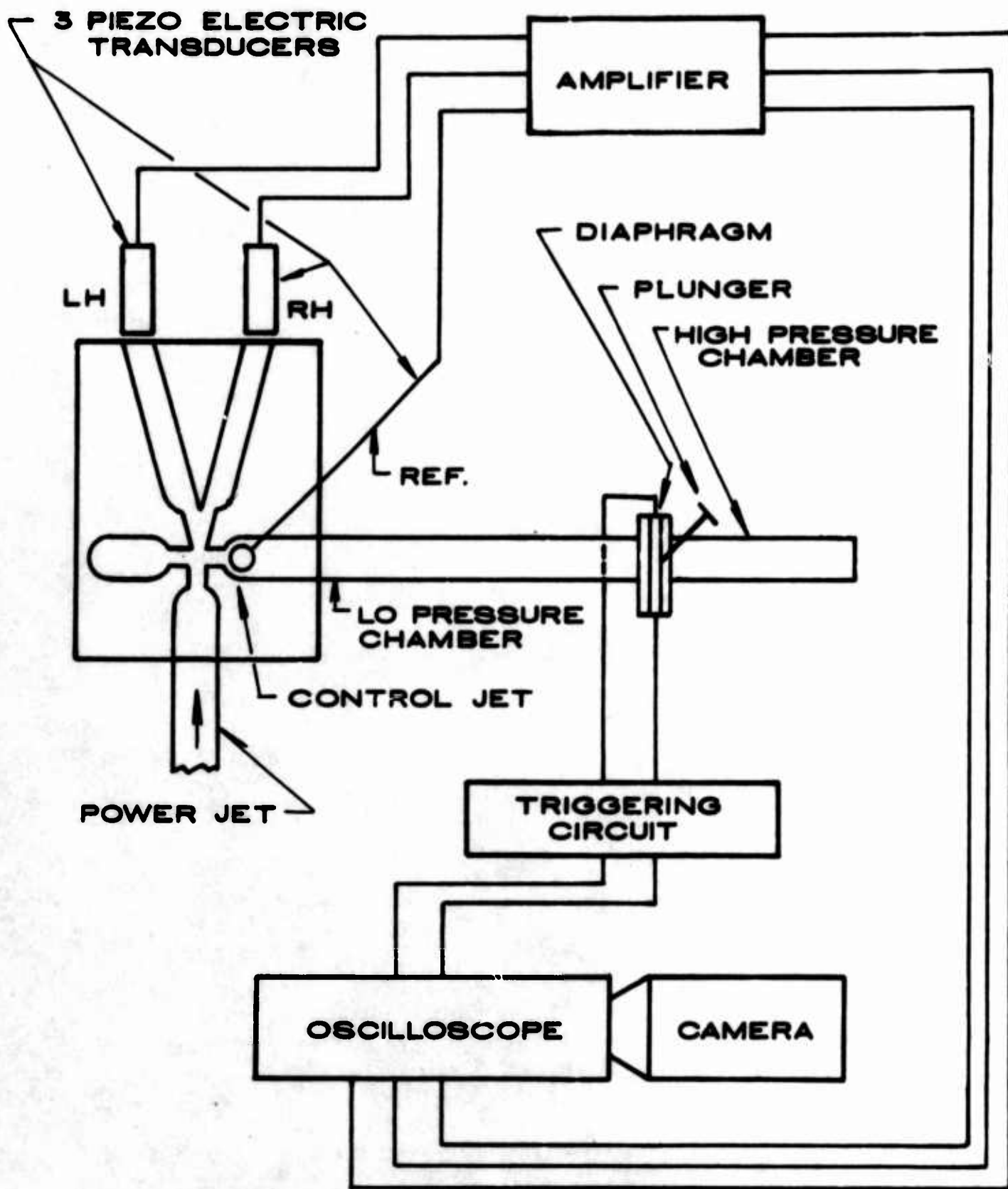
FIGURE 4. INSTRUMENTATION SCHEMATIC

333
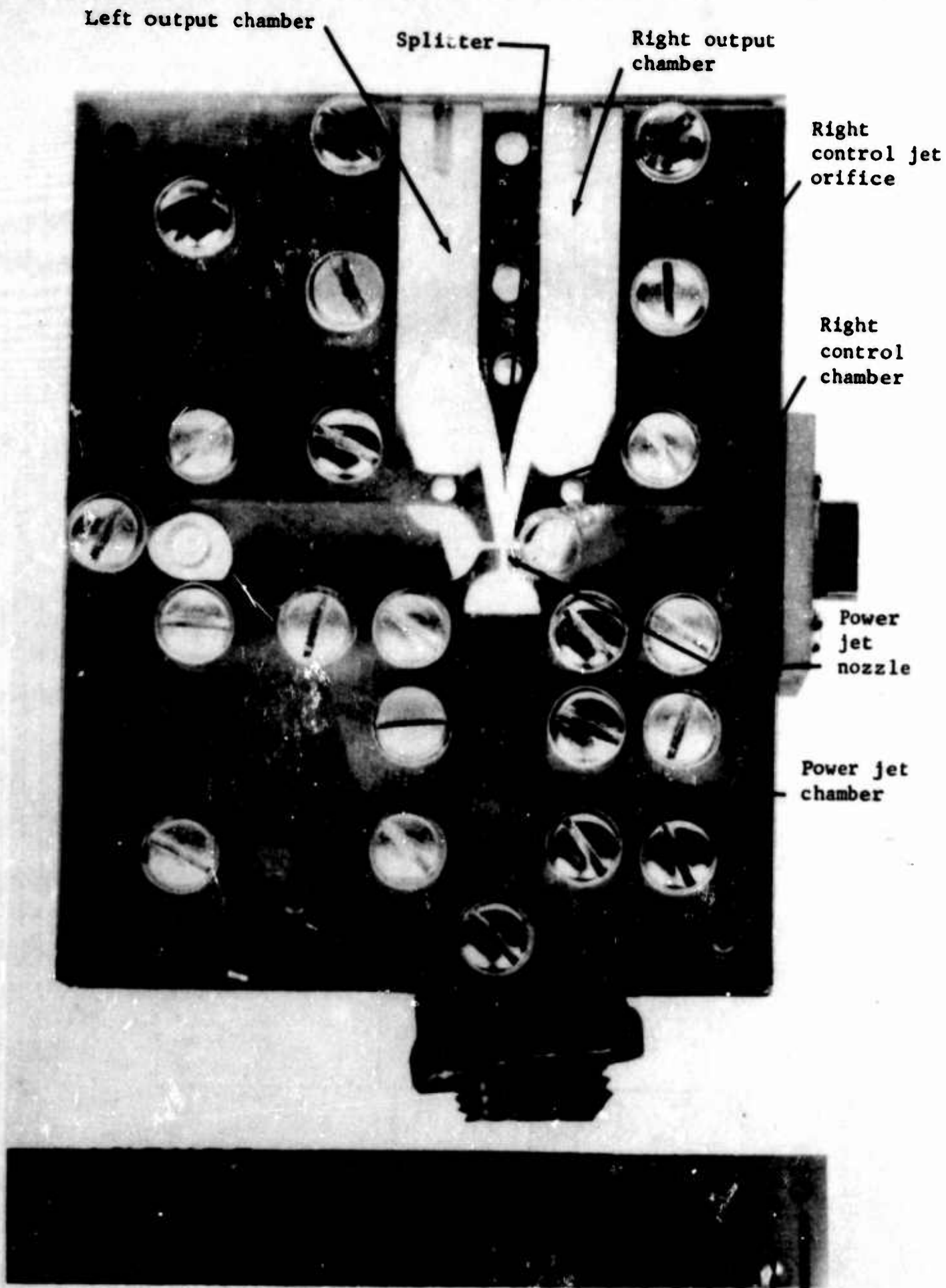
Figure 5. Bistable test element 1.

662-61

334
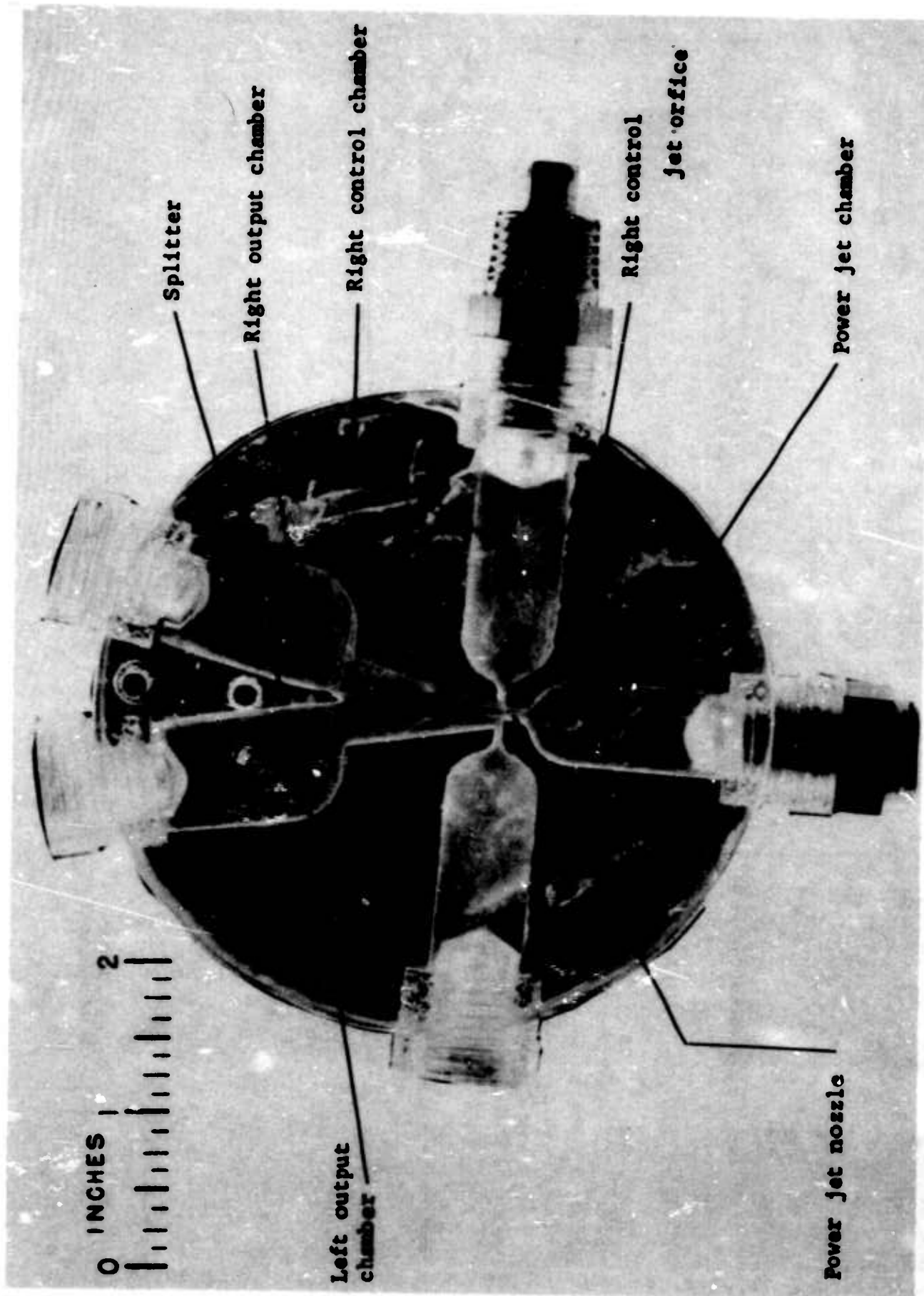
Figure 6. Bistable test element 2.
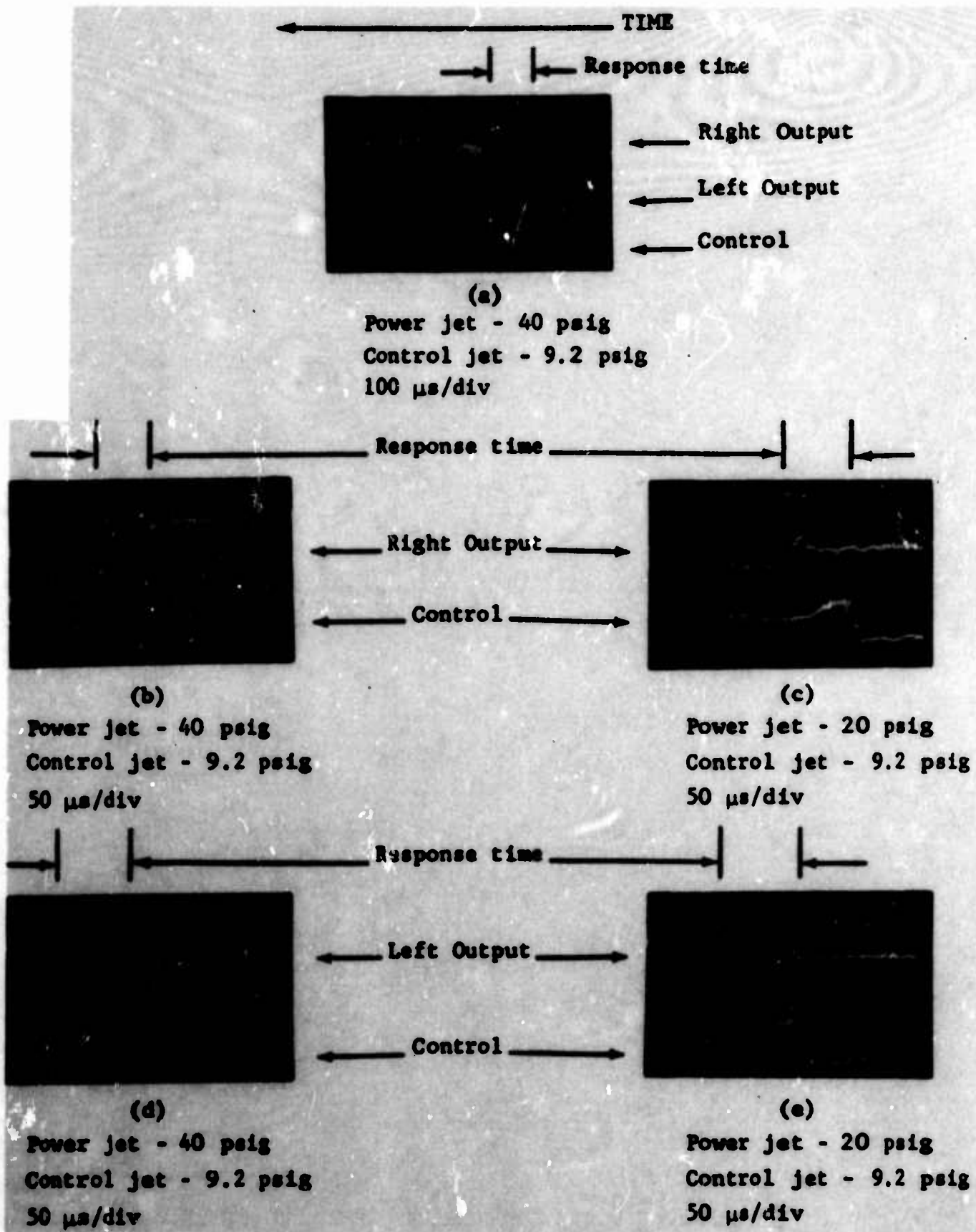
829-61

Figure 7. Typical response time test data - test element 1.

724-61
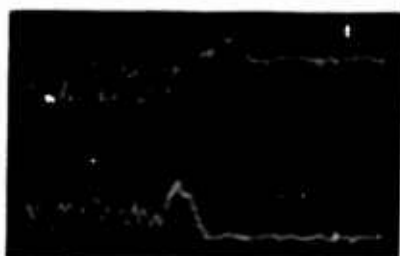
TIME

(a)

Power jet - 10 psig
Control jet - 9.2 psig
20 μs/div
Swithching time - 16 μs

(b)

Power jet - 20 psig
Control jet - 9.2 psig
20 μs/div
Switching time - 16 μs
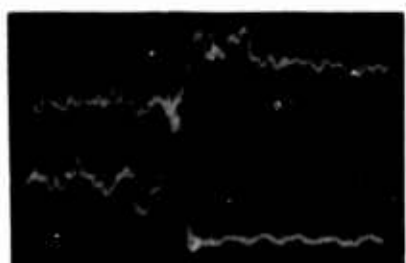
(c)

Power jet - 30 psig
Control jet - 9.2 psig
20 μs/div
Switching time - 14 μs

(d)

Power jet - 40 psig
Control jet - 9.2 psig
50 μs/div
Switching time - 40 μs

(e)

Power jet - 50 psig
Control jet - 9.2 psig
50 μs/div
Switching time - 35 μs

(f)

Power jet - 60 psig
Control jet - 9.2 psig
50 μs/div
Switching time - 35 μs

725-61

Figure 8. Typical switching time test data for test element 1.

TIME

Power jet - 20 psig
Control jet - 9.2 psig
50 μs/div
Switching time - 120 μs

Right Output ⟶

Left Output ⟶

(a)

Power jet - 40 psig
Control jet - 9.2 psig
50 μs/div
Switching time - 130 μs

Right Output ⟶

Left Output ⟶

(b)

Power jet - 60 psig
Control jet - 9.2 psig
50 μs/div
Switching time - 150 μs

Right Output ⟶

Left Output ⟶

(c)

-61

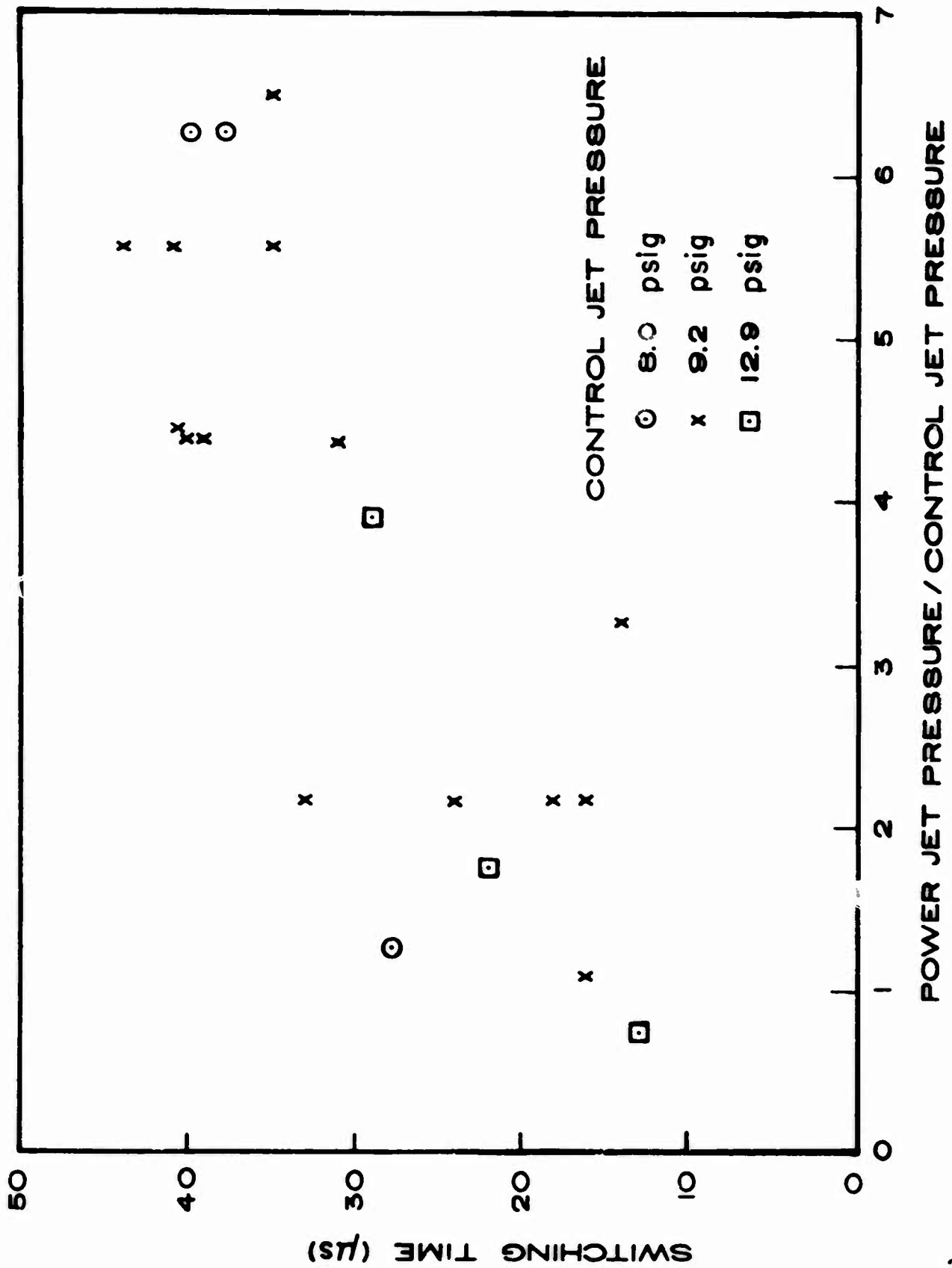Figure 9. Typical switching time test data for test element 2.

FIGURE IO. TEST DATA, ELEMENT I

339

THE EFFECT OF GEOMETRIC CHANGES UPON THE SWITCHING POINT IN A MODEL BI-STABLE FLUID AMPLIFIER*

Henry F. Hrubecky[1] and Larry N. Pearce[2]

INTRODUCTION

The present study was concerned with the effect of varying the principal geometric parameters upon the switching point in a model bi-stable fluid amplifier. The ability for considerable geometric variation was built into a single model system, and of the same nature as described in a previous paper presented at the Symposium.[3] Consequently, the system as conceived and designed was capable of giving a maximum of geometric flexibility which enabled a systematic evaluation of the effect of geometry on amplifier operation.

For the model amplifier under consideration, it was possible to vary the following geometric and flow parameters: (1) the primary and control jet pressures and flow rates, (2) the primary and control jet intersection angle, (3) the setback, (4) the position proximity of the control jet with respect to the primary jet, (5) the width of the mixing region, (6) the diffuser angle, (7) the flow divider wedge position, (8) the flow divider wedge angle, (9) the diffuser length, (10) the primary and control jet aspect ratios, and (11) the diffuser exit pressures or amplifier loads

The present experiments were conducted under no-load conditions (item 11 in the above) as well as without the flow divider wedge in position, no variations in the diffuser length, or variations in primary and control jet aspect ratios. Experiments involving the above variables are at present underway, and in some instances have been completed.

II. EXTENT OF VARIATION OF GEOMETRIC PARAMETERS

The previous section described the various parameters which are capable of variation in the model. Fig. 1 illustrates the flow geometry and the various parameters under consideration. The extent to which each of these parameters was varied is as follows:

A. Angles of flow intersection of from 10° (near parallel) to 105° (slight counterflow). The angle is defined by the centerline of the primary and control jets.

B. Setback from one to eight nozzle widths. Setback is defined as the distance from the primary nozzle centerline to the exit face of the control nozzle.

C. Control proximity from one to eight nozzle widths. Proximity is defined as the distance from the exit face of the primary nozzle to the centerline of the control nozzle.

D. Width of mixing region, bounded on the lower limit by the size of the nozzle and unbounded on the upper limit.

E. Diffuser angles from 0° to 35°, included angle.

F. Diffuser wall length up to 26 nozzle widths long.

III. EXPERIMENTAL PROCEDURE

The apparatus was arranged for a given geometry. With the control flow off, a primary flow was established and maintained at a constant value. The flow in the diffuser was manually made to attach to the wall nearest the control jet. The control jet valve was gradually opened until switching occurred. This established the approximate switching point for the configuration, e.g. between 10 and 20 scfm control flow for a primary flow of 40 scfm. The control flow was then decreased slightly and the flow in the diffuser caused to reattach to the wall nearest the control jet. The control flow was then increased in small steps until switching occurred between 5 and 10 seconds after setting the flow. Readings were then taken of the pressure drop across both flow elements (primary and control).

The control flow was then shut off, and the flow in the diffuser was manually switched with a baffle to the wall nearest the control jet. This procedure was repeated in a number of experiments at the same flow and geometric condition to verify reproducibility of the data. At least four experiments were conducted for each set of conditions.

The flow was then shut off in the apparatus and the geometry was changed. The geometry was varied systematically by fixing all the variables but one and varying this one in 7 or 8 steps between the limits of the design geometry. The geometry was varied from a basic configuration of a setback of 3 nozzle widths, a control proximity of 3 nozzle widths, a flow intersection angle of 90 degrees, and a diffuser angle of 15 degrees.

IV. RESULTS AND DISCUSSION

Results of the study of certain geometric parameters are illustrated in Figures 2 through 6. The length of the bar on the plotted figures is equal to the range of values for the recorded data. Examination of the results from an overall viewpoint reveals that for a constant primary flow of 40 scfm, the amount of control flow needed to switch the flow in the diffuser ranges from 10 to 20 scfm for all independent geometric configurations with the exception of flow intersection angles less than 70° The variation of the data for four experiments made at each configuration was generally less than 10% with minimum of 5% variation. A maximum of 15% was recorded for a few very unstable configurations such as at an intersection angle of 55°.

The effect of varying the jet intersection angle is indicated in Fig. 2. In the experiments in which the jet intersection angle was varied, observation indicated that the flow in the mixing region and diffuser was at steady-state for near perpendicular angles. However, as the angles became more acute, the flow exhibited a pulsating unsteadiness. The exact cause for this was undetermined although it was directly related to the increased amount of flow needed to cause switching. This ensuing flow would cause an increase in the back-flow and vortex formation in the diffuser section. For angles near 90°, the response time for the flow in the mixing region to react to control flow changes was short (approximately 5 seconds) and the switching point was well defined. For angles less than 85°, the response time became increasingly longer, and the switching was less well defined. Below 55° the flow would not switch for control flows up to 40 scfm. At 55° the exact switching point was vague and the amount of flow needed to cause switching (approximately 34 scfm) was more than twice that needed for 85° (approximately 14 scfm).

The above results appear to indicate certain discrepancies in the stagnation bubble theory as a cause of switching. As the above results indicate, it was found that the amount of control flow increased for angles decreasing from 90 degrees. As the angle decreases, one would expect that the momentum vector from the control jet would be directed more and more into the center of the stagnation bubble, thereby being more effective in increasing the static pressure. However, this apparently does not occur, and it appears as though switching is

influenced in these experiments by the direct impact of the two jets. This would account for the minimum of control flow needed to switch occurring near 90 degrees intersection angle.

For the experiments involving a variable setback with a fixed diffuser wall position, illustrated in Fig. 3, the control flow needed to cause switching was seen to be a minimum of approximately 1ᵒ scfm for a setback of one nozzle width. The control flow needed to cause switching increased to approximately 16 scfm for 2 nozzle widths setback, and then it leveled off at 18 scfm for setback greater than 3 nozzle widths. Noting that a shear discontinuity existed downstream of the control nozzle for setback less than 3 nozzle widths, the stagnation bubble was probably enlarged considerably. For small setback, the response time was short (5 seconds) and the switching point well defined. For large setback, the response time increased slightly (approximately 30 seconds).

The apparent inadequacy of the bubble theory is further illustrated in the above results where it appears that the flow is switched more readily with a high velocity stream that exists at the exit of the control nozzle rather than the lower velocity as found some seven nozzle widths downstream from the nozzle exit.

For the experiments involving a variable setback with the position of the diffuser wall with respect to the control nozzle fixed, as illustrated in Fig. 4, it was seen that the switching point varied from 14 scfm at 1 nozzle width setback to 18 scfm at 2 nozzle widths. It then decreased to 12.5 scfm at a setback of 6 nozzle widths. The response time was short and nearly constant, and the switching point well defined.

For experiments involving variable diffuser angles, as illustrated in Fig. 5, the switching point was seen to vary uniformly (nearly linearly) from 13 scfm for parallel walls to 19 scfm for an included angle of 33.5° between the walls. For small angles (0° to 5°) the switching point was vague due to the fact that the spread of the jet was nearly equal to the diffuser width, thereby decreasing the amount of backflow and entrainment. Consequently, this minimized the force unbalance possible in the diffuser. There was, therefore, no strong preference for the flow to attach to either wall. Above 10° the switching point was well defined. The response time was short and uniform for the range of angles used in the experiments.

Changes in control proximity was seen to have little effect on the switching point, as illustrated in Fig. 6. The control flow needed to cause switching was approximately 17.5 scfm for a proximity of 1 nozzle width and decreased linearly to approximately 15 scfm at 7 nozzle widths.

Examination of results in the area of geometric configuration common to all the tests (a setback of 3 nozzle widths, a control proximity of 3 nozzle widths, a diffuser angle of 15°, and a flow intersection angle of 90°) showed that the switching point was approximately 14 scfm for the flow intersection experiment, 15.5 scfm

for setback with the fixed wall experiment, 17 scfm for setback with the movable wall experiment, 18 scfm for the diffuser angle test, and 17 scfm for the control proximity test. This yielded an average of 16.5 scfm with a variation of about $\pm$ 10% between the five different experimental conditions.
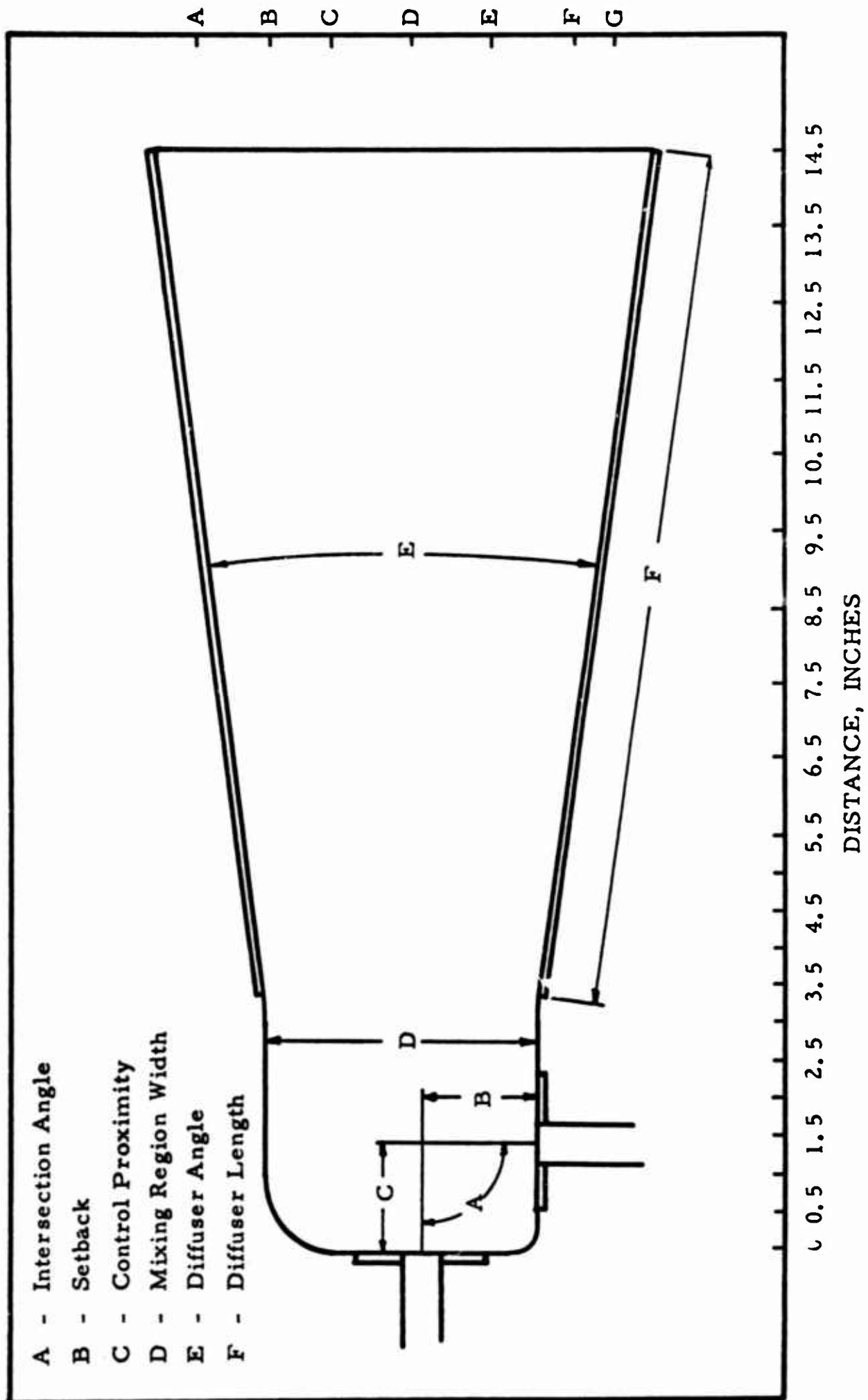
V. SUMMARY

From the results of the study of certain geometric parameters, it can be concluded that for constant primary flow in a two-dimensional model fluid amplifier the amount of control flow needed to cause incipient switching, other geometries being fixed:
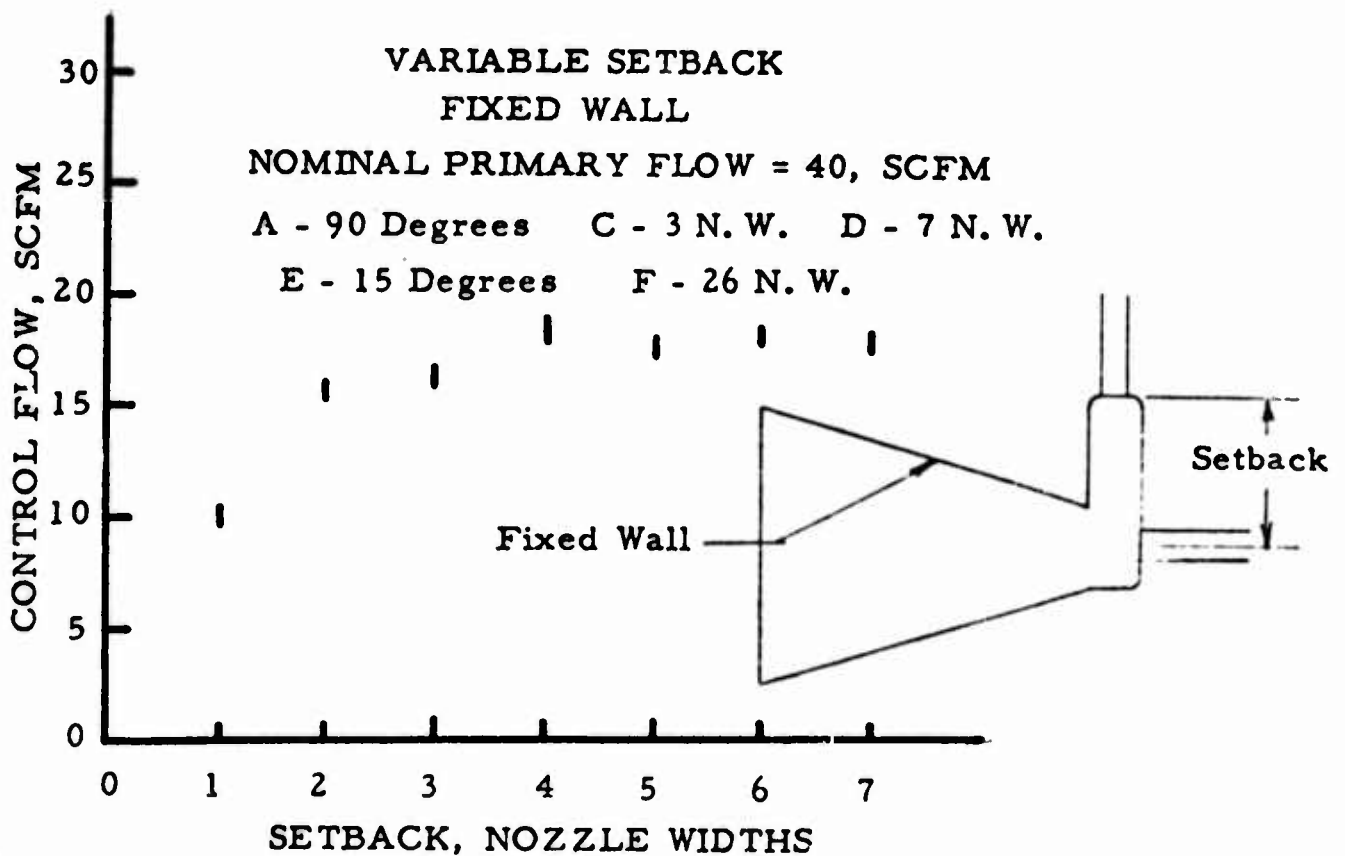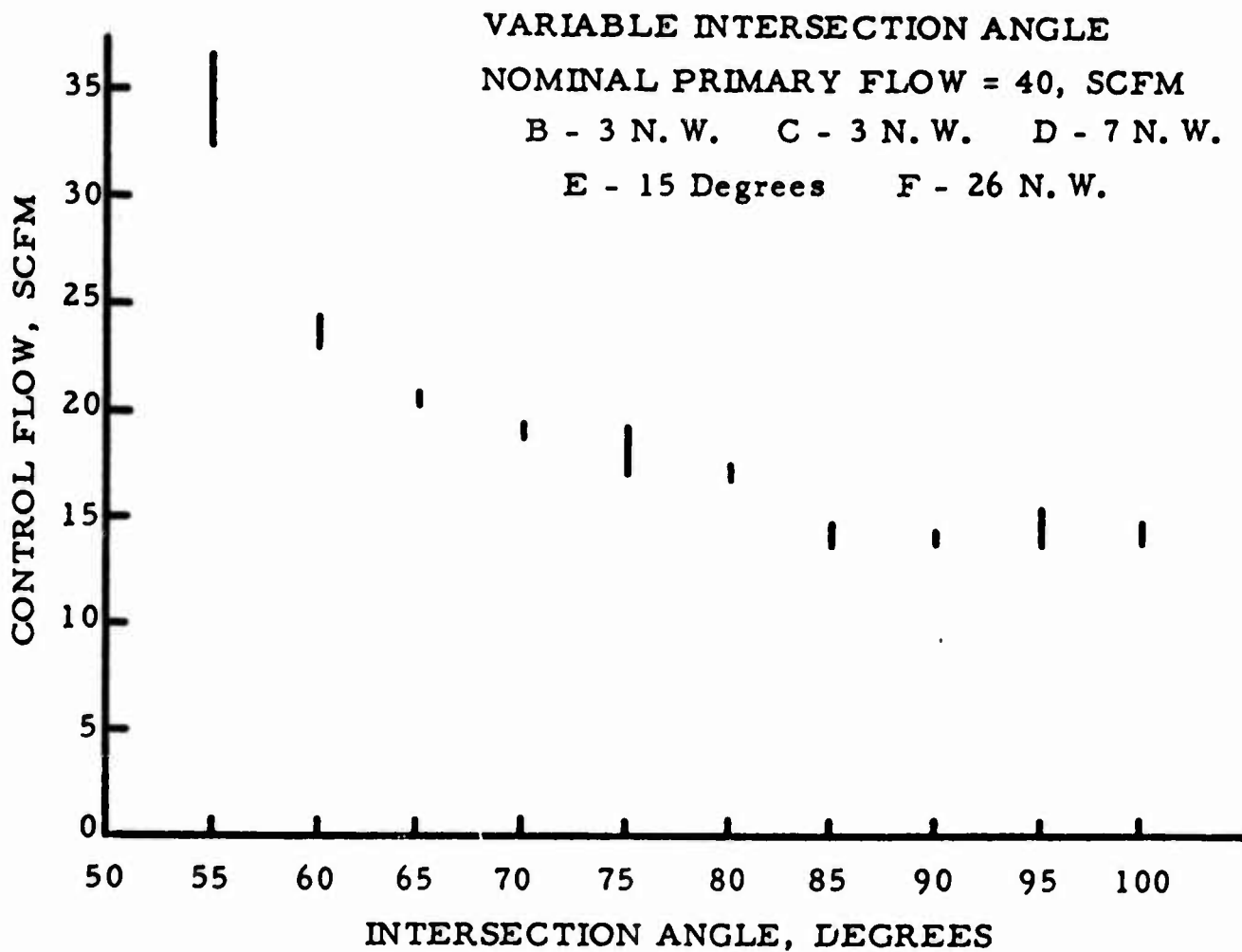
1) decreases for increasing jet intersection angles up to about 85° and then increases slightly for angles greater than 90°.

2) increases for increasing setback up to 7 nozzle widths.

3) increases for increasing diffuser angles up to 33.5°.

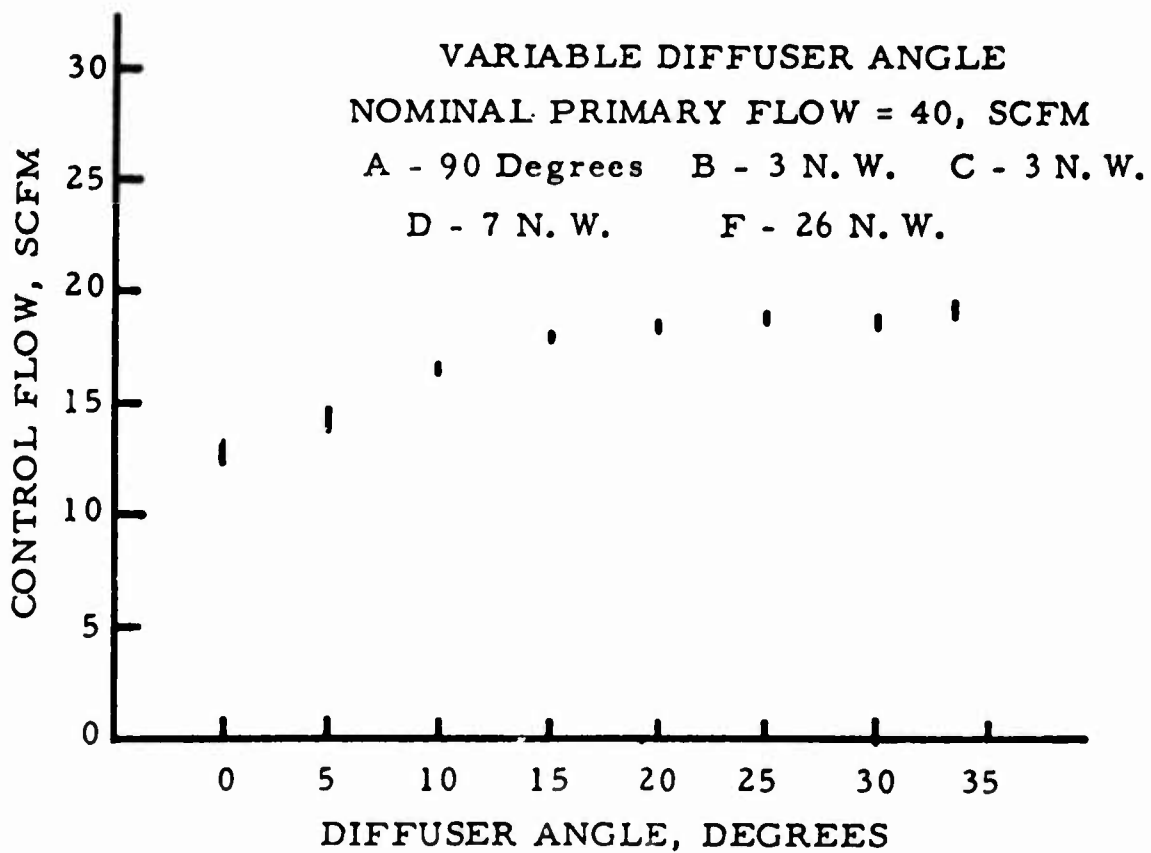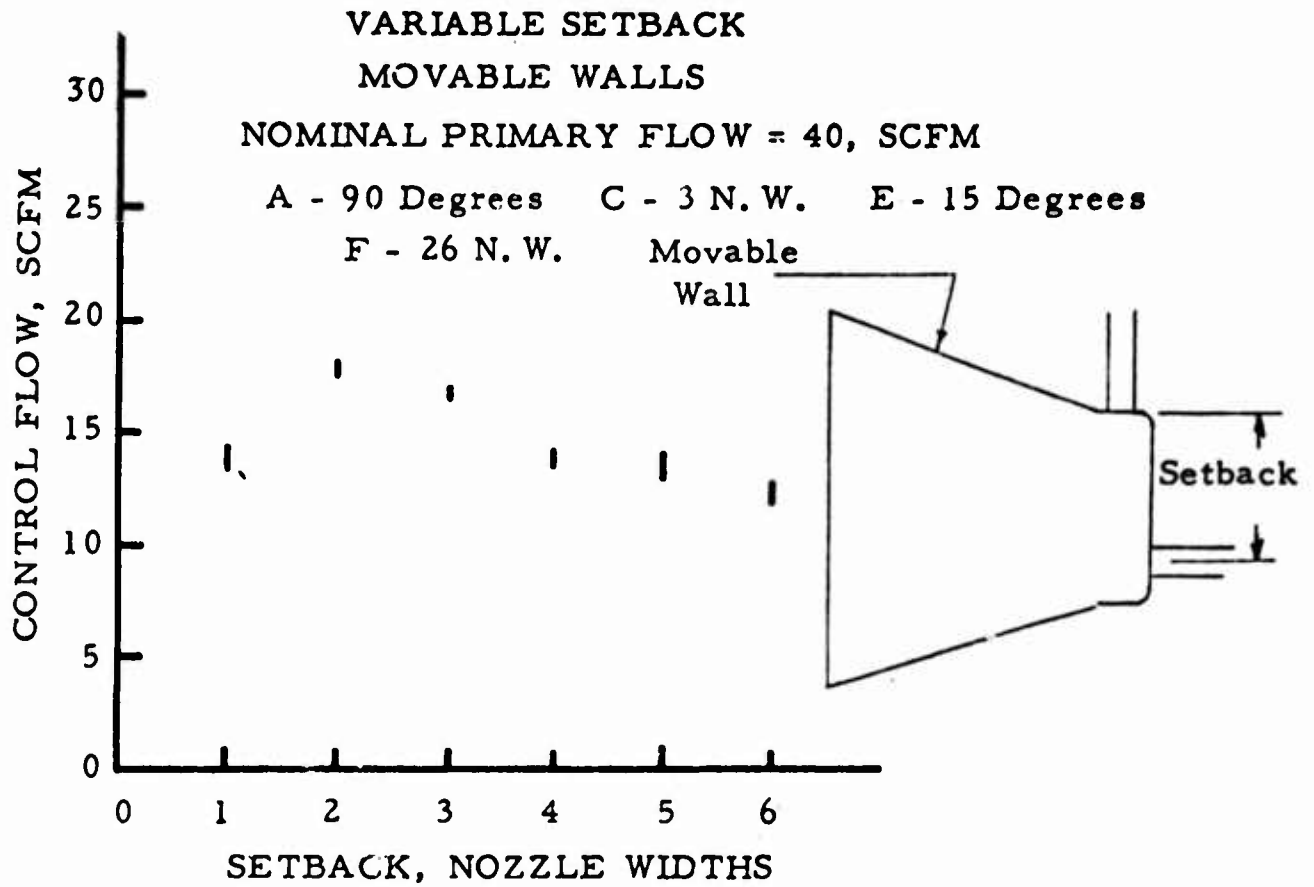4) remains unchanged for changes in control proximity up to 7 nozzle widths.

FIGURES

Fig. 1   Geometric Variables

Fig. 2   Control flow required for switching at various jet
          intersection angles

Fig. 3   Control flow required for switching vs. Setback with fixed
          wall

Fig. 4   Control flow required for switching vs. Setback with
          movable diffuser wall

Fig. 5   Control flow required for switching for various diffuser
          wall angles

Fig. 6   Control flow required for switching vs. control nozzle
          proximity.

346

GEOMETRIC VARIABLES

A – Intersection Angle
B – Setback
C – Control Proximity
D – Mixing Region Width
E – Diffuser Angle
F – Diffuser Length

DISTANCE, INCHES

0.5 1.5 2.5 3.5 4.5 5.5 6.5 7.5 8.5 9.5 10.5 11.5 12.5 13.5 14.5

347

VARIABLE INTERSECTION ANGLE
NOMINAL PRIMARY FLOW = 40, SCFM
B - 3 N.W.   C - 3 N.W.   D - 7 N.W.
E - 15 Degrees   F - 26 N.W.

VARIABLE SETBACK
FIXED WALL
NOMINAL PRIMARY FLOW = 40, SCFM
A - 90 Degrees   C - 3 N.W.   D - 7 N.W.
E - 15 Degrees   F - 26 N.W.

VARIABLE SETBACK
MOVABLE WALLS
NOMINAL PRIMARY FLOW = 40, SCFM
A - 90 Degrees   C - 3 N. W.   E - 15 Degrees
F - 26 N. W.   Movable Wall

VARIABLE DIFFUSER ANGLE
NOMINAL PRIMARY FLOW = 40, SCFM
A - 90 Degrees   B - 3 N. W.   C - 3 N. W.
D - 7 N. W.   F - 26 N. W.

349

VARIABLE CONTROL PROXIMITY
NOMINAL PRIMARY FLOW = 40, SCFM
A - 90 Degrees   B - 3 N. W.   D - 7 N. W.
E - 15 Degrees   F - 26 N. W.

350
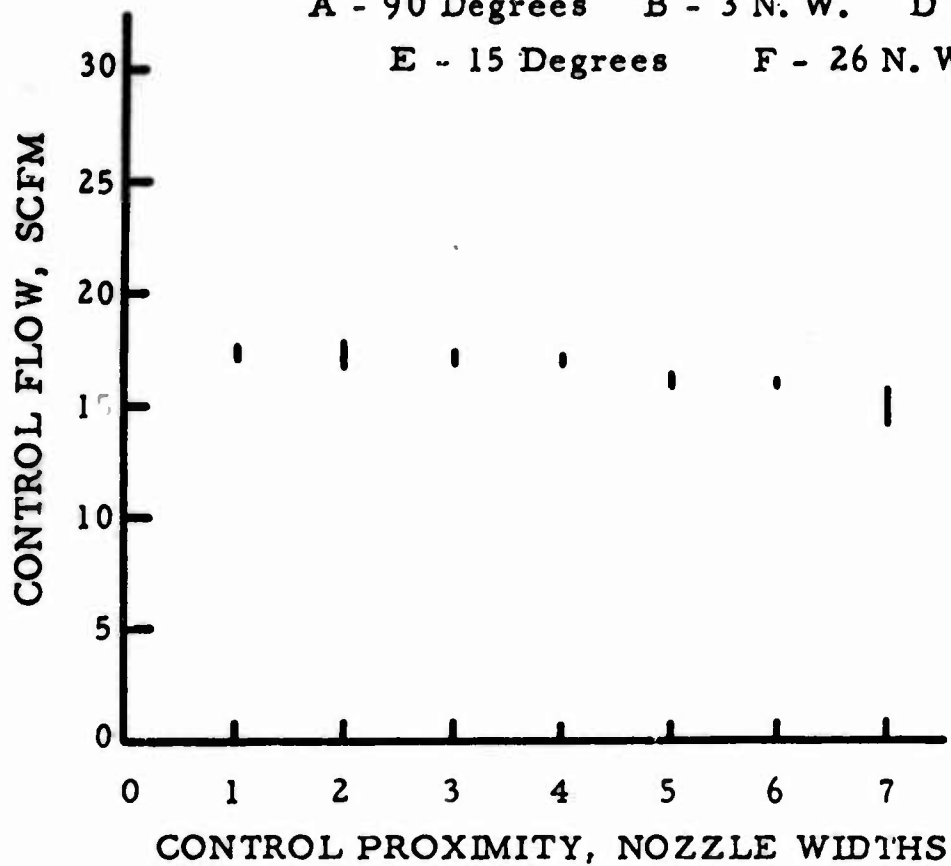
FLOW FIELD CHARACTERISTICS IN A MODEL BI-STABLE FLUID AMPLIFIER*

Henry F. Hrubecky[1] and Larry N. Pearce[2]

I. INTRODUCTION

An experimental investigation as to the nature of the flow field encountered during the intersection and consequent mixing of two different two-dimensional jets under bounded wall conditions was conducted. The jets interacted in a flow geometry, i.e., mixing chamber and diffuser, similar to the one encountered in bi-stable fluid amplifiers. To this end, a model fluid amplifier system was designed and constructed incorporating considerable flexibility in flow conditions and in amplifier geometry. The experimental system is pictured in Figs. la and lb. With the above model system it was possible to vary the following: 1. The primary and control jet intersection angle, 2. Setback, 3. Position proximity of the control jet with respect to the primary jet, 4. The width of the mixing region, 5. The diffuser angle, 6. The primary and control jet pressures and flow rates, 7. Diffuser exit pressures. Recently, the effect of diffuser wall length has been investigated, as well as, the effect of primary and control nozzle aspect ratios. These latter results are not reported in this paper.

The present investigation, in addition to the overall effect upon jet switching of each of the above flow and geometric parameters, was concerned with the nature of the general flow characteristics found in the amplifier, i.e., the static pressure field and velocity field during and after the mixing of the primary and control jets.

With a given amplifier geometry and flow condition, a representative detailed pressure and velocity distribution investigation was conducted for three flow conditions: 1. no control flow, 2. control flow great enough to cause incipient switching, and 3. control flow great enough to assure switching. The latter depicts the flow pattern after the combined jets have switched to the opposite wall.

[1]Professor of Mechanical Engineering, Tulane University, New Orleans

[2]Research Assistant in Mechanical Engineering, Tulane University, New Orleans

The study concerned with the effect of variable amplifier geometry at various mean flow conditions is presented in a separate and following paper at the Symposium. The same amplifier was utilized in both studies.

Prior to consideration of the present experiments, a brief review of certain previous multi-jet flow studies is appropriate.

II. MOTION OF DUAL JETS, PARALLEL OR INTERSECTING

Although the two dimensional and axisymmetric flows has been extensively studied, there is very little information available in the literature for dual jet flows. Corrsin (1) investigated the unstable flow from seven parallel slot nozzles. Temperature, total head, and flow direction were reported. Miller and Comings (2, 3) studied two parallel turbulent jets issuing from parallel slot nozzles in a common wall. End walls prevented interjet air entrainment from the surroundings, and a region of highly convergent flow was formed near the nozzles. Velocity and static pressure measurements were taken and contour maps reveal: 1. A sub-atmospheric pressure exists between the jets that accounts for the jet convergence; 2. The deceleration of the mean flow depends almost entirely on the lateral gradient of turbulent shear stress; 3. A free stagnation point appears on the plane of symmetry; 4. Two stable symmetrical contrarotary vortices recycle air (about 24% of that issuing from the nozzles) located on the concave side of each converging jet; 5. Another large vortex system located outside the jets (on their convex sides); 6. A super atmospheric static pressure further down stream which redirects the merging jet streams in a common down stream direction. Furthermore, the combined stream velocity distribution could be approximated by Gauss' functions. Fully developed velocity profiles were obtained within 12 nozzle widths downstream of the jet exit, while the pressure profiles did not correspond to those of a single jet until some 35 nozzle widths downstream.

It is known that the Reichardt hypothesis concommitant with the assumption of constant pressure mixing leads to the conclusion of the additivity of momentum fluxes from various sources. Bollinger (4) conducted experiments on two intersecting air jets in the atmosphere. He found that for dual parallel jets there is a tendency for this principle to break down. The velocity distribution was obtained from each jet with the other shut off. The combined flow was then measured. The momentum flux was then calculated for various angles of jet intersection. Bollinger's contention was that in those cases where appreciable static pressure gradients exist in the field of flow, the Reichardt hypothesis is no longer applicable to the intersecting jet flow field.

352

Of significicent importance in fluid amplifier operation is the formation of a stagnation bubble in the vicinity of the dual jet interaction. Hence, a detailed study of this region and the surrounding flow was of prime concern. A general review of the phenomenon is given.

III. REVIEW OF STAGNATION BUBBLE FUNCTION AND RESULTING INSTABILITY

Consider a two-dimensional jet issuing from nozzle A as indicated in Figure 2. The jet will spread at a rate proportional to the distance measured from the nozzle exit. The rate of spread depends on the value of the exit momentum of the jet. If its momentum is of a value to yield proportionality such that the jet will have an angle of spread less than the diffuser angle, there will be created regions of backflow and entrainment C on either side of the outer mixing region of the jet. Under symmetric, stable and steady state conditions, the jet will flow down the diffuser centerline. However, if the flow is perturbed from the centerline, say to the left, then the area for entrained flow on the left must decrease slightly. Accordingly, the flow velocity there must increase slightly, if continuity prevails. Simultaneously, the pressure must decrease. This then leads to a net force unbalance and resulting instability tending to force the flow to the left. This causes the flow to "attach" to the left wall. Since there is a discontinuity D at the nozzle exit there must be present a region of high pressure and slow moving fluid E. This stagnation region or bubble is of such a magnitude as to oppose the net force unbalance. Consequently, there must exist an equilibrium position for the jet in which the jet flows close to and parallel to the diffuser wall beyond some point of attachment, F, located at the boundary between the stagnation bubble and the primary flow.

The switching of the jet from one wall to the opposite wall can be accomplished in one of three fundamental ways. First, one could conceivably decrease the pressure in the region of entrained flow below that in the main flow, thereby causing the flow to switch. Secondly, one could conceivably decelerate the main flow velocity close to the wall to yield a static pressure rise great enough to cause switching. Finally, one could increase the pressure in the stagnation bubble E by a net mass influx and cause detachment of the flow from the wall leading then to switching. It is the latter of these methods that is most practical since one can use an outside control flow to accomplish the mass influx in the stagnation bubble.

In previous work, Olson (5) reported that the stagnation point or attachment point occurs from 4 to 7 nozzle diameters downstream of the nozzle exit. Mean pressure ratios (defined as the mean pressure in the stagnation bubble divided by the mean pressure in the primary stream) of 0.9 to 0.7 were found for Mach Numbers 0.7 to 2.0. From momentum considerations pressure ratios were predicted by considering one control volume enclosing only the separation bubble and

another control volume about the separation bubble which includes the primary flow. Simultaneous solution of the momentum equations thus obtained yielded the mean pressure ratios. Experiment agreed well with predicted values. Greber (6) considered the same problem of stagnation pressure ratios from the standpoint of the shear discontinuity generated at the exit of the primary nozzle. He found significant discrepancies between velocity as predicted by boundary layer solutions and asymtotic jet solutions.

IV. DESCRIPTION OF THE MODEL FLUID AMPLIFIER

A plan view of the apparatus is illustrated in Fig. 3.

A. Nozzles.

With air as the working medium, a Reynold's Number of 13,000 based on nozzle width at exit was chosen as being a representative value for the detailed study. To assure a fully developed turbulent profile at the nozzle exit, a long length (40 nozzle widths) of constant area led up to the nozzle exit. Upstream of this section was a stabilizing section with honeycomb flow straighteners in an area of approximately 15 times the nozzle exit area. To approximate two-dimensional flow, an aspect ratio of 10 was chosen for the nozzle exit. This yielded a distance between the base plate and cover plate of approximately 5 inches, large enough to permit easy access with measuring probes. The nozzles were constructed of plexiglas to permit flow visualization.

B. Mixing Section.

The mixing section was designed to accomodate the two nozzles at various angles and relative distances while insuring a closed mixing region with no leakage across the boundary. This was accomplished by machining flanges into the nozzles and diffuser walls and inserting a section of 1/4" thick rubber sheeting. This provided an excellent seal and a relatively smooth transition be-tween the components. The diffuser walls had a pivot point located at the upstream end and a bracket fixed to the lower end, which permitted angular changes but added rigidity to the wall. The base plate was made of 1/2" cold rolled steel, and the cover plate was made of 3/8" plexiglas.

C. Indexing Table for Locating Measuring Probes.

Since there exist large velocity and pressure gradients in the mixing region of the model amplifier, and since the probes were small, in particular, the hot-wire with a wire diameter of 0.00035 inch, it was desirable to locate the probe with as much precision as possible. The device to locate the probe should permit rapid positional changes of the probes and also permit easy probe inter-change. Therefore, a table as indicated in Fig. 1b was designed as

an integral part of the model which utilized a carriage supported by linear ball bushings sliding on stainless steel rods. The carriage had two degrees of freedom, and the movement in each was measured by means of calibrated rods graduated in 1 inch increments with interpolation by means of a micrometer head graduated in thousandths of an inch over a 1 inch range.

V. INSTRUMENTATION

Flow rate measurement was accomplished by utilizing a Meriam Instrument Company Laminar Flow Element. This element features a very small bore honeycomb inserted into the flow. The size of the honeycomb openings assures laminar flow and taps are provided to measure the pressure drop across the honeycomb. This pressure drop was measured with a micromanometer. The flow rate can be ascertained with appropriate calibration values. Corrections for temperature variations were made. The accuracy of the element is better than 1% of full scale reading (100 scfm).

Average velocity measurements were accomplished by means of a constant current hot-wire anemometer (Flow Corporation Model HWB - 3). The hot-wire (Fig. 4) was made of 0.00035 inch diameter tungsten and was 0.044 inch long. The wire was located to within $\pm$ 0.002 inch by means of the indexing table. The probe was calibrated before and after the velocity studies by means of a calibrated wind tunnel, (Flow Corporation Model WT-4).

Static pressure was measured by utilizing a disk type probe fashioned in a manner similar to the one used by Miller (2) in connection with a micromanometer of the null type (Flow Corporation Model MM-3). The probe produced flow along a flat surface parallel to the flow and, consequently, the micromanometer measured the static pressure at a point "on a wall". The micromanometer utilized N-butyl alcohol as a working fluid, and could be read to 0.0001 inch, corresponding to a pressure of 0.000006 psi. The response of the micromanometer was excellent, requiring approximately 10 seconds to stabilize.

Flow direction was ascertained by injecting smoke and observing the flow, and, also, by means of a specially designed, highly sensitive vane.

VI. EXPERIMENTAL PROCEDURE FOR VELOCITY AND PRESSURE FIELD STUDY

Since the parametric study was conducted concurrently with the flow field study, the former, in addition to pertinent results in literature, dictated a suitable configuration for the flow field study. A geometrical configuration of a setback of 3 nozzle widths, a proximity of 3 nozzle widths, a flow intersection angle of 90°, a width of mixing region of 7 nozzle widths, and a diffuser angle of 15° was chosen for the flow field study. For this geometry, three flow

conditions were utilized: (1) no control flow, (2) control flow great enough to produce incipient switching (15 scfm), and (3) control flow great enough to assure switching (16,8 scfm), all for a nominal flow of 40 scfm in the primary nozzle. For each of these conditions measurements were taken with the hot-wire anemometer at some 110 points throughout the mixing region. These points were located on the mid-plane between the base plate and cover plate (similar to nodal points on a grid). The hot-wire probe was inserted from the diffuser end of the amplifier and positioned at one of the predetermined points by means of the indexing table. A traverse of the grid system was made, readings taken and velocities were subsequently obtained from calibration curves.

The probe was calibrated both before and after the velocity tests. This was done by positioning the probe in a stream of known velocity and recording the current necessary to balance the hot-wire circuit. The shift in calibration due to wire aging and contamination during the tests was found to be negligible.

The geometric and flow conditions used for the velocity tests were reproduced for the static pressure tests. Static pressure readings were taken following the same basic procedure used for the velocity readings. The static pressure probe (Fig. 4) was connected to a Flow Corporation Model MM-3 Micromanometer. The probe was positioned at the same points previously used for the velocity readings and the differential static pressure head between the test point and the ambient atmosphere was recorded.

Visual flow observations were made by injecting smoke into the primary nozzle. This was accomplished by igniting a smoke bomb in a closed container and drawing the smoke into the primary nozzle by means of the sub-atmospheric pressure region created by an orifice installed for this purpose in a tee section upstream of the nozzle. The flow patterns were observed for the three conditions. The smoke proved to be a very effective means of determining streamlines.

VII. RESULTS

Results of the velocity and pressure study are contained in Fig. 5 through Fig. 7. Isovels are plotted in Figures 5a, b and c. Isobars are plotted in Figures 6a, b and c. Lines of constant total head are plotted in Figures 7a, b and c. Results show that both with conditions of no control flow and flow after switching, there exists a region of highly unstable vortices along the centerline of the diffuser. The vortex region is created by the attached flow on one side and a region of backflow and entrainment on the opposite side of the diffuser. At the switching point, however, the backflow and entrainment is minimal. (Reasons for this are advanced in the Discussion of Results). The results, quantitatively, verify the high peaked velocity profile across the diffuser exit which makes possible

amplifier operation. Plots of the total head show regions of negative total head that account for the backflow. Regions of high positive total head are located in the mid-stream of the main exit flow from the diffuser, indicating relatively small energy losses. The dissipation of energy is fairly uniform for all three cases. Static pressure profiles indicate stagnation regions responsible for redirecting the flow.

Since turbulence measurements were not taken, the extent of the potential core and the range of the mixing region cannot be defined. However, visualization by smoke injection into the nozzles showed that the potential core vanished in about 8 to 10 nozzle widths and that the flow was, from a visual standpoint, uniform upon exit from the diffuser. The flow visualization study also illustrated the approximation to the two-dimensionality of the apparatus by indicating uniform streamlines parallel to the base plate throughout the mixing region and diffuser section.

VIII. DISCUSSION OF RESULTS

The results indicate that there is a definite flattening and sperading out of the velocity peak at the switching point as opposed to the sharp peak for the other two conditions. Whether this is attributed to the mixing of the two streams, or to the incipient switching is unknown. Also there is the possibility that this is caused directly by the momentum exchange upon impact of the two streams. Investigations of intermediate steps are needed to clarify the spreading of the velocity.

As shown on Figure 5a and 7a, there were regions of unstable vortex flow for conditions of no control flow and flow after switching. They were seen during the smoke studies and were verified by the erratic average velocity data taken in the region. The anemometer indicated large fluctuation in the velocity components. This region of instability was created by the mixing zone between the backflow and the main stream. The backflow exhibited a sluggish, pulsating flow indicating a low energy level. This was verified by the total head data. The backflow as seen from the smoke studies coincided with the regions of low total head.

It was observed that the response time varied widely, depending on the geometry. This would indicate a transient build-up until switching takes place. This is consistent with the theory of stagnation bubble pressure as a cause of switching, but it is definitely not a part of the momentum theory. The response time was probably affected by two factors: the gradual build-up of the stagnation bubble pressure and the transient instability of the vortices formed.

IX. CONCLUSIONS

From the results of the study it can be concluded that:

1) there exist large velocity gradients near one wall of the diffuser with relatively small gradients from the axis to the opposite side of the diffuser thereby yielding the momentum division necessary for amplifier type operation.

2) total head considerations indicate well the regions of back-flow and entrainment.

3) a region of unstable vortices exists between the backflow and the attached flow, which has an influence on the response time of the amplifier.

Although the present experiments clarified some aspects of flow field behavior and its relation to switching in fluid amplifiers, considerable study still remains. Specifically, additional experimental evidence is needed in certain critical regions, such as: the point of attachment of the main stream to the diffuser wall, the effect of size and location of the stagnation pressure bubble, and the influence of vortex instability on response time.

LITERATURE CITED

1. Corrsin, S., <u>Investigations of Flow in an Axially Symmetrical Heated Jet of Air</u>, NACA Wartime Report W-94.

2. Miller, D. R., Ph.D. Dissertation, Purdue University, 1957.

3. Miller, D. R. and Comings, E. W., <u>Force-Momentum Fields in a Dual-jet Flow</u>, Journal of Fluid Mechanics, Vol. 7, 1960.

4. Bollinger, E. H., M.S. Thesis, University of Illinois, 1950.

5. Olson, R. E. <u>Reattachment of a Two-Dimensional Compressible Jet to an Adjacent Plate</u>, Fluid Jet Control Devices. American Society of Mechanical Engineers' Publication, F. T. Brown, Editor. New York, 1962.

6. Greber, I. <u>Bubble Pressures under Reattaching Laminar Jets and Boundary Layers</u>, Fluid Jet Control Devices. American Society of Mechanical Engineers' Publication, F. T. Brown, Editor. New York, 1962.

FIGURES

360

Figure 1a

Figure 1b

TYPICAL VELOCITY PROFILES

——— BEFORE ATTACHMENT

— — — AFTER ATTACHMENT

DISTANCE, INCHES

0   0.5   1.5   2.5   3.5   4.5   5.5   6.5   7.5   8.5   9.5   10.5   11.5   12.5   13.5   14.5

362

PLAN VIEW OF APPARATUS

Micrometer Head

Polished Rods

Linear Ball Bearing Slides

Adjustable Slide

Plastic Diffuser Wall

Pivot Point

Rubber Wall

Flow Straighteners

Thermometer

Plastic Nozzles

VELOCITY PROBE

0.00035 Diameter Tungsten Filament, 0.044 long

Needle Tip Supports

Plastic Seal 1/4 Stainless Metal

Current and Voltage Leads
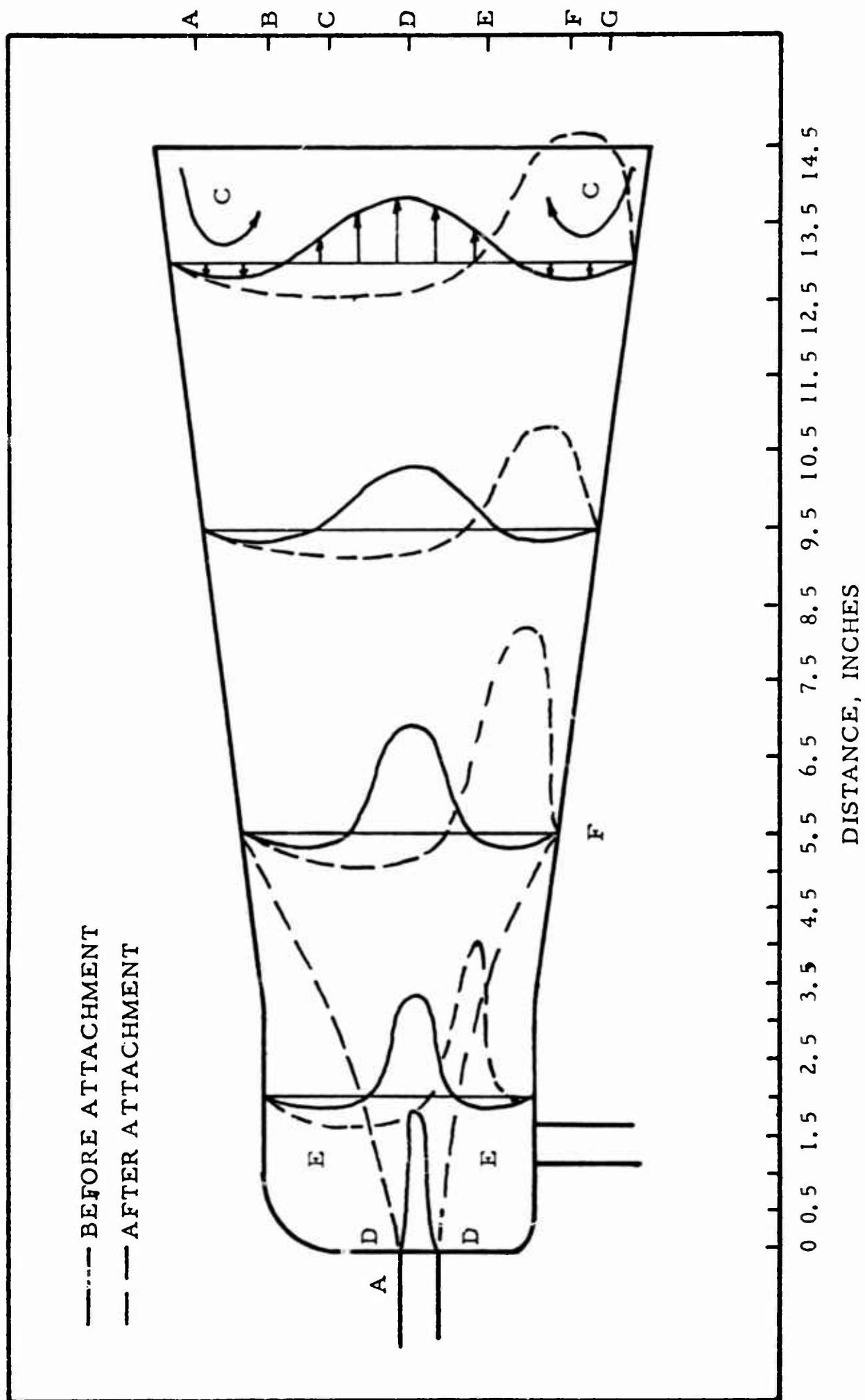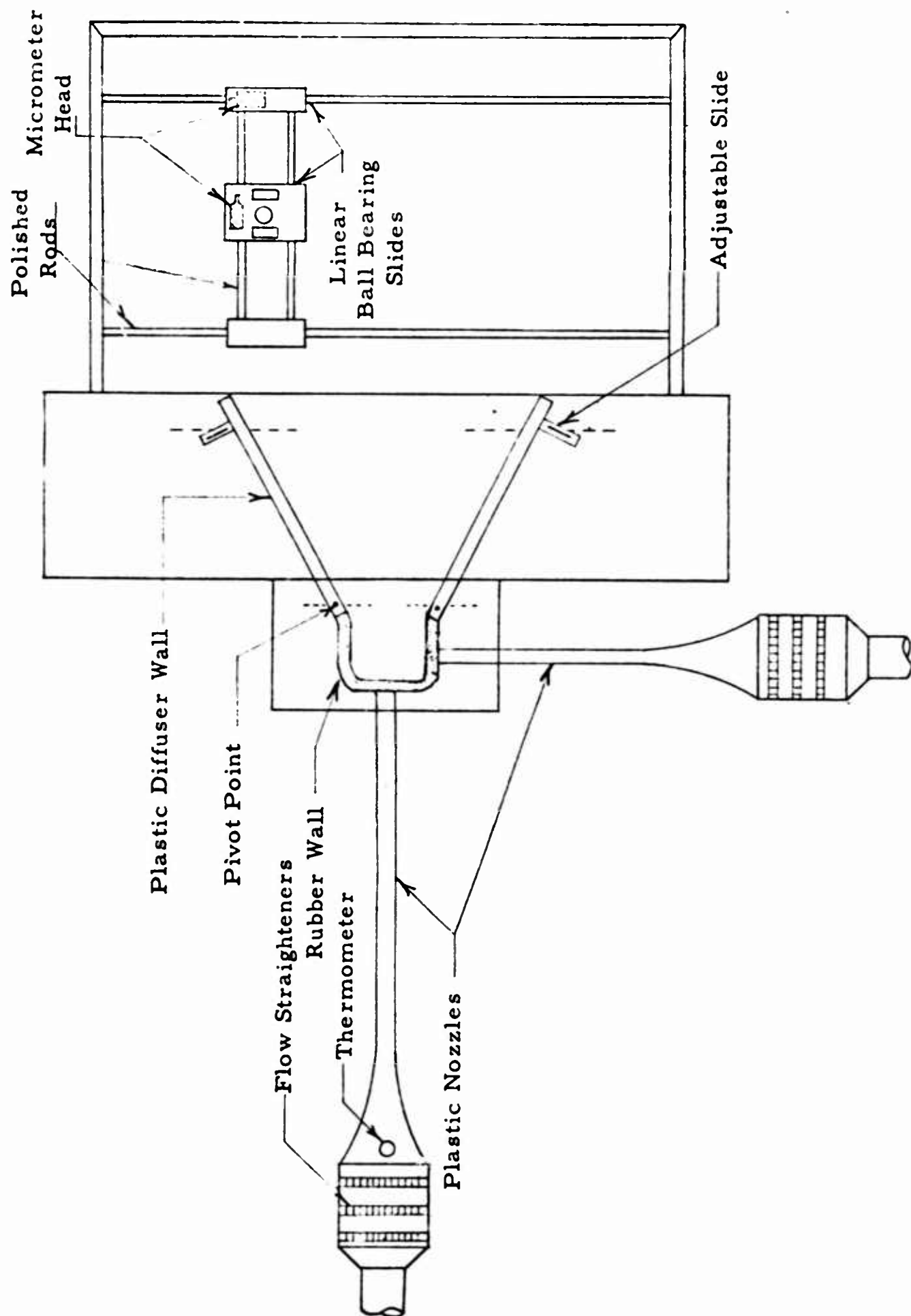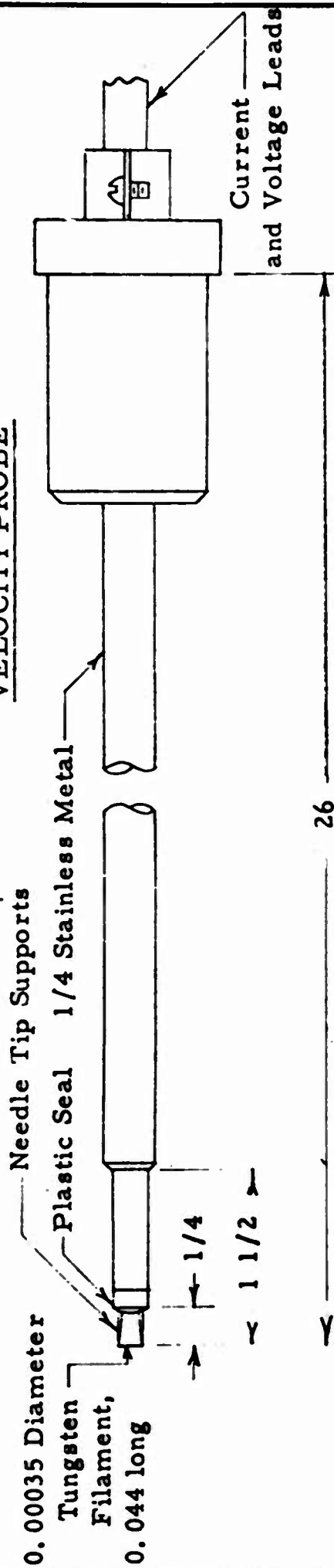
All Dimensions in Inches

1/4

1 1/2

26

STATIC PRESSURE PROBE

1/4 Brass Tubing

Solder

1/8 Copper Tubing

9° Angle

Steel

Solder

Flow

1/2

1 1/2

6

26
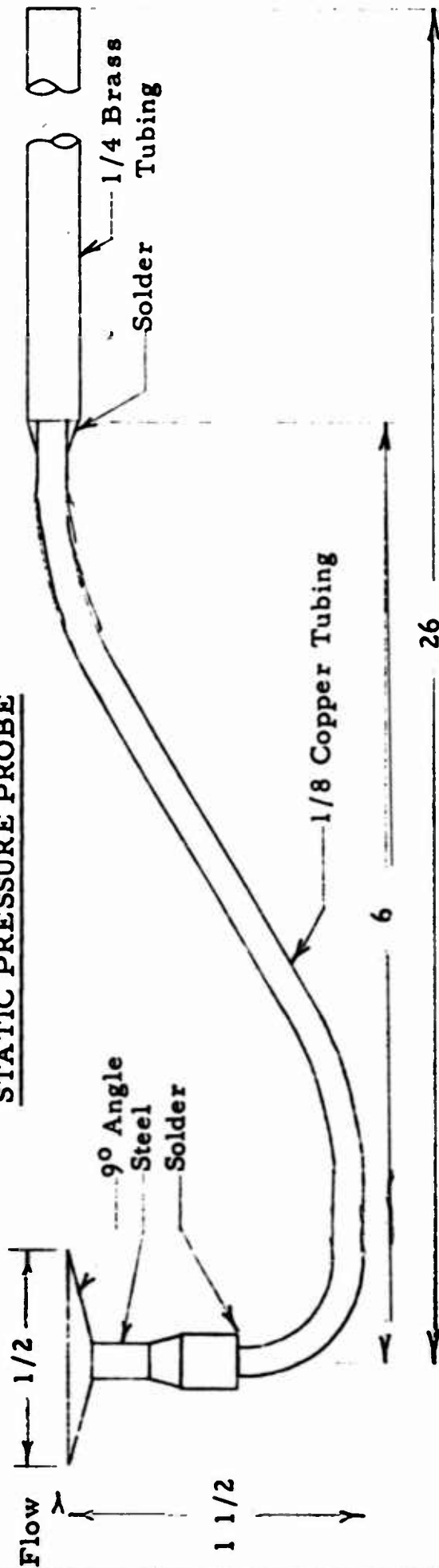
DIRECTIONAL VANE PROBE

Steel Rod

Fine Pivot Point

Brass

Dynamically Balanced Vane

1/4

1 1/4

1/4

26

364
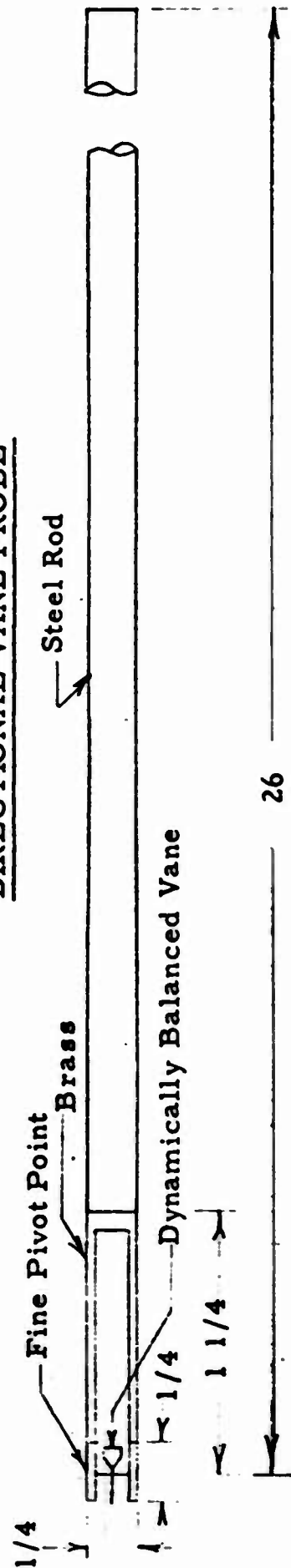
DETAILED STUDY
NO CONTROL FLOW
VELOCITY, FPM

PRIMARY FLOW = 40, SCFM
CONTROL FLOW = 0, SCFM
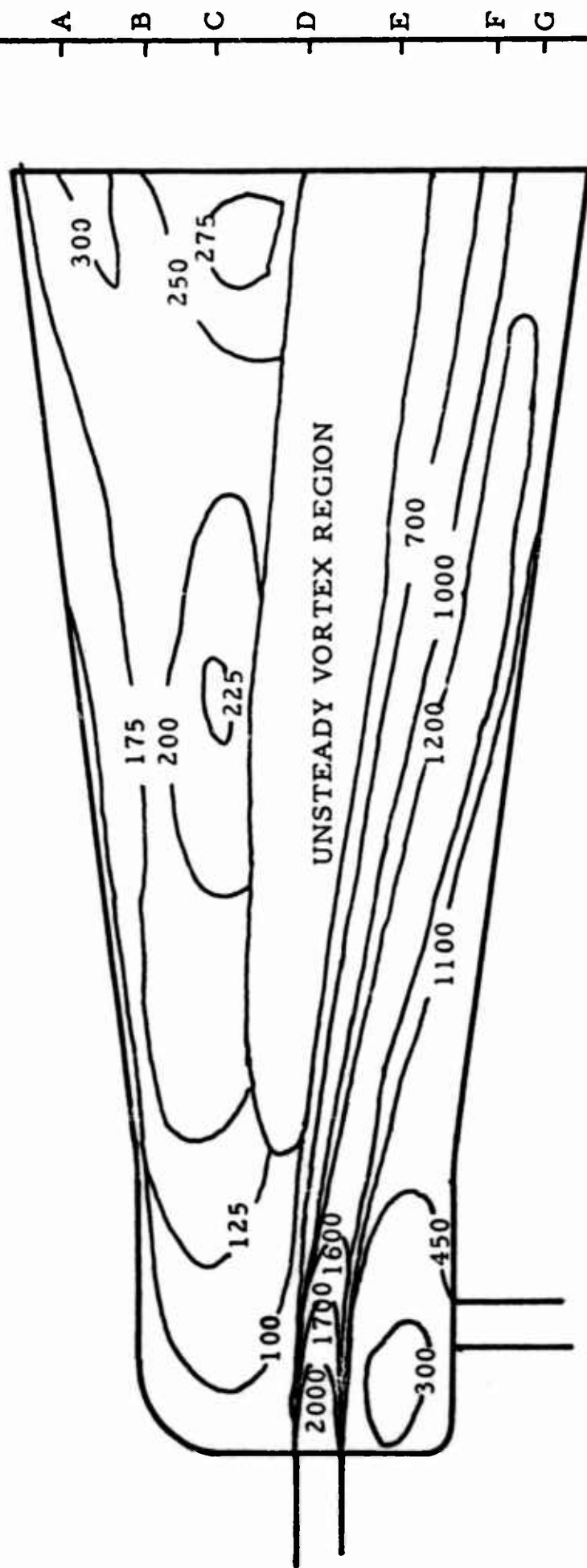
UNSTEADY VORTEX REGION

DISTANCE, INCHES

DETAILED STUDY
BEFORE SWITCHING
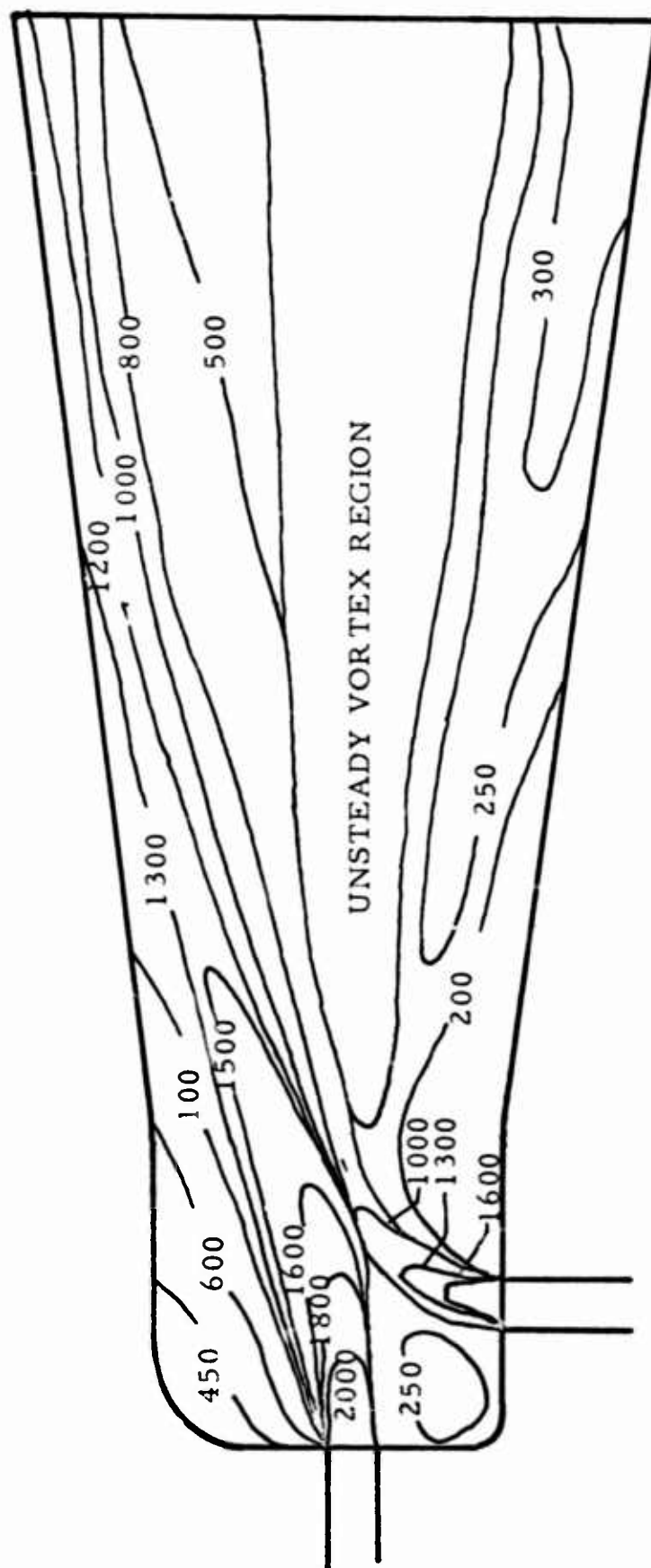VELOCITY, FPM
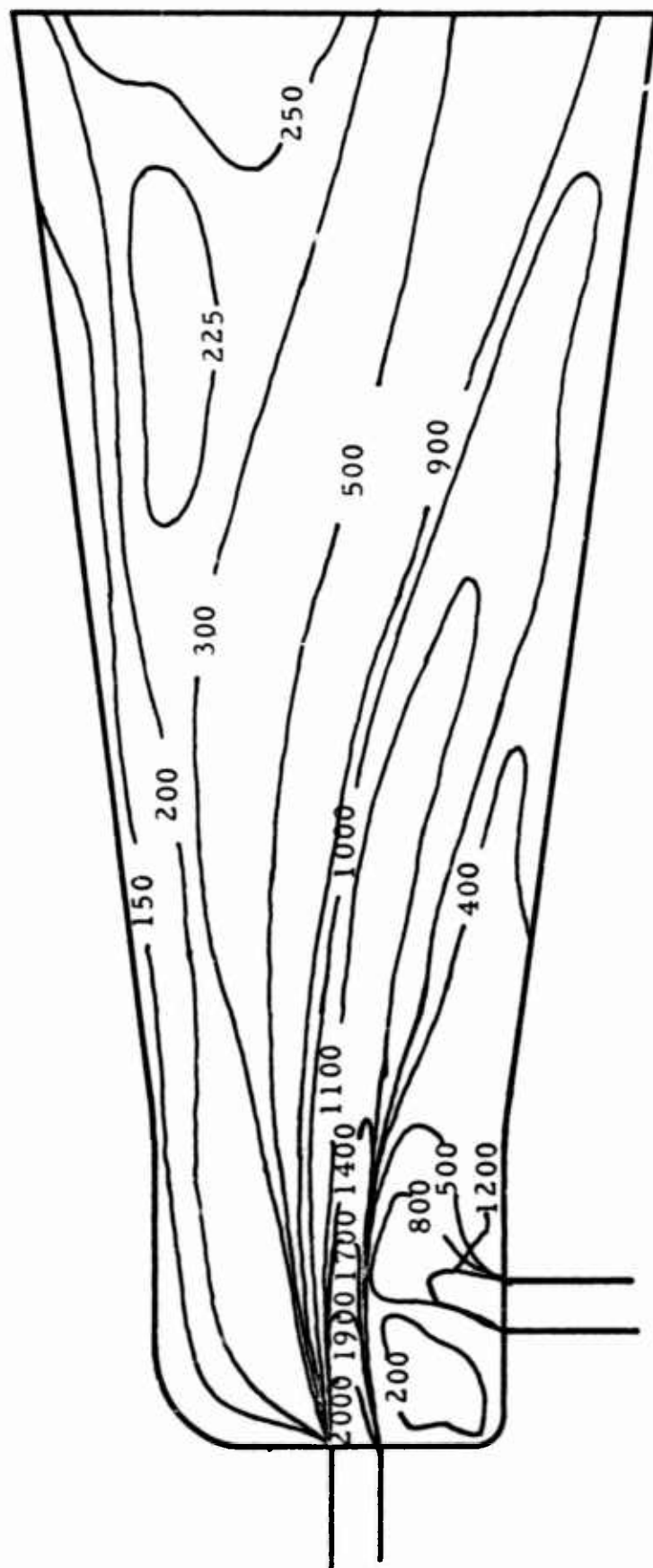
PRIMARY FLOW = 40, SCFM
CONTROL FLOW = 15, SCFM

366

DETAILED STUDY
AFTER SWITCHING
VELOCITY, FPM

PRIMARY FLOW = 40, SCFM
CONTROL FLOW = 16.8, SCFM

367

DETAILED STUDY

NO CONTROL FLOW

STATIC PRESSURE, BELOW ATMOSPHERIC, INCHES OF WATER
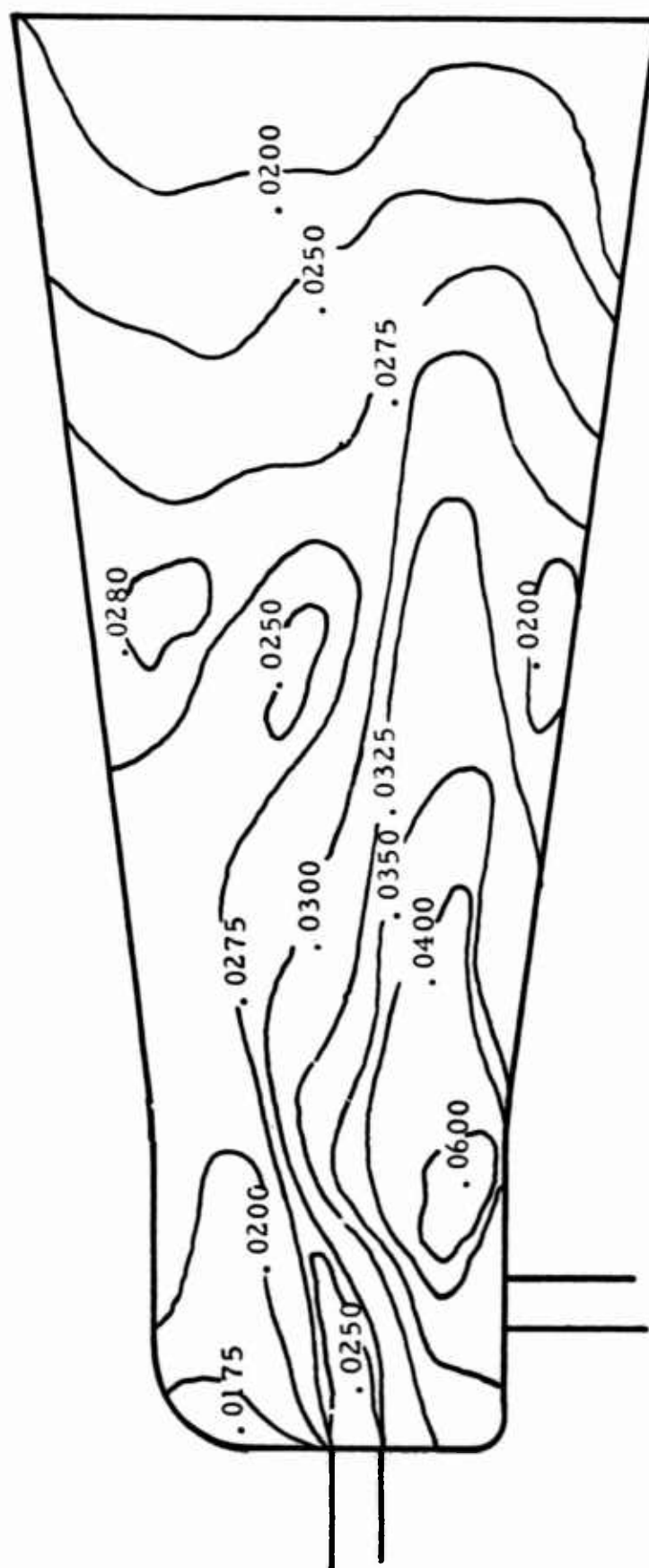
PRIMARY FLOW = 40, SCFM

CONTROL FLOW = 0, SCFM

DISTANCE, INCHES

360

DETAILED STUDY

BEFORE SWITCHING

STATIC PRESSURE, BELOW ATMOSPHERIC, INCHES OF WATER

PRIMARY FLOW = 40, SCFM

CONTROL FLOW = 15, SCFM

DISTANCE, INCHES
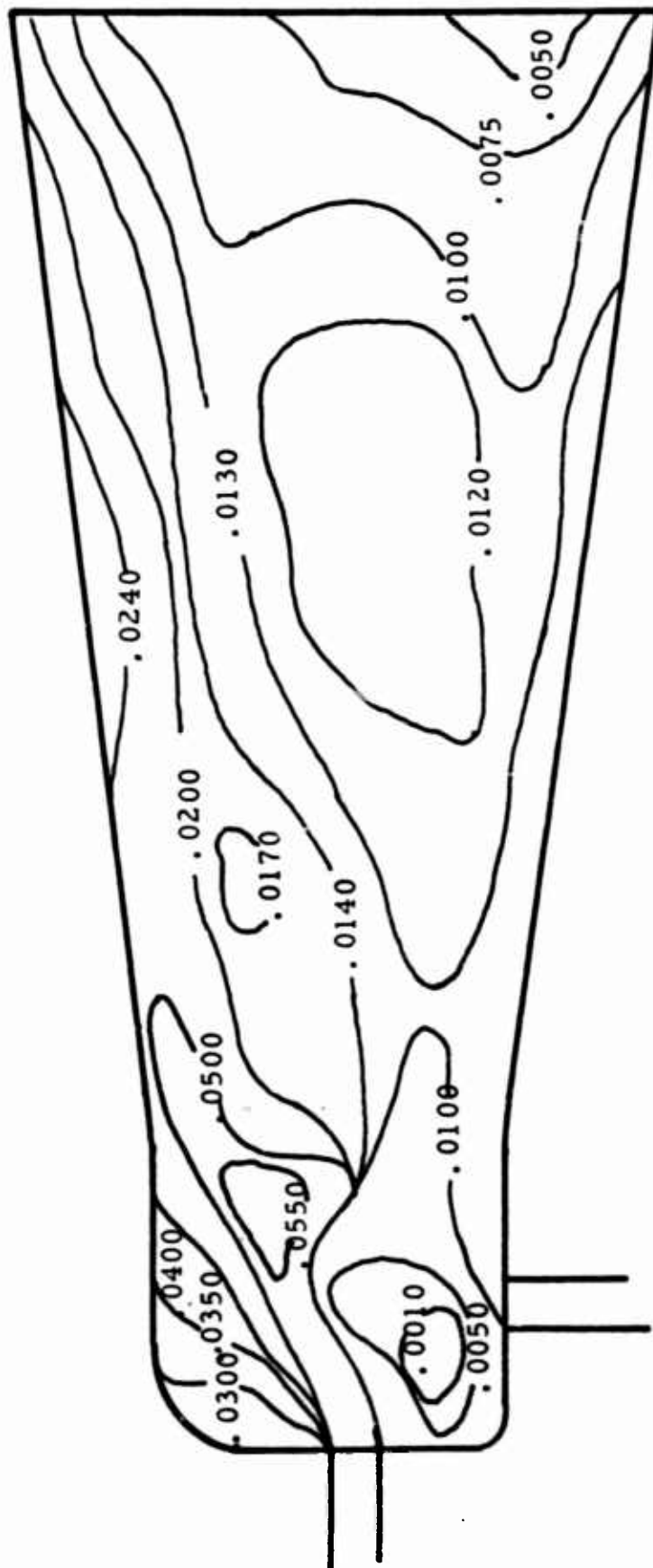
369

DETAILED STUDY

AFTER SWITCHING

STATIC PRESSURE, BELOW ATMOSPHERIC, INCHES OF WATER

PRIMARY FLOW = 40, SCFM

CONTROL FLOW = 16.8, SCFM

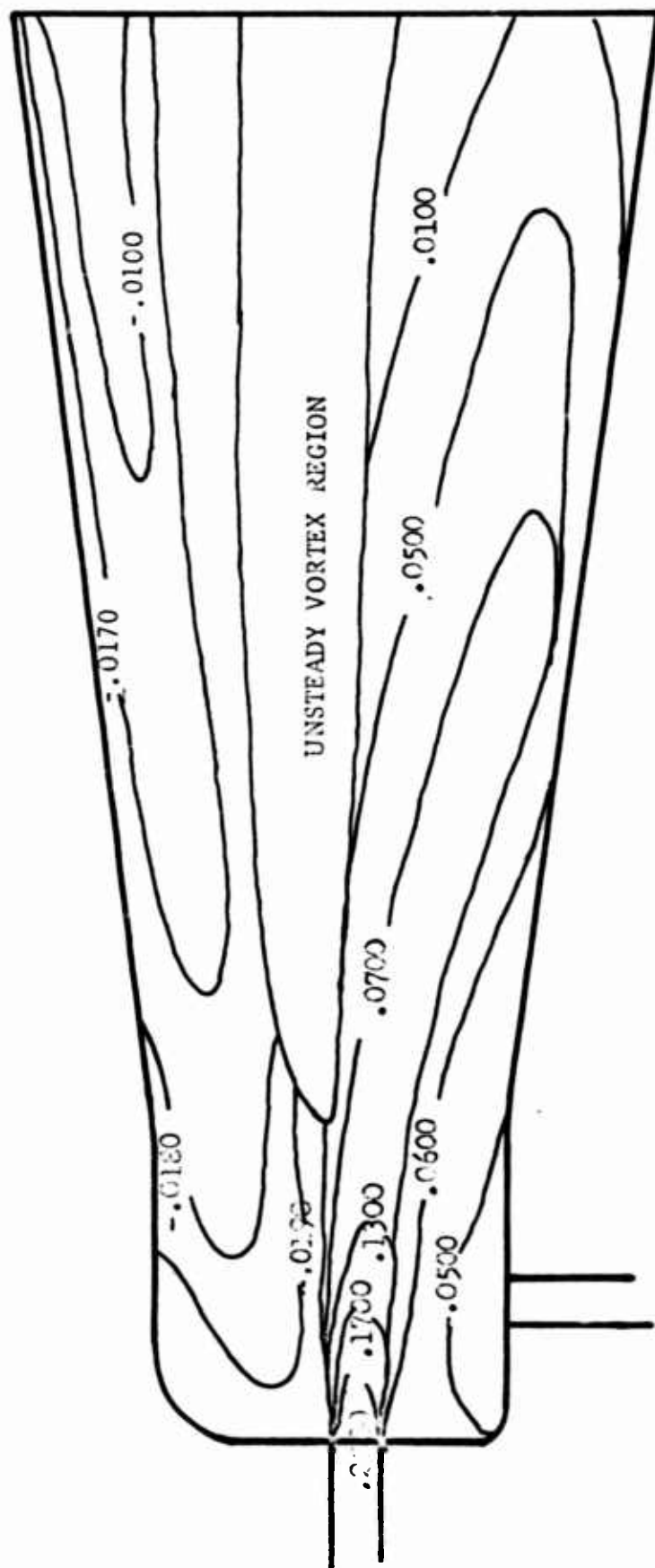DISTANCE, INCHES

370

DETAILED STUDY

NO CONTROL FLOW

TOTAL HEAD, INCHES OF WATER

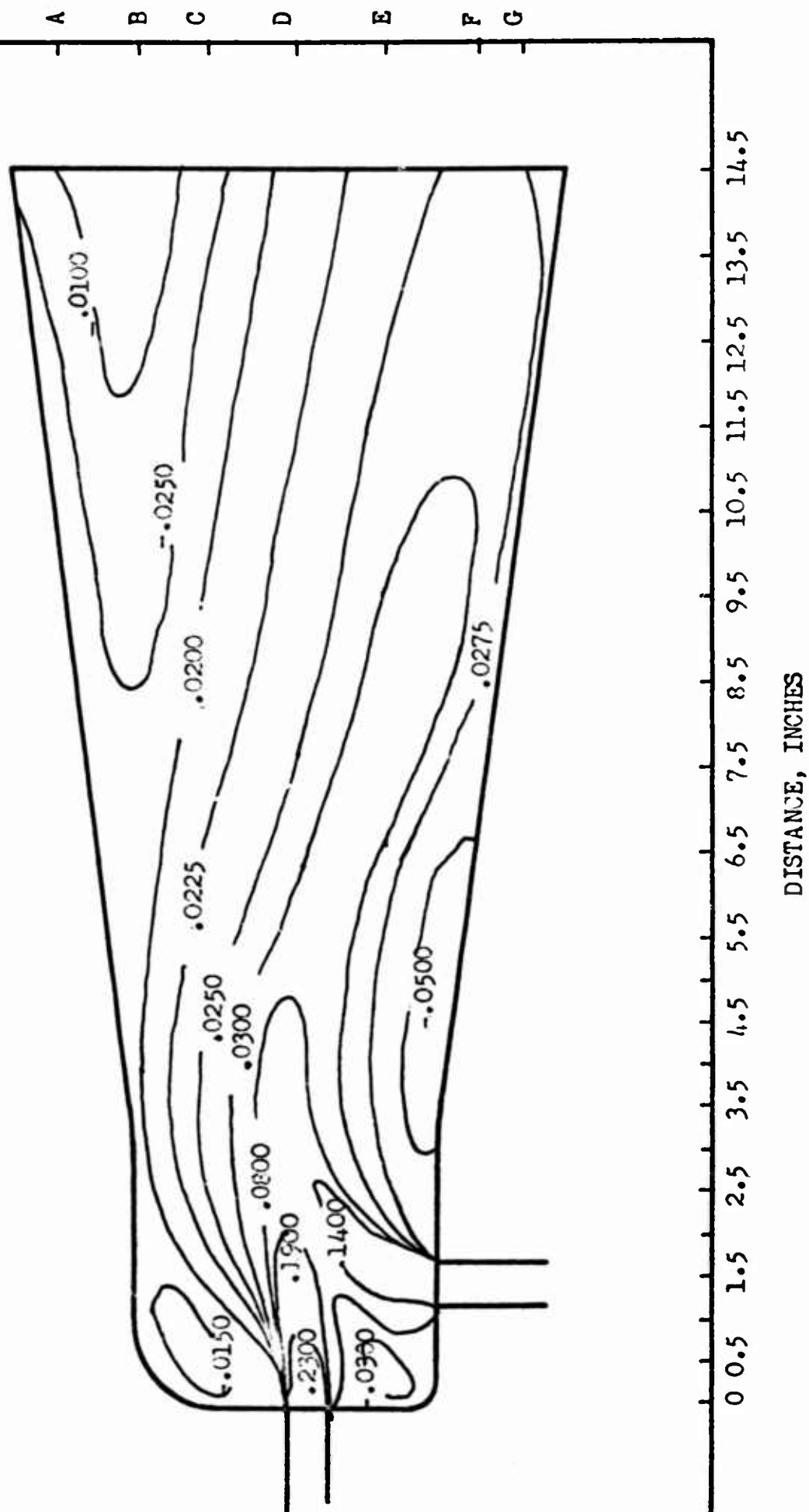PRIMARY FLOW = 40, SCFM
CONTROL FLOW = 0, SCFM

UNSTEADY VORTEX REGION

DISTANCE, INCHES

DETAILED STUDY

BEFORE SWITCHING

TOTAL HEAD, INCHES OF WATER

PRIMARY FLOW = 40, SCFM
CONTROL FLOW = 15, SCFM

DISTANCE, INCHES

DETAILED STUDY

AFTER SWITCHING

TOTAL HEAD, INCHES OF WATER
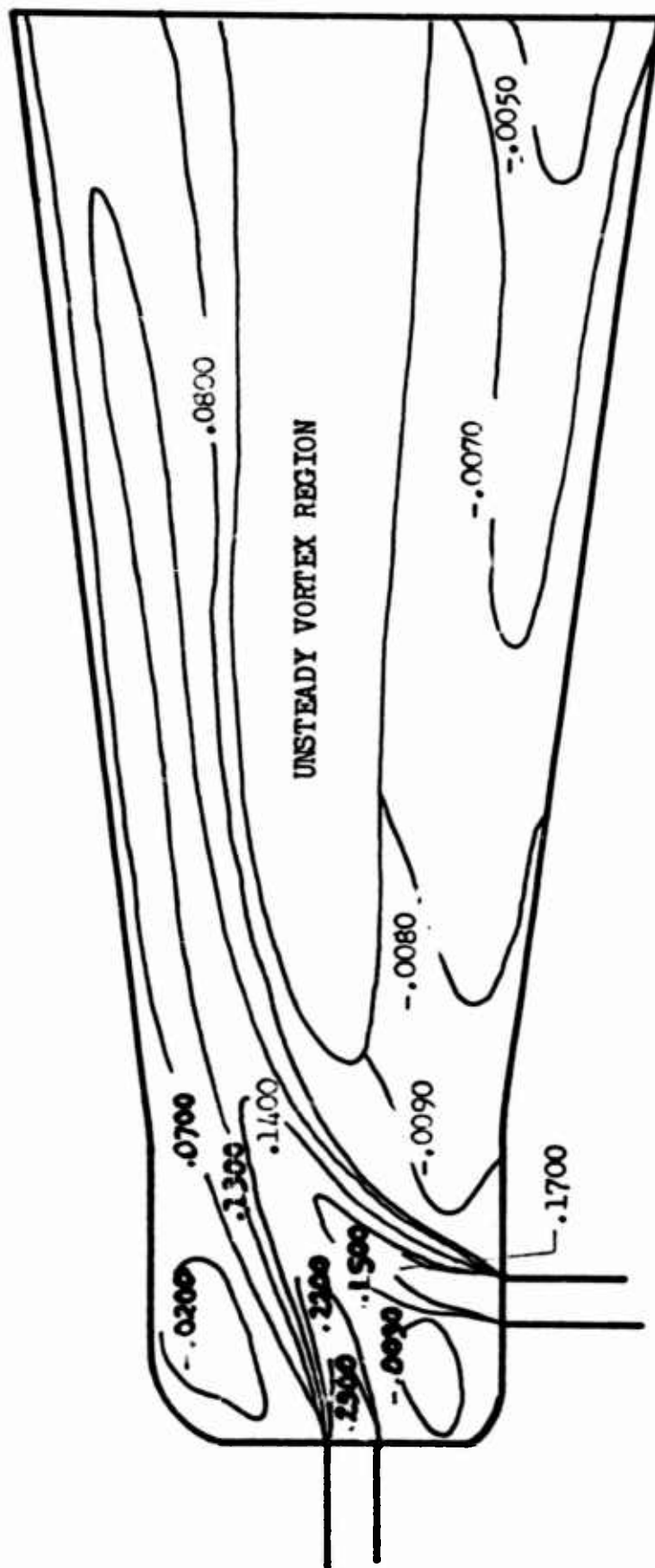
PRIMARY FLOW = 40, SCFM
CONTROL FLOW = 16.8 SCFM

UNSTEADY VORTEX REGION

DISTANCE, INCHES

A HIGH GAIN PROPORTIONAL FLUID STATE FLOW AMPLIFIER

by

M. B. Zisfein *
H. A. Curtiss **

Giannini Controls Corporation
Astromechanics Research Division
Malvern, Pennsylvania

INTRODUCTION

During the past three years the authors and their associates have been engaged in the invention, design and development of a new generation of high performance analog fluid state components. These efforts have dealt with all facets of the cybernetic loop, encompassing sensors, amplifiers, logic and compensation devices, and actuators; the ultimate objectives being the combination of these into advanced fluid state systems.

This paper deals with our development of components for mass flow amplification. These high gain flow amplifying components of ours are almost completely analogous to the electronic transistor in that the input of a control flow (current) is able, over a broad frequency band, to modulate a much larger flow fed from a supply reservoir so that it becomes an output flow which follows faithfully the time variant fluctuations of the small input control flow. We will define first the overall nature of this flow amplification and then the configurations and hardware with which it is accomplished. Consider first the flow amplifier and the electronic transistor shown side by side in Figure 1. Note that the flow amplifier, which will be described later, is here treated symbolically as a black box.

In the left diagram a supply current goes to the transistor through its Emitter. In the right diagram a supply flow goes to our fluid amplifier through its Supply Passage. In the left diagram a small current controlling signal is fed to the transistor through its Base; i.e., the base current. In the right diagram a small control flow is fed to our fluid amplifier through its Control Passage. The modulated output of the transistor goes to the load from the Collector, whereas the fluid amplifier modulated output flow goes to the load through the Output Passage. Note that both right and left diagrams show an energy source in the load circuit; in the transistor sketch it is an emf source such as a battery or generator, in the fluid amplifier sketch it is a flow source such as a compressor, pump, accumulator, or gas generator.

There are some minor discrepancies in the analogy such as the reversed bias current directions, but on the whole the analogy is a good one with one important reservation. The transistor modulates flow in the load

*   General Manager, Astromechanics Research Division
**   Chief, Applied Fluid Dynamics

circuit by changing the flow of electrons, much as a throttling valve changes the flow of a fluid. The fluid amplifier, on the other hand, modulates flow in the load circuit by proportionally distributing the supply flow between the load circuit and another output passage. In other words, the transistor can be regarded as a current or flow amplifier which is a throttling valve, and the proportional fluid amplifier is a flow amplifier which is a diverting valve.

This paper is directed at a summary of the conception, design, development and performance measurement of the linear, high gain, proportional, mass flow amplifier which was represented as a black box in Figure 1. Much of the applied research reported here was performed under Army Contract DA 36-034-ORD-3722Z, sponsored by the Army Missile Command, Guidance and Control Laboratory, under the technical cognizance of Messrs. T. G. Wetheral and J. L. Byrd.

AMPLIFIER PRINCIPLES

The nucleus of our approach to proportional fluid amplification was a search for "sensitive flows." We defined a fluid flow as "sensitive" (for amplification) when it had properties such that the introduction of a small secondary or control flow at the proper location would produce a large change in a substantial portion of the primary flow. The primary sensitive flow upon which our high gain mass flow amplifier is based is the flow in an elbow or sharply curved channel.

Consider the curved channel shown in Figure 2. A typical supply flow velocity distribution is shown at the curved channel inlet. By making the inner wall radius suitably small, we can effect an inner wall separation at, say, point (A). The velocity profile of this separated flow at the curved channel exit is shown as the solid line U_A. If we consider the region contained in the dimension (d) as the output region of the curved channel, we find that large changes in the momentum flux through this output region can be effected by moving the separation point from (A) to, say (B). This momentum flux change can in turn be produced by relatively small changes in a secondary flow directed to operate on the inner wall boundary layer between points (A) and (B). The velocity distribution at the curved channel exit when the separation point has been forced from (A) to (B) is shown in Figure 2 as the dotted line U_B. Thus, by using a small flow to manipulate the inner wall separation point, we cause a large change in the main flow (U_A to U_B).

The small flow, which can manipulate the inner wall separation point, is a control flow. It may be applied to the inner wall boundary layer to promote early separation as from (A) to (B), or alternately, to delay separation from (B) to (A), depending on design requirements. The closeup views of the inner wall in Figure 3 show four of the control flows which the authors have found useful. The first two of these in Figures 3 (a) and (b) are the familiar wing-aerodynamicists' boundary layer control techniques of energizing and removal. In Figure 3 the energizing control flow ducted in through the control passage keeps a boundary layer which would

normally separate at point (B) attached until it reaches point (A). In Figure 3 (b) the boundary layer removal passage carries away the boundary layer at some point ahead of its normal separation point (B), causing the flow to stay attached until it reaches point (A).

Figures 3 (c) and (d) show two control flow application techniques which do not correspond to conventional aerodynamic practice. In Figure 3 (c) it is assumed that curved channel parameters have been selected to ensure a laminar boundary layer which, with no control flow, would separate in laminar fashion at point (B). The tripping control flow emanating from the control passage tends to change the boundary layer from laminar to turbulent and keep it attached until it reaches point (A). In Figure 3 (d) our most successful technique to date is shown. The counterflow control stream emerges from the control passage in the opposite direction from the local boundary layer flow. The stronger the control flow, the farther upstream the separation point is moved from its original or zero-control position.

The success of the counterflow approach in Figure 3 (d) illustrates a recurring facet of fluid state control work. The best flows and techniques are likely to be those which the conventional aerodynamicist might like least. Many techniques, such as the forced separation shown here, are the opposite of usual aerodynamic philosophies related to good vehicle or turbomachine design. For this reason, the flows which appear to be most useful in fluid state control have had relatively little analytical consideration in the past and, to make matters worse, many of these are inherently among the more difficult flows to approach theoretically. In current practice, device design is frequently delayed or thwarted because of the lack of usable analytical solutions.

Summarizing to this point, we have described how the momentum distribution of separated curved channel flow can be manipulated by the proper introduction of a relatively small control flow.

The extrapolation of this technique to high-gain proportional mass flow amplification is accomplished through utilization of another sensitive flow; i.e., oblique flow impingement. This can be illustrated by what we call our Double Leg Elbow Amplifier shown diagrammatically in Figure 4. Here the curved channel or elbow and its control flow are shown inside the dotted boundary a-a. This channel is controlled by the counterflow technique of Figure 3 (d).

The inlet flow of the curved channel is about one half of the desired total supply flow. The other half of the desired supply flow is ducted through the passive leg which is so arranged that the two halves of the supply flow (the modulated half and the unmodulated half) impinge at the curved channel exit. A splitter vane has been used to ensure that the modulated flow emanating from the curved channel exit is the flow passing through region (d) of Figure 2. The two halves of the supply flow merge and from the total power stream. Pickoffs are so arranged that this combined power stream exits entirely through channel 1 for no control flow, and entirely

through channel 2 for full control flow. Between these extremes the output flow is divided between channels 1 and 2 in proportion to the amount of control flow.

In operation, the supply flow is fed to the inlets of both the curved channel and the passive leg. A control flow (say, the output of a fluid state sensor) is fed to the counterflow control passage at the inner wall of the curved channel. The control flow modulates the power stream, which is the merged output of the supply flows. Hence, the control flow modulates the output flows through channels 1 and 2.

The novel principles and devices which have been described above are currently protected by patent actions (Ref. 1) pursued by Giannini Controls Corporation.

The following sections of this paper describe the experimental program conducted to evaluate these sensitive flow concepts and their application to a fluid state amplifier.

EXPERIMENTAL DEVELOPMENT

Experimental studies were conducted in such a way that a logical stepping stone approach to evolvement of a workable high-gain linear proportional fluid state amplifier would result. Therefore, flow in a curved channel with various control flow techniques was studied first to determine the important parameters and select the most promising configuration. These tests were followed by studies of obliquely impinging flows using the modulated curved channel flow as one leg. And finally, studies of a complete amplifier element with output flow pick-offs were conducted to develop and evaluate the Double Leg Elbow Amplifier.

All of the developmental experiments were conducted using laboratory instrument air as the test medium under controlled flow and pressure conditions. All test models contained only rectangular passages. Test velocities were in general maintained low enough (less than 300 feet per second) to eliminate compressibility considerations, but still provide turbulent boundary layer flow conditions in the regions of interest. Reynolds numbers based on effective passage lengths were in the 10^4 to 10^5 range.

Separating Curved Channel Flow

To study the sensitivity of separating curved channel flow, a curving channel or elbow of sufficiently small curvature to promote flow separation on the inner wall was utilized. Small control flows were injected into this separating flow region in one of the boundary layer control techniques previously mentioned (Figure 3). Velocity profiles were obtained from pitot probe surveys at various locations near the channel exit and further downstream. These data, along with gross measurements of the input control and supply stream mass flows and pressures, were used to study the effectivness of the various control schemes in effecting a redistribution of the supply stream momentum.

An example of the flow from this elbow with no control flow injection is shown in Figure 5* where constant velocity lines representing 90% of the peak velocity are shown in relation to a typical channel geometry. Velocity profiles at three streamwise locations are superimposed on the figure.

In Figure 6, velocity profiles, for a constant elbow supply mass flow, at the channel exit for three different control input schemes are compared with the no control case. We call the method of blowing normal to the stream, "cross-flow", and indicate in the Figure the angular location of the injection slot with respect to the exit plane as diagrammed in Figure 5. The 30⁰ cross-flow slot is very near the separation region. The redistribution and resulting increase in the stream momentum and mass flow over a controlled region to the right of the channel for each of the control injections are clearly evident in the figure. It is also evident that the counterflow injection technique is somewhat superior in effecting this flow redistribution.

By suitable placement of a splitter vane in the region to the right of the channel exit, d in Figure 2, linear mass flow gains of over 6:1 have been obtained with the curved channel configuration alone. Since the elbow configured in this manner is in fact an amplifier, we call it the Single Elbow Amplifier to distinguish from the double leg configuration. Typical input-output mass flow results for a Single Elbow Amplifier with a fixed splitter vane location are shown in the lower portion of Figure 7. These data represent a linear proportional mass flow gain of 5.7. It is also significant that this gain is accomplished with essentially no loss in supply pressure.

For our purpose of developing a high gain flow amplifier the prime function of the single elbow is to provide the maximum possible momentum change, since this is the essential factor in deflecting the combined power stream in the Double Leg Elbow Amplifier (DLEA) configuration. The upper curve in Figure 7 shows the momentum flux imparted to the elbow exit flow for the same test run. The resulting momentum relation for these data in terms of the control mass flow is:

$$\frac{M_o}{M_{ei}} = 19 \frac{\dot{m}_c}{\dot{m}_s} + 0.7$$

or; for example, the momentum is nearly doubled with a control flow increase of only one tenth the supply flow.

Many variables enter into the resulting performance of the Single Elbow Amplifier including geometric factors such as control slot width, location of the injection port, splitter vane location and passage aspect ratio, not to mention elbow curvature and flow parameters. Space and continuity considerations preclude presenting here the data showing the effects of such

---

* A considerable portion of the results reported herein were published in three Giannini Controls Corporation reports (References 2,3 and 4).

variations. However, much data of this nature have been obtained and are published in Reference 4.

It is worthy of noting that the power gain can be increased at the expense of flow gain by increasing the width of the control injection port. We have never had occasion to maximize power gain, hence we do not presently know how much power gain can be increased.

It would obviously be desirable to develop a satisfactory analytical technique to describe all the observed flow phenomena - particularly, the separation characteristics. As a start, a search was made of the available published literature. The authors found no effective applicable theoretical work covering flow in curved channels with separation present, let alone with the additional problem of injected auxiliary flows. For this reason the authors and their associates at the Astromechanics Research Division have devoted considerable effort to the derivation of the needed analysis. Progress has been typically slow and painful but in some areas the work has been particularly illuminating. A more detailed study of separating flow in curved channels is presented in another paper (Ref. 5) as part of this symposium. Such studies are essential to a reasonable understanding of high gain flow amplification. We are particularly indebted to the Mechanics Division of the Air Force Office of Scientific Research, under the technical cognizance of Capt. L. P. Gregg, for sponsoring the basic studies reported in Reference 5.

Impinging and Intermixing Flows

It was mentioned earlier that the redistributed momentum exiting from the elbow was utilized to obtain a large proportional amplification by impinging this flow against a passive flow. The interacting streams form a merged jet with a variable deflection angle which is proportional to the original elbow control flow. This section discusses the power jet deflections resulting from this impingement and the additional strong effect of an adjacent boundary; i.e., the splitter vane wall contour.

Output flows from two of the above described elbows, or one elbow and one straight channel, one of which was modulated by a control flow, were impinged obliquely in a region close to the channel exits as shown in the sketch of Figure 8. The effects of the adjacent splitter vane wall curvature and the importance of the incoming flow magnitude and kinetic characteristics on the deflection of the resulting power jet were studied along with the influence of the resultant intermixing on the turbulent diffusion of the jet. This was accomplished by pitot probe measurements of local velocities at various downstream locations for a range of active, passive and control flows.

A typical deflection pattern of the resulting power jet is presented in Figure 8. For this figure, the two impinging flows are inclined approximately at right angles to each other. The power jet flow boundaries are represented by lines where the velocity has fallen to 90% of the peak velocity and by median lines between these 90% boundaries. With no control flow

into the modulated leg, the resulting power jet was at position (A). By imposition of a control flow of 0.019 times the total supply flow, the power jet was deflected to position (B). The net deflection of the power jet was approximately 17°, <u>even though the net deflection would have been only 6° for a perfect momentum interchange</u>. Thus a considerable bonus in jet deflection and thereby a higher potential amplification is obtained. Our experiments show, further, that an even greater bonus in jet deflection occurs when the two impinging flows are inclined at an oblique angle of 60°.

The cause of this bonus in deflection of the combined stream power jet is clearly an important factor in utilizing these concepts since a sizeable boost in gain results. Our experiments indicate that the effects of flow attachment to the adjacent splitter vane wall and subsequent separation induced by the modulated flow cause the increased deflection. For example, referring again to Figure 8, if there were no wall present, the power jet would be inclined 6° to the right of the jet bisecting reference line with no control flow, assuming perfect momentum interchange. Instead, the power jet is inclined 7° to the left toward the adjacent splitter vane wall, where (our experiments show) it clearly is entrained before separating into a free jet.

Therefore, the shape of the splitter vane contour is an important factor in determining the deflection characteristics of the power jet. If the contour is a smooth unbroken wall and does not have a large curvature to promote free boundary separation, the power jet will stay attached to this wall and become bistable. The tendency toward bistability is eliminated by adding an abrupt contour change in the form of a forward facing step or spoiler as shown in the sketch below or by introducing a restrictive bleed opening, as also shown in the sketch. The spoiler has the effect of forcing
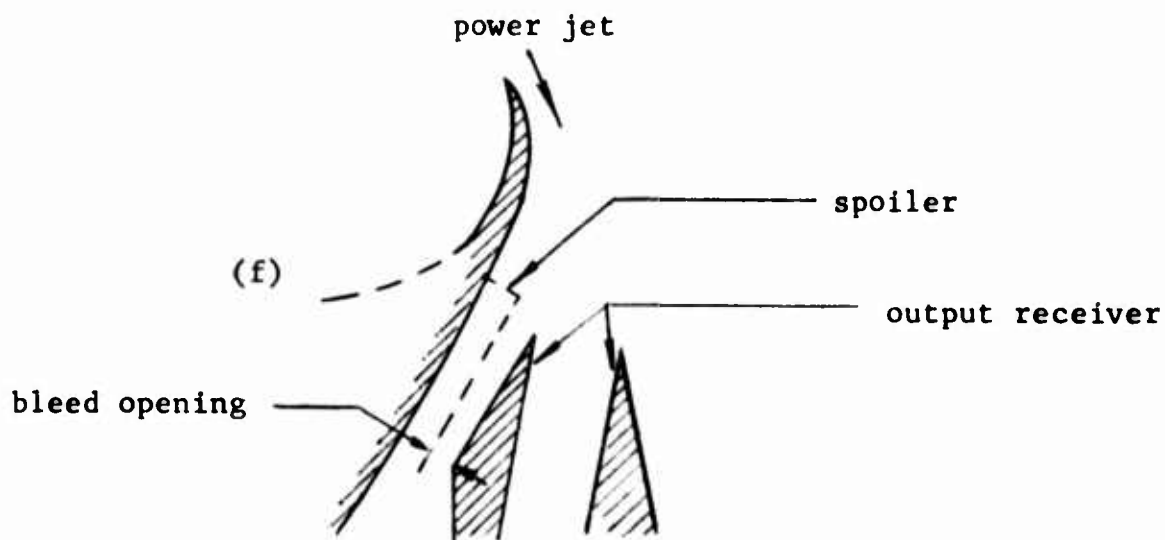
the power jet to separate from the splitter wall whereas the restrictive bleed accomplishes the same end by providing too much impedance for the power jet to remain attached. However, we have found this latter approach to be inferior because it also reduces the deflection sensitivity.

Another approach, that of providing a relatively large curvature as in (f) of the above sketch, reduces the bistability by fixing the point of separation from the splitter wall so that there is no deflection of the power jet. This latter effect was also observed in previous tests with a rearward facing step.

It was also observed during these tests that the maximum gains occur when the power jet is almost unstable or "critically stable" in whatever deflection angle it is located. This shows up as a mild oscillation of the output flows for a fixed control flow. In general, an optimized DLEA configuration provides critically stable operation where the oscillations are ± 3% or less. Undoubtedly, this critically stable condition is a function of the boundary layer separation tendencies from the splitter vane wall. Thus it is clear that the physical contour of the adjacent wall is a very important factor in determining the overall deflection of the power jet.

Typical velocity distributions of the power jet at a downstream distance five times the channel width for various control stream modulations of the active leg are shown in Figure 9. The impinging flows were inclined at an approximate angle of 60° for these data. It is seen that the power jet is deflected in proportion to the momentum modulation of the active leg.

The velocity distributions of Figure 9 are very nearly Gaussian curves, indicating that the combined stream power jet is roughly equivalent to a single turbulent submerged jet in the region past the so-called core region (Albertson, et al, Ref.6) and that the free jet assumption of velocity profile similarity is valid here.

The dynamic pressure of the power jet is shown, in Figure 10, to decrease linearly in proportion to the reciprocal of the distance downstream. This agrees with calculations for a two dimensional submerged jet for constant momentum flux and similarity; e.g., Schlicting, Ref 7. This inverse distance dependence is seen to be independent of the impingement angle and the degree of flow attachment to the splitter vane wall. Thus the behavior of the combined stream power jet can be handled analytically once its initial direction is known. Determining this direction, however, is beyond the range of any known theoretical analysis at the present time. As in the curved channel, the problem of a separating curved flow is involved, but with the added complexity that one boundary is free and the flow pattern will depend strongly on the kinetic characteristics and direction of both impinging streams. In all likelihood, a considerable body of empirical knowledge on this phenomenon will be required before an adequate theoretical treatment is possible.

The above demonstrates that impinging two roughly similar jet flows adjacent to a properly contoured wall and modulating one of the flows will produce a large deflection of the resulting power jet. This deflection is utilized to provide a large mass flow amplification as described in the next section.

AMPLIFIER PERFORMANCE

Earlier in this paper we described how we combined a sharp elbow, an injected control flow, a passive impinging leg and a splitter vane to make the Double Leg Elbow Amplifier in Figure 4. Next we briefly described some of our flow experiments directed at maximizing our understanding of this kind of amplifier. We now summarize some of our test programs which were directed at optimizing and precisely measuring amplifier static and dynamic performance.

We have conducted a wide range of experimental studies of the Double Leg Elbow Amplifier in an operational configuration with instrumented output receiver pickoffs. An optimized mass flow amplification configuration of the DLEA was derived from an extensive series of tests with variable geometry models, one of which is shown in Figure 11. Performance tests of this optimized configuration were conducted with various sized models over a broad range of flows, pressures, and output loadings.

In addition, we have explored the dynamic characteristics of both Single Elbow and Double Leg Elbow Amplifiers over a wide range of input frequencies and also with transient inputs, and finally, we have conducted static performance tests with staged elements. Some of the salient results of these tests are presented in the following discussion.

Static Performance

As mentioned above a DLEA configuration was optimized to obtain high mass flow gain using a variable geometry model. In all of the DLEA models the power stream was directed into one of two output receiver passages which contained low-impedance venturi sections for measuring output flows. Sufficient bulk measurements of control input, supply and output mass flow and pressure characteristics were obtained to define element gains in conjunction with pertinent stream momentums, power levels, and impedance levels.

We define gain herein in the usual differential form; i.e., the ratio of the change in output to the change in input control, which for the DLEA becomes $\Delta(\dot{m}_{or} - \dot{m}_{ol})/\Delta\dot{m}_c$ for mass flow gain and $\Delta(W_{or} - W_{ol})/\Delta W_c$ for power gain. An example of the high gain capability of the DLEA is shown in Figure 12 where differential output mass flow and power are shown as functions of the input control mass flow and power. The output is a linear, proportional, mass flow with a differential gain of 220 and a corresponding differential power gain of 37. The mass flow gain is greater than any other demonstrated technique known to the authors, and furthermore, the power gain is substantial considering the fact that this DLEA was optimized for mass flow gain only.

There are many geometric and flow parameters that affect the overall performance of the DLEA; too many to include an appropriate discussion in this paper. The reader is referred to Reference 4 for applicable test results. However, it is worth noting here that the ratio of passive supply flow to the active leg supply flow does not have a strong influence on gain over a sizeable range of flow ratios. Geometric variables of importance in addition to those mentioned earlier include the location and width of the

receiver openings (typical of other fluid state type amplifiers), location and orientation of the splitter vane, width of the passive leg, and the size of the bleed opening (referring back to the sketch on page 7).

An analytical approach for describing the performance characteristics of the DLEA for varying flow and geometric conditions is presented in Ref. 4. The method, which is a combined theoretical-empirical approach, is presently being refined so that a more complete understanding of DLEA operating principles can be obtained without recourse to extensive testing.

Typical output loading characteristic data for the DLEA is shown in Figure 13 where single output total pressure vs. output mass flow is presented for a series of output impedances. We define impedance here as $P/\dot{m}^2$ since this is almost constant in a given flow geometry with turbulent flow. The element static performance is not affected by increasing the impedance until Z is greater than 4×10^3 $sec^2/in^2 lb$ where the gain begins to drop off from 200 although it is still a respectable 100 for a further four-fold increase of impedance.

For a nearly fixed DLEA configuration, performance tests at similar flow velocities and Reynolds numbers were conducted with three different scale models spanning a flow passage area range of 16. The results demonstrated that roughly similar high gain performance is obtained although some of the operating characteristics are different. Scaling is an inherently difficult problem in fluid state work because boundary layer growth (Reynolds number), flow velocity and flow impedance are all related to a different power of the scale and yet each influences amplifier performance.

A single DLEA element can be operated over a broad range of flows and pressures as shown in Figure 14. Flow and power gains and bias flow required are shown in this figure for a tenfold supply flow range which corresponds to an approximate supply power range of 0.6 to 600 watts. It is evident from this figure that the DLEA mass flow gain is not affected by this large variation in supply conditions.

Recent tests have been conducted with a two stage cascade of DLEA elements with typical results shown in Figure 15. Here, differential second stage output flow is presented as a function of the first stage input control flow for a factor of two difference in supply flow. The mass flow gains are seen to exceed 6,000 for the higher supply flow condition.

Dynamic Characteristics

Dynamic and transient tests of both the Single Elbow Amplifier and DLEA have been conducted to define the dynamic characteristics for use in system synthesis. The dynamic measurements of output response to control flow fluctuations were carried out using a two-channel constant-temperature hot-wire anemometer arrangement. Simultaneous readings of input control and output stream velocity fluctuations were recorded on a dual-trace oscilloscope and/or a recording oscillograph. Approximate harmonic

control input modulations were applied using a rotating valve arrangement, illustrated in Figure 16, for frequencies above 100 cps and using a pneumatic servo-valve for the lower frequencies.

Some typical data of these studies for the Single Elbow Amplifier are shown in Figure 17. Oscilloscope traces of output responses to 25 and 1000 cps approximate sine wave control inputs are reproduced in the figure. The input and output flow hot-wire anemometer readings are displayed as companion traces. The upper trace in each pair represents the velocity measured upstream of the control injection slot while the lower trace represents a measurement at the controlled curved channel exit. The traces shown are voltages across the hot-wire bridge circuit and, as such, are proportional to the fourth root of the instantaneous velocity at the hot wire.

The flow gain for this set of Single Elbow Amplifier data is about 5. It is interesting to point out that recognizable modulations are obtained at frequencies in the kilocycle range - and probably higher since only our equipment limited the input frequencies.

Typical input-output oscilloscope traces of a DLEA are shown in Figure 18 for a 10 cps harmonic input and for a step input. A corresponding Bode diagram for this same model in the 0.1 to 75 cps range is presented in Figure 19. Three sets of data are indicated on the figure; that is, two different supply mass flows, and one test with no output receivers present and the hot-wire mounted where the receiver would have been (see the inset sketch). The curve labeled "A" in this figure was corrected to the dashed curve by eliminating the transport lag which was measured from transient tests.

A Fourier integration method was applied to the step transient data shown in Figure 18 as an independent method of determining the dynamic characteristics. The results of this analysis were identical with the measured phase lags and within 3 db of the measured gain reductions shown in the Bode plot of Figure 19 up to 20 cps. The agreement was striking, particularly considering that the step transient was not abrupt enough to provide other than low frequency harmonic content for the analysis.

Several interesting observations can be ascertained from the Bode diagram of Figure 19. In particular, it can be seen that the amplitude ratio of this amplifier without output receivers is flat in the range tested indicating that the receiver and venturi cause some output attenuation in the frequency range tested, and that higher mass flows and pressures have less attenuation but do not seem to have a different phase shift. An analysis of the amplitude characteristics of Figure 19 indicates that the transfer function is approximately that for a linear first order system or:

$$\frac{K}{\mathcal{T} s + 1}$$

where the time constant, $\mathcal{T}$, is from .01 to .015 sec. for the two curves based on a 6 db/octave attenuation rate. The phase shift, corrected for transport lag, is considerably less than would be expected for a linear system of the amplitude attenuation indicated above since the phase lag at

the -3 db point is less than 45°.

These measurements demonstrate conclusively that the dynamic response of the DLEA and Single Elbow Amplifier are more than adequate for most control system requirements.

CONCLUDING REMARKS

"Sensitive" flows have been developed and successfully integrated into a method for high gain proportional amplification in fluid state control systems. The concept of separated curved flow modulation is a useful means of directly amplifying stream momentum while the concept of jet impingement with adjacent wall entrainment is clearly a powerful means of converting a modulated momentum into large mass flow gains. Linear proportional differential mass flow gains of over 220 are obtained with this Double Leg Elbow Amplifier technique over a broad range of element sizes, flows and output loads.

Dynamic and transient response tests, conducted over a broad frequency range from 0.1 to over 1000 cps, demonstrated the excellent dynamic characteristics of these elements and their applicability to fluid state systems. Finally, it is pointed out that an extensive theoretical and experimental effort in applied fluid mechanics will be required to fully understand and further exploit this already fruitful fluid state amplification technique.

ACKNOWLEDGMENTS

NOMENCLATURE

Symbol	Description		Subscripts	
$\dot{m}$	mass flow		a	active leg
M	momentum		b	bias
P	pressure		c	control
q	dynamic pressure, $\frac{1}{2}\rho u^2$		e	elbow exit
u,U	streamwise velocity		i	initial (no control flow)
w_a	active leg passage width		j	power jet
W	power, $P\dot{m}$		l	left leg
X,y	coordinate axis		o	output
Z	flow impedance, $P/\dot{m}^2$		p	passive leg
τ	time constant		r	right leg
( )'	primary stage		s	supply
			t	total

REFERENCES

1. Zisfein, M. B., G. E. Martin and H. A. Curtiss, Fluid State Amplifier, Giannini Controls Corporation patent Application Dockets 594-597.

2. Curtiss, H. A., A Preliminary Experimental Study of a Pure Fluid Proportional Flow Amplification Technique, Giannini Controls Corporation Report Nr. ARD-06-003, March 1962.

3. Zisfein, M. B. and H. A. Curtiss, The Use of Separated Curved Flow for Proportional Fluid State Amplification, Giannini Controls Corporation Report Nr. ARD-06-009, March 1963.

4. Curtiss, H. A. and D. J. Liquornik, Research Studies in Proportional Fluid State Control Components, Giannini Controls Corporation Report Nr. ARD TR-013-01, September 1963.

5. Curtiss, H. A., O. G. Feil and D. J. Liquornik, Separated Flow in Curved Channels, HDL Fluid Amplification Symposium, May 1964.

6. Albertson, M. A., Y. B. Dai, R. A. Jensen and H. Rouse, Diffusion of Submerged Jets, Transactions of the ASCE, December 1948.

7. Schlichting, H., Boundary Layer Theory, 4th ed., New York, McGraw Hill 1960.
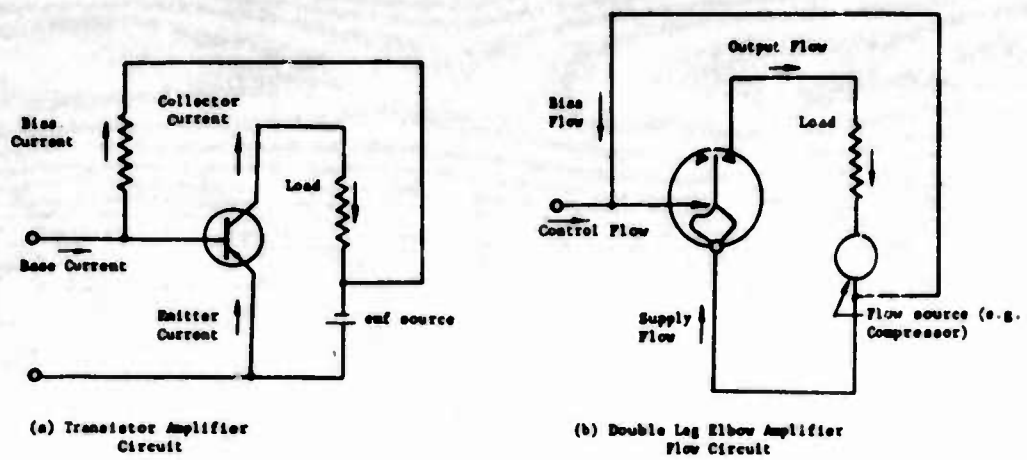
Fig. 1 Simplified Analogy Between Transistor and
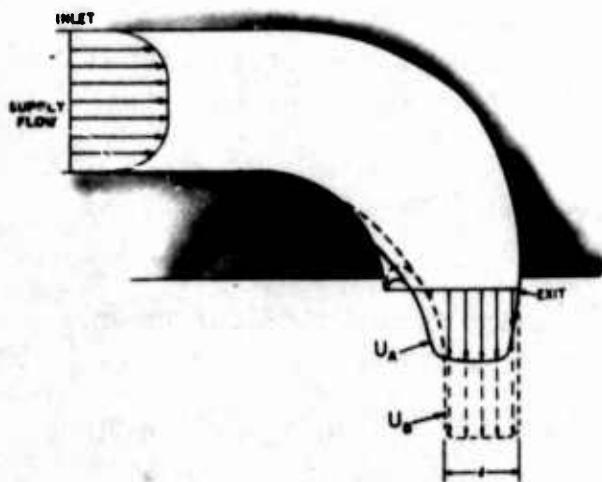Fluid State Proportional Mass Flow Amplifier
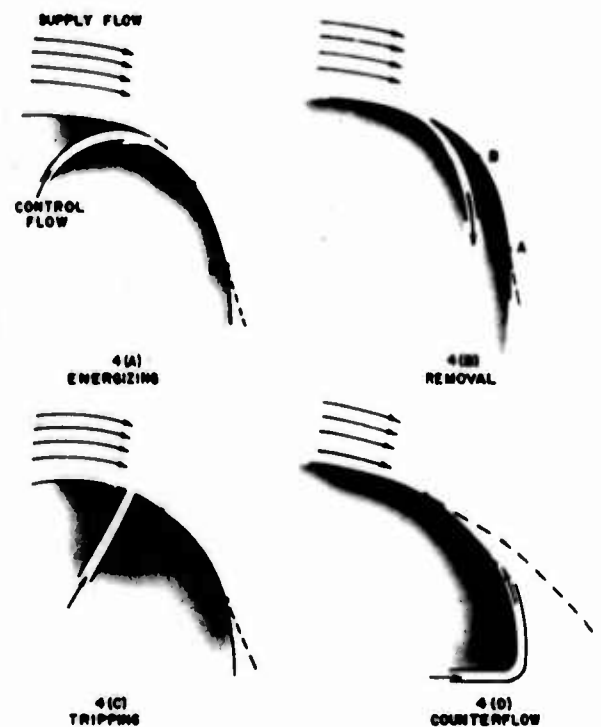

Fig. 2 Separated Flow in a
Curved Channel

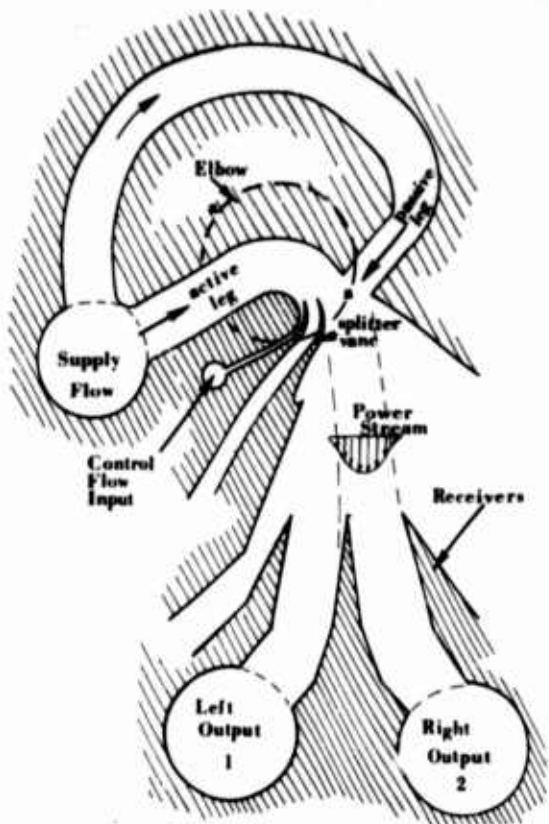Fig. 3 Boundary Layer Control
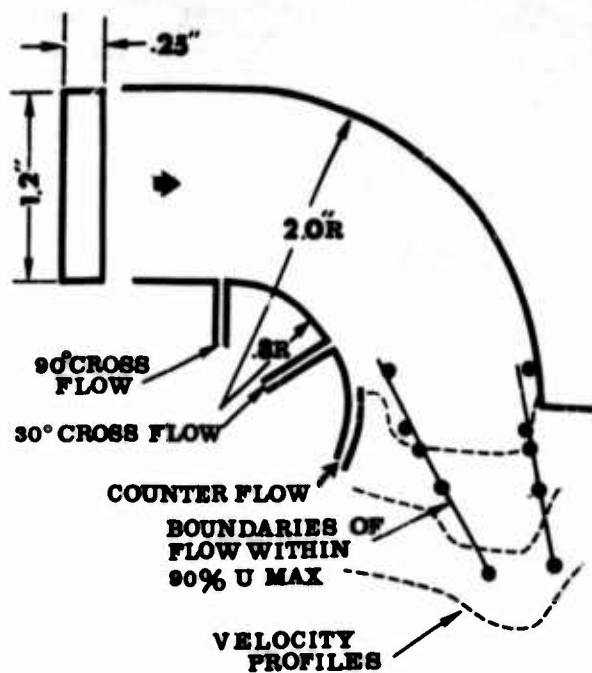Methods

Fig. 4   Double Leg Elbow Amplifier

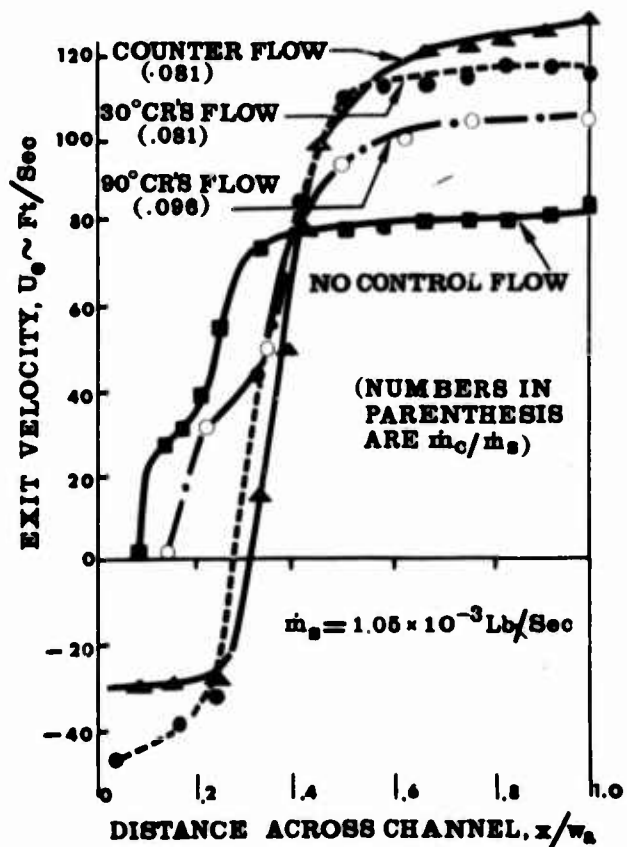Fig. 5   Curved Channel Flow
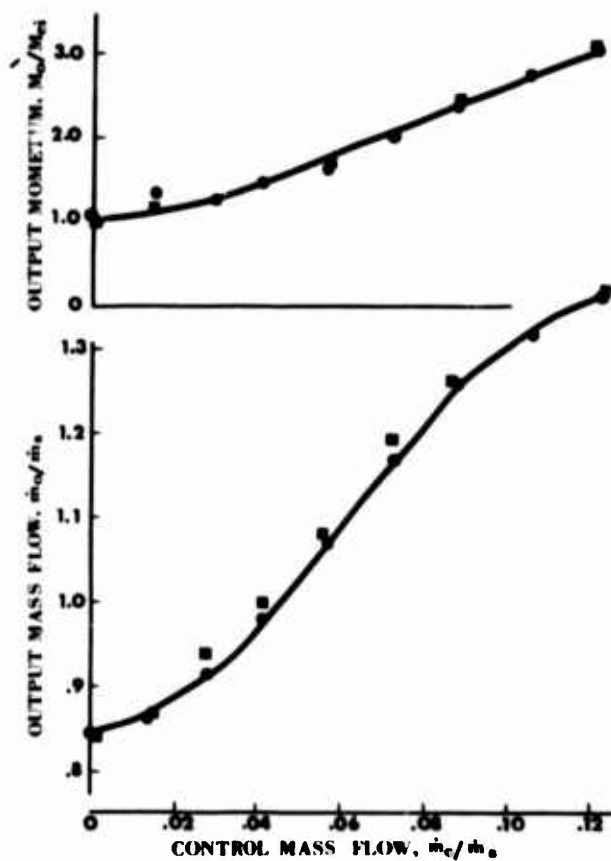

Fig. 6   Curved Channel Exit
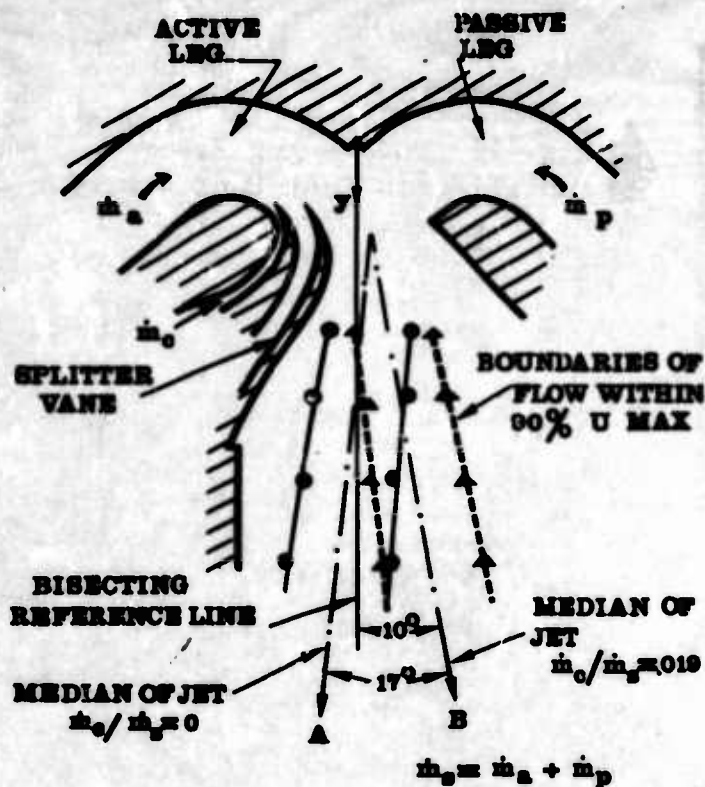Velocity Profiles

Fig. 7   Single Elbow
Amplifier Performance

389

Fig. 8 Power Jet Flow Deflection
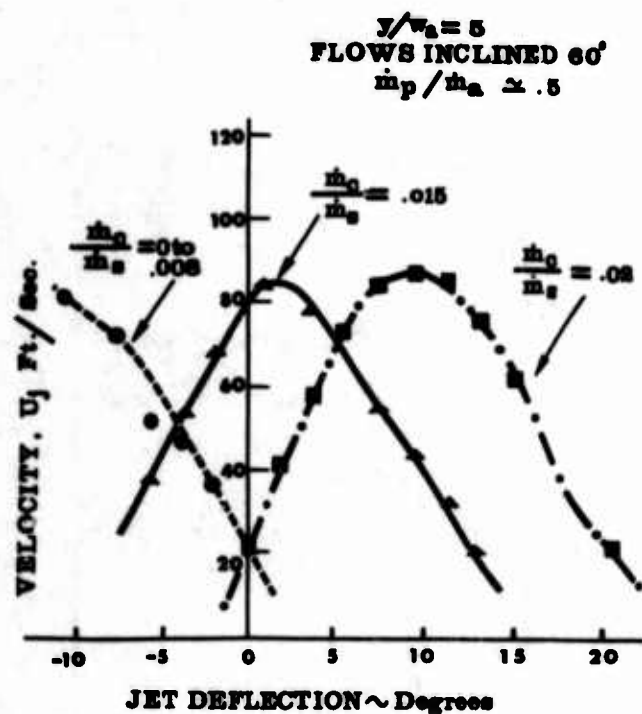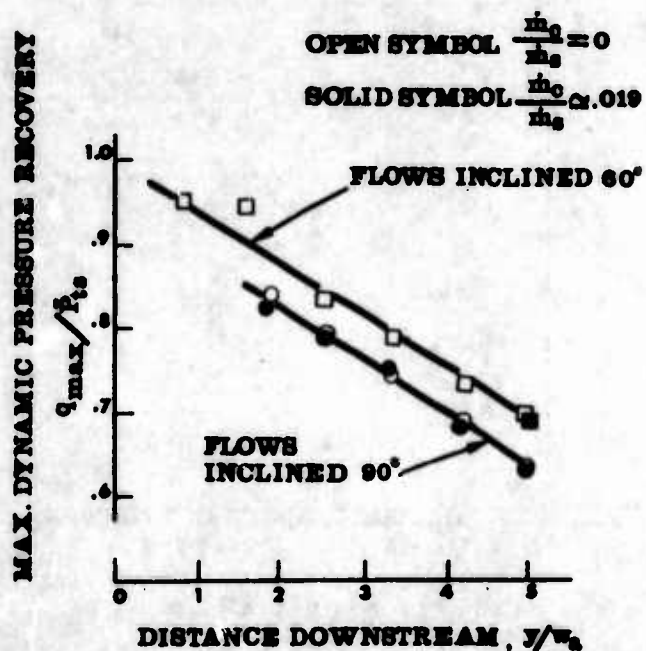
Fig. 9 Power Jet Velocity Profiles

Fig. 10 Power Jet Pressure Decay

Fig. 11 Double Leg Elbow
Amplifier in Test Configuration
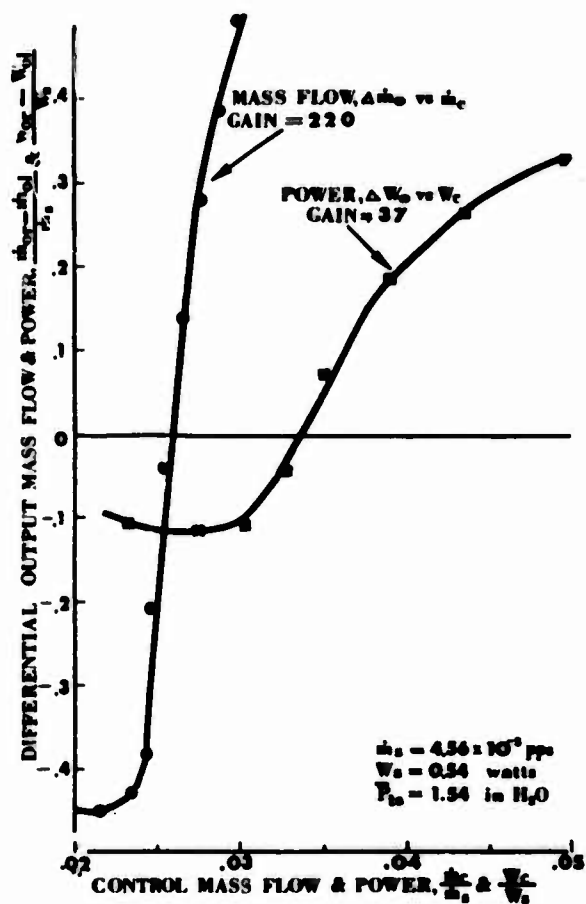
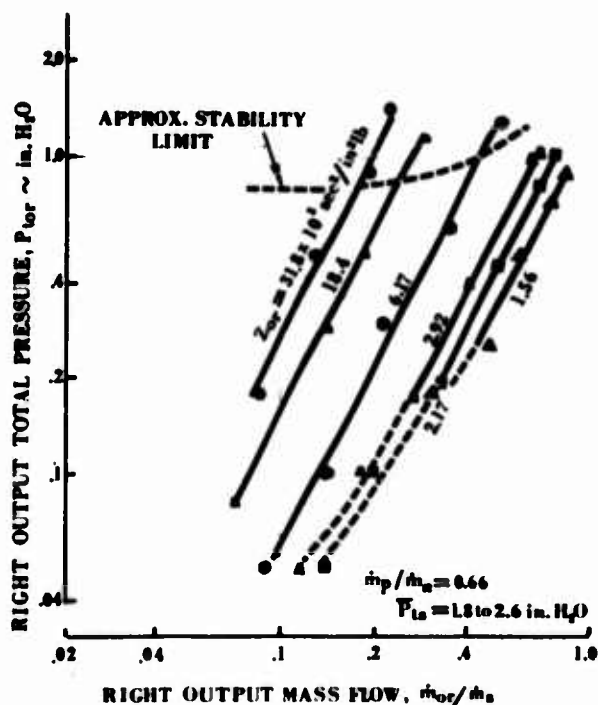Fig. 12 Differential Gains of
Optimized DLEA

Fig. 13 Output Loading Charac-
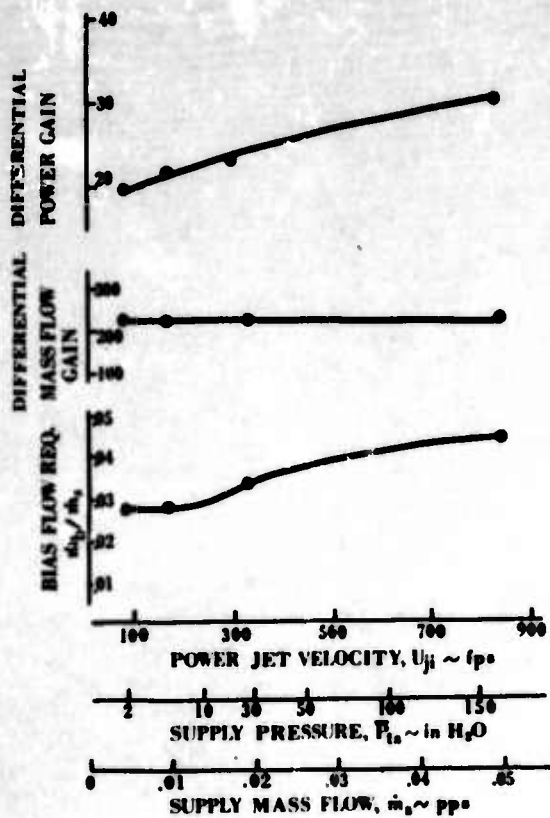teristics of DLEA

391

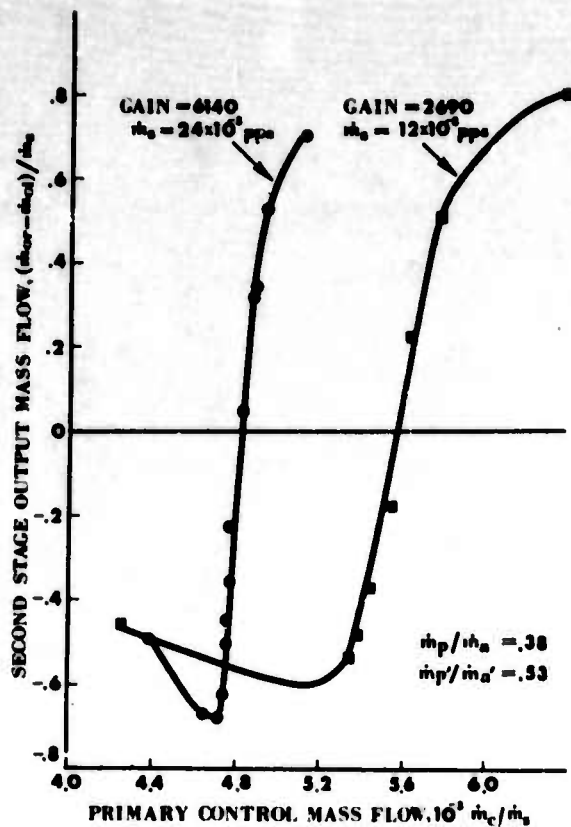Fig. 14 DLEA Performance With Variable Supply Flows

Fig. 15 Differential Gains for 2 Stage DLEA Cascade
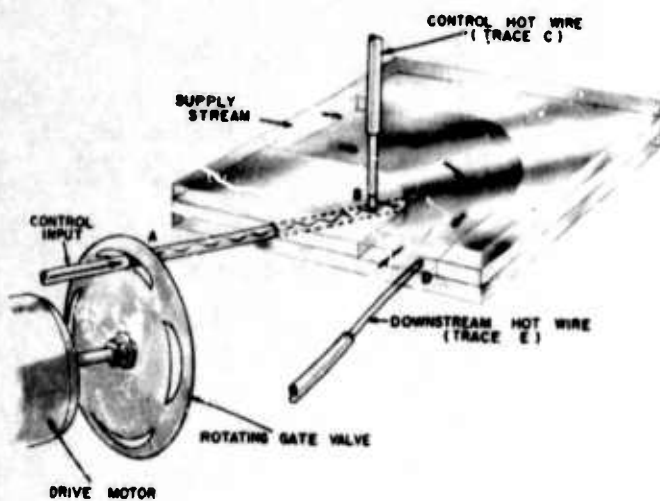

Fig. 16 Configuration for High Frequency Dynamic Tests

(b) 25 cps, time scale: .02 sec/cm.

(c) 1 kc, time scale: 0.5x10-3 sec/cm.

Fig. 17 Dynamic Response Oscilloscope Traces Single Elbow Amplifier
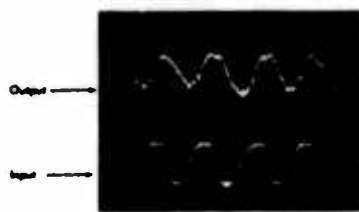
(a) Time Scale: .05 Sec/cm (10 cps)
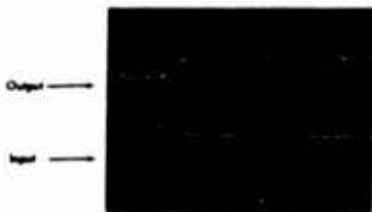
(b) Time Scale: .02 Sec/cm

Fig. 18 Typical DLEA Dynamic Response Oscilloscope Traces

Fig. 19 Typical Bode Diagram of DLEA

393
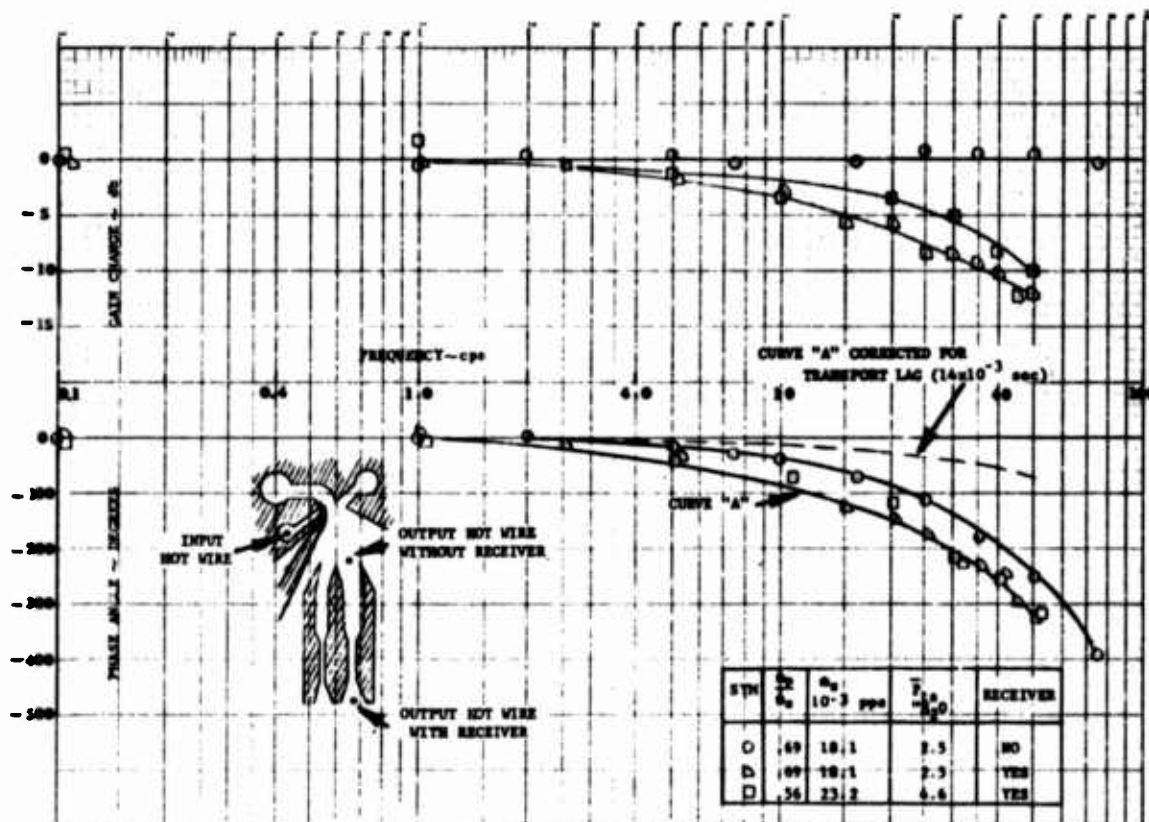
(a) Time Scale - .05 Sec/cm (10 cps)

(b) Time Scale - .05 Sec/cm

Fig. 18 Typical DLEA Dynamic
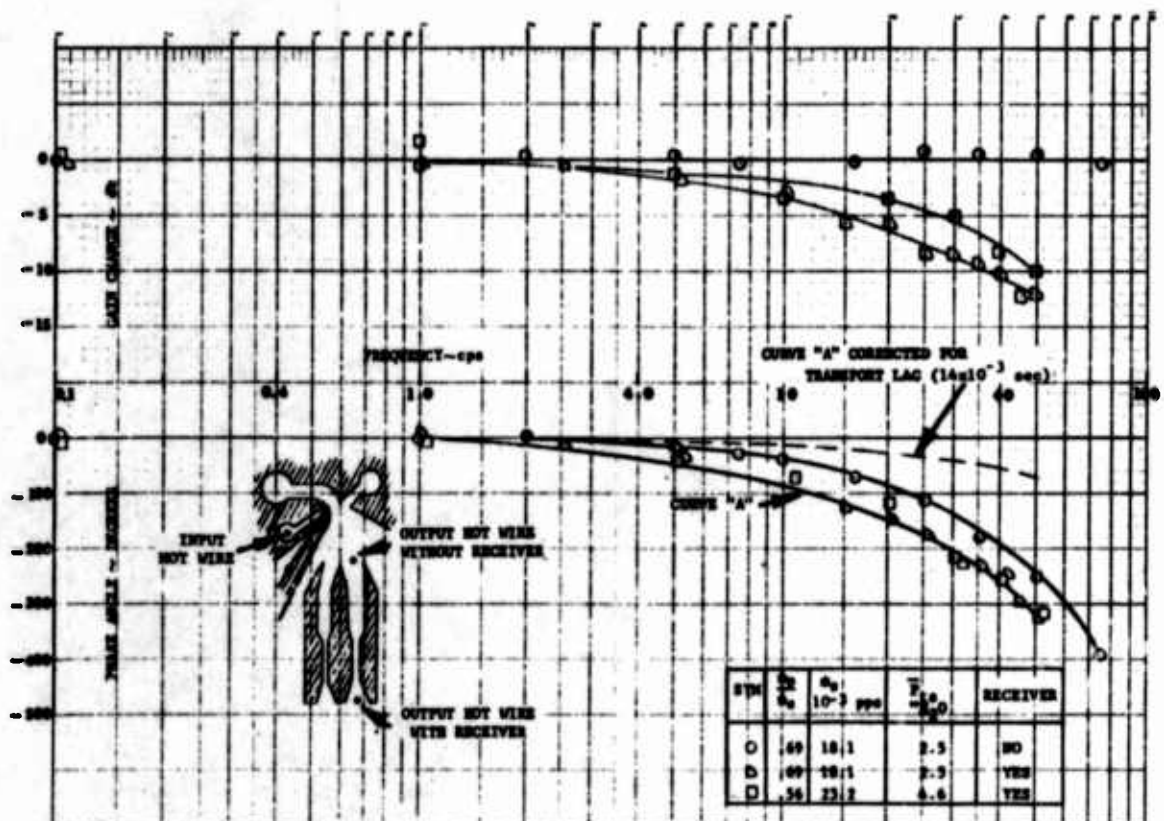Response Oscilloscope Traces

Fig. 19 Typical Bode Diagram of DLEA

393

DISTRIBUTION

Office of the Dir. of Defense
    Research and Engineering
The Pentagon, Washington 25, D. C.
        Attn: Tech Library (Rm 3C128)

Director
Advanced Research Projects Agency
Washington 25, D. C.
        Attn: Fred A. Koether

C. A. Lejonhud
D.C.N.O. (Development)
Op-07T8
The Pentagon (Rm5E621)
Washington 25, D. C.

Director, Army Research Office
Office, Chief of R & D
Washington 25, D. C.
        Attn: Library

Department of the Army
Office of the Chief of R & D
Washington 25, D. C.
        Attn: Chief, Combat Material Div.

Director, Special Weapons
Office of the Chief of R & D
Department of the Army
Washington 25, D. C.

Department of the Army
Office, Chief of R & D
Physical Science Div
Washington 25, D. C.
        Attn: Dr. R. B. Watson

Commanding General
Army Materiel Command
Washington 25, D. C.
        Attn: R & D Directorate, AMCRD-RS-CM
                AMCRD-DE-MI
                AMCRD-DE-N
                AMCRD-RS, Major W. Kerttula

Commanding General
Army Munitions Command
Dover, New Jersey
        Attn: Technical Library

Commanding Officer
U.S. Army Munitions Command
Frankford Arsenal
Philadelphia 37, Pennsylvania
        Attn: Library, 0270

Commanding Officer
Aberdeen Proving Ground, Md.
        Attn: J. A. Tolen

Commanding Officer
U.S. Army Limited War Lab.
Aberdeen Proving Ground, Md.
        Attn: Lt. Col. J. T. Brown

Commanding Officer
Picatinny Arsenal
Dover, New Jersey
        Attn: Tech Library (3 cps)
                SMUPA-VA6

Commanding Officer
U.S. Army Biological Lab
Fort Detrick
Frederick, Maryland

Commanding General
U.S. Army Engineer Research & Dev Lab.
Fort Belvoir, Virginia
        Attn: Tech Library
        Attn: Office of Patents, R. Lucke
Army Security Agency
Arlington Hall Station
Arlington 12, Virginia
        Attn: OACS DEV (OBJ-Div)

Commanding Officer
Army Research Office - Durham
Box CM - Duke Station
Durham, N. C.

Commanding Officer
Artillery Combat Dev Agency
Fort Sill, Okla.

Redstone Scientific Info Center
U.S. Army Missile Command
Redstone Arsenal, Alabama
        Attn: Chief, Document Section
                    (10 copies)

Commanding General
U. S. Army Missile Command
Redstone Arsenal, Alabama
        Attn: Charles Schriener
                    Bldg 7446

Commanding General
U.S. Army Weapons Command
Technical Information Branch
Rock Island, Ill.

Commanding Officer
U.S. Army Weapons Command
Springfield Armory
Springfield, Mass.
        Attn. TIU

Commanding Officer
U.S. Army Materials Research Agency
Watertown Arsenal
Watertown 72, Mass.
        Attn: Tech Info Center

Commanding General
White Sands Missile Range
White Sands, New Mexico
        Attn: Tech Library

Army Mathematics Research Center
University of Wisconsin
Madison 6, Wisconsin
        Attn: Librarian

Commanding Officer
Watervliet Arsenal
Watervliet, New York
        Attn: Tech Library B-C

Department of the Navy
Bureau of Naval Weapons
Washington 25, D. C.
        Attn: S. J. Gorman, RRRE-3

Director
U.S. Naval Research Laboratory
Washington 25, D. C.
        Attn: Code 2027

Office of Naval Research
Washington 25, D. C.
        Attn: Code 492, Dr. Morscher

Department of the Navy
Chief, Bureau of Ships
Washington 25, D. C.
        Attn: Code 210L, 442, 632

Commander
U.S. Naval Ordnance Laboratory
Corona, Calif.
        Attn: Tech Library

Commander
Naval Ordnance Laboratory
White Oak, Silver Spring, Maryland
        Attn: B. Gilbert

Commander
U.S. Naval Ordnance Test Station
China Lake, Calif.
        Attn: Tech Library

Commandant
U.S. Marine Corps
Washington 25, D. C.
        Attn: Code A04F

DDC Headquarters
Cameron Station, Bldg 5
5010 Duke Street
Alexandria, Virginia
        Attn: TISIA (20 copies)

Mr Pervy Griffin
CIA Headquarters
Langley, Virginia
143-7671

396

Aeronautical Systems Division
Wright-Patterson AFB, Ohio
      Attn: ASRMOD (Mr. M. Shorr)
      Attn: ASRMC-ZO (Mr. Wible)

Aeronautical Systems Division
Avionics Laboratory
Wright Patterson AFB, Ohio
      Attn: ASRNG-1

Aeronautical Systems Division
Propulsion Laboratory
Wright Patterson AFB, Ohio
      Attn: ASRMP-1 (Mr. Bentz)

Air Force Special Weapons Center
Kirtland Air Force Base
Albuquerque, New Mexico
      Attn: Tech Library - SWOl

Commander
Air Proving Ground Center
Eglin AFB, Florida
      Attn: Library APGC(PGAPI)

Commander
Edwards Air Force Base, Calif.
      Attn: M. Jones AFTTC (FTOOT)

Sandia Corporation
Sandia Base
Albuquerque, New Mexico
      Attn: Tech Library

U.S. Atomic Energy Commission
Space Nuclear Propulsion Office
Washington 25, D. C.
      Attn: F. C. Schwenk

U.S. Atomic Energy Commission
Washington 25, D. C.
      Attn: Library

Oak Ridge National Lab
P.O. Box Y
Oak Ridge, Tennessee
      Attn: Technical Library Y-12

Los Alamos Scientific Laboratory
P.O. Box 1663
Los Alamos, New Mexico
      Attn: Reports Librarian

Marshall Space Flight Center
Huntsville, Alabama
      Attn: Roy Currie (R-ASTR-TN)
      Attn: Dr. Walter P. Krause

Scientific & Technical Info Facility
P.O. Box 5700
Bethesda, Maryland
      Attn: NASA Representative
             (S-AK/DL)-A366

National Aeronautics & Space Agency
Lewis Research Center
Cleveland 35, Ohio
      Attn: K. Hiller

Library of Congress
Science & Technology Div.
Washington 25, D. C.

National Bureau of Standards
Washington 25, D. C.
      Attn: Chief, Sec. 14.01

National Bureau of Standards
Boulder, Colorado
      Attn: Tech Library

Patent Office
Washington 25, D. C.
      Attn: Scientific Library
       Acquisitions, Rm 1886-C
      Attn: Group 220, R. Stahl
      Attn: Group 360, W. O'Dea
      Attn: Group 370, R. Nilson
      Attn: Group 430, M. Hoffman
      Attn: Miss Steddom

Armour Research Foundation of
  Illinois Inst. of Tech.
Chicago 16, Illinois
      Attn: George I. Jacobi
           10 W. 35th Street

Franklin Institute of the State of
  Pennsylvania
Philadelphia 5, Pennsylvania
        Attn: C. W. Hargens, Tech Dir
        Attn: Charles A. Belsterling

Johns Hopkins University
Applied Physics Lab
8621 Georgia Avenue
Silver Spring, Maryland
        Attn: Tech Library (2 copies)

University of Maryland
College Park, Maryland
        Attn: W. Sherwood, College of
                Aero Engineering
        Attn: Dr. Donald S. Gross,
                Director,Wind Tunnel
        Attn: Dr. S. Pai

University of Southern California
University Park
Los Angeles 7, California
        Attn: Library

University of California
Engineering Library
405 Hilgard Avenue
Los Angeles 24, California
        Attn: Mr. J. Tallman

Cornell Aeronautical Laboratories
P.O. Box 235
Buffalo, New York
        Attn: Librarian

New York University
Engineering Library
University Heights
Bronx 53, New York

Arizona State University
Measurement Engr. Lab. Library
Engineering Center
Tempe, Arizona

University of Minnesota
St. Anthony Falls Hydraulic Lab
Mississippi River at 3rd Ave S. E.
Minneapolis, Minnesota 55414

Purdue University
Mechanical Engineering Library
Mechanical Engineering Building
West Lafayette, Indiana

Wichita State University
Documents Department
Wichita 8, Kansas
        Attn: Library

Johnson Service Company
507 East Michigan Street
Milwaukee 1, Wisconsin
        Attn: Thomas J. Lechner

Purdue University
West Lafayette, Indiana
        Attn: Librarian

Carnegie Institute of Technology
Pittsburgh, Pennsylvania
        Attn: Technical Library
        Attn: Dr. E. M. Williams
University of California
Engineering Library
Berkeley 4, California

Cornell University
Ithaca, New York
        Attn: Dr. Ed Resler, Jr.

Engineering Societies Library
345 East 47th Street
New York 17, New York

Illinois Institute of Technology
Research Institute
10 West 35th Street
Chicago, Illinois
        Attn: Mr. Roy Kamo

Worcester Polytechnic Institute
Worcester, Massachusetts   01609
        Attn: Library

Mass. Inst. of Technology
Dept of Mech. Engineering
Cambridge, Mass.
      Attn: J. L. Shearer - B
             Rm 3-453

Manhattan College
Riverdale 71, New York
      Attn: Technical Library

Fairleigh Dickenson University
Teaneck, New Jersey
      Attn: Engineering Library

University of Michigan
Institute of Science & Technology
Ann Arbor, Michigan
      Attn: Tech Documents Serv (Box 618)

Ohio State University
M.E. Department Library
206 W. 18th Ave
Columbus 10, Ohio

University of New Mexico
Albuquerque, New Mexico
      Attn: Dr. A. H. Koschmann

Case Institute of Technology
Pittsburgh, Pennsylvania
      Attn: E. M. Williams

Catholic University
Department of Mech Engineering
Washington, D. C.
      Attn: Prof. P. K. Chang

University of Nebraska
Lincoln 8, Nebraska
      Attn: Prof. T. Sarpkaya

Oklahoma State University
Stillwater, Oklahoma
      Attn: Dr. Glen Zumwalt

New York State University
School of Engineering
6 Chemistry Road
Buffalo 14, N. Y.
      Attn: Tech Library

Rutgers University
University Library
New Brunswick, N. J.
      Attn: Dr. D. F. Cameron

University of Arizona
Physics Department
Tucson, Arizona
      Attn: Prof. Ulrich H. Bents

Linda Hall Library
5109 Cherry Street
Kansas City 10, Mo.
      Attn: Joseph C. Shipman

Ohio State University
1858 Neil Avenue
Columbus 10, Ohio
      Attn: Documents Division

Pennsylvania State University
201 Hammond Bldg
University Park, Pennsylvania 16802
      Attn: Engineering Librarian
      Attn: David P. Margolis
University of Notre Dame
Notre Dame, Indiana
      Attn: Prof F. N. M. Brown
             Dept of Aeronautical Eng.

Minneapolis-Honeywell Regulator Co.
Military Products Group Research Dept.
2600 Ridgway Rd. Mail Station 340
Minneapolis, Minnesota

NASA
Langley Research Center
Langley Station
Hampton, Virginia
      Attn: Tech Library

Horton, B. M./McEvoy, R. W., Lt. Col.
        Apstein, M./Gerwin, H. L./Guarino, P. A./Kalmus, H. P.
Hardin, C. D., Lab 100
Sommer, H., Lab 200
Hatcher, R. D., Lab 300
Hoff, R. S., Lab 400
Nilsen, H. Lab 500
Flyer, I. N., Lab 600
Campagna, J. H./Apolenis C.J., Div 700
DeMa_i, R., Div 800
Landis, P. E., Lab 900
Seaton, J. W., 260
Kirshner, J., 310 (350 copies)
Garver, R. V., 250
Harris, F. T., 320
Tech Reports Unit, 800 (2 copies)
Tech Info Office, 010 (10 copies)
HDL Library (5 copies)
Rotkin, I./Godfrey, T. B./Bryant, W. T.
Distad, M. F./McCoskey, R.,E./Moorhead, J. G.
Bonnell, R. 040